From Active to Passive Margins:
The Basin and Highland Evolution of the Weddell Sea Sector, East Antarctica

Dem Fachbereich Geowissenschaften

der

UNIVERSITÄT BREMEN

zur Erlangung des Grades

Dr. rer. nat.

vorgelegte

DISSERTATION

von

M.Sc. Nicole Krohne (geb. Lucka)

geboren am 12.01.1985 in Oldenburg

Bremen, den 16.05.2017

Erstgutachter	PD Dr. Frank Lisker
Zweitgutachter	Prof. Dr. Wolfgang Bach
Datum des Kolloquiums:	14.11.2017

Acknowledgements

This thesis was supported by the German Research Foundation (DFG) in the framework of the priority program SPP 1158 'Antarctic Research with comparative investigations in Arctic ice areas' by grants LI 745/15 to F. Lisker and LA 1080/9 to A. Läufer.

I would like to thank my first supervisor PD. Dr. Frank Lisker for providing the opportunity to carry out this captivating topic. I am very grateful for his constructive scientific and methodical support, as well for his open ears for the matters during my PhD process.

I sincerely thank my second supervisor Prof. Dr. Wolfgang Bach for the critical appraisal of my thesis. Prof. Dr. Cornelia Spiegel as head of the working group Geodynamics of the Polar Regions is appreciated for general support and interest for my topic. Vera Kolb, Anke Toltz, Angelika Freesemann, Christiane Schott, Dr. Patrick Monien, Dr. Barbara Ventura, Petra Witte, Giesela Haack, Maria Petrogiannis, and Leslie Sütterlin are cordially thanked for the practical and technical aid, and the kind conversations.

A special thank is dedicated to Prof. Dr. Georg Kleinschmidt. He is heartily appreciated for his assistance, for providing additional field information and sample material of the Shackleton Range, for the nice and constructive meetings, discussions and his deep interest for my research topic concerning the Shackleton Range.

Furthermore, I thank Dr. Andreas Läufer for his general help, the inspiring meetings, and discussions all throughout my PhD time. I would express my thanks to Prof. Dr. Joachim Jacobs for his aid especially during the fieldwork in Sør Rondane. I thank Prof. Dr. Marlina Elburg and Dr. Detlef Damaske for the support in the field, discussions and feedback.

Many heartfelt thanks goes to my PhD colleagues Antonia Ruppel, Dr. Jannis Prenzel, Dr. Wolfgang Reiter, Dr. Julia Lindow, Dr. Simon Elfert, Dr. Nina Dörr, Dr. Maximilian Zundel, Dr. Ruben Rosenkranz and Mohammed Sohi for all the productive discussions, cordial conversations and genial working weekends in the lab.

A very special thank is dedicated to my husband Farian and my two-year old daughter Clara, my parents and my parents-in-law for their steady motivation and for the great support in the daily routine. Kerstin, Sonja, Constanze, Michael, Krissi, Sabrina, Imke, Anne thank you so much for your motivation and proofreading.

Summary

The Weddell Sea sector in East Antarctica is a key area for exploring the dynamic development of continental margins and their landscape evolution in relation to supercontinent cycles. The research area covers the regions Coats Land and Dronning Maud Land, which lie in the gore of the former active continental margin and the interior of Gondwana. Here, the final amalgamation, as well as the initial break-up of Gondwana took place. Due to the extensive lack of Phanerozoic cover rocks, a direct and detailed reconstruction of the Phanerozoic geological history is not possible. Therefore, thermochronological methods have been applied to evaluate the thermal history of the basement rocks. The thermal history allows drawing conclusions about dynamic changes in the past. Existing thermal history interpretations are mainly based on monotonous cooling concepts and either imply a stepwise evolution of the passive continental margin or propose no direct influence to the break-up. However, the monotonous cooling concepts contradict to the regional geomorphology. Ubiquitous remnants of flat surfaces were locally superimposed by Permian sediments. This restricts monotonous cooling. The discrepancy between the geology/geomorphology and the thermal history interpretations result in an overestimation of erosion amounts and the omission of potential reheating episodes. Thus, extensive knowledge about the dynamic development and the landscape in the interior and the continental margin of Gondwana before, during, and after its break-up is lacking. This requires a more comprehensive consideration and (re-)interpretation of thermochronological data.

This thesis is based on an interdisciplinary research approach. Combined thermal history modeling was directly linked to additional geomorphological and geological information. The geological and geomorphological observations are established with petrographic, geochemical, and geochronological methods to determine the exposure age of the paleosurfaces. This was ensued either by sediment deposition ages on the surface, or by analogies to the environment and geomorphological conditions. Two representative areas with a contrasting paleotectonic setting were examined: The Shackleton Range was located on the active continental margin of Gondwana, whereas Sør Rondane was located in the interior of Gondwana, at the triple junction to Sri Lanka and Africa. Both areas developed to passive continental margins due to the breakup of Gondwana.

For the Shackleton Range, a Permian as well as a Jurassic surface exposure of the mountain range is verified by an interdisciplinary approach. A new stratigraphic unit was determined in the Shackleton Range. In Sør Rondane, the Permian and Jurassic surface exposure is very probable. 24 analyzed locations from the Shackleton Range show apatite fission track ages between 124-225 Ma and apatite (U-Th-Sm)/He age between 95-169 Ma. 32 analyzed loca-

tions from Sør Rondane show apatite fission track ages between 136-226 Ma and apatite (U-Th-Sm)/He age between 98-237 Ma. The combined thermal modeling provided a similar thermal history, with varying maximum paleotemperatures. Comparisons of thermal history models show the similarities in evolution, whereas the paleotemperatures were higher in the western part. The paleosurface was reheated between 300–230 Ma, 170–135 Ma and 120–30 Ma. In both regions, the reheating was caused by sedimentary overburden due to basin formation. This implies the simultaneous existence of shallow sedimentary basins that were inverted at the Triassic-Jurassic transition and at the Jurassic-Cretaceous boundary. The intermittent basin inversions were most likley attributed to magmatic events and major changes in plate directions.

The landscape of Gondwana and Antarctica in the area of the Weddell Sea was most of the time characterized by sedimentary basins of various types. The western basins were deeper and were related to tectonics at the active boundary, whereas the interior parts were mostly shallow and related to far-field stress. Basin formation and the kinematics of the basins potentially followed reactivated pan-African structures.

The dynamic development with alternating basins and highlands provides further implications for the landscape response to supercontinent cycles. The Weddell Sea Sector was long term occupied by alternating basin and upland landscapes related to the interplay of tectonic and mantle response. The region formed part of the radial Permian basins that probably persisted to the Eo/Oligocene.

The results demonstrate the importance of applying and combining interdisciplinary methods, to obtain conclusions on geology and landscape evolution.

Zusammenfassung

Der Weddellmeer Sektor in der Ostantarktis ist ein Schlüsselgebiet für die Erforschung der dynamischen Entwicklung von Kontinentalrändern und deren Landschaftsentwicklung in Bezug zu Superkontinentzyklen. Das Forschungsgebiet umfasst die Regionen Coats Land und Dronning Maud Land, die im Zwickel des ehemaligen aktiven Kontinentalrandes von Gondwana und Zentralgondwanas liegen. Hier fand sowohl die finale Verschweißung zu Gondwana, als auch der initiale Aufbruch statt. Aufgrund des weiträumigen Fehlens phanerozoischer Deckschichten ist eine direkte Rekonstruktion der phanerozoischen geologischen Geschichte nicht möglich. Daher wurden in der Vergangenheit thermochronologische Methoden angewandt, um aus den Grundgebirgsgesteinen Rückschlüsse auf vergangene geologisch-dynamische Veränderungen zu ermitteln. Bestehende thermochronologische Interpretationen implizieren eine schrittweise Evolution des passiven Kontinentalrandes im Zuge des Gondwanaaufbruches, wobei andere Interpretationen keinen Einfluss zum Auseinanderbrechen erkennen lassen. Diese Interpretationen beruhen hauptsächlich auf monotonen Abkühlszenarien. Diese Szenarien stehen im starken Widerspruch zu der regionalen Geomorphologie: Reste einer überregionalen Erosionsoberfläche und permische Sedimentgesteine erlauben keine monotone Abkühlgeschichte. Die Diskrepanz der bestehenden Interpretationen zur Geologie/Geomorphologie resultiert in einer Überschätzung der Erosionsbeträge, eine Fehlinterpretation der Abkühlzeitpunkte, der Zeiten stabiler Temperaturen, der Geomorphologie und der zugrundeliegenden Geodynamik. Somit fehlt gültiges Wissen über die Geodynamik und das Landschaftsbild im Inneren und am Kontinentalrand Gondwanas vor, während und nach seinem Zerfall.

Dieses bedingt eine umfassendere Betrachtung und eine Neuinterpretation der thermochronologischen Daten. Daher wurde im Rahmen dieser Arbeit folgender Forschungsansatz verfolgt: Die Modellierung des thermochronologischen Datensatzes wurde direkt mit zusätzlichen geomorphologischen und geologischen Daten verknüpft. Des Weiteren wurden strukturgeologische und geophysikalische Daten in die Interpretation mit einbezogen. Die weitgehend unbedeckten Paläooberflächen bedingen eine zeitliche Eingrenzung. Dieses wurde entweder anhand von petrographischen, geochemischen und geochronologischen Methoden an Sedimentresten etabliert, oder anhand von Analogien zur Umgebung und geomorphologischen Bedingungen eingegrenzt.

Es wurden zwei Stellvertretergebiete mit einer konträren Paläotektonischen Ausgangslage untersucht: The Shackleton Range befand sich am aktiven Kontinentalrand von Gondwana, wohingegen Sør Rondane im Inneren von Gondwanas, an der Grenze zu Sri Lanka und Afrika

lag. Beide Gebiete entwickelten sich zu passiven Kontinentalrändern im Zuge des Auseinanderbrechens von Gondwana.

Für die Shackleton Range konnte anhand des interdisziplinären Ansatzes sowohl eine permische als auch eine jurassische Oberflächenexposition des Grundgebirges nachgewiesen werden und eine neue Gesteinseinheit für die Shackleton Range beschrieben werden. In Sør Rondane ist sowohl eine permische als auch die jurassische Oberflächenexposition sehr wahrscheinlich. 24 analysierte Lokationen aus der Shackleton Range zeigen Apatit Spaltspuralter zwischen 124–225 Ma und Apatit (U-Th-Sm)/He Alter zwischen 95–169 Ma. 32 analysiere Lokationen aus Sør Rondane lieferten Apatit Spaltspuralter zwischen 136–226 Ma und Apatit (U-Th-Sm)/He Alter zwischen 98–237 Ma.

Die kombinierte thermische Modellierung lieferte eine ähnliche thermische Geschichte, wobei die maximalen Paläotemperaturen variieren. Die Paläooberfläche wurde jeweils zwischen 300–230 Ma, 170–135 Ma und 120–30 Ma wieder aufgeheizt. Die Wiederaufheizungen konnten hauptsächlich auf sedimentäre Auflast zurückgeführt werden. Das impliziert die zeitgleiche Existenz flacher Sedimentbecken, die sowohl an der Trias-Jura Grenze, als auch an der Jura-Kreide Grenze invertiert worden sind. Die zwischenzeitlichen Beckeninvertierungen stehen sehr wahrscheinlich im Zusammenhang mit magmatischen Ereignissen und Veränderungen der Plattenbewegungsrichtungen. Die Heraushebung der Massive erfolgte erst nach dem Eo/Oligozän.

Die Landschaft Gondwanas und der Antarktis im Bereich des Wedellmeeres war lange Zeit geprägt von Sedimentbecken unterschiedlichen Typs. Der westliche Teil des Weddell Sea Sectors war bis zum Jura beeinflusst vom aktiven Kontinentalrand, wobei der östliche Teil geprägt war von far-field Extension. Die jurassische Beckenbildung bzw. die Kinematik der Becken erfolgte wahrscheinlich entlang reaktivierter Pan-Afrikanischer Strukturen.

Die Ergebnisse zeigen die Wichtigkeit der Anwendung und Kombination fachübergreifender Methoden, insbesondere bei fehlenden direkten Indikatoren, um Rückschlüsse auf die Geologie und die Landschaftsentwicklung zu erhalten.

Content

1. Introduction

The Weddell Sea Sector in East Antarctica is located between 25°W–30°E and 70°S–82°S. It is framed by the Weddell Sea Embayment in the west, by the Pensacola Mountains in the southwest, by the South Atlantic and the Indian Ocean in the north, by the Lützow-Holm Bay in the east, and by the vast polar ice plateau in the south (Figure 1). The research area is characterized throughout by a passive margin landscape facing the African continent, and is largely covered by up to 3 km thick glaciers that drain the oceans perpendicular to the shoreline. Ice-free areas form highly elevated escarpment-bound massifs that trends parallel to the recent shoreline, and are characterized by ice-molded peaks or are topped by flat surfaces

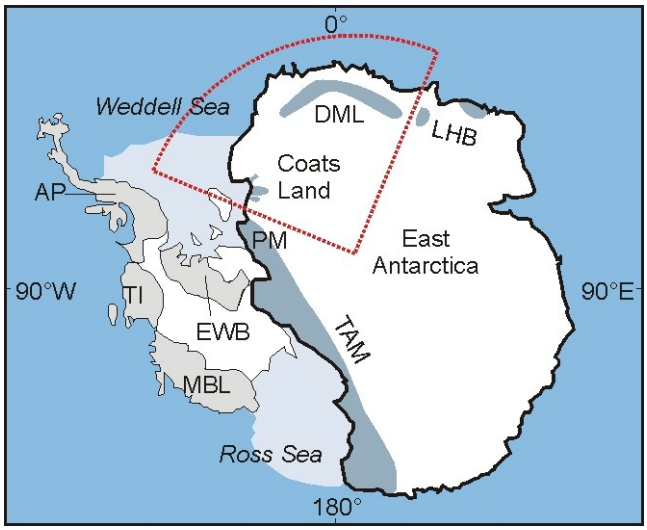

Figure 1: Overview of the Weddell Sea Sector (red quadrant), that is located on the Antarctic continent. Grey shaded areas mark the West Antarctic terrane assemblage and marginal embayments. Blue shaded regions outline important regions for the frame of this study. Abbreviations: AP: Antarctic Peninsula, DML: Dronning Maud Land, EWB: Ellsworth-Whitmore Block, LHB: Lützow Holm Bay, MBL: Marie-Bryd Land, PM: Pensacola Mountains, TAM: Transantarctic Mountains, TI: Thurston Island

Coats Land and Dronning Maud Land (DML) formed part of the final suture zone of Gondwana and cover different paleogeographic and paleotectonic settings within Gondwana during Mesoproterozoic to Jurassic times. The eastern part of the area was situated at the margin close to the active boundary of the Paleo-Pacific (Panthalassa) and the collage of crustal blocks of W-Antarctica, whereas the central and eastern parts were located in the interior Gondwana at the junction of Africa/Madagascar and India/Sri Lanka. Here, initial separation ensued and makes the passive margin to one of the oldest of Gondwana. Hence, the Weddell Sea Sector represents the key area to investigate the Gondwana supercontinental cycle in terms of geodynamics and landscape formation, and helps here to distinguish between local and regional dynamic responses to break-up.

In general, the geological record of the research area comprises the Archaen to Cambrian basement, as extensive cover rocks or substantial cover sequences are lacking. The direct

Phanerozoic record is restricted to thin remnants of Cambro-Ordovician or Permian sediments or Jurassic magmatic rocks (summarized by Boger, 2011), and few directly examined marine deposits (Barker *et al.*, 1990). Further implications of landscape evolution is only provided by the flat surfaces, which are thought to be remnants of one or several regional Permian erosion surface(s) (e.g. Skidmore & Clarkson, 1972; Näslund, 2001). Hence, these deposits and features can only provide a glimpse of Gondwana evolution, so that an evaluation of dynamic processes is not possible.

The application of thermochronological methods is a suitable tool to trace long-term geological history of the rocks. The fission track- and the (U-Th-Sm)/He analysis on apatite, zircon and titanite provide time and style of rock cooling within a temperature window of 40–300°C, conventionally referring to crustal depths between 2–12 km (Wagner, 1972; Yamada *et al.*, 1995; Wolf *et al.*, 1996; Coyle *et al.*, 1997; Figure 2). The apatite fission track (AFT) method is the most common used, and allows the additional elicitation of kinetic parameters that provide information about the style of cooling. Rock cooling is a response to geodynamic changes that are related to either exhumation processes or to post-magmatic cooling processes (e.g. Ring *et al.*, 1999). A comparatively new technical advancement is the thermal history modeling (e.g. HeFTy, Ketcham, 2005) that incorporates independent age data and kinetic data inputs to simulate best-matching time-temperature paths. HeFTy allows the integration of non-thermochronological geological evidence/time temperature-markers. Prenzel *et al.* (2013) demonstrate the need of thermal history modeling for deriving the timing of cooling. A comprehensive overview concerning thermochronology is provided by Hurford & Green (1982), Gallagher *et al.* (1998), Ehlers & Farley (2003),Lisker *et al.* (2009) and Reiners & Ehlers (2005).

Thermochronological methods were applied in the Shackleton Range and in several massifs of western and central DML (Jacobs, 1991; Jacobs *et al.*, 1992; Schnellbach, 1992; Jacobs *et al.*, 1996b; Schäfer, 1998; Jacobs & Lisker, 1999; Lisker *et al.*, 1999; Meier, 1999; Meier & Olesch, 1999; Meier *et al.*, 2004; Emmel *et al.*, 2007; Emmel *et al.*, 2008; Emmel *et al.*, 2009). No thermochronological studies were obtained in eastern DML yet. International standards for modern applications (e.g. thermal history modeling via HeFTy) were regarded and incorporated by Emmel *et al.* (2007), Emmel *et al.* (2008), Emmel *et al.* (2009), Jacobs & Lisker (1999), Lisker *et al.* (1999). Hence, these works reflect the state of the art and allow data and thermal history comparison.

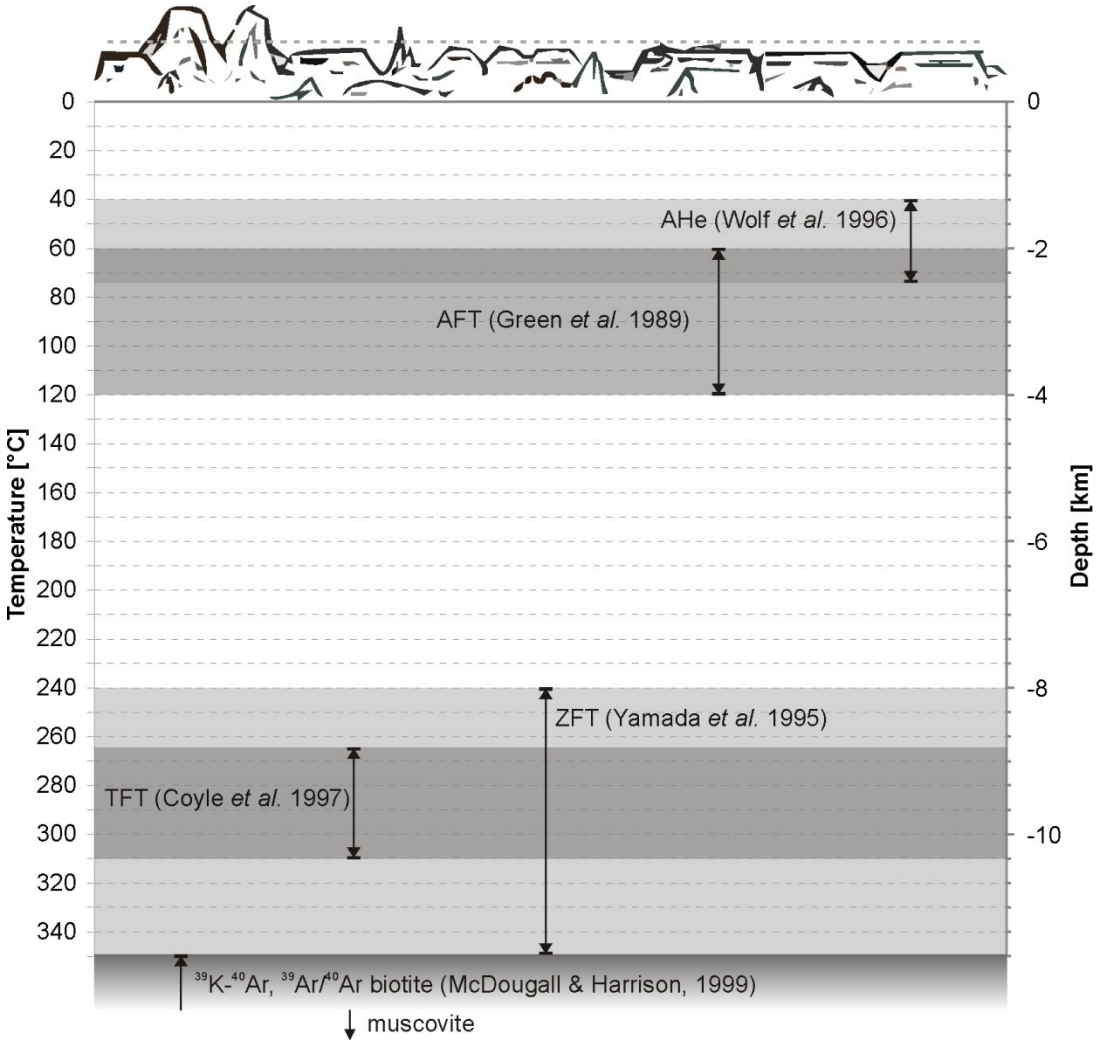

Figure 2: Temperature range of the various thermochronometers and corresponding crustal depths with respect to a common geothermal gradient of 30°C/km. Abbreviations: AHe: (U-Th-Sm)/He thermochronometer, AFT: Apatite fission track thermochronometer, TFT: Titanite fission track thermochronometer, ZFT: Zircon fission track thermochronometer.

The spectrum of apatite fission track ages for western and central DML and the Shackleton Range ranges from 81±8 to 366±16 Ma. The related kinetic parameters vary broadly. The AFT ages show crosscutting relationships to other thermochronometers: Apatite (U–Th)/He ages from western and central DML vary between 87±7 and 304±28 Ma, often with older single grain ages as related AFT ages (Emmel *et al.*, 2007; Emmel *et al.*, 2008). Zircon fission track ages from the Shackleton Range ranges from 160±20 to 215±24 Ma (Lisker *et al.*, 1999). Titanite fission track ages from central DML vary between 323±30 to 516±50 Ma.

The thermal history models show throughout a stepwise cooling pattern, with stages of rapid cooling interrupted by long-term stages of enhanced and stable temperatures (Figure 3). The main cooling phases are concentrated at 230–180 Ma and were related to uplift due to precursive stages of the Ferrar/Karroo magmatic event. Carboniferous (Emmel *et al.*, 2007) and Cretaceous cooling phases were related to flexural uplift and exhumation due to graben

formation in front of the massifs; or at 50–30 Ma to an Eo-Oligocene cooling step by erosion due to flexural response to ice sheet development.

To summarize, the thermal history models show variable and contrasting thermal histories, with variable onset of erosion and depths of exhumation across the research area. Some authors relate their thermal histories closely to the Jurassic break-up mechanisms (Jacobs & Lisker, 1999), whereas others postulate the insignificance of the break-up processes for to the studied region (Emmel *et al.*, 2009).

A closer look to the preserved geological setting indicates discrepancies between the geological record and the thermal history models. In a key location in western DML, the basement paleosurface is covered by few meters of Permian coaly red-beds including Karoo sills and lava flows (Näslund, 2001; Bauer, 2009, Figure 3b). (I) The existence of a paleosurface on basement requires former surface exposure whilst formation and excludes monotonous cooling concepts. (II) Both, the Permian sediments and the magmatic/volcanic rocks indicate times of surface exposure, or close-to-surface positions. (III) All analyzed AFT ages are younger than metamorphic, stratigraphic, or magmatic ages (Jacobs & Lisker, 1999). (IV) Post-Jurassic enhanced temperature/ reheating was suggested by Jacobs & Lisker (1999) by burial of 2 km thick lava flows. However, the competence of the lava flows to erosion does not support the required quick erosion. The slightly tilted paleosurface is well preserved. This would require the complete erosion of the lava without eroding or modifying the basement paleosurface. This seems doubtful.

Remarkably, all studies did not fully consider the Paleozoic erosion surface as an essential time-temperature feature for thermal history modeling. A consequent and direct integration of the time and temperature information provided by the paleosurfaces into thermal history models is missing. Hence, the existent concepts resulted in misestimation of timing, duration and amounts of erosion, and lead to inconsistent passive margin evolution suggestions.

The thesis deals with the revision of the geological history and landscape evolution for the Weddell Sea Sector. An interdisciplinary approach was applied to resolve the inconsistency between geological record and thermal history interpretations. It is founded on thermal history modeling and additional integration of geological evidence that follows the basic steps of the concept presented by Prenzel (2014). In the Weddell Sea Sector however, the exposed paleosurfaces are mostly bare and require additional research to gain or constrain exposure ages of the paleosurface on a geologic time scale. Depending on coverage and degree of preservation, two different approaches were required: I) constrain exposure times by combined petrographical, geochemical, and geochronological data on overlying, thin sedimentary remnants, or II) deducing the sequence of paleosurface creation, exposure ages and

thermochronological data by geological analogies, thermochronological implications and geomorphological observations.

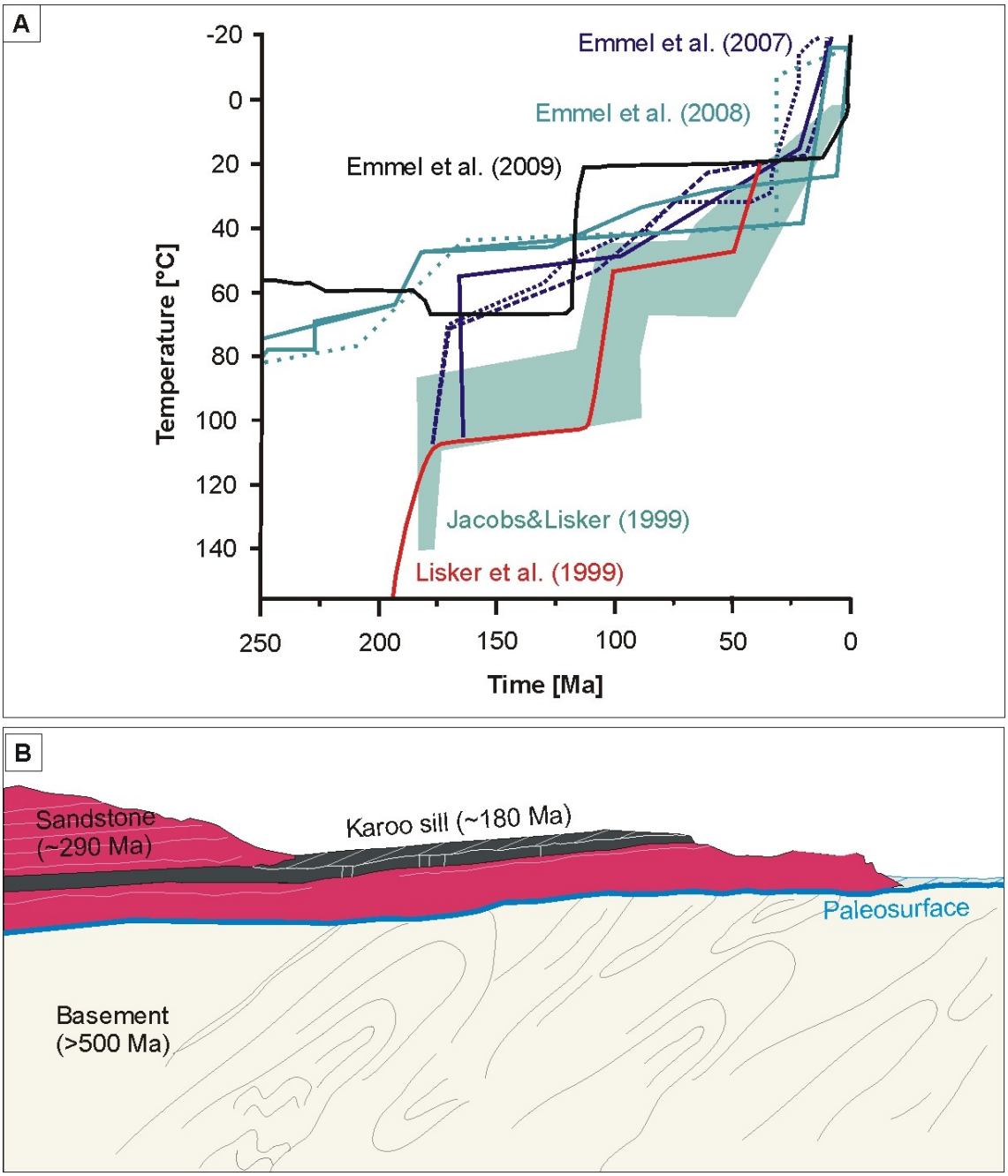

Figure 3: a) Thermal history models from various massifs in DML and Coats Land showing all stepwise and monotonous cooling with varying times and amounts of cooling. Red path: Shackleton Range. Green paths: western DML. Blue and black paths: central DML. b) Sketch of a key outcrop illustrating the geologic setting in the Weddell Sea Sector. The highly deformed Pan-African basement is truncated and features the ubiquitous paleosurface. Permian clastic glacial withdrawal deposits, with thin coal seams were deposited upon the unconformity. Early Jurassic Karroo dolerites and lava flows mark the youngest rocks. Modified after Juckes (1972); Jacobs *et al.* (1992); Bauer *et al.* (1997).

To identify possible differences or coherencies in evolution between the active Gondwana margin and the interior Gondwana, two representative end-member massifs in terms of their paleotectonic placement were studied: The Shackleton Range was placed at the Gondwana

active margin, whereas Sør Rondane was located in the interior of Gondwana at the triple junction between Africa/Madagascar and India/Sri Lanka. Representative AFT and AHe sample suites following horizontal or vertical profiles were sampled directly from the paleosurface remnants or beneath and carefully analyzed. A basic task was to infer the sequence between geological evidence and the thermochronological data, as well as its vertical relation to the paleosurface.

Chapter 2 and 3 provide an overview on the geology and geomorphology of the Weddell Sea Sector. Chapter 4 deals with the geological and landscape evolution history of the Shackleton Range. The Shackleton Range is the main outcrop in Coats Land that is placed at the active margin of Gondwana. Here, the ubiquitous paleosurface is established on the basement and is well preserved, but mostly uncovered. A small outcrop of sediments represents the key for determination of time-temperature markers. The petrology and age of the thin cover rocks was controversially discussed (Buggisch *et al.*, 1994a; Tessensohn *et al.*, 1999a) so that the timing of paleosurface exposure was not clear. In this thesis, different methods where used to describe and qualify the strata and to verify depositional age and milieu. This was realized by (a) the petrographic description of mineral phases, fabric, texture by thin section petrography and X-Ray Diffraction, (b) geochemical fingerprint by major and trace element analysis via Inductively Coupled Plasma Mass Spectrometry and X-Ray Fluorescence and (c) estimation of depositional age by $^{40}Ar/^{39}Ar$ analysis with regarding the other results for correct interpretation of the $^{40}Ar/^{39}Ar$ data. Subsequent thermal history modeling of the thermochronological data was complemented with available external ZFT raw data for incorporation (Lisker *et al.*, 1999). The outcome represents a well-constrained thermal history model and a new stratigraphic unit for the Shackleton Range related to the Ferrar/Karoo event

Chapter 5 addresses the evolution of Sør Rondane. Although Sør Rondane is located at a key position ideally for resolving supercontinental cycles, including the Gondwana formation and breakup, the region is only sparsely studied yet. The Paleozoic geological history is mostly unknown. The times of surface exposure of the paleosurface remnants are not constrained, as overlying rocks were absent. However, the exposition of the paleosurface was deducted by regional analogies and implications by the thermochronological data. The landscape evolution is discussed with additional brittle structural- and geophysical data. The foundation for interpretation was supplemented by identification of different crustal blocks, faults and their movement sense and temperature (=depth) by U-Pb, Lu-Hf, structural analysis, gravity and magnetic measurements on the same sample suite by the publications of Mieth (2014),

Ruppel (2012), Elburg *et al.* (2015b), Ruppel *et al.* (2015) and Elburg *et al.* (2016) (Chapter 6-8).

The topic of this thesis is embedded in a joint project with geochronology, structural geology and geophysical research. The project Geodynamic Evolution of East Antarctica (GEA) aimed to link upper and lower crustal structures to gain essential insights to supercontinental cycles and dynamics. This includes the assembly of Proterozoic nucleus to Gondwana and the location of its suture, the intra-Gondwana evolution and landscape situation and dynamic evolution of the dispersal and break-up. The project included six weeks of field work in Sør Rondane, East Antarctica. The thesis here focuses on the Phanerozoic geological and landscape evolution of the Weddell Sea Sector. The approach aims to obtain timing, distribution, and depths of erosion, geometry, and segmentation of the upper crust in different paleogeodynamic settings. This will help to quantify and evaluate the regional geological and long-term landscape evolution and to verify the geological and paleogeographic setting of the research area within Gondwana. The results will help to understand Gondwana breakup and passive margin/sheared margin formation and provide insights to the long-term landscape evolution of Sør Rondane within Gondwana and Antarctica.

The outcome of the research is presented in the following:

Manuscript 1: (Krohne *et al.*, 2016, Geological Magazine). The principal author extended the initial conception by F. Lisker, conducted the thermochronological, petrographic and XRD analyses, the integration and common interpretation of the whole, cumulative data set, and is responsible for the discussion of the involved processes and edition of the paper. The contribution of the co-authors comprised conception and throughout supervision (F. Lisker), field work (G. Kleinschmidt), geochemical and geochronological analyses (A. Klügel, S. Estrada), regional and thermochronological expertise (A. Läufer, C. Spiegel), and comments and feedback. The manuscript was accepted with minor revisions and is available online since 12.12.2016

Manuscript 2 (Krohne et al., ready for submission). The principal author planned and conducted thermochronological field work, thermochronological analysis, integration and interpretation of the whole data set, is responsible for the discussion of the involved processes and edition of the paper. The manuscript is readily prepared for submission in Tectonics. One section (brittle tectonics) including figure needs to be finally prepared by co-author A. Ruppel. A. Ruppel conducted the structural measurements. The contribution of the co-authors consists of conception and supervision, common fieldwork and sampling, and minor comments and feedback.

Manuscripts 3–5 (Elburg *et al.*, 2015b; Ruppel *et al.*, 2015; Elburg *et al.*, 2016) rely on common field work during the GEA II expedition and provide the base for the main chapters of this thesis. The three papers deal with the Precambrian evolution of Sør Rondane, especially with the formation and the development of the Pan-African orogen, including timing of pan African events and regional structural evolution. N. Krohne contributed in field work, discussion and proofreading.

Chapter 9 will discuss the evolution of the Wedell Sea Sector. Chapter 10 will outline the conclusions, open questions and provides future research options.

2. Geological and tectonic setting of Gondwana and the Weddell Sea Sector

East Antarctica represents the connecting link within the supercontinent Gondwana (Figure 4a). All Gondwana fragments, Africa/Madagascar, India/Sri Lanka, Australia/Tasmania, New Zealand, and South America were assembled at the northern, eastern, and southern margins of East Antarctica. The western margin was occupied by the Paleo-Pacific subduction zone since the Precambrian (Figure 4). The Gondwana assembly was a long-term process (e.g. Elburg *et al.*, 2016) and culminated in the formation of apparently crossing orogens that are radially distributed along the former active margins (e.g. Jacobs & Thomas, 2004; Boger, 2011).

The Gondwana stage is mostly characterized by basin formation and widespread deposition in the interior, whereas the western margin was influenced by the active margin of Panthalassa (e.g. Collinson *et al.*, 1994). Devonian to Carboniferous basins formed at least along the western margin of Gondwana (e.g. Transantarctic Mountains, South Africa), whereas vast Gondwana wide basins formed at the Permo-Carboniferous transition. The most prominent stratigraphic successions are the Beacon Supergroup in the Transantarctic Mountains and the Karroo Supergroup in East Africa. Throughout, Permo-Carboniferous diamictites were deposited upon truncated basement rocks, followed by deposition of Permian to Triassic red-beds and plant material (Barrett *et al.*, 1972; Catuneanu *et al.*, 1998). Multiform Ferrar or Karoo magmatic rocks intruded the basement and sediment or emplaced subaerially. The Ferrar/Karoo igneous activity was a magmatic event, which occurred during ~200–170 Ma, with its main phase at 185–172 Ma (e.g. Encarnación *et al.*, 1996; Duncan *et al.*, 1997; Fleming *et al.*, 1997; Zhang *et al.*, 2003). It comprises rhyolitic to dacitic intrusions, rhyolitic to mafic dyke and sill emplacements, and basaltic lava flows (e.g. Brewer, 1989; Elliot & Fleming, 2000; Elliot & Fleming, 2004; Leat *et al.*, 2005). The diachronous deposition and formation of regional paleosurfaces and paleosols in the Beacon and Karoo supergroups indicate times of subaerial exposure. Correlatives and analogues of the Beacon or Karoo supergroup can be found elsewhere in East Antarctica, and on the Australian, African and South American parts of Gondwana (e.g. Veevers & Powell, 1994).

The common geological history in the Weddell Sea Sector starts with the final amalgamation of Archean to Mesoproterozoic terranes of different generic and paleogeographic origins in the Neoproterozoic and resulted in the formation of the East African-Antarctic Orogen, EAAO that trends from northern Africa towards Coats Land (Stern, 1994; Jacobs & Thomas, 2004; Jacobs *et al.*, 2015; Elburg *et al.*, 2016, Figure 4).

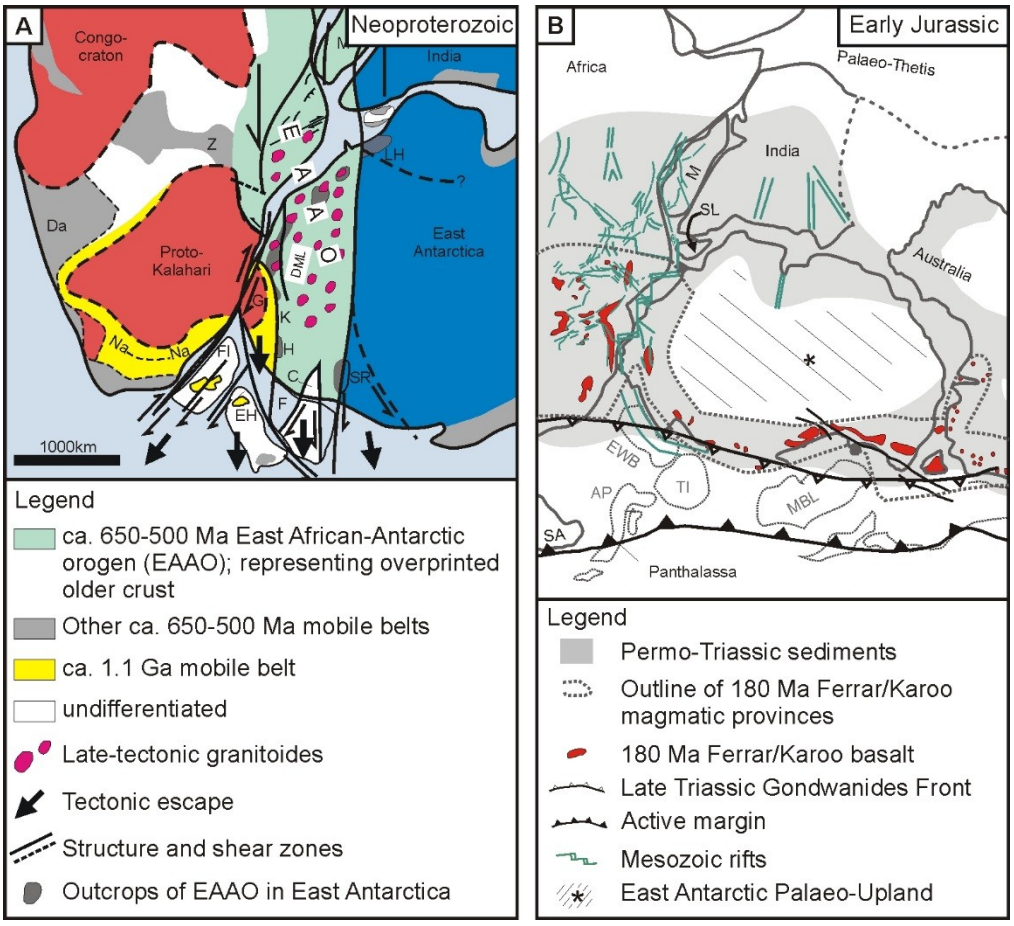

Figure 4: Paleogeographic and geological overview of Antarctica within Gondwana. A) Geological map illutstrating the formaion and late kinematic movements of the EAAO, adapted from Jacobs & Thomas (2004). Abbreviations: C: Coats Land, Da: Damara belt, DML: Dronning Maud Land, EH: Ellsworth-Haag block, F: Filchner Block, FI: Falkland Islands, H: Heimefrontfjella, K: Kirwanveggen, LH: Lützow Holm Bay, M: Madagascar, Na: Natal belt, Z: Zambesi belt. B) Late Triassic-Early Jurassic geological and geographic situation, redrawn according to Veevers (1988), Collinson *et al.* (1994) and Harrowfield *et al.* (2005). Position of the Ellsworth Whitmore Block (EWB) according to Grunow *et al.* (1991), Grunow (1993), Flowerdew *et al.* (2012) and Elliot *et al.* (2015). Abbreviations: AP: Antarctic Peninsular, EWB: Ellsworth-Whitmore Block, G: Grunehogna Craton, M: Madagascar, MBL: Marie-Bryd Land, SA: South America, SL: Sri Lanka, TI: Thurston Island.

In most parts of DML and in the northern Shackleton Range collision led to up to HP/HT metamorphism and intense structural overprint, whereas the southern Shackleton Range, the Kapvaal-Grunehogna Craton, the Bertrab-Littlewood-Mountains and some Weddell Sea microplates remain rheologically unaffected (Figure 4a). This is proposed by Jacobs & Thomas (2004) due to lateral escape towards the south as a result of orogenic collapse and is documented by ductile to brittle detachment faults and several major shear zones that formed throughout the EAAO. The collapse was accompanied by root delamination as indicated by widespread late-tectonic intrusions (e.g. Spaeth *et al.*, 1995; Bauer & Jacobs, 2001; Li *et al.*, 2003; Ruppel *et al.*, 2015). The timing of orogeny trends from north (Sør Rondane) to the south (Shackleton Range) with 650–500 Ma to 540–490 Ma (Shiraishi *et al.*, 2008; Will *et al.*, 2009; Osanai *et al.*, 2013; Elburg *et al.*, 2015a). Erosional unroofing of the EAAO started in

the Cambro-Ordovician and is documented by remnants of molasse-type rocks that are exposed in the Kirwanveggen and in the Shackleton Range (Buggisch *et al.*, 1999; Kleinschmidt *et al.*, 2000).

The Panthalassan trench advanced toward East Antarctica until the Triassic-Early Jurassic transition (Collinson *et al.*, 1994; Figure 4b). The geological record in the research area since the Cambro-Ordovician is limited to Coats Land and western DML. Here, 10–600 m thick relicts of the typical Gondwana strata are preserved (Stephenson, 1966; Bauer *et al.*, 1997). Deposition of basal Permo-Carboniferous diamictites upon the erosion surface was followed by alternating clastic sediments and plant residues that were deposited in freshwater environments (Coats Land) or in shallow marine environments (western DML) (Collinson *et al.*, 1994). Basement and sediments were penetrated and overflowed by igneous rocks between 200–175 Ma that are related to Karoo/Ferrar Large Igneous Province. Up to 900 m thick lava flows, decimeter thick sills and few meters thin steep verging dykes are preserved. The lavas and the sills seem to be bound to remaining sediments, whereas the dykes intruded the basement preferentially along steep verging brittle faults (Stephenson, 1966; Brook, 1972; Owada *et al.*, 2003; Hutton, 2009). An exception may depict Sør Rondane that lacks evidence of Jurassic magmatism so far. Although by field evidence, mafic dykes are present but not all of them are dated yet.

Initial disruption of Gondwana occurred at 155 Ma as first sea floor was formed in the Riiser-Larsen Sea, followed at 147 Ma in the Weddell Sea and 140–135 Ma in the Lazarev Sea (Jokat *et al.*, 2003; König & Jokat, 2006; Leinweber & Jokat, 2012). Then break up preceded clockwise ending in the complete isolation of Antarctica between late Cretaceous/Paleocene times (e.g. Veevers, 2012). The complete isolation and migration to the south is thought to be related to climatic cooling and enhanced erosion that initiates river incision and relief increase (Sugden *et al.*, 2014).

3. Geomorphology of the Weddell Sea Sector

Coats Land and DML are largely covered by thick ice sheets. Ice-free massifs trend roughly parallel to the recent shoreline and are located in 150-200 km distance from the shoreline. The bedrock underneath the ice was mapped in high resolution via geophysical methods and was published by Fretwell *et al.* (2013). Based on this map, the regional relief can be generally divided in two domains: The region west of 0° is characterized by roughly W-E and NW–SE trending grabens, horsts and escarpments. The grabens are up to 2 km in depth and the highest horsts are elevated up to 3 km (Figure 5). The region east of 0° appears less faulted and with generally lower relief differences compared to the west. Only one linear depression can be inferred from the map at the eastern boundary of Sør Rondane (Figure 5). The elevated massifs trending parallel to the shoreline and rise up to 3.2 k m. DML forms the typical passive margin landscape, with the low-lying flat plain and an elevated, escarpment-bound hinterland.

The high-standing massifs were often fault bounded and form steep cliffs (Figure 5). The massifs were mostly topped by plateau surfaces. The plateau surfaces were interrupted by glacially molded alpine-type peaks. The ratio between plateau surfaces and sharp peaks is divergent throughout the region. The largest pieces of the paleosurface are preserved in the western part, whereas the plateau surfaces in the eastern part are retreated to mesas or buttes, and more peak surfaces occur. The plateau surfaces are mostly bare. On few tiny spots, the flat basement surface is covered by Mesozoic debris and Ferrar/Karroo magmatic rocks (Figure 3b). Erosional processes can be dated back to the Paleozoic for at least the Shackleton Range and the western DML. Here, the flat, smoothly undulating surfaces are independently thought to be a Paleozoic erosion surface (Skidmore & Clarkson, 1972; Näslund, 2001). The flat erosion surfaces are a common feature for East Antarctica as well for Gondwana. Paleosurfaces are known for almost every part of Antarctica and are typical features for Gondwana, such as the Kukri peneplain of the Transantarctic Mountains, the East Antarctic Erosion surface in Mac.Robertson Land or the West Antarctic Erosion Surface in Marie Byrd Land (Grindlay & Warren, 1964; LeMasurier & Rex, 1983). Minimum ages of these erosion surfaces are established usually on the base of relics of the sedimentary overburden or overlying volcanic and volcaniclastic rocks. Accordingly, the exposition of some of them is well constrained and distinctive, while others are poorly dated or were exposed repeatedly or diachronously (for example, the Transantarctic Mountains).

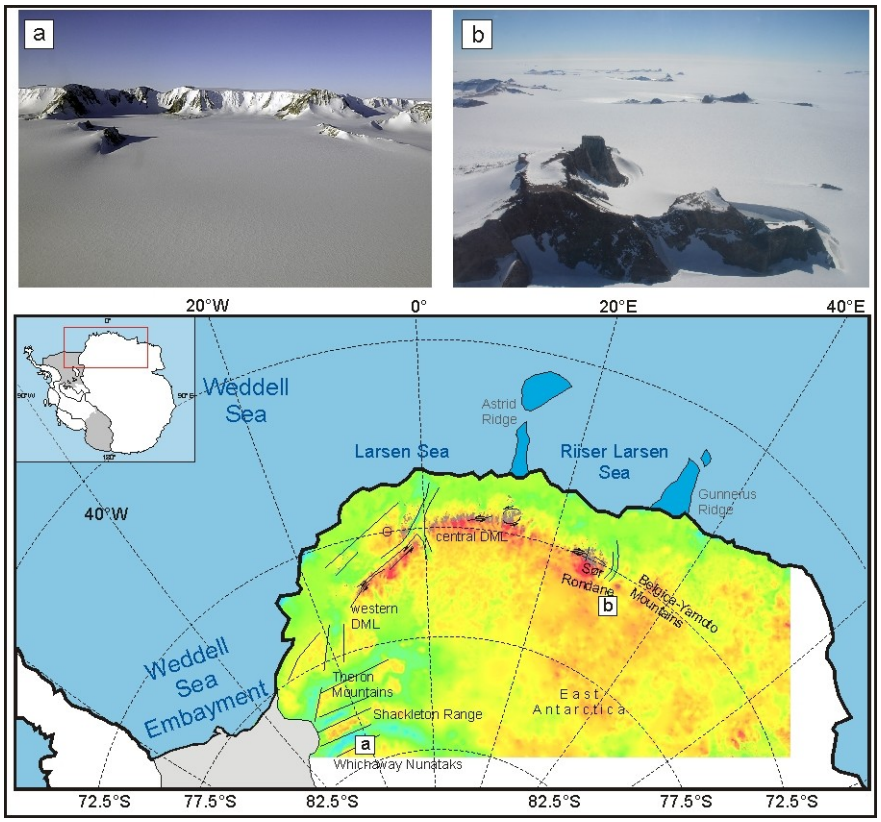

Figure 5: Topographic and morphological overview of the Weddell Sea Sector. Color map shows the bedrock elevation (Bedmap2, Fretwell *et al.*, 2013). The subparallel and nearly continuous chain of DML is well visible, as well the horst and grabens in the western part. Faults and major structures are outlined in black, major structures according to Bauer *et al.* (2003b). Letters a-b refer to representative geomorphic features that exemplify ubiquitous remnants of the regional paleosurface(s) in both research areas. Examples of further surfaces can be found in e.g. Näslund (2001). Photo a) by M. Studinger.

4. The Shackleton Range (East Antarctica): an alien block at the rim of Gondwana?

Nicole Krohne[*], Frank Lisker[*], Georg Kleinschmidt[‡], Andreas Klügel[*], Andreas Läufer[§], Solveig Estrada[§] & Cornelia Spiegel[*]

[*]University of Bremen, Department of Geosciences, PO Box 330440, D-28334 Bremen, Germany

[‡]Goethe University Frankfurt, Institute of Geosciences, Altenhöferallee 1, D-60438 Frankfurt/Main, Germany

[§]Federal Institute for Geosciences and Natural Resources (BGR), Stilleweg 2, D-30655 Hannover, Germany

Geological Magazine 2016 - DOI: 10.1017/S0016756816001011

Keywords

thermochronology, paleosurface, Gondwana break-up, landscape evolution, Ferrar/Karoo volcanism

Abstract

The Shackleton Range is a truncated Pan-African Orogen situated at the Weddell Sea margin of East Antarctica. It almost exclusively consists of basement rocks exposed at an elevated, escarpment-bound paleosurface and is covered locally by patchy remnants of Ordovician, Permian and, controversially, Jurassic terrestrial deposits. This inventory does not match the geological record of any other place in Antarctica. Here we reconstruct the Phanerozoic evolution of the Shackleton Range by means of a multi-disciplinary approach combining petrological, geochemical and geochronological data with thermal history models of zircon and apatite fission track (ZFT, AFT) and (U-Th-Sm)/He (AHe) data. Petrographic, geochemical, and $^{40}Ar/^{39}Ar$ analyses of a sedimentary cover sequence identify volcaniclastic rocks related to the Ferrar/Karoo magmatic event. Thermal history modeling of ZFT ages of 160–215 Ma, AFT ages of 124–225 Ma, AHe ages of 95–169 Ma and kinematic proxies in combination with geological information indicates a complex thermal history comprising at least three cooling episodes interrupted by reheating pulses. Thermal history refers to inversion of part of the Carboniferous–Triassic Transantarctic Basin prior to the 180 Ma Ferrar/Karoo Event and formation of an up to 3.4 km deep extensional Jurassic–Early Cretaceous basin due to Weddell Sea rifting. Basin depth was diminished by regional middle Cretaceous stress field changes. Final basin inversion and surface uplift were likely triggered by far-field tectonics and climatic influence. This history represents a typical example for the transition from an active to passive margin setting along the outer rim of Gondwana.

4.1. Introduction

The Shackleton Range forms a highland at 80–81°S and 19–31°W between Slessor and Recovery Glacier and Filchner Ice Shelf, and dominates the Coats Land region of Antarctica (Figure 6). Situated at the hinge of the Weddell Sea, at the intersection of the Panthalassan (Paleo-Pacific) coast of Gondwana and the newly developing Atlantic margin, and at the border between the stable East Antarctic Craton and the mobile West Antarctic terrane assemblage, the range occupies a crucial position for the Phanerozoic history of Gondwana and Antarctica. This unique setting means that the Shackleton Range is a key location to study the transition from an active to a passive Gondwana margin, the opening of the Weddell Sea and the formation of the rifted margins to the Weddell Sea and South Atlantic Ocean. However, none of these processes appears preserved even implicitly in the known geological record. Exposed mountain massifs almost exclusively consist of truncated metamorphic basement, while patchy Phanerozoic deposits are restricted to Cambro-Ordovician molasses of the Pan-African Orogen and a single outcrop of thin Permo-Carboniferous glacial strata (e.g. Buggisch *et al.*, 1999; Tessensohn *et al.*, 1999a). Other sedimentary sequences or igneous units that are typical for the Panthalassan margin of Gondwana elsewhere, such as thick Mesozoic active margin foreland deposits or the *c.* 180 Ma aged basaltic Ferrar/Karoo sills or flows, are not preserved.

Indirect evidence for the geological history from thermochronological data is also scarce. Only one set of zircon and apatite fission track (ZFT, AFT) data has been published so far (Lisker *et al.*, 1999), and was interpreted as reflecting three exhumation and uplift stages of the basement at *c.* 190 Ma, *c.* 110 Ma and, tentatively, at *c.* 50 Ma. Such a Phanerozoic record does not match the geological history anywhere else in Antarctica or adjacent Gondwana fragments, and makes the Shackleton Range an alien block in the continent.

On the contrary, a close inspection of stratigraphic record, thermochronological data, and geomorphological features reveals several problems. A first problem refers to the timing of depositional episodes. Sediment relicts in the eastern Shackleton Range, resting above truncated basement, were generally considered as Permo-Carboniferous tillite sequence; an alternative theory is that the uppermost strata are Lower Jurassic tuffites (Buggisch *et al.*, 1994a; Buggisch *et al.*, 1994b; Tessensohn *et al.*, 1999a). More severe is a second concern about the thermal history interpretation of ZFT and AFT data in terms of monotonous cooling paths that does not account for events of near-surface exposition (Lisker *et al.*, 1999). The occurrence of either upper Paleozoic or Mesozoic deposits upon truncated basement requires coeval heating of the rock column beneath. This disproves the proposed exhumation concept

including any estimates of timing and amounts and rates of exhumation, and requires a revision of the exhumation and tectonic history.

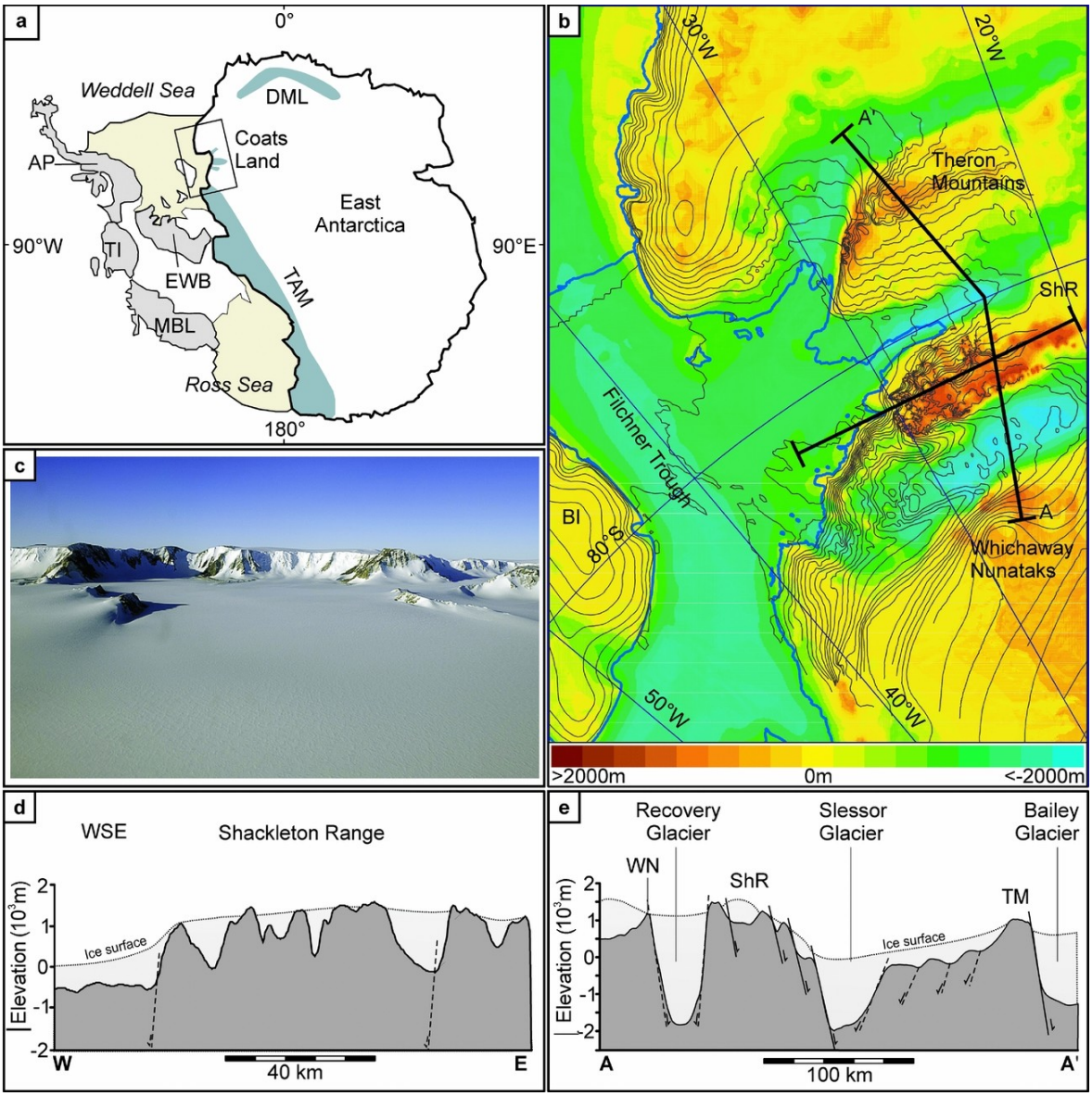

Figure 6: (a) Simplified overview of the East and West Antarctic plate pattern. The East Antarctic plate is outlined by the thick solid black line; West Antarctic mobile terranes and coastal embayments are outlined by thin solid black lines. Blue shaded areas within East Antarctica indicate significant ice-free regions in the frame of this study. AP–Antarctic Peninsula; DML–Dronning Maud Land; EWB–Ellsworth-Whitmore Block; MBL–Marie Byrd Land; TAM–Transantarctic Mountains; TI–Thurston Island. The inset shows the area of map plotted in (b). (b) Regional map of the study area in the Weddell Sea embayment with shaded colors reflecting the sub-ice topography. Contour lines indicate recent (ice-) surface elevations. Thick solid lines delineate cross-sections drawn in (d) and (e). BI–Berkner Island; ShR–Shackleton Range. (c) Photograph of the Shackleton Range, displaying the paleosurface and escarpments of the Read Mountains. Cliff heights are c. 400 m. Photograph (taken by M. Studinger) faces north. (d) W–E-aligned cross-section through the basement of the Shackleton Range. Notable is the high-standing, deeply incised paleosurface of the Shackleton Range and the steep escarpment towards the Weddell Sea coast. Stippled lines indicate inferred normal faults. WSE–Weddell Sea Embayment. (e) Cross-section through the basement from Whichaway Nunataks (WN) to Theron Mountains (TM) via Shackleton Range (ShR), highlighting the enormous relief differences between glacial troughs and rock outcrops, and the obvious normal fault pattern. Stippled lines indicate inferred normal faults. Bedrock elevation data of (b), (d), and (e) are based on Bedmap 2 data (Fretwell *et al.*, 2013); contour lines were supplied by the Antarctic Digital Database.

Here, we aim to revise the stratigraphic position of the uppermost strata of the Shackleton Range to identify episodes of basement exposition and deposition and to reconstruct the Mesozoic and Cenozoic exhumation and tectonic history. This study relies on an interdisciplinary approach combining petrological, geochemical and geochronological data with thermochronological data. The first step is to establish rock type and facies of the deposits–diamictite or volcaniclastic rock–via petrographic thin-section analyses, X-ray diffraction (XRD) analysis, inductively coupled plasma mass spectrometry (ICP-MS) and X-ray fluorescence (XRF) analyses. Radiometric age data ($^{40}Ar/^{39}Ar$) will then determine either detritial ages or the timing of the last metamorphic event or–in the case of volcanic detritus–provide a deposition age and therefore also the date of near-surface position of the truncated basement. Finally, this information will provide a crucial input to set the frame for thermal history modeling of existing and new ZFT, AFT and AHe data.

The new stratigraphic data and thermal history models provide key constraints to develop consistent burial and exhumation scenarios of the Shackleton Range and derive timing, depths and rates of basin infill and exhumation amounts. The results have major implications for the general geological evolution and tectonic processes at the Panthalassan margin of Gondwana and the initiation of the Weddell Sea Basin.

4.2. Geological and geomorphological setting

4.2.1. Geological framework

East Antarctica is formed by a collage of Precambrian terranes that amalgamated stepwise during Precambrian–Cambrian time (e.g. Boger, 2011). Its western margin is framed by Paleozoic West Antarctic mobile crustal blocks, which were bounded in the outermost west by the (Paleo-) Pacific subduction zone during Paleozoic–Mesozoic time (Figure 6a). Along the western margin of Gondwana, in the Transantarctic Mountains, Beacon Group sediments were deposited diachronously during Devonian–Triassic time. They mainly consist of clastic red-bed sediments deposited upon truncated Proterozoic–lower Paleozoic basement rocks. Further components of the Beacon Strata are clastic Permian freshwater to shallow-marine sequences and Permian–Triassic coal seams. Paleosols and erosion surfaces are abundant within the strata and indicate times of subaerial periods. Typically for the Beacon Supergroup, the youngest rocks depict multiform Ferrar/Karoo magmatic rocks, somehow related to the beginning break-up of Gondwana (e.g. Barrett, 1992; Collinson *et al.*, 1994). The Ferrar/Karoo igneous activity was a magmatic event which occurred during ~200–170 Ma, with its main phase at 180–175 Ma. Ferrar-related rocks include rhyolitic to dacitic intrusions, rhyolitic to mafic dyke and sill emplacements, and basaltic lava flows (e.g. Brewer,

1989; Elliot & Fleming, 2000; Elliot & Fleming, 2004; Leat *et al.*, 2005). Correlatives and analogues of the Beacon sequence including the Ferrar/Karroo rocks can be found elsewhere in East Antarctica (e.g. Dronning Maud Land), as well in the Australian, African and South American parts of Gondwana. However, at least some West Antarctic blocks (e.g. Ellsworth Mountains) comprise different sediments of Cambrian–Permian age, folded during the Gondwanide Orogeny during Middle–Late Triassic time (e.g. Craddock, 1972; Curtis, 2001).

In Coats Land, the structural continuation of the Transantarctic Mountains, the Shackleton Range forms the largest rock outcrop surrounded by the steep escarpment of the Theron Mountains in the north and the patchy Whichaway Nunataks in the south. It forms a topographic high elevated up to 1800 m and flanked by two major, up to 2000 m deep, glacial troughs that host westwards-flowing ice streams (Figure 6b). It occupies an area of ~15300 km^2 with a length of 170 km in the E–W direction and a maximum width of 90 km in the N–S direction. Outcrops form rock massifs that are dissected by snowfields and ice streams. In clockwise order, these are: LaGrange Nunataks, Herbert Mountains, Pioneers Escarpment, Read Mountains, Stephenson Bastion, Otter Highlands and Haskard Highlands (Figure 7).

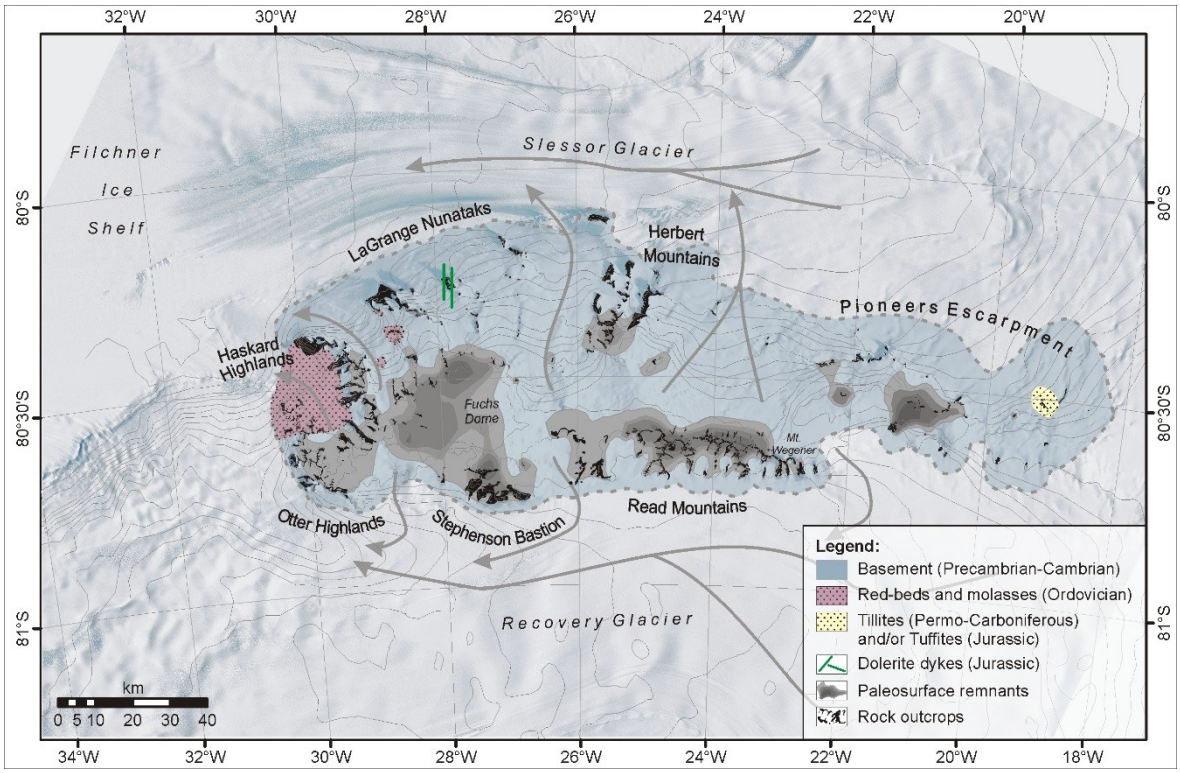

Figure 7: Combined geomorphic and simplified geologic overview of the Shackleton Range modified after Tessensohn *et al.* (1999b) and Kleinschmidt *et al.* (2002). Arrows mark the flow direction of selected glaciers (Höfle & Buggisch, 1995); green lines indicate the location and strike of Jurassic dolerite dykes (Spaeth *et al.*, 1995). Data from Bedmap2 (paleosurfaces), Antarctic Digital Database (contour lines) and LIMA data (Landsat image).

The basement of the Shackleton Range consists of a nappe stack which formed during the Pan-African Orogeny at ~500 Ma. It comprises medium- to high-grade crystalline rocks, partly

eclogized ophiolites, and non- to low-grade metamorphic sedimentary rocks of Paleoproterozoic–early Paleozoic age (e.g. Clarkson, 1981; Kleinschmidt *et al.*, 1992; Tessensohn *et al.*, 1999b; Kleinschmidt *et al.*, 2002; Boger, 2011). The Phanerozoic sedimentary record of the Shackleton Range is restricted to small, isolated patches. Subhorizontal Ordovician red-bed molasse and fossiliferous sediments of the Blaiklock Glacier Group in the west document the initial exhumation of the Pan-African Orogen (Buggisch *et al.*, 1999). Controversially discussed Permo-Carboniferous glacial deposits or Jurassic tuffaceous rocks crop out at a small nunatak in the east and represent the youngest sedimentary deposits (Buggisch *et al.*, 1994a; Buggisch *et al.*, 1994b; Tessensohn *et al.*, 1999a). Post-orogenic dykes of mostly mafic composition yield amphibole, biotite and whole-rock ^{40}K–^{39}Ar ages ranging over 177–426 Ma (Hotten, 1993; Spaeth *et al.*, 1995; Brommer, 1998; Brommer & Henjes-Kunst, 1999). Sills were not observed in the Shackleton Range. The brittle tectonic inventory includes thrusts, shear zones, and normal and reverse faults. These as-yet undated structures were related to the latest orogenic event. Skidmore & Clarkson (1972) describe the Shackleton Range as a rectangular horst with major N–S-trending faults. Major ice streams appear to utilize tectonic structures that separate the metamorphic basement of the Shackleton Range from adjacent early Permian deposits and massive Jurassic dolerite sills in the Theron Mountains and in the Whichaway Nunataks, respectively (Stephenson, 1966; Brook, 1972; Hofmann *et al.*, 1980; Hutton, 2009; Figures 6, 7).

4.2.2. Geomorphological pattern

The morphology of the Shackleton Range is dominated by almost-horizontal ridges, plateaus and mesas. Summits reach elevations of 400–1800 m, and are bound by up to 400 m steep cliffs. The terrain is highest at the Fuchs Dome ice cap in the SW and across to Mount Wegener (Read Mountains). It declines slightly to the NW and finally plunges towards the Weddell Coast, where isolated and conical nunataks appear at low elevation. At the eastern rim, outcrops submerge beneath the ice cover. The flat topped ridges, plateaus and mesas were interpreted as remnants of an undulating continuous ‘peneplain’ or paleosurface (Stephenson, 1966; Skidmore & Clarkson, 1972; Marsh, 1985). The paleosurface was supposedly formed during Middle Ordovician–Permian time. Its remnants occur across all mountain massifs and are dissected by faults of unknown age, resulting in an exposure at different elevations (Stephenson, 1966). The largest remnant of the paleosurface is exposed at 1600–1800 m in the Read Mountains. Further remnants (in clockwise direction) are observed at the following elevations: Stephenson Bastion at 1450 and 1600 m; Haskard Highlands at 1000–1150 m; LaGrange Nunataks at 1200–1330 m; and Herbert Mountains at 1640 m. In the Pioneers Escarpment, a large amount of the paleosurface is covered by ice. Nevertheless, Stephenson

(1966) refers to the existence of the paleosurface in the east; its subglacial existence is also evident with regards to the sub-ice topography (Fretwell *et al.*, 2013; Figure 7). The paleosurface is slightly tilted to the east (Stephenson, 1966). The ground of the surfaces appears frost-shattered and covered by up to 0.40 m till (Stephenson, 1966; Höfle & Buggisch, 1995; Sugden *et al.*, 2014). The Quaternary erosion rate is low at 0.10–0.35 m Ma^{-1} (Fogwill *et al.*, 2004).

4.3. Petrological, geochemical and geochronological analyses

4.3.1. The sedimentary succession in the eastern Shackleton Range

The formation age of the Shackleton Range paleosurface and timing of (re-)exposition are poorly constrained. A nunatak at 80.5°S 19°W contains a 30 m thick unfossiliferous succession that is debated as being either Permo-Carboniferous glacial deposits or Jurassic tuffites (Figures 7, 8; Buggisch *et al.*, 1994a; Buggisch *et al.*, 1994b; Tessensohn *et al.*, 1999a). The nonconformity to the basement is not exposed, but the basement paleosurface is exposed a few kilometers apart (Figure 7, Figure 8). The tilting direction and dip of the paleosurface coincide with the tilting of the sedimentary succession (Tessensohn *et al.*, 1999a). The sedimentary sequence, chiefly reported by Tessensohn *et al.* (1999a), can be divided into five stratigraphic units according to physical properties. The base of the succession (Unit A) contains non-sorted arenaceous matrix-supported sediments with grain sizes ranging from boulder to clay size. The boulder–pebble-sized clasts are made up of sandstones, phyllites and mica schists and are sub-rounded to rounded with striated and faceted surfaces. Some of these clasts are surrounded by a white halo of a few centimeters thickness. Unit B comprises dark-grey shales with imbedded faceted clasts. It is overlain by pale-colored pebbly sand–siltstones with slumping, as well as load and convolute bedding structures (Unit C). Sandy clasts in this unit are poorly sorted and consolidated. Unit D consists of black shales and millimeter-sized clasts. The uppermost unit (E) comprises pale white sandstone and siltstones (Tessensohn *et al.*, 1999a; Figure 8). The occurrence of secondary chlorite and the white haloes of unidentifiable composition in the basal units (A and B) may refer to a mild metamorphic overprint of these strata.

Based on the striated and faceted surfaces of the boulders and the occurrence of dropstones, Tessensohn *et al.* (1999a) interpreted the sequence as glacial debris and correlated its basal layer with the Permo-Carboniferous base of the Beacon Supergroup that was deposited throughout the Transantarctic Mountains (e.g. Barrett, 1992; Collinson *et al.*, 1994). In analogy, the sedimentary cover on the paleosurface was suggested to be of Permo-Carboniferous age. However, the origin of Units D and E was discussed controversially. Buggisch *et al.*

(1994a) and Buggisch *et al.* (1994b) sampled the dark shales of Unit D below Unit E. Petrographic thin-section analysis showed clusters of angular quartz and feldspar in a matrix of fine-grained quartz and white mica. $^{40}K–^{39}Ar$ whole-rock age determinations on fine-grained fractions yielded ages of 181±2 Ma for 0.6–2 µm and 186±2 Ma for 2–6 µm fractions. The authors classified the rock as a tuffite that may be related to the ~180 Ma Ferrar volcanic event. In contrast, Tessensohn *et al.* (1999a) considered the whole strata as part of the Permo-Carboniferous glacial cycle; this may have been affected by Jurassic contact metamorphism, probably due to an unexposed Jurassic intrusion.

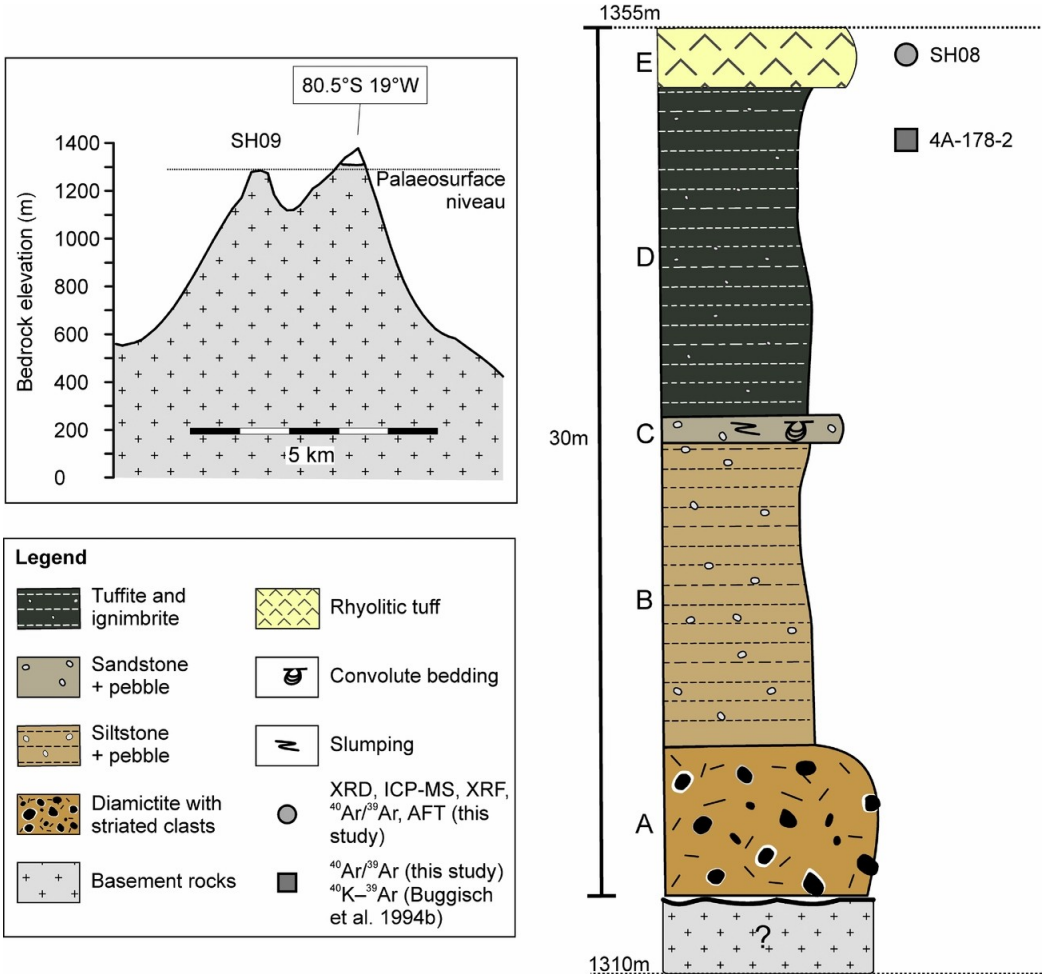

Figure 8: Simplified topographic sketch and stratigraphic section describing the sedimentary deposits of the easternmost nunatak at 80.5°S, 19°W modified after Tessensohn *et al.* (1999a). Capital letters refer to stratigraphic units.

We aim to specify the nature and the age of these strata by petrographic, geochemical and geochronological analyses of the uppermost beds (Units D, E) as they mark a crucial time–temperature constraint for the interpretation of thermochronological data obtained from basement rocks beneath.

4.3.2. The lithology of the cover sequence (Unit E)

Hand specimen SH08 from Unit E is a massive whitish to pale-grayish rock slightly indicating flow fabric. Individual minerals or clasts are hardly discernible by the naked eye except for local blackish sharp spherical fragments and 0.5–1.5 mm sized spheroids that are partly filled with a whitish, porous and soft material (Figure 9a-c).

Thin-section analysis reveals a micro- to cryptocrystalline groundmass of felsic minerals with intermediate relief and first-order interference colors, interspersed by very-fine-grained dark minerals and up to 50 µm sized phenocrysts. Within the matrix, the same mineral grains are joined to clusters and patches with a lobate or cloudy appearance. Furthermore, very-fine-grained secondary-phase minerals with high-order interference colors and also with low first-order interference colors are aligned spheroidically. Phenocrysts comprise subhedral quartz, tabular orthoclase, plagioclase laths and opaque mineral phases. Accessory minerals are subhedral amphibole, zircon and apatite. Notably, many of these minerals occur as angular and broken fragments (Figure 9d-f). The flow fabric is also evident within the thin-section. Some mineral phases may not have been detected optically, due to micro- to cryptocrystalline grain sizes (Appendix B.1.1).

X-ray diffraction (XRD) analysis of powder of sample SH08 was conducted for qualitative and semi-quantitative mineral determination. The analysis was carried out using $CuK\alpha_{1,2}$ radiation at ambient temperature conditions. Rietveld refinement was implemented to exclude diffraction shifts. The XRD pattern shows substantial reflexes at the 2Θ angles, where mineral phases quartz (2Θ=26.6512), albite (2Θ=27.89), orthoclase (2Θ=27.76) and apatite (2Θ=31.871) are placed (Figure 9e). The relative intensity is highest for quartz, albite and orthoclase with more than 80000 counts. Further mineral phases show only very low relative intensities and tend to be obscured by the high-intensity counts. The 100-intensity peak of one mineral phase is placed at 2Θ = 6.212 with a d-spacing of 14.230 Å. This peak can either refer to zeolites (faujasite), chlorite group minerals or to hydrated clay minerals. Hydration of clayous minerals changes lattice parameters and can therefore cause a substantial shift in 2Θ angles. Morkel *et al.* (2006) and Dietze *et al.* (2007) report d-value ranges of 13–18 Å at 4.9–6.8 2Θ for smectite group minerals, so may be present in the studied sample. A further peak of very low relative intensities (~1%) at 10.48 2Θ angles refers to a rather uncommon mineral phase. d-values of 8.44 Å (1), 2.816 Å (0.47) and 2.544 Å (0.45) would suggest euchlorine. The complete reflex list and XRD measurement conditions are listed in Appendix B (Appendix B.1, Table S 2 and Table S 3).

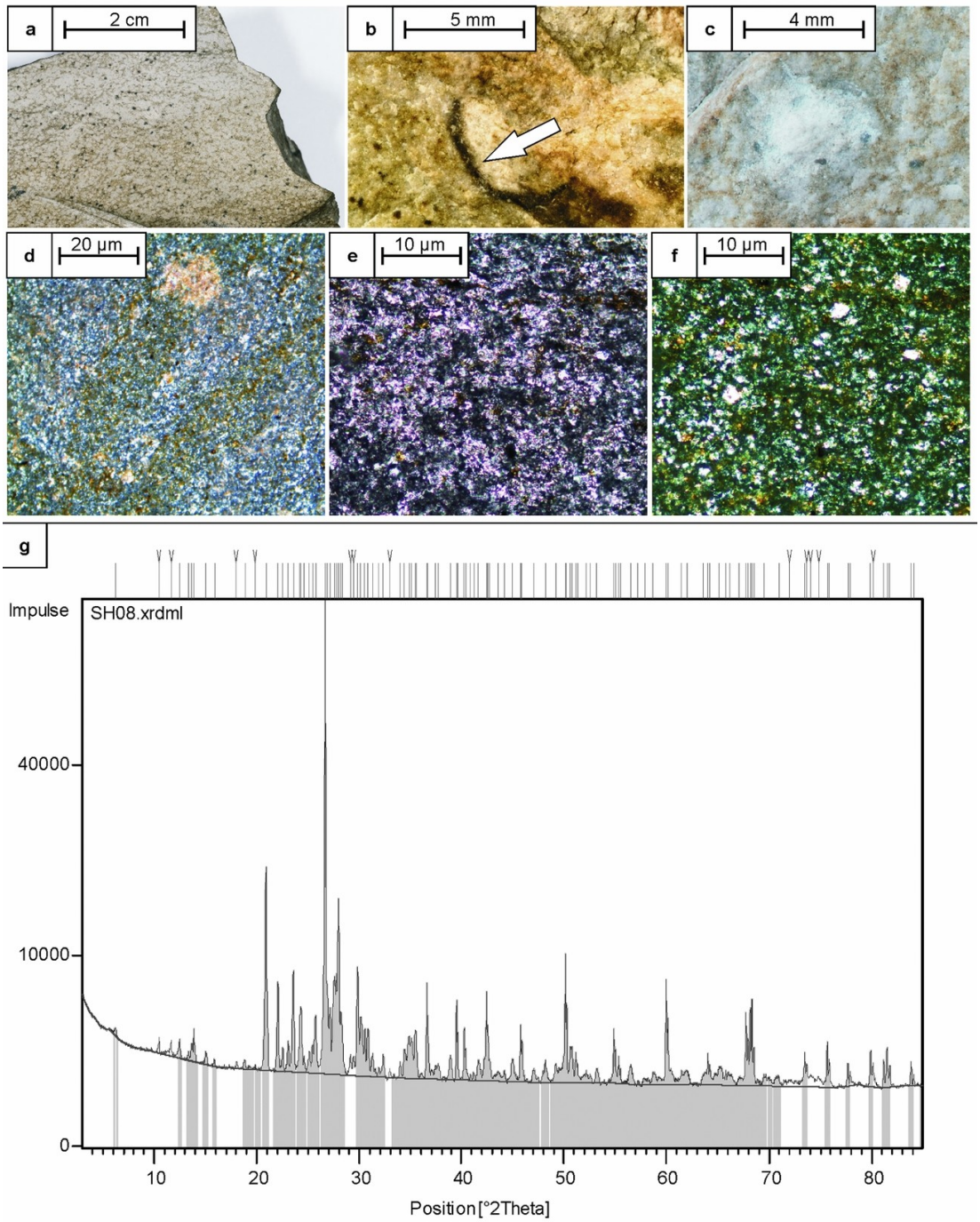

Figure 9: (a) Photograph of polished hand specimen of SH08 displaying internal flow texture. (b) Photograph of blackish bubble wall shards (white arrow). (c) Photograph of spherical structure composed of very soft material. (d) Thin-section microphotograph (crossed polarizers) showing dark very-fine-grained matrix, flow structure and secondary mineral phases. (e) Thin-section microphotograph under plain polarized light and (f) crossed polarizers show the micro- to cryptocrystalline matrix and abundant crystal fragments. (g) XRD diffraction diagram of SH08. Measurement was conducted with $CuK\alpha_{1,2}$ radiation at ambient temperatures. 'V's at the top represent undescribed reflexes.

As a result, mineralogy, fabric and texture of the rock resemble those of ash falls and pyroclastic flows from explosive volcanic eruptions. The sharp vesicular blackish fragments and the spheroids most likely represent bubble wall shards and lapilli, respectively. Sample SH08/Unit E most likely represents a rhyolitic tuff that is rich in vitric components.

4.3.3. Geochemistry of the rhyolitic tuff

To investigate the geochemical character, ICP-MS/XRF measurements were performed (Table 1; Appendix B.1). A molar $Al_2O_3/(CaO+Na_2O+K_2O)$ ratio of 0.64 defines SH08 as a SiO_2-rich, metaluminous rhyolite according to the TAS diagram of LeBas *et al.* (1986). Concentrations of Fe_2O_3 (2.9 wt%), MgO (1.7 wt%) and TiO_2 (0.7 wt%) are comparatively low. An incompatible-element diagram of the sample, normalized to primitive mantle, shows troughs for Nb, Ta, Sr and Ti and spikes for Pb, indicating enrichment of more incompatible relative to less incompatible elements (Figure 10a). The Nb, Ta and Pb anomalies are characteristic of continental crust and volcanic rocks at convergent plate boundaries. The chondrite-normalized rare Earth element (REE) pattern displays light REE considerably enriched relative to heavier REE (La_N/Lu_N = 9.29), and is almost identical to that of average upper continental crust (Taylor & McLennan, 1985; Figure 10b). A plot of REE normalized to average upper continental crust (UCC; Taylor & McLennan, 1985) shows an almost uniform distribution in contrast to other Jurassic magmatic rocks from Coats Land (Figure 10b). In the Rb v. (Yb+Ta) discrimination diagram of Pearce *et al.* (1984), the sample plots in the field for volcanic-arc granites. Rb and most other fluid-mobile elements (K, Cs, Ba and Pb) are enriched in sample SH08, which suggests that Unit E was not subject to major hydrothermal alteration and metasomatism.

Apart from the REE, the overall incompatible trace-element distribution of sample SH08/Unit E resembles the Jurassic dolerite intrusions from the neighboring LaGrange Nunataks, Theron Mountains and Whichaway Nunataks (Brewer, 1989; Spaeth *et al.*, 1995; Leat *et al.*, 2005; Figures 10a, b). In particular, the negative anomalies for Nb, Ta, Sr and Ti and positive anomalies for Pb are similar. The TAS diagram of the dolerite intrusions and SH08 refers to subalkaline volcanic series.

Table 1: Major- and trace-element concentrations of sample SH08.

Major Elements [wt. %]		Trace Elements [µg/g]					
SiO_2	71.09	Li	12.7	Nb	12.8	Er	3.82
Al_2O_3	10.38	Sc	8.66	Cs	0.59	Tm	0.57
Fe_2O_3	2.86	V	50.3	Ba	585	Yb	3.50
MnO	0.09	Cr	47.9	La	44.5	Lu	0.51
MgO	1.67	Co	8.82	Ce	90.6	Hf	3.24
CaO	4.16	Ni	26.4	Pr	11.1	Ta	0.75
Na_2O	3.08	Cu	5.07	Nd	43.4	Pb	14.9
K_2O	3.28	Zn	54.1	Sm	8.47	Th	11.8
TiO_2	0.65	Ga	10.0	Eu	1.62	U	2.42
P_2O_5	0.18	Rb	107	Gd	7.41		
SO_3	0.07	Sr	92.0	Tb	1.16		
L.O.I	2.46	Y	42.1	Dy	6.76		
SUM	99.97	Zr	208	Ho	1.31		

Data in italics analyzed by ICP-MS, data in roman by XRF.

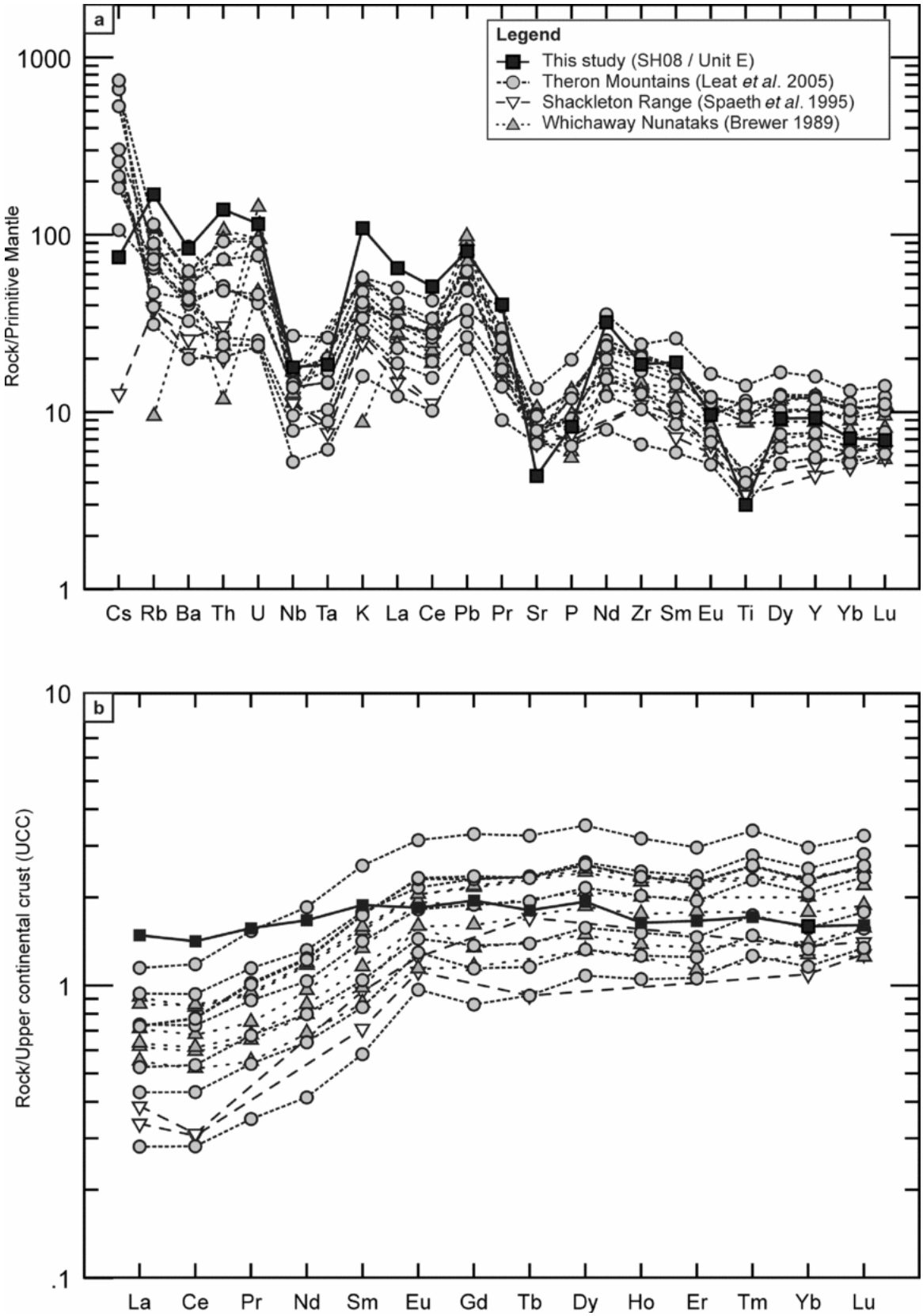

Figure 10: (a) Comparison of incompatible-element diagrams of Jurassic magmatic rocks in Coats Land. The patterns look similar for all samples and are consistent with volcanic-arc affinities. Normalizing values from Sun & McDonough (1989). (b) Upper continental crust normalized rare Earth element (REE) plot of the same Jurassic magmatic rocks. The small nearly horizontal REE spectrum of sample SH08 and the enrichment of the heavier relative to the lighter REE of the tholeiitic rocks are obvious. Normalizing values from Taylor & McLennan (1985).

4.3.4. Geochronology: $^{40}Ar/^{39}Ar$ analyses

Buggisch *et al.* (1994b) performed ^{40}K–^{39}Ar whole-rock analyses on two fine-grained fractions (0.6–2 µm and 2–6 µm) from Unit D, and obtained ages of 181±2 Ma and 186±2 Ma, respectively. To define the time relationship between the top layers of the cover sequence, $^{40}Ar/^{39}Ar$ measurements were conducted on two samples from Units D and E (Table 2: $^{40Ar}/^{39Ar}$ data., Figure 11, Appendix B.1.4).

Table 2: $^{40}Ar/^{39}Ar$ data.

4A-178-2 / Unit D
Mixed quartz-Fe minerals-feldspar-biotite separate

T [°C]	$^{38}Ar/^{39}Ar$	$^{37}Ar/^{39}Ar$	$^{36}Ar/^{39}Ar$	$^{39}Ar/^{40}Ar$	$^{36}Ar/^{40}Ar$	Ca/K	^{39}Ar cum. [%]	Age [Ma]	±1σ
215	0.3501	0.1175	1.5795	0.0022	0.0034	0.22	0.90	0.0	0.0
460	0.0798	0.0584	0.2159	0.0105	0.0023	0.11	3.54	135.2	1.6
586	0.0524	0.0300	0.0276	0.0218	0.0006	0.05	19.18	161.5	1.6
701	0.0529	0.0151	0.0865	0.0137	0.0012	0.03	69.10	201.6	2.0
811	0.0379	0.0191	0.0305	0.0175	0.0005	0.04	84.28	204.2	2.1
913	0.0556	0.0376	0.1299	0.0114	0.0015	0.07	91.96	208.4	2.1
1012	0.1015	0.0976	0.3516	0.0066	0.0023	0.18	96.65	206.1	2.2
1144	0.3562	0.1366	1.6901	0.0019	0.0031	0.25	98.95	173.9	3.2
1220	0.2890	0.4296	1.1712	0.0025	0.0030	0.79	99.44	198.4	7.5
1329	0.4801	0.3108	2.2011	0.0014	0.0031	0.57	100.00	233.1	8.3

SH 08 / Unit E
Whole rock (>355µm)

T [°C]	$^{38}Ar/^{39}Ar$	$^{37}Ar/^{39}Ar$	$^{36}Ar/^{39}Ar$	$^{39}Ar/^{40}Ar$	$^{36}Ar/^{40}Ar$	Ca/K	^{39}Ar cum. [%]	Age [Ma]	±1σ
457	0.5264	0.1228	1.0203	0.0029	0.0030	0.22	1.70	150.3	1.7
523	0.0506	0.0465	0.0509	0.0165	0.0008	0.09	5.14	191.2	1.9
604	0.0203	0.0364	0.0214	0.0203	0.0004	0.07	20.58	181.7	1.8
681	0.0399	0.0143	0.1434	0.0118	0.0017	0.03	32.75	175.6	1.8
773	0.0163	0.0145	0.0141	0.0219	0.0003	0.03	52.05	176.0	1.8
860	0.0206	0.0242	0.0290	0.0201	0.0006	0.04	64.13	174.7	1.8
943	0.0295	0.0347	0.0443	0.0187	0.0008	0.06	72.62	171.1	1.7
1007	0.0439	0.0387	0.0447	0.0187	0.0008	0.07	80.72	169.8	1.7
1112	0.0609	0.0679	0.0582	0.0169	0.0010	0.12	93.48	176.8	1.8
1308	0.0774	0.4233	0.1186	0.0117	0.0014	0.77	100.00	209.8	2.1

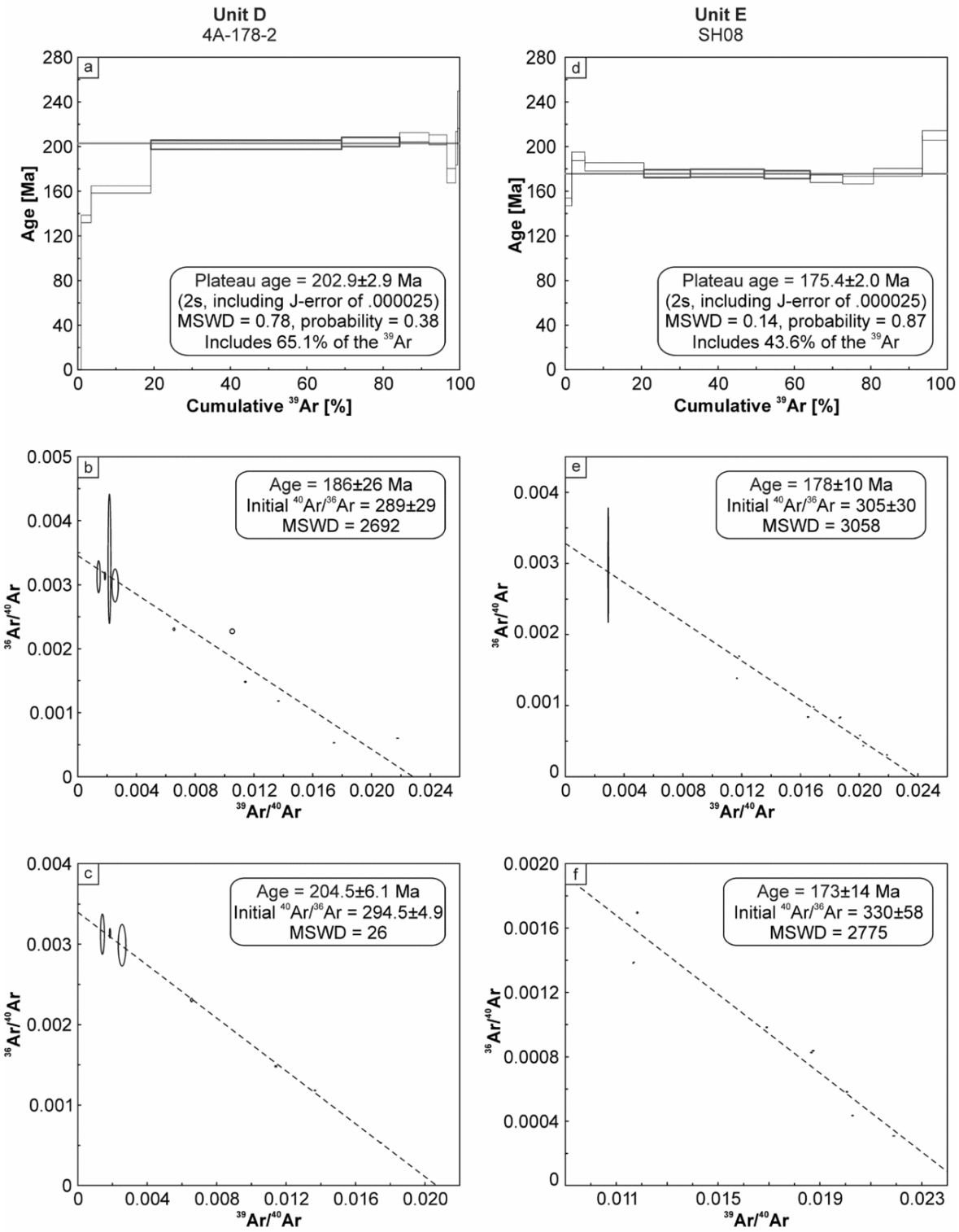

Figure 11: $^{40}Ar/^{39}Ar$ data plots. (a) Age spectrum plot of sample 4A-178-2, Unit D. Bold rectangles show plateau steps; thin rectangles illustrate rejected plateau steps; box heights display the 2σ error; horizontal line shows plateau age. (b) Inverse isochron plot of all data points. (c) Inverse isochron point without outliers. (d) Age spectrum plot of sample SH08, Unit E (legend as for (a)). (f) Inverse isochron plot of all data points. (g) Inverse isochron point without outliers. (b, c, f, g) Ellipses display 2σ error.

Sample 4A-178-2 is a dark, fine-grained, feldspar-bearing sediment from Unit D. Thin-section analysis validates the observations made by Buggisch *et al.* (1994a), referring to a

volcaniclastic rock. Limited sample material did not allow the separation of a pure feldspar fraction. A mixed separate consisting of quartz, Fe minerals, feldspar and minor biotite yielded a total fusion age of 193.1±2.0 Ma and involves a plateau age of 202.9±2.9 Ma (MSWD 0.78) for 65% of the released ^{39}Ar with constant low Ca/K ratios (0.03–0.04). These ages are slightly older than the ^{40}K–^{39}Ar ages of Buggisch *et al.* (1994a). Dating of the >355 µm whole-rock fraction of sample SH08 from Unit E yielded a total fusion age of 178.2±2.2 Ma, and a plateau age of 175.4±2 Ma (MSWD 0.14) was calculated for 44% of the released ^{39}Ar. Although this plateau age does not represent >50% of the released ^{39}Ar, it is characterized by constant low Ca/K ratios (0.03–0.04) and is, within the error, identical to the total fusion age. The inverse isochron calculations of both samples yield ages with high MSWD values, and will therefore not be used further. We interpret the plateau ages of 203±3 Ma and 175±2 Ma as the currently best estimates for Unit D and Unit E, respectively, while being consistent with the stratigraphic order.

4.3.5. Synopsis: Jurassic volcaniclastic rocks on Permian tillites

The metaluminous composition and overall geochemical character of SH08 refers to an I-type granite/rhyolite magma that was generated by partial melting of mafic lower crust. The sedimentary flow fabric of this sample in conjunction with abundant crystal fragments, as well as the occurrence of lapilli and bubble wall shards, is consistent with ash deposits from a violent rhyolite eruption. The ^{40}Ar/^{39}Ar ages of the sample from Units D/E bracket the volcanogenic sediment emplacement between 202 Ma and 175 Ma. Compared to Unit E, similar geochemical patterns and ages (163±13–183±11 Ma) of dolerite dykes and sills from the nearby La-Grange Nunataks, Whichaway Nunataks and Theron Mountains (Hofmann *et al.*, 1980; Spaeth *et al.*, 1995; Leat *et al.*, 2005) imply a relation to the Ferrar event. Furthermore, the ^{40}Ar/^{39}Ar age of Unit E is consistent with the ^{40}Ar/^{39}Ar age of 176.6±1.8 Ma on the Ferrar tholeiitic rocks as a whole (Fleming *et al.*, 1997).

The petrological, geochemical and geochronological analyses characterize Unit D and Unit E as products of the early and main phase of the Ferrar/Karoo magmatic cycle. These volcaniclastic sediments rest conformably or unconformably upon a few meters of basal Permo-Carboniferous sediments deposited during the initial Gondwana glaciation. These basal strata in turn nonconformably cover basement that has previously been truncated. The interpretation of our petrographic and geochemical data therefore indicates repeated basement (near-) surface exposition at least during early Permian and Late Triassic–Early Jurassic time, and defines a reliable frame for thermal history modeling of thermochronological data.

4.4. Thermochronology

4.4.1. Sampling

Twenty-eight *in situ* rock samples were collected from basement outcrops in the central and eastern Shackleton Range during GEISHA and EUROSHACK expeditions of the German Federal Institute for Geosciences and Natural Resources (BGR) in 1987/88 and 1994/95, mainly from the following mountain massifs: Herbert Mountains, Pioneers Escarpment, Read Mountains and Haskard Highlands (Figure 12; Appendix B, Table S 1). Twenty-two specimens were used for AFT analysis, with 13 of them being re-analyzed. Seven samples were suitable for AHe measurement. Zircons from seven locations had already been dated by ZFT thermochronology (Lisker *et al.*, 1999). As a result, each of the 22 individual sample locations were analyzed with up to three independent thermochronometers for maximum paleotemperature coverage and resolution. The spatial coverage of the samples did not contain vertical profiles, so paleogeothermal gradients could not be determined.

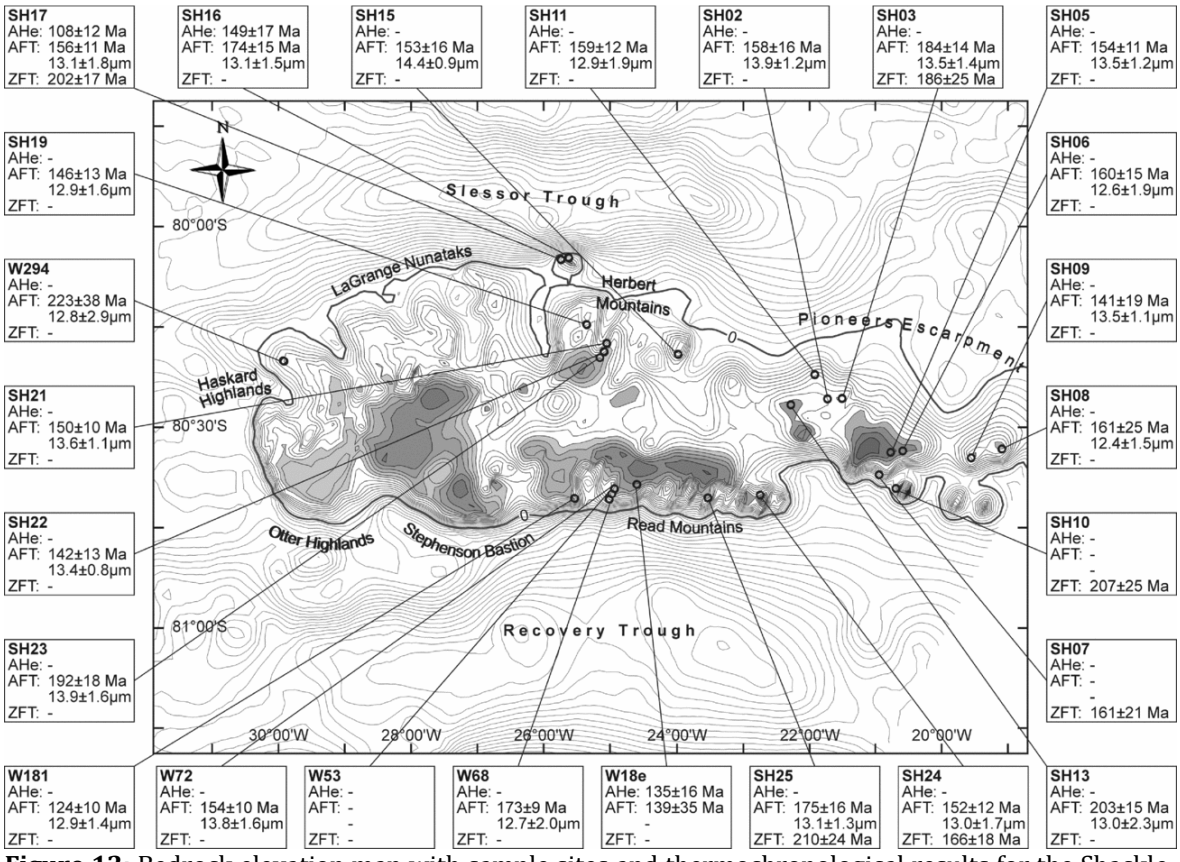

Figure 12: Bedrock elevation map with sample sites and thermochronological results for the Shackleton Range, including AHe ages, AFT ages and mean track lengths and ZFT ages. Dots mark the sites of the thermochronology samples. AHe ages reported reflect central ages calculated using HelioPlot (Vermeesch, 2010). Bedrock elevation is based on Bedmap2 data (Fretwell *et al.*, 2013). Grey areas illustrate the remnants of the former plateau paleosurface, recently exposed at different elevation levels in nearly all rock massifs (Stephenson, 1966; Skidmore & Clarkson, 1972; Marsh, 1985)

4.4.2. Published ZFT data

Lisker *et al.* (1999) published ZFT ages between 161±20 Ma and 214±24 Ma from seven locations in the southern and eastern Shackleton Range directly at or a few meters below the original paleosurface (Figure 12).

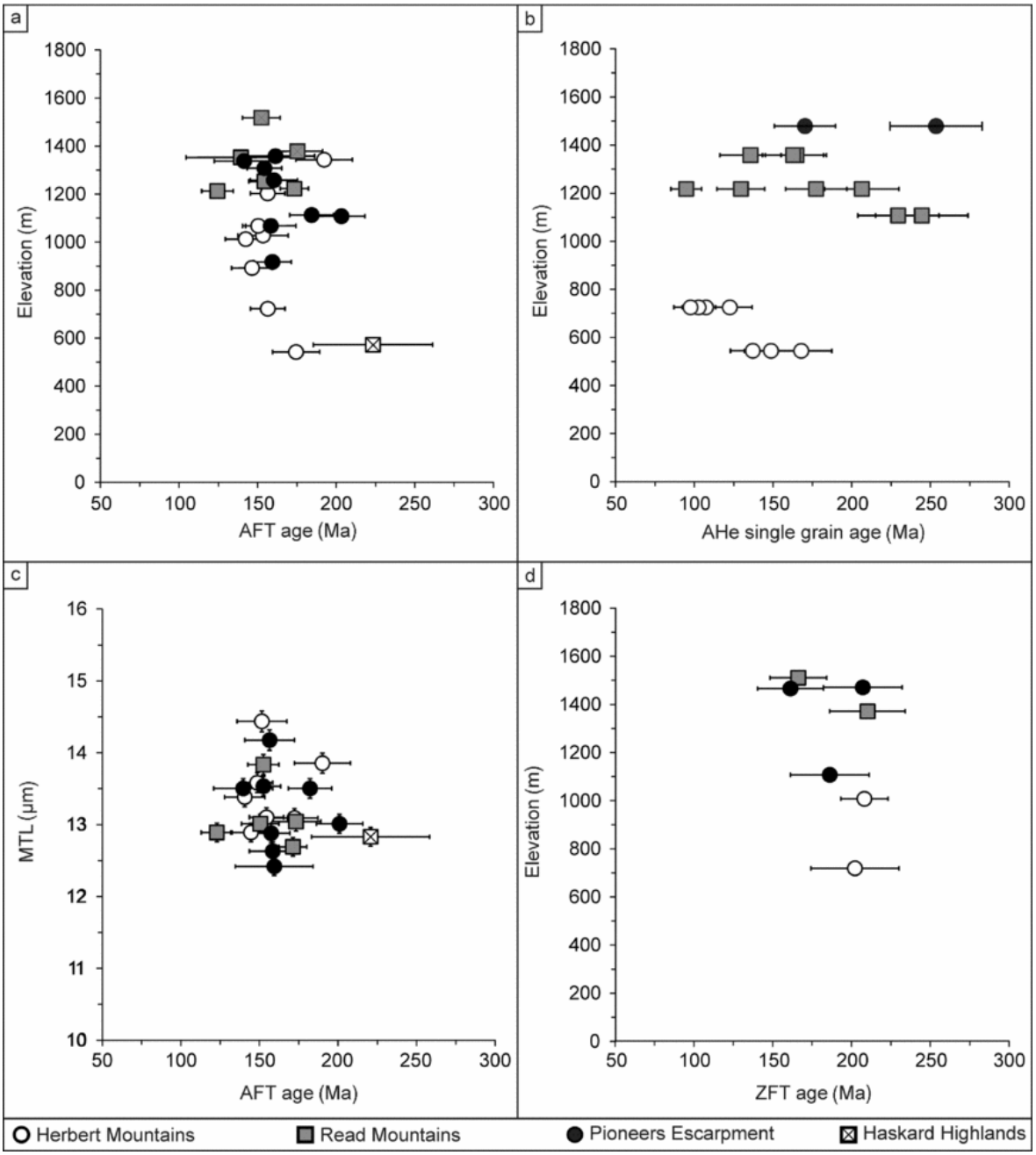

Figure 13: Thermochronological data plots. (a) Apatite fission track (AFT) age v. elevation. (b) Apatite (U-Th-Sm)/He single grain age v. elevation relation. (c) Mean track length (MTL) v. AFT age ('boomerang plot'). (d) Zircon fission track (ZFT) age v. elevation. Symbols refer to the distinct massifs of the Shackleton Range.

Mean ZFT ages cluster narrowly around ~190 Ma and are substantially younger than the time of rock formation and the latest Pan-African metamorphism (Will *et al.*, 2009). Furthermore, the reported high χ^2 probabilities refer to single-age populations for all samples; all ages

therefore reflect the same cooling event. The ages show no correlation with elevation and no trend between southern or northern units (Figure 13d).

4.4.3. AFT data

New AFT mounts were etched after the recommendations of Donelick *et al.* (2005). For etching conditions and calibration of existing mounts see Appendix B.1.5. AFT sample ages vary between 124±10 and 223±38 Ma. Mean track lengths vary between 12.4±0.1 and 14.4±0.2 µm, with standard deviations of 1.0–2.9 µm. The kinetic parameter D_{par} ranges from 1.73±0.35 to 2.38±0.25 µm. The ages of all individual samples pass the χ^2 test with high χ^2 probabilities, referring to a single-age population (Table 3; Figure 12, Figure 13a–c; Appendix B.1.5.2, Figure S 1 and Figure S 2). AFT ages of all samples are, within error, younger than the respective ZFT ages and postdate the last metamorphic overprint. There is no general correlation of AFT ages with mean track lengths, sample elevation or structural trends (Figure 13a, c). However, the age spread within the different mountain massifs is similar: sample ages of the Pioneers Escarpment range over 141–203 Ma (with relief differences Δh = 470 m), in the Herbert Mountains 142–193 Ma (Δh = 800 m) and in the Read Mountains 124–175 Ma (Δh = 385 m). The AFT age of 161±25 Ma from sample SH08 is little younger, but within error of the $^{40}Ar/^{39}Ar$ plateau age of 175±2 Ma obtained from the same site.

4.4.4. AHe data

Apatite grains from seven samples yielded 3–5 aliquots that match the criteria for AHe measurement (e.g. Farley, 2002; Appendix B.1.5.3). A total of 19 of the 25 measured aliquots were considered for further interpretation, whereas either ^{238}U or ^{232}Th concentrations of aliquots SH02#1–3, SH05#1–3 and W53#2 were below the 'hot blank' of 0.0058 ng U and 0.0106 ng Th. Single grain ages were calculated using the ^4He ingrowth equation, described by Farley (2002). F_T-corrected single grain ages range from 95±11 to 255±30 Ma and replicate within error in most of the samples, except for SH07 and W181 (Table 4; Figure 13b). Effective uranium (eU) values scatter strongly between 0.4 and 1082 ppm. F_T-corrected single grain ages do not seem to correlate with eU (r_{xy} = –0.29, r^2=0.08) and grain radius (r_{xy} = –0.27, r^2=0.08). This excludes substantial ^4He implantation from neighboring U-, Th- or Sm-rich minerals (Spiegel *et al.*, 2009) as well as enhanced ^4He retention due to radiation damage (Shuster *et al.*, 2006; Flowers *et al.*, 2009).

Table 3: Apatite fission track results

Sample / Location	Elev. [m] Lithology	N_D ρ_D [10^6 cm^{-2}]	N_s ρ_s [10^6 cm^{-2}]	N_i ρ_i [10^6 cm^{-2}]	$P(\chi^2)$ [%]	Age ± 1σ [Ma] N_G	MTL ± 1σ [µm] SD [µm]	N_L	D_{par} ± 1σ [µm] SD	U [ppm]
SH 02	1065	7249	164	248	97	158±16	13.93±0.18	13	1.90±0.02	15
Pioneers Escarpment	Meta Turbidite	1.46	7.44	11.22		30	1.24		0.18	
SH 03	1110	8274	337	512	95	184±14	13.51±0.18	102	2.13±0.03	17
Pioneers Escarpment	Meta Turbidite	1.71	12.79	19.43		20	1.35		0.17	
SH 05	1305	7249	380	587	100	154±11	13.54±0.18	95	1.89±0.02	37
Pioneers Escarpment	Gneiss	1.46	24.10	37.23		33	1.20		0.19	
SH 06	1255	8274	185	324	90	160±15	12.64±0.16	79	1.71±0.02	10
Pioneers Escarpment	Gneiss	1.71	7.39	12.93		20	1.89		0.17	
SH 08	1355	7249	68	101	100	161±25	12.43±0.16	19	2.18±0.03	25
Pioneers Escarpment	Rhyolitic. Tuff	1.46	16.22	24.10		28	1.50		0.28	
SH 09	1335	8274	84	167	100	141±19	13.51±0.18	66	2.09±0.03	8
Pioneers Escarpment	Gneiss	1.71	4.87	9.67		19	1.09		0.23	
SH 11	915	8274	322	565	65	159±12	12.89±0.17	83	2.67±0.03	22
Pioneers Escarpment	Gneiss	1.71	12.55	22.03		22	1.90		0.29	
SH 13	1105	7249	358	420	100	203±15	13.02±0.17	83	1.95±0.03	28
Pioneers Escarpment	Gneiss	1.46	27.76	27.87		31	2.29		0.21	

Table 3 continued

Sample / Location	Elev. [m] Lithology	N_D ρ_D [10^6 cm^{-2}]	N_s ρ_s [10^6 cm^{-2}]	N_i ρ_i [10^6 cm^{-2}]	P(χ^2) [%]	Age ± 1σ [Ma] N_G	MTL ± 1σ [µm] SD [µm]	N_L	D_{par} ± 1σ [µm] SD	U [ppm]
SH 15	1025	8274	140	257	100	153±16	14.44±0.19	8	2.38±0.03	9
Pioneers Escarpment	Gneiss	1.71	4.44	8.15		20	0.87		0.19	
SH 16	540	7249	225	350	99	174±15	13.11±0.17	94	1.97±0.03	35
Herbert Mountains	Gneiss	1.46	30.15	41.75		19	1.50		0.12	
SH 17	720	7249	396	604	56	156±11	13.11±0.17	82	1.98±0.03	16
Herbert Mountains	Gneiss	1.46	10.39	15.84		31	1.84		0.12	
SH 19	890	8274	216	413	34	146±13	12.90±0.17	5	2.26±0.03	28
Herbert Mountains	Gneiss	1.71	19.32	26.95		13	1.59		0.22	
SH 21	1065	8274	421	785	45	150±10	13.59±0.18	56	2.44±0.03	19
Herbert Mountains	Gneiss	1.71	12.37	23.07		22	1.11		0.28	
SH 22	1010	8274	176	348	96	142±13	13.39±0.17	4	2.06±0.03	14
Herbert Mountains	Gneiss	1.71	8.91	17.61		19	0.77		0.19	
SH 23	1340	8274	197	287	97	192±18	13.86±0.18	23	2.22±0.03	10
Herbert Mountains	Gneiss	1.71	9.10	13.25		20	1.62		0.24	
SH 24	1515	8274	250	462	68	152±12	13.02±0.17	57	2.04±0.03	15
Read Mountains	Meta Turbidite	1.71	9.42	17.40		21	1.72		0.20	

Table 3 continued

Sample / Location	Elev. [m] Lithology	N_D ρ_D [10^6 cm^{-2}]	N_s ρ_s [10^6 cm^{-2}]	N_i ρ_i [10^6 cm^{-2}]	P(χ^2) [%]	Age ± 1σ [Ma] N_G	MTL ± 1σ [µm] SD [µm]	N_L	D_{par} ± 1σ [µm] SD	U [ppm]
SH 25	1375	8274	195	311	91	175±16	13.05±0.17	2	2.15±0.03	26
Read Mountains	Meta Turbidite	1.71	14.69	23.43		15	1.29		0.31	
W18e	1350	7249	25	43	25	139±35	-	-	1.73±0.02	49
Read Mountains	Pegmatite	1.46	27.83	47.87		3	-		0.37	
W68	1220	8831	701	1168	56	173±9	12.70±0.17	101	2.58±0.03	57
Read Mountains	Gneiss	1.77	44.74	74.54		20	2.01		0.17	
W72	1250	8831	426	801	100	154±10	13.84±0.18	99	2.09±0.03	35
Read Mountains	Gneiss	1.77	24.53	46.13		20	1.63		0.18	
W181	1210	7249	234	450	25	124±10	12.90±0.17	48	1.89±0.02	44
Read Mountains	Granite	1.46	22.99	44.21		32	1.43		0.19	
W294	570	8831	62	80	100	223±38	12.84±0.17	101	2.24±0.03	8
Haskard Highlands	Gneiss	1.77	7.22	9.32		19	2.93		0.20	

ζ= 332±6 for IRMM 540 Dosimeter glasses (N. Krohne). Ages were calculated using the software TRACKKEY, Version 4.2.g (Dunkl, 2002). ρ_D, ρ_S, ρ_i, N_D, N_s and N_i denote the density and number of counted dosimeter, spontaneous and induced tracks; N_G is number of counted apatite grains; N_L is number of confined track lengths measured; P[χ^2] is probability, where P[χ^2]>5% indicates a single-age population (Galbraith, 1981); 1σ errors: conventional method; Green (1981).

Table 4: Apatite (U-Th-Sm)/He results

Sample	R_s [μm]	mass [mg]	^{4}He [ncc]	^{238}U+ ^{235}U [ppm]	^{232}Th [ppm]	^{147}Sm [ppm]	eU [ppm]	raw Age [Ma]	error (±1σ) [Ma]	F_T-factor	corr. age [Ma]	error (±1σ) [Ma]
Pioneers Escarpment												
SH 02 #1	80.94	0.005	0.112	0.000	0.000	6.060	0.006	-		0.14	-	-
SH 02 #2	52.55	0.003	0.100	1.858	0.000	1.547	1.860	-		0.71	-	-
SH 02 #3	41.98	0.001	0.048	0.000	0.000	5.696	0.006	-		0.13	-	-
SH 05 #1	41.05	0.001	0.005	0.000	0.000	1.052	0.001	-		0.13	-	-
SH 05 #2	45.99	0.002	0.173	4.638	0.000	13.41	4.651	-		0.67	-	-
SH 05 #3	47.68	0.002	0.025	0.000	0.000	0.877	0.001	-		0.13	-	-
SH 07 #1	72.01	0.005	0.919	7.180	0.744	8.244	8.848	198	12	0.78	255	30
SH 07 #2	115.00	0.022	0.094	0.208	0.066	1.493	0.357	147	9	0.86	171	20
Herbert Mountains												
SH 16 #1	73.13	0.006	1.928	23.40	6.483	20.34	37.89	113	7	0.77	148	17
SH 16 #2	70.30	0.004	1.551	25.73	6.729	26.71	40.78	106	7	0.77	138	16
SH 16 #3	58.69	0.002	0.143	3.423	3.505	5.123	11.25	123	8	0.73	169	20
SH 17 #1	82.53	0.006	0.274	3.527	1.890	16.299	7.763	86	5	0.80	107	13
SH 17 #2	87.62	0.010	0.858	7.926	3.374	18.251	15.48	80	5	0.82	98	12
SH 17 #3	84.14	0.010	0.786	6.260	1.549	11.412	9.729	100	6	0.82	123	15
SH 17 HB	74.70	0.003	0.436	12.78	6.554	22.635	27.43	81	5	0.79	103	12

Table 4: continued

Sample	R_s [μm]	mass [mg]	^{4}He [ncc]	^{238}U+ ^{235}U [ppm]	^{232}Th [ppm]	^{147}Sm [ppm]	eU [ppm]	raw Age [Ma]	error (±1σ) [Ma]	F_T-factor	corr. age [Ma]	error (±1σ) [Ma]
Read Mountains												
W181 #1	51.09	0.002	1.560	37.738	30.458	96.92	105.8	143	9	0.69	208	25
W181 #2	38.77	0.001	0.937	93.968	442.46	133.3	1082	55	3	0.58	95	11
W181 #3	61.97	0.004	3.906	44.466	178.13	83.71	442.1	93	6	0.72	130	15
W181 #4	47.15	0.001	2.775	311.05	119.49	150.9	577.9	118	7	0.66	178	21
W18e #1	36.01	0.001	0.246	27.64	0.586	32.21	28.98	93	6	0.57	162	19
W18e #2	39.93	0.007	0.361	27.44	70.11	23.59	183.9	99	6	0.60	166	20
W18e #3	43.95	0.001	0.611	36.11	59.04	24.26	167.9	86	5	0.63	136	16
W53 #1	42.67	0.001	0.338	15.67	7.761	16.73	33.01	144	9	0.62	231	27
W53 #2	47.87	0.002	0.153	3.175	0.000	5.303	3.180	-	-	0.68	-	-
W53 #3	45.30	0.001	0.219	7.994	0.245	7.876	8.549	161	10	0.65	246	29

^{4} He, ^{238}U, ^{232}Th and ^{147}Sm were measured at the Department of Sedimentology and Environmental Geology of the University in Göttingen, Germany. Sample SH17 HB was measured at the Department of Geosciences, University of Bremen. The eU concentration calculated according to Shuster *et al.* (2006), Flowers *et al.* (2009) and Spiegel *et al.* (2009). R_S: sphere radius; F_T-factor: α-ejection correction (Farley *et al.*, 1996). Discarded aliquots are formatted in italics (section 4.4.4).

Single grain ages of SH16, SH17 and W18e replicate within error. They are, together with the age of W181#2, slightly younger than corresponding AFT ages. All other single grain ages are older than corresponding AFT and ZFT ages. Such 'cross-over' ages seem typical for old, slowly cooled metamorphic rocks (Flowers *et al.*, 2009). Ternary U–Th–He plots illustrate large intra-sample variations of isotopic compositions for the aliquots with cross-over AHe ages (Appendix B, Figure S 3). Inhomogeneous fission track distributions within some apatite grains implies zoning of U (and probably also Th) concentration, which results in over- or under-correction of alpha-ejection (Fitzgerald *et al.*, 2006). As a consequence, aliquots with divergent intra-sample isotopic ratios from the replicating group (i.e. outside the 2σ error) and aliquots with cross-over AHe single grain ages are discarded from further interpretation.

The samples from the Herbert Mountains (SH16#1–3, SH17#1–HB) are located within a short distance of each other. They show consistent isotopic ratios and have similar ages that correlate tightly with AFT ages. The AHe ages of the whole sample suite do not correlate with elevation or with structural or lithological trends of the mountain massifs (Figure 13b).

4.4.5. Thermal history modeling and interpretation

Thermal history modeling is a powerful tool to quantitatively deduce best-fitting time–temperature paths from the combined thermochronological dataset, covering a temperature range of 40–300°C. Modeling was conducted with HeFTy software, version 1.8.3 (Ketcham, 2005). The program independently computes random time–temperature paths by applying various kinetic models and statistical tests. Modeled thermochronological data are compared to the observed thermochronological data, and characterized according to their matching ('goodness of fit'). For this study we selected AFT samples comprising more than 50 confined track length measurements, and more than 19 dated single apatite grains if available, supplemented by AHe (up to three independent aliquot data) and ZFT age data. Sixteen samples from four mountain massifs matched these criteria. All input and model parameters for time–temperature history modeling are provided in the Apendix B (Table S 3 - Table S 5). Thermal history modeling follows the approach described by Prenzel *et al.* (2013). It relies on the basic assumption that a morphologically homogeneous mountain range topped by a paleosurface results from uniform exhumation processes. Exhumation stages are identified by similar timing of cooling episodes for the whole sample suite, while maximum paleotemperatures of individual samples may vary. At first, random thermal history paths produce best-fitting time–temperature paths for all samples individually by inverse HeFTy modeling. Afterwards, the best composite thermal history of individual HeFTy forward models serves as the base for a generic thermal history of all samples.

'Inverse modeling' was conducted on each sample to derive various best-fitting time–temperature paths according to 'constraint boxes' set on the basis of thermochronological data and geological markers (Appendix B, Table S 5). Geological time and temperature markers for the paleosurface position are: (1) initial basement burial of tillites imply surface temperatures at ~300 Ma; (2) ZFT data indicate cooling through the zircon partial annealing zone (~320–180°C) at ~200 Ma (ZPAZ; Yamada *et al.*, 1995); (3) deposition of Jurassic volcaniclastic rocks mark Jurassic surface position (Jurassic atmospheric temperature was c. 20°C; Chandler *et al.*, 1992); and (4) recent surface temperatures with consideration of the orographic gradient are required due to recent surface exposure (Appendix B, Table S 6). All inverse modeling specifications were put into an input ASCII-textfile ('batch mode') to warrant equal modeling conditions for each sample run. A total of 250000 individual thermal history paths were tested and areas of the statistical best fitted paths were outlined.

Subsequent 'forward modeling' aimed to merge the individual thermal histories to one common, consecutive scenario for the whole sample suite. Resulting representative time–temperature paths rely on the distinct best-fit inverse modeling results and compelling constraints, such as timing of temperature changes and spatial relationships.

Inverse time–temperature models of all samples are very similar, with only minor variation. They imply: (1) fast cooling ~200 Ma to Jurassic surface temperatures; (2) reheating during 175–130 Ma; and (3) cooling during 130–55 Ma to low temperatures (Appendix B, Figure S 4). Common time–temperature paths obtained from *forward* modeling favor rapid cooling from 300–320°C to temperatures of 20±10°C between 205 and 175 Ma, subsequent reheating to 60–95°C at 170 Ma and to 70–100°C at 135 Ma (Figure 14). Temperatures of all samples decrease below 40°C at 120 Ma. Furthermore, thermal history modeling of two samples with multiple AHe age data tentatively support a temperature increase of up to 50°C during 94–33 Ma, which is also integrated into thermal history models without AHe age information. Final cooling to recent surface temperatures is interpolated on the basis of the best fits of the thermochronological modeling program and the achievement of a common history valid for all samples. This scenario suggests rapid cooling from up to 50°C to 5°C at 25 Ma and ongoing surface cooling according to polar conditions.

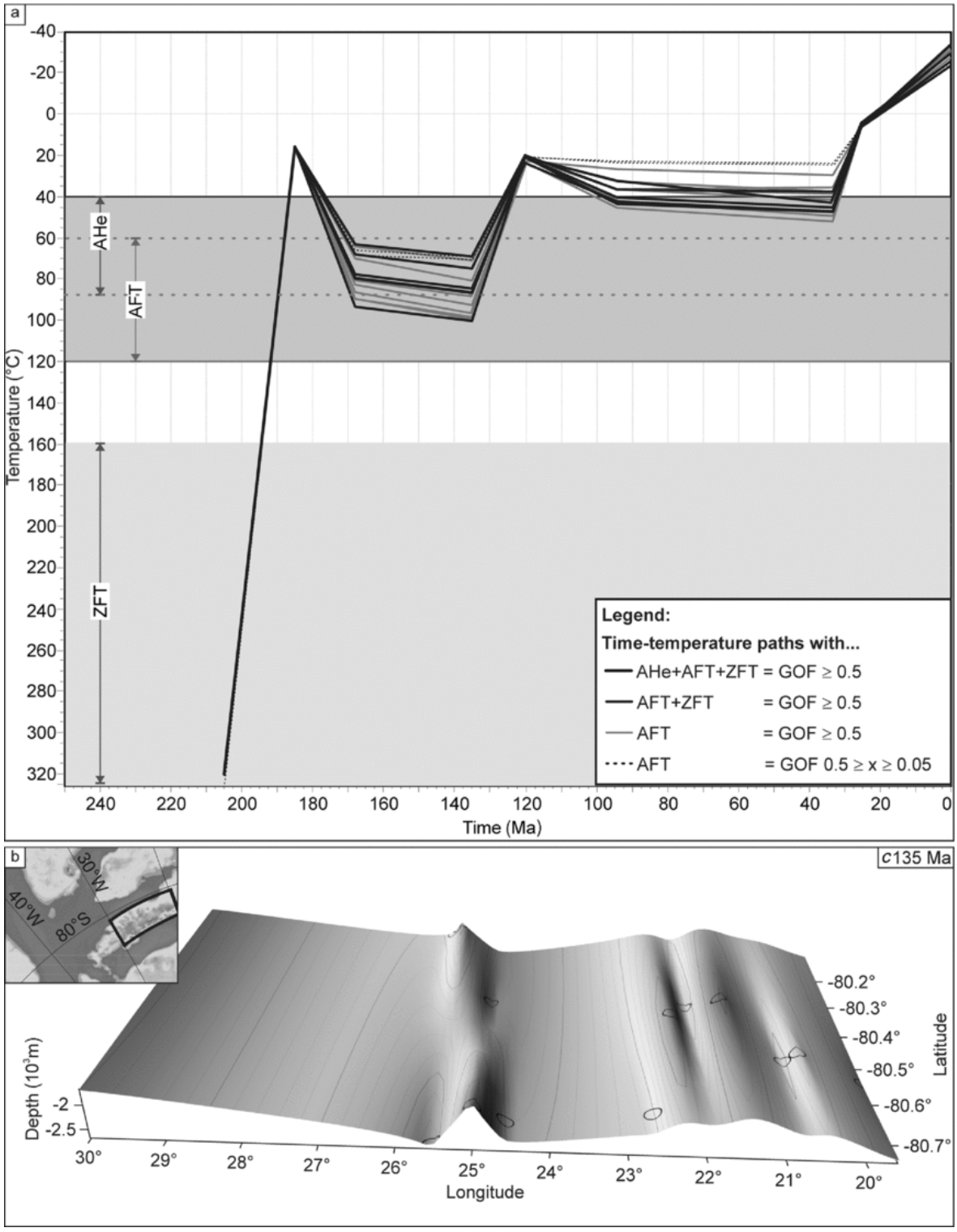

Figure 14: (a) Compilation of common thermal history models from the Shackleton Range modeled with HeFTy. Grey areas illustrate the temperature sensitivity zones of the different thermochronometers: (U-Th-Sm)/He (AHe) over the range 40–85°C (Wolf *et al.*, 1996), apatite fission track (AFT) over 60–120°C (Wagner, 1972) and ZFT over 160–320°C (Yamada *et al.*, 1995). For thermal history inversion of the particular samples see Appendix B (Figure S 3). (b) Interpolated 3D map of maximal depths of the Shackleton Range Basin at ~135 Ma based on thermal history models. Circles indicate the sample positions. The map infers a general N–S-aligned trend of troughs, suggested here likely to represent N–S-trending faults. This is well in line with the geological observations for the Weddell Sea and Coats Land region (e.g. Brommer *et al.*, 1999; Ferris *et al.*, 2000). Thick rectangle in the inset provides an overview of the interpolated area. For a more detailed orientation according to sample locations and recent (sub-) ice morphology, see Figure 12.

4.5. Exhumation and long-term landscape evolution of the Shackleton Range

4.5.1. Transantarctic Basin

The Shackleton Range formed part of the active outer Panthalassan margin of Gondwana since the amalgamation of the supercontinent. Pan-African molasse fanglomerates and sandstones are preserved in the Ordovician Blaiklock Glacier Group in the western Shackleton Range (Clarkson & Wyeth, 1983). Duration and original thickness of the respective basin are not constrained and cannot be specified by our data, but the nonconformity of Permo-Carboniferous tillites on basement indicates that most of the Blaiklock Glacier strata must have been eroded during late Paleozoic time.

The glacial deposits in the eastern Shackleton Range are key to the late Paleozoic–early Mesozoic evolution of the Weddell Sea region. Such tillite strata within Beacon rocks can be traced along the whole Panthalassan Gondwana margin in the adjacent Theron Mountains, Whichaway Nunataks, Pensacola Mountains and Ellsworth-Whitmore Mountains, but also throughout the massifs of the Transantarctic Mountains and in Dronning Maud Land and Namibia (Collinson *et al.*, 1994; Isbell *et al.*, 2008). They rest either above a nonconformity on basement or (e.g. in the central Transantarctic Mountains) disconformably on Devonian strata. Deposition of the largely unfossiliferous tillites commenced diachronously between Late Carboniferous time in the Ross Sea sector of the Transantarctic Mountains and Permian time in the Weddell Sea region. These sediments are referred to as the Pagoda Formation at the base of the Victoria Group, that piles up to a 1500 m thick Permian and 1200 m Triassic rock column in the central Transantarctic Mountains (Barrett, 1992). They were deposited in the Permo-Triassic Transantarctic Basin, a series of narrow, subduction-related epicontinental- and back-arc basins along the Panthalassan margin of Gondwana (Collinson *et al.*, 1994; Figure 15).

The Permo-Triassic succession of the Shackleton Range was originally far thicker than the present remnants. Burial depths can be determined from maximum paleotemperatures derived from geochronological and thermochronological data. On the one hand, the uniform ZFT age cluster at ~190 Ma (Lisker *et al.*, 1999) indicates a complete reset of the ZFT system. Depending on the degree of α damage, fission tracks in natural zircons are completely annealed at temperatures of 240–350°C during a heating duration of 10–25 Ma (Yamada *et al.*, 1995; Garver *et al.*, 1999; Rahn *et al.*, 2004). On the other hand, amphibole and biotite ^{40}K–^{39}Ar ages of basement rocks of 499–598 Ma reflect post Pan-African cooling without any indication of ^{39}Ar loss (Buggisch *et al.*, 1994b; Brommer, 1998; Brommer & Henjes-Kunst, 1999), and limit heating to the closure temperature of the biotite ^{40}K–^{39}Ar system, which is ~350±50°C (e.g.

Purdy & Jäger, 1976). A combination of the thermal constraints and thermal history modeling therefore suggests heating of the Permian surface to Late Triassic temperatures of 240–350°C before rapid cooling to surface temperatures commenced around the time of the Karoo/Ferrar emplacement.

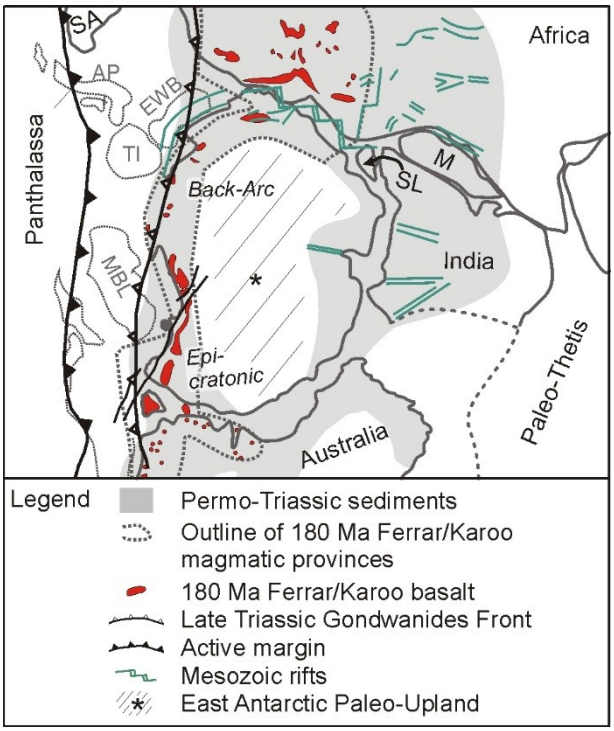

Figure 15: Paleogeographic and tectonic reconstruction of Permian–Early Jurassic Gondwana according to Veevers (1988), Collinson *et al.* (1994) and Harrowfield *et al.* (2005). Position of the Ellsworth Whitmore Block (EWB) according to Grunow *et al.* (1991), Grunow (1993), Flowerdew *et al.* (2012) and Elliot *et al.* (2015). AP–Antarctic Peninsula; M–Madagascar; MBL–Marie Byrd Land; S–South America; SL–Sri Lanka; TI–Thurston Island.

Permo-Triassic burial depths cannot be calculated in detail since the Paleogeothermal gradient of Coats Land is not yet known. However, the evolution of a volcanic back-arc basin in intermediate distance to the Shackleton Range would likely have enhanced heat flux and resulted in an increased gradient. The paleogeographic reconstruction of Collinson *et al.* (1994) locates the Shackleton Range ~500 km from the magmatic trench. Recent geothermal gradients of volcanic back-arc basins (e.g. north Sumatra Basin, 400 km from the trench) are 35–63°C km^{-1}, with an average of 44°C km^{-1} (Aadland & Phoa, 1981; Humphreys *et al.*, 1994). Application of a geothermal gradient of 35–60°C km^{-1} stacks a sediment column of 4–10 km on the basement of the Shackleton Range. Even the minimum estimate of a 4 km thick Permo-Triassic Beacon overburden exceeds the thickness of the Victoria Group in the Transantarctic Mountains. It implies a systematic increase of this sequence along the Panthalassan margin from the present Australian towards the present African segment. The composition of this vanished rock section must necessarily remain speculative, but timing and thickness correlate well with the deposition pattern in adjacent regions. The abundance of calc-alkaline vol-

canic detritus in tightly to non-folded Permian sequences in central Transantarctic Mountains, Ellsworth-Whitmore Mountains and in the Theron Mountains marks the evolution of a volcanic forearc and back-arc basin system between the present Ross Sea and the proto-Weddell Sea region during the Permian–Late Triassic Gondwanide Orogeny with migration of the fold belt towards the east (Panthalassan margin by Collinson *et al.*, 1994; Curtis, 2001; Flowerdew *et al.*, 2012; Elliot *et al.*, 2015). Coats Land, including the Shackleton Range, the Whichaway Nunataks and Theron Mountains, represents a main depocentre within an extensive Permo-Triassic Transantarctic Basin (system).

Our thermal history models and recognition of Ferrar/Karoo volcaniclastics suggest sudden Late Triassic–Early Jurassic cooling in the Shackleton Range until re-exposition of the Middle Ordovician–Carboniferous paleosurface (Figure 14). This exhumation episode is obviously caused by rapid erosion of almost the complete Permo-Triassic cover due to basin inversion. Near-surface emplacement of Ferrar/Karoo sills within the Permian strata of the Theron Mountains (Hutton, 2009) proves coeval exhumation there, and can also be assumed for the Whichaway Nunataks. Late Triassic basin inversion appears to be part of a distinctive erosional episode observed between at least 210 and 195–190 Ma along the whole length of the Transantarctic Mountains that separates two phases of deposition. This stage was associated with considerable magmatic activity, at first silicic then mafic, represented by Late Triassic–Early Jurassic deposition of volcaniclastic sandstones and rhyolitic tuffs followed by extrusion of the tholeiitic Ferrar basalts (and its intrusive correlatives) at ~180 Ma in the Transantarctic Mountains (e.g. Collinson *et al.*, 1994; Elliot & Fleming, 2000; Elliot *et al.*, 2007; Elsner *et al.*, 2013).

4.5.2. Weddell Sea rifting

The Panthalassan margin of Gondwana was subject to Early Jurassic extension, accompanied by bimodal igneous activity within the previous Permo-Triassic Transantarctic Basin (Dalziel *et al.*, 1987; Collinson *et al.*, 1994; Elliot & Fleming, 2000; this study). In the Shackleton Range, extension and bimodal igneous activity is marked by the ejection of silicic volcaniclastic rocks and their deposition upon a few tens of meters thick Permo-Carboniferous basal strata overlying the paleosurface, and the emplacement of almost vertical N–S-trending mafic dykes at 186–179 Ma (Spaeth *et al.*, 1995; Brommer & Henjes-Kunst, 1999; Brommer *et al.*, 1999). Our thermal history models record subsequent Jurassic–Early Cretaceous basement heating to temperatures up to 100°C. This temperature increase cannot be explained by enhanced heat flux from magmatic activity as the Jurassic dykes in the Shackleton Range are just a few meters thick and not younger than ~179 Ma (Spaeth *et al.*, 1995).

Instead, this long-term temperature increase implies burial of the basement, potentially in a structurally bound basin. Long-lasting subsidence, extension and crustal thinning of the Weddell Sea embayment is generally confirmed by stretching factors of 1.5–2 and by the formation of contemporaneous rift structures such as the Filchner Rift (Studinger & Miller, 1999; Ferris *et al.*, 2000; King, 2000; Jordan *et al.*, 2013). The predominantly N–S- to NE–SW-oriented magnetic trends of Weddell Sea embayment and offshore Weddell Sea (Hübscher *et al.*, 1996a, b; Golynsky & Aleshkova, 2000; Jordan *et al.*, 2013) prove orthogonal extension. Spaeth *et al.* (1995), Brommer & Henjes-Kunst (1999) and Brommer *et al.* (1999) report similar trends of dykes and normal faults from the northern Shackleton Range.

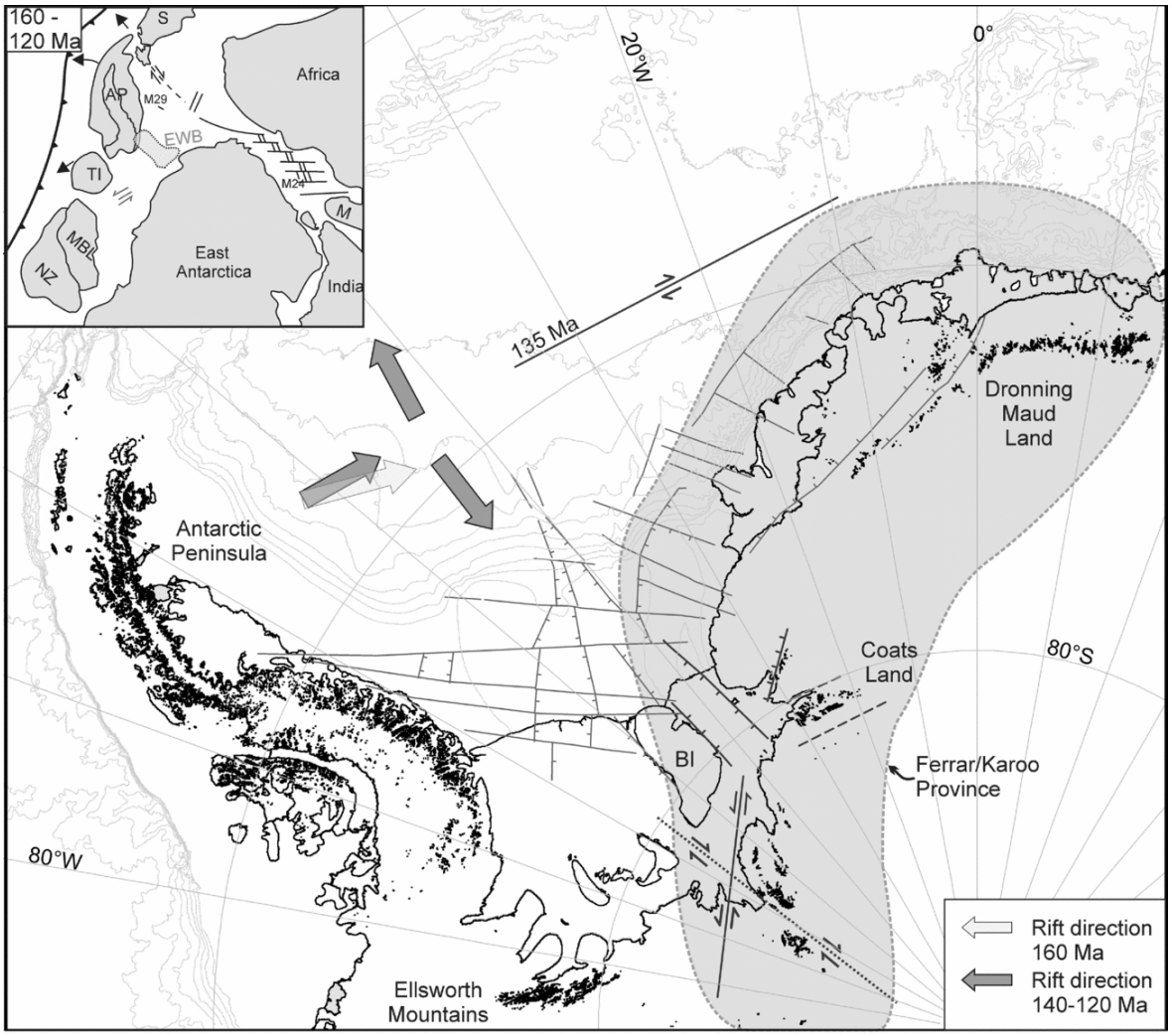

Figure 16: Compilation of offshore faults, magnetic anomalies and general rifting directions during Jurassic and Cretaceous time (Brook, 1972; Marsh, 1985; Peters, 1989; Kristoffersen & Hinz, 1991; Hübscher *et al.*, 1996a; Leitchenkov *et al.*, 1996; Ferris *et al.*, 2000; Kovacs *et al.*, 2002; König & Jokat, 2006; Jordan *et al.*, 2013). Outline of the Ferrar/Karoo province after Elliot (1992). Stippled lines indicate inferred faults. Contour lines originated from the Antarctic Digital Database. Inset: overview of the plate configuration and structures during 160–120 Ma, modified after Martin (2007). Position of the Ellsworth Whitmore Block (EWB) according to Grunow *et al.* (1991). Abbreviations as for Figure 15.

This structural coincidence and our thermal histories place the Shackleton Range in a basin that became involved later in the rifted margin of the Weddell Sea. Thermochronological data

are not available from the Whichaway Nunataks and the Theron Mountains, but NE–SW-aligned faults are consistent with this scenario (Figure 16).

A depocentre of similar spatial trend, the Mesozoic Victoria Basin, evolved contemporaneously along the Transantarctic Mountains (Lisker & Läufer, 2013). The coexistence between Mesozoic Victoria Basin and the Jurassic basin along the eastern Weddell Sea margin favors a regional extension/transtension regime along the Panthalassan margin during Jurassic time, and may indicate initial passive margin transformation. Paleogeothermal gradients within the Mesozoic Victoria Land Basin were calculated by means of combined thermochronological and organic maturity data by Prenzel *et al.* (2014). They decrease from ~45°C km^{-1} during the Ferrar event at ~180 Ma to conventional 25°C km^{-1} during the Cenozoic. For this gradient and a Jurassic surface temperature of 15–20°C (e.g. Chandler *et al.*, 1992), maximum paleotemperatures of 70–100°C (Figure 14a) refer to 2.0–3.4 km of Late Jurassic overburden. Varying burial depths may be related to a pre-rift topographic surface characterized by narrow N–S-trending valleys and ranges (Figure 14b), perhaps induced by the Jurassic stress regime.

The post-Gondwana thermal history of the Shackleton Range is dominated by Early Cretaceous uniform cooling from 70–100°C to below 40°C. Fast erosion of the sedimentary overburden and basin inversion commencing at ~135 Ma correlate with a significant change of spreading direction and plate movements in the Weddell Sea at 130 –135 Ma (e.g. Grunow *et al.*, 1991; Kristoffersen & Hinz, 1991; Kovacs *et al.*, 2002; König & Jokat, 2006). This event led to stagnation of the N–S-trending rifts, including the Filchner Rift (Kristoffersen & Hinz, 1991; Martin, 2007) and the initiation of sinistral transtensional movement in the Weddell Sea (Kristoffersen & Haugland, 1986). Plate motion changes offshore probably modified the onshore stress regime oblique to the rift structures of the Shackleton Range. Such a transition to oblique extension relative to basin margin faults often results in basin inversion (De Paola *et al.*, 2005), and incorporated the Shackleton Range into the Weddell Sea rift shoulder. A further active sinistral strike-slip movement between the Ellsworth-Whitmore Block and East Antarctica can be traced at the Filchner Rift and implies that the Shackleton Range was bordered by two divergent strike-slip faults trending oblique to the faults (Fig. 11; Grunow, 1993; Jordan *et al.*, 2013). We suggest that oblique transtension (partitioned transtension) initiated basin inversion in the Shackleton Range.

4.5.3. Landscape evolution since Cretaceous time

Implementation of the AHe age information into the thermal history models indicates renewed heating of the paleosurface on the Shackleton Range to temperatures of ~50°C during

~120–33 Ma, referring to shallow burial in the order of ~1 km for a conventional geothermal gradient. Burial beginning at 120 Ma could be linked with the termination of the Ellsworth-Whitmore movement relative to East Antarctica and protracted extension, related to ongoing rifting and dispersion of Gondwana (e.g. Kristoffersen & Haugland, 1986; Hübscher *et al.*, 1996a, b; Leitchenkov *et al.*, 1996; Martin, 2007). The presence of a shallow Cretaceous basin close to the Weddell Sea embayment places the surface of the Shackleton Range near paleo sea-level elevations. It challenges the hypothesis of the Eocene–Oligocene upland area in the Weddell Sea embayment by Wilson *et al.* (2012) that relies on the interpolation of largely uncertain stratigraphic units from geophysical properties in the Weddell Sea.

Final cooling from ~50°C to surface temperatures beginning at 35 Ma implies the erosion of the Late Cretaceous–Paleogene sedimentary overburden and provides the minimum time constraint for basin inversion and uplift of wide parts of Coats Land. These processes do not appear to be associated with any significant tectonic event in the immediate vicinity, but could be related to large-scale plate processes of either the separation between Patagonia and the Antarctic Peninsula (Livermore & Woollett, 1993) or the enhanced activity along the West Antarctic Rift system and uplift of the Transantarctic Mountains (Behrendt & Cooper, 1991; Prenzel *et al.*, 2014). A similar influence of far-field tectonics on passive margins long after break-up is confirmed by the late reactivation of regional faults along African and Brazilian passive margins (Gallagher & Brown, 1997). In this context, even minor far-field effects of remote tectonism would have been sufficient to initiate exhumation of the Shackleton Range.

Furthermore, the Eocene–Oligocene transition at 34 Ma marks a time of a major climate change that triggered the permanent glaciation of Antarctica and created an enormously efficient glacial erosion regime until Miocene time (Robert & Maillot, 1990; Poole *et al.*, 2005; Thorn & DeConto, 2006). Swift Neogene sedimentation of thick transitional continental and glacial deposits in the offshore Weddell Sea manifests as enhanced sediment supply due to increased onshore erosion which was, in turn, climatically influenced (Rogenhagen *et al.*, 2005; Huang *et al.*, 2014). Fast exhumation of the little consolidated Cretaceous and Paleogene basin deposits again exposed the paleosurface on the Shackleton Range, with only some protected remnants of its Permo-Triassic and Jurassic cover remaining preserved, and triggered uplift and relief formation. Subsequent surface modification and relief development is assumed to have been controlled by fluvial and glacial bedrock incision along pre-existing faults (Sugden *et al.*, 2014) and seem to be restricted to it. The rather homogenous, slight dip of the paleosurface and sedimentary remnants indicates late tilting. Tilting, as well as the disection and displacement of the paleosurface patches, were likely provoked due to onwards uplift and associated with reactivation of local faults, now hosting local glaciers (Figure 7).

The uplift of the Shackleton Range to recent elevations appears to be mostly triggered by composed isostatic response to the removal of the sedimentary overburden, massive bedrock incision and vertical down-wearing close to valley/trough margins.

4.6. Conclusions

The study demonstrates the great potential of combined petrologic, geochemical and geochronological data to determine age and setting of unfossiliferous sequences and to serve as key constraints for the age determination of paleosurfaces and thermal history modeling of thermochronological data. It also helps to substantially improve the resolution of the thermal history models.

The Shackleton Range was originally postulated to have been exposed during most of the Phanerozoic Eon, and to have experienced very little deposition during this time. Episodic exhumation and uplift was mainly assumed to have occurred during Jurassic and Cretaceous times. However, this scenario was rather unusual for the Panthalassan margin of Gondwana, and could be thoroughly revised in this study.

Instead, a regional erosion surface, similar to the Kukri peneplain on the Transantarctic Mountains, established soon after truncation of the Pan-African Orogen. Contrary to traditional perception, this surface was buried for most of the time beneath a kilometer-thick sedimentary cover, and became exposed only episodically. Permo-Triassic burial to depths of 4–10 km within the 'Transantarctic Basin' identifies this basin as a truly trans-Gondwanan feature with a general trend of increasing basin depth towards the Weddell Sea.

There are also striking similarities with the evolution of the Mesozoic Victoria Basin in the Ross Sea region (Lisker & Läufer, 2013). Both basins are characterized by long-lasting basin extension initiated by the Jurassic Ferrar Event, diffuse crustal thinning accompanying the disintegration of Gondwana, and a final switch to discrete rifting and basin inversion. Rifting of the Weddell Sea commenced during Early Cretaceous time, while the Mesozoic Victoria Basin persisted until the late Eocene Epoch.

Inversion of both the Transantarctic Basin and the Jurassic (proto-) Weddell Sea Basin were controlled by regional-scale tectonic processes. In contrast, final exhumation and uplift of the Shackleton Range from early Oligocene time seems to be mainly driven by climatic influence, primarily by the glaciation of the Antarctic continent and resulting fast down-wearing, glacial incision, and the respective isostatic response. In summary, the geological history of the Shackleton Range revealed here is not in contrast to the established evolution of the active Panthalassa margin; rather, it represents a typical example for the transition from an active to passive margin setting along the outer rim of Gondwana (Figure 17).

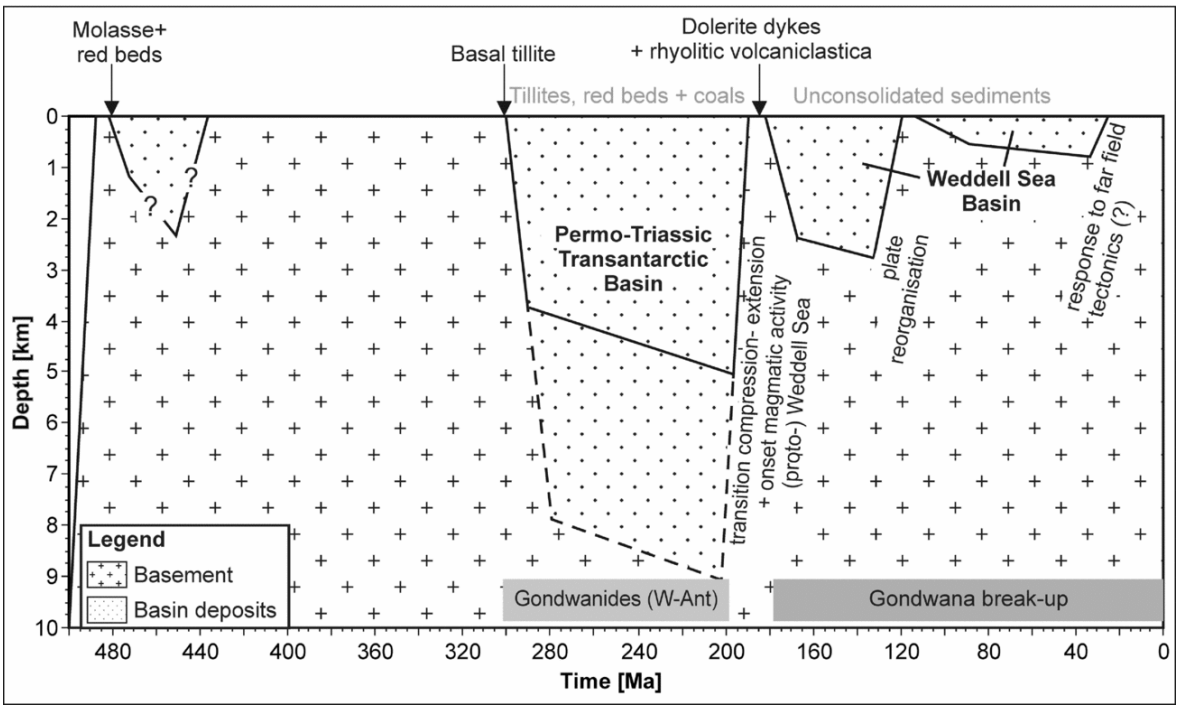

Figure 17: Conclusive sketch of the post Pan-African geological history for the uppermost crust of the Shackleton Range, based on geological and geomorphological evidence and the thermal history models. Arrows indicate the timing of deposition of the sediments and light grey text the inferred basin deposits. Bold text highlights the individual basins. Text within the figure and the boxes at the bottom mark the geodynamic background and the tectonic history for the (proto-) Weddell Sea/Coats Land. For detailed information see section 4.5.

4.7. Acknowledgements

This work was supported by the German Research Foundation (DFG) in the framework of the priority program SPP 1158 'Antarctic Research with comparative investigations in Arctic ice areas' by grants LI 745/15 to F. Lisker and LA 1080/9 to A. Läufer. U. Schnellbach, M. Olesch and F. Henjes-Kunst collected the rock samples during the GEISHA and EUROSHACK Expeditions of the Federal Institute for Geosciences and Natural Resources (BGR). We thank R.X. Fischer and the crystallography research group of the University of Bremen for XRD analyses. P. Stutz and S. Heidrich (University of Hamburg) are acknowledged for the XRF analysis and Y. Kapusta (Actlabs Canada) for discussions on the $^{40}Ar/^{39}Ar$ dating results. S. Boger, G. Eagles and W. Jokat are acknowledged for discussions and valuable comments, and M. Studinger for providing aerial photographs of the Shackleton Range. The comments of an anonymous reviewer are gratefully acknowledged. We thank M. Allan for editorial handling.

5. Passive margin formation in Sør Rondane (East Antarctica)

Nicole Krohne[1], Frank Lisker[1], Andreas Läufer[2], Antonia S. Ruppel[2], Joachim Jacobs[3,4], Marlina A. Elburg[5], Detlef Damaske[2] and Cornelia Spiegel[1]

[1]University of Bremen, Department of Geosciences, P.O. Box 330440, D-28334 Bremen, Germany

[2]Federal Institute for Geosciences and Natural Resources (BGR), Stilleweg 2, D-30655 Hannover, Germany

[3]University of Bergen, P.O. Box 7800, 5020 Bergen, Norway

[4]Norwegian Polar Institute, Fram Centre, N-9296 Tromsø, Norway

[5]University of Johannesburg, P.O. Box 524 Auckland Park 2006, Johannesburg, South Africa

Keywords

Exhumation, transpression, Gondwana break-up, passive margin

Abstract

Sør Rondane in eastern Dronning Maud Land is located at the junction of Africa/Madagascar and India/Sri Lanka that separated during Gondwana break-up. The recent landscape represents a passive margin setting, comprising an escarpment-bound and highly elevated massif topped by plateau remnants or intensely ice-molded peaks. Here we study the Phanerozoic geological and long-term landscape evolution of western Sør Rondane by means of thermochronological data supplemented with brittle structural inventory and geomorphological implications. Apatite fission track (AFT) ages vary between 136 and 226 Ma, with mean track lengths of 11.6 to 13.5 µm and broad track length spectra. Apatite (U-Th-Sm)/He (AHe) ages vary between 98 Ma and 237 Ma. The post Pan-African brittle structural inventory comprises conjugate fault system with NE–SW left lateral, and NNE–SSW right lateral faults, pointing to a WNW–ESE paleostress direction. The direction of faults is similar to that of offshore faults and to the strike of spreading axes and evidences far field influence of extension. Thermal history modeling of these data indicates at least two post-Permian long-term reheating phases to maximum temperatures of 110°C that were interrupted by cooling phases at 215 Ma, 140 Ma and ~50–40 Ma. The first reheating is related to a shallow Permo-Triassic basin, inverted at 140 Ma and post-Jurassic reheating is linked to burial in a shallow continental basin. Post-Jurassic basin formation was likely supported by faulting. Substantial exhumation, morphological modification, uplift and faulting occurred in the last 30 Ma, superimposed by isostatic readjustments and crustal response to downwearing, bedrock incision, and adjacent glacial load.

5.1. Introduction

Sør Rondane is located between 22–28°E and 71–72.5°S in the eastern part of Dronning Maud Land (DML), Antarctica (Figure 18). Sør Rondane is 180 km in length and 100 km in width. The nearest rock-exposed regions are the mountain ranges in central DML, including the Schirmacher Oasis in the west and the Belgica-Yamoto Mountains and the Lützow-Holm Bay in the east. DML forms a passive margin region at the South Atlantic and Indian Ocean facing the African continent.

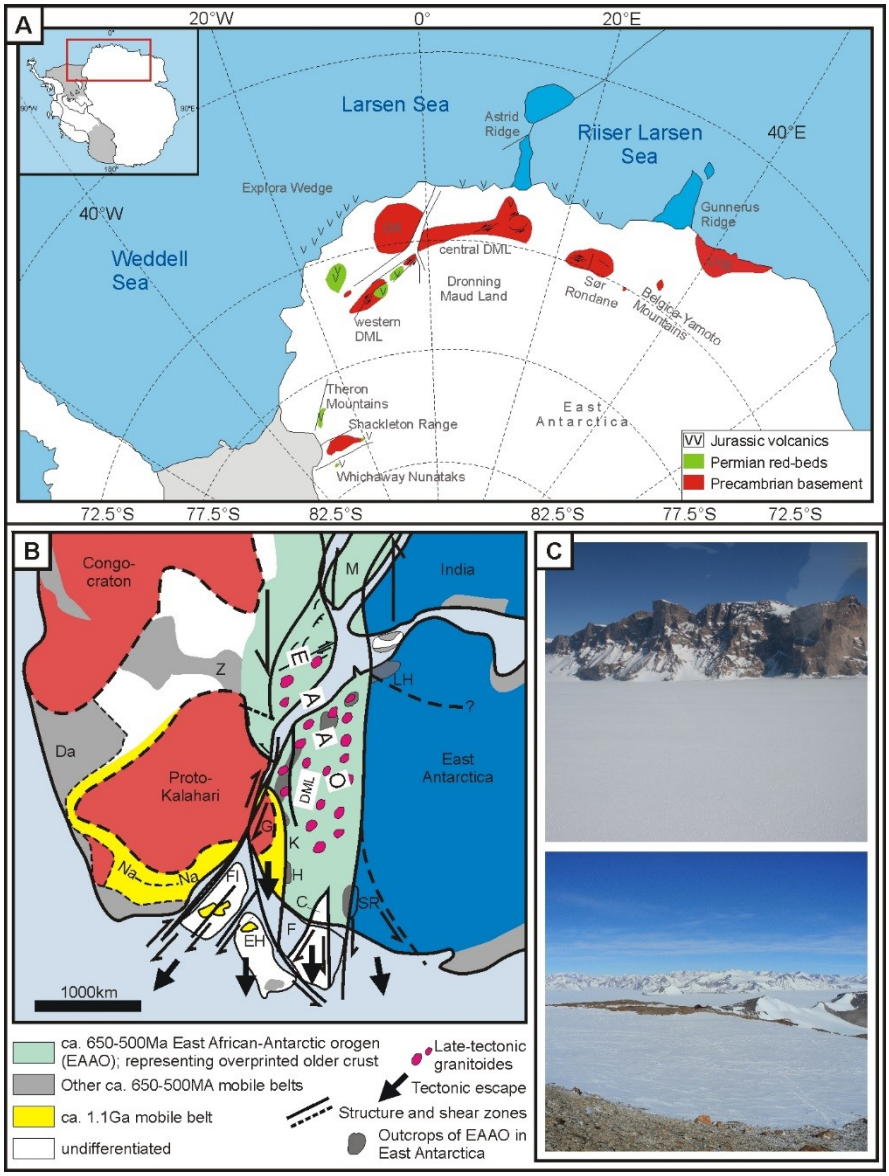

Figure 18: (a) Geographic and geological overview of DML and adjacent regions redrawn after (Bauer *et al.*, 2003b). Major offshore features are outlined. Solid lines indicate major brittle tectonic features. (b) Paleogeographic and tectonic overview of central Gondwana at ~550–500 Ma, redrawn after (Jacobs & Thomas, 2004). Abbreviations: C: Coats Land, Da: Damara belt, DML: Dronning Maud Land, EH: Ellsworth-Haag block, F: Filchner Block, FI: Falkland Islands, H: Heimefrontfjella, K: Kirwanveggen, LH: Lützow Holm Bay, M: Madagascar, Na: Natal belt, Z: Zambesi belt. (c) Field photographs showing examples of flat and high-standing paleosurface remnants and alpine type morphologies.

It is characterized by a fault bound highland relict trending parallel to the shoreline ~200 km off the initial ridge. The highland is often topped by plateau surfaces or alpine type peaks that are dissected by mainly ~N–S trending glaciers (Näslund, 2001).

The plain in front of the escarpment is buried by a thick ice cover and positioned 1000 m below sea level (Fretwell *et al.*, 2013). DML was once situated in the hinge of Gondwana directly at the locus to Africa/Madagascar and India/Sri Lanka and hence represents a key area for studying the evolution of supercontinent dispersal (e.g. Yoshida *et al.*, 1992; Leinweber & Jokat, 2012; Veevers, 2012). Here, dispersal of Gondwana initiated between eastern DML and Mozambique (Jokat *et al.*, 2003) and makes the conjugate margin pair to the oldest one of Gondwana.

The regional geological history throughout DML is similar since at least 650–500 Ma, when the Precambrian basement was metamorphically and structurally reworked as a consequence of Gondwana amalgation. Prominent structural features of DML are syn-to late orogenic major strike-slip faults trending sub-parallel to the length of the highlands (e.g. Jacobs & Thomas, 2004; Figure 18). The Phanerozoic geological record is poor and restricted to isolated and thin remnants of molasse-type rocks, upper Permian red-beds and Jurassic magmatic rocks. Hence, the long-term Phanerozoic geological evolution, including the evolution of the passive margins is not preserved. An effective method to resolve the undisclosed long-term geological history from exposed rocks is the application of thermochronological methods, such as fission track and (U-Th-Sm)/He analyses. The combination of both thermochronometers provides insights to the thermal history of the crust to temperatures between 40–120°C. Temperature changes within the crust are either a result of exhumation processes (such as tectonic faulting) or post-magmatic cooling processes (related to convective and conductive thermal influence). Applying a conventional geothermal gradient, these temperatures reflecting crustal depths of ~1.2–3 km and are in the same crustal depth where the crust reacts brittly to deformation.

Only little is known about the Phanerozoic geological evolution of Sør Rondane as neither thermochronological data nor investigation of the brittle inventory have been published before. However, thermochronological studies were applied in massifs from the western and central parts of DML by Jacobs & Lisker (1999), Meier *et al.* (2004), Emmel *et al.* (2007), Emmel *et al.* (2008) and Emmel *et al.* (2009). Apatite fission track (AFT) and (U–Th)/He (AHe) data comprise ages of 81–366 Ma and corresponding proxies, and are complemented by crosscutting relationships. Thermal history modeling based on these data rely on monotonous cooling concepts, reflecting three different cooling stages since ~250 Ma. The thermal history models throughout were interpreted as stepwise exhumation related to stages of the

Gondwana break-up. Exhumation stages were related to flexural or rift flank uplift, or magmatic cooling, and stages of constant elevated temperatures to burial by lava flows. In central DML, Permian and Triassic exhumation as well as Cretaceous exhumation was postulated (Emmel *et al.*, 2009) whereas exhumation in the western DML was postulated by the Jurassic and mid-Cretaceous passive margin evolution (Jacobs & Lisker, 1999). However, the authors of former studies did not fully recognize the flat paleosurface as a central time-temperature feature, and hence did not completely exploit its potential as key constraint for thermal history modeling, although their samples originated from or beneath it. The existence of the paleosurface remnants provides implications of the dynamic history of the basement. Furthermore, sedimentary remnants offer times of minimal exposure ages and related subsurface temperatures. In western DML, the erosion surface is covered unconformably by Permian diamictites that are intruded or topped by 180 Ma aged Karoo/Ferrar dykes, sills and lava flows. This implies that the present surface was exposed during the Permian and in the Early Jurassic-and disproves monotonous cooling concepts. This contrast has major implications on the comprehension of course, timing, processes and amount of exhumation, the relationship between dynamic evolution and long-tem surface processes, and the view on the general geological history and requires the integration of geomorphological information to thermal history modeling.

Here, thermal history modeling of AFT and AHe data was complemented with probable paleosurface exposure times, following the basic approach of Prenzel (2014) and Krohne *et al.* (2016). The paleosurfaces in Sør Rondane lack a sedimentary cover and hence formation or exposure ages are not known. Here, the integration of paleosurface follows the assumption that formation of a flat surface has a regional extent and cannot form between a high relief mountain range. Furthermore, the time-span of thermochronological ages excludes paleosurface formation, and pre- or postdates paleosurface creation.

Thermal history paths provide implications to timing, depth and areal distribution to faulting. They hence provide implications on the geodynamic evolution and may be able to provide timing on brittle tectonic events. This approach will improve our knowledge about the geological evolution of the passive margins, fault controlled dynamic movements and the geometry of passive margin evolution.

5.2. Geological overview

5.2.1. Basement of Sør Rondane

The basement of Sør Rondane is generally classified by two terranes that amalgated during the Pan-African orogeny (e.g. Osanai *et al.*, 1988; Shiraishi *et al.*, 1994). The *NE-Terrane* is

composed of amphibole to granulite facies supracrustal rocks, whereas the *SW-Terrane* consists of amphibole/greenschist facies supra- and infracrustal rocks and granulite metasedimentary and metaigneous rocks (Osanai *et al.*, 1988; Shiraishi *et al.*, 1994; Elburg *et al.*, 2015b; Figure 19). The Sør Rondane Suture is postulated as part of the frontal fold zone between both terranes whereas the Main Tectonic Boundary is described as the main suture between the *NE-Terrane* and *SW-Terrane* (Osanai *et al.*, 2013). The exact position of the Main Tectonic Boundary differs between petrographic and aerogeophysical evidence, whereas the existence of the Sør Rondane Suture is not confirmed by geophysical measurements (Osanai *et al.*, 2013; Mieth *et al.*, 2014). Within the SW-Terrane, the well defined Main Shear Zone (MSZ) divides amphibole/greenschist facies supracrustal rocks from the Gabbro-Tonalite-Tronthjemite-Granodiorite complex and depicts the most prominent structural feature of Sør Rondane (Mieth *et al.*, 2014; Elburg *et al.*, 2015b; Ruppel *et al.*, 2015; Figure 19). The MSZ is a 120 km long and >100 m wide WSW–ENE trending dextral shear zone occurring in western Sør Rondane, and appears to terminate at the N–S trending Gjelbreen Lineament, which likely represents a N–S trending fault zone (Kojima & Shiraishi, 1986; Mieth *et al.*, 2014; Ruppel *et al.*, 2015; Figure 19). However, the likley synchronous dextral Grophelia Shear Zone in eastern Sør Rondane is indicative for widespread strike-slip movements in Sør Rondane (Ishikawa *et al.*, 2013; Ruppel *et al.*, 2015). The MSZ comprises protomylonitic to ultramylonitic rocks with general subhorizontal to shallow E or W inclined stretching lineations, and the mylonitic foliation dips steeply towards the south or south-east (Ruppel *et al.*, 2015). The high strain ductile deformation happened under peak amphibolite facies, and its dextral strike-slip movement was active between ~560 and ~530 Ma, including different deformation phases under ductile to late brittle conditions. Temperatures reached max 600°C to finally ~300°C (Ruppel *et al.*, 2015). Further strike-slip boundaries are proposed in the southern Sør Rondane by geophysical observation or are inferred on the geological map (Shiraishi *et al.*, 1997). A NE–SW trending magnetic anomaly boundary within the Gabbro-Tonalite-Tronthjemite-Granodiorite subterrane is proposed as a result of dextral strain whereas an inferred shear zone further south cannot be confirmed by geophysical observation(Mieth *et al.*, 2014).

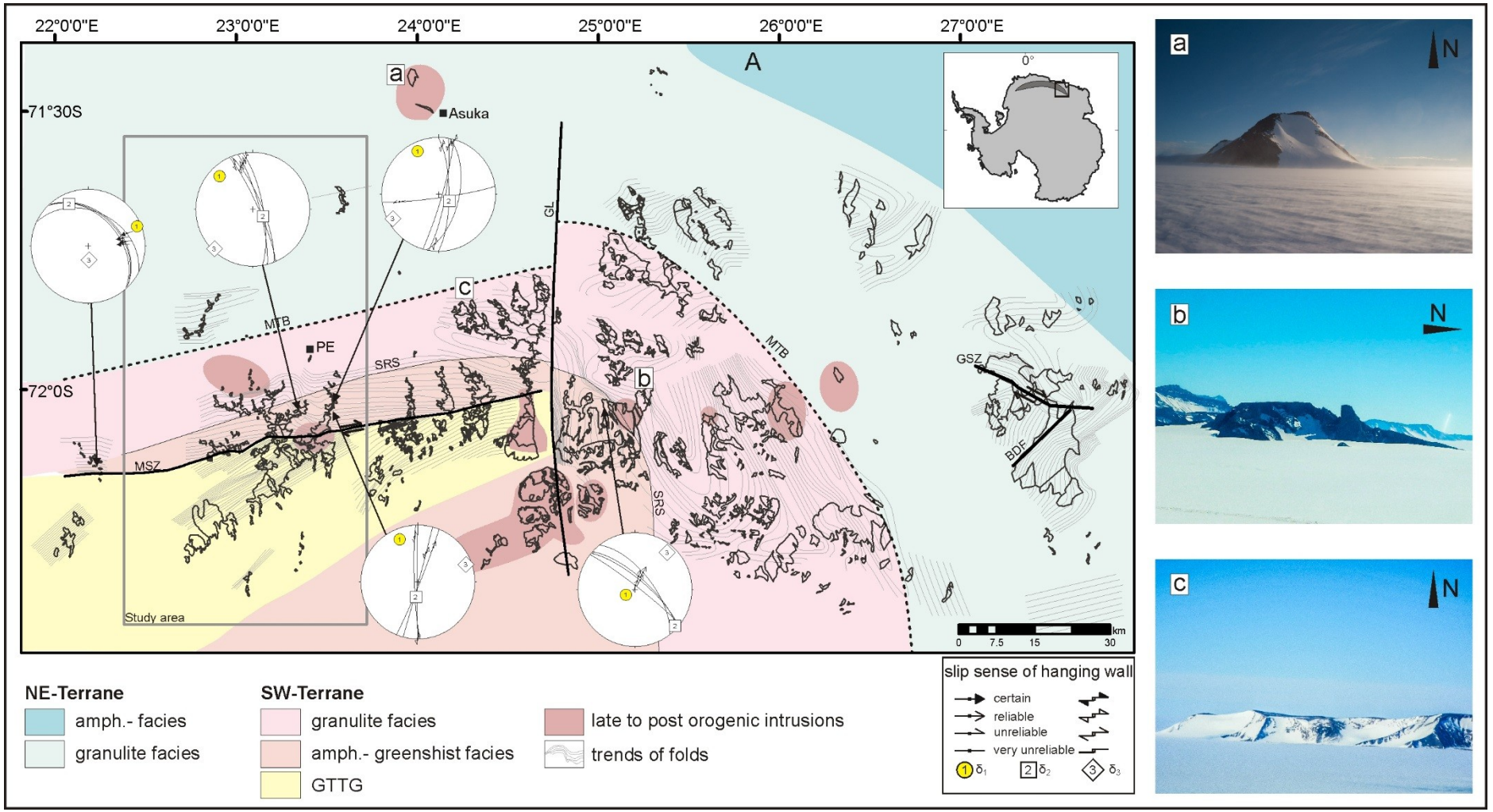

Figure 19: Geologic map of Sør Rondane showing terranes and the associated structures. Brittle tectonic inventory is drawn in great circles, lower hemisphere projection. Fine contour lines indicate the structural sense. Modified after Ruppel (2012), Ishikawa *et al.* (2013), (Osanai *et al.*, 2013). Toyoshima *et al.* (2013), Mieth *et al.* (2014), and Ruppel *et al.* (2015). Rectangle outlines the study area. Site names are outlined for orientation. Abbreviations : MTB - Main tectonic boundary, SRS - Sør Rondane Suture, MSZ - Main Shear Zone, GL - Gjelbreen Lineament, GSZ -Grophelia Shear Zone, BDF - Balchen Detachment Fault., PE: Princess Elisabeth Station

Late stages of deformation at the strike-slip boundaries, ductile detachment faults and overall late to post tectonic plutonism by granite and syenite intrusions and mafic dykes (Li *et al.*, 2003; Shiraishi *et al.*, 2008; Elburg *et al.*, 2016) were related to stages of lateral orogenic collapse at ~600–460 Ma and NW–SE extension (e.g. Shiraishi *et al.*, 2008; Ishikawa *et al.*, 2013). Post-orogenic cooling and ongoing exhumation is represented by whole rock ^{40}K–^{39}Ar and $^{40}Ar/^{39}Ar$ ages of 490–420 Ma (Takigami *et al.*, 1987; Takigami & Funaki, 1991; Osanai *et al.*, 2013).

5.2.2. Phanerozoic evolution of adjacent regions

No Paleozoic and Mesozoic geological record is preserved in Sør Rondane and the geological evolution can be inferred only via analogies with adjacent regions. Cambro-Ordovician deposition and compaction of molasse-type sediments in the western DML and the Shackleton Range and on the African continent prove ongoing exhumation and relief decay of the Pan African orogen (e.g. Jacobs & Thomas, 2004). At least to the Early Permian, the topography is completely leveled down forming regional planation surfaces (Näslund, 2001). Subsequent deposition of mainly continental detritus took place, and is preserved in western DML (Bauer *et al.*, 1997). It starts with Permo-Carboniferous diamictites that unconformably cover the striated paleosurface. Cemented clastic red-bed deposits, intercalated by low-rank coal seams were deposited during the Permian and possibly during the Triassic times (Juckes, 1972; Bauer *et al.*, 1997). Regional Early Jurassic (~180 Ma) igneous rocks intruded the basement and the sediments or lavas were emplaced subaerially. The igneous rocks are related to the Karoo/Ferrar Large Igneous Province. The igneous activity was a short term but widespread and voluminous event, named Karoo/Ferrar Event (e.g. Leat *et al.*, 2005). Seaward dipping magmatic reflectors of the Explora Wedge at the continental rise at western and central DML and possibly Jurassic volcanic intrusion in the Riiser Larsen Sea classifies the DML margin as a magmatic passive margin (Hinz & Krause, 1982; Leitchenkov *et al.*, 1996; Leitchenkov *et al.*, 2008; Mieth *et al.*, 2014). Sør Rondane is surrounded by Karroo/Ferrar volcanic rocks but lacks direct evidence of this magmatic episode (Figure 18). There is an ongoing debate if magmatism as well as continental break-up requires the existence of the Karoo-Maud Plume (Cox, 1992; Heinonen *et al.*, 2010b). First ocean floor was created at ~155 Ma in the Riiser Larsen Sea between eastern DML and Mozambique and marks the initial separation of Gondwana (Jokat *et al.*, 2003). Initial spreading was directed N–S and NNE–SSW as documented by NNE–SSW trending depressions, transform faults and strike slip faulted ridges (e.g. Astrid Ridge and Gunnerus Ridge). However, major spreading and dispersal occurred under ENE–WSW to NW–SE directions (axis strike WNW–ESE) (Jokat *et al.*, 2003; Nogi *et al.*, 2004; Leitchenkov *et al.*, 2008; Reeves *et al.*, 2016). The depositional history of the Riiser-

Larsen Sea is based on seismostratigraphic evidence (Leitchenkov *et al.*, 2008; Mieth *et al.*, 2014). Sedimentary deposits are up to 7 km in thickness, whereas the depocentre is bounded to the SW foot of the Gunnerus Ridge that most likely represents a pull-apart basin.

5.2.3. Geomorphology of Dronning Maud Land and Sør Rondane

Sør Rondane hosts massifs of 1000–3200 m elevation that protrude up to 1600 m from the ice sheet. The terrain in Sør Rondane is highest in the southwest sloping irregularly down to the north and redirects major ice streams from the polar plateau to the eastern and western terminations (e.g. van Autenboer & Decleir, 1978). Glacial troughs are often overdeepened and at least some of them seem to be fault-controlled (e.g. Gjelbreen; Pattyn *et al.*, 1992; Mieth *et al.*, 2014). The massifs are characterized by escarpment-bound summit plateau surfaces intersected by extensive ice-molded peaks. The flat or slight undulating plateau surfaces occur throughout the area and are elevated diversely between 1000 m in the north and 2600 m in the south (Figure 19, Appendix E, Figure S 9). There is no lithological difference between plateau surfaces and the alpine type peaks. Furthermore, surfaces must have been formed prior Cenozoic times, as the lowermost exposed surface Romnoesfjellet (1284 m) does not provide any indications for Neogene to Quaternary ice-override (van Autenboer, 1964). Also some other surfaces were elevated significantly higher than maximum ice-sheet elevations since the Neogene, and evidences that they cannot have been formed during that time (Pattyn *et al.*, 1989; Matsuoka *et al.*, 2006; Suganuma *et al.*, 2014). The same morphological pattern trends towards the east as well as to the west (Figure S 9). Hence, the morphology of DML can be constrained as one mega feature. Alpine landscape formation pre-dates the late Cenozoic and hence postdates the paleosurface formation (Näslund, 2001).

In western and central DML, the flat surfaces were interpreted as remnants of one or several regional and planation surfaces (Näslund, 2001). Flow directions of the Permian ice sheet indicate regional low relief landforms in the Permian (Bauer *et al.*, 1997). An exposition age of the paleosurface is given by the preserved thin remnants of the Carboniferous-Permian tillite in the western part. Striae on the basement paleosurface are in direct contact to the overlying diamictites (Poscher, 1992). This combination proves surface exposure, modification, and subsequent burial. Repeated near-surface exposure of the basement paleosurface and thin Permian strata is indicated by the intrusion of 182 Ma aged sills, dykes and the effusion of lavas (e.g. Duncan *et al.*, 1997) at least directly indicated in western DML and in parts of central DML. This altogether suggests a similar situation for eastern DML.

5.3. Brittle structural inventory of Sør Rondane

Published brittle structures are related to the late stages of Pan-African orogenic collapse and lateral extrusion along the strike-slip boundaries (Toyoshima *et al.*, 1995; Ruppel, 2012; Ishikawa *et al.*, 2013; Toyoshima *et al.*, 2013; Ruppel *et al.*, 2015). Evidence of younger brittle deformation is not provided in literature yet.

Here, the brittle tectonic inventory of western Sør Rondane was studied during GEA I and II expeditions (Geodynamic Evolution of East Antarctica, 2010–12) of the German Federal Institute for Geosciences and Natural Resources. 128 fault-slip measurements on fault planes and slickensides were obtained in eight localities, comprising up to three distinctive fault-slip events. The sense of hanging wall block movement was obtained by inspection of Riedel shears, fiber steps or tearing edges on the fault planes or slickensides.

Three different paleostress tensor groups were obtained: (I) NW–SE striking, subvertical normal faults point to NE–SW directed extension (II) NW–SE directed contraction (III) Conjugate fault systems NE–SW left-lateral and NNE–SSW right lateral faults point to a WNW–ESE maximum paleostress direction. Co-genetic (?) reverse faults at the MSZ with NW–SE maximum tension and NE–SW minimum stress point to the generation of positive flower structures (Figure 19). The latter (III) fault-slip data indicate at least one younger brittle deformation event as late Pan-African times; however, the exact timing of movement was not possible to determine.

5.4. Thermochronology

5.4.1. Sampling strategy

Thirty in-situ rock samples for fission track and (U–Th–Sm)/He analysis were collected in western Sør Rondane during GEA I and II expeditions. Sampling intended to cover the entire relief between 1300–3200 m and all tectonic domains, to investigate the relationship between the different structural boundaries and geomorphology to cooling (Figure 20). Sampling includes a general horizontal N–S transect traversing three litho-tectonic boundaries (Main Tectonic Boundary; Sør Rondane Suture and MSZ) and two semi-vertical transects at the two highest mountains Widerøefjellet and Vikinghøgda that are separated by narrow standing and steep dipping dextral shear planes of the MSZ (Ruppel *et al.*, 2015). Morphologically, both summits were separated by a dry valley that pins Vikinghøgda to the north and Widerøefjellet to the south.

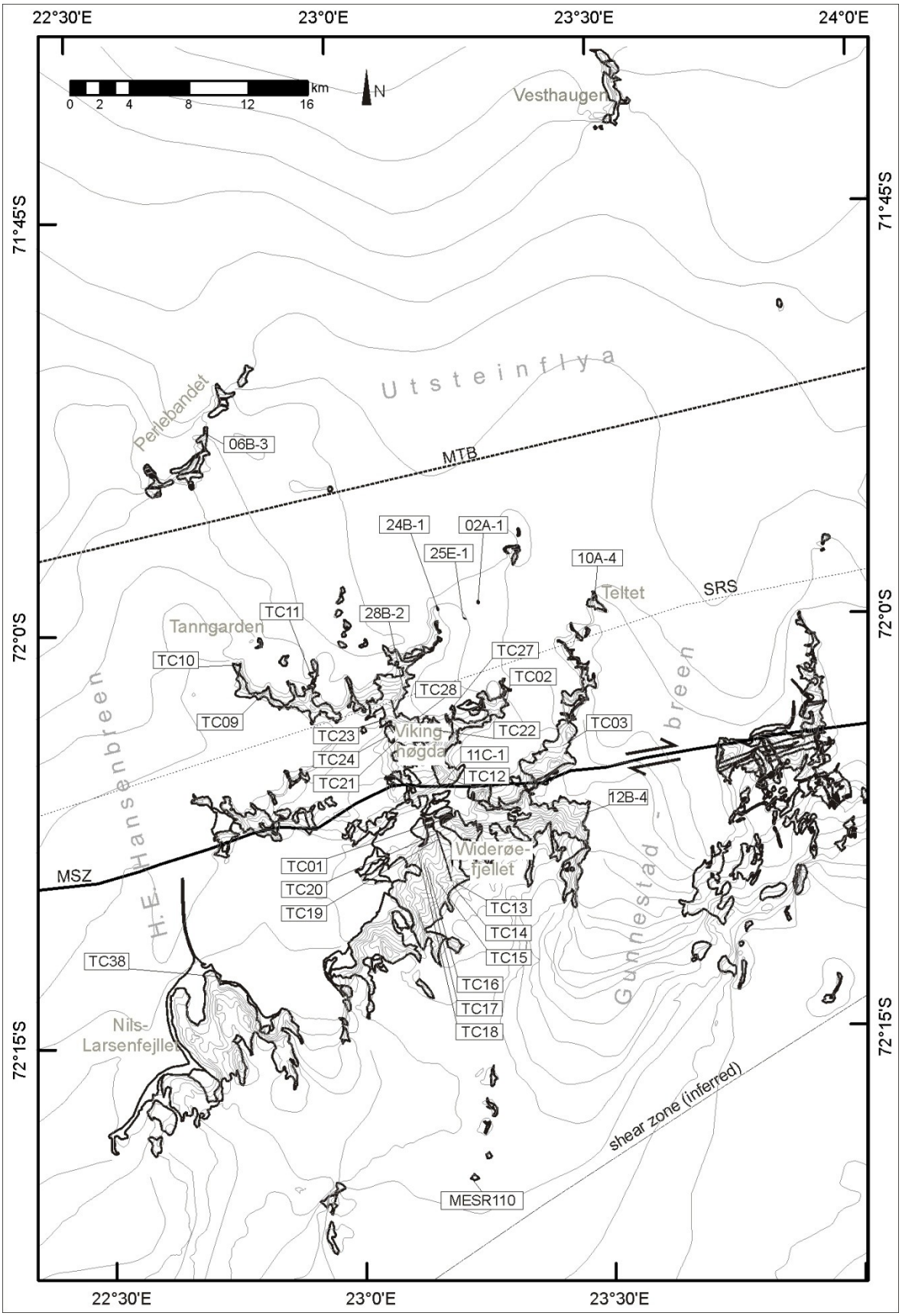

Figure 20: Map of the study area, showing the location of the thermochronological samples. See Figure 19 for general overview of the area. Structures as in Figure 19. Regional names are outlined for orientation.

Paleosurface remnants are exposed between 1000 and 2800 m. In the study area, small Paleosurface remnants top Vikinghøgda and Nils-Larssenfjellet. All other samples were collected from alpine type morphologies. The dissection and the different elevation of the paleosurface remnants restrict backstacking of the vertical distance to the former paleosurface prior thermal history modeling, and furthermore do not allow the calculation of paleogeothermal gradients.

AFT and AHe thermochronometry covers temperature span of 80°C, referring to a vertical coverage of ~2.5 km. This exceeds the recent vertical relief. Hence, interpretation of all samples must consider and allow Permian and Jurassic low-temperatures placement.

5.4.2. Apatite fission track results

Thirty AFT ages range from 136±12 to 226±32 Ma, and are hence substantially younger than the times of rock formation, the latest metamorphic overprint and 430–490 Ma ^{40}K–^{39}Ar and $^{40}Ar/^{39}Ar$ cooling ages (Takigami & Funaki, 1991; Shiraishi *et al.*, 2008; Osanai *et al.*, 2013 and references therein; Table 5). Details to sample preparation and technical information are given in Appendix C.1.2. All samples pass the χ^2 test with high χ^2-probabilities referring to a single age population. Mean track lengths (MTL) vary between 11.6 and 13.5 µm with broad track length spectra and standard deviations of 1.3–2.7 µm. Values of the kinetic parameter D_{par} range between 1.5 and 2.2 µm. Both MTL and D_{par} values from the horizontal profile correlate with elevation. Most shortened tracks are preserved in the oldest and youngest samples, while long MTL of 13.1–13.5 µm were measured in samples with AFT ages between 183–193 Ma (Figure 21). The standard deviations of the mean track lengths correlate negatively with MTL values (Figure 21).

The AFT ages of Widerøefjellet and Vikinghøgda range from 136±12 to 226±32 Ma. In general, they correlate inversely with elevation, with an apparent offset in the Widerøefjellet profile (Figure 21). Mean track lengths of both semi-vertical profiles vary between 11.7±1.8 and 13.5±1.4 µm and do not correlate with elevation. Apatite grains from Widerøefjellet are generally smaller in size compared to those from other locations and most of the non-analyzed grains show curved dislocations, most possibly developed due to tectonic stress.

The AFT data from the different terranes of Sør Rondane do not show any systematic AFT age or track length cluster.

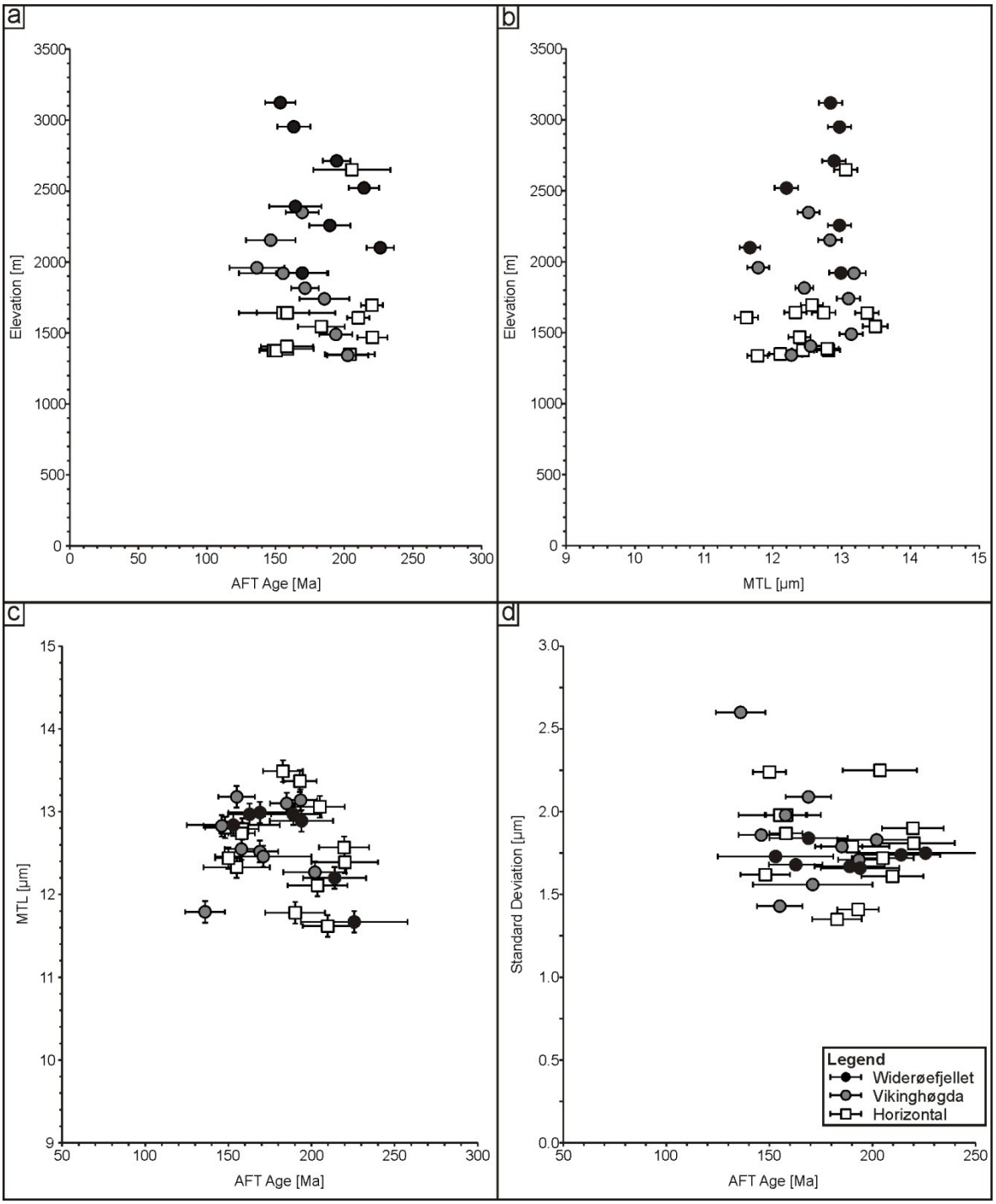

Figure 21: Apatite fission track (AFT) results. a) Diagram showing the age vs. elevation relationship. Note that AFT ages of the vertical transects correlate inversely with elevation. Error bars indicate the standard deviation of pooled fission track ages. b) Plot showing mean track lengths (MTL) against elevation, with 1σ error bars. c) Mean track lengths are plotted against AFT and show a banana pattern. Vertical error bars indicate 1σ error, horizontal error bars indicate the standard deviation of pooled AFT ages. d) Standard deviation of the MTL plotted against AFT age. The largest standard deviations, and hence the broadest mean track length histogram occur in the youngest samples, whereas the lowest standard deviations are present in the samples with the largest MTL.

Table 5: Apatite Fission Track Results

Sample / Location	Elev. [m] Lithology	N_D ρ_D *	N_s ρ_s *	N_i ρ_i *	$P(\chi^2)$ [%]	Age ± 1σ [Ma] N_G	MTL ± 1σ [µm] SD [µm]	N_L	D_{par} ± 1σ [µm] SD	U [ppm]
TC_01	1922	8182	129	205	100	169±19	12.99±0.17	75	2.19±0.03	23.94
Widerøefjellet	Granodiorite	1.643	14.86	23.61		22	1.84		0.17	
TC_02	1406	8380	446	779	75	158±10	12.55±0.16	83	1.79±0.02	17.51
Ketelersbreen	Grey Gneiss	1.683	11.94	20.86		22	1.98		0.19	
TC_03	1643	8274	396	798	18	135±9	12.33±0.16	77	1.68±0.02	30.06
Gunnestadbreen	Grey Gneiss	1.661	19.58	39.46		20	1.98		0.16	
TC_09	1642	8274	839	1442	18	158±8	12.74±0.17	100	1.74±0.02	32.39
Tanngarden	Grey Gneiss	1.661	20.55	35.33		21	1.87		0.12	
TC_10	1639	8274	702	986	89	193±10	13.37±0.17	80	2.11±0.03	32.15
Tanngarden	Grey Gneiss	1.661	27.16	38.15		20	1.41		0.18	
TC_11	1545	8274	441	655	33	183±12	13.49±0.18	27	1.90±0.02	26.59
Tanngarden	Grey Gneiss	1.661	20.27	30.11		21	1.35		0.04	
TC_12	1920	8274	337	590	90	155±11	13.18±0.17	19	1.87±0.02	26.99
Vikinghøgda	Granite	1.661	17.41	30.47		20	1.43		0.15	
TC_13	3120	8574	82	147	69	157 ± 22	12.84±0.17	11	1.74±0.02	11.94
Widerøefjellet	Granodiorite	1.722	8.23	14.76		13	1.73		0.12	

*[10^6 cm^{-2}]

Table 5 (continued)

Sample / Location	Elev. [m] Lithology	N_D ρ_D *	N_s ρ_s *	N_i ρ_i *	$P(\chi^2)$ [%]	Age ± 1σ [Ma] N_G	MTL ± 1σ [µm] SD [µm]	N_L	D_{par} ± 1σ [µm] SD	U [ppm]
TC_14	2950	7249	267	391	23	163±13	12.97±0.17	100	1.91±0.02	27.61
Widerøefjellet	Granodiorite	1.456	19.56	28.65		21	1.68		0.15	
TC_15	2710	8620	180	262	92	194±19	12.89±0.17	77	1.99±0.03	16.79
Widerøefjellet	Tonalite	1.731	13.77	20.04		21	1.66		0.23	
TC_16	2520	7249	264	293	59	214±19	12.20±0.16	52	1.94±0.03	24.61
Widerøefjellet	Granodiorite	1.456	21.33	23.68		20	1.74		0.18	
TC_17	2390	8597	36	62	84	164±35	-	-	2.02±0.03	8.70
Widerøefjellet	Granodiorite	1.726	6.81	11.72		5	-		0.33	
TC_19	2257	8643	211	316	72	189±17	12.97±0.17	29	1.82±0.02	13.13
Widerøefjellet	Granodiorite	1.736	9.48	14.2		22	1.67		0.20	
TC_20	2100	7249	98	103	100	226±32	11.67±0.15	21	1.50±0.02	4.54
Widerøefjellet	Granodiorite	1.456	4.12	4.33		21	1.75		0.15	
TC_21	2153	8552	286	552	61	146±11	12.83±0.17	91	2.00±0.03	26.09
Vikinghøgda	Hbl-Bt-Gneiss	1.717	17.72	34.20		22	1.86		0.18	
TC_22	1816	8529	58	95	48	171±29	12.46±0.16	42	1.85±0.02	15.51
Vikinghøgda	Hbl-Bt-Gneiss	1.713	12.11	19.83		6	1.56		0.17	

*[10^6 cm^{-2}]

Table 5 (continued)

Sample / Location	Elev. [m] Lithology	N_D ρ_D *	N_s ρ_s *	N_i ρ_i *	$P(\chi^2)$ [%]	Age ± 1σ [Ma] N_G	MTL ± 1σ [µm] SD [µm]	N_L	D_{par} ± 1σ [µm] SD	U [ppm]
TC_23	1741	7249	767	986	21	185±10	13.10±0.17	116	1.83±0.02	47.96
Vikinghøgda	Hbl-Bt-Gneiss	1.456	28.36	36.46		20	1.79		0.18	
TC_24	2348	7249	467	659	97	169±11	12.52±0.16	88	1.74±0.02	44.14
Vikinghøgda	Hbl-Bt-Gneiss	1.456	32.78	46.26		21	2.09		0.10	
TC_27	1344	8666	200	281	73	202±19	12.27±0.16	93	1.57±0.02	8.68
Vikinghøgda	Hbl-Bt-Gneiss	1.740	7.20	10.11		19	1.83		0.13	
TC_28	1491	7249	788	696	25	193±10	13.14±0.17	114	1.92±0.02	32.78
Vikinghøgda	Hbl-Bt-Gneiss	1.456	25.64	31.52		21	1.71		0.15	
TC_38	1696	8380	429	536	89	220±15	12.57±0.16	84	2.06±0.03	28.56
Nils-Larssenfjellet	Tonalite	1.683	28.33	35.4		20	1.90		0.18	
02A-1	1338	8182	214	302	78	190±18	11.78±0.15	102	1.74±0.02	9.66
Ketelersbreen	Grey Gneiss	1.643	7.54	10.64		23	1.79		0.13	
06B-3	1388	8380	416	707	67	162±11	12.79±0.17	103	1.95±0.03	23.88
Perlebandet	Hbl- Plag-Gneiss	1.683	16.64	28.28		22	1.98		0.16	
10A-4	1350	8182	249	328	72	204±18	12.11±0.16	81	1.87±0.02	9.33
Teltet	Grey Gneiss	1.643	8.39	11.05		20	2.25		0.12	

*[10^6 cm^{-2}]

Table 5 (continued)

Sample / Location	Elev. [m] / Lithology	N_D ρ_D *	N_s ρ_s *	N_i ρ_i *	$P(\chi^2)$ [%]	Age ± 1σ [Ma] N_G	MTL ± 1σ [µm] SD [µm]	N_L	D_{par} ± 1σ [µm] SD	U [ppm]
11C-1	1959	8274	215	432	60	136±12	12.31±0.16	51	1.77±0.02	20.66
Vikinghøgda	Metarhyolite?	1.661	12.70	25.51		20	1.77		0.18	
12B-3	1607	8182	399	510	80	210±15	11.62±0.15	19	1.81±0.02	17.5
Ketelersbreen	Hbl-Bt-Gneiss	1.643	6.73	8.6		23	1.61		0.19	
24B-1	1377	8274	260	480	90	148±12	12.81±0.17	22	1.87±0.02	15.22
Duboisbreen	Grey Gneiss	1.661	9.87	18.22		22	1.62		0.14	
25E-1	1376	8274	632	1147	97	150±8	12.44±0.16	100	1.84±0.02	45.92
Duboisbreen	Grey Gneiss	1.661	30.89	56.06		21	2.24		0.13	
28B-2	1469	8182	241	260	95	220±20	12.39±0.16	13	2.13±0.03	10.36
Gunnestadbreen	Gneiss	1.643	10.17	10.97		22	1.81		0.05	
ME SR 110	2648	8274	386	514	63	204±14	13.06±0.17	51	2.15±0.03	36.88
Caussinknappen	Tonalite	1.661	30.75	40.95		21	1.72		0.19	

*[10^6 cm^{-2}]

ζ= 332±6 for IRMM 540 Dosimeter glasses (N. Krohne). Mounts were prepared and etched according to the recommendations of Donelick *et al.* (2005). Ages were calculated using the software TRACKKEY, Version 4.2.g (Dunkl, 2002). Abbreviations: Elev: Elevation. ρ_D, ρ_S, ρ_i, N_D, N_s, N_i describe the density and number of counted dosimeter, spontaneous and induced tracks. N_G: Number of counted apatite grains. N_L: Number of confined track lengths measured. $P[\chi^2]$: probability, with $P[\chi^2]$>5% referring to a single age population (Galbraith, 1981). 1σ errors: conventional method; Green (1981).

5.4.3. (U–Th–Sm)/He results

79 single grain ages were calculated from 25 sample locations by applying the ^{4}He ingrowth equation (Farley, 2002) and are listed in Table 6 and shown in Figure 22. Details to sample preparation and technical information are given in Appendix C.1.3. F_T-corrected single grain ages vary strongly between 44±6 and 348±41 Ma, with some aliquot ages being significantly older as the corresponding fission track age. U–Th–He ternary plots indicate few samples with replicating ages and uniform geochemistry. Most of the samples show either clustering single grain ages or a randomly distributed age scatter. Central ages vary between 98±10 Ma and 237±5 Ma (Appendix C, Figure S 7). The eU ratios range from 4–253 ppm, and may correlate slightly with single grain AHe ages which may represent radiation damage (Shuster *et al.*, 2006; Flowers *et al.*, 2009) (r_{xy}=0.32, r^2=0.11), whereas no correlation exists to the grain radius (r_{xy}=0.00, r^2=0.13) and mass (r_{xy}=0.01) (Figure 22). F_T–corrected single grain ages and eU values of the Widerøefjellet somehow correlate with a coefficient of 0.31. All other r_{xy} values are below 0.2 and indicate no correlation with eU. AHe single grain ages, older than corresponding fission track ages, are confined to proximity to the MSZ. 81% aliquots from the Widerøefjellet have significantly higher AHe single grain ages than corresponding AFT ages. Analogously, 55% Vikinghøgda AHe single grain ages predate the respective AFT ages, while only 22% samples remote from the MSZ show such a reverse/inverse relationship. Apatite grains close to the MSZ are smaller and of poorer quality than the others, and some grains within the AFT mounts show indications of intracrystal deformation (curved dislocations) and irregular ^{238}U and ^{235}U zonation. The broad scatter of single grain ages reflects the typical scenario for cratonic regions (Flowers, 2009), and is also reported in adjacent regions (Emmel *et al.*, 2007).

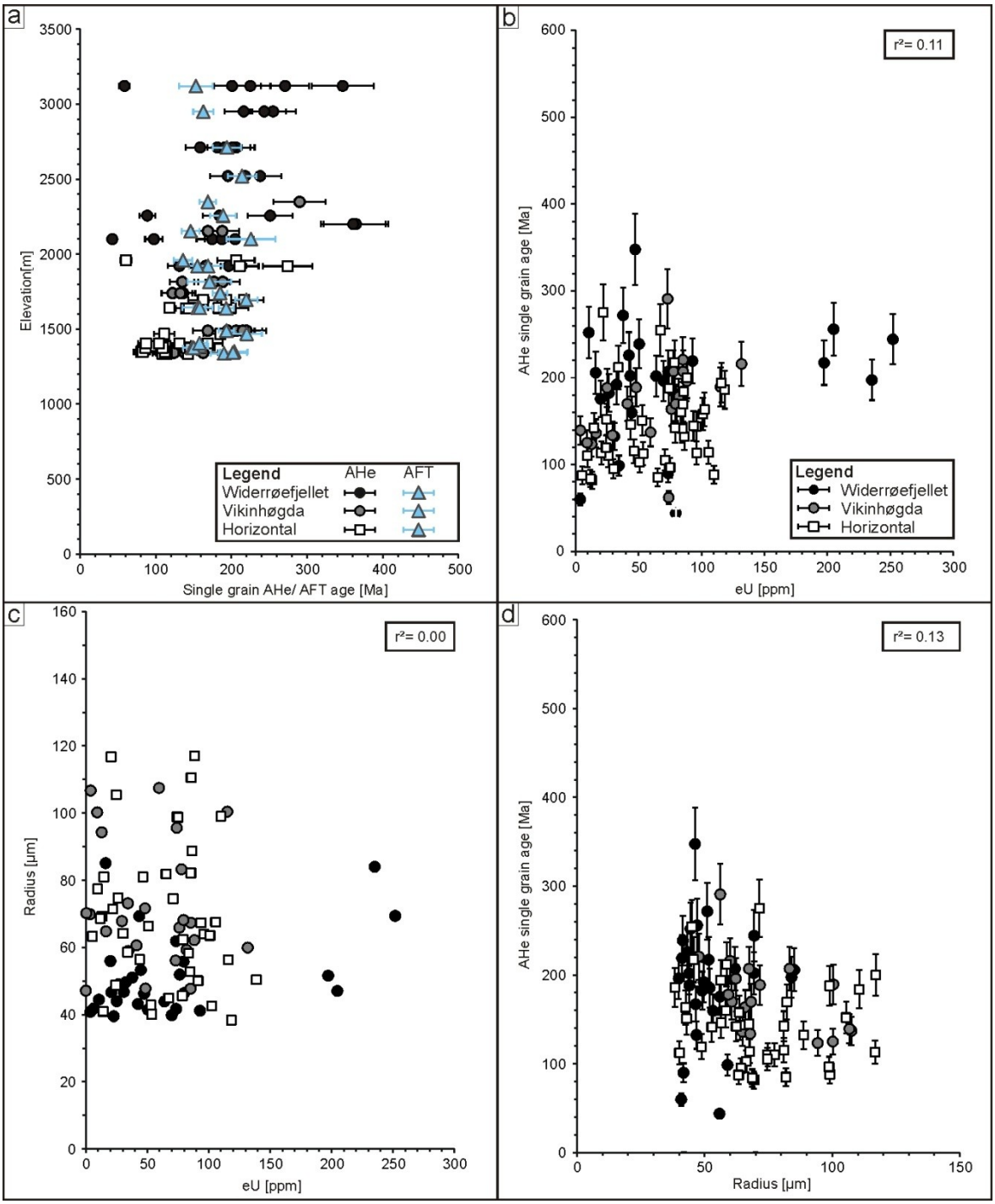

Figure 22: Apatite (U-Th-Sm)/He (AHe) results: a) AHe single grain ages and corresponding apatite fission track (AFT) ages were plotted against elevation. Error bars indicate the 1σ error of the AHe data. b) eU values were plot against AHe single grain ages, showing a rough correlation and broad distribution of eU values. Error bars indicate the 1σ error of the AHe data. c) eU relation to the mean sphere radius of the distinctive apatite grains. No trends and no correlation are obvious. d) The FT-corrected single grain ages correlate negatively with radius. Error bars indicate the 1σ error of the AHe data.

Table 6: AHe Results

Sample	R_s	mass [mg]	^{4}He [ncc]	$^{238+235}U$ [ppm]	^{232}Th [ppm]	^{147}Sm [ppm]	eU [ppm]	uncorr. age [Ma]	SD [Ma]	F_T-factor	corrected age [Ma]	SD [Ma]
TC01#1	84.03	0.005	6.698	42.321	86.395	55.053	235.210	159.51	9.89	0.808	197.3	23.2
TC01#2	46.47	0.002	0.544	21.000	26.494	16.720	80.152	105.35	6.53	0.631	167.1	19.7
TC01#4	46.79	0.002	0.241	9.371	9.639	33.176	30.919	89.01	5.52	0.672	132.4	15.6
TC02 #1	88.76	0.011	4.525	25.420	27.320	4.200	86.403	106.78	6.62	0.807	132.3	15.6
TC02 #2	99.05	0.013	4.678	31.833	34.977	5.279	109.907	73.85	4.58	0.837	88.2	10.4
TC02 #4	82.21	0.008	4.090	23.356	27.825	3.107	85.465	134.10	8.31	0.791	169.5	20.0
TC02 #5	74.53	0.005	1.149	15.798	24.765	3.611	71.076	82.43	5.11	0.783	105.3	12.4
TC03 #1	98.93	0.013	8.523	29.484	20.055	18.748	74.266	154.99	9.61	0.825	187.9	22.1
TC03 #2	42.90	0.001	0.450	26.119	12.015	11.412	52.947	96.66	5.99	0.641	150.9	17.8
TC03 #3	48.77	0.002	0.176	10.122	6.337	12.747	24.279	77.05	4.78	0.646	119.2	14.0
TC09 #1	117.08	0.023	20.628	37.356	22.942	46.767	88.609	170.39	10.56	0.852	199.9	23.5
TC09 #2	110.57	0.017	18.188	49.996	15.949	97.402	85.693	157.08	9.74	0.854	183.9	21.6
TC09 #3	105.46	0.018	3.762	11.984	5.705	65.855	24.784	126.91	7.87	0.835	152.0	17.9
TC10 #1	52.80	0.002	0.979	31.950	23.621	54.380	84.726	95.44	5.92	0.675	141.4	16.6
TC10 #2	62.35	0.002	1.071	32.809	20.711	64.991	79.102	105.66	6.55	0.744	142.0	16.7
TC10 #3	67.36	0.002	1.254	30.641	28.234	51.655	93.711	110.46	6.85	0.764	144.6	17.0
TC12 #1	40.96	0.001	0.287	5.543	3.801	30.549	14.058	314.28	19.49	0.619	(507.4)	(59.7)
TC12 #2	58.59	0.003	0.538	7.787	11.748	56.742	34.064	152.74	9.47	0.721	211.8	24.9
TC12 #3	71.48	0.005	0.847	4.107	8.000	40.035	22.003	211.94	13.14	0.770	275.2	32.4
TC13 #1	46.24	0.001	0.420	7.220	17.995	33.636	47.419	215.91	13.39	0.621	347.6	40.9
TC13 #2	43.91	0.001	0.306	17.362	20.871	30.012	63.976	128.06	7.94	0.635	201.7	23.7
TC13 #3	40.84	0.002	0.017	1.703	0.905	1.181	3.724	38.17	2.37	0.638	59.8	7.0
TC13 #4	51.05	0.002	0.440	7.518	13.534	37.673	37.764	184.99	11.47	0.681	271.7	32.0
TC13 #5	43.18	0.001	0.278	7.730	15.534	21.678	42.424	144.49	8.96	0.640	225.8	26.6
TC14 #1	47.06	0.001	1.950	66.371	62.036	9.437	204.845	168.69	10.46	0.659	255.8	30.1
TC14 #2	51.59	0.001	1.996	59.862	61.592	12.532	197.347	149.71	9.28	0.690	217.1	25.6

Table 6 (continued)

Sample	R_s	mass [mg]	^{4}He [ncc]	$^{238+235}$U [ppm]	^{232}Th [ppm]	^{147}Sm [ppm]	eU [ppm]	uncorr. age [Ma]	SD [Ma]	F_T-factor	corrected age [Ma]	SD [Ma]
TC14 #3	69.40	0.003	6.562	73.001	80.148	10.884	251.901	188.05	11.66	0.770	244.2	28.8
TC15#1	53.30	0.002	0.314	9.458	15.806	6.642	44.743	111.33	6.90	0.697	159.7	18.8
TC15#2	61.90	0.003	1.462	24.306	22.029	6.395	73.481	153.53	9.52	0.741	207.1	24.4
TC15#3	69.33	0.005	1.591	15.717	12.443	5.640	43.496	151.81	9.41	0.751	202.2	23.8
TC15#4	49.07	0.002	0.235	4.968	9.700	5.252	26.625	125.08	7.76	0.686	182.4	21.5
TC15#5	49.66	0.002	0.346	7.819	11.059	4.472	32.507	132.14	8.19	0.688	192.1	22.6
TC16 #1	39.84	0.001	0.353	19.501	22.596	7.551	69.942	119.00	7.38	0.607	196.1	23.1
TC16 #2	41.46	0.001	0.523	21.793	12.895	8.313	50.584	149.57	9.27	0.626	238.8	28.1
TC16 #3	41.16	0.002	0.942	28.293	28.960	8.058	92.940	139.24	8.63	0.636	219.1	25.8
TC19 #1	41.72	0.001	0.442	44.361	13.031	21.164	73.467	57.17	3.54	0.636	89.9	10.6
TC19 #2	44.47	0.002	0.113	2.277	3.720	22.387	10.602	164.45	10.20	0.653	252.0	29.7
TC19 #3	51.94	0.002	1.805	52.353	10.784	43.681	76.467	129.18	8.01	0.697	185.3	21.8
TC20#1	55.96	0.003	0.207	3.420	7.410	18.881	19.977	120.93	7.50	0.689	175.6	20.7
TC20#2	55.82	0.002	0.989	25.619	24.165	55.725	79.611	31.26	1.94	0.713	43.9	5.2
TC20#3	58.96	0.002	0.267	11.140	10.458	37.923	34.521	71.72	4.45	0.727	98.7	11.6
TC20#4	85.12	0.006	0.630	3.697	5.546	24.118	16.099	166.32	10.31	0.808	205.7	24.2
TC20#5	44.00	0.001	0.102	4.392	9.272	40.335	25.128	118.58	7.35	0.630	188.3	22.2
TC21 #2	71.66	0.006	3.656	29.649	8.272	20.914	48.133	148.35	9.20	0.786	188.8	22.2
TC21 #3	60.62	0.003	1.041	25.280	7.147	19.147	41.251	125.16	7.76	0.736	170.0	20.0
TC22 #1	59.31	0.002	1.072	23.677	26.095	16.455	81.937	129.88	8.05	0.729	178.0	21.0
TC22 #2	100.43	0.012	11.946	43.079	32.288	22.615	115.169	156.34	9.69	0.825	189.4	22.3
TC22 #3	64.80	0.004	0.342	5.585	4.826	6.659	16.363	100.03	6.20	0.735	136.0	16.0
TC23 #1	94.30	0.012	1.094	6.189	2.993	45.940	12.914	100.46	6.23	0.814	123.4	14.5
TC23 #2	107.51	0.010	4.098	25.803	15.091	109.000	59.596	116.58	7.23	0.851	137.1	16.1
TC23 #3	67.84	0.003	0.625	15.113	6.355	33.330	29.330	102.17	6.33	0.764	133.7	15.7
TC27 #1	100.23	0.014	0.793	3.971	2.334	12.164	9.194	103.33	6.41	0.826	125.1	14.7

Table 6 (continued)

Sample	R_s	mass [mg]	^{4}He [ncc]	$^{238+235}$U [ppm]	^{232}Th [ppm]	^{147}Sm [ppm]	eU [ppm]	uncorr. age [Ma]	SD [Ma]	F_T-factor	corrected age [Ma]	SD [Ma]
TC27 #2	106.73	0.016	0.610	2.376	0.691	11.725	3.930	116.45	7.22	0.836	139.3	16.4
TC27 #5	65.90	0.005	2.283	25.667	22.584	35.373	76.109	121.37	7.52	0.741	163.7	19.3
TC28 #1	62.20	0.003	3.302	61.616	11.948	58.907	88.343	141.03	8.74	0.720	195.9	23.1
TC28 #2	67.38	0.006	5.238	43.329	18.865	27.988	85.463	160.22	9.93	0.774	207.1	24.4
TC28 #3	47.73	0.002	1.742	58.574	11.949	46.246	85.290	141.71	8.79	0.642	220.7	26.0
TC28 #4	68.19	0.005	4.217	54.366	11.237	33.535	79.480	127.21	7.89	0.749	169.8	20.0
TC28 #5	59.95	0.002	4.061	84.442	21.198	51.602	131.807	158.36	9.82	0.734	215.9	25.4
TC38 #1	56.37	0.002	1.459	41.911	33.106	21.276	115.826	139.10	8.62	0.717	194.1	22.8
TC38 #3	42.59	0.001	0.293	24.176	35.053	21.697	102.436	101.99	6.32	0.624	163.4	19.2
TC38 #4	45.65	0.001	0.582	24.431	24.266	14.858	78.607	141.08	8.75	0.649	217.5	25.6
02A-1 #1	81.01	0.007	1.066	9.531	16.555	12.533	46.494	90.57	5.62	0.785	115.4	13.6
02A-1 #2	74.70	0.006	0.496	5.473	9.286	16.620	26.216	84.56	5.24	0.768	110.1	13.0
02A-1 #3	63.96	0.004	1.339	15.247	36.172	21.524	96.005	104.89	6.50	0.731	143.6	16.9
06B-3 #1	66.33	0.005	1.203	22.586	12.667	26.723	50.885	76.38	4.74	0.743	102.7	12.1
06B-3 #2	64.21	0.004	0.557	14.154	7.169	27.765	30.183	69.57	4.31	0.733	94.9	11.2
06B-3 #3	67.59	0.004	1.817	33.652	32.219	32.085	105.597	86.77	5.38	0.761	114.0	13.4
10A-4 #1	69.34	0.004	0.221	5.931	3.204	54.013	13.137	62.56	3.88	0.764	81.8	9.6
10A-4 #2	116.78	0.021	2.317	7.451	5.826	51.460	20.506	95.95	5.95	0.848	113.1	13.3
10A-4 #3	68.63	0.005	0.325	7.613	1.836	77.701	11.789	63.89	3.96	0.761	83.9	9.9
11C-1 #1	95.62	0.011	1.325	12.187	27.685	28.476	74.008	50.53	3.13	0.816	61.9	7.3
11C-1 #2	83.28	0.009	3.222	10.218	30.286	28.604	77.845	167.48	10.38	0.809	207.1	24.4
11C-1 #3	73.15	0.006	2.528	9.171	11.205	16.783	34.197	278.35	17.26	0.786	354.4	41.7
24B-1 #1	77.44	0.004	0.242	4.813	2.056	26.146	9.429	87.34	5.42	0.792	110.3	13.0
24B-1 #2	63.30	0.003	0.134	5.234	0.032	13.991	5.319	65.19	4.04	0.746	87.4	10.3
24B-1 #3	81.01	0.008	1.248	10.477	1.869	37.032	14.686	112.22	6.96	0.788	142.5	16.8

Table 6 (continued)

Sample	R_s	mass [mg]	^{4}He [ncc]	$^{238+235}$U [ppm]	^{232}Th [ppm]	^{147}Sm [ppm]	eU [ppm]	uncorr. age [Ma]	SD [Ma]	F_T-factor	corrected age [Ma]	SD [Ma]
25E-1 #1	56.46	0.003	0.931	24.550	8.598	82.923	43.823	101.84	6.31	0.696	146.2	17.2
25E-1 #2	63.55	0.003	2.728	55.120	20.537	84.823	101.044	118.03	7.32	0.747	158.0	18.6
25E-1 #3	58.29	0.003	1.569	31.977	23.126	76.480	83.672	112.94	7.00	0.705	160.1	18.8
28B-2 #1	40.11	0.001	0.101	11.956	18.674	34.933	53.672	67.22	4.17	0.598	112.4	13.2
28B-2 #3	38.34	0.001	0.268	15.099	46.330	21.449	118.529	101.67	6.30	0.546	186.2	21.9

Measurement of ^{4}He, ^{238}U, ^{232}Th and ^{147}Sm was conducted at the department of Geosciences of the University of Bremen. The eU concentration calculated after (Shuster *et al.*, 2006; Flowers *et al.*, 2009; Spiegel *et al.*, 2009). Abbreviations: R_S: sphere radius, F_T-factor: α-ejection correction (Farley *et al.*, 1996).

Similar to the AFT age trend, the AHe single grain ages generally correlate with elevation, except at Widerøefjellet and Vikinghøgda (Figure 22). Higher locations generally show a higher scatter of aliquot ages. A broad scatter of individual ages is obvious, especially in samples from the Gabbro-Tonalite-Tronthjemite-Granodiorite subterrane. Samples in the north have significantly younger aliquot and central ages as the corresponding AFT ages. Towards the south the samples are only somewhat younger than or as old as the AFT ages. Top samples from Widerøefjellet and Vikinghøgda show an inverted/crosscutting AHe/AFT relationship. Samples from the highest elevations have as old or significantly older AHe central and aliquot ages. These samples occur all above ~2000 m. Samples below ~1400 m show the normal age distribution with younger AHe dates than AFT ages. This pattern may reflect a transition between the usual and the inverted AHe/AFT age relationship between 1400 and 2000 m with as old or even older as AFT ages.

5.4.4. Thermal history modeling

Thermal history modeling with HeFTy (version 1.8.7; Ketcham, 2005) was applied to derive discrete time-temperature paths from thermochronological data and geological master constraints. Twenty samples match requirements for thermal history modeling that include an adequate number of grain ages and track length measurements and no crossover relationships between AHe and AFT ages.

Thermal history modeling is based on the approach described by Prenzel *et al.* (2013). It relies on the elemental assumption that a mountain range topped by a paleosurface results from consistent exhumation processes. Exhumation stages are marked by similar timing of cooling episodes for the whole sample suite, while maximum paleotemperatures of individual samples may vary.

For thermal history modeling, a sequence of geological record and thermochronological data can be deduced: All thermochronological samples were recently in close vertical relationship to the erosional surface. Hence paleosurface formation (=erosion) cannot precede simultaneously to fission track cooling. Fission track cooling postdates paleosurface formation.

As inferred in section 5.2.3, the paleosurfaces in DML must be a pre-Cenozoic feature. The thermochronological age range does not allow simultaneous paleosurface formation (but exposure). Hence, the paleosurfaces must have been created prior the main AFT and AHe record. By analogy to juxtaposed regions, paleosurface formation was likley in the Paleozoic, with Permian and Jurassic re-exposure.

Following constraints were defined:

(1) The last known date of higher paleotemperatures than 120°C is provided by ^{40}K–^{39}Ar and $^{40}Ar/^{39}Ar$ ages of 430–490 Ma (Takigami *et al.*, 1987). Whole rock ages obtained on biotite and hornblende rich gneiss mark paleotemperatures >300°C.

(2) Upper Permian formation or re-exposition of low-relief erosional surfaces mark surface temperatures at ~300 Ma (cf. section 5.2.3).

(3) Early Jurassic shallow crustal position and exposition of the paleosurface is narrowed down in section 5.2.3. Constraints were set between 15–60°C, in the order of the recent paleosurface dissection.

(4) The recent mean annual surface temperature is -18°C at Asuka Station (~800 m) (calculated from Yamanouchi *et al.*, 1988; Aoki, 1989; Matsuoka *et al.*, 1990; Meshida *et al.*, 1991; Iwasaki & Yamanouchi, 1992; Sukegawa & Yamanouchi, 1993). These temperatures were used to calculate the distinctive surface temperatures under consideration of the orographic gradient (Appendix C, Table S 7).

(5) Further constraint boxes between 40–170 Ma and 200–300 Ma were set widely to allow all iterations between surface temperatures as well as complete resetting (i.e. temperatures higher as the apatite partial annealing zone). Furthermore, the lower limit of boxes was adjusted to Mesozoic and Cenozoic surface temperatures.

A complete overview of input preferences and constraints is provided in the appendix (Appendix C, Table S 8 and Table S 9).

The course of the inverse thermal history models is very similar throughout, however with some paleotemperature variation (Appendix C, Figure S 8). As constrained by K/Ar dates at 450Ma, cooling proceeded further on. Since 300 Ma reheating to 80–110°C is marked with subsequent cooling to below 60°C around 180–230 Ma. The reheating between 250 and 200 Ma indicates an almost complete reset and hence, limits high-resolution thermal information to the time after 200 Ma. Thermal history models show some reheating between 160 and 135 Ma to temperatures of 50–110°C, with subsequent cooling to present day surface temperatures, tentatively with an acceleration of cooling around 40 Ma. In general, the shapes of the paths and the maximum paleotemperatures do not correlate with present elevation.

Best fitting common forward thermal histories were achieved for all samples. Common thermal history of western Sør Rondane indicates temperatures of 95–110°C at ~215 Ma with cooling to very low temperatures at 182 Ma. Uniform reheating followed between 182–140 Ma with high heating rates between 182 and 165 Ma, and with lower rates until 140 Ma. Cooling is shown subsequently until 115 Ma. A stagnation or slight of cooling is offered until ~40

Ma. Since 40 Ma the models cooled all below 40°C and hence, the thermal histories relay only on total cooling.

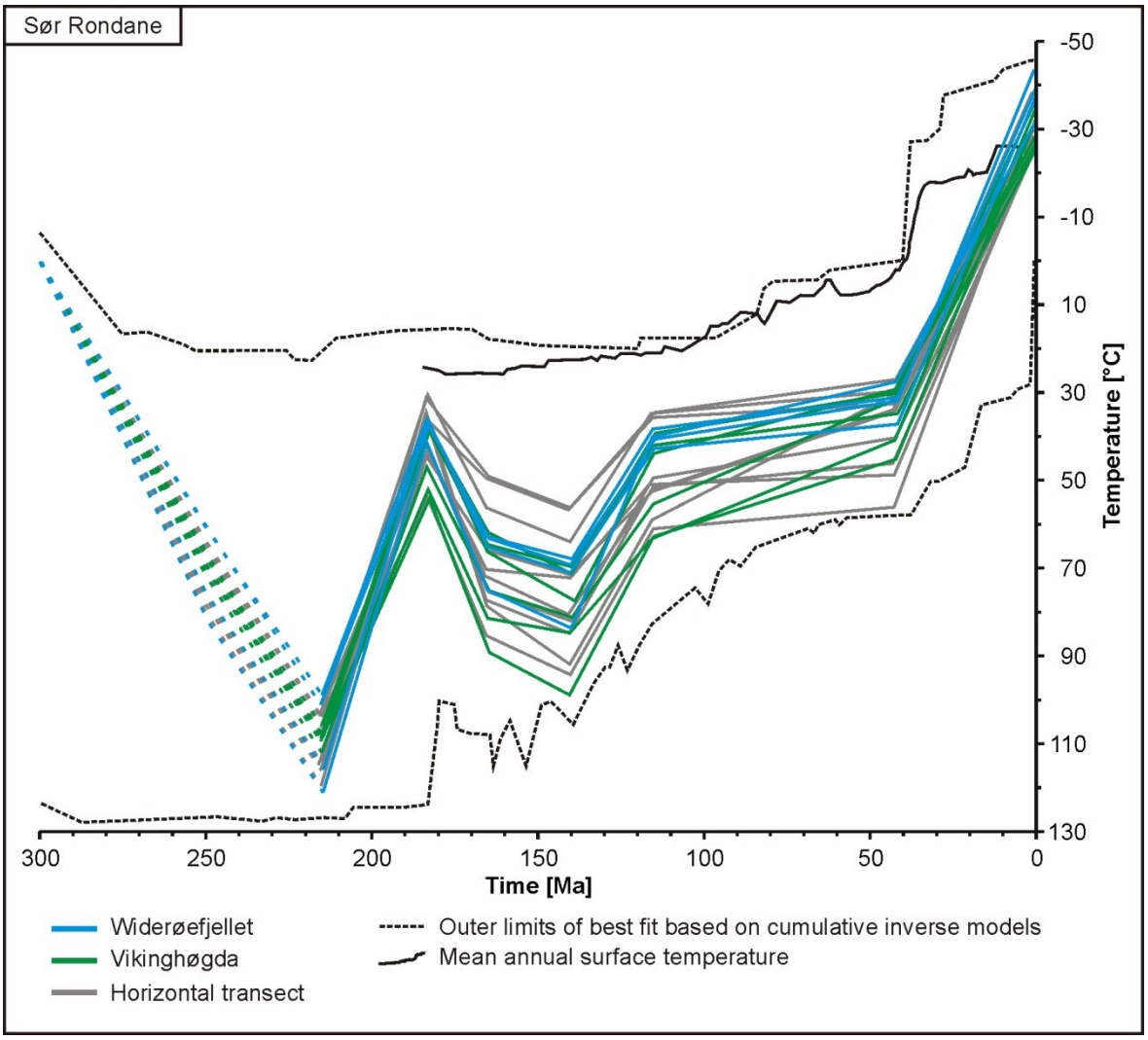

Figure 23: Compilation of thermal history models of Sør Rondane. All thermal history models (except TC14) are supported by GOF>0.5 (Appendix C). The stippled lines illustrates areas that are blurred by subsequent main cooling. For thermal history inversion see Appendix C, Figure S 8. Temperature variation curve by (Prenzel *et al.*, 2014)

TC38 and TC24 were sampled closely beneath paleosurface remnants. Same courses and temperatures (or even lower) of thermal history models were interpreted here as representing the original paleosurfaces.

5.5. Discussion

5.5.1. Permo-Triassic basin evolution

Sør Rondane hosts paleosurface remnants that are not dated as sediments are lacking. However, Early Permian exposure of the basement paleosurface is indicated by subsequent deposition of sediments in western DML. Thermal history modeling based on fission track and AHe dating on apatites supports Early Permian near surface position of the paleosurface and

the basement in Sør Rondane, with subsequent reheating to maximum paleotemperatures of 105–120°C until ~215 Ma (Figure 23). The lowermost temperature of 105°C refers to the temperature of the paleosurface. The only mechanism to substantially and consistently reheat surface rocks over great areal distances is burial of the basement by deposition of sediments. This implies that western Sør Rondane was buried by sediments during the Permian and the Triassic. Congeneric Permo–Triassic basins are known from adjacent regions: western DML (Bauer *et al.*, 1997), Mozambique (Salman & Abdula, 1995) and further East Africa (Kreuser, 1995). Assuming a conventional geothermal gradient of 25–30°C/km and a Late Triassic surface temperature of 25–35°C (Fawcett *et al.*, 1994), these paleotemperatures refer to maximum basin depths of 2.8 km in the vicinity of Sør Rondane. Maturity data of lower Permian coals from western DML suggest post-Permian maximal paleotemperatures of 80°C, implying basin depths not exceeding ~2.5 km. Remarkably, geohistory diagrams for East African intracontinental grabens infer maximal basin depths of 2.6 km (Kreuser, 1995). Regarding the geometry and the depth of the East African grabens or basins, a southward relation or perhaps a continuation to the DML basins is likely (Figure 24). This fits well with the revised paleogeographic reconstructions (Kristoffersen *et al.*, 2014) that place the coastline of DML closer to north Mozambique. However, a detailed determination of the structural architecture of the DML continental sags requires a more narrow-spaced thermochronological sampling.

These basins were formed due to Gondwana extension and sagging (e.g. Veevers & Tewari, 1995). Taking this altogether, the region was characterized by shallow intercontinental grabens indicating far-field extensional stress.

Subsequent and overall cooling of the Sør Rondane basement since ~215 Ma suggests regional degression of overburden and implies unroofing and the basin inversion. The formation of the Permo-Triassic basins documents the widespread stress regime. Ongoing extension likely formed areas of enhanced crustal weakness. The rift model of Huismans *et al.* (2001) implies, that once a critical lithospheric thinning is reached, the buoyancy of asthenosphere triggers active rifting, leading to tensional stresses within and compression around the upwelling region, likely accompanied by surface uplift and increasing denudation. Basin inversion predates the onset of magmatic activity of the Ferrar/Karoo LIP by ~20 Ma.

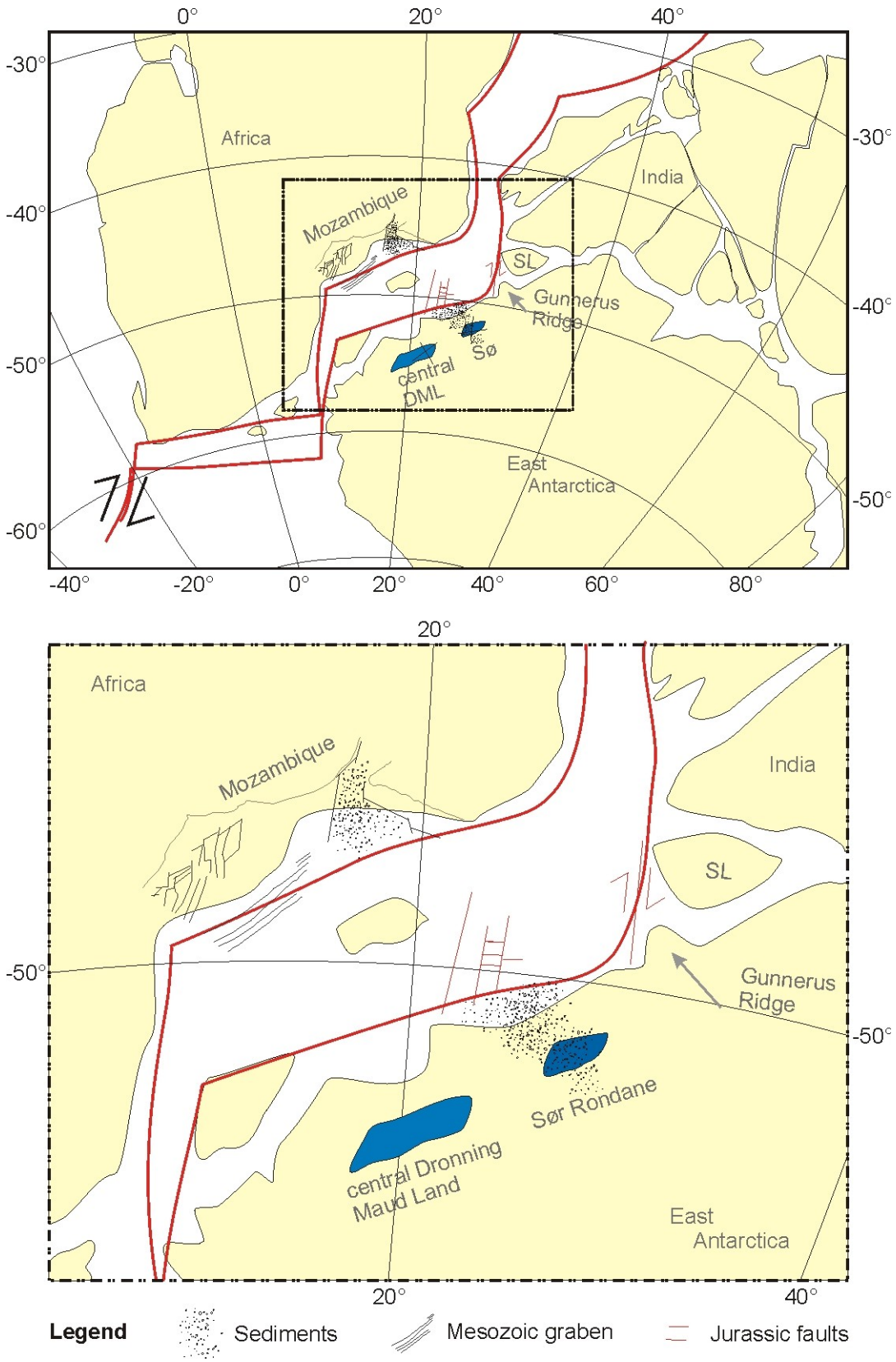

Figure 24: Outline of the Permian basins and Jurassic rift features illustrating the relationship and the distribution of Permian sediments. Modified after Salman & Abdula (1995), Owada *et al.* (2003), Leitchenkov *et al.* (2008) and Reeves *et al.* (2016).

Corresponding to that, the basin inversion is coeval with stratigraphic hiatus and changes in sedimentary pattern in the main Karoo basins as well in the East African basins (Kreuser,

1995; Catuneanu *et al.*, 2005). This process, in this context often described as epirogenic uplift in East Africa, seems to have a regional extent.

5.5.2. Jurassic rifting and margin evolution

The ongoing extensional regime since basin inversion is documented by magmatism as suggested by Jurassic intrusions in the transitional crust (Leitchenkov *et al.*, 2008; Mieth *et al.*, 2014), and more obvious by the creation of first sea floor in the Riiser-Larsen Sea at 155 Ma and formation of NNE–SSW trending strike-slip ridges and NE–SW trending spreading axes (Jokat *et al.*, 2003; Leitchenkov *et al.*, 2008). The same structural trend is obvious in Sør Rondane and would strongly evidence for a congenic formation. This would imply the far-field tectonic influence of extension. This fits well to structural observations in central DML. Here, conjugate fault systems point to the similar paleostress direction and resembles the offshore structures in the Larsen Sea.

Early Jurassic temperatures of ~20–60°C modeled in this study indicate that the basement and the Permian paleosurface of Sør Rondane was re-exposed to the surface or placed near the surface. This event initiated reheating to maximum temperatures of ~60–100°C between 185 and 140 Ma. Individual thermal histories are similar with reheating until 165 Ma attenuating until 140 Ma. Reheating must be related either to igneous activity or to burial heating.

Not all mafic dykes are dated yet. However, intensive igneous activity would enhance crustal temperatures and heat would be transported convectively (hydrothermal activity) and conductively (enhanced geothermal gradient). Both processes would be characterized by local variation in temperatures and would result in heterogeneous thermal overprint. Such irregular pattern is not obvious in Sør Rondane. Moreover, igneous Karoo/Ferrar event was short-term event and terminated at ~178 Ma (e.g. Riley & Knight, 2001), while temperatures remained homogenously stable and high until 140 Ma. Hence, heat flow increase due to magmatic and hydrothermal activity unlikely accounts as here as cause of reheating. Instead, igneous or sedimentary burial must be considered as main cause for reheating.

In central DML, Emmel *et al.* (2007) report a similar reverse relationship between ages and elevation of the topographically uppermost samples between 2600 and 3000m. The authors relate the reverse relationship to thermal imprint of Jurassic intrusion. In general, a thermal aureole is twice to triple as thick as corresponding thickness of an intrusion (e.g. Bauer *et al.*, 1997). Thus, the heat supplied by near-surface intrusions to create a 0.5 km thermal aureole would require ~1.5 km thick intrusion in minimum. This theory seems to be invalid, as the underlying samples do not allow such thick overburden.

In western DML Jurassic to Cretaceous burial of the basement paleosurface by up to 2 km thick lava flows was postulated by Jacobs & Lisker (1999) via thermochronological methods. Indeed, a Jurassic lava pile of 900 m thickness is preserved in the vicinity. However, the required quick cooling at 100 Ma seems difficult to explain by erosion of ~1 km of the basalts with regard to the competence of trap basalts. However, the stepwise cooling pattern consisting of stages of rapid erosion followed by a stage of enhanced temperatures during the whole Cretaceous is hardly explainable by erosion of a rheological homogenous rock column.

Instead, rapid cooling that is related to exhumation can be explained better by erosion of softer material. This implies erosion of a more incompetent material. In this view, the incompetent deposits require a shallow morphological sink for accumulation and preservation until rapid removal. With regard to the regional extensional regime the formation of shallow continental basins seem probable. Jurassic graben structures within the conjugate basin (Mozambique Basin) hosts Jurassic Karoo Lavas and rhyolites of unknown thickness and up to 900 m Jurassic red beds (Salman & Abdula, 1995). Speculatively, the same material may have been deposited in the Sør Rondane basin.

In Sør Rondane the general temperature increase with declining heating rates between 165 and 140 Ma indicates sedimentary overburden with slighter sedimentation rates and would imply ongoing extension with decreasing subsidence rates. Varying paleotemperatures within the Jurassic basin provides insights into basin geometries. Assuming a conventional geothermal gradient the maximum overburden on the paleosurface was between 1 km in the southernmost and westernmost part and 1.5 km near Ketelersbreen. This suggests a dissection of the paleosurface. The highest paleotemperatures were obtained in the western Vikinghøgda region and near Ketelersbreen, referring to 2.5 km of burial, including here the amount of basement overburden and the thickness of the deposits.

5.5.3. Cretaceous to Eocene basin

Further cooling occurred contemporaneously in Sør Rondane commenced in Sør Rondane at ~140 Ma to temperatures between ~30–65°C. The overall event indicates the onset of erosion , and hence basin inversion. The similar to slightly higher paleotemperatures with regard to the Jurassic to Cretaceous mean annual temperature (MAT) with 26–30°C (Jenkyns *et al.*, 2012) would imply the virtually or complete erosion of basin-fill. The basin inversion is contemporaneous with the change in spreading direction in the Indian Ocean and the onset of widespread igneous activity in the Riiser Larsen Sea and Larsen Sea (for example, Astrid Ridge, Mozambique Ridge) (Hinz *et al.*, 2004; König & Jokat, 2010; Leinweber & Jokat, 2012; Reeves, 2014). This tectonic episode is also reported by Emmel *et al.* (2009) in central DML,

as well as on the conjugate part in Mozambique (Daszinnies *et al.*, 2009; Emmel *et al.*, 2012). The regional coincidence would imply the timing of tectonic (re-)activation and landscape modification along the passive margin, probably associated with decoupling between Africa and Antarctica in the Riiser-Larsen Sea and Larsen Sea.

The Sør Rondane thermal history models collectively show a declination of cooling to 25–56°C beginning at 115 Ma until ~40 Ma. The rate of cooling is very low and nearly similar to the long term rate of atmospheric temperature drop. A stable geothermal gradient would imply steady state conditions, whereas a lower geothermal gradient would imply reheating, and a higher gradient would imply cooling.

The assumption of a paleogeothermal gradient of 25°C/km increases the surface temperatures and crustal paleotemperatures. This would require compensational basement heating with a maximal overburden of 0.8 km on the paleosurface.

Varying temperatures and cooling rates are aligned roughly along the MSZ and at the southwestern flank of Vikinghøgda relative to its northern flank including Widerøefjellet, and can be explained by tectonic movements with maximum offsets of ~600 m (Figure 23).

Conjugate brittle shear zones (σ1: WNW–ESE) in the vicinity of the MSZ, with possibly congenic reverse faults perpendicular to σ1 point to the formation of positive flower structures. Crucially, same σ1 directions for conjugate fault systems with congenic creation of reverse faults/positive flower structures occur in central DML (Owada *et al.*, 2003). This points to regional oblique compression and implies likely a large-scale tectonic influence. Compressive stress occurred between 54 and 72 Ma due to major changes in seafloor spreading direction, including reorganization of the mid oceanic ridge and relative motion direction of DML to Africa (Reeves *et al.*, 2016). Offshore evidence of this compressional event is attested in the Riiser Larsen Sea by reverse faulting in an originally extensional graben structure (Rao *et al.*, 1992). The transpression was accompanied by minor displacements, but it likely initiated the final basin inversion. An increasing erosion is also documented by enhanced sediment supply on the continental margin (Leitchenkov *et al.*, 2008).

5.5.4. Glaciation and long-term landscape evolution

In Sør Rondane, the remnants of the Permian paleosurface are recently elevated up to 3200m. Low relief formation and the preservation of regional flat paleosurfaces required its stay in low energy environments and/or coverage by a protective sheet. Both necessitate–at least for formation and initial coverage–near sea level placements. Furthermore, the ongoing extensional stress regime and the thermal histories discussed above do not allow high elevation settings prior to the transpression. The recent high elevation and topographic relief require

substantial uplift and morphological modification since the Eocene. Thermal history models indicate cooling/erosion initiating at 40 Ma. However, the low paleotemperatures and the lack of external constraints, such as sediments or datable geomorphological features restrict full resolution of the thermal history.

Paleotemperatures between 27–56°C , surface temperatures of ~7°C and the assumption of an Eocene geothermal gradient of ~25°C/km of the Transantarctic Mountains (Prenzel *et al.*, 2014), suggest an overburden of 0.8 km on top of the basement. The maximum paleotemperatures of 56°C determine the maximum erosion of 1.6 km to recent times. Enhanced erosion is documented by a substantial increase of sediment supply in the Eo/Oligocene that resulted in the formation of 1.5 km thick sedimentary layers in the proximal Riiser Larsen Sea (Solli *et al.*, 2007; Leitchenkov *et al.*, 2008). Morphological modification and progressive relief formation is proposed to have begun by fluvial incision, followed by wet based glacial erosion, especially along pre-existing faults (Sugden *et al.*, 1995). A positive feedback is suggested further on between rock incision and isostatic compensation that is manifested by increasing relief formation (Sugden *et al.*, 1995; Näslund, 2001).

The mapped crustal thickness in eastern DML is in the order of 40 km, and more ~55 km in central DML. Our thermal history models only support a late crustal thickening. Gravity data indicates an elongated Bouger anomaly that trends from central DML to Sør Rondane parallel to the recent shoreline (Mieth, 2014). The anomaly is interpreted as either thicker than normal crust or a crust with low-density. The thicker than normal crust can explain the recent high elevations of central and eastern DML. Furthermore, isostatic models of the crust indicate isostatic disequilibria and a current isostatic uplift of central DML. Resulting relief increase most likely prompts gravitational instability and triggers normal faulting likely on preexisting faults. Neogene or Quaternary normal faulting is obvious in our data: same Jurassic to Eocene paleotemperatures occur recently at different vertical levels and can be explained either by post Eocene independent movement along steep verging listric faults or by reactivation of shear planes of the MSZ. The highest rates of relative faulting occurred along the Main Shear Zone (Dry Valley) close to glacial valley flanks.

Tentatively, at 20–10 Ma, the basement temperatures coincide with the surface temperature of ~-10°C and indicate subaerial exposure. However, cooling of the basement does not terminate with the basement exposure to the surface. The supposed late and varying paleosurface exposure and differential erosion would also explain the morphologic evolution with partially preservation of the surfaces. Calvet *et al.* (2015) describe that elevated and uncovered erosion surfaces/plateausurfaces are easy to destroy and are stable for 10 Ma in maximum. The varying erosion rates resulted in varying surface modification. Surfaces that were bare at 20

Ma were glacially shaped until ca. 15 Ma, while others were protected under sediment and/or possibly hard Karoo magmatic rocks. The preservation of the surfaces is supported by the hyperarid conditions with very low Quaternary erosion rates (Matsuoka *et al.*, 2006; Suganuma *et al.*, 2014).

5.6. Conclusions

The combined thermal history modeling and integration of time-temperature markers constrained by evidence of paleosurface exposure and brittle structural inventory, revealed a well-resolved evolution history of western Sør Rondane since the Permian. The outcome also revises the recent knowledge about exhumation and landscape evolution of the regions in the vicinity to the highly exposed passive margins: The current premise concerning the evolution of the passive margins in Dronning Maud Land of stepwise exhumation and solely burial by thick lava flows subsequent to volcanism is not valid, as burial by magmatic lavas alone cannot explain the required exhumation pattern. Instead, we propose another scenario that is consistent with geomorphology, thermal history models, and geophysical observation and to the evolution history of adjacent regions (Figure 24).

This excludes a highland setting as suggested by former thermal history models that would have existed in the Triassic. Instead, continental basins cover most of the time the area and the topographic highlands as such were a Cenozoic feature.

The assumption of a temporal correlation of the paleosurface exposure in other parts of DML was supported by thermal history models. Eastern DML was covered by 2.5 km thick sedimentary deposits during the Permo-Triassic. The region formed presumably part of the Permo-Triassic (Karoo) Basins of East Africa that stretches along the structural trend of the truncated Pan-African orogen (EAAO, Jacobs and Thomas 2004), including the Mozambique Basin. Furthermore, at least the basins close to the imminent mid-ocean ridges were inverted and uplifted between in the Late Triassic, before shallow burial by mostly incompetent detritus. The similar conjugate fault systems revealed in the basement in Sør Rondane resembles the fault pattern offshore and indicates Far-field tectonic stress. The faults may be responsible for basin formation. A barely NE–SW- related trend between paleotemperatures is obvious. Basin inversion at 140 Ma seems to be related to changes in spreading directions and magmatic emplacements. Most probably, a slight veneer remains on the paleosurface that tend to increase until the Cenozoic. Probably, the structures were reactivated or inverted by Cenozoic to Eocene compression. Another plate motion change occurred during Late Cretaceous-Early Paleocene. The new paleostress field triggered reactivation of the Pan-African conjugate fault systems leading to faulting and dissection of the Sør Rondane Mountains, especially obvious

close to the MSZ. This scenario might also be the case for central Dronning Maud Land. Thermochronological data close to the major shear zone in central DML show similar age elevation relationships with inverse profiles (Emmel *et al.*, 2007). Inverse AFT age/elevation profiles can be explained by reverse faulting and are supported by regional brittle structural inventory. Furthermore, similar ages and brittle structural data hint strongly for a collective evolution. A similar scenario is also reported from passive margins in Namibia (Wildman *et al.*, 2015) and would imply a general process along shear zones.

Enhanced erosion since Eo-Oligocene supports the existent climate and landscape evolution models. Our data indicate late block faulting, and major dissection of 2000 m not earlier as the Eo-Oligocene and support only late uplift scenarios. This suggests that the crustal thickening revealed by geophysics must have been ensued very late.

5.7. Acknowledgements

This work was supported by the German Research Foundation (DFG) in the framework of the priority program SPP 1158 'Antarctic Research with comparative investigations in Arctic ice areas' by grant LI745/15 to F. Lisker and LA 1080/9 to A. Läufer. N. Krohne, J. Jacobs and M. Elburg are indebted to the German Federal Institute of Geosciences and Natural Resources (BGR) for the invitation to participate in the GEA II expedition (Geodynamic Evolution of East Antarctica). We thank the International Polar Foundation, Alain Hubert and the crew of Princess Elisabeth Station for support in the field. Many thanks go to the SkyHeli Helicopter Team.

6. Early Neoproterozoic metagabbro-tonalite-trondhjemite of Sør Rondane (East Antarctica): Implications for supercontinent assembly

Marlina Elburg[a, b], Joachim Jacobs[c, d], Tom Andersen[e], Chris Clark[f], Andreas Läufer[g], Antonia Ruppel[g], Nicole Krohne[h], Detlef Damaske[g]

[a] Discipline of Geology, SAEES, UKZN, Westville, South Africa

[b] Department of Geology, University of Johannesburg, PO Box 524, Auckland Park 2006, South Africa

[c] Department of Earth Science, University of Bergen, Allégaten 41, 5007 Bergen, Norway

[d] Norwegian Polar Institute, Fram Centre, 9296 Tromsø, Norway

[e] Department of Geosciences, University of Oslo, PO Box 1047 Blindern, N-0316, Norway

[f] Department of Applied Geology, Curtin University, GPO Box U1987, Perth, WA 6845, Australia

[g] Federal Institute of Geosciences and Natural Resources (BGR), Stilleweg 2, 30655 Hannover, Germany

[h] Department of Geosciences, University of Bremen, PF 330 440, 28334 Bremen, Germany[a]

Precambrian Research 259, 2015, 189-206 - doi 10.1016/j.precamres.2014.10.014

Highlights

- The ca. 1 Ga meta-igneous rocks of the Sør Rondane Mountains (E. Dronning Maud Land, Antarctica) were generated in an oceanic arc setting.
- Subduction halted around 950 Ma, giving rise to more diverse magmatism.
- Igneous ages and isotopic characteristics suggest a pre-Gondwana connection to India-Sri Lanka-Madagascar.

Keywords

Antarctica; Rodinia; Gondwana; Oceanic arc; Zircon U-Pb Lu-Hf

Abstract

New data for intrusive meta-igneous rocks from the Southwest terrane of the Sør Rondane Mountains confirm the view that this is a juvenile oceanic arc terrane, with the main phase of subduction-related magmatic activity around 995–975 Ma. Younger magmatism (960–925 Ma) is more varied: a high Sr/Y ('adakitic') suite is present, as well as high-Ti mafic dykes, and one sample of A-type granite. This is interpreted as reflecting the end of subduction. The occasional presence of Archaean inherited zircons suggests proximity of Sør Rondane to an older continental nucleus from which detritus was shed. Although the 'meta-igneous sector' appears to be unique in representing a juvenile oceanic arc terrane, igneous

ages and isotopic compositions around 1000–900 Ma suggest a broad coherence between outcrops ranging from Schirmacher Oasis (11° E) to Yamato Mts (35° E). This area seems unrelated to the slightly older, and isotopically and geochemically more enriched Mesoproterozoic rocks of central and western Dronning Maud Land. A closer relation appears to exist with Sri Lanka-India-Madagascar during the earliest Neoproterozoic than with southern Africa.

6.1. Introduction

The Sør Rondane Mountains, located in the eastern part of Dronning Maud Land, have been subjected to an appreciable amount of geological research recently, as they have been proposed to lie in an area where several fold belts, related to the amalgamation of Gondwana, interact (Jacobs *et al.*, 1998; Meert, 2003; Boger, 2011; Osanai *et al.*, 2013). To correctly interpret Gondwanan events it is important to characterize the fragments involved in amalgamation, and their similarities and distinctions to neighboring areas. In this context, interesting differences between the ca. 1 Ga meta-igneous samples from Sør Rondane and those from the more westerly parts of Dronning Maud Land were noted recently (Shiraishi *et al.*, 2008; Kamei *et al.*, 2013; Owada *et al.*, 2013).

With the present contribution, we want to add to the data and discussion provided by previous authors on the 1.0–0.9 Ga meta-igneous rocks (the 'metatonalite suite' of Kamei *et al.*, 2013) in the southwestern part of Sør Rondane. We will focus on the integration of zircon U-Pb, Lu-Hf and trace element data with whole rock geochemical data to assess the models proposed for the tectonic setting in which the magmas were generated. A comparison with data from neighboring areas in Antarctica and its Gondwana neighbors will be used to assess the tectonic implications for the Rodinia as well as Gondwana supercontinent.

6.2. Geological background

The first geological investigations of the Sør Rondane Mountains were carried out by Belgian expeditions in the 1950–60s, who recognized that an older series of metamorphic rocks (metatonalites and related lithologies) was intruded by younger (now known to be Pan-African) granites (van Autenboer *et al.*, 1964). More recent mapping has been done by Japanese expeditions, who also published a geological map of the area (Shiraishi *et al.*, 1997), and whose most recent efforts were described in a special issue of *Precambrian Research* (volume 234, 2013).

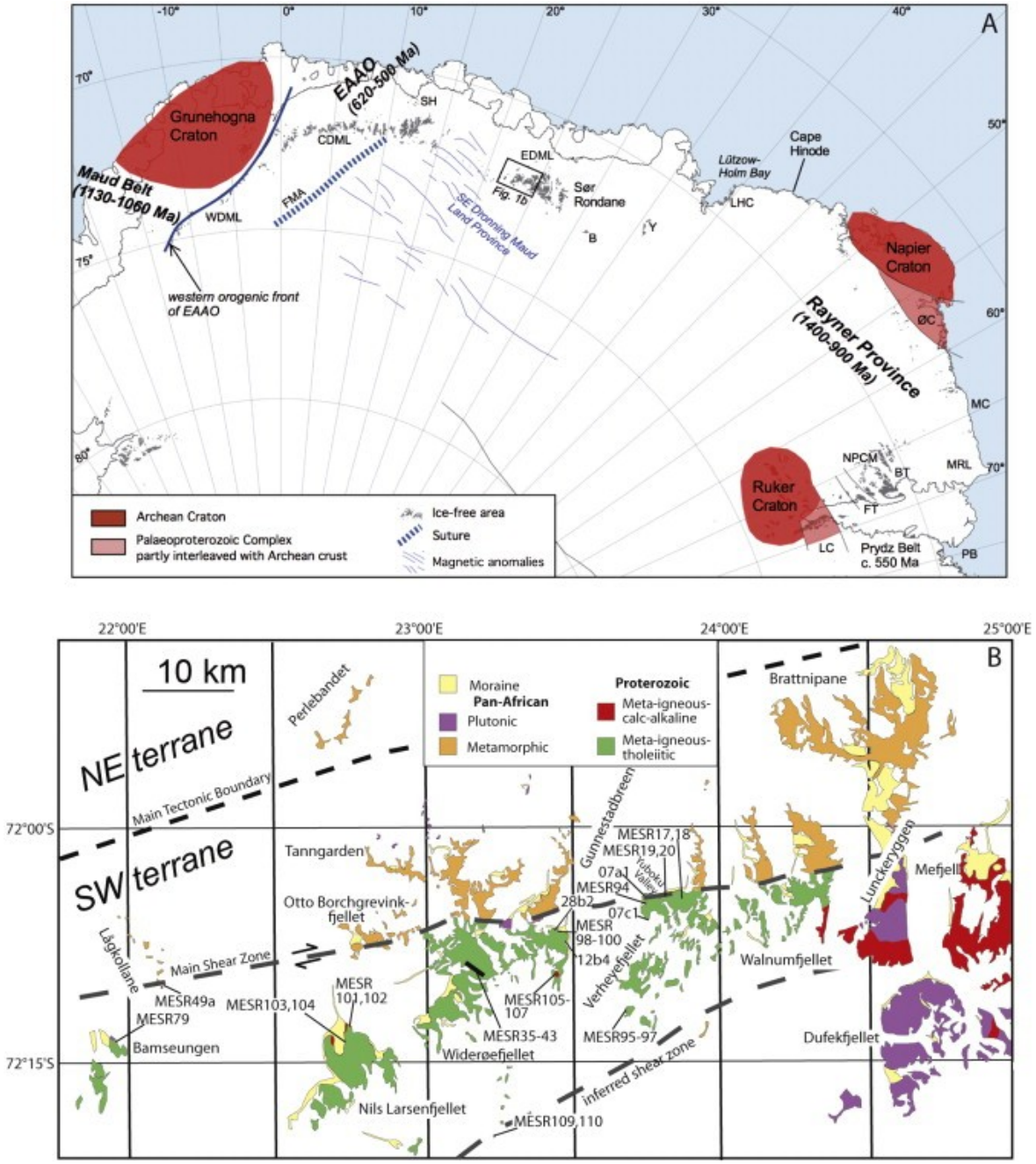

Figure 25: Regional tectonic framework of the Sør Rondane Mountains, eastern Dronning Maud Land. Sør Rondane is located halfway between the Grunehogna and the Napier cratons. The Grunehogna Craton is surrounded by the Mesoproterozoic Maud Belt with African (Kalahari) affinities, whilst the Napier Craton, which is fringed by the ca. 1.4–0.9 Ga Rayner Complex, has affinities to greater India. The Forster Magnetic Anomaly (FMA) has been recognized as a significant Late Neoproterozoic suture zone. The area may be dissected by additional Late Neoproterozoic suture zones that are, however, less well defined. *Abbreviations*: B, Belgica Mts.; BT, Beaver Terrane; CDML, central Dronning Maud Land; EAAO, East African-Antarctic Orogen; FT, Fischer Terrane; LC, Lambert Complex; LHC, Lützow-Holm Complex; MC, Mawson Coast; MRL, Mac. Robertson Land; NPCM, northern Prince Charles Mts.; PB, Prydz Bay; SH, Schirmacher Hills; WDML, western Dronning Maud Land; Y, Yamato Mts; ØC, Øygarden Complex. (B) Geological map of the Sør Rondane mountains after Kamei *et al.* (2013), Osanai *et al.* (2013), Shiraishi *et al.* (1997) and our own data, indicating the location of the samples analyzed in this study.

The Sør Rondane Mountains have been divided into two areas of different metamorphic affinities, the granulite-amphibolite-facies Northeast (NE) terrane and amphibolite-greenschist-

facies Southwest (SW) terrane. The boundary between the two areas, first named the 'Sør Rondane Suture' (Shiraishi *et al.*, 1997) has recently been redefined as the 'Main Tectonic Boundary' (Osanai *et al.*, 2013), and shifted slightly northwards compared to its location inferred previously. What will be referred to as the 'meta-igneous sector' is part of the SW-terrane, located between the Main Shear Zone (MSZ; with a dextral sense of shear Ruppel, 2012) in the north and another, inferred, shear zone north of Dufekfjellet in the south(Figure 25), where the rocks consist almost wholly of meta-igneous rocks, at amphibolite-greenschist-facies. The part of the SW-terrane located north of the MSZ consist largely of metasedimentary, rather than meta-igneous rocks, and has experienced granulite- to amphibolite-facies metamorphism (Osanai *et al.*, 2013).

Data on the meta-igneous suite have been provided by the reports to the individual geological maps of Sør Rondane Shiraishi *et al.* (1992a), and by Ikeda & Shiraishi (1998), but a more detailed study was done by Kamei *et al.* (2013), and additional data, focused on the mafic end member, were presented by Owada *et al.* (2013). The work by Kamei *et al.* (2013) divides the area in several suites: a 998–995 Ma (SHRIMP U-Pb zircon) gneissose Bt-Hbl metatonalite, with tholeiitic affinities in terms of (elevated) FeO*/MgO ratios, with associated mafic enclaves; and four suites of calc-alkaline rocks (hbl-bt metatonalite, hbl metagabbro, hbl-bt tonalitic gneiss, and bt metatonalite), which yielded ages of 945–920 Ma, apart from a sample of bt metatonalite in Nils-Larsenfjellet, which gave an age of 772 Ma. On the basis of the geochemical characteristics of the two suites, Kamei *et al.* (2013) proposed a juvenile oceanic arc setting for the tholeiitic suite, and interpreted the calc-alkaline suite as having formed by an 'adakite scenario', i.e. melting of a subducted oceanic slab with residual garnet, also in a subduction setting.

In contrast, Owada *et al.* (2013) focused on the mafic rocks associated within the meta-igneous sector, and divided them into a ca. 995 Ma low-Ti (TiO_2 <1.2 wt.%) suite of mafic enclaves and a ca. 945 Ma high-Ti (TiO_2 >1.2 wt.%) suite of dykes. Owada *et al.* (2013) also interpreted the low-Ti samples to have formed in a juvenile arc terrane, but the younger, high-Ti group was, interpreted to have been formed in a back-arc setting, contrasting with the subducted slab-melt scenario of Kamei *et al.* (2013).

6.3. Sample description

6.3.1. Field appearance

A total of thirty-four samples was collected from the outcrops occurring to the south of the 'Main Shear Zone' (Shiraishi *et al.*, 1997; Figure 24) during the German-led 'Geodynamic Evolution of East Antarctica' (GEA) expeditions I and II in the Austral summer of 2010–2011 and

2011–2012. The rocks are dominantly coarse-grained and mesocratic in appearance, with a distinctly green tinge. More melanocratic rocks can be fine- or coarse-grained. The melanocratic rocks occur as discrete mappable bands or as mafic enclaves or dykes within the more mesocratic rocks (Figure 26A–F).

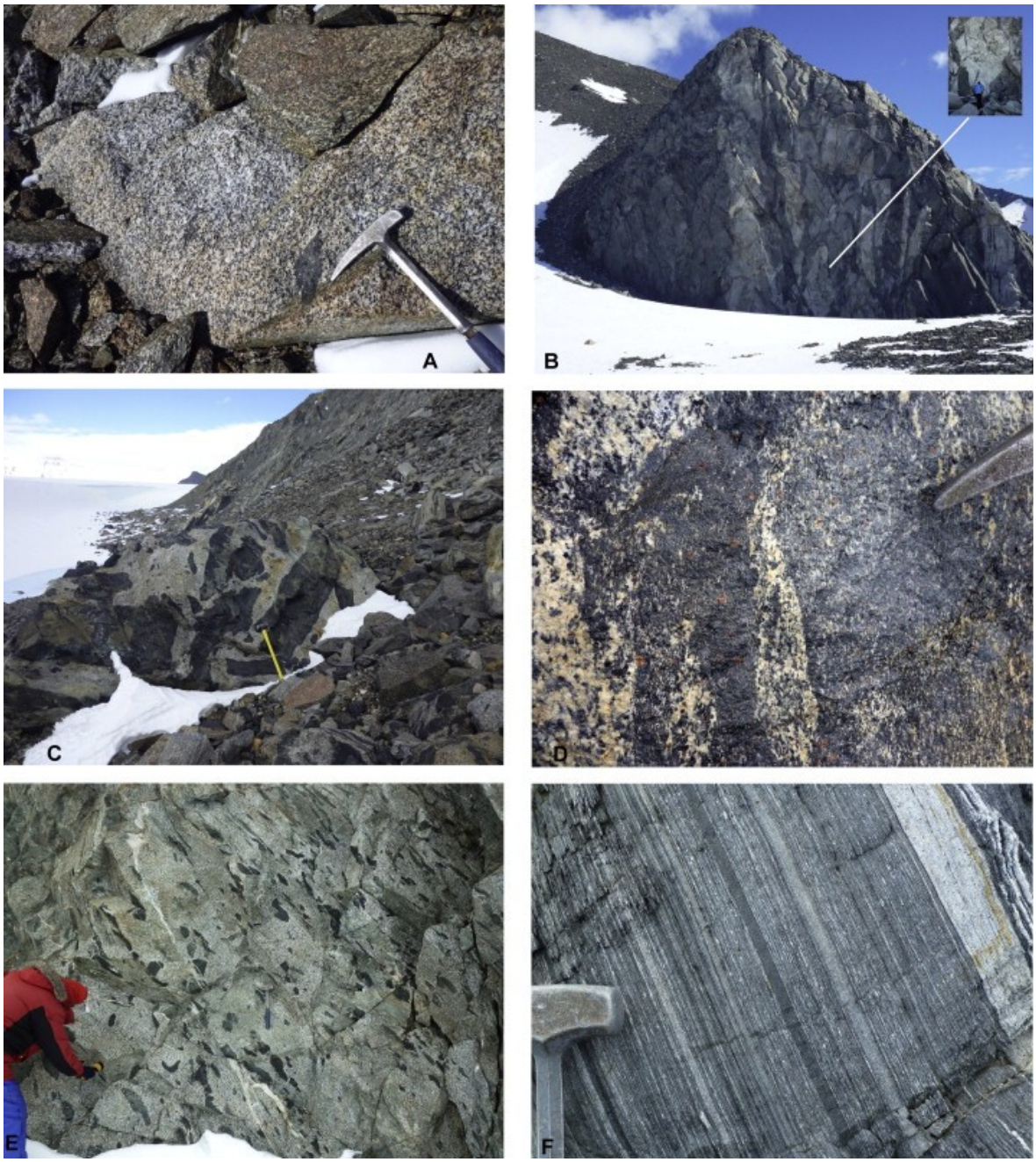

Figure 26: Field photographs of the sampled lithologies. (A) Metatonalite with quartz-gabbroic enclave on central Widerøefjellet (sample MESR38). (B) Outcrop at the east side of Widerøefjellet. Sample MESR99 was taken from the most leucocratic material. Inset shows person for scale. (C) Enclave-bearing metatonalite on the east side of Nils-Larsenfjellet (MESR101-102). Note the scalloped rims of the mafic enclaves, indicative of an origin by magma mingling. (D) Caussinknappen nunatak, showing intermingling of mafic and felsic (MESR110) material, and the presence of garnet. (E) Undeformed enclave-bearing metatonalite from which sample 07C1 was taken. (F) Area from which sample 07A1 originates, interpreted to be the deformed equivalent of panel E.

In some cases, the mafic enclaves can be seen to originate from mafic dykes. Leucocratic dykes of up to 5 m width have also been observed. There is plenty of evidence of ductile deformation in the field, especially close to the 'Main Shear Zone', but the intensity of this deformation is variable. In some instances, it is possible to recognize textures that can be interpreted to be of igneous origin, such as the presence of (subvolcanic) quartz phenocrysts (Figure 27A) and larger feldspar crystals that are likely to have been phenocrysts before becoming porphyroclasts.

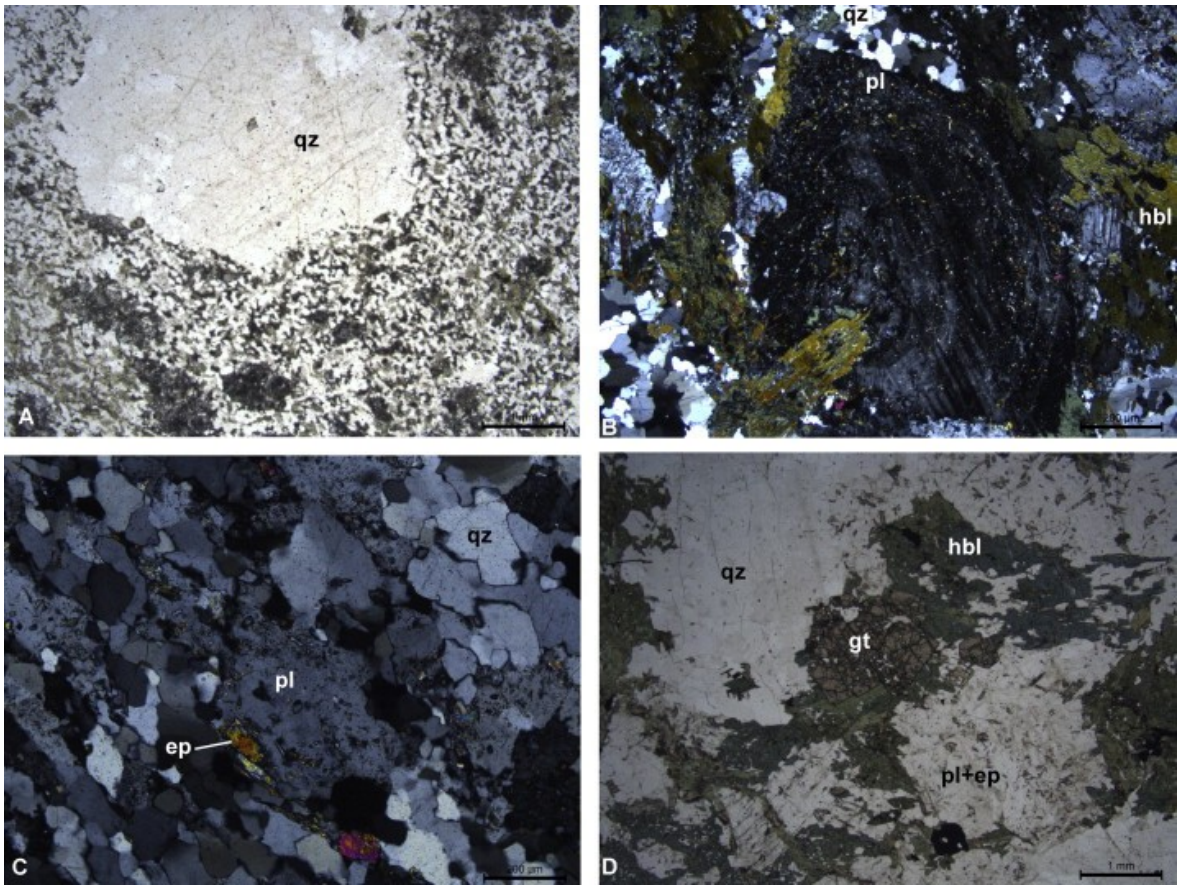

Figure 27: Photomicrographs of selected samples. (A) Sample MESR97, with quartz phenocrysts in a fine-grained matrix, interpreted to represent a shallow-intrusive origin of the sample. (B) Sample MESR100, showing broad oscillatory zoning in the plagioclase crystal, interpreted to be a relict of the igneous protolith. (C) Sample MESR99, the oldest sample analyzed, consisting predominantly of quartz and plagioclase, partially altered to epidote. This sample could either be a felsic cumulate, or a crystal-rich tuff; the texture is clearly metamorphic, and does not permit a choice between the two options. (D) Sample MESR104, containing subhedral garnet, interpreted to be of metamorphic origin.

6.3.2. Petrography

All samples analyzed are, essentially, metamorphic rocks, with epidote and chlorite as the most obvious metamorphic minerals, but the extent to which they have been metamorphosed is variable. In some samples, plagioclase crystals are wholly replaced by finer-grained epidote, while in other samples igneous oscillatory zoning may still be visible within the plagioclase (Figure 27B).

Because of the metamorphic overprint, the samples have been classified (Figure 28) on the basis of their normative mineralogy and intrusive QAPF classification (Le Maitre, 2002), with the additional category of trondhjemite based on the Ab-An-Or diagram of Barker (1979) (see Appendix D, which also gives data on the modal mineralogy).

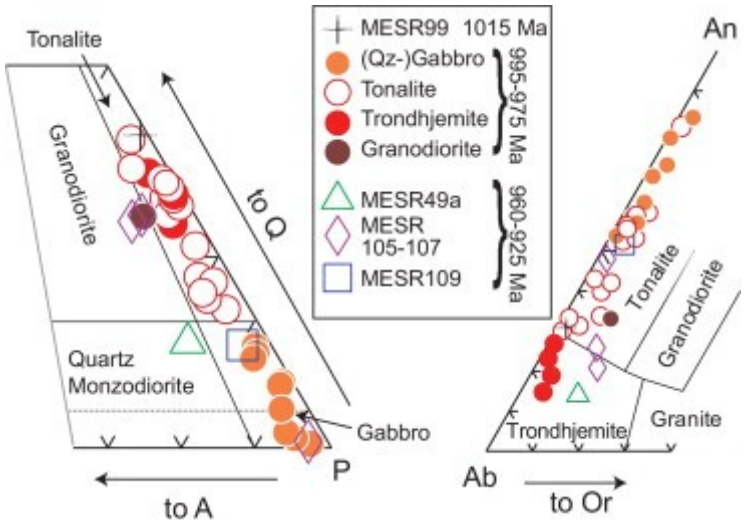

Figure 28: Relevant parts of QAPF (Le Maitre, 2002) and Ab-An-Or normative diagrams (Barker, 1979) on which the classification of the samples has been based.

The texture of the meta-(quartz-)gabbros is variable: it can be foliated, porphyroclastic, coarse- or fine-grained equigranular, meta-porphyritic, meta-ophitic, or poikilitic, with large oikocrysts of amphibole. In some cases, amphibole is zoned from cores with a more olive-green color to rims where the green has a more bluish tinge. Plagioclase in variable stages of epidotisation is present in all samples, as is minor quartz. Chlorite is more common in the sheared samples. Opaque minerals are present in most samples, and titanite in some. Apatite is an accessory phase, apart from sample MESR109, in which it occurs at the percent level; this sample also contains more abundant oxides than other meta-gabbros.

Intermediate samples mainly classify as metatonalites, and contain lower modal amounts of amphibole, while chlorite and quartz increase in abundance, with biotite in more potassium-rich samples. Accessory minerals are apatite, zircon, titanite, and opaque minerals, and more rarely rutile. In some samples, the opaque minerals are partially replaced by titanite. Amphibole is sometimes riddled with small inclusions of opaque minerals and/or rutile, often elongated in certain orientations with respect to the host crystal, suggesting they were formed by exsolution. Garnet occurs as eu- to subhedral crystals in samples with higher FeO*/MgO ratios. It can contain inclusions of opaque minerals, and does not display reaction rims; it is therefore interpreted to be formed during prograde metamorphism of the tonalites. Calcite occurs as a secondary mineral in some samples. Sample MESR99 classifies as a tonalite, but is extremely low in mafic minerals (leucotonalite).

The metatrondhjemites mainly differ from the metatonalites in their lower modal amount of amphibole, the absence of titanite and higher quartz contents, but the distinction between tonalite (modal An% >30) and trondhjemite (modal An% <30) is gradual.

One sample (MESR49a) is an only slightly metamorphosed quartz-monzodiorite, and, unlike all the other samples, contains microcline. Samples MESR97, 105 and 106 are classified as metagranodiorites, and contain white mica.

All samples show some signs of deformation, varying from undulose extinction of the quartz, to sutured grain boundaries and a porphyroclastic texture, whereby larger plagioclase crystals are enveloped by ribbons of quartz, amphibole, epidote and chlorite defining an S-C fabric. Neither the intensity of metamorphism, as evidenced by the extent of epidote formation, nor the intensity of deformation appears to be related to the age (varying between ca. 1015 and 925 Ma, see below) of the samples.

6.4. Analytical techniques

A more detailed description of the analytical techniques used is given in Appendix D. Major and trace elements were analyzed at the Discipline of Geological Sciences, University of KwaZulu-Natal, by X-ray fluorescence (XRF) spectrometry on fused discs and pressed pellets respectively, using a PANalytical Axios–minerals sequential XRF spectrometer. Lower-level trace elements were analyzed by laser ablation (LA) inductively coupled plasma mass spectrometry (ICPMS) of the XRF fused discs using an NWR UP-213 laser and Perkin-Elmer Nexion quadrupole ICPMS. Trace elements in zircon were also analyzed using the latter setup.

Laser-ablation U-Pb and Lu-Hf isotopic analyses were performed at the Department of Geosciences, University of Oslo, using an NWR UP-213 laser and a Nu Instruments multi-collector ICPMS, following techniques described by Elburg *et al.* (2013). Four samples were dated by U-Pb on zircon using a Sensitive High Resolution Ion-Microprobe (SHRIMP) at Curtin University (Perth, Western Australia; Appendix D). Two samples were analyzed for Sr and Nd isotopes at the Department of Geological Sciences of the University of Cape Town.

6.5. Zircon U-Pb and Lu-Hf data

Zircon U-Pb data were acquired on a total of twelve samples, spanning the geographic area from which the samples were obtained. Eight of these were analyzed by LA-MC-ICPMS (sample identifiers starting with 'MESR') and four by SHRIMP (sample identifiers starting with a number). The full data set can be found in Appendix D. All uncertainties are quoted at the 2-sigma level (Table 7).

Table 7: Summary of zircon U-Pb ages and Hf isotopes.

Sample	Age type	Age (Ma)	2σ (Ma)	n	Interpretation	εHf_i	2σ
07A1	Concordia	979	5	15	Igneous		
	$^{207}Pb/^{206}Pb$ wtd. av.	987	13				
07C1	Concordia	986	3	18	Igneous		
	$^{207}Pb/^{206}Pb$ wtd. av.	987	6				
12B4	Concordia	984	6	12	Igneous		
	$^{207}Pb/^{206}Pb$ wtd. av.	994	8				
	Upper intercept	1024	14	4	Inherited		
	$^{207}Pb/^{206}Pb$ wtd. av.	1039	13				
28B2	Concordia	991	5	11	Igneous		
	$^{207}Pb/^{206}Pb$ wtd. av.	990	6				
MESR99	Concordia	1015	4	20	Igneous	+6.5	2.6
	$^{207}Pb/^{206}Pb$ wtd. av.	1010	5				
MESR43	Concordia	991	4	25	Igneous	+6.5	2.0
	$^{207}Pb/^{206}Pb$ wtd. av.	986	4				
MESR104	Concordia	986	6	14	Igneous	+6.3	1.7
	$^{207}Pb/^{206}Pb$ wtd. av.	984	7				
MESR79	Concordia	986	7	15	Igneous	+7.3	2.4
	$^{207}Pb/^{206}Pb$ wtd. av.	990	18				
MESR110	Upper intercept	979	18	8	Igneous	+4.2	1.2
	$^{207}Pb/^{206}Pb$ wtd. av.	979	15				
MESR106	Concordia	957	8	11	Igneous	+7.5	2.1
	$^{207}Pb/^{206}Pb$ wtd. av.	957	5				
	$^{207}Pb/^{206}Pb$	1006 – 1070		4	Inherited	+7.9	0.8
	$^{207}Pb/^{206}Pb$	2910 – 2966		1	Inherited?	+3.6	0.9
MESR49a	Concordia	947	8	10	Igneous	+7.7	1.8
	$^{207}Pb/^{206}Pb$ wtd. av.	960	7				
MESR109	Upper intercept	927	+37/−22	2	Igneous	+6.9	5.2
	$^{207}Pb/^{206}Pb$ wtd. av.	929	14				
	Upper intercept (with MESR106)	2970	+32/−30	1	Inherited	−2.1	

n, number of analyses on which the age is based. Samples 07A1, 07C1, 12B4 and 28B2 analyzed by SHRIMP, others by LA-MC-ICPMS.

The zircons that were dated by LA-ICPMS were also analyzed for their Lu-Hf isotope systematics to determine the initial $^{176}Hf/^{177}Hf$ ratios and assess the degree of homogeneity within the samples.

Sample 07C1 comes from a mesoscopically undeformed tonalite, containing abundant mafic enclaves (Figure 26E). This locality is ca. 1 km S of the MSZ (Figure 25). The up to 400 µm large zircons are clear to light brownish with few inclusions. In cathodoluminescence (CL) imaging, zircons show irregular sector zoning, and sometimes a faint oscillatory zoning. Eighteen spots were analyzed on eighteen crystals. Typical U-concentrations range from 100 to 900 ppm (Th/U: 0.15–0.28). The 18 analyses define a concordia age of 986 ± 3 Ma (Figure

29A), which is interpreted as the crystallization age of the tonalite. This is indistinguishable of the weighted average $^{207}Pb/^{206}Pb$ age of 987 ± 6 Ma.

Sample 07A1 represents the mylonite equivalent of the metatonalite (Figure 26F), as exposed in the southern part of the MSZ, west side of Yuboku Valley (Figure 25). It contains zircons that appear as anhedral fragments up to 200 μm in size. Zircons are clear to light brownish and have numerous inclusions. In CL images, they show oscillatory or sector zoning. Some zircons have high-U rims, which are too thin to be analyzed. Eighteen crystals were analyzed with one spot each. The zircons are low in U (70–210 ppm) with Th/U from 0.13 to 0.24. Two spots yielded discordant ages, and one spot gave an age that was ~50 Ma younger than the other analyses. The remaining fifteen analyses yielded a concordia age of 979 ± 5 Ma (Figure 29B), which is interpreted to be the age of the tonalitic protolith to the mylonite. The weighted average 207Pb/206Pb age is similar at 987 ± 13 Ma. The discordant analyses probably reflect Pb-loss as the result of deformation.

Sample 12B4 comes from the east side of Widerøefjellet and is a heterogeneous, fine-grained felsic gneiss of trondhjemitic composition. The zircons are mostly small and clear, often not exceeding 100 μm in size. In CL imaging, the zircons show moderate zoning. Some zircons have metamict cores others have thin high-U rims. Sixteen grains were analyzed from the main weakly oscillatory-zoned parts, which have typical U concentrations of 250–500 ppm (Th/U: 0.36–0.48). Fourteen analyses define a concordia age of 984 ± 6 Ma (Figure 29C), albeit with a slightly high MSWD of concordia of 4.5. This age is the best estimate of the igneous crystallization age of the sample, and within error of the weighted average $^{207}Pb/^{206}Pb$ age of 994 ± 8 Ma. The remaining four analyses can be used to give a discordia with a very poorly defined lower intercept and an upper intercept of 1024 ± 14 Ma (weighted average $^{207}Pb/^{206}Pb$ age is 1039 ± 13 Ma). The MSWD of this discordia is 0.58, and its relevance will be discussed in conjunction with the LA-MC-ICPMS data for sample MESR99 from the same general area.

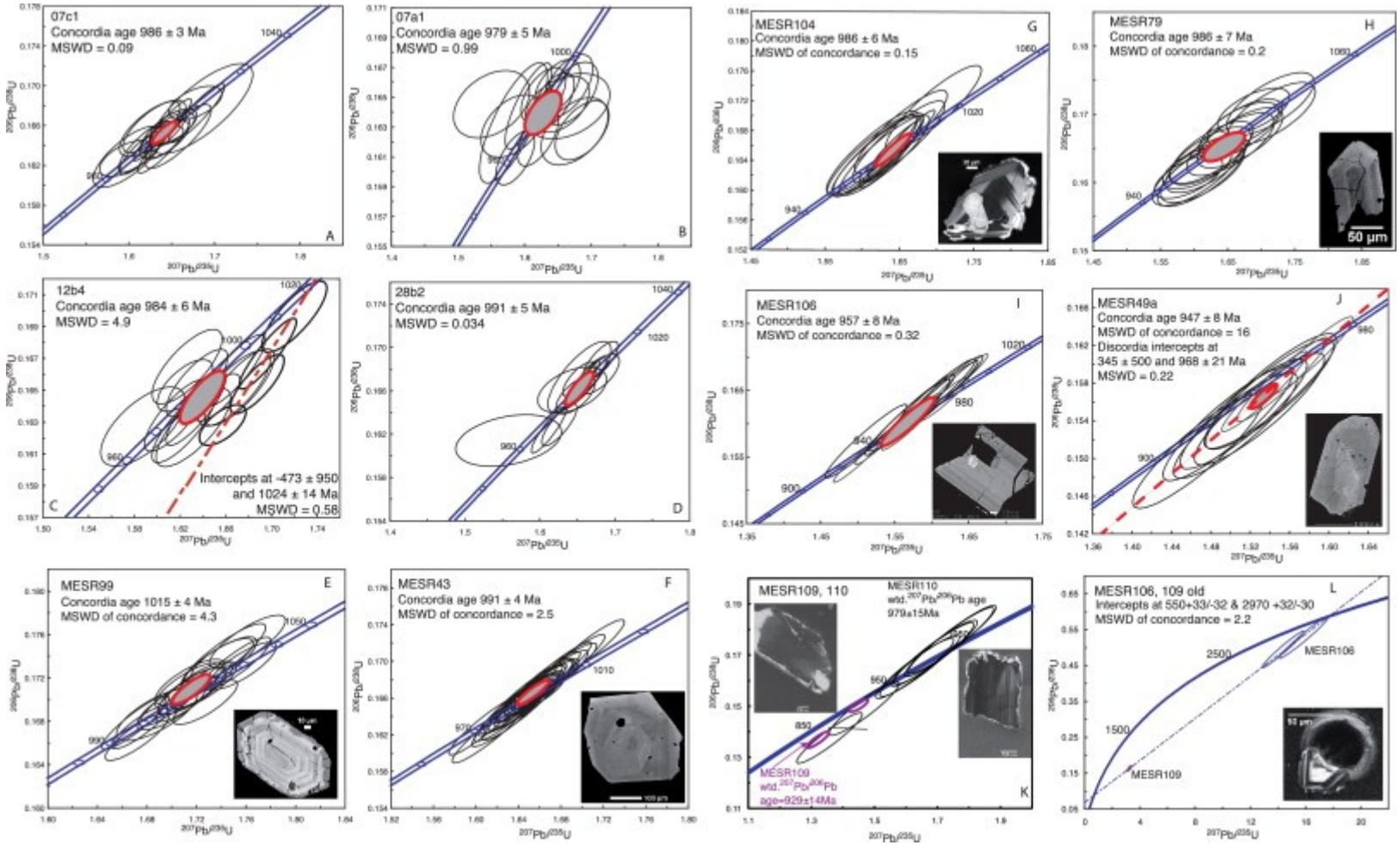

Figure 29: Zircon U-Pb data. Only the analytical points that were used for age calculation are shown; full analyses are given in Appendix D. All uncertainties are 2σ. (A–D) Sample analyzed by SHRIMP (Curtin University, W. Australia); (E–L) samples analyzed by LA-MC-ICPMS (Oslo University, Norway), which were also analyzed for Lu-Hf and trace elements. Zircon portraits are BSE images, apart for panels G, H, K and L (CL). The ~3 Ga zircon in sample MESR106 (panel L) was only imaged after ablation, hence the crater.

Sample 28B2 comes from an area to the northwest of 12B4 and is a foliated metatonalite. The zircons are stubby, light brownish and mostly anhedral. In CL, the zircons show a core-rim relationship, with dark cores and very bright irregular rims. Twelve crystals were analyzed, targeting eight cores and 4 rims. One core yielded a strongly discordant analysis. Whilst the high-U cores have U from 500 to 2200 ppm (Th/U: 0.14–0.52), the rim analyses have much lower U ranging from 60 to 150 ppm (Th/U: 0.38–0.41). However, the seven core and four rim analyses are indistinguishable in age and yield a concordia age of 991 ± 5 Ma (Figure 29D), which is interpreted as the crystallization age of the protolith, indistinguishable from the weighted average $^{207}Pb/^{206}Pb$ age of 990 ± 6 Ma.

Sample MESR99 comes from an area between 12B4 and 28B2 on the east side of Widerøefjellet (Figure 25 and Figure 26). The outcrop consists of a variety of undeformed rock types, ranging from mesocratic to leucocratic metatonalite. The most mafic compositions are represented as mafic enclaves within an intermediate fairly coarse-grained intrusive. The most leucocratic material is present as 10 m-sized semi-angular patches with equidimensional to elongate shapes. The geological relationships between the different phases is unclear from field observations, as no chilled contacts were observed. The dated sample is of the leuco-tonalite, which is homogeneously fine-grained. Its zircons are euhedral, with aspect ratios <2:1 and typically only 100–150 μm in their longest dimension. Many of them have a turbid brown appearance, but clear ones are found as well. Back-scattered electron (BSE) imaging shows that some zircons display well-defined oscillatory zoning (Figure 29E), but others have more patchy zoning; the latter crystals typically yielded discordant analyses with significant common Pb. Many zircons have a thin, darker rim, which was not of sufficient size to be analyzed. Thirty-six crystals were analyzed, and yielded U-contents of 600–1200 ppm, with Th/U ratios (determined by LA-Q-ICPMS) of 0.4–1. Sixteen analyses yielded discordant and/or common-Pb influenced analyses. The remaining twenty analyses had $^{206}Pb/^{204}Pb$ ratios >8000 and yielded a concordia age of 1015 ± 4 Ma, with an MSWD of 4.3 (weighted average 207Pb/206Pb age is 1010 ± 5 Ma). The somewhat high MSWD reflects a range in the ages of the individual points between 1031 and 998 Ma (Figure 29E). The homogeneity in crystal size and shape, and their oscillatory zoning indicates that this is a single population of igneous zircons, and the age is interpreted to be the crystallization age of the zircons. A similar age is found from the discordia of four zircons in sample 12B4, from slightly further north. However, the main igneous age there is younger at 984 ± 6 Ma. This may reflect a next phase of magmatism, which may also have been responsible for the (undated) thin rims on the zircons in MESR99.

The average initial $^{176}Hf/^{177}Hf$ ratio of the 29 zircons analyzed is 0.282334 ± 0.000089 (2 sigma; Figure 30). The scatter is slightly outside that expected from analytical uncertainty, based on the repeated analyses of the Temora standard. The two lowest analyses might be outliers, and if these are left out the average comes to 0.282341 ± 0.000074, which translates to an εHf_i of 6.5 ± 2.6.

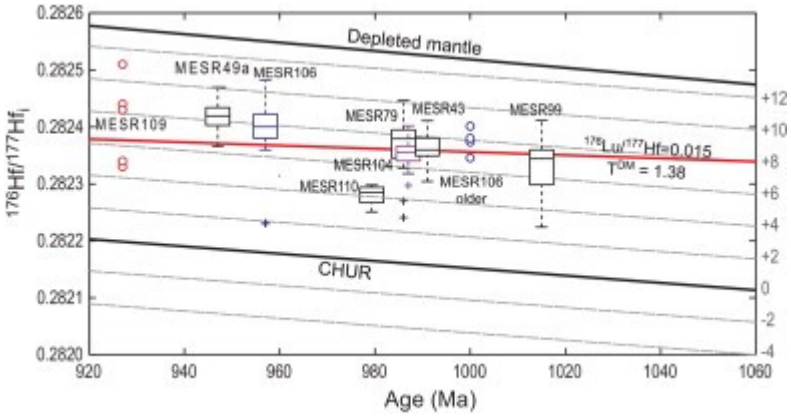

Figure 30: Box-and-whisker plot of initial zircon Hf isotopic composition versus age, with labeled contour lines for epsilon Hf. Because of the limited number of zircons analyzed for MESR109, only the data points are shown. Other data points shown are outliers from the main population. The reference line with $^{176}Lu/^{177}Hf = 0.015$ indicates the typical evolution of crust with a depleted mantle extraction age of ca. 1.4 Ga, which passes through most of the ca. 995–975 samples.

Sample MESR43 was taken near the bottom of a traverse down the south-central part of Widerøefjellet (Figure 25), and it is a moderately deformed, coarse-grained metatonalite. Its zircons are generally clear, with a light-purple color and aspect ratios <2:1. Their size is around 200–350 µm. Zoning is only poorly visible in BSE images, but appears to be oscillatory (Figure 29F). Twenty-six crystals (with U concentrations of 200–500 ppm; Th/U ratios around 0.25) were analyzed, of which only one is discordant. The other twenty-five analyses define a concordia age of 991 ± 4 Ma, albeit with a slightly elevated MSWD of 2.5. This age is within error of the weighted average $^{207}Pb/^{206}Pb$ age of 986 ± 4 Ma, and is interpreted as the crystallization age of the intrusion.

The twenty-six Lu-Hf analyses constitute a homogeneous population, with the spread in data within that expected from analytical uncertainty. The average initial $^{176}Hf/^{177}Hf$ ratio is 0.282360 ± 0.000056, or εHf_i of 6.5 ± 2.0.

Sample MESR104 comes from Nils-Larsenfjellet and is a moderately deformed metatonalite, which in places contains mafic enclaves. Zircons in this sample are about 200 µm and have aspect ratios from 1:1 to 3:1. Cathodoluminescence (CL) imaging shows well-defined oscillatory zoning in most crystals. Nineteen grains (U contents 200–600 ppm, Th/U = 0.25–0.5) were ablated, of which five gave discordant analyses. The other fourteen gave a concordant age of 986 ± 6 Ma (Figure 29G; weighted average $^{207}Pb/^{206}Pb$ age is 984 ± 7 Ma), with an

MSWD of 0.15, and this age is most likely to reflect the igneous crystallization age of the sample.

Twenty zircons yielded a homogeneous Hf isotope population with an initial $^{176}Hf/^{177}Hf$ ratio of 0.282353 ± 0.000049, or εHf_i of 6.3 ± 1.7.

Sample MESR79 is a coarse-grained metatrondhjemite from Bamseungen. Its zircons are between 100 and 200 μm, with aspect ratios up to 3:1, and show oscillatory zoning, which is poorly defined in BSE images, but clearly visible in CL. Some featureless cores are present too. Twenty-five ablations were performed on 23 grains. U concentrations were variable, from 50 to 200 ppm, but with spikes up to 3000 ppm; Th/U ratios were 0.4–1, with the higher values for the U-enriched grains. Some grains caused problems, because of elevated count rates for ^{206}Pb (>1 Mcps) causing dead-time problems and deviation from ion-counter linearity, resulting in reversely discordant analyses. Only fifteen analyses could therefore be used to obtain the igneous age of this sample, which is a concordia age of 986 ± 7 Ma (MSWD = 0.2; Figure 29H), within error of the weighted average $^{207}Pb/^{206}Pb$ age of 990 ± 18 Ma.

Twenty-seven zircons were analyzed for Lu-Hf systematics, of which two gave values that were significantly lower than the main population, and the CL image of one of these zircons showed the presence of a core, with a slightly discordant $^{207}Pb/^{206}Pb$ age of 1043 ± 32 Ma. Without these two analyses, the average initial $^{176}Hf/^{177}Hf$ ratio is 0.282380 ± 0.000067, or εHf_i of 7.3 ± 2.4.

Sample MESR106 was taken from the southeastern side of Widerøefjellet in an area with both felsic and mafic intrusives. It is a fine-grained granodiorite, with zircons of 100–200 μm. They are euhedral with aspect ratios from 2:1 to 5:1, and show concentric zoning, generally mimicking the outline of the crystal, in BSE images. Slightly brighter cores, with cracks around them, are present in some crystals. Twenty-six spots were ablated, with U contents typically 200–800 ppm, and Th/U between 0.25 and 0.45. One crystal gave an age of ~3 Ga, and four crystals yielded ages of 1050–995 Ma. Eleven other analyses gave concordant analyses, which together defined an age of 957 ± 8 Ma (Figure 29I; weighted average $^{207}Pb/^{206}Pb$ age is 957 ± 5 Ma), which is likely to be the crystallization age of the intrusion.

The igneous population (n = 21) gave an initial $^{176}Hf/^{177}Hf$ ratio of 0.282406 ± 0.000059, or εHf_i of 7.5 ± 2.1. The four grains that are slightly older give a marginally lower initial $^{176}Hf/^{177}Hf$ ratio of 0.282374 ± 0.000049. The initial $^{176}Hf/^{177}Hf$ ratio of the ca. 3 Ga grain was 0.28096 ± 0.000028 or εHf_i of 3.6 ± 0.9.

Sample MESR49a comes from the southernmost nunatak of the Lågkollane group, which consists of moderately deformed coarse-grained quartz-monzodiorite, intruded by undeformed

finer-grained granitoid and a pegmatite dyke. The sample is of the deformed quartz-monzodiorite. It contains numerous euhedral zircons between 200 and 400 μm in length and aspect ratios around 3:1. Cracks and inclusions are quite common. Several contain cores that are very bright and patchy in BSE images, but the majority of crystals displays fine-scale oscillatory zoning. Thirty-six spots were analyzed, but many of them were discordant and rich in common Pb, probably as a result of the many cracks and inclusions. U contents are 200–500 ppm, and Th/U ratios around 0.35. Only twelve analyses were of sufficient quality to be retained, and ten of these yielded a concordia age of 947 ± 8 Ma (Figure 29J). However, since most analyses plotted below the concordia, the MSWD of concordance is as high as 14. A discordia through the same sample set gives an upper intercept of 968 ± 21 Ma, which is within error of the concordia age, and the weighted average $^{207}Pb/^{206}Pb$ age of 960 ± 7 Ma. The other two analyses gave significantly younger ages at 880–910 Ma. The ca. 950 Ma age is taken as the best estimate of the igneous age for this sample.

MESR49a yielded a homogeneous Hf-isotope population of zircons (n = 34), with an average of $^{176}Hf/^{177}Hf$ = 0.282419 ± 0.000050, or εHf_i of 7.7 ± 1.8.

Sample MESR109 and 110 both come from the very small Caussinknappen nunatak, which consists of tonalite (MESR110) with garnet-bearing mafic enclaves and schlieren (Figure 26D). Garnet-free mafic material is also present, which has a sharper contact with the host rock and which we interpret to being a (poorly exposed) dyke; this constitutes sample MESR109.

MESR110 contains clear, virtually colorless zircons, typically with prismatic shape, and up to 300 μm in their longest dimension. Aspect ratios are typically 3:1. They show fine oscillatory zoning in CL imaging. Ten crystals were ablated, and gave U contents of 200–800 ppm. Two zircons are discordant and give $^{207}Pb/^{206}Pb$ ages of 940–950 Ma, and may have been affected by partial resetting by the magma that yielded MESR109 (see below). The other eight spots gave a weighted average $^{207}Pb/^{206}Pb$ age of 979 ± 15 Ma (MSWD = 0.06), and intercept ages at 979 +19/−18 and 66 +280/−60 Ma (Figure 29K).

This sample yielded a very homogeneous Hf isotopic population: 12 grains gave an average initial $^{176}Hf/^{177}Hf$ ratio of 0.282283 ± 0.000034, or εHf_i of 4.2 ± 1.2.

Zircons in MESR109 are rare and small (100 μm), and elongated in shape. Small zircons have aspect ratios up to 4:1, but larger ones are generally 2:1. They are typically cloudy brown in color, and give a very poor CL response. Only nine crystals could be ablated, of which one grain is clearly older ($^{207}Pb/^{206}Pb$ age >2 Ga). Of the seven other grains, only two show less than 15% discordance; the other five show a combination of Pb-loss and common Pb, yielding

$^{207}Pb/^{206}Pb$ ages between 950 and 1570 Ma, and $^{206}Pb/^{204}Pb$ ratios as low as 300. The two least discordant grains, with the highest $^{206}Pb/^{204}Pb$ ratios define a two-point isochron with an upper intercept of 927 +37/−22 Ma (Figure 29K), which is within error of the weighted mean $^{207}Pb/^{206}Pb$ age of 929 ± 14 Ma, which we take as the best estimate of the igneous age. When the older grain is combined with the two analyses of the old crystal in MESR106, a discordia with intercepts at 550 +33/−32 and 2970 +32/−30 Ma (MWSD 2.2) can be constructed (Figure 29L).

Only 6 grains were suitably large for Hf isotope analysis, and one of them was the inherited grain. The five igneous grains give a scattered distribution (Figure 30) with an average of $^{176}Hf/^{177}Hf$ of 0.282408 ± 0.000147, or εHf_i of 6.9 ± 5.2. If an age of 2.97 Ga is taken for the inherited grain, its initial Hf isotopic composition is 0.280821 or εHf_i of −2.1.

6.6. Geochemistry

In order to facilitate the presentation and discussion of the data, three main groups of samples are defined on the basis of their age: one sample, MESR99, with an age of ca. 1015 Ma; the main group of samples with ages between 995 and 975 Ma; and the younger samples (960–925 Ma). The main group has been subdivided on the basis of their mineralogy (Figure 28) into (quartz-)gabbros (nine samples), tonalites (fifteen samples), trondhjemites (four samples), and a single granodiorite (MESR97). The younger samples are quartz-monzodiorite MESR49a from Lågkollane, the quartz-gabbro MESR109 from Caussinknappen, and the two granodiorites and a gabbro from the SE of Widerøefjellet (MESR105–107). Note that the samples are referred to by their igneous name from now on, although all are strictly speaking metamorphic rocks.

6.6.1. Major and trace elements

Figure 31 shows selected Harker variation diagrams of major and trace elements (all analyses can be found in Appendix D), while Figure 32 and Figure 33 show normalized rare earth element (REE) and trace element diagrams. The main age (995–975 Ma) group of samples shows coherent trends that broadly conform to those expected from a consanguineous group of igneous rocks, related to each other by the fractionation of plagioclase and ferromagnesian mineral phases: CaO (as well as $Fe_2O_3^*$, MnO and MgO) decrease, whereas Na_2O and to a lesser extent K_2O increase with increasing SiO_2 content. The tonalite sample from Caussinknappen (MESR110) is unusual in its low sodium and high calcium content. Data for TiO_2 are somewhat scattered on the low-SiO_2 side of the diagram, but decrease from tonalite to trondhjemite. For the trace elements, V (as well as Cr, Ni, Sc and Co) decrease with increasing SiO_2 content, Y and Zr (as well as Rb, Ba and REE) show a scattered increase, while Sr con-

tents remain more or less constant after an initial increase. REE patterns are typically flat to slightly LREE-enriched for the (quartz-)gabbros, while LREE concentrations increase in tonalitic and trondhjemitic samples. Both positive and negative Ce- and Eu-anomalies occur, unrelated to the modal composition of the samples. Two (undated) samples show somewhat aberrant behavior: quartz-gabbro MESR18 has higher TiO_2, P_2O_5, Y and REE contents than other samples of this group, while granodiorite MESR97 has higher K_2O, Rb and Ba concentrations.

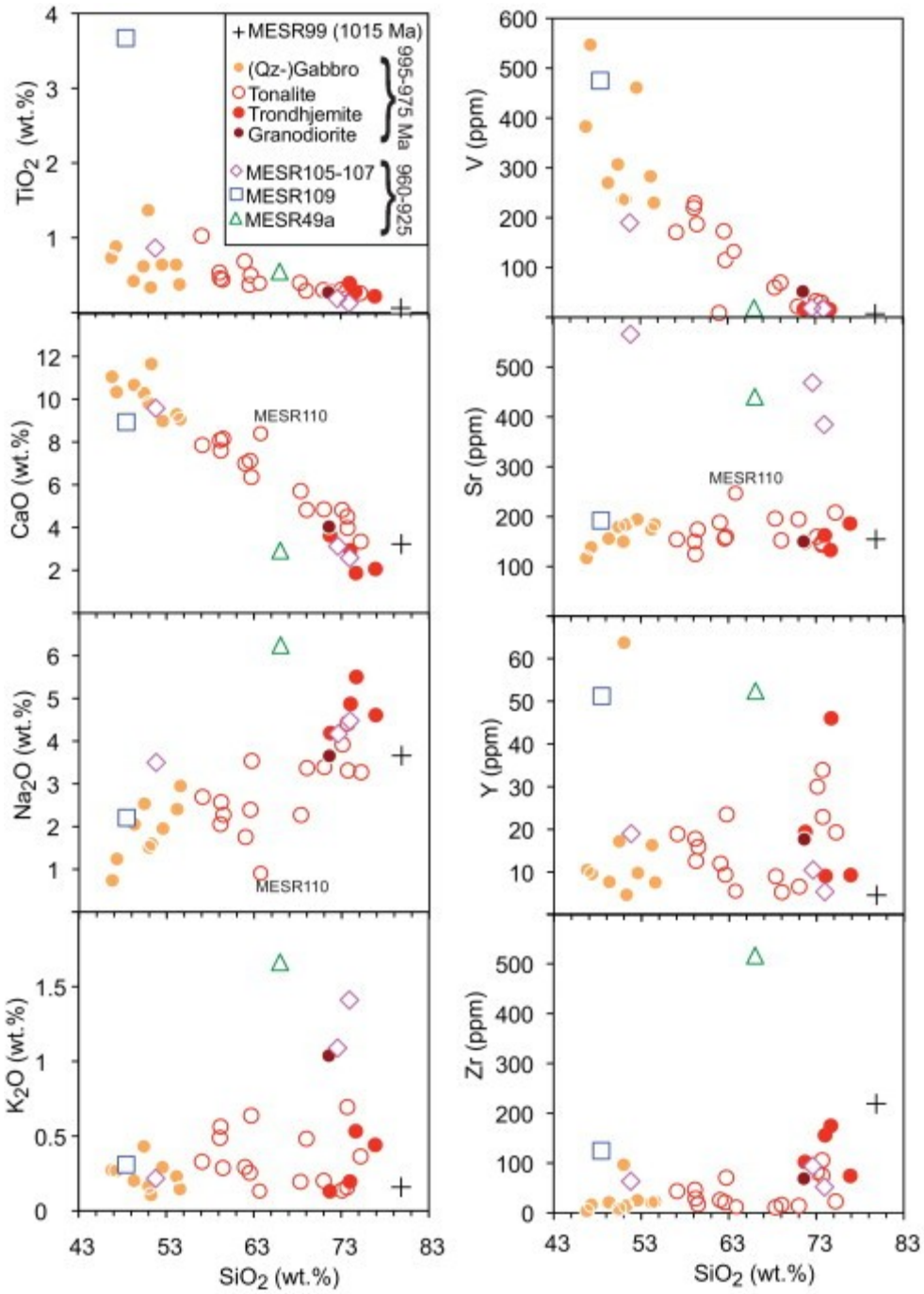

Figure 31: Harker variation diagrams for selected oxides and elements. Legend is given in the figure.

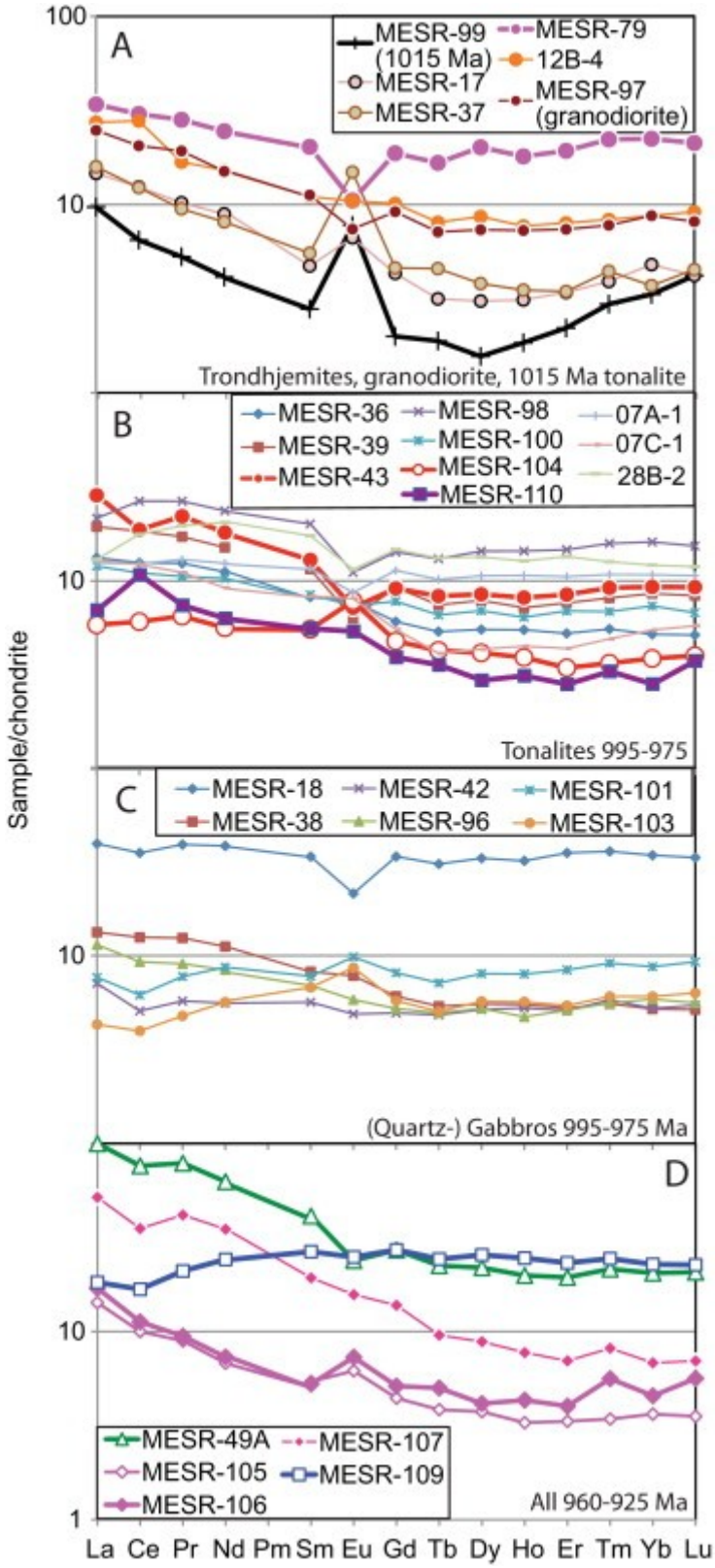

Figure 32: CI-normalized Rare Earth Element diagrams. Normalizing values from Evensen *et al.* (1978). Dated samples given in bold lines. (A) Patterns for the 995–975 Ma trondhjemites, granodiorite and the one older, high-SiO2 tonalite MESR99. (B) Patterns for the 995–975 Ma tonalites. (C) Gabbroic samples assumed to belong to the 995–975 Ma age group. (D) Mafic and felsic samples 960–925 Ma.

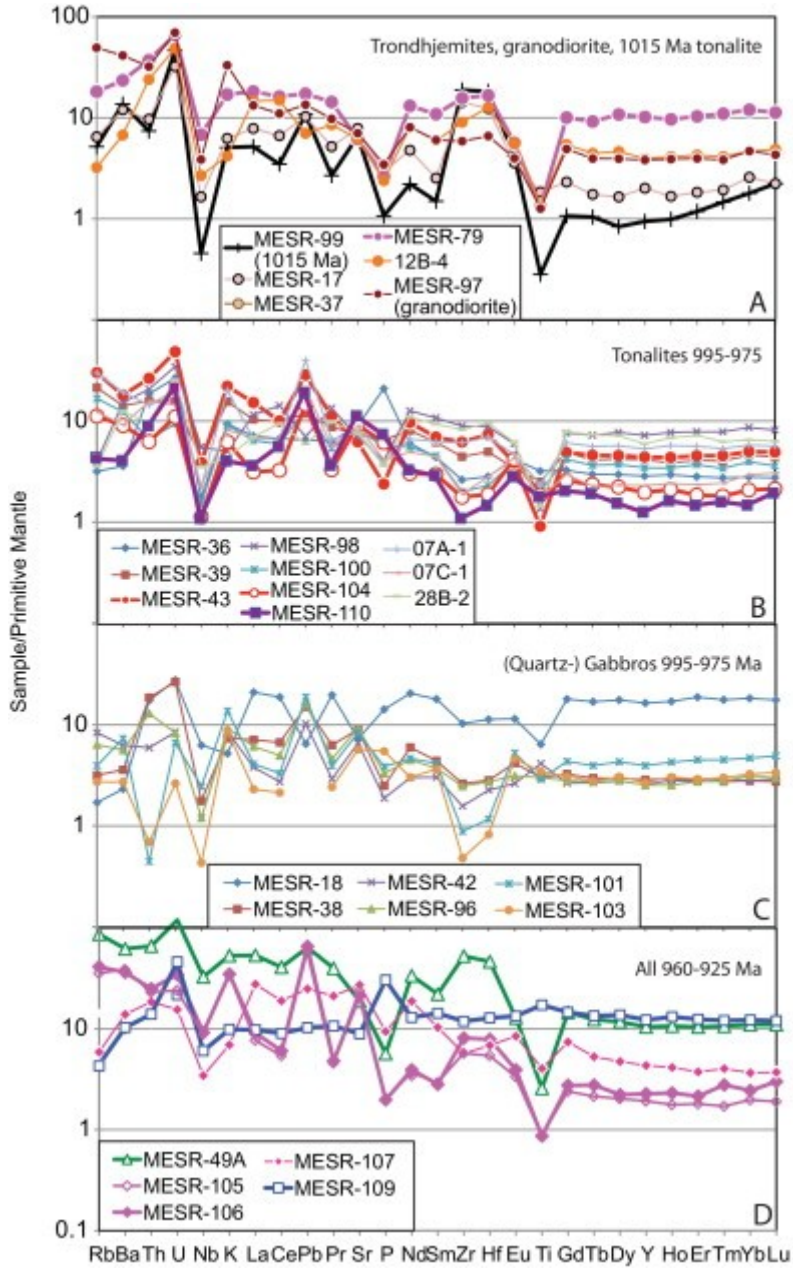

Figure 33: Primitive mantle-normalized trace element patterns. Normalizing values from Palme & O'Neill (2003). Legend and panels as for Figure 32.

The one sample that gave a marginally older age at ca. 1015 Ma has the highest SiO_2 content, and lies on the extension of the trend for the 995–975 Ma age group for most variation diagrams. Its REE pattern shows MREE depletion and a very pronounced positive Eu-anomaly (Eu/Eu* = 3.3), but is not too dissimilar to that of some of the trondhjemitic samples (Figure 32A).

Of the younger (960–925 Ma) samples, MESR105–107 as well as MESR49a stand out with respect to their high Sr, and for the felsic samples also high K_2O, Rb and Ba concentrations. Additionally MESR49a also has high Zr, Y, Nb, Ga and REE concentrations compared to the

995–975 age group. The qz-gabbro from Caussinknappen, MESR109, has very high TiO_2 (and P_2O_5) contents, and is the only sample to show LREE depletion.

Most samples, apart from some of the most felsic ones, are metaluminous (Figure 34). They classify as calcic in the modified alkali-lime diagram of Frost *et al.* (2001), apart from MESR49a, which is alkali-calcic and MESR109 which comes up as marginally calc-alkalic.

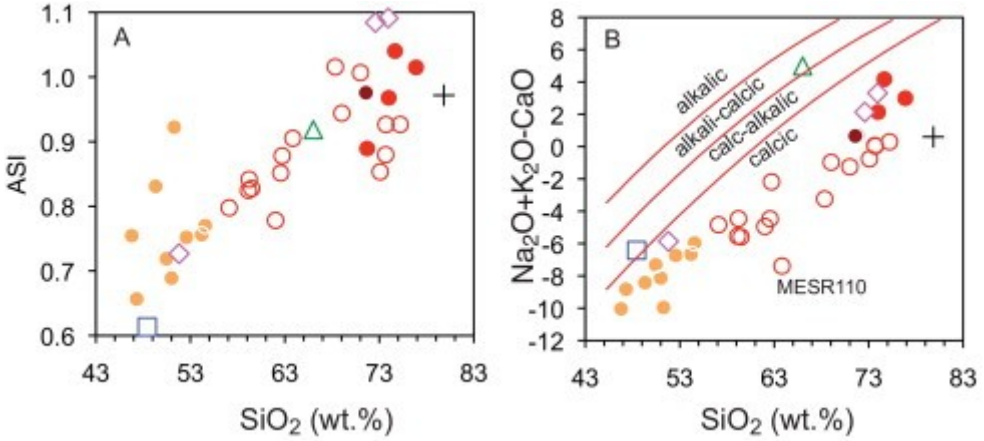

Figure 34: Classification diagrams. (A) Aluminum-saturation index (ASI = molar $Al_2O_3/(Na_2O + K_2O + Na_2O)$) versus SiO_2. (B) Modified alkali-lime diagram (Frost *et al.*, 2001). Most data classifies as being calcic, with MESR49a being a notable exception.

6.6.2. Sr and Nd isotopic systems

Only two samples were analyzed for Sr and Nd isotope ratios, since a major body of data on these systems was already presented by Kamei *et al.* (2013) and Owada *et al.* (2013). Sr isotopic ratios may be affected by metamorphism, and are therefore less reliable than the Nd isotopic values. The initial $^{87}Sr/^{86}Sr$ ratios are around 0.7033 for both MESR106 and MESR43 (Table 8), which is more or less the value for the Bulk Earth at that time. The $^{143}Nd/^{144}Nd$ ratios are, however, decidedly superchondritic (initial ε_{Nd} +3 to +4), with a somewhat higher value for MESR106 than for MESR43.

Table 8: Representative whole rock analyses.

Sample name	MESR43 Widerøe-fjellet C	MESR49A Lågkollane	MESR79 Bamseungen	MESR99 Widerøefjellet E	MESR104 Nils-Larsenfjellet W	MESR106 Widerøefjellet SE	MESR109 Caussinknappen	MESR110 Caussinknappen
SiO_2	73.70	66.01	74.66	79.85	68.34	72.59	48.43	63.77
TiO_2	0.19	0.55	0.28	0.06	0.40	0.19	3.67	0.39
Al_2O_3	12.43	15.97	13.54	11.70	14.54	14.87	12.39	15.30
$Fe_2O_3^*$	3.57	4.61	2.85	0.85	6.25	2.22	17.18	7.67
MnO	0.08	0.11	0.03	0.02	0.15	0.05	0.27	0.16
MgO	0.51	0.73	0.83	0.22	1.26	0.58	4.80	1.84
CaO	3.97	2.92	1.86	3.22	5.71	3.12	8.93	8.41
Na_2O	3.31	6.25	5.50	3.66	2.27	4.17	2.21	0.90
K_2O	0.69	1.66	0.53	0.16	0.20	1.09	0.31	0.13
P_2O_5	0.05	0.11	0.05	0.02	0.12	0.04	0.60	0.15
LOI	1.05	0.45	1.59	0.73	1.36	1.18	0.36	0.31
Sum	98.59	99.14	100.22	99.83	99.29	99.02	99.33	98.81
Sc	11	9	9	5	17	4	46	27
V	30	19	16	7	60	19	475	132
Zn	45	83	26	7	62	34	128	70
Ga	12	24	17	10	15	15	25	13
				LA-ICPMS				
Rb	18.3	52.3	11.0	3.1	6.8	24.9	2.7	2.6
Sr	126	381	125	134	186	433	181	231
Y	19.3	45.6	44.6	4.1	8.6	9.9	53.4	5.5
Zr	66.9	567	169.2	203.5	19.1	87.4	128.1	11.9
Nb	2.3	19.6	4.1	0.3	0.7	5.5	3.6	0.7
Cs	1.0	1.9	0.5	0.2	0.3	0.5	0.1	0.2
Ba	121.6	418.7	158.7	92.3	61.0	244.2	69.4	27.7
La	10.5	36.6	12.5	3.6	2.1	6.2	6.7	2.5
Ce	17.9	72.8	29.0	6.2	5.8	10.8	16.1	10.1
Pr	3.0	10.8	3.9	0.7	0.9	1.3	2.9	1.0

Table 8 (continued)

Sample name	MESR43 Widerøe-fjellet C	MESR49A Lågkollane	MESR79 Bamseungen	MESR99 Widerøefjellet E	MESR104 Nils-Larsenfjellet W	MESR106 Widerøefjellet SE	MESR109 Caussinknappen	MESR110 Caussinknappen
Nd	12.9	44.5	17.5	2.9	4.0	5.2	17.2	4.4
Sm	3.0	9.5	4.7	0.6	1.3	1.2	6.1	1.3
Eu	0.63	2.08	0.92	0.67	0.68	0.64	2.17	0.46
Gd	2.79	8.30	5.74	0.61	1.47	1.57	8.32	1.18
Tb	0.48	1.30	0.97	0.11	0.25	0.29	1.41	0.20
Dy	3.24	8.33	7.68	0.60	1.58	1.58	9.73	1.10
Ho	0.69	1.69	1.54	0.16	0.33	0.37	2.09	0.26
Er	2.11	4.84	4.81	0.55	0.86	1.00	5.77	0.69
Tm	0.33	0.77	0.79	0.11	0.13	0.20	0.87	0.12
Yb	2.31	5.08	5.55	0.83	0.96	1.13	5.65	0.69
Lu	0.35	0.79	0.81	0.16	0.15	0.21	0.86	0.14
Hf	2.21	13.88	5.01	5.47	0.57	2.36	3.84	0.44
Ta	0.19	1.09	0.32	0.04	0.05	0.63	0.31	0.08
Pb	8.22	13.42	3.72	4.79	1.76	15.13	1.89	4.56
Th	2.21	5.51	3.11	0.62	0.52	2.08	1.16	0.76
U	1.06	2.61	1.45	1.01	0.24	0.75	1.00	0.47
87Sr/86Sr	0.708200					0.705215		
2se	0.000012					0.000012		
87Rb/86Sr	0.3489					0.1289		
87Sr/86Sri	0.703256					0.703452		
εSri	−1.25					0.97		
143Nd/144Nd	0.512412					0.512588		
2se	0.000009					0.000012		
147Sm/144Nd	0.1364					0.1577		
143Nd/144Ndi	0.511525					0.511598		
εNdi	3.24					3.81		

LOI, loss on ignition; $Fe_2O_3^*$, all Fe as Fe_2O_3.

6.6.3. Zircon trace element data

Trace element analyses were performed on some of the zircons for which Hf data were obtained in order to compare them to the whole rock analyses and assess whether the latter could represent liquid compositions, or that they are influenced by cumulate or alteration processes. Since the analyses were quite homogeneous only average data are shown and discussed.

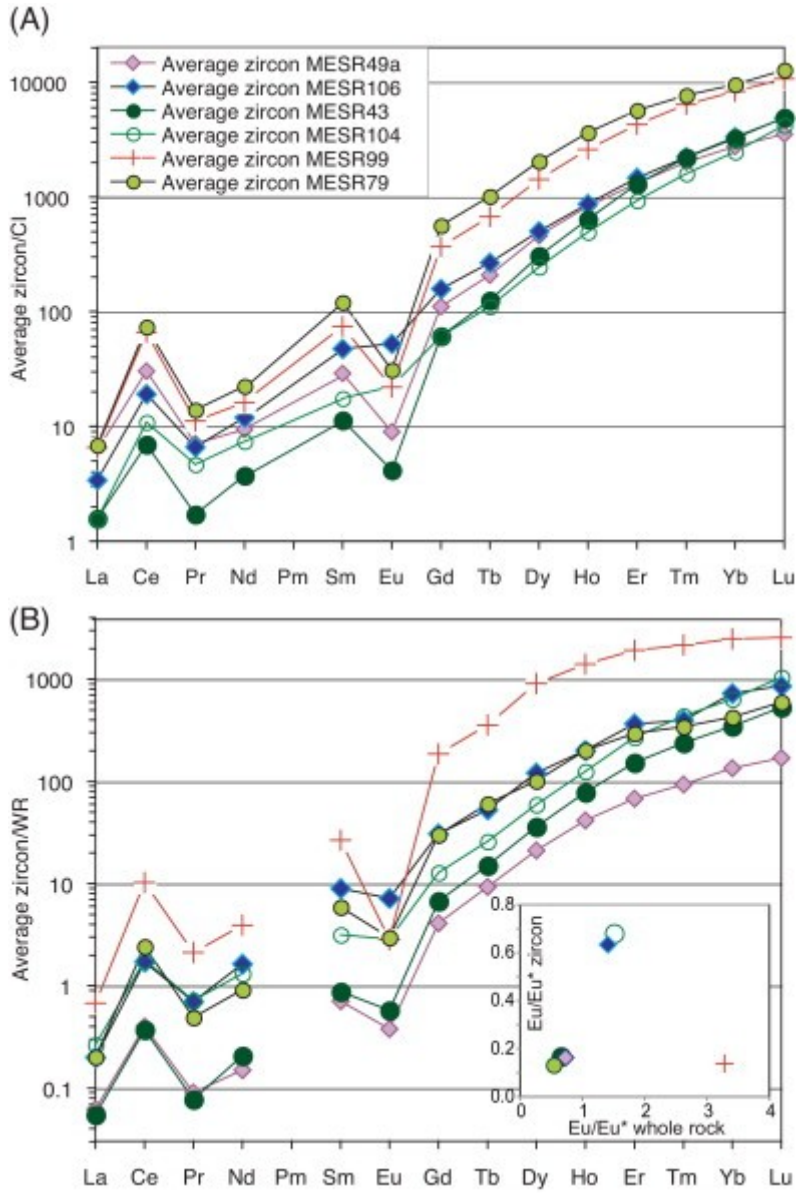

Figure 35: Zircon trace element data, averaged per sample. (A) Chondrite-normalized REE patterns for average zircons from the different sample, showing the positive Ce- and negative Eu-anomalies expected from the zircon's crystal chemistry. Samples MESR104 and 106 display a reduced negative Eu-anomaly compared to the other samples. (B) Whole rock-normalized zircon REE patterns. The very low zircon/whole rock Eu ratio for MESR99 indicates that the whole rock composition is unlikely to represent a liquid. Samples MESR104 and 106 have a Eu-anomaly within the range expected for zircon/liquid distribution coefficients, indicating that the positive Eu-anomaly in the whole rock samples is unlikely to be a cumulate effect.

The chondrite-normalized REE patterns (Figure 35A) show the features expected for zircon, with very low LREE/HREE ratios and a positive Ce-anomaly. There is slightly less than an order of magnitude variation in the absolute concentration of the REE between the samples, with MESR43 having the lowest, and MESR79 the highest concentrations. Most samples display negative Eu-anomalies, but these are much reduced for MESR106 and MESR104, which both show positive Eu-anomalies in their whole rock REE pattern too. MESR99, which has a very noticeable positive Eu-anomaly in its whole rock REE pattern, shows a clear negative anomaly in its zircon REE pattern.

When the zircon REE-patterns are normalized over the whole rock patterns (Figure 35B), the results can be interpreted to represent the zircon/liquid distribution coefficient (Kd), provided the whole rock compositions represent liquid compositions. All samples have a steeply sloping Kd pattern, with positive Ce- and negative Eu-anomalies, as is expected from zircon's crystal structure (Belousova *et al.*, 2002). MESR99 displays the strongest Eu-anomaly in its Kd pattern, being as low as 0.04. This lies outside the range found experimentally for varying conditions of temperature and oxygen fugacity (Trail *et al.*, 2012), and outside the trend seen for the other samples (Figure 35B inset). The positive Eu-anomaly of the whole rock pattern for MESR99 is therefore highly likely to be an accumulative feature. The whole rock patterns for MESR106 and MESR104, with their positive Eu-anomaly, might be a reflection on the liquid composition, since their Kd Eu-anomaly is 0.4, and thereby higher than for the samples without a WR positive Eu-anomaly, and within the experimentally determined range.

Sample MESR43 displays a, potentially metamorphism- or alteration-related, negative Ce-anomaly in its WR REE pattern. The value for the Ce-anomaly in the zircon/WR REE pattern is 5.7, and thereby lower than those for MESR99 or 79, and within the range of experimentally determined values. The question whether this WR Ce-anomaly is a primary feature can therefore not be answered unambiguously, but we think it is related to metamorphism and/or alteration.

Apart from REE, the zircons analyzed also contain quantifiable amounts of Th and Nb. High Th/Nb ratios are a feature of subduction-related magmas, and the WR analyses show quite a range of Th/Nb ratios (Figure 33). Zircon Th/Nb ratios also vary strongly, with a more systematic variation of Nb than Th on a per-sample basis (Figure 36). There is a broad correlation between Nb contents of the zircons and of the whole rock, in that the sample with the highest WR Nb contents (MESR49a) also has the higher zircon Nb concentrations and lower Th/Nb ratios than, for instance MESR104 with low Nb concentrations and high Th/Nb ratios for both zircon and whole rock. The exception is again MESR99, which has very high WR Th/Nb ratios, and the lowest Nb concentrations, whereas the zircon data are similar to those

for MESR79. Calculated zircon/WR ratios for MESR99 are 43 for Nb and 1290 for Th, whereas literature values are 0.3–27 and 11–69 respectively (Nardi *et al.*, 2013). So this confirms the non-liquid composition of the WR sample, as already deduced from the REE patterns. The Nb zircon data for the other samples appears to be compatible with a cogenetic crystal-liquid relationship between zircon and whole rock, since calculated zircon/WR ratios for Nb are 0.5–4.4, while the results for Th are less convincing, with an apparent average Kd of 27–630.

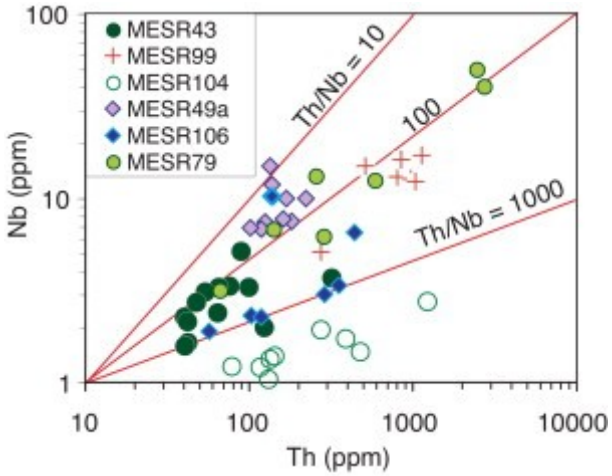

Figure 36: Nb versus Th concentrations for zircons. Note log scale on both axes. Although not highly systematic, there is a relationship between whole rock and zircon data, with sample MESR104 also showing a pronounced negative Nb anomaly for the whole rock, whereas this anomaly is very much reduced for MESR49a.

6.7. Discussion

6.7.1. U-Pb zircon age groups

Our U-Pb zircon dating shows that the majority of samples have an igneous crystallization age between 975 and 995 Ma, independent of the analytical technique used for dating (SHRIMP or LA-MC-ICPMS); these ages are similar to, but slightly younger than those reported by Kamei *et al.* (2013) and Owada *et al.* (2013) for the main group of (tholeiitic/low-Ti) meta-igneous rocks (998–995 Ma).

Our three younger ages of 957 ± 8, 947 ± 8 and 929 ± 14 Ma are similar to up to marginally higher than the SHRIMP dates reported previously. Shiraishi *et al.* (2008) obtained an igneous age of 920 ± 8 Ma for a metatonalite sample from Mefjell, and this age could correspond to the one obtained for our more mafic sample MESR109. Kamei *et al.* (2013) dated three (CA, high-Sr) samples at 945–930 Ma, while Owada *et al.* (2013) obtained a single zircon from a high-Ti mafic dyke with an age of 945 ± 9 Ma. An igneous age of 951 ± 17 Ma, so within the time frame of our analyses, has been reported by Shiraishi *et al.* (2008) for an enderbitic gneiss from northern Brattnipene; this is located north of the Main Shear Zone, but still south of the Main Tectonic Boundary (Figure 25), and is thus part of the SW terrane. The slightly

older ages from sample MESR106 at 1070–1060 Ma are likely to represent inherited zircons. A similar age of 1048 ± 12 Ma was reported by Osanai *et al.* (2013) for garnet-biotite gneiss from Mefjell South, within the SW-terrane. The ca. 3 Ga single zircons in MESR106 and MESR109 are quite remarkable. Although laboratory cross-contamination can never be completely excluded, no rocks of a similar age were treated in the laboratory at the same time. Also, old ages are not completely unknown from the Sør Rondane Mountains, but only north of the Main Tectonic boundary: Shiraishi *et al.* (2008) reports a single ca. 3260 Ma grain within a paragneiss from northern Austkampane while Pasteels & Michot (1968) report zircon fractions from granitoids to the SW of Austkampane that yielded an ca. 2700 Ma upper intercept. Within the broader Antarctic context, igneous activity around 2990 Ma has been reported in the Napier Craton (Kelley & Harley, 2005) and similar ages also exist in the Ruker Complex (see overview in Liu *et al.*, 2013). Whether it is statistically relevant that we only found Archaean zircons in the younger intrusions is unclear.

One of our samples, MESR99, yielded an older age of 1015 ± 4 Ma. Four zircons from a nearby sample, 12B4, give a similar upper intercept age. Similar, inherited U-Pb zircon ages of 1014 ± 15 and 1009 ± 13 Ma have been reported by Shiraishi *et al.* (2008) from gneiss samples in the NE terrane (Perlebandet and Utnibba), while Osanai *et al.* (2013) report inherited ages of 1030–1040 Ma from Bamseungen within the meta-igneous sector of the SW terrane.

The ages presented here strengthen the connection between the SW- and NE-terrane of Sør Rondane. The two areas show different *P–T–t* paths related to the amalgamation of Gondwana, and were also thought to differ in the maximum age of inherited zircon, with ages older than 1100 Ma previously unreported for the SW terrane (Osanai *et al.*, 2013). If we accept the validity of the two ca. 3 Ga inherited zircons presented here, then this distinction has ceased to exist. However, 900–1000 Ma ages are noticeably scarcer in the NE- than the SW-terrane (Shiraishi *et al.*, 2008; Osanai *et al.*, 2013), which could be related to the difference in crustal level between the two terranes, as the NE-terrane is dominated by metasedimentary rocks.

Our ages, together with those published previously, reinforce the idea that Meso-Neoproterozoic magmatism in the Sør Rondane Mountains occurred significantly later than in Central and Western Dronning Maud Land where it has been dated at 1130–1060 Ma (Jacobs *et al.*, 1998; Jacobs *et al.*, 2003c), similar to ages found in the South African Natal Belt (McCourt *et al.*, 2006). The area furthest west from Sør Rondane in Antarctica where 900–1000 Ma (Sm–Nd isochron) ages are found is the Schirmacher Hills (Rao *et al.*, 2000; Ravikant, 2006), although these are interpreted to reflect metamorphism, rather than a magmatic event. Towards the east, there is a scarcity of data for the Yamato-Belgica complex,

but Shiraishi *et al.* (1994) present a U-Pb zircon protolith age of ca. 1000 Ma. From the Lützow-Holm to the Rayner Complex ca. 1000 Ma ages are quite common (Shiraishi *et al.*, 2008; Liu *et al.*, 2013), e.g. in the Cape Hinode metatrondhjemites (1017±13 Ma, Shiraishi *et al.*, 2008) and Mawson Coast charnockites (Halpin *et al.*, 2012). This is most widely interpreted as reflecting a connection between this part of Antarctica and Sri Lanka–India–Madagascar prior to Gondwana amalgamation (e.g. Boger *et al.*, 2014). In this reconstruction, the Vijayan Complex of Sri Lanka would be closest to Sør Rondane, and ages of 900–1100 Ma are indeed found there (Kröner *et al.*, 2013).

6.7.2. Comparative geochemistry

In the following section we compare our data to those published by others to interpret the likely tectonic setting in which the magmas were generated and their similarity to similarly-aged (meta-)igneous rocks within Sør Rondane, neighboring areas in Antarctica (central Dronning Maud Land and Schirmacher Hills; Rao *et al.*, 2000; Mikhalsky & Jacobs, 2004; Ravikant, 2006) and the Vijayan Complex in Sri Lanka (Milisenda *et al.*, 1994; Kröner *et al.*, 2013). Connections between the Sør Rondane Mountains, the Namuno block of Mozambique and the Central Highlands Complex of Sri Lanka have been proposed by Grantham *et al.* (2008), based on the available geochronological and structural data. The SHRIMP U-Pb zircon ages for a charnockite from the Ocua and a tonalitic gneiss from the Marupa complex in Mozambique of 994 ± 61 and 951 ± 44 Ma respectively (Grantham *et al.*, 2008) are indeed similar to the ages reported here, but no geochemical data are available to further investigate the connection.

Relationships within SW-terrane Sør Rondane: tectonic interpretation

The one sample (MESR99) that gave the older, ca. 1015 Ma, age is more SiO_2-rich than any of the other samples. The homogeneity of the age and Hf isotopic composition of the zircons composition demonstrates that it is an igneous rock. However, its whole rock composition is unlikely to represent a liquid composition, as indicated by the zircon/whole rock trace element ratios, which do not fall within the range for published distribution coefficients. The sample is very rich in quartz and plagioclase (partially replaced by epidote), and has unusually high zirconium and hafnium concentrations compared to its REE contents; we therefore interpret it to be a felsic cumulate or crystal-rich tuff. Considering the similarity in zircon Hf isotope ratios and trace element contents to some of the 995–975 Ma samples, its parental magma must have shown a strong geochemical resemblance to the magmas of this age group, and we will therefore consider it together with these samples. Because of its aberrant whole rock composition and unknown age, qz-gabbro MESR18 may not belong to this group. Alt-

hough the ca. 980 Ma age of Caussinknappen tonalite MESR110 falls into the 995–975 Ma age group, its geochemical (low sodium, high calcium) and isotopic characteristics (lower Hf isotopic composition) are aberrant; this could be related to its position further south than the other samples. It lies close to an inferred shear zone (Figure 25A), and the boundary with the SE Dronning Maud Land Province of Mieth *et al.* (2014).

Our samples that are interpreted to belong to the main 995–975 Ma age group have low TiO_2 (<0.6 wt.%), Sr (<200 ppm) and Zr (<200 ppm) concentrations. They have flat to slightly LREE-enriched rare earth element patterns (at CI-normalized values between 40 and 4), and their zircons show an average εHf of 6.3–7.3. They closely resemble the 'main lithotype' (tholeiitic biotite-hornblende metatonalite and associated enclaves) of Kamei *et al.* (2013) and the low-Ti microgabbros of Owada *et al.* (2013) in terms of Sr/Y, La/Lu, Ga/Al, V/Ti ratios and initial epsilon Nd ratios (Figure 37), but also the ca. 950 Ma enderbitic gneisses from the Brattnipene area, north of the Main Shear Zone (Shiraishi & Kagami, 1992).

In common with Kamei *et al.* (2013) and Owada *et al.* (2013), we interpret the samples from this age group to have formed in an oceanic arc environment. All the hallmarks for a subduction setting are present in the normalized trace element diagrams: negative Nb anomalies, positive Sr anomalies in the gabbros and enrichment in REE relative to Zr and Hf. The interpretation of an oceanic rather than continental arc is based on the flat REE patterns for the gabbros and the low absolute concentrations of incompatible trace elements. In this respect, our samples resemble data for e.g. the mid-crustal section of the Jurassic Talkeetna oceanic arc (Greene *et al.*, 2006). There is a strong chemical coherence between the mafic, intermediate and felsic samples which is interpreted as a cogenetic relationship. The dominance of intermediate samples (tonalites) is typical for arc terranes (e.g. Reubi & Blundy, 2009). The occurrence of the (quartz-)gabbros as enclaves within the more felsic intrusives, and the crenulated margins on these enclaves (Figure 26C), implies that both were (partially) liquid at the same time, and it is therefore likely that the intermediate to felsic magmas were derived from the more mafic magmas by crystal fractionation. The presence of a small positive Eu-anomaly in some samples, of which the zircon trace element data show that it is likely to be a feature of the magmatic liquid could be related to the fractionation sequence being dominated by amphibole rather than plagioclase; this is in line with the concave REE patterns for the felsic samples, and the fairly constant Sr concentrations with increasing SiO_2 content. In the less fractionated (quartz-)gabbro samples, it could be a result from preferential mobilization of divalent Eu during dehydration of the slab in the sub-arc mantle (Bau & Knittel, 1993).

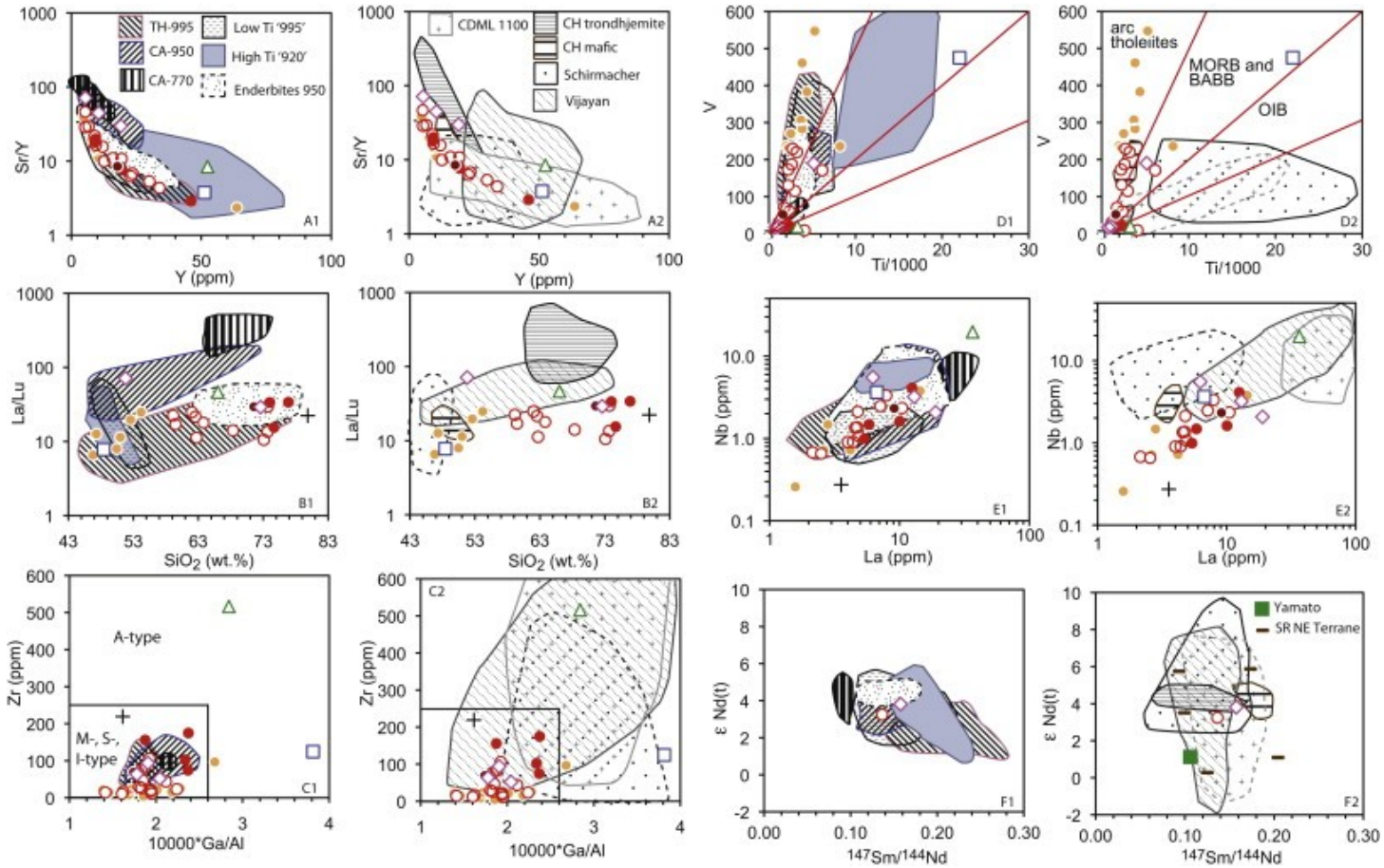

Figure 37: Comparison between samples analyzed in the present study and published data; symbols as in Figure 31 and given in diagram. Panels on left show data from the SW-terrane of Sør Rondane: ca. 995 Ma tholeiites, 920–945 and ca. 770 Ma calc-alkaline: Kamei *et al.* (2013); low-Ti enclaves (ca. 995 Ma) and high-Ti dykes (ca. 920 Ma): Owada *et al.* (2013); ca. 950 Ma enderbites: Shiraishi & Kagami (1992). Panels on right show data from the broader region: Central Dronning Maud Land: Jacobs *et al.* (1998), Mikhalsky & Jacobs (2004); Cape Hinode trondhjemite: Ikeda *et al.* (1997); Cape Hinode mafics: Suda *et al.* (2008); Schirmacher Hills: Rao *et al.* (2000), Ravikant *et al.* (2007); Vijayan Complex, Sri Lanka: Milisenda *et al.* (1994), Kröner *et al.* (2013). (A) Sr/Y versus Y (note log scale for y-axis); (B) La/Lu (log scale) versus SiO2; (C) Zr versus 10,000 × Ga/Al with fields for different granite types from Whalen *et al.* (1987); (D) V versus Ti/1000 with fields for different types of basalts from Shervais (1982); (E) Nb versus La (double log scale); (F) initial εNd value versus 147Sm/144Nd, with additional data from Shiraishi *et al.* (2008) for Yamato Mts, and Grew *et al.* (1992) for NE-terrane gneisses.

Our samples that have been dated as at 960–925 Ma have variable geochemical characteristics and do not form a coherent group. They are enriched in Sr compared to the older group (leading to higher Sr/Y ratios), and can have high TiO_2 and P_2O_5 contents (MESR109) or high Zr concentrations (MESR49a). REE patterns vary from LREE depleted (MESR109) to LREE-enriched (MESR107). The Nd and Hf isotopic characteristics are marginally more depleted (i.e. higher values) than for the older age group. These characteristics indicate that high-Sr samples MESR105–107 are most closely related to the 920–950 Ma calc-alkaline group of Kamei *et al.* (2013), while high-Ti sample MESR109 resembles the ca. 950 Ma high-Ti dykes of Owada *et al.* (2013). Sample MESR49a has uniquely high Nb and Zr concentrations, but could potentially be related to the high-Ti clan of rocks by fractionation processes.

Considering the geochemical variety of magmas present between 960 and 925 Ma, the interpretation of the tectonic setting is more difficult. Kamei *et al.* (2013) interpreted their calc-alkaline series as adakites, based on the Sr/Y ratios, reflecting slab melting; Owada *et al.* (2013) suggested a back-arc environment based on the V versus Ti diagram for his high-Ti dykes. The evidence for an adakitic signature in the felsic samples of this time period is not as strong as for the Cape Hinode metatrondhjemites (Ikeda *et al.*, 1997), which have a much higher La/Lu and Sr/Y ratios (Figure 37A and B), but a geochemical shift is nevertheless noticeable, also towards slightly more depleted isotopic characteristics. The high-Ti samples are characterized by LREE-depleted patterns and low La/Nb ratios (Figure 37E), a-typical for arc-related magmatism, and also have Ti–V characteristics more typical for Mid-Ocean Ridge (MORB) or Back-arc Basin Basalt (BABB) than for arc-related magmas (Figure 37D). However, samples with HFSE enrichments compared to 'classical' arc rocks are found both in back-arc basins (Sinton *et al.*, 2003; Sorbadere *et al.*, 2013) and arc settings (Peate *et al.*, 1997; Kuritani, 2001; Kratzmann *et al.*, 2010; Gazel *et al.*, 2011; Sorbadere *et al.*, 2013). In both environments, the geochemical signature can be explained by a small contribution from the subducted slab and a more important role for adiabatic melting of asthenospheric mantle compared to typical arc settings, where melting is mainly induced by a hydrous flux from the slab. Since the degree of melting is smaller than for flux-melting, or for the more extensive adiabatic upwelling at Mid-Ocean Ridges, fluid-immobile incompatible trace elements are more enriched than in either arc or MOR magmas. In an arc setting, this type of high-HFSE magma is typically found when there are heterogeneities within the subducting slab, such as a ridge (Peate *et al.*, 1997; Kratzmann *et al.*, 2010), a seamount chain (Peate *et al.*, 1997) or a hotspot track (Gazel *et al.*, 2011), which can lead to slab tear or break-off, and enhanced mantle upwelling compared to a classical subduction situation. This is also an environment in which adakites can form (Yogodzinski *et al.*, 2001).

The fact that this diverse group of magmas intruded after the typical arc-type magmas at 995–975 Ma indicates that a profound change in tectonic regime has occurred. This is most likely the end of a real subduction scenario, either due to collision with a microcontinent or oceanic plateau, or slab break-off. A limited number of samples with similar geochemical characteristics to the 960–925 Ma adakite-like materials was dated at ca. 770 Ma by Kamei *et al.* (2013). Whether this reflects resumption of subduction or reworking of pre-existing crust is not clear; the isotopic data permit either interpretation.

7.2.2. Relationships within wider Antarctica and Gondwana

Comparing the geochemistry of 900–1200 Ma samples from different areas in Antarctica, and the Vijayan Complex of Sri Lanka, to those from the SW-terrane of Sør Rondane, there a some clear differences and similarities.

The biotite- and pyroxene-bearing gneisses from the NE-terrane analyzed by (Grew *et al.*, 1992) for Nd isotopes, and the one gneiss sample from the Yamato Mountains (Shiraishi *et al.*, 2008) extend to marginally lower initial ratios (Figure 37F); however, major and trace element characteristics were not given, apart from Sm and Nd concentrations, which are similar to the 960–925 Ma samples from the SW-terrane.

The mafic and felsic samples from Cape Hinode (Ikeda *et al.*, 1997; Suda *et al.*, 2008) are very similar in terms of Nd isotopes to the meta-igneous samples from the SW-terrane. The felsic samples are slightly more typically trondhjemitic in trace element composition, as described before. The mafic samples are similar to the (quartz-)gabbros.

The orthogneisses from Central Dronning Maud Land (Mikhalsky & Jacobs, 2004; Jacobs *et al.*, 2008) overlap with, but extend to lower values for initial Nd isotopic ratios, similar to the gneisses from the NE-terrane. However, they are geochemically very different, and have much higher contents of (relatively immobile) incompatible elements, such as the REE, Zr, Th and Nb (Figure 37A, C and E). Similarly, the granulites from Schirmacher Hills show a clear overlap in Nd isotopes (Rao *et al.*, 2000; Reading, 2006), but Ti, Nb and Zr contents are significantly enriched. The granitoid gneisses of the Vijayan Complex (Sri Lanka) largely overlap with the gneisses from Central Dronning Maud Land, rather than with our Sør Rondane samples, in geochemistry and isotopic composition. The Hf isotopic composition of the Vijayan zircons is also typically lower than that of the Sør Rondane samples (Figure 38A). Although our sample MESR49a shows similarly enriched trace element characteristics to CDML, Schimacher and Vijayan, it distinguishes itself with its depleted Hf isotopic signature for the zircons (Figure 38A).

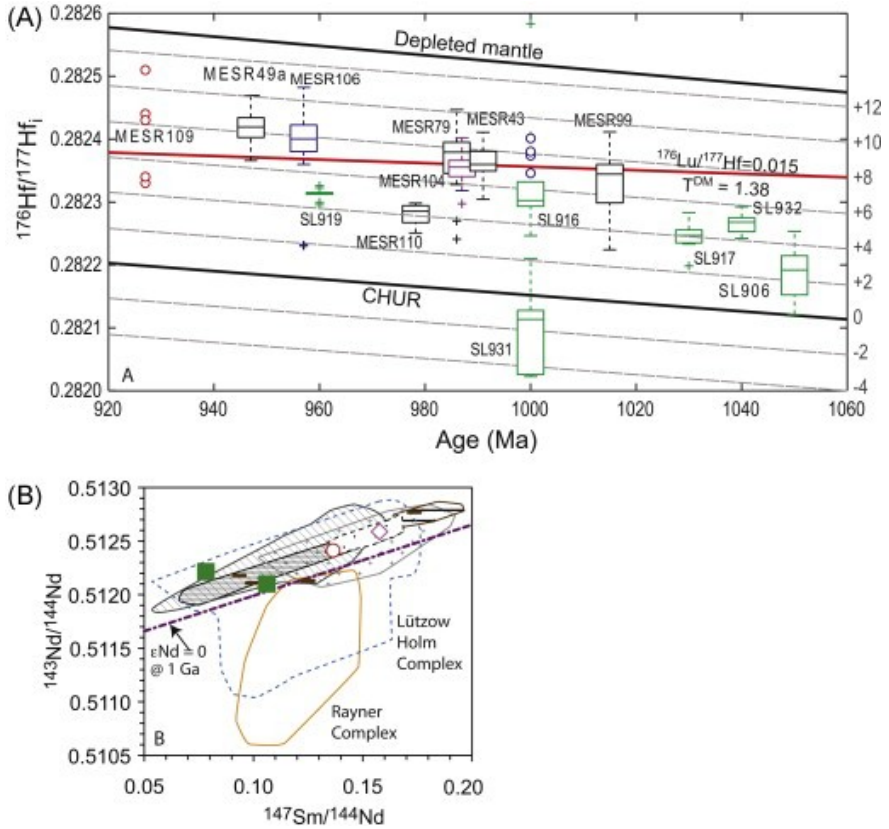

Figure 38: As Figure 30, but with data for the Vijayan Complex of Sri Lanka (SL sample numbers) from Kröner *et al.* (2013). (B) Present-day 143Nd/144Nd versus 147Sm/144Nd; data sources and symbols as for Figure 37, with additional data from the compilation by Shiraishi *et al.* (2008). Reference line for εNd = 0 at 1000 Ma shown for comparison. Data for the Lützow-Holm and Rayner Complex extend to far lower 143Nd/144Nd ratios than the Sør Rondane samples, indicative of an old crustal component in their source.

So the meta-igneous sector of the SW-terrane compares poorly to the Central Dronning Maud Land orthogneisses in both age (younger) and geochemical composition (more depleted). Despite the overlapping ages and Nd isotopic composition, the samples from Schirmacher Hills do not match in geochemical composition, while the Vijayan complex is both marginally older (up to 1100 Ma), and more enriched in Nd and Hf isotopic signature as well as trace element composition. A reasonably good match exists with the mafics and metatrondhjemites from Cape Hinode, although the latter are ca. 1015 Ma rather than <960 Ma for the Sør Rondane samples that most closely match them in geochemical composition. Not only this age difference is problematic in proposing a match between the two areas, but also the fact that samples from the Lützow-Holm Complex that lie geographically between Cape Hinode and Sør Rondane have Nd isotopic compositions that point towards a more significant role for crustal reworking (Shiraishi *et al.*, 2008; Figure 37B)–and the presence of the Main Tectonic Boundary, which separates the SW- and NE-terranes. Rocks from the Rayner Complex (Figure 25A), where ca. 900–1000 Ma ages are common too (Boger *et al.*, 2000; Corvino *et al.*, 2008; Mikhalsky & Sheraton, 2011; Grew *et al.*, 2012; Halpin *et al.*, 2012), extend to even more isotopically enriched values (Figure 38B), reflecting a much longer crustal prehistory.

6.7.3. Timeline of events and possible tectonic scenarios

The data and comparison shown here have implications for both the Rodinia and Gondwana supercontinents. The disparity in igneous ages between Central Dronning Maud Land and Sør Rondane clearly shows that the latter was more closely related to the Indo-Antarctic Craton (Sri Lanka–India–Madagascar) whereas the former shows strong ties with the Kalahari Craton, being a close match to the South African Natal Belt.

Our data confirms that the meta-igneous sector of the SW-terrane was formed in an oceanic arc setting around 995–975 Ma, and we interpret the signature of the younger rocks to reflect stalling subduction from 950 Ma onwards. No deformation or metamorphism has been recognized in the area around this time, so the halting of the subduction process may be a far-field effect of a collision elsewhere. The dimensions of the meta-igneous sector of the tonalite terrane are more in keeping with either N- or S-dipping subduction in present-day coordinates (rather than E or W), but we have no constraints on the vergence. The rare occurrence of Archaean inherited zircons within the <960 Ma intrusives suggests the proximity to an older craton, which may have been the collider that halted subduction. This could have been part of the aeromagnetically defined Southeast-Dronning Maud Land (SE-DML) Province of Mieth *et al.* (2014), located directly southwest of the meta-igneous sector. However, it could also be the craton from which the sediments, which are now found in the NE-terrane, have been shed, in which case a more easterly location seems more plausible–although it is unclear what the relative positions of the SW- and NE-terranes were at this stage.

The northern, dominantly supracrustal, sector of the SW-terrane seems related to the meta-igneous terrane in terms of ages and geochemical composition, even though the two sectors are separated by the much younger dextral Main Shear Zone of Pan-African age (Ruppel, 2012).

The ca. 770 Ma ages for calc-alkaline magmatism in the SW-terrane reported by Kamei *et al.* (2013) can be interpreted to reflect resumption of subduction. This age and type of magmatism is also known from Sri Lanka (Wanni Complex, Willbold *et al.*, 2004) and Madagascar (see overview by Boger *et al.*, 2014; Boger *et al.*, 2015). However, Central and Western Dronning Maud Land were part of Rodinia (Powell & Pisarevsky, 2002), which was in the process of splitting up around this time, and do not appear to record this phase of magmatism. Zircons with 800–700 Ma ages are also found in Schirmacher Hills (Mikhalsky & Sheraton, 2011) and within a metadiorite in the NE-terrane of Sør Rondane (Osanai *et al.*, 2013).

The next event is the 650–600 Ma high-grade metamorphism in Sør Rondane (see overview of geochronology in Osanai *et al.*, 2013), which has also been recognized in the Yamato Mountains (Asami *et al.*, 2005) as well as Schirmacher Hills (Ravikant *et al.*, 2004), but not in the Lützow-Holm area (Asami *et al.*, 2005; Shiraishi *et al.*, 2008). This may point towards a crustal boundary between the Yamato Mountains and Lützow-Holm area, as also proposed on the basis of magnetic anomalies (Osanai *et al.*, 2013). For Sør Rondane, the ca. 600 Ma metamorphic event has been linked to the collision between the SW- and NE-terrane, as the downgoing and overthrust blocks respectively. The Dufekfjellet granite (Li *et al.*, 2006; Figure 24) intruded at the same time (ca. 620 Ma) into the SW-terrane, so into the low-grade portion of the downgoing block, which seems somewhat mysterious from a tectonic point of view, unless another block was being underthrust underneath the SW-terrane from the south. This could then be the SE-DML Province.

The final event is wide-spread intrusion of granitoids and minor syenites (570–510 Ma) in both the SW- and NE-terrane, which were amalgamated at this stage, and associated retrograde metamorphism.

On a larger scale, the juxtaposition of terranes with both ca. 630 and ca. 550 Ma metamorphic ages has also been noted by Boger *et al.* (2015) for the Vohibory-Androyen and Anosyen domains of SW Madagascar, has been and connected to the events in Antarctica and eastern Africa. Collision between the Vohibory and Androyen terrane was interpreted to have occurred around 630 Ma, so at a similar time to the inferred collision between the NE- and SW-terrane in Sør Rondane. It was followed by collision with the Androyen Terrane, connected to greater India, at ca. 550 Ma. Boger *et al.* (2015) extend this scenario into Antarctica with the Sør Rondane-Yamato domain (containing ca. 630 Ma ages) colliding with the Lützow-Holm area around 550 Ma during the final amalgamation of Gondwana. Although the Madagascan Vohibory Domain resembles the meta-igneous sector of the SW-terrane of Sør Rondane in being a juvenile oceanic arc terrane, the Vohibory protoliths were formed at 850–700 Ma (Jöns & Schenk, 2008), rather than around 980 Ma. Also, the inferred vergence of the ca. 630 Ma collision in Madagascar is opposite to what has been suggested for the SW- and NE-terranes of Sør Rondane, so a simple one-to-one correlation between SW Madagascar and Sør Rondane does not exist. However, it confirms the idea that Sør Rondane holds an important place in the final amalgamation of Gondwana.

6.8. Conclusions

- The meta-igneous sector of the SW-terrane of Sør Rondane was the mid-crustal part of a juvenile oceanic arc terrane around 1020–975 Ma, as indicated by whole

rock trace element patterns typical for subduction-related magmas (negative Nb anomalies in mantle-normalized diagrams, positive LREE/HFSE ratios), combined with a high (typically ca. +7) zircon initial epsilon Hf and fairly flat REE patterns. Comparison of zircon and whole rock REE patterns suggest that some of the moderately positive Eu-anomalies may be a feature of the magmatic liquid rather than reflecting cumulate processes.

- Younger igneous samples (960–920 Ma) are more variable: they are either characterized by high Sr/Y rations ('adakitic' signature) or have a reduced to absent subduction signature in terms of trace element patterns; all have higher zircon Hf isotopic ratios. This is interpreted as signifying the end of subduction, and magmatism related to adiabatic upwelling of subduction-modified or unadulterated depleted mantle, and/or slab melting.
- Rare inherited zircons with Archaean and late Mesoproterozoic ages in the <960 Ma intrusives could indicate increasing proximity to a cratonic area, potentially the fragment that caused subduction to halt.
- Compared to neighboring areas in Antarctica and in a wider Gondwanan context, the meta-igneous sector of the SW-terrane is unique with respect to the combination of protolith age, geochemical and isotopic signature.
- The 1000–900 Ma ages are younger than those of the classic 'Grenville' orogeny (as seen in central and western Dronning Maud Land and the South African Natal Belt) that formed Rodinia, and more similar to ages observed in India–Sri Lanka–Madagascar. This supports the idea that greater India was not part of or was located in a peripheral position to the Rodinian supercontinent (Powell & Pisarevsky, 2002).
- The ca. 630 and 550 Ma metamorphic and igneous history of Sør Rondane documented by other workers reflects the progressive amalgamation of Gondwana, and may be connected to events in SW Madagascar and eastern Africa (Boger *et al.*, 2015).

6.9. Acknowledgements

The whole GEA II team would like to thank the helicopter pilots Knut Wagner, Florian Tauber and Jörn Hergenröder of Sky Heli, Germany, for their flying skills, and Alain Hubert, Gigi Johnson-Amin and the whole crew of the Belgian 'Princess Elisabeth' Station for their hospitality and support during the field season. The analytical work was funded by grant # 90036 from the South African National Research Foundation to MAE; Carishma Ramchurran and Pat Suthan are thanked for their help with the analytical work at UKZN, and Christel Tinguely,

Phil Janney and Petrus Le Roux at UKZN. Siri L. Simonsen and Magnus Kristoffersen helped with the analyses at the University of Oslo. J. Jacobs, N. Lucka and M. Elburg are indebted to BGR for the invitation to participate at the GEA expeditions. J. Jacobs wishes to thank Alfred-Wegener-Institute for Polar and Marine Research (AWI) and M. Elburg International Polar Foundation (IPF) and BELARE for providing polar clothing. The study was partly supported by the Deutsche Forschungsgemeinschaft (Grants LA 1080/9 to A. Läufer, BGR, and LI 745/15 to F. Lisker, Univ. Bremen) in the framework of the priority program "Antarctic Research with comparative investigations in Arctic ice areas". J. Jacobs work was funded in part by NFR-NARE. The manuscript benefited greatly from reviews by A. Kamei and S. Boger; their considerable efforts have been very much appreciated.

7. The Main Shear Zone in Sør Rondane, East Antarctica: Implications for the late-Pan-African tectonic evolution of Dronning Maud Land

Antonia S. Ruppel[1], Andreas Läufer[1], Joachim Jacobs[2,3], Marlina Elburg[4], Nicole Krohne[5], Detlef Damaske[1], and Frank Lisker[5]

[1]Federal Institute for Geosciences and Natural Resources, Hannover, Germany

[2]University of Bergen, Bergen, Norway

[3]Norwegian Polar Institute, Tromsø, Norway

[4]University of Johannesburg, Johannesburg, South Africa, [5]University of Bremen, Bremen, Germany

Tectonics 34(6), 2015, 1290-1305 doi:10.1002/2014TC003763

Abstract

Structural investigations in western Sør Rondane, eastern Dronning Maud Land (DML), provide new insights into the tectonic evolution of East Antarctica. One of the main structural features is the approximately 120 km long and several hundred meters wide WSW-ENE trending Main Shear Zone (MSZ). It is characterized by dextral high-strain ductile deformation under peak amphibolite-facies conditions. Crosscutting relationships with dated magmatic rocks bracket the activity of the MSZ between late Ediacaran to Cambrian times (circa 560 to 530 Ma). The MSZ separates Pan-African greenschist- to granulite-facies metamorphic rocks with "East African" affinities in the north from a Rayner-age early Neoproterozoic gabbro-tonalite-trondhjemite-granodiorite complex with "Indo-Antarctic" affinities in the south. It is interpreted to represent an important lithotectonic strike-slip boundary at a position close to the eastern margin of the East African-Antarctic Orogen (EAAO), which is assumed to be located farther south in the ice-covered region. Together with the possibly coeval left-lateral South Orvin Shear Zone in central DML, the MSZ may be related to NE directed lateral escape of the EAAO, whereas the Heimefront Shear Zone and South Kirwanveggen Shear Zone of western DML are part of the south directed branch of this bilateral system.

7.1. Introduction

The continuation of the East African Orogen (Stern, 2001) into Dronning Maud Land (DML) in East Antarctica is of major importance for the reconstruction of the final amalgamation of Gondwana during the Late Proterozoic and early Paleozoic, including the number of crustal fragments involved. It is generally assumed that multiphase collision of various crustal blocks of proto-E and proto-W Gondwana led to at least two more or less continuous and apparently

crossing Pan-African orogenic belts in late Neoproterozoic to early Paleozoic times circa 650–490 Ma ago (Meert, 2003; Boger, 2011; Satish-Kumar *et al.*, 2013).

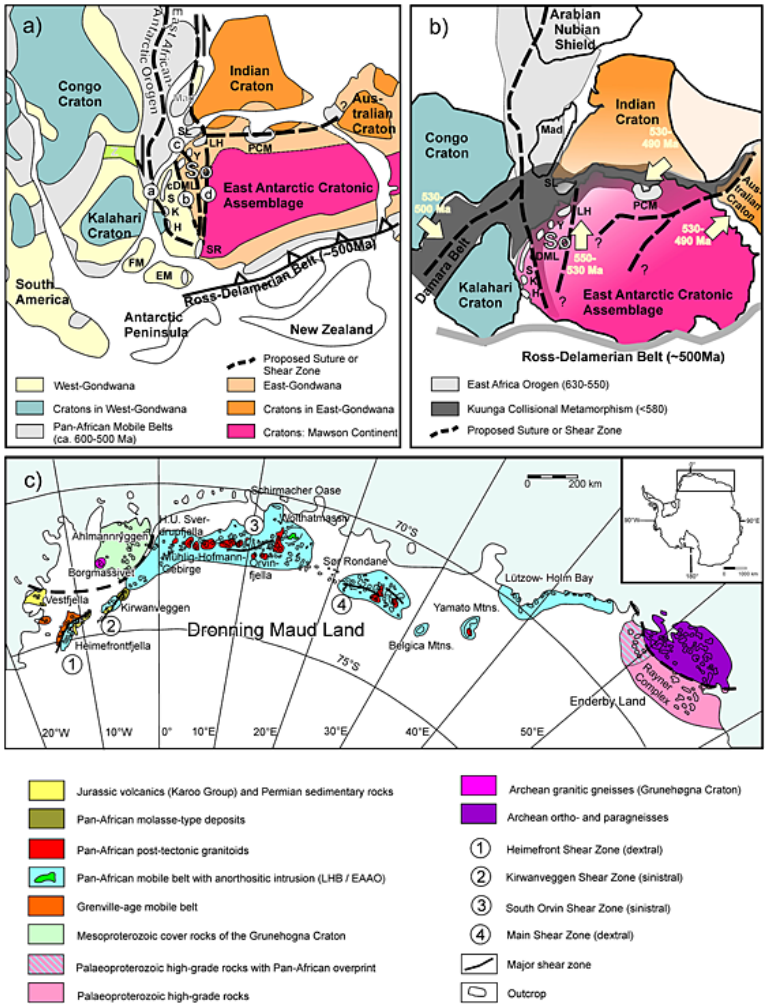

Figure 39: Overview of late Neoproterozoic to early Paleozoic plate tectonic reconstructions indicating the position of Dronning Maud Land and Sør Rondane (Sø) within two apparently crossing Pan-African orogenic belts. East Antarctica, formerly considered to represent a stable entity (the "East Antarctic Craton"), consists of several separate cratons welded together during Proterozoic and early Paleozoic orogenies (e.g. Boger, 2011). Therefore, we use the term "East Antarctic Cratonic Assemblage" here. (a) Continuation of the East African-Antarctic Orogen (circa 630–550 Ma) from the Arabian Peninsula in the north through East Africa into Dronning Maud Land in the south (modified after Grunow *et al.*, 1996 and Jacobs *et al.*, 1998). Labels (a)–(d) indicate four different scenarios of where the E-W Gondwana suture has been proposed to be located (a) Shackleton (1996); (b) Jacobs *et al.* (1998); (c) Moyes *et al.* (1993); and (d) Grunow *et al.* (1996). (b) Slightly younger Pan-African metamorphic ages are observed, e.g., in the Damara Belt, Lützow-Holm Belt, Prince Charles Mountains, and in the Denman Glacier region, and are referred to as the Kuunga Orogen (<580 Ma) (modified after Meert, 2003). (c) Geological map of Dronning Maud Land indicating the presence of four major shear zones (labeled 1–4)(adapted from Bauer *et al.*, 2003b), topographic base from Antarctic Digital Database, and Grunehogna Craton boundary after Bauer *et al.* (2003b) and Marschall *et al.* (2013). Abbreviations: DML, Dronning Maud Land; EM, Ellsworth-Whitmore Mountains; FM, Falkland Microplate; H, Heimefrontfjella; K, Kirwanveggen; LH, Lützow-Holm Bay; PCM, Prince Charles Mountains; S, Sverdrupfjella; SL, Sri Lanka; Sø, Sør Rondane; SR, Shackleton Range; and Z, Zambezi Belt.

In this scenario, the East African-Antarctic Orogen (EAAO) or Mozambique Belt (Stern, 1994; Jacobs *et al.*, 1998; Jacobs *et al.*, 2003c) was formed by the accretion of multiple arc terranes and continental collision of the African plate assembly and the Antarctic Coats Land Block at

circa 650–540 Ma followed by late-stage extension at circa 530–490 Ma (Figure 39a); it stretches from the Arabian Peninsula along the margin of East Africa into western DML in East Antarctica.

The Kuunga Orogen (Figure Figure 39b), extending from Australia across eastern India, the Prince Charles Mountains-Prydz Bay region and eastern DML in East Antarctica and farther into Mozambique and beyond, is the result of the collision of Indo-Antarctica and Australo-Antarctica, with its main phase, depending on the author, at either circa 570–530 Ma (e.g. Meert, 2003), circa 550–500 Ma (e.g. Fitzsimons, 2003), or circa 530–490 Ma (e.g. Boger *et al.*, 2001; Boger & Miller, 2004). Here Sør Rondane in eastern DML holds a key position since it appears to be located close to the likely crossing point of the EAAO and the Kuunga Orogen (Satish-Kumar *et al.*, 2013; Mieth *et al.*, 2014).

The structure of the EAAO changes significantly along its length. Its northern part is to a large extent characterized by middle Late Proterozoic accretion of juvenile volcanic arc terranes separated by ophiolitic sutures that are sinistrally sheared and metamorphosed under low- to medium-grade conditions; the southern part experienced up to granulite-facies metamorphism and polyphase deformation of late Neoproterozoic-Cambrian age, which overprinted an Archean-Mesoproterozoic basement and was followed by late-tectonic voluminous high-temperature plutonism and collapse tectonics (Jacobs & Thomas, 2004). Evidence for a slightly younger Kuunga orogenic event (Figure 39b) in the Antarctic region is observed as significant high-grade regional metamorphic overprint in the Lützow-Holm Bay region around circa 530–500 Ma (U-Pb zircon ages) (Shiraishi *et al.*, 1994) and in the Prince Charles Mountains at circa 530–490 Ma, representing the collision between Indo-Antarctica and west Gondwana (Boger, 2011). The final collision phase of the Australo-Antarctic plate with west Gondwana is thought to have occurred around 530–490 Ma (Boger, 2011). To the west, similar ages of circa 530–500 Ma were reported for peak deformation/metamorphism in the Damara Belt in the African part of west Gondwana (e.g. Gray *et al.*, 2008).

A major question in reconstructing the amalgamation of Gondwana is the location of the suture zone between proto-east and proto-west Gondwana and the margins of the EAAO. Figure 39a presents four different scenarios of the proposed east/west Gondwana suture in DML. One of these scenarios suggests the suture to pass through the target region between central and eastern DML (Moyes *et al.*, 1993). The western margin of the EAAO is represented by the Heimefront Shear Zone, an approximately 20 km wide major dextral transpression zone in western DML (e.g. Jacobs *et al.*, 1997; Jacobs *et al.*, 1998). The Heimefront Shear Zone separates Grenville-age rocks unaffected by Pan-African overprint to the west from Mesoproterozoic rocks that suffered widespread and intense polyphase high-grade defor-

mation and metamorphism of Pan-African age to the east (e.g. Jacobs *et al.*, 1996a; Jacobs *et al.*, 1998) and is characterized by a prominent magnetic anomaly pattern (Golynsky & Jacobs, 2001). However, the position of the eastern margin of the EAAO remains unclear. In this regard, structural investigations in Sør Rondane may help to answer the question if a possible suture zone is preserved in the main mountain range or may provide evidence for the location of an eastern boundary of the EAAO.

Therefore, a combined structural and geophysical survey was carried out over three consecutive Antarctic seasons in the Sør Rondane region between 2010 and 2013. One of the main targets was the Main Shear Zone (MSZ), which represents a prominent structural element in Sør Rondane. So far, only little is known about the kinematics along the MSZ, and a modern structural characterization, its extent, timing, and role during the Pan-African orogenic cycle are largely lacking. Here we present for the first time detailed structural and kinematic analysis of the MSZ combined and integrated with the main geophysical and petrological/geochemical results of our expeditions (Mieth *et al.*, 2014; Elburg *et al.*, 2015b; Jacobs *et al.*, 2015). The paper addresses the following main questions: (1) which kinematics are involved and what is the geodynamic significance of the MSZ within the EAAO; (2) does the MSZ represent an important regional structure of the EAAO, or is it rather of minor significance as presumed so far; and (3) are there any hints for the location of the eastern front and thus the width of the EAAO in Sør Rondane?

7.2. Geological Overview of Sør Rondane

Sør Rondane is divided into a granulite-facies northeastern terrane (NE terrane) and an amphibolite- to greenschist-facies southwestern terrane (SW terrane), separated by the Sør Rondane Suture (Osanai *et al.*, 1992; Osanai *et al.*, 1996a; Osanai *et al.*, 1996b). This structure was interpreted as a large fault or shear zone with unknown kinematics along which the NE and SW terranes collided in Late Proterozoic times. Peak metamorphism of the NE terrane occurred around 650–600 Ma (SHRIMP U-Pb zircon ages, Shiraishi *et al.*, 2008; Laser ablation-inductively coupled plasma-mass spectrometry U-Pb zircon ages, Osanai *et al.*, 2013). Collision was followed by subsequent retrograde metamorphism, orogenic collapse, and exhumation, which was dated at circa 590–530 Ma in both terranes (Shiraishi *et al.*, 2008; Osanai *et al.*, 2013).

Osanai *et al.* (2013) refined the terranes and lithotectonic units of Sør Rondane (Figure 40), mainly based on new petrological and geochronological data, namely contrasting PTt loops of different types of granulite-facies rocks (Adachi *et al.*, 2013; Baba *et al.*, 2013) and detritial zircon provenances in the NE and SW terranes. The newly defined Main Tectonic Boundary is

interpreted to represent the suture between the NE and SW terranes, apparently associated with SW directed reverse ductile shearing around 650–600 Ma (Osanai *et al.*, 2013). In this scenario, the former Sør Rondane Suture does not represent a suture but is part of the frontal fold zone of the Main Tectonic Boundary.

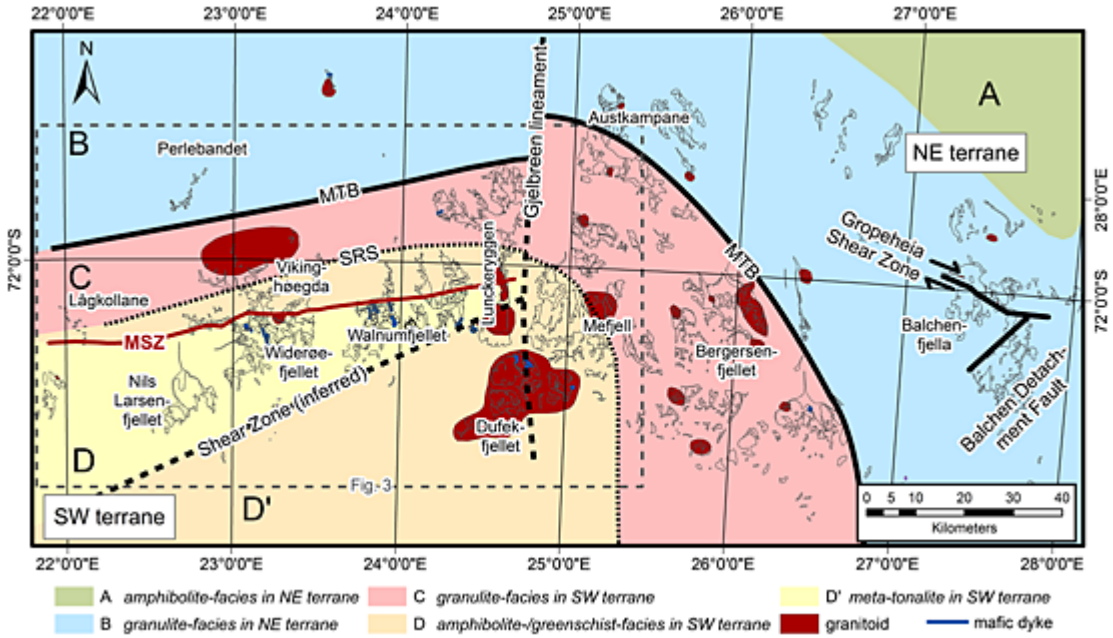

Figure 40: Geological overview of Sør Rondane indicating the subdivision of tectonic terranes and units (modified after Osanai *et al.*, 2013) including representative place names. Units A and B belong to the NE terrane and units C, D, and D′ to the SW terrane. The Main Tectonic Boundary (MTB) separates NE and SW terranes. The previously assumed boundary between these terranes, the Sør Rondane Suture (SRS), is redefined as part of a frontal fold zone of the MTB within the SW terrane (Osanai *et al.*, 2013). The GTTG complex is separated from the northern greenschist- to granulite-facies rocks by the Main Shear Zone (MSZ). An inferred shear zone is indicated in the south of the GTTG complex (Shiraishi *et al.*, 1992a; Osanai *et al.*, 1996a). Another structural feature trending N-S with as yet unknown characteristics is termed the Gjelbreen lineament (Mieth *et al.*, 2014). Age relation of Gropeheia Shear Zone and Balchen Detachment Fault based on aerogeophysical data (Mieth *et al.*, 2014).

The amphibolite to granulite-facies NE terrane is mainly composed of metasupracrustal rocks deposited after 750 Ma but before Pan-African high-grade metamorphism at circa 650–600 Ma or, alternatively, on a postulated circa 1.1–1 Ga basement before or at circa 800–750 Ma, based on detritial zircon data (Shiraishi *et al.*, 2008). Mafic and locally ultramafic metavolcanic rocks indicate a formation in oceanic and island arc to continental margin environments (Osanai *et al.*, 1992; Ikeda & Shiraishi, 1998). The northern part of the SW terrane consists of metasedimentary and metaigneous rocks, which reached granulite-facies conditions in the north and amphibolite- to greenschist-facies conditions in the south, both units separated by the Sør Rondane Suture (Figure 40). The southern part of the SW terrane is represented by a gabbro-tonalite-trondhjemite-granodiorite (GTTG) complex. Kamei *et al.* (2013) determined two different geochemical series with different ages of emplacement for the GTTG complex that is interpreted to have formed along a juvenile oceanic arc. SHRIMP U-Pb zircon ages of circa 998–995 Ma were derived for the intrusion of tholeiitic tonalites and

of circa 945–920 Ma for calc-alkaline tonalites. The GTTG complex shows evidence of tectono-thermal overprint under greenschist- to lower amphibolite-facies conditions at circa 590–530 Ma (Osanai *et al.*, 2013). However, our own observations show that the GTTG rocks still preserve igneous textures on a mesoscopic scale apparently without indications of strong deformation except close to the MSZ (e.g. Mieth *et al.*, 2014; Elburg *et al.*, 2015b).

The transection of the SW terrane along the MSZ (Kojima & Shiraishi, 1986) in an approximately E-W direction separates the low-grade to granulite-facies rocks in the north from the GTTG complex in the south. Toyoshima *et al.* (1995) presented an overview of the structural evolution for the central part of Sør Rondane and reported E-W to ENE-WSW striking mylonitic foliation with NE-SW to N-S trending mineral lineations dipping to the south. A top-to-the-SW to south displacement is interpreted to be associated with retrograde mylonitization and tonalite intrusion at circa 950 Ma. Recent structural work of Toyoshima *et al.* (2013) revises the deformation history of Sør Rondane into multiple stages. They propose that the SE dipping detachment fault in Balchenfjella, which is thought to have formed in an extensional regime after circa 600 Ma (Ishikawa *et al.*, 2013), possibly represents the eastern continuation of the MSZ.

Two late to posttectonic phases of Pan-African age can be recognized in Sør Rondane. Metamorphic U-Pb zircon ages between circa 570 and 530 Ma (e.g. Picciotto *et al.*, 1964; Pasteels & Michot, 1970; Shiraishi *et al.*, 2008; Adachi *et al.*, 2013; Grantham *et al.*, 2013; Osanai *et al.*, 2013) are interpreted to represent a postcollisional retrograde hydration event caused by regional magmatic activity, which affected the granulite-facies rocks in the NE terrane. This event is thought to be associated with extensional tectonics as well as the development of the Balchen detachment fault in easternmost Sør Rondane (Ishikawa *et al.*, 2013). Postpeak-metamorphic plutonism is documented by the intrusion of late- to posttectonic granitoids that are classified into three groups based on ages and magnetic signatures (Mieth *et al.*, 2014 and references therein). Plutonism is recorded for both terranes and is related to a major extensional phase (Li *et al.*, 2003; Li *et al.*, 2006; Shiraishi *et al.*, 2008). Mafic lamprophyre dykes and high-K dolerite dykes intrude the entire area with no systematic orientation and are interpreted as postkinematic and possibly linked to the extensional stage after Pan-African collision (Kojima & Shiraishi, 1986; Takigami *et al.*, 1987; Owada *et al.*, 2008).

New detailed aeromagnetic measurements refine the geological framework of Sør Rondane based on geological information (Mieth *et al.*, 2014). Seven distinct magnetic domains were identified and correlated with distinct tectonic domains. The data suggest an E-W division of Sør Rondane, possibly related to extensional tectonics. Main Shear Zone, Main Tectonic Boundary, and Sør Rondane Suture have a significant magnetic expression and can be traced

underneath the ice cover. However, the geologic and magnetic boundaries differ in some places (cf. Figure 40 and Figure 41). The magnetic anomalies of the GTTG complex are collinear to the general SW-NE foliation trend in this unit. Additionally, it is suggested that a curvilinear magnetic anomaly within the GTTG complex developed as the result of major dextral shear strain.

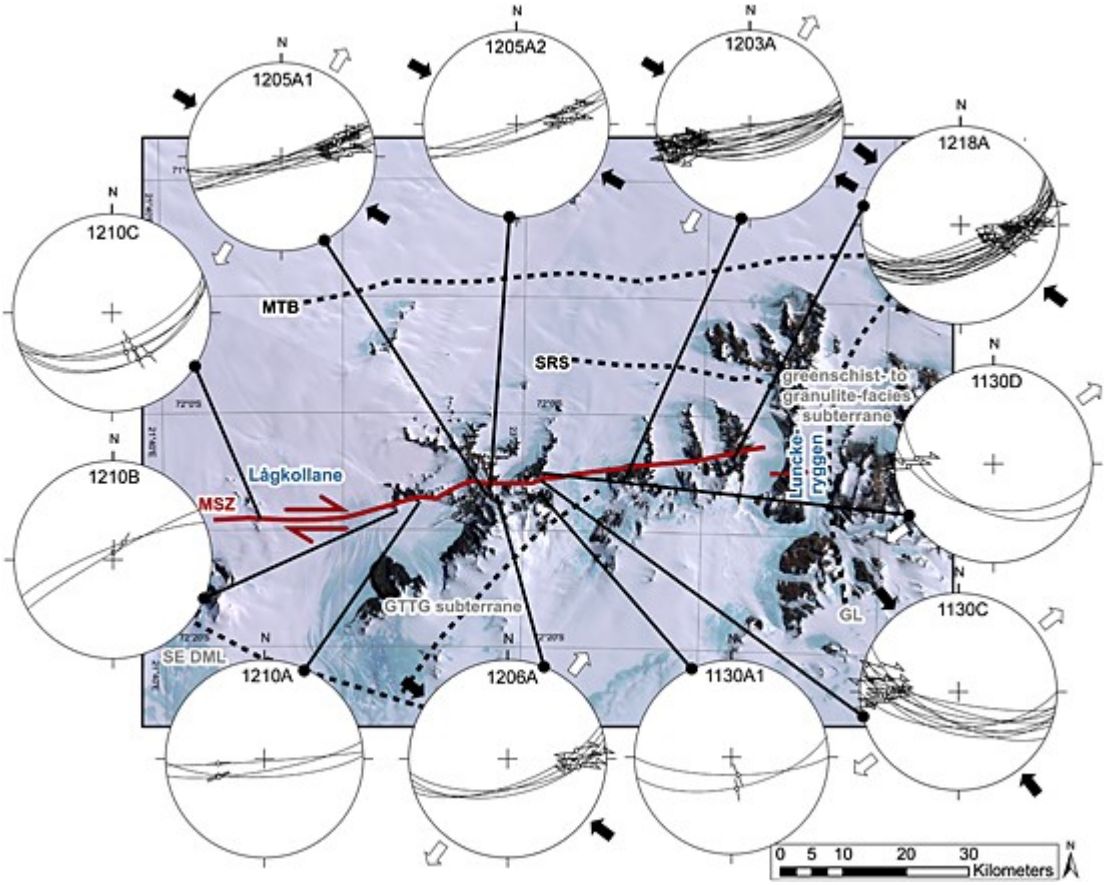

Figure 41: Map with equal-area lower hemisphere projections of kinematic analyses of mylonites along the MSZ. Foliation planes are plotted as great circles, and lineations and shear senses are marked as arrows. Thick arrows indicate horizontal stress directions: black = maximum horizontal stress, white = minimum horizontal stress. Dashed lines represent magnetic boundaries, based on aerogeophysical data and field observations (Mieth *et al.*, 2014). Stereoplots were computed by using the Win-Tensor software by Delvaux & Sperner (2003). Abbreviations: GL, Gjelbreen lineament; GTTG, gabbro-tonalite-trondhjemite-granodiorite; MSZ, Main Shear Zone; MTB, Main Tectonic Boundary; SE DML, southeastern Dronning Maud Land province; and SRS, Sør Rondane Suture.

7.3. Structural Geology

The MSZ (Kojima & Shiraishi, 1986), which measures up to several hundreds of meters in width by roughly 120 km in length, represents a high-strain ductile shear zone of intense mylonitic deformation between Lågkollane in the west and Lunckeryggen in the east (Figure 41). It divides the SW terrane in a northern subterrane consisting of greenschist- to granulite-facies metamorphic and plutonic rocks and a southern subterrane dominated by a gabbro-tonalite-trondhjemite-granodiorite (GTTG) complex. The general strike direction of the MSZ is WSW-ENE but locally its strike changes to a more southwesterly direction. The mylonitic

foliation dips steeply to moderately to the south or SE with angles between 45°–89°. Mineral stretching lineations plunge either shallowly east or west, less frequently they are moderately to steeply inclined and oriented downdip (Figure 41 and Figure 42).

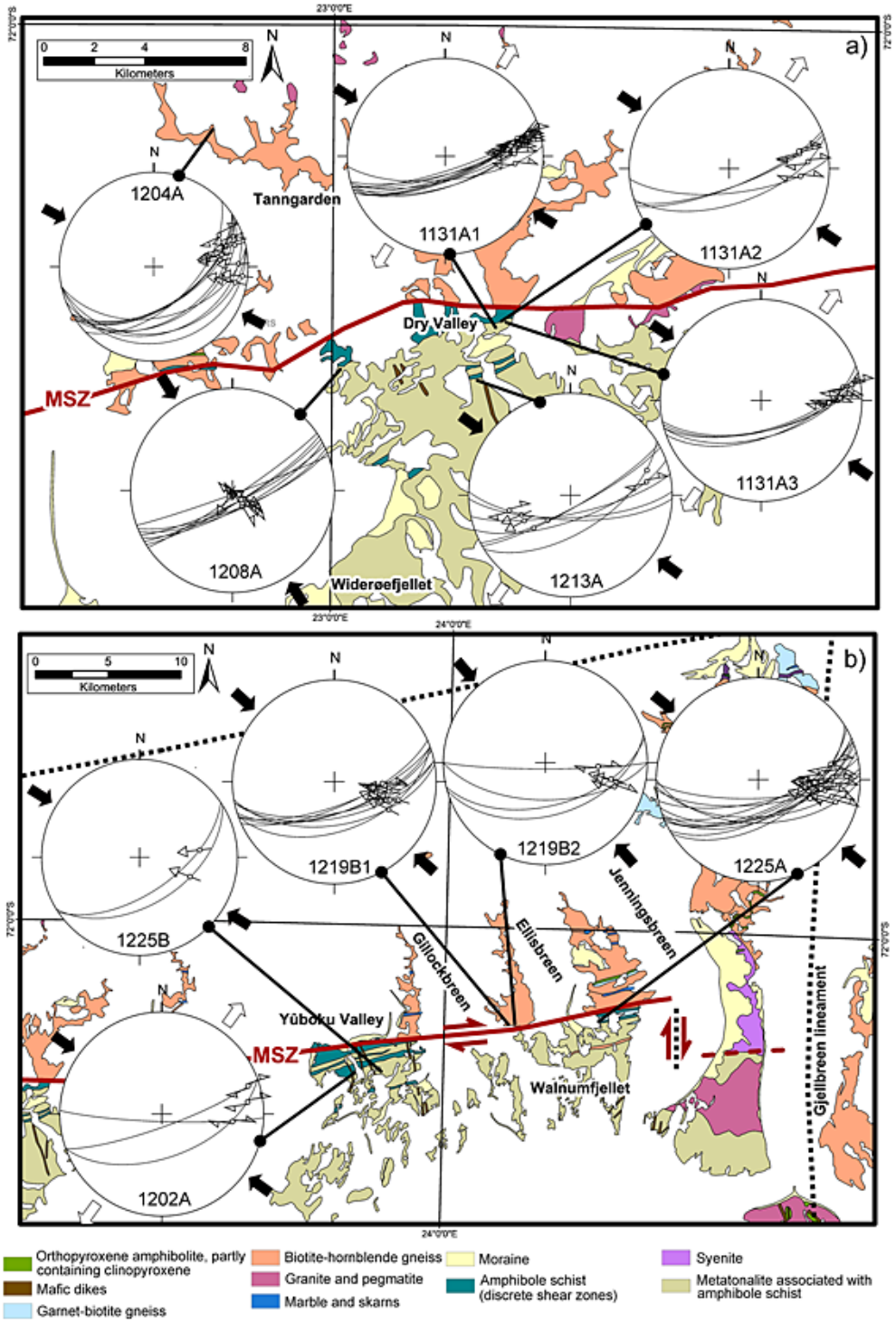

Figure 42: Geological map showing the position of additional structural measurements along the MSZ comprising foliation and lineation data sets characterized by a dextral sense of movement with apparent transpressive component for the regions (a) Dry Valley, Tanngarden and (b) Yûboku Valley, Ridges between Gillockbreen and Jenningsbreen. Amphibol schists represent discrete dextral shear zones following MSZ-related fabrics. Stereoplots were computed by using the Win-Tensor software by Delvaux & Sperner (2003).

Kinematic indicators both in the field and on polished rock slabs and in thin sections (Figure 43 and Figure 44) indicate a dextral sense of shear with either transpressive or subordinate transtensive components suggested by foliation/lineation dip directions (cf. Figure 42).

Figure 43: Photographs of key locations and examples of shear sense indicators of the MSZ in western Sør Rondane. (a) The MSZ along the valley between Vikinghøgda in the north and Widerøefjellet in the south with the typical appearance of the MSZ as a depression due to the diminished competence of the mylonitic rocks. (b) Example of a metatonalite with mafic enclaves from the GTTG complex ~3 km to the south of the MSZ. (c) Mylonitized metatonalite of the GTTG complex shown in Figure 43b but close to the MSZ. Dark streaks are interpreted as transposed enclaves. (d) S-C fabrics and *σ*-clasts point to a right-lateral sense of movement for mylonitic rocks at location 1205A. (e) Right-lateral sense of movement indicated by z-shaped quartz veins in grey gneisses at Wallnumfjellet (ridge between Gillockbreen and Ellisbreen). (f) Protomylonite from the central part of the MSZ at Yûboku Valley (1203A). (g) Kink bands in the central part of the MSZ in mylonitic rocks east of Ellisbreen (1218A).

The main deformation zone of the MSZ is characterized by a large variety of mylonitic rocks, ranging from protomylonites to ultramylonites, apparently largely depending on original composition and grain size of the rocks. Microstructural analyses of rocks of the GTTG subterrane show mylonitic textures with plagioclase and K-feldspar porphyroclasts that have been ductilely deformed (undulose extinction, deformation twins, grain-boundary migration, and dynamic recrystallization mainly along the margins of larger grains) with no brittle component, which points to deformation temperatures of 450–600°C (Passchier & Trouw, 2005).

Plagioclase porphyroclasts are partially replaced by clinozoisite and epidote, which is, however, independent of the deformation event (Elburg *et al.*, 2015b). Asymmetric pressure shadows are composed of dynamically recrystallized quartz, greenish-blue hornblende, and minor chlorite. Most frequently, *σ*-clasts and minor δ-clasts can be observed confirming the right-lateral sense of movement observed in the field (Figure 44a and b). Quartz is to a large extent dynamically recrystallized, and individual grains show undulose extinction, subgrain formation, and grain-boundary migration. Ribbon quartz is very common. These fabrics are typically found in low- to medium-grade mylonitic rocks (Passchier & Trouw, 2005).

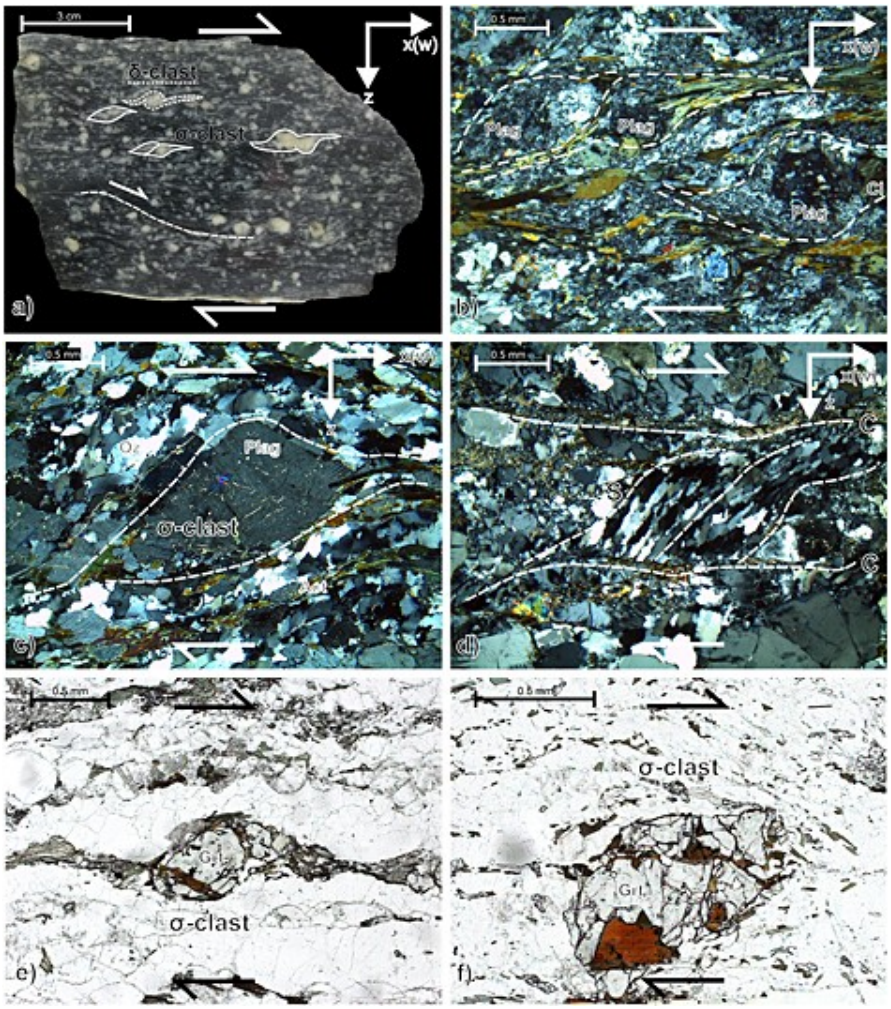

Figure 44: Polished rock slab of an orthomylonite showing right-lateral sense of shear indicated by *σ*-clasts, δ-clasts, and shear bands (1203A). (b) Photomicrograph of an orthomylonite with saussuritized plagioclase porphyroclasts (Plag) and asymmetric pressure shadow tails composed of actinolite (Act) and chlorite (Cl). These *σ*-clasts are evidence of a right-lateral sense of movement (1203A). (c) Photomicrograph of a mylonitic rock with asymmetric plagioclase porphyroclasts indicating dextral shear sense (1205A). (d) Photomicrograph of a mylonitic rock. Quartz is dynamically recrystallized, shows sutured grain boundaries, and is elongated. Elongated quartz grains form the south surface and micas the C surface of a right-lateral S-C fabric (1130C). Cl, chlorite; Plag, plagioclase; Qz, quartz. (e and f) Mylonitic bt-hbl-gneiss with ductilely deformed and elongated garnet *σ*-clasts within the main foliation from the ridge between Ellisbreen and Jenningsbreen indicating dextral shearing (1218A).

Large garnet porphyroclasts were observed in ultramylonitic rocks in the main deformation zone. The clasts are ductilely deformed and elongated within the main foliation and show

asymmetric, mostly σ-like geometries (e.g., locations 1203A, 1218A, Figure 41, Figure 44e, and f). Some smaller euhedral grains show an internal straight S_i rotated in the main foliation and are interpreted as intertectonic porphyroblasts (cf. Passchier & Trouw, 2005).

North of the principal deformation zone, MSZ-related mylonitic textures with right-lateral shear senses are preserved in both metaigneous and metasedimentary rocks of the greenschist- to granulite-facies subterrane, as well as in late-tectonic granitoids that intruded along the MSZ (e.g., Vengen granite, unnamed granitic intrusion east of Gillocksbreen). Thin sections of mylonitic rocks show right-lateral plagioclase *σ*-clasts and S-C fabrics (Figure 44c and d). With increasing distance from the main deformation zone, grey gneisses of the SW terrane show decreasing grades of ductile deformation toward the north. Weak S-C fabrics and poorly developed plagioclase *σ*-clasts again indicate a dextral sense of shear. The mylonitic foliation is formed mainly by biotite and hornblende. Epidote occurs as an accessory mineral.

The late-tectonic Vengen granite, which was dated at circa 560 Ma (SHRIMP U-Pb zircon) (Shiraishi *et al.*, 2008), intruded along the MSZ but also shows dextral ductile deformation and late-stage brittle offsets, particularly visible along the western margin of Ketelersbreen. This may indicate that the Vengen granite intruded during the waning stages of shearing. The northern margin of the GTTG subterrane is strongly deformed by the MSZ, where the plutonic protoliths are transformed to mylonitic greenish epidote-hornblende ± biotite ± garnet schists and orthogneisses (Figure 43c). South of the MSZ, mylonitic deformation gradually decreases, and only right-lateral discrete shear zones consisting of low-grade schists with general trends (sub)parallel to the MSZ occur in certain domains of apparently rather undeformed GTTG rocks (Figure 43b). Discrete shear zones show sigmoidal internal foliation and phacoid bodies again indicating a right-lateral shear sense.

Several ductile-brittle transitional and brittle structures can be observed along the MSZ. These chevron folds and kink bands (Figure 43g) and conjugated fault systems with MSZ-parallel dextral displacement of both aplitic and mafic dykes occur along brittly reactivated mylonitic foliation planes. Furthermore, MSZ-parallel slickensides with subhorizontal striations and fibers composed of feldspar and hornblende were recorded in the late-tectonic syenite stock at Lunckeryggen, which gave U-Pb zircon crystallization ages of circa 560 Ma (Elburg *et al.*, 2016). These slickensides occur in the direct extension of the MSZ farther to the west (see also Osanai *et al.*, 1996b) and may be interpreted as brittle activity of the shear zone overprinting the syenitic intrusion (Figure 45). In addition, negative flower structure-like arrays linked to MSZ-parallel faults are visible at the northern end of Lunckeryggen, again indicative of dextral strike-slip tectonics (e.g., Figure 45b).

Figure 45: Photographs of MSZ-related brittle structures in the syenite of northern Lunckeryggen. Main rock types are melanocratic and quartz syenites, both intruded by granites. (a) View to SW across the eastern face of Lunckeryggen. The stippled rectangle shows the position of the outcrop in photo (Figure 45b). The Lunckeryggen Syenite (sy) is located in the front. Lunckeryggen Granite (gr) and GTTG complex (to) are visible in the background. The granite intrudes the GTTG complex as well as the syenite and contains xenoliths of both. The morphological depression between granite and syenite (labeled to/f) represents the foliated and mylonitized contact zone of syenite and GTTG complex (Osanai *et al.*, 1996b) and is interpreted as the eastern continuation of the MSZ from Ellisbreen into Lunckeryggen dextrally offset by a postulated N-S oriented fault along Jenningsbreen. (b) Eastern wall of northern Lunckeryggen. The wall shows subvertical and steeply inclined brittle faults with an approximate E-W strike direction parallel to the MSZ. The flower-like structure visible on the right side of the picture suggests strike-slip movements along the faults. (c) Large E-W striking slickenside with subhorizontal striations along one of the faults seen in photo (Figure 45b). A right-lateral movement is indicated by fiber steps on the fault plane. (d) Example for slickensides in the syenite with kinematic indicators showing a dextral movement.

7.4. Discussion

7.4.1. The Main Shear Zone of Sør Rondane

The MSZ is characterized by a right-lateral sense of movement with a suggested transpressional and minor transtensional character along strike. The activity of the MSZ caused upper low- to medium-grade high-strain ductile to late-stage brittle deformation, affecting both the Pan-African metamorphic rocks of the greenschist- to granulite-facies subterrane north of it and the early Neoproterozoic GTTG subterrane to the south. Low-grade schists reflect foliation-parallel, discrete high-strain dextral shear zones in the GTTG complex. Shiraishi *et al.* (1992b) specify these rocks as greenschists or amphibole schists with mineral assemblages being identical with that of the tonalite, which is confirmed by our own observa-

tions (Elburg *et al.*, 2015b). The schists contain epidote, zoisite, and chlorite as secondary products and are characteristic for at least greenschist-facies conditions during activity of the MSZ. On a larger scale, these schists, as they are mapped in the Japanese Antarctic Geological Map Series in the vicinity of the MSZ, show a sigmoidal trend, which may indicate a strain increase toward the internal parts of the MSZ leading to a rotation of the preexisting fabric of the rock into the general trend of the MSZ. These macrostructures swinging into the MSZ and the corresponding curvilinear magnetic anomalies are observed for the GTTG complex and may tentatively be interpreted as a result of major dextral shear strain along the MSZ (Mieth *et al.*, 2014). One major curvilinear magnetic anomaly continues along the schists at Walnumfjellet and finally meets the east trending MSZ. This may indicate that the western region of Sør Rondane records deformation caused by dextral shearing and this is supported by a general ENE-WSW trend of magnetic anomalies in the western part of the NE terrane (Mieth *et al.*, 2014).

Since robust age determinations of the mylonites are lacking so far, the activity of the MSZ can only be narrowed down based on crosscutting relationships with dated magmatic rocks. The lower age limit for the activity of the MSZ is provided by the youngest group of granitoid intrusions, which gave an age of circa 530–510 Ma (Tainosho *et al.*, 1992; Li *et al.*, 2003; Li *et al.*, 2006; Shiraishi *et al.*, 2008; Elburg *et al.*, 2016) and appear to be unaffected by dextral ductile shearing. The intrusion of the Vengen granite at circa 560–550 Ma (U-Pb zircon) (Shiraishi *et al.*, 2008; Elburg *et al.*, 2016), which has undergone ductile deformation, gives an upper age constraint for the time of shearing. This is also supported by slickensides with the same orientation and kinematics as the MSZ and fibers composed of feldspar and hornblende, which were observed in the syenite complex at Lunckeryggen also dated to circa 560 Ma (U-Pb zircon) (Elburg *et al.*, 2016) in direct extension of the MSZ west of it. The mineral association on the slickensides implies that brittle deformation occurred under elevated temperatures of up to approximately 300°C and likely increased fluid activities during faulting. These slickensides may represent late-stage activities of the shear zone within the syenite. However, the syenite is intruded by and included as angular xenoliths in the Lunckeryggen granite, the main body of which is located farther to the south (e.g. Li *et al.*, 2003). Both syenite and granite may tentatively be regarded to be of roughly the same age. Based on U-Pb zircon age data of 564 ± 2 Ma of a postkinematic lamprophyre dyke and crosscutting relationships of this dyke with other magmatic rocks, Owada *et al.* (2010) and Owada *et al.* (2013) assume that both lamprophyre dykes and Lunckeryggen granite are roughly coeval and may be attributed to the same age group as the Vengen granite. Also, Li *et al.* (2003) interpret both syenite and the Vengen-type granite group to have evolved from the same magma source by crystal fractionation processes. The granites of this age group plot in the volcanic arc and collisional field

in Y-Nb discrimination diagrams, and can be classified as A types on the basis of their Ga/Al ratios (Jacobs *et al.*, 2015). The syenites have a similar geochemical signature and resemble the lamprophyre dykes in terms of their Sr and Nd isotopic signature (Elburg *et al.*, 2016). The geochemical coherence between all these rock types suggests mantle melting with subsequent crystal fractionation with or without crustal contamination.

Another possibility is that the MSZ is offset along a roughly N-S striking fault underneath Jenningsbreen, paralleling the Gjelbreen lineament (Figure 42b). The slickensides at Lunckeryggen would then represent brittle equivalents of the mylonitic MSZ located at some distance away from the principle deformation zone. Taking into account the simple approximation that the MSZ follows the boundary between the GTTG subterrane and the greenschist- to granulite-facies subterrane, the location of the mylonitic principle deformation zone may be assumed to be located in central Lunckeryggen possibly close to or within the boundary of the syenite and the northernmost tonalitic rocks of the GTTG subterrane (Figure 42b). In this regard, Osanai *et al.* (1996b) report that the syenite "shows remarkable mylonitic structures which are parallel to the contact plane of the mass." This consequently suggests a considerable apparent right-lateral offset of a postulated fault underneath Jenningsbreen of several tens of kilometers.

Further structural features are marked in the Japanese Antarctic Geological Map Series north and south of the MSZ as the "Sør Rondane Suture" and "Shear Zone (inferred)," respectively (Figure 40). Osanai *et al.* (2013) describe the Sør Rondane Suture as a feature that separates areas of different metamorphic grades but preserves no evidence of significant thrusting or fault movement as it would be expected within a collision boundary. The SRS rather seems to define a simple shear zone as part of the frontal fold zone of the overthrusting NE terrane over the SW terrane along the Main Tectonic Boundary. Since age and kinematics of the Sør Rondane Suture remain unknown, it might also be possible that it represents a dextral shear zone of late Pan-African age, similar to the MSZ. This is supported by our own field observations at the southern outcrops of Perlebandet, where steeply dipping, approximately E-W oriented foliation planes, contains a prominent subhorizontal stretching lineation. However, this does not exclude that this structure has an older contractional increment. Another enigmatic shear zone is inferred to the south of the MSZ; however, this structure is ice-covered and structural data are missing (Figure 40). Furthermore, there is no evidence in the aeromagnetic data for the existence of this shear zone (Mieth *et al.*, 2014).

In any case, our data show that the MSZ can be interpreted as a large scale, at least 120 km long late Pan-African strike-slip structure of most likely late Ediacaran to Cambrian age. In this regard, Ishikawa *et al.* (2013) suggest that the eastern Balchenfjella area underwent the

most intensive dextral and normal sense shear strain in Sør Rondane. According to the authors, the Gropeheia Shear Zone in this region results from high-grade dextral transpression during late Neoproterozoic times. These and our own observations from the MSZ may indicate that the whole area of Sør Rondane was affected by widespread, significant dextral shear in Pan-African times.

7.4.2. Geodynamic Significance of the MSZ in the EAAO

Major questions regarding the geodynamic evolution of the EAAO in Gondwana concern the location of the suture(s) and the width of this mobile belt. Possible locations of the E/W Gondwana suture in DML (Figure 39) were proposed by Grunow *et al.* (1996), Helferich *et al.* (2004) Jacobs *et al.* (1998), Kleinschmidt *et al.* (2002), Kleinschmidt *et al.* (2000) Moyes *et al.* (1993) and Shackleton (1996) assume that the suture runs from the Shackleton Range into eastern DML passing southern Kirwanveggen to its SE and reaching the Southern Ocean at about 20°E. In agreement with this hypothesis, Riedel *et al.* (2013) describe a pronounced set of NE trending magnetic anomalies east of Jutulstraumen, which separates two areas with fundamentally different magnetic signatures. The authors interpreted the Forster Magnetic Anomaly as a major tectonic block boundary and/or suture zone within the EAAO, possibly between east and west Gondwana. Therefore, it is likely that a suture zone may be located west of Sør Rondane, possibly outcropping in the area of Wohlthat Massif. However, there seems to be no continuation of the Forster Magnetic Anomaly farther to the NE of Wohlthat Massif. It either terminates in this region or is cut off by a yet unknown structure. Further support for this idea are reported by Shiraishi *et al.* (2008) who describe various types of mafic dykes linked to Pan-African orogenesis in central and eastern DML. Analyses of Sr and Nd isotopic signatures of mafic dykes show different crustal sources for the Mühlig-Hofmann-Gebirge and Sør Rondane (Owada *et al.*, 2008). This indicates a different geologic history for the underlying crust of the Mühlig-Hofmann-Gebirge in central DML and Sør Rondane. Thus, these authors suggest a crustal boundary, potentially related to the suture zone of east and west Gondwana, passing between the Mühlig-Hofmann-Gebirge and Sør Rondane. Furthermore, discrepancies between the timing of magmatic and metamorphic activity in (i) Sør Rondane (Shiraishi *et al.*, 2008; Osanai *et al.*, 2013), the Schirmacher Oasis (Ravikant, 2006; Ravikant *et al.*, 2007), and Yamato-Belgica Mountains (e.g. Shiraishi *et al.*, 2003; Shiraishi *et al.*, 2008) against (ii) central DML for Pan-African (Jacobs *et al.*, 2003d) as well as Grenvillian events (Elburg *et al.*, 2016) support the hypothesis that a possible suture zone that resulted from oblique collision is located between central and eastern DML.

The MSZ separates the SW terrane into (i) a northern subterrane with circa 650–600 Ma greenschist- to granulite-facies peak metamorphism and 590–530 Ma retrogression

(Shiraishi *et al.*, 2008; Osanai *et al.*, 2013) and (ii) a southern GTTG subterrane consisting of juvenile rocks with early Neoproterozoic protolith ages of circa 995–920 Ma (Kamei *et al.*, 2013; Elburg *et al.*, 2015b) and greenschist to lower amphibolite-facies thermal overprint at circa 590–530 Ma (Osanai *et al.*, 2013). The northern subterrane shows in many aspects close similarities to the area of Schirmacher Oasis, where Pan-African high-grade metamorphism is not younger than circa 600 Ma and has thus clear "East African" affinities (Ravikant *et al.*, 2007; Boger, 2011; Osanai *et al.*, 2013). In contrast, the rocks of the GTTG subterrane are interpreted to have formed in an intraoceanic arc environment with affinities to the Indo-Antarctic Rayner complex farther to the east rather than the central and western DML basement (Elburg *et al.*, 2015b). On a mesoscopic scale, the GTTG subterrane contains large domains with apparently completely undeformed igneous textures, whereas strain seems to concentrate at its northern border along the MSZ and in discrete shear zones paralleling MSZ-related fabrics. So far, our observations do not provide any proof of pervasive deformation and high-grade >600 Ma old reworking of the GTTG subterrane. The rather weak tectonic overprint of the main body of the TTG subterrane could be explained by strong strain partitioning due to rheology contrasts between the plutonic rocks and the neighboring metasedimentary units. Therefore, the MSZ marks the boundary between two major lithotectonic units and separates East African-type crust in the north from Rayner-age, Indo-Antarctic crust in the south.

The MSZ does, on the other hand, not represent the eastern margin of the EAAO as previously speculated (e.g. Mieth & Jokat, 2014). This is indicated by new geological evidence and geochronological data from previously unvisited nunataks west of Sør Rondane proving the presence of similar Rayner-age, circa 1000–900 Ma old juvenile arc and metasedimentary cover rocks, however, with intense medium- to high-grade reworking at circa 630–520 Ma and abundant felsic melt injections (Jacobs *et al.*, 2015). This region is characterized by a pronounced NW-SE trending magnetic pattern, namely the SE DML province (Mieth & Jokat, 2014), which terminates at the Forster Magnetic Anomaly to the NW and continues into the ice-covered region south of Sør Rondane (Mieth *et al.*, 2014). The SE DML province may thus represent the westward extension of Rayner-age crust of accretionary origin, which has suffered protracted Pan-African overprint and abuts at the Foster Magnetic Anomaly (Jacobs *et al.*, 2015). The north-eastern margin of the SE DML province marks the boundary between its typical weak magnetic anomaly pattern with elongated positive anomalies to the SW and a pronounced magnetic low to the NE. This line can tentatively be traced from NE of Schirmacher Oasis (Mieth & Jokat, 2014) to the region south of Sør Rondane (Mieth *et al.*, 2014) and may thus be referred to as the Schirmacher-Rondane Lineament (Figure 46). Due to the close similarities in the geology of the Schirmacher Oasis and Sør Rondane metamor-

phic basement north of the MSZ, it may be assumed that the Schirmacher-Rondane Lineament coincides with a major NW-SE striking shear zone with considerable dextral offset. Consequently, the MSZ may be regarded to be part of this major shear system transecting the eastern DML basement.

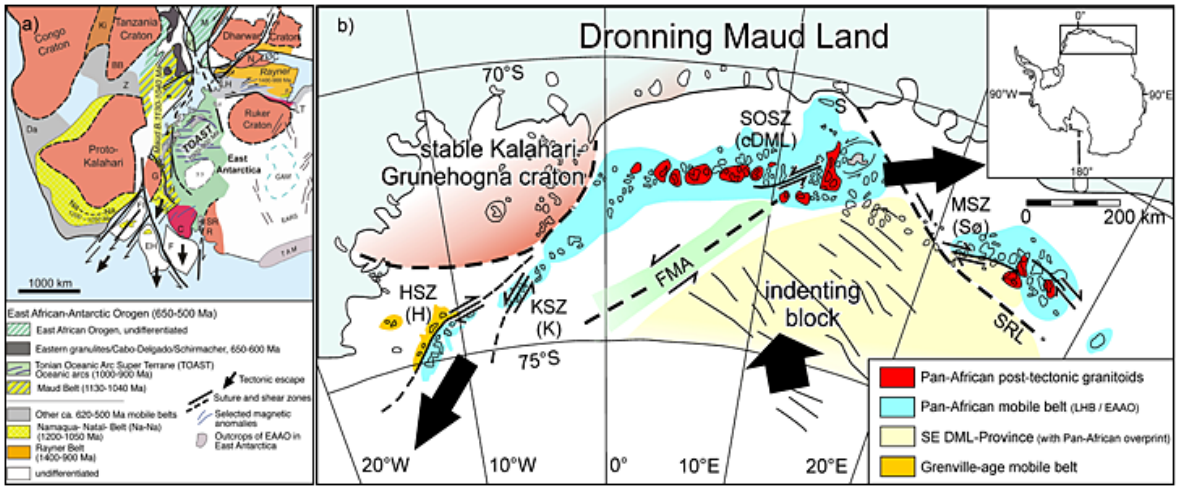

Figure 46: Lateral tectonic escape model for the southern and north-eastern terminations of the East African-Antarctic orogen (EAAO) within (a) Gondwana configuration (modified after Jacobs *et al.*, 2015) and within (b) Dronning Maud Land. The dextral MSZ and the sinistral South Orvin Shear Zone are interpreted in terms of NE directed escape of the EAAO (geographic NE is related to the relative positions of Africa and Antarctica within Gondwana). For further explanations see text. Abbreviations: C, Coats Land; cDML, central Dronning Maud Land; Da, Damara Belt; EH, Ellsworth-Haag; F, Filchner block; FI, Falkland Islands; FMA, Forster Magnetic Anomaly; G, Grunehøgna Craton; H, Heimefrontfjella; HSZ, Heimefront Shear Zone; K, Kirwanveggen; KSZ, Kirwanveggen Shear Zone; L, Lurio Belt; LA, Lambert Terrane; M, Madagascar; N, Napier Complex; MSZ, Main Shear Zone; Na-Na, Namaqua-Natal; ØC, Øygarden Complex; S, Schirmacher Oasis; Sø, Sør Rondane; SR, Shackleton Range; SRL, Schirmacher-Rondane Lineament; TAM, Transantarctic Mountains; LH, Lützow-Holm Bay; R, Read Block; V, Vohibori; Y, Yamato Mts.; Z, Zambesi Belt.

The high-grade metamorphic basement of DML is characterized by a number of large-scale shear zones of likely late Pan-African age, which are shown in the tectonic diagram of Figure 46b. These shear zones include from west to east the dextral Heimefront Shear Zone (e.g. Jacobs *et al.*, 1998; Jacobs *et al.*, 2009) and the sinistral South Kirwanveggen Shear Zone in western DML (e.g. Helferich *et al.*, 2004), the sinistral South Orvin Shear Zone in central DML (e.g. Bauer & Siemes, 2004), and the dextral MSZ in eastern DML. The MSZ may be interpreted in terms of an important strike-slip zone probably related to NE directed lateral escape of the EAAO, possibly together with the presumably coeval South Orvin Shear Zone. The geographic direction "NE" is related to the relative positions of Africa and Antarctica within the supercontinent Gondwana. This model would fit well to the bilateral tectonic escape of the EAAO proposed by Jacobs & Thomas (2004) (Figure 46a). We suggest that the Heimefront Shear Zone together with the South Kirwanveggen Shear Zone represents part of the south directed and the South Orvin Shear Zone and the MSZ with the Schirmacher-Rondane Lineament part of the NE directed branch of this bilateral system. The SE DML province may be regarded as

the indenting block, while the Grunehogna-Kalahari Craton acted as its stable counterpart on the opposite side of the EAAO, forcing the southward and northeastward translation of various tectonic blocks. Focusing on our target area, in particular, NE directed escape of crustal blocks and the accommodation of space may have been facilitated by (i) subduction and ocean closure between Indo-Antarctica and Australo-Antarctica between 560 and 520 Ma (e.g. Boger & Miller, 2004; Boger, 2011), (ii) a late Neoproterozoic to Early Cambrian passive continental margin setting along north and NE Indo-Antarctica (e.g. Jiang *et al.*, 2003; Boger & Miller, 2004), and (iii) the presence of several crustal blocks and fragments to the north and NE of the greater Sør Rondane region, which formed during previous collisional events of Grenville and Pan-African age (Figure 45a; Boger, 2011; Jacobs *et al.*, 2015). Large numbers of late collisional to postcollisional igneous rocks are found in central DML, decreasing in amount toward western and eastern DML. Jacobs *et al.* (2008) presume that these circa 510 Ma high-temperature A2-type granitoids result from a delaminated thickened lithosphere, followed by the influx of asthenospheric mantle material and subsequent orogenic collapse. The most frequent occurrences of these granitic intrusions may represent the central part of the collapsing EAAO. This in turn is accompanied by the development of the late-tectonic Pan-African shear systems and bilateral escape tectonics in western and eastern DML.

7.5. Conclusions

The MSZ is characterized by dextral high-strain ductile deformation under mostly upper low- to medium-grade metamorphic conditions. Except for its northern margin, MSZ-related deformation in the GTTG subterrane is limited to discrete low-grade shear zones.

The activity of the MSZ can be narrowed down based on relative age constraints with dated magmatic rocks between an upper age around 560 Ma and a lower age of circa 530 Ma. Therefore, the MSZ can be interpreted as a large-scale late Pan-African strike-slip structure of late Ediacaran to Cambrian age.

The MSZ represents an important lithotectonic boundary separating East African from "Indo-Antarctic" Rayner-age crust presumably close to the eastern margin of the EAAO, which is assumed to be located farther south in the ice-covered region.

Together with the Heimefront, South Kirwanveggen, and South Orvin Shear Zones, the MSZ may be related to bipolar lateral escape of the EAAO toward the NE and south. In this scenario, the central part of this orogen, preserved today in central DML, is characterized by the delamination of thickened lithosphere and followed by the influx of asthenospheric mantle

material and subsequent orogenic collapse associated with late Pan-African opposite-directed tectonic escape along major regional shear zones.

7.6. Acknowledgments

This study was part of the collaborative research program “Geodynamic Evolution of East Antarctica” (GEA) of the German Federal Institute of Geosciences and Natural Resources (BGR) and the Alfred Wegener Institute Helmholtz Centre for Polar and Marine Research (AWI). J. Jacobs, M. Elburg, and N. Krohne are indebted to BGR for the invitation to participate in the expeditions and to AWI for providing polar clothing. We would like to express our sincere thanks to Alain Hubert and his team at the Belgian Princess Elisabeth station for the wonderful time there and support in the field. Many thanks go also to the crew of Sky Heli, Germany, who took the geological party safely to the field and back to the station. This study was supported by the Deutsche Forschungsgemeinschaft (grants LA1080/9 to A. Läufer and LI 745/15 to F. Lisker) in the framework of the priority program 1158 “Antarctic Research with comparative investigations in Arctic ice areas.” M. Elburg was the recipient of an NRF-SANAP grant SNA2011110200002, which is gratefully acknowledged. J. Jacobs received funding through NFR-NARE, which is equally gratefully acknowledged. Finally, we thank Robert Thomas and Wilfried Bauer for the critical and helpful reviews. Data can be provided on request by contacting A. Ruppel or A. Läufer (BGR).

8. One Hundred Fifty Million Years of Intrusive Activity in the Sør Rondane Mountains (East Antarctica): Implications for Gondwana Assembly

Marlina A. Elburg[1,*], Tom Andersen[1,2], Joachim Jacobs[3,4], Andreas Läufer[5], Antonia Ruppel[5], Nicole Krohne[6] and Detlef Damaske[5]

[1]Department of Geology, University of Johannesburg, Auckland Park 2006, Johannesburg, South Africa

[2]Department of Geosciences, University of Oslo, PO Box 1047 Blindern, N-0316 Oslo, Norway

[3]University of Bergen, Department of Earth Science, PB 7803, 5020 Bergen, Norway

[4]Norwegian Polar Institute, Fram Centre, 9296 Tromsø, Norway

[5]Bundesanstalt für Geowissenschaften und Rohstoffe, Stilleweg 2, D-30655 Hannover, Germany

[6]Department of Geosciences, University of Bremen, PF 330 440, 28334 Bremen, Germany

The Journal of Geology 124 (1), 2016, 1-26–doi: 10.1086/684052

Abstract

New U-Pb zircon ages for the younger phase of magmatism in the Sør Rondane Mountains (East Antarctica) are combined with published igneous and metamorphic zircon ages and show evidence for at least four thermal pulses: at 650–600 Ma, 580–550 Ma, ca. 530 Ma, and a magmatic tail between 510 and 500 Ma. No igneous U-Pb ages younger than 500 Ma have been found, in contrast to the situation in central and western Dronning Maud Land. Zircon Lu-Hf isotopic data are best explained as reflecting both crustal reworking and juvenile input, with the latter more obvious during the 580–550 Ma period. The Hf isotopic data, together with the presence of mafic and silica-undersaturated intrusives, argue against purely intracrustal melting as a petrogenetic process. Apart from the observed temporal trend, there is also a geographic trend in Hf isotopic compositions, with lower initial ε Hf values toward the northeast. However, the Hf isotopic shifts are gradual and do not show evidence for a dramatic change between the two previously defined metamorphic terranes. This observation, together with the long duration of magmatism, suggests that the Sør Rondane Mountains may be a collage of several different (sub-)terranes that were amalgamated over a longer period of time.

8.1. Introduction

The geology of the Sør Rondane Mountains (East Antarctica) has been the focus of intensive research for the past few years, as it was interpreted to be the locus where two orogens—the ca. 660–600 Ma East African–Antarctic Orogen (EAAO; Figure 47A) and the later (ca. 560–530

Ma) Kuunga Orogen—crossed (e.g. Satish-Kumar *et al.*, 2008; Satish-Kumar *et al.*, 2013). This has led to a wealth of new data, especially high-quality U-Pb zircon age data, with a strong focus on the metamorphic history of the area.

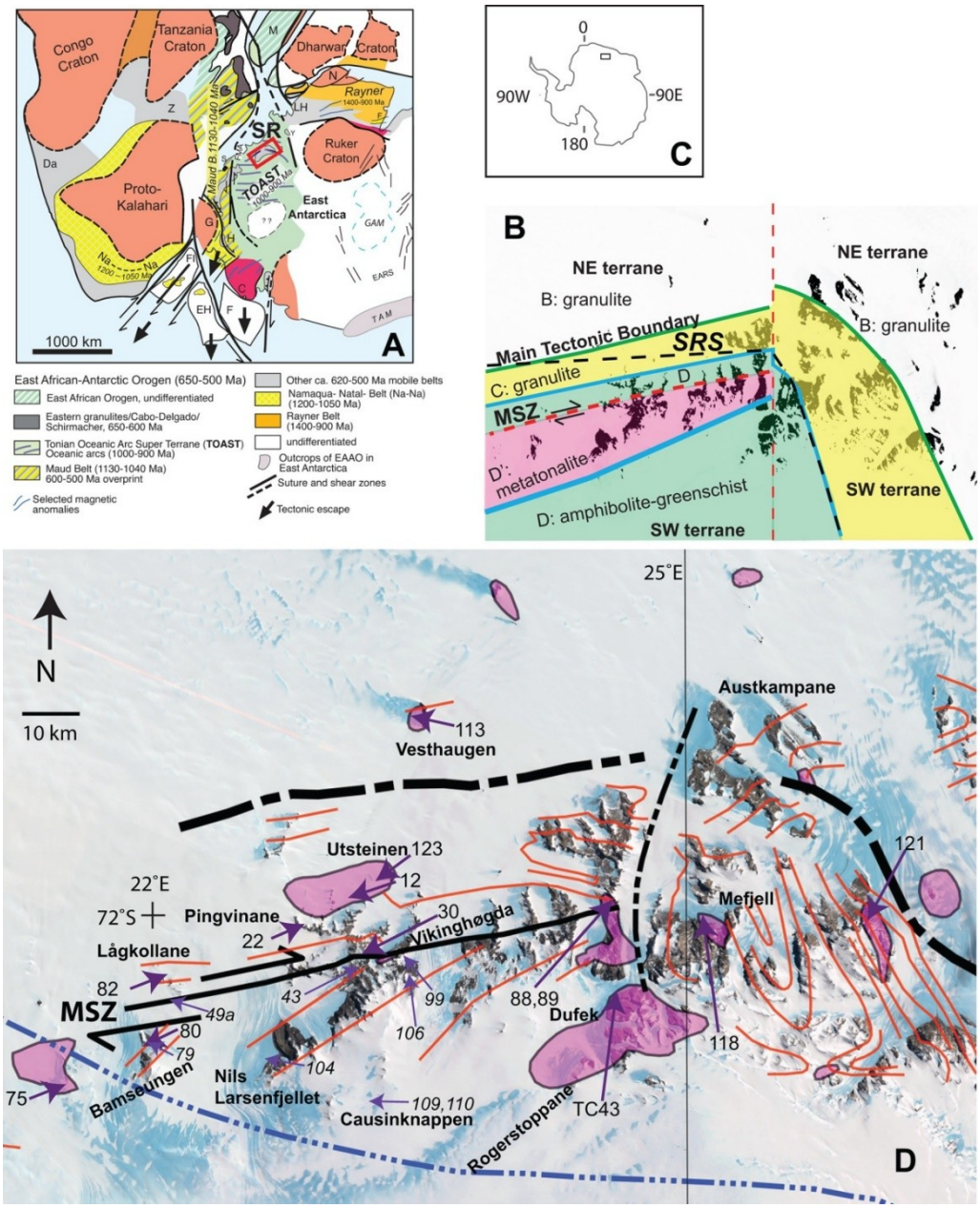

Figure 47: *A*, Position of the Sør Rondane Mountains (SR) within the East African–Antarctic Orogen, after Jacobs *et al.* (2015). Abbreviations: C, Coats Land; Da, Damara Belt; EARS, East Antarctic Rift System; EH, Ellsworth-Haag; F, Filchnerblock; FI, Falkland Islands; FMA, Forster Magnetic Anomaly; G, Grunehøgna; GAM, Gamburtsev Mountains; H, Heimefrontfjella; LH, Lützow-Holm Complex; M, Madagascar; N, Napier Complex; Na–Na, Namaqua–Natal; R, Read Block; S, Schirmacher Hills; TAM, Trans-Antarctic Mountains; Z, Zambesi Belt. *B*, Overview map of the Sør Rondane Mountains (from Google Earth, air photo date 1999) showing the various sectors within the NE and SW terranes, following Osanai *et al.* (2013). The previously assumed boundary between the two terranes, the Sør Rondane Suture (SRS), is shown as a thin dashed line. MSZ, Main Shear Zone. *C*, Location of the Sør Rondane Mountains within Antarctica. *D*, Map with the magnetic boundaries (black and blue dashed lines) and structural trendlines (in red) following Mieth *et al.* (2014), and sample locations (prefix MESR omitted for clarity). Smaller italic sample numbers refer to samples from Elburg *et al.* (2015b). Pink areas indicate the extent of granitoid bodies, as interpreted from aeromagnetic data and ground truthing.

With this contribution, we want to emphasize the magmatic development during these orogenic periods in terms of not only ages and their relationship to deformational events but also the Hf isotopic composition of the dated zircons. For this, we obtained U-Pb and Lu-Hf zircon data on 13 samples that span most of the area and the known Pan-African age range of the Sør Rondane Mountains. Our new data are integrated with previous zircon U-Pb ages on the Sør Rondane Mountains—as well as the neighboring Yamato-Belgica Mountains in the east and the central and western Dronning Maud Land in the west—to document spatial and temporal magmatic trends, which will help to build a better picture of the final amalgamation of the Gondwana supercontinent. The integration of the new and published data also adds to the discussion of whether magmatism in the EAAO and Kuunga belts is related to intracrustal melting only (Grantham *et al.*, 2008) or that the mantle played a pivotal role, as, for instance, during lithospheric delamination (Jacobs & Thomas, 2004).

8.2. Regional Geology

The Sør Rondane Mountains have been the subject of a considerable number of studies, first in the frame of the Belgian Antarctic Research Expeditions following the International Geophysical Year in 1957–1958 and later mainly reflecting the results of the Japanese Antarctic Research Expeditions. The current understanding of the area has been detailed in a special issue of *Precambrian Research* (vol. 234), with Osanai *et al.* (2013) giving the most comprehensive overview of the tectonic development of the area. The existence of two terranes—the southwest (SW) and northeast (NE) terranes—has been known for a longer time (Shiraishi *et al.*, 1997), but the boundary between the two has now been shifted to what has been called the Main Tectonic Boundary (Figure 47B) from a more southerly position for what used to be the Sør Rondane Suture. The SW terrane, in its most recent definition, consists of both greenschist-amphibolite (D and D′) and granulite-facies (C) sectors, with a counterclockwise *PTt* path; while the NE terrane consists of amphibolite- and granulite-facies sectors (sectors A and B, respectively), with a clockwise *PTt* path (Osanai *et al.*, 2013). Within the SW terrane, the D′ sector consists of a suite of amphibolite to greenschist facies meta-intrusives (Kamei *et al.*, 2013; Owada *et al.*, 2013; Elburg *et al.*, 2015b), separated from the D sector to the north by the Main Shear Zone, a dextral strike-slip fault with a length of ca. 120 km (Ruppel *et al.*, 2015). The southern boundary of the D′ sector may be another shear zone hidden under the ice (Shiraishi *et al.*, 1997), although magnetic anomalies appear to define a different trend (Mieth *et al.*, 2014).

The D′ sector consists of greenschist- to amphibolite-grade gabbro, tonalite, trondhjemite, and minor granodiorite, with ages ranging from 920 to 1015 Ma. The trace element and isotopic signature of the samples have been interpreted to reflect magmatism in an oceanic arc

setting until ca. 975 Ma (tholeiitic signature), after which magmatism became somewhat more variable (calc-alkaline signature), which could be interpreted as reflecting a postsubduction stage, perhaps linked to slab break-off (Elburg *et al.*, 2015b). Only very sparse zircons with ages older than ca. 1040 Ma were found in this area, in the form of two ca. 3 Ga grains in the 970–920 Ma intrusive (Elburg *et al.*, 2015b). Kamei *et al.* (2013) also described a spatially limited occurrence of calc-alkaline intrusives with ages around 770 Ma in the Nils-Larsenfjellet area.

The other sectors consist mainly of metamorphosed supracrustal rocks intruded by Pan-African granitoids. The depositional ages of these supracrustals has been established as being Late Tonian–Early Cryogenian (880–790 Ma) on the basis of the isotopic composition of marbles found in both the SE and the NW terrane (Otsuji *et al.*, 2013). This agrees with the youngest U-Pb zircon ages found in detritial rocks, which are around 780 Ma, for both the NW and the SE terranes (Osanai *et al.*, 2013). Zircons with ages older than ca. 1 Ga are more common in the NE than in the SW terrane. The oldest detritial age recorded within the C and D sectors of the SW terrane are ca. 1200 Ma, whereas detritial ages in the NE terrane include Paleoproterozoic and Archaean (up to ca. 3.3 Ga) components (Shiraishi *et al.*, 2008; Kamei *et al.*, 2013; Osanai *et al.*, 2013; Owada *et al.*, 2013; Elburg *et al.*, 2015b).

An inferred large-scale tectonic feature is an NS lineament (Figure 47), which offsets the boundary between the two terranes (Osanai *et al.*, 2013) but which is hidden under the ice. A magnetic boundary has been observed in roughly the same location (Mieth *et al.*, 2014). The latter authors tentatively relate this central Sør Rondane corridor to late-stage extensional tectonics following the main collisional event.

Previous workers have divided the Pan-African granitoids into four different groups, on the basis of their geochemical characteristics (Li *et al.*, 2001; Li *et al.*, 2003). The group 1 granites comprise the Dufek and Lunkeryggen granites, with an arc-type trace element signature located within the SW terrane, whereas the group 2 granites (Austkampane, Pingvinane, Rogerstoppane, and Vikinghøgda; both SW and NE terrane) were classified as having a within-plate signature. The Lunkeryggen Syenite Complex was classified as a separate group, as were the syenitic and granitic rocks from the Mefjell Plutonic Complex (both SW terrane). The ages of the different granites are, however, poorly known, since most dates were obtained by K-Ar, Ar-Ar, and Rb-Sr dating, which yielded (closure) ages between 530 and 460 Ma. Only the ages of the Vikinghøgda (562 ± 7 Ma; Shiraishi *et al.*, 2008) and Dufek granite (619 ± 7 Ma; Li *et al.*, 2006) have been obtained by U-Pb zircon dating, and they are notably older than the earlier ages reported. The uncertainty in the age of the granitoids also hampers the interpretation of their isotopic signature, since the initial Sr isotopic signature for these

rather high Rb/Sr samples changes significantly when ages shift tens of millions of years. This may explain why the initial $^{87}Sr/^{86}Sr$ ratios appear to vary between 0.703 and 0.73 within a single group (see compilation in Li *et al.*, 2003).

8.3. Samples and Methods

Thirteen samples were collected from a wide area of the Sør Rondane Mountains (Figure 47) during the German-led expedition Geodynamic Evolution of East Antarctica II in the Austral summer of 2011–2012. Unfortunately, the sampling was done on the basis of the previous interpretation of the Sør Rondane Suture (e.g. Shiraishi *et al.*, 2008) as the boundary between the SW and NE terrane rather than the new interpretation of the more northerly Main Tectonic Boundary (Osanai *et al.*, 2013); thus, the SW terrane is now overrepresented with 11 samples (Figure 47), while only one sample comes from the NE terrane (MESR113 from Vesthaugen) and one sample on the boundary between the two terranes (MESR121). The position of the latter sample is, however, still to the west of the magnetic boundary that Mieth *et al.* (2014) propose to represent the Main Tectonic Boundary.

Analytical techniques employed were identical to those described by Elburg *et al.* (2013), using the LA-MC-ICPMS laboratory at the Department of Geosciences of Oslo University. Zircons used for U-Pb standardization were GJ-1 (207Pb/206Pb age 608 ± 1 Ma; Jackson *et al.*, 2004), 91500 (207Pb/206Pb age 1065 ± 1 Ma; Wiedenbeck *et al.*, 1995), and A382 (concordia age = 1877 ± 2 Ma; Huhma *et al.*, 2012). Internal structures of zircons were obtained with backscattered electron (BSE) imaging at the Geology Division of the School of Agricultural, Earth, and Environmental Sciences at the University of KwaZulu-Natal.

For the U-Pb data, common Pb–affected analyses were not corrected but were either used for an intercept age in a Tera-Wasserburg diagram or not used for age calculations. All data are provided in Table 9. Ages were calculated using the ISOPLOT add-in for Microsoft Excel 2003 (ver. 3.71; Ludwig, 2008). Errors are quoted at the 2σ level and at a 95% confidence level for weighted average ages. The MSWD for the concordant ages are for combined concordance and equivalence.

For some of the samples, the spread in concordant dates is larger than can be explained by the uncertainty of the individual measurements. This could reflect the presence of different age groups within the population, the presence of (minor) common Pb, or Pb loss. In these instances, the age spread has been visualized by sorting the concordant analyses in order of ascending $^{206}Pb/^{238}U$ age, with error bars representing the uncertainty of each analytical point. This approach is based on the treatment proposed for $^{207}Pb/^{206}Pb$ ages obtained from zircon evaporation dating (Dougherty-Page & Bartlett, 1999). Because analyses with high

$^{206}Pb/^{204}Pb$ ratios are less likely to be influenced by common Pb, this ratio has also been shown in the diagrams and is represented by the size of each data point. This way of representing the data facilitates identifying the presence of different age groups by visual inspection.

For the Hf isotopic compositions, the homogeneity of the zircons can be assessed by comparison to the statistics of the standards that were measured during the analytical period (Table 9). The Mud Tank standard yielded an initial $^{176}Hf/^{177}Hf_{732}$ of 0.282510 ± 0.000036 (2σ; n = 65), which translates into an uncertainty of 1.3 ε units. Since this zircon is extremely low in heavy rare earth elements (HREEs) ($^{176}Yb/^{177}Hf < 0.003$), both interference and age corrections are minimal, so this is the best possible uncertainty we can obtain with the method. For the Temora 2 standard ($^{176}Yb/^{177}Hf$ = 0.03–0.1), the 2σ uncertainty on the initial ratio increases to 0.000068 (2.4 ε units), and the high-HREE standard LV-11 ($^{176}Yb/^{177}Hf$ = 0.1–0.35) yields 0.000083 (3 ε units). Most zircons analyzed in this study had a $^{176}Yb/^{177}Hf$ ratio similar to that of Temora 2, so the expected 2σ uncertainty on a homogeneous population is around 2.5 ε units, unless the zircons were exceptionally rich in Hf, which typically improves the statistics. A few analyses with $^{176}Yb/^{177}Hf > 0.35$ ($^{176}Lu/^{177}Hf > 0.005$) were discarded, since we noted a change in the initial ratios for the LV-11 standard above this value, casting doubt on the efficiency of our interference correction at these high Yb/Hf ratios.

Table 9: Zircon U-Pb and Hf Isotope Data for Samples and Standards Analyzed

Sample	latitude S	longitude E	type age	n	age±2σ[1]	MSWD[2]	type age	$\varepsilon Hf_i \pm 2\sigma$	$^{176}Hf/^{177}Hf_i \pm 2\sigma$	n
TC43	72° 10.360’	24° 38.454’	$^{206}Pb/^{238}U$ wtd. av.	2	950 ± 18	1.6	inherited, igneous prot.	+3.9 ± 2.4	0.28228 ± 3	2
			$^{206}Pb/^{238}U$	6	664-800		inherited	ca. +6	0.28247 - 252	4
			$^{206}Pb/^{238}U$ wtd. av.	7	637 ± 6	1.0	preferred igneous age	+4.3 ± 1.7	0.28250 ± 5	10
			$^{206}Pb/^{238}U$	1	603 ± 7		metamorphic?	+2.5 ± 0.9	0.28247 ± 3	1
MESR12	71° 59.889’	23° 14.360’	concordia	9	577 ± 6	1.6	igneous age			
			$^{206}Pb/^{238}U$ wtd. av.	8	575 ± 5	0.75	preferred igneous age	+5.0 ± 1.0	0.28256 ± 3	27
MESR82	72° 7.296’	22° 1.122’	$^{206}Pb/^{238}U$	1	644 ± 3		inherited	+2.7	0.28246	1
			$^{206}Pb/^{238}U$ wtd. av.	21	572 ± 4	5.4	preferred igneous age	+2.4 ± 2.2	0.28249 ± 6	32
MESR89	72°1.981’	24°35.865’	$^{206}Pb/^{238}U$	1	960		inherited, igneous prot.	+8.4 ± 1.2	0.28241 ± 4	2
			$^{206}Pb/^{238}U$	1	715		inherited, igneous prot.	+5.6 ± 0.3	0.28249 ± 1	2
			$^{206}Pb/^{238}U$ wtd. av.	4	617 ± 14	1.9	inherited, metam. prot.	+2.6 ± 0.7	0.28247 ± 2	4
			$^{206}Pb/^{238}U$ wtd. av.	6	560 ± 9	1.9	preferred igneous age	+0.3 ± 2.8	0.28244 ± 8	11
MESR88	72°1.981’	24°35.865’	assumed		560		assumed	+1.3 ± 1.0	0.28247 ± 3	15
MESR75	72° 17.081’	21° 26.114’	concordia	5	556 ± 4	1.5	preferred igneous age	+2.4 ± 1	0.28250 ± 3	21

Table 9 (continued)

Sample	latitude S	longitude E	type age	n	age±2σ[1]	MSWD[2]	type age	$\varepsilon Hf_i \pm 2\sigma$	$^{176}Hf/^{177}Hf_i \pm 2\sigma$	n
MESR30	72° 5.846’	23° 10.923	$^{206}Pb/^{238}U$	2	ca. 1000		inherited	+7 - +8.5	0.28241 ± 2	3
			$^{206}Pb/^{238}U$	1	803 ± 8		inherited	+6.5 ± 1	0.28246 ± 3	1
			$^{206}Pb/^{238}U$ wtd. av.	3	742 ± 7	1.0	inherited	+2 - +8	0.28239 - 56	6
			$^{206}Pb/^{238}U$	1	670 ± 5		inherited	+3.1 ± 1.0	0.28245 ± 3	5
			$^{206}Pb/^{238}U$ wtd. av.	2	616 ± 9	0.4	inherited	+2.1 ±1.2	0.28246 ± 5	1
			$^{206}Pb/^{238}U$ wtd. av.	11	551 ± 8	6.1	preferred igneous age	0.0 ± 2.9	0.28244 ± 8	44
MESR121	72° 3.970’	26° 0.769’	$^{206}Pb/^{238}U$ wtd. av.	19	532 ± 3	2.9	preferred igneous age	-5.9 ± 1.6	0.28228 ± 5	23
MESR80	72° 13.736’	21° 57.217’	concordia	9	529 ± 3	1.6	preferred igneous age	+1.3 ± 1.4	0.28249 ± 4	30
MESR123	71° 56.824’	23° 20.813’	$^{206}Pb/^{238}U$ wtd. av.	43	528 ± 4	1.6	preferred igneous age	-1.8 ± 1.6	0.28240 ± 5	47
MESR118	72° 2.810’	25° 3.449’	$^{206}Pb/^{238}U$ wtd. av.	12	527 ± 5	1.7	preferred igneous age	-4.4 ± 2.9	0.28233 ± 8	42
MESR113	71° 41.610’	23° 33.462’	$^{206}Pb/^{238}U$	3	600-535		inherited	-0.8 ± 1.0	0.28238 ± 3	1
			$^{206}Pb/^{238}U$ wtd. av.	4	509 ± 12	2.2	preferred igneous age	-2.5 ± 1.6	0.28239 ± 4	18
MESR22	72° 2.309’	22° 50.998’	concordia	12	506 ± 4	0.9	preferred igneous age	-1.3 ± 2.1	0.28243 ± 6	36

Table 9 (continued)

standard	type age	n	age±2σ[1]	recommended[5]	MSWD[2]	$^{176}Hf/^{177}Hf_i$±2σ	recommended[5]	n
Plesovice	$^{206}Pb/^{238}U$ wtd. av.	12	340.2 ±1.4	337.1 ± 0.4	1.1			
C	$^{207}Pb/^{206}Pb$ wtd. av.	61	560.7 ± 1.4	556.4 ± 1.5	0.9			
Mud Tank	initial[3]		732			0.282510 ± 36	0.282507±6	65
Temora	initial[3]		414			0.282683 ± 68	0.282686±8	27
LV11	initial[3]		290			0.282818 ± 107	0.282837±28	73
LV11	initial[3]		290			0.282832 ± 834	0.282837±28	63

TW=Tera Wasserburg plot. $^{206}Pb/^{238}U$ wtd. av. = weighted average of the $^{206}Pb/^{238}U$ ages. cPb = common Pb; prot. = protolith

[1] weighted average $^{206}Pb/^{238}U$ quoted at the 95% confidence level.

[2] the MSWD of the concordia ages is for concordance and equivalence

[3] only analyzed for Lu-Hf isotope systematics; age used for calculation of initial Hf isotope ratio.

[4] only analyses with $^{176}Yb/^{177}Hf$ <0.35

[5] recommended ages and intial Hf isotopic compositions from Slama *et al.* (2008), Kristoffersen *et al.* (2013), Woodhead & Hergt (2005), Heinonen *et al.* (2010a)

8.4. Results

The data are presented in order of their U-Pb zircon ages, from older to younger. The full data set can be found in Table 9. Field photographs are given in Figure 48 and photomicrographs in Figure 49.

Figure 48: Field photographs. *A*, Vertical granite dyke (with hammer) from which MESR12 was taken, crosscutting gneisses but also showing a steep foliation itself. *B*, Granite dyke (labeled) from which sample MESR82 originates, clearly discordant to host gneisses and calc-silicates. *C*, Pink syenites, similar to sample MESR89, intruding more melanocratic rocks of the Lunkeryggen complex. *D*, Vertical granite dyke (sample MESR113) with a scalloped contact against host diorite at Vesthaugen. *E*, Contact between Utsteinen granite and host gneisses at Princess Elisabeth Antarctica Station. *F*, Pegmatite veins (MESR88) with amazonitic feldspar crosscutting other syenitic phases at Lunkeryggen. *G*, Red granite (MESR75) with small mafic enclave.

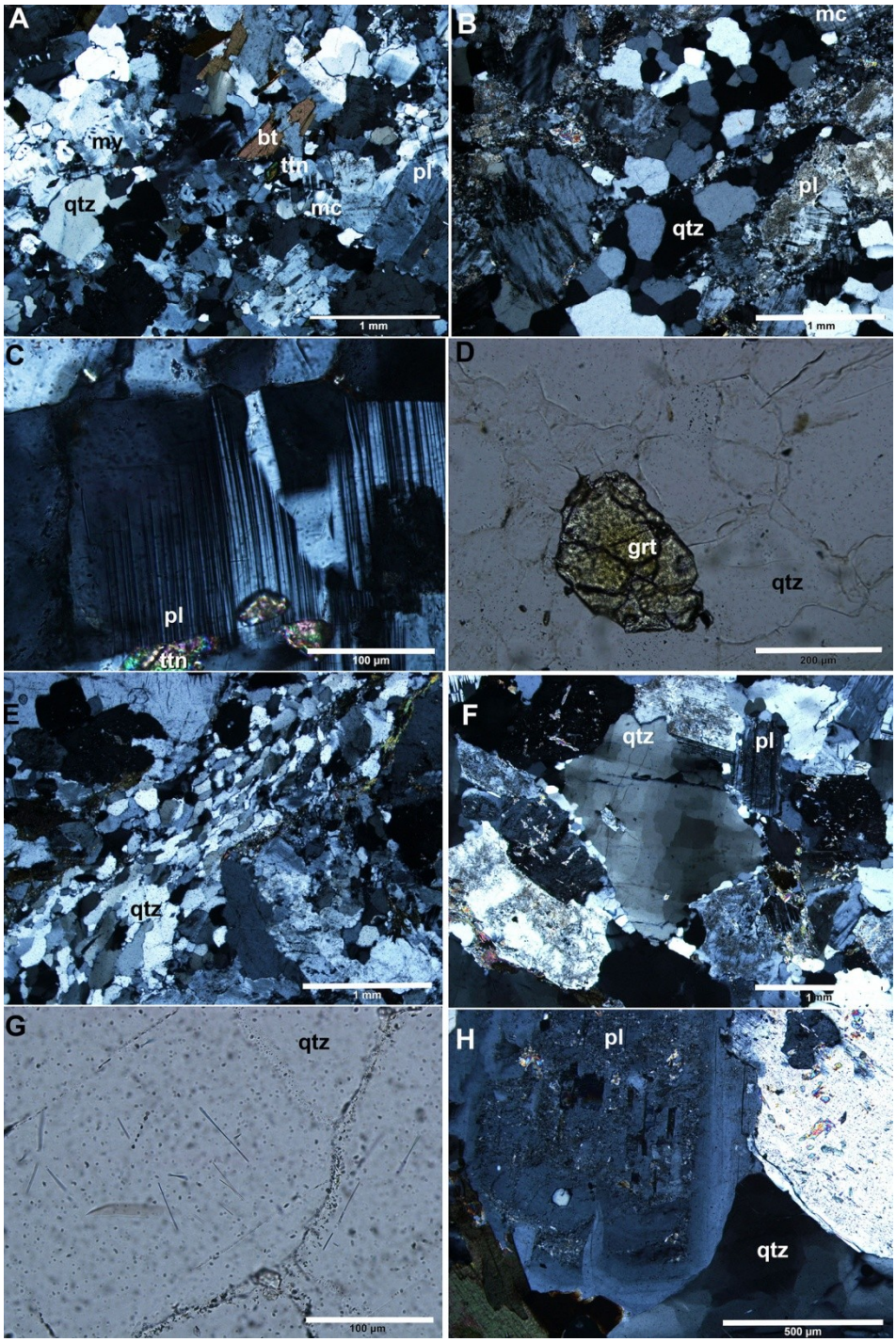

Figure 49: Photomicrographs of selected samples. Abbreviations following Kretz (1983): my, myrmekite; xpl, crossed polars; ppl, plane polarized light. *A*, Sample TC 43 from Dufek, with little evidence for deformation; xpl. *B*, MESR12, showing fine-grained bands defining the foliation and recrystallized domains of quartz; xpl. *C*, Bent plagioclase twins as the only evidence for deformation in syenite sample MESR89. *D*, Yellow garnet in pegmatitic sample MESR88 within the Lunkeryggen syenite complex; ppl. *E*, Sample MESR30 from the sheared Vengen/Vikinghøgda granite, showing elongate and serrated quartz grains; xpl. *F*, Sample MESR80 from Bamseungen, showing compositionally zoned plagioclase and chessboard deformation in quartz; xpl. *G*, Putative rutile needles within quartz of sample MESR123; ppl. *H*, Sample MESR22, the youngest granite analyzed, with zoned plagioclase and undulose quartz; xpl.

TC43 is an unfoliated, medium-grained sample from the Dufek granite. This pluton is located within the amphibolite-greenschist-facies D sector of the SW terrane, stitching a N-S running

shear zone with apparent sinistral displacement (Osanai *et al.*, 2013). The main minerals are quartz, K-feldspar (typically perthitic microcline), and plagioclase, with lesser amounts of biotite. Myrmekite is quite common (Figure 49A). Plagioclase shows minor sericitization, and some of the biotite has been altered to chlorite. Quartz shows undulose extinction or has undergone dynamic recrystallization. Accessory minerals are opaque minerals, titanite, apatite, and zircon. Zircons are colorless and clear, and they vary from equidimensional to elongated, with aspect ratios up to 3 and a typical length of 150 μm. Equidimensional crystals often have an anhedral shape. Internal structures, as viewed in BSE imaging, are variable (Figure 50).

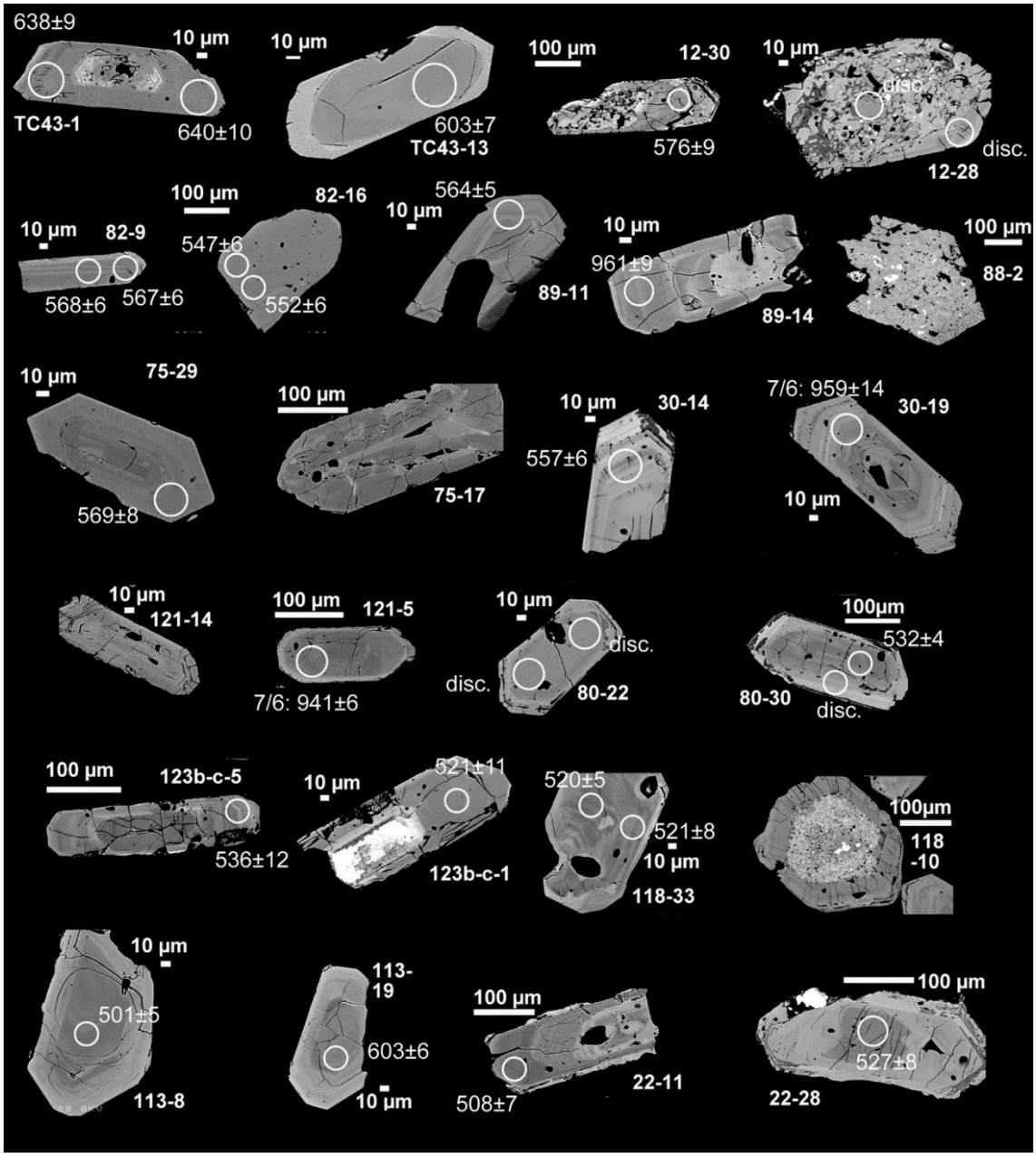

Figure 50: Typical zircon backscattered electron images for the samples analyzed. The first number is the sample without the prefix MESR, and the second is the number of the individual zircon, as also used in the text and Table 9. $^{206}Pb/^{238}U$ dates (in Ma) are given next to the indicated ablation spots, unless badly discordant because of common Pb (disc.); for slightly discordant analyses, the $^{207}Pb/^{206}Pb$ date is given (7/6).

Some crystals show indistinct oscillatory zoning, sometimes surrounding a euhedral, BSE-bright patchy core; others have a homogeneous, rounded core and BSE-bright rim; while others are homogeneous or patchy throughout. A total of twenty-four spots were analyzed on 21 grains, yielding unsystematic variations in U concentrations between 200 and 3000 ppm. $^{206}Pb/^{204}Pb$ ratios varied between 60 and 80,000, with the lower ratios in strongly discordant analyses. The unfiltered data give intercepts in a Tera-Wasserburg plot at 645 ± 54 and 1995 ± 900 Ma, but the MSWD of 79 indicates the severity of scatter, supported by the presence of different textures in the zircons. Two near-concordant grains (2, 12) yield a combined weighted average $^{206}Pb/^{238}U$ age of 950 ± 18 Ma and are thought to represent an inherited component from an igneous protolith, since both zircons show oscillatory zoning in the analyzed areas.

One grain (14) with a homogenous, rounded, BSE-dark core and BSE-bright rim gives a concordant 664 ± 10 Ma $^{206}Pb/^{238}U$ date for the core and ca. 750 Ma—but strongly reversely discordant (and likely meaningless)—for the rim. Four more grains (8, 15, 21 and 22) with patchy to absent zoning yield near-concordant to (reversely) discordant dates around 750 Ma. Of the remaining analyses, eight are (near-) concordant, of which one (13) gives a slightly younger date of 603 ± 7 Ma. This is a homogeneous, rounded, BSE-dark core, with a low U content (180 ppm) surrounded by a BSE-light rim (Figure 50). The other seven analyses on weakly oscillatory-zoned parts of crystals are tightly clustered (Figure 51A) and give a weighted average $^{206}Pb/^{238}U$ age of 637 ± 6 Ma (concordia age 636 ± 8 Ma), which we interpret to reflect the crystallization of the granitic magma. The one zircon with the ca. 600 Ma age may reflect metamorphic resetting.

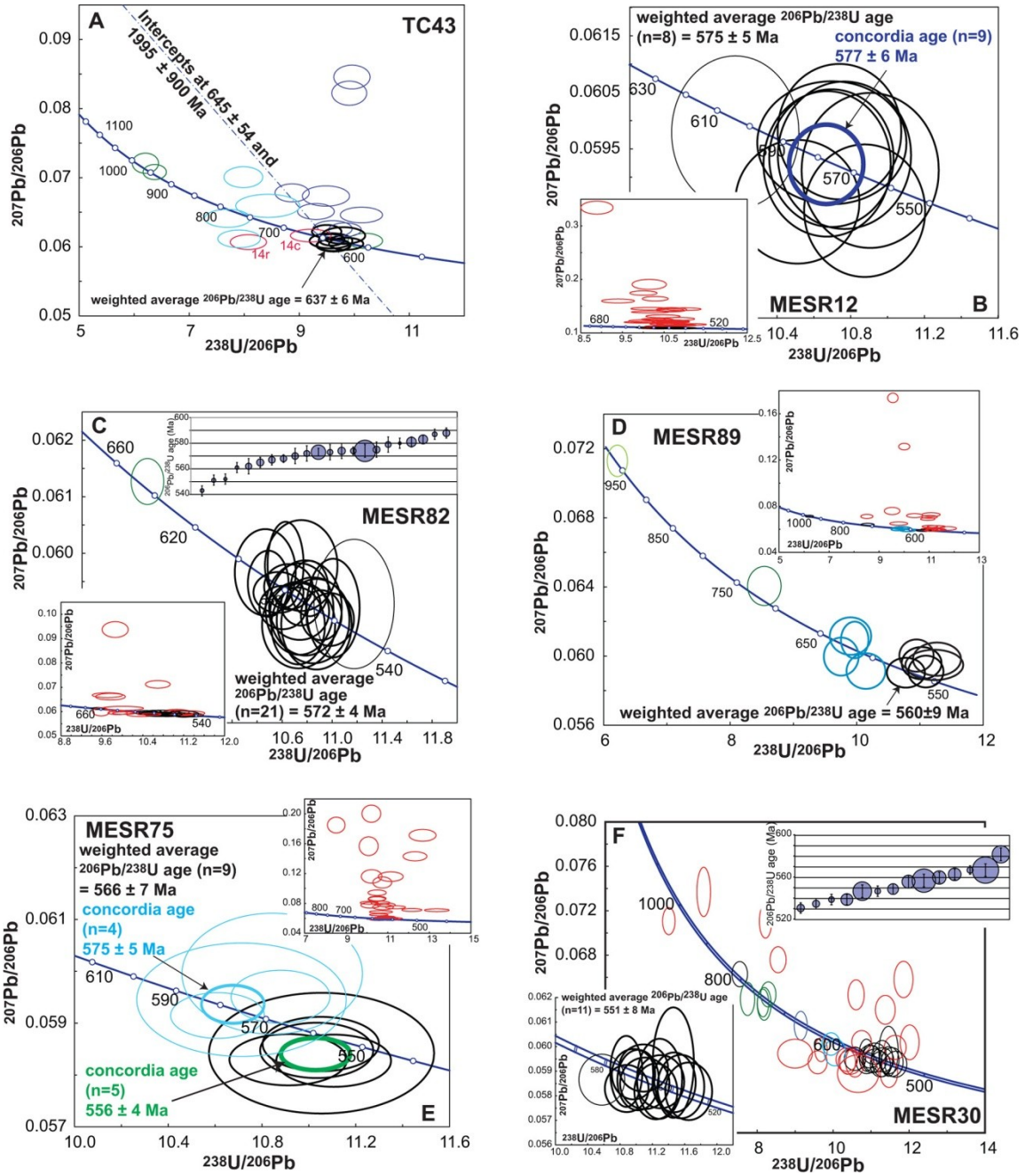

Figure 51: Tera-Wasserburg diagrams for all dated samples. All error ellipses are 2σ. Thick black circles are the analyses used for establishing the igneous age of the sample. *A*, Sample TC43 from Dufek. *B*, Sample MESR12 from northern D sector of the SW terrane. Inset includes discordant data points (in red), not used for igneous age calculation. *C*, Sample MESR82 from the Lågkollane group. Insets show Tera-Wasserburg diagram for all data and the concordant $^{206}Pb/^{238}U$ ages in ascending order, with bubble size proportional to the $^{206}Pb/^{204}Pb$ ratio. *D*, Sample MESR89 from the Lunkeryggen syenite complex; red data points (inset) show discordant points, blue and green circles are interpreted as inherited components. *E*, MESR75 from the western part of the SW terrane, with two apparent age populations of zircons that show identical internal structures and Hf isotopic compositions. The youngest age group is provisionally taken as representing the igneous age of the sample. Inset shows discordant points in red. *F*, MESR30 of the northern side of the sheared Vengen/Vikinhøgda granite, with discordant points in red. Inset shows close-up of data for igneous zircon; blue and green colors represent inherited components. *G*, MESR121 from the boundary between the NE and the SW terranes. *H*, MESR80 from Bamseungen. *I*, MESR123 from Utsteinen (Princess Elisabeth Antarctica Station). *J*, MESR118 from Mefjell. *K*, MESR113 from Vesthaugen (NE terrane). *L*, MESR22 from the northern D sector of the SW terrane.

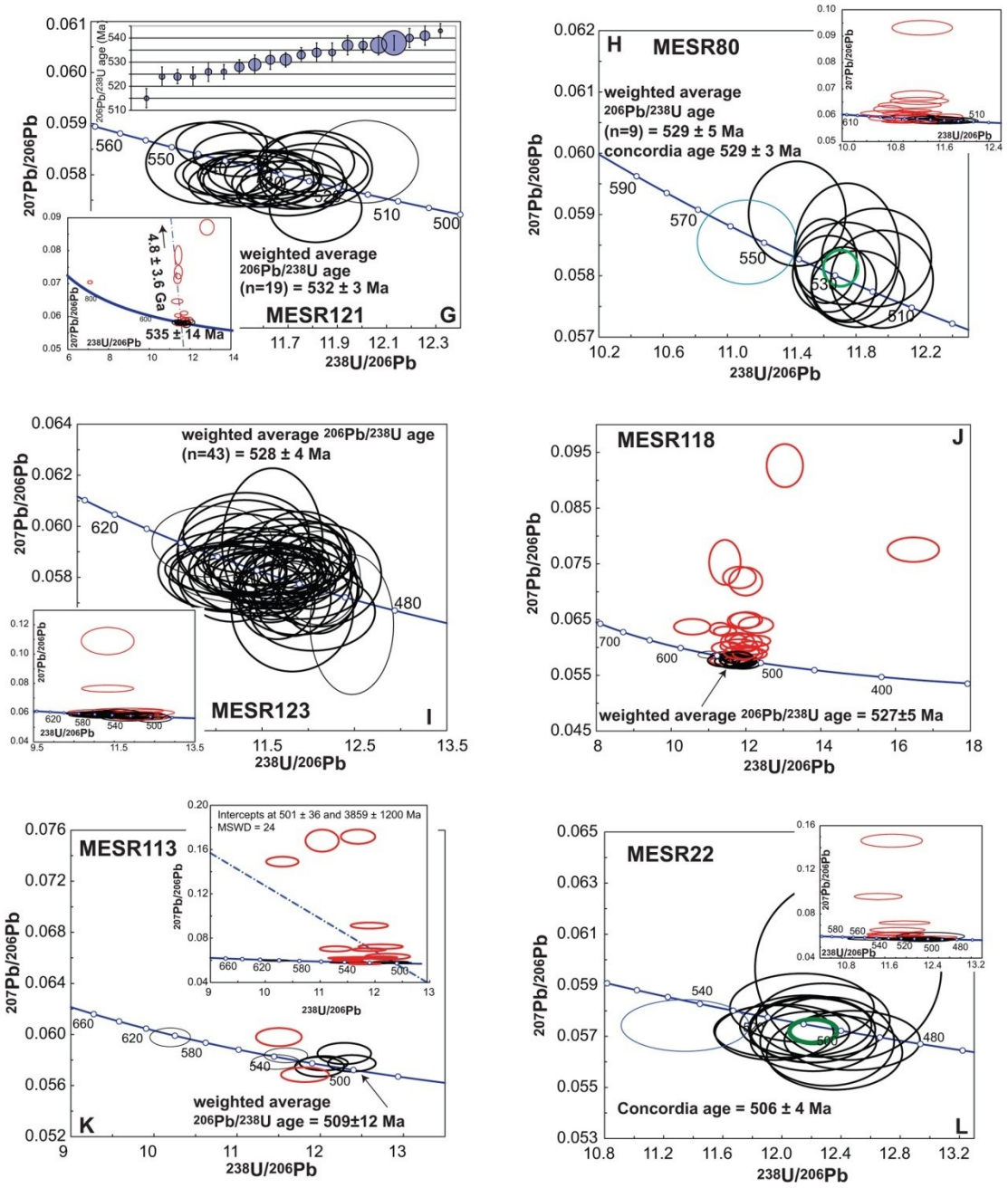

Figure 51 (continued)

The 10 Lu-Hf analyses on igneous grains with an ca. 640 Ma age give an εHf_{637} value of +4.3 ± 1.7, or $^{176}Hf/^{177}Hf_{637}$ = 0.282500 ± 0.000049 (Table 9; Figure 51 and Figure 52). The one grain that gave a younger age around 600 Ma also has a slightly lower εHf_i at 2.5 ± 0.9. The two inherited grains with ca. 950 Ma ages have initial values between +3 and +5, while the 750 Ma analyses have an average around +6. $^{176}Yb/^{177}Hf$ ratios vary unsystematically between 0.04 and 0.18.

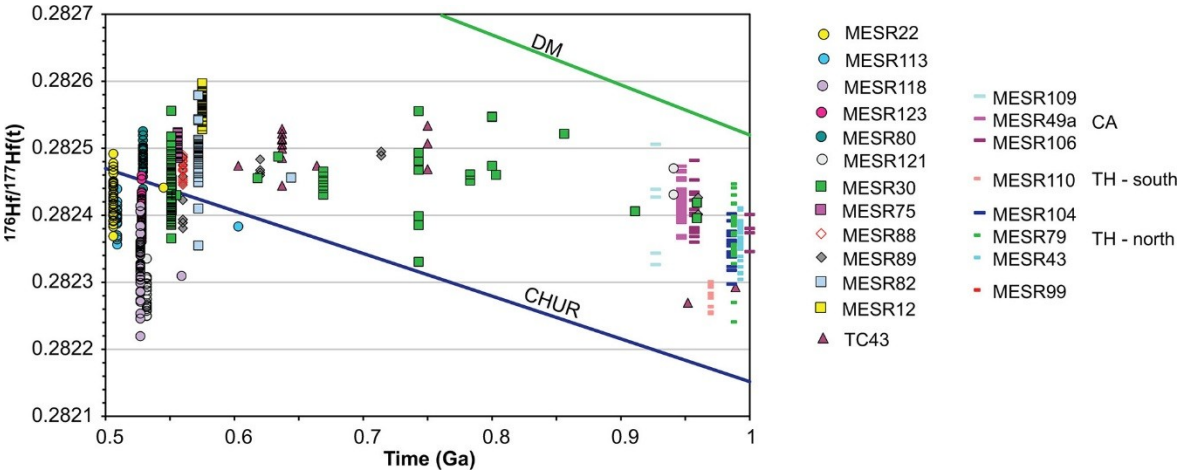

Figure 52: Initial $^{176}Hf/^{177}Hf$ isotopic ratio versus age for all samples analyzed in this study, plus those from Elburg *et al.* (2015b) for the 0.9–1.0 Ga meta-igneous rocks from the D′ sector of the SW terrane. Errors on individual data points not shown for clarity. The line of $^{176}Lu/^{177}Hf = 0.015$ gives the evolution curve for a typical crustal reservoir. $^{176}Lu/^{177}Hf = 0.00$ is the limiting case of a Lu-free reservoir, similar to the evolution curve for a zircon. CHUR, Chondritic Uniform Reservoir; DM, depleted mantle; TH, tholeiitic; CA, calc-alkaline.

MESR12 is a fine-grained leucocratic granite sheet (ca. 1.5 m wide) that crosscuts the foliation defined by the grey gneisses in the area (Figure 48A), which is the granulite-facies section of the SW terrane. The sample itself is also foliated, mainly defined by anastomosing bands of more fine-grained materials (predominantly quartz and feldspar). Somewhat coarser quartz seems to contain very thin needles, which may be rutile. Quartz crystals often display 120° triple junctions (Figure 49B). Microcline and plagioclase are the next most abundant minerals, with the latter often sericitized. Biotite is scarce, often altered to chlorite. Accessory minerals are opaques and zircon.

The sample contains mostly turbidly brown zircons up to 300 µm long, with typical aspect ratios of 3. Quite a few show spongiform areas, often surrounded by radial cracks (Figure 50). Zoning outside of those areas is typically oscillatory.

Thirty-nine spots were analyzed on 32 grains, with U contents varying between 300 and 3000 ppm. Most points were discordant as a result of high common Pb content, with $^{206}Pb/^{204}Pb$ ratios down to 60. Nine concordant analyses yielded a concordia age of 577 ± 6 Ma (MSWD = 1.6; Figure 51B), which is within the uncertainty of the weighted average $^{206}Pb/^{238}U$ age of 575 ± 5 Ma (MSWD = 0.75; one analysis rejected on statistical grounds). This is deemed to be the best estimate of the igneous age of this dyke.

The 27 Lu-Hf analyses define a tightly clustered population at an εHf_{575} value of +5.0 ± 1, or $^{176}Hf/^{177}Hf_{575} = 0.282563 \pm 0.000029$ (Figure 52). $^{176}Yb/^{177}Hf$ ratios are around 0.05.

MESR82 is a medium-grained granite from the western side of Sør Rondane (Lågkollane), located within the D sector of the SW terrane, if the sector boundaries—as defined by Osanai *et al.* (2013)—are extended westward. The cream-colored granitoid body crosscuts the main

layering of the outcrop and intrudes gneisses and calc-silicate rocks (Figure 48B). Deformation of the granite is evidenced by the dynamically recrystallized quartz and a weak foliation defined by the preferential alignment of biotite. K-feldspar is typically perthitic. Plagioclase is often slightly sericitized, but biotite in only rarely altered to chlorite. Titanite is a minor phase, and allanite is found sporadically, often overgrown by or associated with biotite. Apatite, opaque minerals, and zircon are relatively abundant accessory phases. Muscovite and calcite also occur but appear to be secondary phases.

Zircons are colorless and clear and typically 100–200 μm long, with aspect ratios up to 5. Elongated grains are often euhedral, while more stubby ones are generally sub- to anhedral. Zoning is typically faint and can be oscillatory or patchy. Forty spots were analyzed on 22 grains, with U contents varying between 80 and 1300 ppm but most within the 200–300 ppm range. Common Pb is a problem for a number of grains, but 23 analyses gave concordant dates. Of these, one core (22c) was clearly older at 644 ± 3 Ma, although BSE imaging did not reveal a striking difference between core and rim at the level of exposure. The remaining analyses give a spread in dates that is greater than can be explained by analytical uncertainty and therefore do not provide a concordia age. A weighted average $^{206}Pb/^{238}U$ age is 572 ± 4 Ma (with the youngest age rejected on statistical grounds) but with an MSWD of 5.4. When the individual $^{206}Pb/^{238}U$ dates are put in ascending order, a plateau is visible from 572–575 Ma (Figure 51C), which includes the analyses with the highest $^{206}Pb/^{204}Pb$ ratios (up to 110,000, indicated by the bubble size) and thus the least influence of common Pb. We therefore propose that the ca. 572 Ma weighted average $^{206}Pb/^{238}U$ age reflects the crystallization of the granitoid. Using the unmixing function of IsoPlot gives the same result, with a dominant age population at 575 ± 3 Ma and a subordinate one at 554 ± 4 Ma.

The one grain of ca. 644 Ma is similar to the other zircons in terms of Lu-Hf, with an εHf_{644} value of +2.7 ($^{176}Hf/^{177}Hf_{644}$ = 0.282456). Of the other 33 analyses, one BSE-bright undated core has an εHf_{572} value of −2.5 ($^{176}Hf/^{177}Hf_{572}$ = 0.282355). The remaining 32 analyses give an average εHf_{572} value of +2.4 ± 2.2, or $^{176}Hf/^{177}Hf_{572}$ = 0.282492 ± 0.000062. $^{176}Yb/^{177}Hf$ ratios are low, around 0.02.

MESR89 is a pink syenite from the complex at Lunkeryggen, within the amphibolite-greenschist-facies D sector of the SW terrane. The pink syenite crosscuts the more melanocratic rocks of the complex (Figure 48C) but is itself crosscut by pegmatites similar to sample MESR88 (below). The sample is rich in K-feldspar, typically with coarse patchy perthitic exsolution. Plagioclase and quartz occur in subordinate amounts; the former occasionally shows bent twins (Figure 49C), while the latter can show 120° triple junctions between individual crystals. Sericitization of the feldspars is very minor. The dominant ferro-

magnesian phase is amphibole, with greenish-blue to brown pleochroism. Greenish-brown biotite is a minor phase. Titanite and apatite are relatively abundant, and an opaque phase occurs as equant crystals. Zircon and allanite are accessory phases. Fluorite and calcite occur interstitially, while rare epidote is found as larger, anhedral crystals.

The sample contains a small number of zircons, varying from colorless to brownish-pink, of variable sizes and shapes. The largest ones are fragments of more than 400 μm in their longest dimension, whereas most crystals are no longer than 200 μm and have aspect ratios up to 4. The zoning visible in BSE images varies from oscillatory to patchy. Twenty-four analyses were performed on 16 crystals. Uranium content varied between 70 and 2000 ppm. About half of the crystals contained appreciable common Pb, with $^{206}Pb/^{204}Pb$ ratios between 100 and 44,000, resulting in a significant number of discordant analyses. The 12 (near-) concordant analyses yielded a spread of dates (Figure 51D). The core of grain 14 yielded a $^{206}Pb/^{238}U$ date of 961 ± 9 Ma, and oscillatorily zoned crystal 02a gave 714 ± 9 Ma, while four analyses on homogeneous-looking parts of three grains (6, 16, 20) gave a weighted average $^{206}Pb/^{238}U$ age of 617 ± 14 Ma. These ages are interpreted to reflect inheritance from igneous (961, 714 Ma) or metamorphic (617 Ma) protoliths. The remaining six analyses (on oscillatorily zoned or homogeneous crystals) yielded a weighted average $^{206}Pb/^{238}U$ age of 560 ± 9 Ma (MSWD = 1.9), and a concordia age of 564 ± 9 Ma (MSWD = 2.8).

Two analyses on the ca. 961 Ma grain yielded an εHf_{960} value of +8.4 ± 1.2, or $^{176}Hf/^{177}Hf_{961}$ = 0.282414 ± 0.000035, while the ca. 714 Ma grain yielded an εHf_{714} value of +5.6 ± 0.3 ($^{176}Hf/^{177}Hf_{714}$ = 0.282492 ± 0.000008). Four analyses of the ca. 617 Ma age group yielded εHf_{617} = +2.6 ± 0.7 ($^{176}Hf/^{177}Hf_{620}$ = 0.282469 ± 0.000021); $^{176}Yb/^{177}Hf$ ratios are around 0.03. The values for the 11 grains with igneous ages of ca. 560 Ma yielded an average εHf_{560} of +0.3 ± 2.8, or $^{176}Hf/^{177}Hf_{560}$ = 0.282441 ± 0.000078 (Figure 52), with $^{176}Yb/^{177}Hf$ ratios around 0.06. The spread in initial ratios is slightly high for a homogeneous population with these Yb/Hf ratios.

MESR88 is a leucocratic late pegmatite dyke from the Lunkeryggen syenite complex, of which the K-feldspar has an amazonitic color (Figure 48F). In thin section, it can be seen to have microcline twinning and only limited exsolution. Granophyric intergrowths occur around some of the larger microcline crystals. Plagioclase and quartz are the other common minerals. There is hardly any sericitization of the feldspars. Ferromagnesian minerals are green clinopyroxene and a yellow garnet (Figure 49D). Titanite and opaque minerals are additional subordinate phases. Fluorite occurs interstitially.

The sample contains zircons up to 700 μm long with a milky brown to gray color. BSE imaging showed bright patchy zoning with many U-rich inclusions (Figure 50). No dates could be

obtained from these zircons because of their extreme uranium contents and metamict nature. The age of the sample was assumed to be within error of the ca. 560 Ma age for MESR89.

Despite the uncertainty in age, the 15 zircons analyzed form quite a tight population in terms of their Hf isotopic composition, with an εHf_{560} of +1.3 ± 1.0, or $^{176}Hf/^{177}Hf_{560}$ = 0.282469 ± 0.000027, with $^{176}Yb/^{177}Hf$ ratios around 0.05. The good statistics on this sample reflect the high intensities of LA-MC-ICPMS signal for the Hf isotopes, which is a reflection of high Hf contents in pegmatitic zircons (Elburg *et al.*, 2013). The Hf isotope array overlaps with and lies toward the high side of that for MESR89 (Figure 52).

MESR75 is a sample of a bright red granite from the far western side of the study area, of which the macroscopically visible deformation appears to be limited to minor brittle features. No contacts with host rocks were observed. More mafic enclaves occur sporadically (Figure 48G) and are interpreted as evidence for mingling between mafic and felsic magmas (Elburg & Nicholls, 1995). The sample contains K-feldspar with coarse perthitic exsolution lamellae, plagioclase (with some sericitization), and quartz. The latter can show 120° triple junction with neighboring quartz crystals. Plagioclase twins are occasionally bent. Blue-green amphibole and green-brown biotite occur in subequal proportions; titanite, opaque minerals, and apatite are common. Minor fluorite occurs interstitially.

Zircons can be clear and colorless or murky yellowish brown. They are typically 200 µm long and have aspect ratios up to 4, but most are around 2. The majority of the crystals is cracked, and inclusions are common. Oscillatory zoning is observed in most crystals, and only few have developed patchy zoning. Thirty-five spots were ablated on 22 grains, which have U contents between 200 and 1500 ppm. Most grains contained appreciable common Pb and gave very discordant dates. Nine analyses were concordant. Together, they define a weighted average $^{206}Pb/^{238}U$ age of 566 ± 7 Ma but with an MSWD of 3.1. The dates are not equivalent, so a concordia age cannot be calculated. Visual inspection of the data points in the concordia diagrams suggest the existence of two clusters, with four points defining a concordia age of 575 ± 5 Ma (MSWD = 1.5) and five others an age of 556 ± 4 Ma (MSWD = 1.5). The areas analyzed look similar in BSE imaging in terms of zoning patterns and have similar $^{206}Pb/^{204}Pb$ ratios, but the older areas have higher U contents (600–900 vs. 200–500 ppm). On the basis of the presence of mafic enclaves, it seems possible that there are different intrusive phases present, and we tentatively take the age of the younger cluster as the most likely representative for the igneous age.

Despite the spread in dates, the 21 analyzed zircons define a very tight cluster in terms of Hf isotopic composition. The average εHf_{556} is +2.4 ± 1.0, or $^{176}Hf/^{177}Hf_{556}$ = 0.282502 ± 0.000027. The $^{176}Yb/^{177}Hf$ ratios are around 0.03.

MESR30 is a sample from the Vengen/Vikinghøgda granite, taken just north of the Main Shear Zone. The granite is located within the amphibolite-greenschist facies D sector of the SW terrane and is hosted by a series of metasedimentary rocks, including calc-silicates and chlorite-garnet schists. The granite sample has a tectonic foliation, mainly defined by bands of a finer grain size, consisting largely of white mica or deformed quartz (Figure 49E). Plagioclase (with some sericitization), quartz, and microcline, with flame perthite, are the main minerals. Larger quartz crystals display undulose extinction, while patches of finer-grained quartz typically show mutual 120° triple junction. The main ferromagnesian mineral is dark-brown biotite (sometimes with minor alteration to chlorite), but patches of finer-grained epidote, interpreted to be secondary, are also present.

The sample contains zircons of variable shapes and sizes, with the majority being euhedral, about 200 μm long, and with an aspect ratio of 2, but more rounded or equidimensional grains are found as well. Their colors vary from colorless and pinkish to yellowish brown. Zoning patterns can be oscillatory or patchy, but some grains do not display any zoning apart from core-rim structures. Some have BSE-bright high-U cores, with radial cracks in the mantling zones. Forty-four spots were analyzed on 32 grains, with widely varying U contents between 100 and 3000 ppm. Common Pb and discordance are a problem in some grains, but 21 spots yielded concordant dates. Inheritance is pronounced, with a number of different age groups. Two spots (19, 6) yielded discordant dates around 1 Ga, and the oscillatory zoning of those zircons suggests an igneous protolith. One core with oscillatory zoning (21c) gave a concordant date of 803 ± 8 Ma, another one (24c, with less distinct zoning) at 783 ± 7 Ma, and three analyses on two zircons (both with oscillatory zoning) yielded a combined weighted average $^{206}Pb/^{238}U$ age of 742 ± 7 Ma. One grain with wavy zoning is concordant at 669 ± 5 Ma, and two other analyses (17, 24r, both with oscillatory zoning) combine to give a date of 616 ± 9 Ma. Fourteen grains give dates between 531 and 582 Ma but do not constitute a single concordant population. A weighted average $^{206}Pb/^{238}U$ age is 551 ± 8 Ma (with the oldest date rejected on statistical grounds) but with a high MSWD of 6.1. The zircons with the clearest oscillatory zoning are those in the 556–557 Ma age bracket (e.g., grain 14), while the three youngest analyses (<540 Ma) have somewhat lower $^{206}Pb/^{204}Pb$ ratios; we therefore take this ca. 550 Ma age as the best estimate of igneous crystallization. Some of the younger dates could be a result of resetting during late shearing in the granite.

Because of the complicated age pattern, a large number of Lu-Hf analyses were done, with 22 analyses representing inherited grains and 44 for the igneous age group (Figure 52). If the initial $^{176}Hf/^{177}Hf$ ratios for the two groups are compared, the younger grains fall within the range observed for the older grains: the inherited grains range from 0.282331 to 0.282556,

while the ca. 550 Ma age group gives a range in $^{176}Hf/^{177}Hf_{551}$ of 0.282366–0.282517. The average for the igneous population is 0.282438 ± 81, or εHf_{551} 0.0 ± 2.9. The spread in the initial ratios for this group is not much greater than what can be expected from the analytical uncertainty, considering that the $^{176}Yb/^{177}Hf$ ratios are on the high side, with values in the 0.03–0.25 range (average = 0.1).

Sample MESR121 comes from a granite in the border area between the granulite-facies area of the SW terrane and the NE terrane, as defined by Osanai *et al.* (2013), where it intrudes more mafic host rocks. The sample consists of quartz (with undulose extinction), plagioclase (which can be zoned, with sericitization mainly confined to the cores of the crystals), microcline (with flame perthite), and myrmekitic intergrowths. Biotite is dark brown to straw yellow in color and shows minor alteration to chlorite; it often contains zircon inclusions. Titanite is often associated with equant opaque minerals, and apatite is a conspicuous accessory phase.

Colorless to light yellow zircons are 100–200 μm long and have aspect ratios varying from 2 to 5. More than half the grains are sub- to anhedral. Zoning, as observed in BSE imaging, varies from indistinct to oscillatory. Thirty-five points were analyzed on 22 grains, which typically yielded U concentrations of 300–600 ppm. One homogeneous, BSE-dark core (grain 5) gave a $^{207}Pb/^{206}Pb$ date of 941 ± 6 Ma, which constitutes the only obvious evidence for inheritance. A significant number of other grains also gave mildly to severely discordant dates, and the whole data set defines a discordia with a lower intercept at 535 ± 14 Ma, albeit with an MSWD of 67. A total of 20 points are concordant, but their spread is greater than can be explained by analytical error, frustrating attempts to obtain a concordant age. The weighted average $^{206}Pb/^{238}U$ age is 532 ± 3 Ma (with the youngest age rejected on statistical grounds; MSWD = 2.9). There is no obvious plateau within the spread of ages between 524 and 543 Ma, and the ca. 530 Ma age is therefore taken to represent the intrusive age of the granitoid.

The one zircon with the ca. 941 Ma age yielded two Hf isotope points around εHf_{941} +9 ($^{176}Hf/^{177}Hf_{941}$ = 0.28245). The remaining 23 analyses define a homogeneous population, with an average εHf_{532} of −5.9 ± 1.6, or $^{176}Hf/^{177}Hf_{532}$ = 0.282282 ± 0.000045. The $^{176}Yb/^{177}Hf$ ratios are around 0.03.

Sample MESR80 is a fine-grained red granite sample from Bamseungen in the D′ sector of the SW terrane, with ca. 1 Ga metatonalites (Elburg *et al.*, 2015b) as host rocks. Quartz displays a chessboard pattern (Figure 49F) and rarely contains very thin needles of presumably rutile. Both plagioclase (which can be zoned) and microcline have undergone some alteration, and secondary muscovite has formed. Biotite is dark brown to very light brown in color and

shows only minor alteration to chlorite. Allanite and fluorite are found as accessories. Calcite is a rare secondary phase.

The sample contains colorless to yellow-brown zircons with largish sizes (up to 400 μm length), aspect ratios around 2, and zoning patterns that are typically oscillatory, sometimes partly replaced by patchy areas. Twenty-two spots were ablated on 17 grains. Uranium concentrations vary between 100 and 5000 ppm, but the latter zircons typically give discordant analyses. Ten analyses were concordant, of which one, with U contents close to 5000 ppm, gave a slightly older age of 578 ± 5 Ma, which we interpret to reflect an analytical artifact, resulting from nonlinearity of the ion counters at high intensities. The other nine points yielded a concordia age of 529 ± 3 Ma (MSWD concordia and equivalence = 1.6), which is in excellent agreement with the weighted average $^{206}Pb/^{238}U$ age of 533 ± 4 Ma (MSWD = 1.8). This ca. 530 Ma age is taken to date the crystallization of the granite.

The zircon population (n = 30) is very homogeneous in its Hf isotopic composition, with an average εHf_{529} of +1.3 ± 1.4 ($^{176}Hf/^{177}Hf_{532}$ = 0.282486 ± 0.000039) and a relatively high $^{176}Yb/^{177}Hf$ ratio of ca. 0.11.

MESR123 comes from the pink Utsteinen granite at the Belgian Princess Elisabeth Antarctica Station within the D sector of the SW terrane. The granite intrudes gneissic host rocks with sharp contacts (Figure 48E). Quartz displays undulose extinction and contains putative rutile needles (Figure 49G), while microcline has coarse to lamellar perthitic exsolution. Plagioclase is somewhat sericitized, and microcline to a lesser extent. Biotite is more abundant than amphibole and shows very dark brown to light brown pleochroism. Amphibole is very dark green to olive green. Apatite, titanite, fluorite, and metamict allanite are accessory minerals. Minor calcite is also present. Zircon crystals can already be seen to contain cores in thin section.

The zircons obtained are typically 200 μm long and vary from equidimensional to elongated, with aspect ratios up to 4. However, most grains are fragmented and/or riddled with cracks. Rims are typically colorless and cores brown and cloudy. Many grains have very high uranium contents (up to 3000 ppm), and different settings were used between sessions to analyze both low- and high-U spots. High uranium contents are often found in euhedral cores, which give a characteristic BSE-bright response (Figure 50). Oscillatory zoning is commonly seen in the BSE-dark rims. Because of the range in U contents, a large number of spots (54) were analyzed on 43 grains. Rims have U contents from <100 to ca. 600 ppm, while BSE-bright cores vary between 1500 and 9000 ppm. Despite the variable U contents, there is no evidence that different age groups are present. Forty-five analyses are concordant, and with the rejection of one high and one low outlier, the weighted average $^{206}Pb/^{238}U$ age came out at 528 ± 4 Ma

(MSWD = 1.5), which agrees with the concordia age of 529 ± 3 Ma. This is interpreted to be the age of igneous crystallization.

Of the 51 analyses performed for Lu-Hf, four had to be discarded because of $^{176}Yb/^{177}Hf$ ratios >0.35. The remaining 47 analyses form a well-defined homogeneous population, without a distinction in isotopic ratios between cores and rims. The εHf_{528} is −1.8 ± 1.6 ($^{176}Hf/^{177}Hf_{528}$ = 0.282399 ± 0.000045). Cores and rims differ in their $^{176}Yb/^{177}Hf$ ratio, with an average of 0.04 for the rims and 0.2 for the cores.

MESR118 comes from Mefjell, located just within the granulite-facies C sector of the SW terrane. The granite is light colored and fine grained, and it crosscuts a more mesocratic intrusive with a sharp contact. The sample is very fresh and is dominated by quartz, plagioclase, and perthitic K-feldspar, which all contain exceedingly thin needles, similar to those seen in the quartz crystals in several other samples. Quartz shows undulose extinction, and myrmekite is abundant. Biotite is very dark brown to light brown in color and is often associated with opaque minerals. Accessories are zircon, apatite, and metamict allanite.

The sample contains colorless to yellow or brown zircons that vary from equidimensional to elongated, with aspect ratios up to 5. Lengths can be up to 500 μm but are more typically in the 200–300 μm range. About one-third of the zircons have large euhedral cores that are riddled with BSE-bright inclusions, show patchy zoning, and have very high U contents, which made it impossible to obtain dates from these cores with the setup used. Oscillatorily zoned rims around these cores often display radial cracks. Another third of the zircons mounted have patchy or indistinct zoning, and the remainder displays oscillatory zoning. A total of 32 points were measured on 32 grains, but many analyses displayed high common Pb contents, with $^{206}Pb/^{204}Pb$ ratios varying between 500 and 48,000. Measured U contents range between 75 and 1300 ppm. Thirteen analyses are concordant and have $^{206}Pb/^{204}Pb$ ratios >6000. One of these analyses (29) has a slightly older $^{206}Pb/^{238}U$ date of 559 ± 6 Ma, and the other 12 analyses yield a weighted average of 527 ± 5 Ma, which we interpret to be the igneous age of the sample.

The 41 analyses done on the ca. 527 Ma zircons show a spread in Hf isotope ratios that is slightly larger than what can be expected from analytical error, considering that the $^{176}Yb/^{177}Hf$ ratios are around 0.08. The average εHf_{527} is −4.4 ± 2.9, or $^{176}Hf/^{177}Hf_{527}$ = 0.282327 ± 0.000082. The one zircon with the apparently slightly older age of 559 Ma does not differ from the main group, with $^{176}Hf/^{177}Hf_{559}$ = 0.282310 ± 0.000070.

MESR113 comes from a granite from Vesthaugen in the B sector of the NE terrane, well north of the Main Tectonic Boundary. It crosscuts a diorite with a sharp but scalloped contact and is

rather inhomogeneous in appearance, with coarser- and finer-grained patches (Figure 48D). The sample appears undeformed but has undergone extensive alteration, with chloritization of the biotite, growth of secondary muscovite at the expense of feldspars, and interstitial calcite. Quartz contains thin needle-like inclusions. Accessory phases are opaque minerals, titanite, apatite, and zircon.

The zircons are colorless to light pink, with aspect ratios up to 4 and a typical length of 200 µm. Many crystals are cracked. Most crystals show clearly visible zoning in BSE images, which can be either oscillatory or more patchy. Nineteen spots were analyzed on 18 crystals. Uranium contents vary between 100 and 1000 ppm, and most crystals contain significant common Pb, resulting in widely varying $^{206}Pb/^{204}Pb$ ratios of 100–35,000. When all data are plotted on a Tera-Wasserburg diagram, they yield an age of 501 ± 36 Ma, but the MWSD of 24 indicates that this is not a meaningful age. The seven (almost) concordant analyses from zircons with oscillatory zoning and high $^{206}Pb/^{204}Pb$ ratios give scattered dates. One (19) is clearly older, with a $^{206}Pb/^{238}U$ date of 603 ± 6 Ma. Two high-U (ca. 1000 ppm) analyses yield $^{206}Pb/^{238}U$ dates of 534 and 539 Ma, and the other four spots range between 501 and 516 Ma. The latter four give a weighted average $^{206}Pb/^{238}U$ age of 509 ± 12 Ma (95% confidence level), with an MSWD of 2.2. Since the ca. 539 Ma age was measured on a rim (grain 8), of which the core gave a concordant age of ca. 501 Ma, we think that the two high-U analyses with slightly older dates are an artifact related to nonlinearity of the ion counters at high count rates. We therefore take the ca. 510 Ma age as the best estimate for the crystallization age of the granite.

The 18 analyses performed for Hf isotopes yielded a homogeneous population, with an average εHf_{509} of −2.5 ± 1.6 ($^{176}Hf/^{177}Hf_{509}$ = 0.282393 ± 0.000043) and an unremarkable $^{176}Yb/^{177}Hf$ ratio of 0.06. The one older grain has a very similar initial Hf isotopic ratio, with $^{176}Hf/^{177}Hf_{603}$ = 0.282383 ± 0.000070.

MESR22 is derived from an ca. 5-m-thick white granite dyke with large K-feldspar crystals from Tanngarden, just within the granulite facies C sector of the SW terrane. It is macroscopically undeformed and intruded subparallel to the bedding of the metamorphic country rocks (calc-silicates and gneisses). Quartz displays equant subgrains and irregular grain boundaries. K-feldspar is largely microcline and shows coarse perthitic exsolution lamellae. Plagioclase displays discontinuous normal zoning (Figure 49H); some crystals appear to be fractured. Slight sericitization is observed in the feldspars. Biotite has dark brown to light brown pleochroism and can be altered to chlorite. Secondary muscovite is present in many feldspar crystals. Fluorite, apatite, and zircon are accessory phases.

Zircons are numerous and large, with lengths up to 400 µm and aspect ratios varying between 2 and 4. Most crystals display well-defined oscillatory zoning in BSE, but some have

dark featureless cores, with low U contents of <200 ppm compared with the 400–2000 ppm of the other areas. These cores have a brownish color, contrasting with the colorless appearance of the rest of the zircons. Some crystals have started to develop patchy zoning that partly obliterates the oscillatory zoning. Twenty-two analyses were performed on 17 grains, and 13 are concordant. Of these, grain 26—with the highest U contents of ca. 2000 ppm—yields a slightly older date at 545 ± 8 Ma, which may reflect an analytical problem at these high U concentrations. The other 12 analyses define a concordia age of 506 ± 4 Ma, which is indistinguishable from the weighted average $^{206}Pb/^{238}U$ age of 507 ± 4 Ma and defines the age of igneous crystallization.

The 36 Lu-Hf analyses gave an average εHf_{506} of −1.3 ± 2.1 ($^{176}Hf/^{177}Hf_{507}$ = 0.282428 ± 0.000059) at a $^{176}Yb/^{177}Hf$ ratio of 0.09 (one analysis was discarded because of its high Yb/Hf ratio). The one grain that had given a slightly older age has an indistinguishable initial ratio of 0.282441 ± 0.000022.

8.5. Discussion

8.5.1. Comparison with Published Pan-African Zircon U-Pb Ages

Sør Rondane

Our data complement previous U-Pb ages from the Sør Rondane Mountains, which were mainly obtained in the framework of the Japanese Antarctic program. The oldest Pan-African intrusive we dated is Dufekfjellet (637 ± 6 Ma), for which a somewhat younger SHRIMP U-Pb zircon age of 619 ± 7 Ma was published by Li *et al.* (2006). Although apparently broadly similar in mineralogy, the sample analyzed by Li *et al.* (2006) came from the western side of the intrusion and contained garnet, while ours was from the north, and no garnet was observed. Another distinction is that our analyses show a prominent inherited component, which was not reported by the previous authors. It is therefore possible that the ≥5 Ma difference in age represents different phases within the intrusive, or it could represent an underestimate of the uncertainty on the age. The fact that our sample yielded one zircon with a younger age (603 ± 7 Ma) could indicate a prolonged magmatic history for the intrusion.

A U-Pb SHRIMP zircon age on the Vengen/Vikinghøgda granite, from which our sample MESR30 is derived, was given by Shiraishi *et al.* (2008) as 562 ± 7 Ma (sample 9091405A); their titanite age is similar at 568 ± 11 Ma. Both are within error of our age of 551 ± 8 Ma. Inherited, xenocrystic zircon was also described by the previous authors, with ages around 1100, 1000, and 600 Ma, of which the latter two compare well with the age fractions present in our sample.

Three SHRIMP U-Pb zircon ages were provided by Jacobs *et al.* (2015) for samples from three locations in the west from the same outcrops where MESR75, 80, and 82 were taken (Jacobs's samples of J1214B, J1216A, and J1216B, respectively). For MESR75, the younger age cluster compares very well (556 ± 4 vs. 557 ± 2 Ma), as is the case for MESR80 (529 ± 3 vs. 534 ± 4 Ma). However, sample MESR82 yields an igneous age of 572 ± 5 Ma, whereas J1216B yields 555 ± 4 Ma; moreover, the former yielded only a single inherited zircon, whereas the latter gave as many inherited as igneous ages. Because the outcrop consists of a significant number of different intrusive phases, the presence of distinct age components can be expected. The dominant age population in J1216B appears as a minor population in MESR82 (Figure 51C), pointing toward a prolonged thermal history for this area. Note that the choice of age has a minimal influence on the initial Hf isotopic composition of the zircons, which would change from +2.4 at 572 Ma to +1.9 at 555 Ma.

No other samples that are close equivalents to the ones analyzed in this study have been dated previously, but a significant body of igneous and metamorphic U-Pb zircon ages already exists on Pan-African metamorphism and magmatism in the Sør Rondane Mountains (Li *et al.*, 2006; Shiraishi *et al.*, 2008; Adachi *et al.*, 2013; Grantham *et al.*, 2013; Higashino *et al.*, 2013; Nakano *et al.*, 2013; Osanai *et al.*, 2013; Owada *et al.*, 2013; Jacobs *et al.*, 2015) as well as for older intrusive (Shiraishi *et al.*, 2008; Kamei *et al.*, 2013; Owada *et al.*, 2013; Elburg *et al.*, 2015b). Focusing on Pan-African ages (≤700 Ma), we compiled the existing U-Pb zircon data, which have been plotted in order of decreasing age (Figure 53). This representation has the advantage over a histogram that age peaks are not influenced by the choice of bin sizes or boundaries; it also permits showing the error on individual analyses. The diagram shows that metamorphism in the NE terrane was contemporaneous with magmatism (such as the Dufek granite) and metamorphism in the SW terrane between ca. 660 and 600 Ma, with perhaps a short hiatus in activity around 630 Ma. This period of zircon formation has been related to the EAAO, whereby the NE terrane was thrust over the SE terrane (Osanai *et al.*, 2013). The next magmatic-metamorphic period peaked between 580 and 550 Ma, which also involved rare magmatism in the NE terrane. This age group was not explicitly mentioned by Osanai *et al.* (2013), but Grantham *et al.* (2013) equate this with the thrusting event. Magmatism around 530 Ma is accompanied by minor (?retrograde) metamorphism in the NE terrane, and there is a tail of magmatism between 510 and 500 Ma. Although this last event is represented with few data points, three out of four are from the NE terrane, which is a noticeably higher proportion of igneous ages for the NE terrane than in any of the previous period, although it cannot be excluded that this just reflects the unreliable statistics of small numbers. Only one age, a metamorphic one, is younger than 500 Ma. Previous authors have viewed the ca. 530 and 500 Ma stages as representing magmatism and associated retrograde metamorphism

resulting from intracrustal melting after crustal thickening (Grantham *et al.*, 2008; Grantham *et al.*, 2013; Osanai *et al.*, 2013).

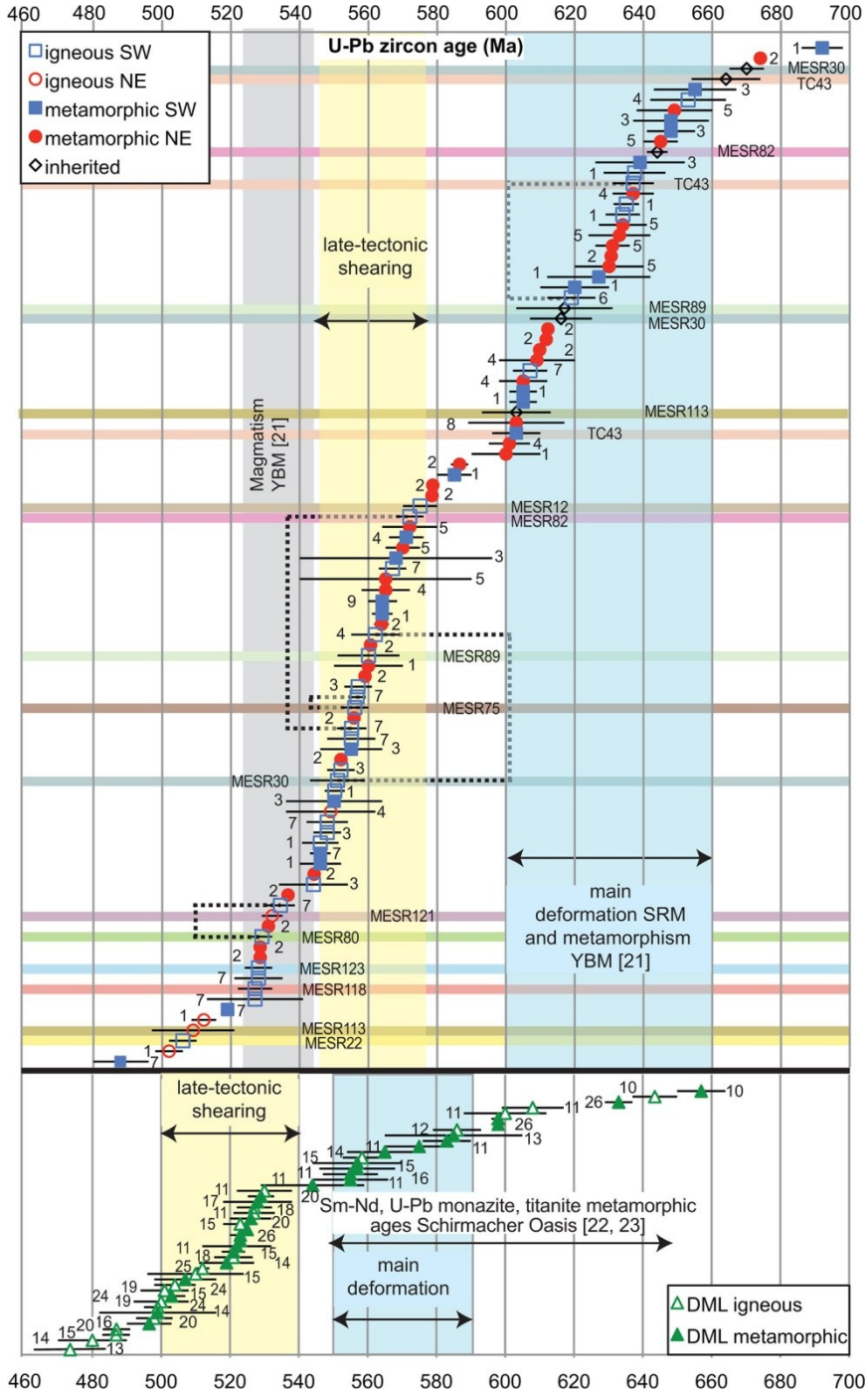

Figure 53: All available igneous and metamorphic U-Pb zircon ages for the NE and SW terrane of the Sør Rondane Mountains (*top*) and central and western Dronning Maud Land (*bottom*). Error bars are 2σ. Our own data are highlighted by colored bars; the inherited components are only from our own data. Dotted lines connect samples from the same outcrops or intrusive bodies. YBM, Yamato-Belgica Mountains. Source: 1, Adachi *et al.* (2013); 2, Grantham *et al.* (2013); 3, Nakano *et al.* (2013); 4, Shiraishi *et al.* (2008); 5, Osanai *et al.* (2013); 6, Li *et al.* (2006); 7 (Jacobs *et al.*, 2015); 8, Higashino *et al.* (2013); 9, Owada *et al.* (2013); 10, Baba *et al.* (2010); 11, Jacobs *et al.* (1998); 12, Bauer *et al.* (2003a); 13, Harris *et al.* (1995); 14, Board (2005); 15, Jacobs *et al.* (2003a); 16, Jacobs *et al.* (2003c); 17, Jacobs *et al.* (2003b); 18, Jacobs *et al.* (2003d); 19, Paulsson & Austrheim (2003); 20, Bisnath *et al.* (2006); 21, Shiraishi *et al.* (2003); 22, Ravikant *et al.* (2004); 23, (Ravikant *et al.*, 2007) R; 24, Jacobs *et al.* (2008); 25, Mikhalsky *et al.* (1997); 26, Baba *et al.* (2015).

Our samples cover all age groups, with TC43 (Dufek, SW terrane) representing the oldest (>600 Ma) age group; MESR12, 82, 89 (Lunkeryggen syenite), 75, and 30 (Vengen/Vikinhøgda), which all come from the SW terrane, fall within the 550–580 Ma group; the ca. 530 Ma group is represented by MESR121 (just within the NE terrane), 80, 123, and 118 (SW terrane); while the two youngest granites are MESR113 from Vesthaugen in the NE terrane and MESR22, which hails from the SW terrane. Inherited zircon is found within granites of all age groups but is limited to ages ≤1 Ga and will be discussed further in the section on Hf isotopes (see below).

Although the number of samples with a particular age may help to define the timing of metamorphic-igneous events, it is unlikely to give an accurate representation of the volumes of magma emplaced at any given time. This is most obvious for the Dufek granitoid, for which two ages are available but which appears to define the single largest intrusion in the area on the basis of the observed large positive magnetic anomaly (Figure 46; after Mieth *et al.*, 2014). However, interpreting the magnetic anomalies as representing a single magmatic body is unlikely to be correct, as can be seen from the fact that samples MESR12 and 123 are from the same interpreted granitoid body, whereas their ages differ by approximately 50 million years, which is consistent with the observed differences in mineralogy and fabric between the two samples.

Neighboring Areas

U-Pb zircon age data from the Yamato-Belgica Mountains bordering the Sør Rondane Mountains to the east are very scarce but point toward metamorphism around 660–600 Ma and magmatism in the ca. 530 Ma age bracket (Shiraishi *et al.*, 2003). This overlaps with two of the age groups seen in Sør Rondane. Whether the other two age groups are also present within the Yamato-Belgica Mountains needs to be clarified by further dating studies.

In central and western Dronning Maud Land, U-Pb zircon evidence for the oldest period of magmatism and metamorphism (680–630 Ma) is found only in the Schirmacher Oasis (Baba *et al.*, 2010), augmented by Sm-Nd isochrones and U-Pb data on titanite and monazite (Ravikant *et al.*, 2004; Ravikant *et al.*, 2007) and by U-Pb zircon ages from Hochlinfjellet (Baba *et al.*, 2015). For the rest of the area, magmatism and metamorphism appear to start between ca. 610 and 550 Ma, with, for instance, the Gruber Anorthosite at ca. 600 Ma (Jacobs *et al.*, 1998). The next pulse of activity was between 530 and 520 Ma, and then another was between ca. 510 and 480 Ma (Mikhalsky *et al.*, 1997; Jacobs *et al.*, 1998; Bauer *et al.*, 2003a; Jacobs *et al.*, 2003a; Jacobs *et al.*, 2003b; Jacobs *et al.*, 2003c; Jacobs *et al.*, 2003d; Paulsson & Austrheim, 2003; Board, 2005; Bisnath *et al.*, 2006; Jacobs *et al.*, 2008). A notable difference

with the Sør Rondane Mountains is the evidence for magmatism younger than 500 Ma, for which no U-Pb zircon ages have been found in the Sør Rondane Mountains.

The greater resemblance of the Sør Rondane Mountains with the Yamato-Belgica Mountains and Schirmacher Oasis than with the remainder of Dronning Maud Land was already noticed by Elburg *et al.* (2015b) regarding the older phase of magmatism (1–0.9 Ga in Sør Rondane vs. 1.2–1.05 in Dronning Maud Land); the apparent absence of the older Pan-African metamorphic period within central and western Dronning Maud Land has been noticed by other workers (Grantham *et al.*, 2008) and has been used for large-scale tectonic reconstructions of Gondwana amalgamation (Grantham *et al.*, 2008; Grantham *et al.*, 2013; Boger *et al.*, 2015; Jacobs *et al.*, 2015). It must be noted that the geochronological data for central and western Dronning Maud Land are scarcer than for the Sør Rondane Mountains, so this apparent later start of magmatism and metamorphism could be a sampling artifact, as the most recent ages published by Baba *et al.* (2015) illustrate. However, the slightly younger age of postcollisional magmatism in central and western Dronning Maud Land appears to be a true difference between the two areas.

8.5.2. Age of Deformation

Only few of the samples studied show macroscopic evidence for deformation. The oldest granitoid (Dufek, TC43, at ca. 640 Ma) is largely undeformed, which could be a result of the relatively large size of this intrusion, which thereby behaved as a rigid block during deformation. It is located within the D sector, which as a whole displays little evidence for deformation, leading to the suggestion of Jacobs *et al.* (2015) that the area behaved as a megaboudin during deformation associated with Gondwana amalgamation.

Sample MESR12, an ca. 575 Ma granitoid dyke crosscutting the main foliation, is foliated itself, so deformation was still ongoing at that time. In sample MESR82, which has the same age within error, evidence for deformation is limited to the presence of dynamically recrystallized quartz and a weak alignment of the micas. The next younger samples (such as the syenite complex sample MESR89 and far western granite MESR75) show very limited evidence for ductile deformation, with rare bent plagioclase twins, although some brittle features were observed, and the contact between the syenites and the host rocks is sheared (Ruppel *et al.*, 2015). Further evidence for the halting of regional deformation around this time comes from the U-Pb zircon age of undeformed and unmetamorphosed minette dykes (Owada *et al.*, 2013) from the SW terrane at 564 ± 2 Ma.

The dextral Main Shear Zone (Ruppel *et al.*, 2015) was clearly active until at least ca. 550 Ma, which is the age of sheared Vengen/Vikinghøgda sample MESR30. Thus, deformation on this

feature appears to have continued longer than the regional deformational event. Perhaps this shear zone also affected the granites at Bamseungen (MESR80), for which the chessboard quartz (Figure 49F) provides for high-temperature deformation (Kruhl, 1996). Because sample MESR123, representing the granite from Utsteinen, does not show any sign of dextral shear, its age of ca. 528 Ma may provide a lower limit for activities of the Main Shear Zone and related structures.

The age of deformation in central and western Dronning Maud Land has been inferred in a similar way by U-Pb zircon dating of intrusives affected and unaffected by deformation (Jacobs *et al.*, 2008 and references therein). The main deformational event in central and western Dronning Maud Land appears to have taken place between 590 and 550 Ma, with late-tectonic shearing in the period of 540–500 Ma and posttectonic intrusives appearing only at 500–480 Ma. Therefore, not only magmatism but also deformation seems to have occurred slightly later in central and western Dronning Maud Land than in the Sør Rondane Mountains (Figure 53).

8.5.3. Lu-Hf Data

The Inherited Components

Hf isotope results for zircons from the Sør Rondane Mountains are appreciably scarcer than U-Pb age data, with only Elburg *et al.* (2015b) providing data for the 0.9–1 Ga metagabbro/tonalite/trondhjemite/ granodiorite from the SW terrane, which are shown in Figure 52 and Figure 54 for comparison. The locations are given in Figure 47. The oldest inherited component in the Pan-African granitoids analyzed yielded ages around 950 Ma (similar to the dominant groups of metatonalites of the SW terrane (Kamei *et al.*, 2013; Owada *et al.*, 2013; Elburg *et al.*, 2015b) and were found in TC43 (Dufek), MESR89 (Lunkeryggen syenite), and MESR30 (Vengen/Vikinhøgda granite), all from the SW terrane. The ca. 950 Ma zircons within the latter two intrusions match the age and average isotopic signature (εHf_i ca. +7.5) of samples MESR106 and 49a, interpreted to belong to a postsubduction calc-alkaline magmatic episode (Elburg *et al.*, 2015b). The ca. 950 Ma inherited component within TC43 has an isotopic signature (εHf_i ca. +4) that is most closely matched by sample MESR110, which comes from the metatonalite outcrop furthest south. However, the Hf isotopic composition of the Pan-African igneous zircons in sample TC43 is too high to be formed by reworking of this tonalite body and resembles the characteristics of the northern tholeiitic bodies more closely (see below).

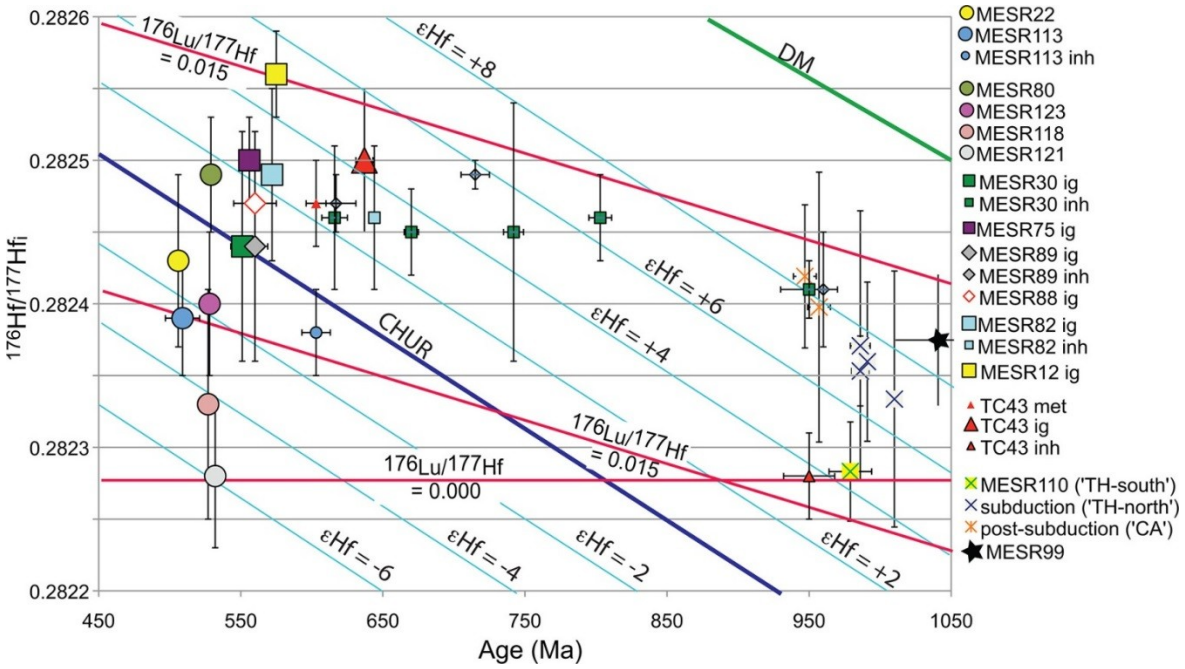

Figure 54: Initial $^{176}Hf/^{177}Hf$ zircon isotopic ratio versus age, averaged per age group. Error bars are 2 SD. The line of $^{176}Lu/^{177}Hf = 0.015$ gives the evolution curve for a typical crustal reservoir; $^{176}Lu/^{177}Hf = 0.00$ is the limiting case of a Lu-free reservoir, similar to the evolution curve for a zircon. CHUR, Chondritic Uniform Reservoir ($^{176}Lu/^{177}Hf = 0.0336$); DM, depleted mantle ($^{176}Lu/^{177}Hf = 0.0388$). The 900–1015 Ma samples are from Elburg *et al.* (2015b), with sample names as in Figure 52.

Inherited zircons in the 700–800 Ma age bracket (in MESR30 [Vengen/Vikinghøgda] and MESR89 [syenite]) could possibly be related to another phase of calc-alkaline magmatism dated at ca. 770 Ma (Kamei *et al.*, 2013). However, the ca. 750 Ma zircons from MESR30 show a large range in εHf_i values (+2 to +8), which may point toward a role for crustal reworking in addition to juvenile magmatic additions at 750 Ma. This period of magmatic activity in the Sør Rondane Mountains still needs further clarification. Zircons with similar ages are commonly the youngest igneous component in metasedimentary samples from the NE terrane. Within the SW terrane, only a single detritial age in this bracket (at 784 ± 2 Ma) has been reported (Adachi *et al.*, 2013) and was interpreted to represent igneous activity. The scarcity of these ages was interpreted to reflect a lack of igneous and metamorphic activity in the SW terrane between 650 and 950 Ma and/or an older depositional age for the SW terrane than the NE terrane (Osanai *et al.*, 2013). Our new data and the evidence for calc-alkaline magmatism in the SW terrane given by Kamei *et al.* (2013) make the distinction between the NE and the SW terrane less pronounced, although the absence of inherited ages older than 1200 Ma within the SW terrane, as noted by Osanai *et al.* (2013), still stands.

Inherited zircons with ages ≤700 Ma overlap in age with the oldest phase of magmatism and metamorphism (Figure 53). They often have an initial $^{176}Hf/^{177}Hf$ ratio that is within error of the igneous population (Figure 54).

The Igneous Populations

The igneous populations of zircons vary in average initial $^{176}Hf/^{177}Hf$ ratios between ca. 0.28225 and 0.28257, or εHf_i values of −6 to +5. Most of the range of Hf isotopic values could potentially just be explained by reworking of the 0.9–1 Ga population of zircons, within a reservoir with a $^{176}Lu/^{177}Hf$ ratio of 0.015 (Figure 54), which is commonly taken as the average ratio for continental crust (Griffin *et al.*, 2004). Only samples MESR118 and 121 have Hf isotopic compositions that are lower and which would necessitate reservoirs with lower $^{176}Lu/^{177}Hf$ ratios, whereby MESR121 can be modeled with only a ratio of 0; this would work only if the lowest Hf isotope population of the 0.9–1 Ga age group was reset in terms of U-Pb age but not in Hf isotopic composition. This seems an unlikely interpretation, also because the ca. 0.9–1 Ga metatonalites are restricted to the D′ sector of the SW terrane at a distance of more than 40 km from the location of MESR121. The depleted mantle extraction ages of the zircons—assuming aging in a crustal reservoir with a $^{176}Lu/^{177}Hf$ ratio of 0.015 before zircon formation—range from 1.15 Ga for MESR12 to 1.8 Ga for MESR121; assuming an upper crustal reservoir with a $^{176}Lu/^{177}Hf$ ratio of 0.010 changes these numbers to 1 and 1.45 Ga, respectively. This is slightly older than the Nd model ages for the SW terrane given by Shiraishi *et al.* (2008), which range between 0.9 and 1.25 Ma.

For the samples of which the isotopic signature could potentially be explained by reworking of the ca. 1 Ga metatonalitic crust (i.e., excluding MESR118 and 121), there is a broad trend of decreasing initial $^{176}Hf/^{177}Hf$ ratios from ca. 575 to 500 Ma. This seems somewhat coincidental if the zircon isotopic signature were a result of intracrustal reworking only, since there would not be an obvious reason why early stages of magmatism would have reworked preexisting crust with higher Hf isotopic compositions than later stages of magmatism. We therefore think that the isotopic signatures are better explained by a decreasing contribution of juvenile material with time. Another observation that argues against intracrustal reworking only is the existence of the Lunkeryggen Syenite Complex, which dominantly consists of quartz-poor syenites to melasyenites that are unlikely to have been formed by remelting of preexisting continental crust. They could possibly be related to the undeformed high-potassium, silica-undersaturated minette dykes that were also dated at ca. 560 Ma by both K-Ar and U-Pb zircon dating and that were interpreted to reflected melting of the lithospheric mantle, modified by the subduction and collision processes at 600–660 Ma (Owada *et al.*, 2013).

The older Dufek granite does not appear to conform to the trend of decreasing Hf isotopic compositions with time and could very well be explained by pure intracrustal reworking of the 0.9–1 Ga subduction-related metatonalites. This interpretation fits better with the tecton-

ic scenario proposed by Osanai *et al.* (2013), whereby the SW terrane is thrust underneath the NE terrane during peak metamorphism at 600–660 Ma than if the Dufek granite is interpreted to have formed in a subduction setting at this time. However, some question remains of how melting was initiated during the isothermal compressional event around this time that was deduced from the *PTt* path of the SW terrane (Osanai *et al.*, 2013).

When looking at the four ca. 530 Ma granitoids only (which include MESR118 and 121), there is a huge spread in zircon Hf isotope ratios. This could potentially be related to the spatial distribution of the intrusives, whereby the ratios decrease from west to east (Figure 55). Sample MESR121, with the lowest value, is located close to the boundary of the SW and NE terranes. This does not mean that there is a significant difference in isotopic ratios between the SW and NE terrane, since the one (younger) sample that is located unambiguously within the NE terrane (MESR113 from Vesthaugen) has an average initial $^{176}Hf/^{177}Hf$ ratio that is within error of that of the similarly aged sample MESR22 from the SW terrane and is higher than Mefjell sample MESR118 from the granulite (C) sector of the SW terrane (Figure 55).

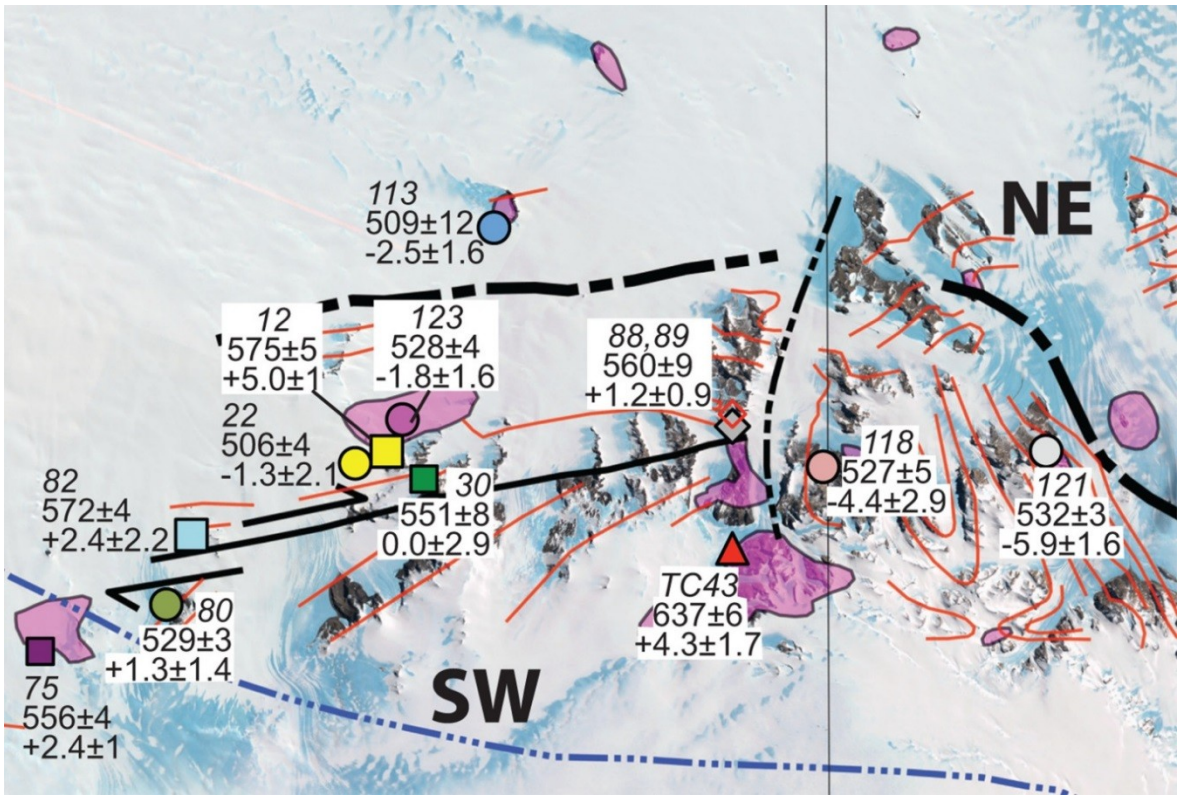

Figure 55: Overview of ages and εHf_i for the different granitoids analyzed.

The tectonic scenario envisaged by Osanai *et al.* (2013), with the NE terrane having been thrust over the SW terrane, implies that the SW terrane could potentially underlie the NE at greater depth, which could explain the similarity between sample MESR113 from Vesthaugen with granitoids of the SW terrane; it cannot, however, explain why the Hf model ages for samples MESR118 and 121 are older than for other granitoids from the SW terrane. These

older model ages point toward the involvement of older crust in their petrogenesis. This could mean that the SW terrane is not a single entity, with a mantle extraction age similar to that of the 0.9–1 Ga metatonalites, but that it is a collage of several domains, with contrasting geological histories. The area from which MESR118 and 121 are derived forms a distinct structural and aeromagnetic domain (Figure 47D), called the central Sør Rondane corridor by Mieth *et al.* (2014). The latter authors speculated that this area with complex tectonic structures might be an extensional corridor, but the distinction in isotopic signatures with the rest of the SW terrane could mean that it is a different crustal domain.

8.6. Recapitulation and Conclusions

Our new data and compilation of published U-Pb zircon ages show a prolonged history of magmatism and metamorphism in the Sør Rondane Mountains. The main metamorphic phase is at 660–600 Ma, recognized most clearly in the NE terrane, accompanied with minor magmatism, of which the Dufek granite is the most important example. This granite may have been formed by reworking of the 0.9–1 Ga metatonalites in the area, since its reported geochemical arc signature (Li *et al.*, 2003) is hard to reconcile with its position in the lower plate, according to the interpretation of the metamorphic terranes by Osanai *et al.* (2013). However, the timing of intracrustal melting in the supposed lower plate during isothermal decompression is also somewhat problematic. This period is also thought to be the main phase of deformation, although distributed inhomogeneously throughout the area. If this period of magmatism and metamorphism indeed represents the EAAO (Osanai *et al.*, 2013), it seems a bit surprising that evidence for magmatism and metamorphism around this time is scarce in central Dronning Maud Land.

The next magmatic and metamorphic period was from 575 to 550 Ma and may represent the final stages of ductile deformation, mainly focused on the Main Shear Zone, as evidenced by a sheared sample of the Vengen/Vikinghøgda granite at ca. 550 Ma. From 575 Ma onward, the zircon Hf isotopic compositions show a decreasing trend, in both absolute and ε units, from an εHf_{575Ma} of +5. The Lunkeryggen syenite complex also falls within this magmatic period and could potentially be genetically linked to the minette dykes of the same ca. 560 Ma age (Owada *et al.*, 2013). The variable Hf isotopic signature, the association of mafic and felsic magmas, and the presence of a syenite complex of which the rocks cannot be generated by crustal remelting suggest the involvement of mantle melts during this magmatic period.

The four samples from the ca. 530 Ma magmatic episode show a strong decrease in zircon Hf isotope ratios from west to east (Figure 55). It is noteworthy that one of the two least radiogenic samples (MESR118 from Mefjell), which fall outside of the isotopic range that could be

explained by simple intracrustal reworking of the 0.9–1 Ga metatonalites, still lies within the SW terrane, as defined by Osanai *et al.* (2013), but on the eastern side of the N-S running lineament that offsets the boundary between the two terranes, within the aeromagnetically (Mieth *et al.*, 2014) defined central Sør Rondane corridor. This could potentially be a slightly older crustal domain than the rest of the SW terrane. Metamorphism and magmatism around this time has been associated with the collision between the Kalahari Craton (to which the Sør Rondane Mountains had already been accreted) and the Indo-Antarctic Craton in the east (Osanai *et al.*, 2013). The available data show that metamorphism in this age bracket is better represented in central Dronning Maud Land than in the Sør Rondane Mountains, so it is somewhat surprising if this event represented a collision with a more easterly block.

Two granitoids, among which is a sample from Vesthaugen in the NE terrane, yielded ages between 510 and 500 Ma and εHf_i around −2. Magmatism of this age and younger is again more prevalent in central Dronning Maud Land.

The observed temporal and spatial isotopic trends in the Sør Rondane Mountains suggest waning importance of juvenile magmatic input over time and a control by the crust into which the granitoids intruded. Although crustal contamination may have played a role, this cannot have been very important for, for example, the silica-poor Lunkeryggen syenite complex, since crustal contamination would rapidly increase the magmas' silica content. It is therefore likely that the lithospheric mantle has had an important influence on the magmas' isotopic composition. This suggests that a process like lithospheric delamination (Jacobs & Thomas, 2004) or postcollisional extension is a more likely cause for the observed magmatism than intracrustal melting related to crustal thickening (Grantham *et al.*, 2008). However, neither a single period of delamination nor crustal thickening can explain the ca. 150 Ma duration of magmatism.

The metamorphic, magmatic, and deformational history of the Sør Rondane Mountains appears to be shifted to an ca. 20–40 Ma older age bracket than what has been documented in central and western Dronning Maud Land (with the possible exception of Schirmacher Oasis). Although data from the Yamato-Belgica complex are scarce, they overlap in age with those for the Sør Rondane Mountains. This reinforces the idea put forward by previous studies (e.g. Riedel *et al.*, 2013; Elburg *et al.*, 2015b; Jacobs *et al.*, 2015) that an important tectonic boundary exists between the Sør Rondane Mountains and central and western Dronning Maud Land, which could be the Forster Magnetic Anomaly (Riedel *et al.*, 2013). This is, however, unlikely to be the one and only large-scale boundary between eastern and western Gondwana, but it more likely represents one of a number of boundaries where different slices of the supercontinent came together. The variation seen within the Sør Rondane Mountains

in terms of inherited zircons between the NE and SW terrane (Osanai *et al.*, 2013; this work) as well as the difference in Hf isotopic composition between different sectors of the SW terrane may favor a collage-style accretionary history. Evidence for this style of accretion also comes from central Dronning Maud Land, where different geographic areas show contrasting metamorphic ages (Baba *et al.*, 2015). Such a collage-style accretion may also be the cause of the extended duration of magmatism in the Sør Rondane Mountains. A modern analog may the Indonesian area, which consists of a collage of fragments with contrasting geological histories (Hall, 2002; van Leeuwen *et al.*, 2007) and where magmatism has been semicontinuous during this assembly (e.g. Elburg *et al.*, 2003).

8.7. Acknowledgments

The Geodynamic Evolution of East Antarctica II team would like to thank the helicopter pilots K. Wagner, F. Tauber, and J. Hergenröder of Sky Heli, Germany, for their flying skills and A. Hubert, G. Johnson-Amin, and the crew of the Belgian Princess Elisabeth Antarctica Station for their hospitality and support during the field season. The analytical work was funded by grant 90036 from the South African National Research Foundation to M. A. Elburg. C. Ramchurran and J. Reinhardt are thanked for their help with the analytical work at the University of KwaZulu-Natal, and we also thank S. L. Simonsen at Oslo University. J. Jacobs, N. Krohne, and M. A. Elburg are indebted to the Bundesanstalt für Geowissenschaften und Rohstoffe (BGR) for the invitation to participate at the Geodynamic Evolution of East Antarctica expeditions. J. Jacobs wishes to thank the Alfred-Wegener-Institute for Helmholtz Centre for Polar and Marine Research, and M. A. Elburg acknowledges the International Polar Foundation, the Belgian Federal Science Policy Office, and the Belgian Antarctic Research Expedition. The study was partly supported by the Deutsche Forschungsgemeinschaft (grants LA 1080/9 to A. Läufer, BGR, and LI 745/15 to F. Lisker, University of Bremen) in the framework of the priority program Antarctic Research with Comparative Investigations in Arctic Ice Areas. J. Jacobs's work was funded in part by Norges Forskningsråd–Norwegian Antarctic Research Expeditions. Helpful reviews by T. Adachi and A. Kamei are gratefully acknowledged.

9. Synthesis: The post Pan-African evolution of the Weddell Sea Sector

The combination of thermochronology with geomorphological information and either petrological/geochronological or structural data revealed a dynamic Phanerozoic evolution for the western as well as for the eastern part of the Weddell Sea sector (Krohne *et al.*, 2016; Krohne *et al.*, prepared for submission). In the Shackleton Range as well as in Sør Rondane, the low temperature history can be confined back to the Permo-Carboniferous boundary, as indicated by the exposure and the beginning burial of the paleosurface(s). The ubiquitous occurrence of the Permian paleosurface(s) together with also significantly younger AFT and AHe ages from western and central DML implies a similar geological history. Hence, this coincidence indicates the large and almost complete truncation of the East African Antarctic Orogen at least to the end of the Carboniferous. Timing, style, and mechanism of pre-Permian exhumation can be roughly estimated by muscovite and biotite $^{40}K–^{39}Ar$ and $^{40}Ar/^{39}Ar$ ages of basement and molasse deposits, and TFT data (Kleinschmidt *et al.*, 2002; Jacobs *et al.*, 2008; Emmel *et al.*, 2009). Biotite and muscovite $^{40}K–^{39}Ar$ and $^{40}Ar/^{39}Ar$ of 530–490 Ma tend to be consistent between all regions and indicate ongoing exhumation, but might have been locally perturbed by synchronous post-orogenic plutonism (Takigami & Funaki, 1991; Brommer, 1998; Henjes-Kunst, 2004; Daszinnies *et al.*, 2009; Jacobs, 2009). In western DML, muscovite and biotite $^{40}K–^{39}Ar$ ages from basement rocks range between ~500 Ma and 470 Ma (summarized by Jacobs, 2009), whereas sericite growth ages in the molasses vary between 470 Ma and 450 Ma (Kleinschmidt *et al.*, 2002). This indicates synchronous exhumation and deposition. Growth of sericite requires burial temperatures of at least 350°C, corresponding to ~10–12 km of overburden (e.g. McDougall & Harrison, 1999). Similar–structurally controlled– molasse deposits are retained in the Shackleton Range and East Africa (Kleinschmidt *et al.*, 2002; Jacobs & Thomas, 2004) also testifies exhumation elsewhere of the EAAO. As suggested by Jacobs & Thomas (2004) the late Pan-African transtensional regime would rather allow formation of isolated pull-apart basins as formation of one vast foreland basin. The approximate duration of deposition can be inferred as well. The youngest $^{40}K–^{39}Ar$ sericite age of 450 Ma provides the time of maximum overburden, and infers the cessation of deposition. Nevertheless, timing of required inversion of the molasse basin and its nearly complete vanishing is terminated to the Late Carboniferous when the formation or erosional modification of the paleosurface is indicated by glacial striae (Poscher, 1992). The inversion might be reflected by TFT data (Emmel *et al.*, 2009): Widespread TFT ages from narrow spaced basement blocks in central DML with the oldest age composed of more than one age population imply multiple cooling events. Multiple cooling events can be explained by burial heating in a ~10 km deep basin and would suggest a larger extend of Paleozoic basins. The youngest

titanite ages of 370–325 Ma probably reflect a cooling event. The cooling must have been related to erosion, as the Permian paleosurface indicates basement exposure at 300–280 Ma.

In summary, the Cambro-Ordovician to Early Permian phase can be seen as a stage of morphological homogenization and leveling. This stage was accompanied by abrasion of the ubiquitous paleosurface by Late-Carboniferous ice sheets (Visser, 1987).

Both, Krohne *et al.* (2016) describe the formation and existence of Permo-Triassic basins in Coats Land as well as in eastern DML and imply the coexistence of the basins. Furthermore, Permo-Triassic sedimentary basins are reported in western DML (Boger, 2011). In central DML, substantially younger AFT ages as the exposure age of the paleosurface require reheating of the basement (Emmel *et al.*, 2007; Emmel *et al.*, 2009). The striking analogy in terms of geomorphology and AFT data to the surrounding massifs argues strongly for burial heating as well. Furthermore, AFT ages of 366 Ma and 320–300 Ma reflect the pre-Permian history, in close distance to Jurassic and Cretaceous ages. The pre-Permian AFT ages infer incomplete resetting, and would suppose temperatures not exceeding ~80–100°C. This temperature refers to a minimum depth of ~2 km that is similar to western DML. The aerial distribution and the shallow depth of the DML basin would refer to an intracontinental sag basin, or a few equal sag basins.

Krohne *et al.* (prepared for submission) propose a relation of the basins in DML to Permo-Triassic rift-related basins along East Africa. This would imply the southern extent of Permo-Triassic intercontinental sags and furthermore would imply different co-existent basins in the research area. This is supported by equal pre-Jurassic structural trends between Antarctica (Grunehogna Craton) and East Africa (Grantham & Hunter, 1991).

Krohne *et al.* (2016) recognized a 4–10 km deep Permo-Triassic basin in Coats Land that formed probably part of the adjacent Permian back-arc basin and evolved to a foreland basin in the Triassic (Collinson *et al.*, 1994). Folded strata in the Ellsworth Mountains confine the western boundary of the foreland basin. To the south (Transantarctic Mountains), a foreland basin was also existent to that time (Collinson *et al.*, 1994). Likewise, both basins were assembled to one foreland basin that follows the trend of the Paleo-pacific subduction zone. The eastern extent to Coats Land is not confined yet. The most proximal site is the western DML basin. The Permian shallow marine sediments indicate a structurally lower placement as the alluvial Coats Land basin (e.g. Collinson *et al.*, 1994). Despite this lower placement, the total burial was lesser. A concluding assignment of a relation to the back-arc basin cannot be drawn, but a stratigraphic comparison between the Lower Permian sediments of the Theron Mountains and the western DML would probably provide further implications to this topic. The research area was covered by co-existent basins with different tectonic backgrounds.

Basin inversion with the almost complete erosion of basin-fill is reported at ~230–215 Ma in Sør Rondane and not earlier than 215 Ma in the Shackleton Range (Krohne *et al.*, 2016; Krohne *et al.*, prepared for submission). Jurassic dykes and only tiny remnants of compacted Permo-Triassic strata prove the equal situation in western DML (Bauer *et al.*, 1997; Bauer, 2009). Thus, most likely, the central DML suffered the same history. In contrast to the trend of the onset of erosion, magmatic imprint and subaerial emplacement was slightly earlier in the Shackleton Range (200–180 Ma) as for the vicinity of Sør Rondane with 178 Ma (Belyatskii *et al.*, 2006). The greater depth of the basin implies a more rapid erosion of Coats Land compared to DML. Likewise, the uplift in Coats Land was associated with slab retreat, extension and enhanced mantle upwelling (Brewer *et al.*, 1996; Martin, 2007).

Both, the onset of basin inversion and the onset of magmatic activity show only minor time differences with regard to the areal extend, and erosion postdates the magmatic activity by 20 Ma. The tight temporal coherency of both processes implies two events of regional dimension, whereas a direct relation of the processes is hard to specify.

Remarkably, the basement was buried in all regions subsequent to magmatism (Jacobs & Lisker, 1999; Krohne *et al.*, 2016; Krohne *et al.*, prepared for submission). Basins of up to 2–3.4 km depth were formed in Coats Land and western DML, whereas the basins in central and eastern DML were up to 1.5 km deep.

The amount of post-magmatic overburden appears to be related to the former depths of the Permian-Triassic basins (Figure 56). Either, the rates of sedimentary supply did not change, or the post-magmatic basins were bounded to the Permian-Triassic faults and the tectonic regime has not changed. Further evidence for sedimentation subsequent to magmatic activity, their processes, and their relation are present in the vicinity: In East Africa, the basins were only inverted prior to magmatic activity and formed a basin again shortly after the main phase of magmatic activity. This implies that the exhumation/ basin inversion was not caused by a horizontal force. The uplift was a short-term phenomenon that is contemporaneous to the main phase of magmatic activity. Hence, the basin inversion is likley related to vertical forces that is associated with magmatic activity. The style of rifting seems to fit well to the proposed rift model concept by Huismans *et al.* (2001), by the conversion of passive to active rifting and its influence to lithospheric upwelling.

Although, the Jurassic basins were most likely placed on continental to slight extended crust, the onshore structure resembles the offshore structural pattern and evidences their relation. The depth of the Jurassic basins was eventually controlled by the direction and velocity of extension, and the placement to the margin.

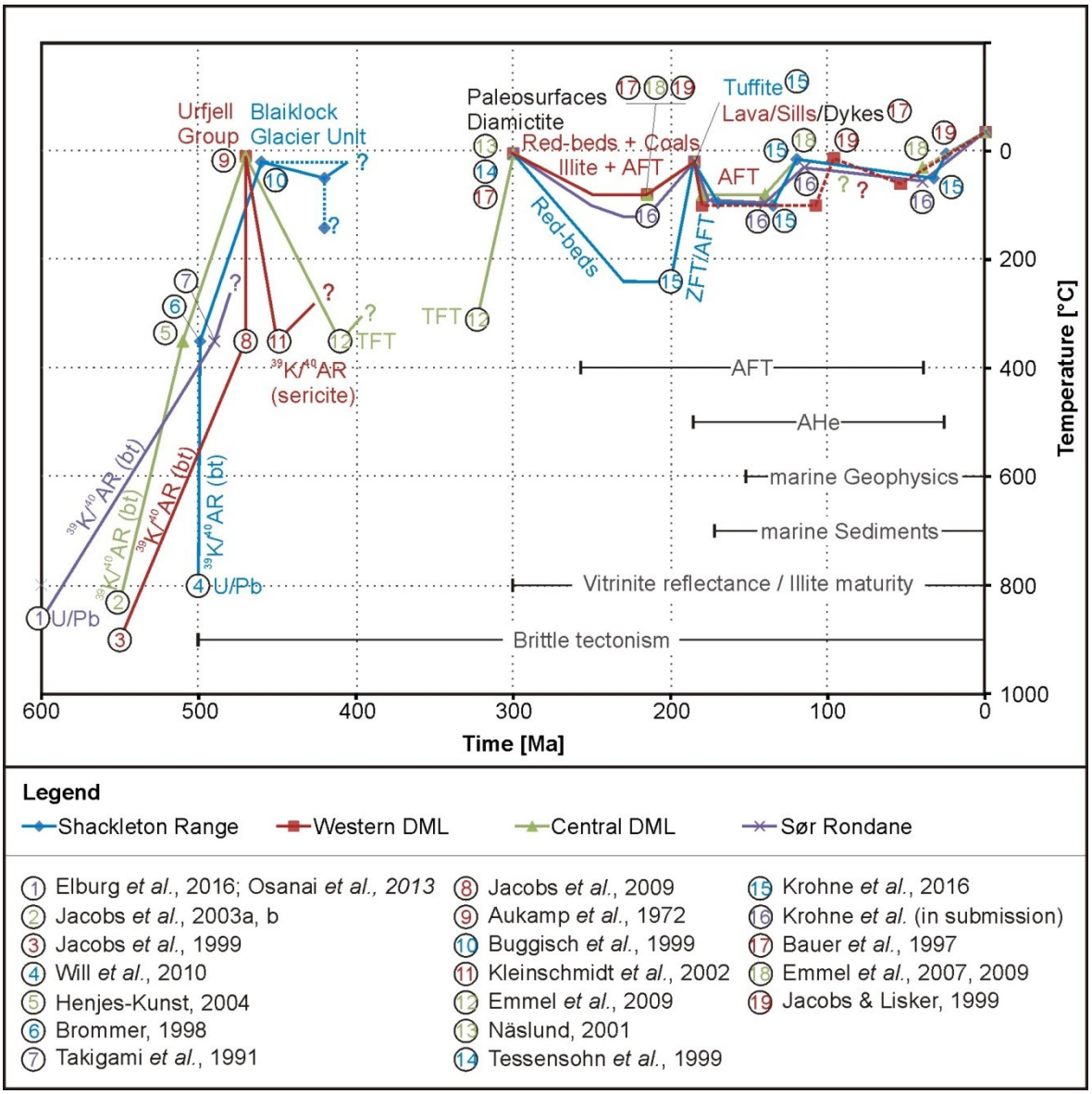

Figure 56: Compilation of all low-temperature data of the Weddell Sea Sector and the corresponding time temperature history.

Inversion of the basin(s), occurred roughly diachronously, beginning in Sør Rondane at 140 Ma and in the Shackleton Range at 135 Ma, and is estimated in central DML as well around 140 Ma and in western DML at 100 Ma (Jacobs & Lisker, 1999; Emmel *et al.*, 2009). This implies that inversion preceded 20 Ma after first sea-floor creation and seem to be linked to changes in rifting directions. The incompetent basin-fill was removed, whereas a more competent layer was slowly eroded or buried again by sediments. The basement in Coats Land and in eastern DML was buried slightly. By the Eocene, the overburden on the basement was still up to 1.6 km in the Shackleton Range and 0.8 km in Sør Rondane (Krohne *et al.*, 2016; Krohne *et al.*, prepared for submission). A burial of ~1.2 km can be inferred from the thermal history models by Jacobs & Lisker (1999) and Emmel *et al.* (2009).

The geological evolution of Coats Land and DML regarding the paleosurface exposition in the Permian, the deposition of red beds and coalification of swamp fauna, and the adjacent emplacement of subsurface lava flows disprove both–high elevation settings and marine settings at least until 140–135 Ma. After that, a probably more distinct evolution took place. In Coats Land the basin persisted until the Eocene, whereas the Cretaceous to Eocene evolution in the eastern DML was probably erosive. The basin evolution discussed here suggests a continental to mild transitional placement of the basins placed at least until the Cretaceous slightly above sea level. The recent high elevation and high relief topography hence require a substantial uplift and morphological modification since the Eocene.

The uplift and erosion of the Shackleton Range can be fully explained by isostatic response due to glacial incision along the pre-existing fault pattern (Paxman *et al.*, 2017). In central and western DML, the uplift seems to be a response of crustal anomalies, revealed by geophysical survey (Riedel, 2009; Mieth, 2014). Hence, the recent morphology with high elevations is a mainly Cenozoic feature.

10. Conclusions and Outlook

The combination of various thermochronometers with geomorphological information, and petrological, geochemical, geophysical methods, and with structural data allowed the elucidation of the long-term geological history (Figure 57). Even tiny and thin sedimentary remnants are able to constrain paleosurface exposure ages and geological history, if the contact to the paleosurface can be examined, and the deposition ages and milieu is constrained. In the case of completely bare surfaces, at least the sequence of events can be deduced by combination of mapping, geomorphological observation, and thermochronological information. Paleosurfaces can be utilized as a horizontal level. It allows the correlation of widely distributed samples, provides aerial correlation of two different blocks in depth as well as in horizontal space. The paleosurfaces permit detection of differential block faulting, basin depths or potential hinge zones. Furthermore, the paleosurfaces determine a paleomorphological setting and rate of incision, and can provide uplift estimations when overlain by sediments.

The approach here revealed a far more dynamic geological evolution than previously suggested. It shows that monotonous cooling concepts for the Weddell Sea Sector are incompatible. The continental margins were rather subject to dynamic changes and were placed in different paleoenvironmental and paleotectonic settings. The revised geological and landscape evolution history is more suitable to the regional tectonic environment, the offshore geological record and to the geological history of the surrounding Gondwana fragments.

The outcome has different implications on the geodynamic and tectonic setting: The recent landscape is not a result of simple downwearing of the Pan-African orogen. Instead, the area was covered by at least three basins placed in different geotectonic milieus since the Gondwana assembly. Cambrian to probably Carboniferous deep isolated molasse basins existed in the western and central DML as well as in the western Shackleton Range. These basins were inverted and nearly completely vanished by Permo-Carboniferous ice sheets. Since the Permian, the Weddell Sea Sector became part of widespread Permo-Triassic basins. The interior part of Gondwana was covered by sediments of up to 2.5 km in thickness, and may belong to the network of Permo-Triassic intracontinental basins that covered the future passive margins. The western part, however, was buried in a back-arc basin, that evolved in the Triassic to a deep forearc basin. A possible Permo-Triassic inversion event is not resolved by thermochronological data. The evidence from the regions shows that the Permo-Triassic basins where more widespread than preserved and supports the theory by Veevers & Tewari (1995) and Harrowfield *et al.* (2005) of extensive and radially distributed Permo-Triassic Gondwana basins and parallel compartments.

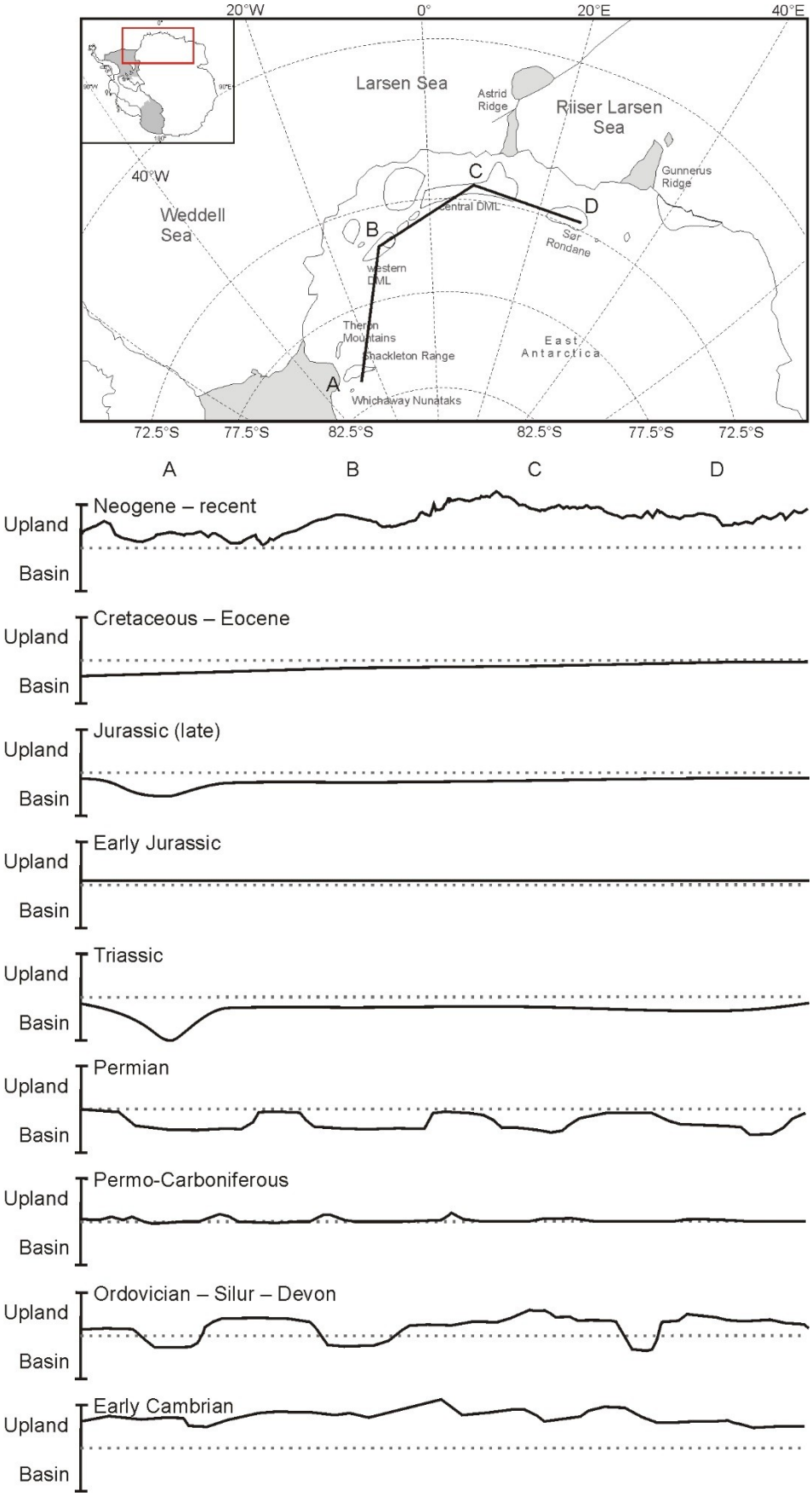

Figure 57: Schematic geographic cross section trough the different sites to various times, illustrating relative depths and highs through time. A general trend of increasing basin depth towards the west since the Mesozoic is obvious.

In the research area, the basins were almost synchronously inverted, resulting in the erosion of most of the basin-fill before magmatic emplacement. Uplift and basin inversion seem to be related to ongoing extension. In the Shackleton Range, the new evidence of a rhyolitic tuffite attested bimodal volcanism. The rhyolite reflects a volcanic-arc granite generated by partial melting of lower mafic crust that seems typical for the Panthalassan margin. It supports the subduction slab-roll back theory and W-E extension (Brewer *et al.*, 1996; Martin, 2007). Synchronously or not much later as Ferrar/Karoo volcanism, Jurassic basins formed presumably along re-activated Permian structures. The foreland basin in Coats Land evolved to the marginal part of the Weddell Sea basin that existed until the Eo-Oligocene. In DML, basins formed almost contemporaneously. Whereas the western DML basins were obviously dominated by orthogonal extension, the basins in central and eastern DML were influenced by a more oblique extensional regime. Burial of the basement was most likely controlled by basin formation and deposition of sediments, but the occurrence of thin sills within the sediments cannot be excluded. The Early Cretaceous inversion of the basins is probably linked to major changes in seafloor spreading direction and offshore magmatic emplacements, proceeding to tectonic decoupling of Africa and Antarctica. However, the basement was buried firmly until the Eo/Oligocene.

The recent high-elevated rocks are a comparatively young feature. Uplift is terminated to Cenozoic times, and since then, the morphological modification took place. This implies that the proposed passive margin evolution concerning escarpment formation and relief formation is not necessarily linked to continental break-up.

The flat erosion surfaces extend beyond the Weddell Sea Sector. The surfaces occur in the Pensacola Mountains in the west and cap parts of the Belgica Mountains in the east. The formation of radial basins in the Permian was probably not an isolated incident, as there were indications for Jurassic to Eocene burial in the Transantarctic Mountains, in Coats Land, in Dronning Maud Land and probably beyond.

The existence of an erosion surface must be recognized and brought into a sequence for correct time temperature interpretation in the region. The better the determination of the formation or exposition and the milieu is, the better is the resolution. Hence, a study with combination of various thermochronometers, petrological and geochronological data, sequence stratigraphy, structural field data, geophysical data, and geomorphological information should be interpreted and reviewed in a regional frame, including Mozambique, South Africa, Sri Lanka, and central DML.

The remaining open questions are illustrated in Figure 56 and could be resolved by application of further thermochronometer and petrographic/geochronological analysis. Titanite

fission track analysis on basement units as well as on rocks from the Blaiklock Glacier Group combined with of petrological work, with focus on secondary growth minerals, and the dating of fossils (Trilobites) would provide paleoenvironmental, structural, maximal basin depths, and probably the time of inversion. Hence, it would contribute to constrain the erosion processes and erosion times of the EAAO.

The application of Zircon (U–Th)/He analysis in Sør Rondane and in central DML would eventually provide insights to basin depths and geometry of the Permo-Triassic basins, since the zircon He thermochronometer covers a temperature range of 150–190°C (Reiners *et al.*, 2004; Reiners, 2005). Furthermore , the interpretation of the results will probably be able to resolve the question of a Early Triassic inversion event that is obvious in the surrounding Karoo basins (Catuneanu *et al.*, 2005). The basement rocks were rich on zircon, and a number of them were dated via U-Pb method. Hence, crystallization and metamorphic ages are known (Elburg *et al.*, 2015b; Jacobs *et al.*, 2015; Elburg *et al.*, 2016).

References

AADLAND, A. J. & PHOA, R. S. K. 1981. Geothermal gradient map of Indonesia: a publication of the Indonesian Petroleum Association (eds. Aadland, A. J. & Phoa, R. S. K.). Indonesian Petroleum Association, Jakarta, Indonesia.

ADACHI, T., OSANAI, Y., HOKADA, T., NAKANO, N., BABA, S. & TOYOSHIMA, T. 2013. Timing of metamorphism in the central Sør Rondane Mountains, eastern Dronning Maud Land, East Antarctica: constrains from SHRIMP zircon and EPMA monazite dating. *Precambrian Research* **234**, pp. 136-160.

ANDERSEN, T., ANDERSSON, U. B., GRAHAM, S., ABERG, G. & SIMONSEN, S. L. 2009. Granitic magmatism by melting of juvenile continental crust: new constraints on the source of Palaeoproterozoic granitoids in Fennoscandia from Hf isotopes in zircon. *Journal of the Geological Society* **2**, 166, pp. 233-247.

AOKI, T. 1989. Meteorological data at Asuka Station, Antarctica in 1988. In *JARE Data Reports*. National Institute of Polar Research. Tokyo, No. 150.

ASAMI, M., SUZUKI, K. & GREW, E. S. 2005. Monazite and zircon dating by the chemical Th-U-total Pb isochron method (CHIME) from Alasheyev Bight to the Sør Rondane Mountains, East Antarctica: a reconnaissance study of the Mozambique suture in eastern Queen Maud Land. *Journal of Geology* **113**, 1, pp. 59-82.

AUCAMP, A. P. H., WOLMERANS, G. & NEETHLING, D. C. 1972. The Urfjell Group, a deformed (?) early Paleozoic sedimentary sequence. Kirwanveggen, western Dronning Maud Land. In *Antarctic Geology and Geophysics* (ed. Adie, R. J.). Universitetsforlaget, Oslo, 1, pp. 557-562.

BABA, S., HOKADA, T., KAIDEN, H., DUNKLEY, D. J., OWADA, M. & SHIRAISHI, K. 2010. SHRIMP zircon U-Pb dating of sapphirine-bearing granulite and biotite-hornblende gneiss in the Schirmacher Hills, East Antarctica: implications for Neoproterozoic ultrahigh-temperature metamorphism predating the assembly of Gondwana. *The Journal of Geology* **118**, 6, pp. 621-639.

BABA, S., OSANAI, Y., NAKANO, N., OWADA, M., HOKADA, T., HORIE, K., ADACHI, T. & TOYOSHIMA, T. 2013. Counterclockwise P–T path and isobaric cooling of metapelites from Brattnipene, Sør Rondane Mountains, East Antarctica: implications for a tectonothermal event at the proto-Gondwana margin. *Precambrian Research* **234**, pp. 210-228.

BABA, S., HORIE, K., T., H., OWADA, M., ADACHI, T. & K., S. 2015. Multiple collisions in the East African-Antarctica Orogen: constraints from timing of metamorphism in the Filchnerfjella and Hochlinfjellet terranes in central Dronning Maud Land. *The Journal of Geology* **123**, 1, pp. 55-77.

BARKER, F. 1979. Trondhjemite: definition, environment and hypotheses of origin. In *Trondhjemites, Dacites, and Related Rocks.* (ed. Barker, F.). Elsevier Scientific Publishing, Amsterdam, pp. 1-12.

BARKER, P. F., KENNETT, J. P. & ET AL. 1990. Proceedings of the Ocean Drilling Program. Ocean Drilling Program, College Station, Texas, Scientifc Results, **113**.

BARRETT, P. J., GRINDLEY, G. W. & WEBB, P. N. 1972. The Beacon Supergroup of East Antarctica. In *Antarctic Geology and Geophysics* (ed. Adie, R. J.). Universitetsforlaget, Oslo, pp. 319-332.

BARRETT, P. J. 1992. The Devonian to Jurassic Beacon Supergroup of the Transantarctic Mountains and correlatives to other places of Antarctica. In *The Geology of Antarctica* (ed. Tingey, R. J.). Oxford Monographs on Geology and Geophysics, **17**, pp. 120-152.

BAU, M. & KNITTEL, U. 1993. Significance of slab-derived partial melts and aqueous fluids for the genesis of tholeiitic and calc-alkaline island-arc basalts – evidence from Mt Arayat, Philippines. *Chemical Geology* **105**, 4, pp. 233-251.

BAUER, W., HAGEMANN, H. W., POSCHER, G., SACHSENHOFER, R. F. & SPAETH, G. 1997. Permian coals from western Dronning Maud Land – composition, environment, and the influence of

Jurassic magmatism on their maturity. In *The Antarctic Region: Geological Evolution and Processes* (ed. Ricci, C. A.). Terra Antartica Publication, Siena, pp. 945-951.

BAUER, W. & JACOBS, J. 2001. The collision orogen of central Dronning Maud Land (Antarctica), a result of the assembly of East and West Gondwana. *Gondwana Research* **4**, 4, pp. 573-574.

BAUER, W., FIELITZ, W., JACOBS, J., FANNING, C. M. & SPAETH, G. 2003a. Mafic dykes from Heimefrontfjella and implications for the post-Grenvillian to pre-Pan-African geological evolution of western Dronning Maud Land, Antarctica. *Antarctic Science* **15**, 3, pp. 379-391.

BAUER, W., THOMAS, R. J. & JACOBS, J. 2003b. Proterozoic-Cambrian history of Dronning Maud Land in the context of Gondwana assembly. In *Proterozoic East Gondwana: Supercontinent Assembly and Breakup* (eds. Yoshida, M., Windley, B. F. & Dasgupta, S.). Geological Society London, London, Special Publications, **206**, pp. 247-269.

BAUER, W. & SIEMES, H. 2004. Kinematics and geothermometry of mylonitic shear zones in the Orvinfjella, central Dronning Maud Land, East Antarctica. In *International GeoMaud Expedition of the BGR to central Dronning Maud Land in 1995/96 - Geological Results* (ed. Paech, H.-J.). E. Schweizerbart´sche Verlagsbuchhandlung (Nägele u. Obermiller), Stuttgart, B96, **Polar Issue No. 10**, pp. 391-422.

BAUER, W. 2009. Permian sedimentary cover, Heimefrontfjella, western Dronning Maud Land (East Antarctica). *Polarforschung* **79**, 1, pp. 39-42.

BEHRENDT, J. C. & COOPER, A. 1991. Evidence of rapid Cenozoic uplift of the shoulder escarpment of the Cenozoic West Antarctic rift system and a speculation on possible climate forcing. *Geology* **19**, 4, pp. 315-319.

BELOUSOVA, E. A., GRIFFIN, W. L., O'REILLY, S. Y. & FISHER, N. I. 2002. Igneous zircon: trace element composition as an indicator of source rock type. *Contributions to Mineralogy and Petrology* **143**, 5, pp. 602-622.

BELYATSKII, B. V., SUSHCHEVSKAYA, N. M., LEICHENKOV, G. L., MIKHAL'SKII, E. M. & LAIBA, A. A. 2006. Magmatism of the Karoo–Maud Superplume in the Schirmacher Oasis, East Antarctica. *Doklady Earth Sciences* **406**, 1, pp. 128-131.

BISNATH, A., FRIMMEL, H. E., ARMSTRONG, R. A. & BOARD, W. S. 2006. Tectono-thermal evolution of the Maud Belt: new SHRIMP U-Pb zircon data from Gjelsvikfjella, Dronning Maud Land, East Antarctica. *Precambrian Research* **150**, 1–2, pp. 95-121.

BOARD, W. S. 2005. Pan-African tectonism in the western Maud Belt: P-T-t path for high-grade gneisses in the H.U. Sverdrupfjella, East Antarctica. *Journal of Petrology* **46**, 4, pp. 671-699.

BOGER, S. D., CARSON, C. J., WILSON, C. J. L. & FANNING, C. M. 2000. Neoproterozoic deformation in the Radok Lake region of the northern Prince Charles Mountains, East Antarctica; evidence for a single protracted orogenic event. *Precambrian Research* **104**, 1–2, pp. 1-24.

BOGER, S. D., WILSON, C. J. L. & FANNING, C. M. 2001. Early Paleozoic tectonism within the East Antarctic craton: the final suture between east and west Gondwana? *Geology* **29**, 5, pp. 463-466.

BOGER, S. D. & MILLER, J. M. 2004. Terminal suturing of Gondwana and the onset of the Ross-Delamerian Orogeny: the cause and effect of an Early Cambrian reconfiguration of plate motions. *Earth and Planetary Science Letters* **219**, pp. 35-48.

BOGER, S. D. 2011. Antarctica – before and after Gondwana. *Gondwana Research* **19**, 2, pp. 335-371.

BOGER, S. D., HIRDES, W., FERREIRA, C. A. M., SCHULTE, B., JENETT, T. & FANNING, C. M. 2014. From passive margin to volcano-sedimentary forearc: the Tonian to Cryogenian evolution of the Anosyen Domain of southeastern Madagascar. *Precambrian Research* **247**, pp. 159-186.

BOGER, S. D., HIRDES, W., FERREIRA, C. A. M., JENETT, T., DALLWIG, R. & FANNING, C. M. T. 2015. The 580-520 Ma Gondwana suture of Madagascar and its continuation into Antarctica and Africa. *Gondwana Research* **28**, 3, pp. 1048-1060.

BOUVIER, A., VERVOORT, J. D. & PATCHETT, P. J. 2008. The Lu-Hf and Sm-Nd isotopic composition of CHUR: constraints from unequilibrated chondrites and implications for the bulk composition of terrestrial planets. . *Earth and Planetary Science Letters* **273**, 1–2, pp. 48-57.

BREWER, T. S. 1989. Mesozoic dolerites from Whichaway Nunataks. *Antarctic Science* **1**, 2, pp. 151-155.

BREWER, T. S., REX, D., GUISE, P. G. & HAWKESWORTH, C. J. 1996. Geochronology of Mesozoic tholeiitic magmatism in Antarctica: implications for the development of the failed Weddell Sea rift system. In *Weddell Sea Tectonics and Gondwana Break-up* (eds. Storey, B., King, B. C. & Livermore, R. A.). Geological Society London, London, Special Publications, **108**, pp. 45-61.

BROMMER, A. 1998. Strukturelle Entwicklung und Petrogenese des nördlichen Kristallingürtels der Shackleton Range, Antarktis: Proterozoischen und Ross-orogene Krustendynamik am Rand des Ostantarktischen Kratons. *Berichte zur Polarforschung* **290**, p. 184 pp.

BROMMER, A. & HENJES-KUNST, F. 1999. Structural investigations and K-Ar geochronology of the northern Herbert Mountains and Mount Sheffield, Shackleton Range, Antarctica. *Terra Antartica* **6**, 3, pp. 279-291.

BROMMER, A., MILLAR, I. L. & ZEH, A. 1999. Geochronology, structural geology and petrology of the northwestern La Grange Nunataks, Shackleton Range, Antarctica. *Terra Antartica* **6**, 3, pp. 269-278.

BROOK, D. 1972. Stratigraphy of the Theron Mountains. *British Antarctic Survey Bulletin* **29**, pp. 67-89.

BUGGISCH, W., KLEINSCHMIDT, G., HÖHNDORF, A. & POHL, J. 1994a. Stratigraphy and facies of sediments and low-grade metasediments in the Shackleton Range, Antarctica. *Polarforschung* **63**, 1, pp. 9-32.

BUGGISCH, W., KLEINSCHMIDT, G., KREUZER, H. & KRUMM, S. 1994b. Metamorphic and structural evolution of the southern Shackleton Range during the Ross Orogeny. *Polarforschung* **63**, 1, pp. 33-56.

BUGGISCH, W., BACHTADSE, V. & HENJES-KUNST, F. 1999. Lithostratigraphy, facies, geochronology and palaeomagnetic data from the Blaiklock Glacier Group, Shackleton Range, Antarctica. *Terra Antartica* **6**, 3, pp. 229-239.

CALVET, M., GUNNELL, Y. & FARINES, B. 2015. Flat-topped mountain ranges: their global distribution and value for understanding the evolution of mountain topography. *Geomorphology* **241**, pp. 255-291.

CATUNEANU, O., HANCOX, P. J. & RUBIDGE, B. S. 1998. Reciprocal flexural behaviour and contrasting stratigraphies: a new basin development model for the Karoo retroarc foreland system, South Africa. *Basin Research* **10**, 4, pp. 417-439.

CATUNEANU, O., WOPFNER, H., ERIKSSON, P. G., CAIRNCROSS, B., RUBIDGE, B. S., SMITH, R. M. H. & HANCOX, P. J. 2005. The Karoo basins of south-central Africa. *Journal of African Earth Sciences* **43**, 1–3, pp. 211-253.

CHANDLER, M. A., RIND, D. & RUEDY, R. 1992. Pangaean climate during the Early Jurassic: GCM simulations and the sedimentary record of paleoclimate. *Geological Society of America Bulletin* **104**, 10, pp. 543-559.

CLARKSON, P. 1981. Geology of the Shackleton Range: IV. The dolerite dykes. *British Antarctic Survey Bulletin* **53**, pp. 201-212.

CLARKSON, P. & WYETH, R. 1983. Geology of the Shackleton Range: III. The Blaiklock Glacier Group. *British Antarctic Survey Bulletin* **52**, pp. 233-244.

COLLINSON, J. W., ISBELL, J. L., ELLIOT, D. H., MILLER, M. F., MILLER, J. M. G. & VEEVERS, J. J. 1994. Permian-Triassic Transantarctic Basin. In *Permian-Triassic Pangean Basins and Foldbelts along the Panthalassan Margin of Gondwanaland* (eds. Veevers, J. J. & Powell, C. M.). Geological Society of America (GSA), Boulder, CO, United States, 184, pp. 173-222.

COMPSTON, W., WILLIAMS, I. S. & MEYER, C. 1984. U-Pb geochronology of zircons from lunar breccia 73217 using a sensitive high mass-resolution ion microprobe. *Journal of Geophysical Research* **89**, S02, pp. B525-B534.

CORVINO, A. F., BOGER, S. D., HENJES-KUNST, F., WILSON, C. J. L. & FITZSIMONS, I. C. W. 2008. Superimposed tectonic events at 2450 Ma, 2100 Ma, 900 Ma and 500 Ma in the North Mawson Escarpment, Antarctic Prince Charles Mountains. *Precambrian Research* **167**, 3–4, pp. 281-302.

COX, K. G. 1992. Karoo igneous activity, and the early stages of the break-up of Gondwanaland. In *Magmatism and the Causes of Continental Break-up* (eds. Storey, B., Alabaster, T. & Pankhurst, R. J.). Geological Society London, London, Special Publications, **68**, pp. 137-148.

COYLE, D. A., WAGNER, G. A., HEJL, E., BROWN, R. & VAN DEN HAUTE, P. 1997. The Cretaceous and younger thermal history of the KTB site (Germany): apatite fission-track data from the Vorbohrung. *Geologische Rundschau* **86**, 1, pp. 203-209.

CRADDOCK, C. 1972. Antarctic tectonics. In *Antarctic Geology and Geophysics* (ed. Adie, R. J.). Universitetsforlaget, Oslo, 1, **Series B**, pp. 449-455.

CURTIS, M. L. 2001. Tectonic history of the Ellsworth Mountains, West Antarctica: reconciling a Gondwana enigma. *Geological Society of America Bulletin* **113**, 7, pp. 939-958.

DALZIEL, I. W. D., STOREY, B. C., GARRETT, S. W., GRUNOW, A. M., HERROD, L. D. B. & PANKHURST, R. J. 1987. Extensional tectonics and the fragmentation of Gondwanaland. In *Continental Extensional Tectonics* (eds. Coward, M. P., Dewey, J. F. & Hancock, P. L.). Geological Society London, London, Special Publications, **28**, pp. 433-441.

DASZINNIES, M. C., JACOBS, J., WARTHO, J.-A. & GRANTHAM, G. H. 2009. Post Pan-African thermotectonic evolution of the north Mozambican basement and its implication for the Gondwana rifting. Inferences from $^{40}Ar/^{39}Ar$ hornblende, biotite and titanite fission-track dating. In *Thermochronological Methods: From Palaeotemperature Constraints to Landscape Evolution Models* (eds. Lisker, F., Ventura, B. & Glasmacher, U. A.). Geological Society London, London, Special Publications, **234**, pp. 261-286.

DE CORTE, F., VAN DEN HAUTE, P., BELLEMANS, F., INGELBRECHT, C. & NICHOLL, C. 1998. The uranium doped glass IRMM-540 distributed by the European Comission: a new tool in fission-track age calibration. In *19th International Conference on Nuclear Tracks in Solids*, Besancon, France.

DE PAOLA, N., HOLDSWORTH, R. E., MCCAFFREY, K. J. W. & BARCHI, M. R. 2005. Partitioned transtension: an alternative to basin inversion models. *Journal of Structural Geology* **27**, 4, pp. 607-625.

DELVAUX, D. & SPERNER, B. 2003. New aspects of tectonic stress inversion with reference to the TENSOR program. In *New Insights into Structural Interpretation and Modelling* (ed. Nieuwland, D. A.). Geological Society London, London, Special Publications, **212**, pp. 75-100.

DIETZE, M., HAUBRICH, F., KLINGER, T. & ULLRICH, B. 2007. Smectites in the porphyrite from Wurgwitz near Dresden (Saxony, Germany). *Geologica Saxonica Journal of Central European Geology* **52/53**, pp. 97-115.

DONELICK, R. A. 1993. Apatite etching characteristics versus chemical composition. *Nuclear Tracks and Radiation Measurements* **21**, 4, p. 604.

DONELICK, R. A., O'SULLIVAN, P. B. & KETCHAM, R. A. 2005. Apatite fission-track analysis. *Reviews in Mineralogy and Geochemistry* **58**, 1, pp. 49-94.

DOUGHERTY-PAGE, J. S. & BARTLETT, J. M. 1999. New analytical procedures to increase the resolution of zircon geochronology by the evaporation technique. *Chemical Geology* **153**, 1–4, pp. 227–240.

DUMITRU, T. A. 1993. A new computer-automated microscope stage system for fission-track analysis. *Nuclear Tracks and Radiation Measurements* **21**, 4, pp. 575-580.

DUNCAN, R. A., HOOPER, P. R., REHACEK, J., MARSH, J. S. & DUNCAN, A. R. 1997. The timing and duration of the Karoo igneous event. *Journal of Geophysical Research* **102**, B8, pp. 18127-18138.

DUNKL, I. 2002. TRACKKEY: a Windows program for calculation and graphical presentation of fission track data. *Computers and Geosciences* **28**, 1, pp. 3-12.

EHLERS, T. A. & FARLEY, K. A. 2003. Apatite (U-Th)/He thermochronometry: methods and applications to problems in tectonic and surface processes. *Earth and Planetary Science Letters* **206**, 1–2, pp. 1-14.

ELBURG, M., ANDERSEN, T., JACOBS, J., LÄUFER, A., LE ROUX, P., RUPPEL, A., HARRIS, C., KROHNE, N. & DAMASKE, D. 2015a. Spatial and temporal influences on the geochemical signature of Pan-African magmatism in the Sør Rondane Mountains (East Antarctica). In *Proceedings of ISAES XII –12th International Symposium on Antarctic Earth Sciences*, Goa, India, 13th-17th July. pp. 39-40.

ELBURG, M., JACOBS, J., ANDERSEN, T., CLARK, C., LÄUFER, A., RUPPEL, A., KROHNE, N. & DAMASKE, D. 2015b. Early Neoproterozoic metagabbro-tonalite-trondhjemite of Sør Rondane (East Antarctica): implications for supercontinent assembly. *Precambrian Research* **259**, 3–4, pp. 189-206.

ELBURG, M., ANDERSEN, T., JACOBS, J., LÄUFER, A., RUPPEL, A., KROHNE, N. & DAMASKE, D. 2016. One hundred fifty million years of intrusive activity in the Sør Rondane Mountains (East Antarctica): implications for Gondwana assembly. *The Journal of Geology* **124**, 1, pp. 1-26.

ELBURG, M. A. & NICHOLLS, I. A. 1995. The origin of microgranitoid enclaves in the S-type Wilson's Promontory Batholith, Victoria: evidence for magma mingling. *Australian Journal of Earth Science* **42**, 3, pp. 423-435.

ELBURG, M. A., VAN LEEUWEN, T., FODEN & MUHARDJO, J. 2003. Spatial and temporal isotopic domains of contrasting igneous suites in western and northern Sulawesi, Indonesia. *Chemical Geology* **199**, pp. 243-276.

ELBURG, M. A., ANDERSEN, T., BONS, P. D., SIMONSEN, S. L. & WEISHEIT, A. 2013. New constraints on Phanerozoic magmatic and hydrothermal events in the Mt Painter Province, South Australia. *Gondwana Research* **24**, 2, pp. 700-712.

ELHLOU, S., BELOUSOVA, E., GRIFFIN, B., PEARSON, N. & O'REILLY, S. 2006. Trace element and isotopic composition of GJ-red zircon standard by laser ablation. *Geochimica et Cosmochimica Acta* **70**, 18, pp. A158-A158.

ELLIOT, D. H. 1992. Jurassic magmatism and tectonism associated with Gondwanaland break-up: an Antarctic perspective. In *Magmatism and the Causes of Continental Break-up* (eds. Storey, B. C., Alabaster, T. & Pankhurst, R. J.). Geological Society London, London, Special Publications, **68**, pp. 165-184.

ELLIOT, D. H. & FLEMING, T. H. 2000. Weddell triple junction: the principal focus of Ferrar and Karoo magmatism during initial breakup of Gondwana. *Geology* **28**, 6, pp. 539-542.

ELLIOT, D. H. & FLEMING, T. H. 2004. Occurrence and dispersal of magmas in the Jurassic Ferrar Large Igneous Province, Antarctica. *Gondwana Research* **7**, 1, pp. 223-237.

ELLIOT, D. H., FLEMING, T. H., FOLAND, K. A. & FANNING, C. M. 2007. Jurassic silicic volcanism in the Transantarctic Mountains: was it related to plate margin processes or to Ferrar magmatism. In *10th International Symposium on Antarctic Earth Sciences* (eds. Cooper, A. K., Raymond, C. R. & Team, t. I. E.), Santa Barbara. USGS, Antarctica: a Keystone in a Changing World – Online proceedings for the 10th International Symposium on Antarctic Earth Sciences Open File Report 2007-1047, p. 5.

ELLIOT, D. H., FANNING, C. M. & HULETT, S. R. W. 2015. Age provinces in the Antarctic craton: evidence from detrital zircons in Permian strata from the Beardmore Glacier region, Antarctica. *Gondwana Research* **28**, 1, pp. 152-164.

ELSNER, M., SCHÖNER, R., GERDES, A. & GAUPP, R. 2013. Reconstruction of the early Mesozoic plate margin of Gondwana by U–Pb ages of detrital zircons from northern Victoria Land, Antarctica. In *Antarctica and Supercontinent Evolution* (eds. Harley, S. L., Fitzsimons, I. C. W. & Zhao, Y.). Geological Society London, London, Special Publications, **383**, pp. 211-232.

EMMEL, B., JACOBS, J., CROWHURST, P. & DASZINNIES, M. C. 2007. Combined apatite fission-track and single grain apatite (U-Th)/He ages from basement rocks of central Dronning

Maud Land (East Antarctica) – possible identification of thermally overprinted crustal segments. *Earth and Planetary Science Letters* **264**, 1–2, pp. 72-88.

EMMEL, B., JACOBS, J., CROWHURST, P., AUSTEGARD, A. & SCHWARZ-SCHAMPERA, U. 2008. Apatite single-grain (U-Th)/He data from Heimefrontfjella, East Antarctica: indications for differential exhumation related to glacial loading? *Tectonics* **27**, 6, pp. 1-13.

EMMEL, B., JACOBS, J. & DASZINNIES, M. C. 2009. Combined titanite and apatite fission-track data from Gjelsvikfjella, East Antarctica – another piece of a concealed intracontinental Permo-Triassic Gondwana rift basin? In *Thermochronological Methods: From Palaeotemperature Constraints to Landscape Evolution Models* (eds. Lisker, F., Ventura, B. & Glasmacher, U. A.). Geological Society London, London, Special Publications, **324**, pp. 317-330.

EMMEL, B., BOGER, S. D., J., J. & DASZINNIES, M. C. 2012. Maturity of central Madagascar's landscape – low-temperature thermochronological constraints. *Gondwana Research* **21**, 2–3, pp. 704-713.

ENCARNACIÓN, J., FLEMING, T. H., ELLIOT, D. H. & EALES, H. V. 1996. Synchronous emplacement of Ferrar and Karoo dolerites and the early breakup of Gondwana. *Geology* **24**, 6, pp. 535-538.

EVENSEN, N. M., HAMILTON, P. J. & O'NIONS, R. K. 1978. Rare-earth abundances in chondritic meteorites. *Geochimica et Cosmochimica Acta* **42**, 8, pp. 1199-1212.

FARLEY, K. A., WOLF, R. A. & SILVER, L. T. 1996. The effects of long alpha-stopping distances on (U-Th)/He ages. *Geochimica et Cosmochimica Acta* **60**, 21, pp. 4223-4229.

FARLEY, K. A. 2000. Helium diffusion from apatite: general behavior as illustrated by Durango fluorapatite. *Journal of Geophysical Research* **105**, B2, pp. 2903-2914

FARLEY, K. A. 2002. (U-Th)/He dating: techniques, calibrations, and applications. *Reviews in Mineralogy and Geochemistry* **47**, 1, pp. 819-844.

FARLEY, K. A., SHUSTER, D. L. & KETCHAM, R. A. 2011. U and Th zonation in apatite observed by laser ablation ICPMS, and implications for the (U–Th)/He system. *Geochimica et Cosmochimica Acta* **75**, 16, pp. 4515-4530.

FAWCETT, P. J., BARRON, E. J., ROBISON, V. D. & KATZ, B. J. 1994. The climatic evolution of India and Australia from the late Permian to mid-Jurassic: a comparison of climate model results with the geologic record. In *Pangea: Paleoclimate, Tectonics, and Sedimentation during Accretion, Zenith, and Breakup of a Supercontinent* (ed. Klein, G. D.). Geological Society of America Colorado, United States, Special Papers, **288**, pp. 139-158.

FERRIS, J. K., VAUGHAN, A. P. M. & STOREY, B. C. 2000. Relics of a complex triple junction in the Weddell Sea Embayment, Antarctica. *Earth and Planetary Science Letters* **178**, 3–4, pp. 215-230.

FITZGERALD, P. G., BALDWIN, S. L., WEBB, L. E. & O'SULLIVAN, P. B. 2006. Interpretation of (U-Th)/He single grain ages from slowly cooled crustal terranes: a case study from the Transantarctic Mountains of southern Victoria Land. *Chemical Geology* **225**, 1–2, pp. 91-120.

FITZSIMONS, I. C. W. 2003. Proterozoic basement provinces of southern and southwestern Australia, and their correlation with Antarctica. In *Proterozoic East Gondwana: Supercontinent Assembly and Breakup* (eds. Yoshida, M., Windley, B. F. & Dasgupta, S.). Geological Society London, London, Special Publications, **206**, pp. 93-130.

FLEMING, T. H., HEIMANN, A., FOLAND, K. A. & ELLIOT, D. H. 1997. $^{40}Ar/^{39}Ar$ geochronology of Ferrar dolerite sills from the Transantarctic Mountains, Antarctica: implications for the age and origin of the Ferrar magmatic province. *Geological Society of America Bulletin* **109**, 5, pp. 533-546.

FLOWERDEW, M. J., TYRRELL, S., RILEY, T. R., WHITEHOUSE, M. J., MULVANEY, R., LEAT, P. T. & MARSCHALL, H. R. 2012. Distinguishing East and West Antarctic sediment sources using the Pb isotope composition of detrital K-feldspar. *Chemical Geology* **292-293**, 23, pp. 88-102.

FLOWERS, R. M. 2009. Exploiting radiation damage control on apatite (U-Th)/He dates in cratonic regions. *Earth and Planetary Science Letters* **277**, 1–2, pp. 148-155.

FLOWERS, R. M., KETCHAM, R. A., SHUSTER, D. L. & FARLEY, K. A. 2009. Apatite (U-Th)/He thermochronometry using a radiation damage accumulation and annealing model. *Geochimica et Cosmochimica Acta* **73**, 8, pp. 2347-2365.

FOGWILL, C. J., BENTLEY, M. J., SUGDEN, D. E., KERR, A. R. & KUBIK, P. W. 2004. Cosmogenic nuclides ^{10}Be and ^{26}Al imply limited Antarctic Ice Sheet thickening and low erosion in the Shackleton Range for >1 m.y. *Geology* **32**, 3, pp. 265-268.

FRETWELL, P., PRITCHARD, H. D., VAUGHAN, D. G., BAMBER, J. L., BARRAND, N. E., BELL, R., BIANCHI, C., BINGHAM, R. G., BLANKENSHIP, D. D., CASASSA, G., CATANIA, G., CALLENS, D., CONWAY, H., COOK, A. J., CORR, H. F. J., DAMASKE, D., DAMM, V., FERRACCIOLI, F., FORSBERG, R., FUJITA, S., GIM, Y., GOGINENI, P., GRIGGS, J. A., HINDMARSH, R. C. A., HOLMLUND, P., HOLT, J. W., JACOBEL, R. W., JENKINS, A., JOKAT, W., JORDAN, T., KING, E. C., KOHLER, J., KRABILL, W., RIGER-KUSK, M., LANGLEY, K. A., LEITCHENKOV, G., LEUSCHEN, C., LUYENDYK, B. P., MATSUOKA, K., MOUGINOT, J., NITSCHE, F. O., NOGI, Y., NOST, O. A., POPOV, S. V., RIGNOT, E., RIPPIN, D. M., RIVERA, A., ROBERTS, J., ROSS, N., SIEGERT, M. J., SMITH, A. M., STEINHAGE, D., STUDINGER, M., SUN, B., TINTO, B. K., WELCH, B. C., WILSON, D., YOUNG, D. A., XIANGBIN, C. & ZIRIZZOTTI, A. 2013. Bedmap2: improved ice bed, surface and thickness datasets for Antarctica. *The Cryosphere* **7**, 1, pp. 375-393.

FROST, B. R., BARNES, C. G., COLLINS, W. J., ARCULUS, R. J., ELLIS, D. J. & FROST, C. D. 2001. A geochemical classification for granitic rocks. *Journal of Petrology* **42**, 11, pp. 2033-2048.

GALBRAITH, R. F. 1981. On statistical models for fission track counts. *Mathematical Geology* **13**, 6, pp. 471-478.

GALLAGHER, K. & BROWN, R. 1997. The onshore record of passive margin evolution. *Journal of the Geological Society* **154**, 3, pp. 451-457.

GALLAGHER, K., BROWN, R. & JOHNSON, C. 1998. Fission track analysis and its applications to geological problems. *Annual Review of Earth and Planetary Sciences* **26**, pp. 519-572.

GARVER, J. I., BRANDON, M. T., RODEN-TICE, M. & KAMP, P. J. J. 1999. Erosional denudation determined by fission-track ages of detrital apatite and zircon. In *Exhumation Processes: Normal Faulting, Ductile Flow, and Erosion* (eds. Ring, U., Brandon, M. T., Willett, S. & Lister, G.). Geological Society London, London, Special Publications, **154**, pp. 283–304.

GAZEL, E., HOERNLE, K., CARR, M. J., HERZBERG, C., SAGINOR, I., DEN BOGAARD, P. V., HAUFF, F., FEIGENSON, M. & SWISHER III, C. 2011. Plume-subduction interaction in southern Central America: mantle upwelling and slab melting. *Lithos* **121**, 1–4, pp. 117-134.

GLEADOW, A. J. W. 1984. Fission track dating methods II – a manual of principles and techniques. In *Workshop on fission track analysis; principles and applications*, Townsville. James Cook University, p. 35.

GOLYNSKY, A. & ALESHKOVA, N. D. 2000. Regional magnetic anomalies of the Weddell Sea region and their geological significance. *Polarforschung* **67**, 3, pp. 101-117.

GOLYNSKY, A. & JACOBS, J. 2001. Grenville-age versus Pan-African magnetic anomaly imprints in western Dronning Maud Land, East Antarctica. *Journal of Geology* **109**, 1, pp. 136-142.

GRANTHAM, G. H. & HUNTER, D. R. 1991. The timing and nature of faulting and jointing adjacent to the Pencksökket, western Dronning Maud Land, Antarctica. In *Geological Evolution of Antarctica; Proceedings of the 5th International Symposium on Antarctic Earth Sciences* (eds. Thomson, M. R. A., Crame, J. A. & Thomson, J. W.). Cambridge University Press, Cambridge, pp. 47-51.

GRANTHAM, G. H., MACEY, P. H., INGRAM, B. A., ROBERTS, M. P., ARMSTRONG, R. A., HOKADA, T., SHIRAISHI, K., JACKSON, C., BISNATH, A. & MANHICA, V. 2008. Terrane correlation between Antarctica, Mozambique and Sri Lanka; comparisons of geochronology, lithology, structure and metamorphism and possible implications for the geology of southern Africa and Antarctica. In *Geodynamic Evolution of East Antarctica: A Key to the East-West Gondwana Connection* (eds. Satish-Kumar, M., Motoyoshi, Y., Osanai, Y., Hiroi, Y. & Shiraishi, K.). Geological Society London, London, Special Publications, **308**, pp. 91-119.

GRANTHAM, G. H., MACEY, P. H., HORIE, K., KAWAKAMI, T., ISHIKAWA, M., SATISH-KUMAR, M., TSUCHIYA, N., GRASER, P. & AZEVEDO, S. 2013. Comparison of the metamorphic history of the Monapo Complex, northern Mozambique and Balchenfjella and Austhameren areas, Sør Rondane, Antarctica: implications for the Kuunga Orogeny and the amalgamation of N and S. Gondwana. *Precambrian Research* **234**, pp. 85-135.

GRAY, D. R., FOSTER, D. A., MEERT, J. G., GOSCOMBE, B. D., ARMSTRONG, R., TROUW, R. A. J. & PASSCHIER, C. W. 2008. A Damara orogen perspective on the assembly of southwestern Gondwana. In *Geodynamic Evolution of East Antarctica: A Key to the East-West Gondwana Connection* (eds. Satish-Kumar, M., Motoyoshi, Y., Osanai, Y., Hiroi, Y. & Shiraishi, K.). Geological Society London, London, Special Publications, **294** pp. 257-278.

GREEN, P. F. 1981. A new look at statistics in fission-track dating. *Nuclear Tracks* **5**, 1–2, pp. 77-86.

GREEN, P. F., DUDDY, I. R., GLEADOW, A. J. W. & LOVERING, J. F. 1989. Apatite fission track analysis as a paleotemperature indicator for hydrocarbon exploration. In *Thermal History of Sedimentary Basins: Methods and Case Histories* (eds. Naeser, N. D. & McCulloh). Springer, New York, pp. 181-195.

GREENE, A. R., DEBARI, S. M., KELEMENT, P. B., BLUSZTAJN, J. & CLIFT, P. D. 2006. A detailed geochemical study of island arc crust: the Talkeetna Arc Section, south-central Alaska. *Journal of Petrology* **47**, 6, pp. 1051-1093.

GREW, E. S., MANTON, W. I., ASAMI, M. & MAKIMOTO, H. 1992. Reconnaissance geochronologic data on Proterozoic polymetamorphic rocks of the eastern Sør Rondane Mountains, East Antarctica. In *Recent Progress in Antarctic Earth Science* (eds. Yoshida, T., Kaminuma, K. & Shiraishi, K.). Terra Scientific Publishing Company, Tokyo, pp. 37-44.

GREW, E. S., CARSON, C. J., CHRISTY, A. G., MAAS, R., YAXLEY, G. M., BOGER, S. D. & FANNING, C. M. 2012. New constraints from U-Pb, Lu-Hf and Sm-Nd isotopic data on the timing of sedimentation and felsic magmatism in the Larsemann Hills, Prydz Bay, East Antarctica. *Precambrian Research* **206**, pp. 87-108.

GRIFFIN, W. L., BELOUSOVA, E. A., SHEE, S. R., PEARSON, N. J. & O'REILLY, S. Y. 2004. Archean crustal evolution in the northern Yilgam Craton: U-Pb and Hf-isotope evidence from detrital zircons. *Precambrian Research* **131**, pp. 231-282.

GRINDLAY, G. W. & WARREN, G. 1964. Stratigraphic nomenclature and correlation in the western Ross Sea region. In *Antarctic Geology* (ed. Adie, R. J.). North Holland Publishing Company, Amsterdam, pp. 314-333.

GRUNOW, A., KENT, D. V. & DALZIEL, I. 1991. New paleomagnetic data from Thurston Island: implications for the tectonics of West Antarctica and Weddell Sea opening. *Journal of Geophysical Research: Solid Earth* **96**, B11, pp. 17935-17954.

GRUNOW, A., HANSON, R. & WILSON, T. 1996. Were aspects of Pan-African deformation linked to Iapetus opening? *Geology* **24**, 12, pp. 1063-1066.

GRUNOW, A. M. 1993. Creation and destruction of Weddell Sea floor in the Jurassic. *Geology* **21**, 7, pp. 647-650.

HALL, R. 2002. Cenozoic geological and plate tectonic evolution of SE Asia and the SW Pacific: computer-based reconstructions, model and animations. *Journal of Asian Earth Sciences* **20**, 4, pp. 353-431.

HALPIN, J. A., DACZKO, N. R., MILAN, L. A. & CLARKE, G. L. 2012. Decoding near-concordant U-Pb zircon ages spanning several hundred million years: recrystallisation, metamictisation or diffusion? *Contributions to Mineralogy and Petrology* **163**, 1, pp. 67-85.

HARRIS, P. D., MOYES, A. B., FANNING, C. M. & ARMSTRONG, R. A. 1995. Zircon ion microprobe results from the Maudheim high-grade gneiss terrane, western Dronning Maud Land, Antarctica. In *Centennial Geocongress*, Johannesburg. pp. 240-243.

HARROWFIELD, M., HOLDGATE, G. R., WILSON, C. J. L. & MCLOUGHLIN, S. 2005. Tectonic significance of the Lambert Graben, East Antarctica: reconstructing the Gondwanan rift. *Geology* **33**, 3, pp. 197-200.

HEINONEN, A. P., ANDERSEN, T. & RÄMÖ, O. T. 2010a. Source constraints from the Hf isotope composition of zircon in the rapakivi granites and associated mafic rocks of southern Finland. *Journal of Petrology* **51**, 8, pp. 1687-1709.

HEINONEN, J. S., CARLSON, R. W. & LUTTINEN, A. V. 2010b. Isotopic (Sr, Nd, Pb, and Os) composition of highly magnesian dikes of Vestfjella, western Dronning Maud Land, Antarctica: a key to the origins of the Jurassic Karoo large igneous province? *Chemical Geology* **277**, 3–4, pp. 227-244.

HELFERICH, S., LÄUFER, A. L., HENJES-KUNST, F. & KLEINSCHMIDT, G. 2004. Pan-African events in southern Kirwanveggen (western Dronning Maud Land, Antarctica) – evidence from structural geology and geochronology. *Zeitschrift der Deutschen Geologischen Gesellschaft* **154**, 4, pp. 453-468.

HENJES-KUNST, F. 2004. Further evidence for Pan-African polyphase magmatism and metamorphism in central Dronning Maud Land, East Antarctica, from rocks at Schirmacheroase: a geochronological study. In *International GeoMaud Expedition of the BGR to central Dronning Maud Land in 1995/96 - Geological Results* (ed. Paech, H.-J.). E. Schweizerbart´sche Verlagsbuchhandlung (Nägele u. Obermiller), Stuttgart, B96, **Polar Issue No. 10**, pp. 255-292.

HIGASHINO, F., KAWAKAMI, T., SATISH-KUMAR, M., ISHIKAWA, M., MAKI, K., TSUCHIYA, N., GRANTHAM, G. H. & HIRATA, T. 2013. Chlorine-rich fluid or melt activity during granulite facies metamorphism in the Late Proterozoic to Cambrian continental collision zone – an example from the Sør Rondane Mountains, East Antarctica. *Precambrian Research* **234**, pp. 229-246.

HINTHORNE, J. R., ANDERSON, C. A., CONRAD, R. L. & LOVERING, J. F. 1979. Single-grain $^{207}Pb/^{206}Pb$ and U/Pb age determinations with a 10 μm spatial resolution using the ion microprobe mass analyser (IMMA). *Chemical Geology* **25**, pp. 271-303.

HINZ, K. & KRAUSE, W. 1982. The continental margin off Queen Maud Land/Antarctica: seismic sequences, structural elements and geological development. In *Geologisches Jahrbuch*, 23, **E**, pp. 17-41.

HINZ, K., NEBEN, S., GOUSEVA, Y. B. & KUDRYAVTSEV, G. A. 2004. A compilation of geophysical data from the Lazarev Sea and the Riiser-Larsen Sea, Antarctica. *Marine Geophysical Researches* **25**, 3, pp. 233-245.

HÖFLE, H.-C. & BUGGISCH, W. 1995. Glacial geology and petrography of erratics in the Shackleton Range, Antarctica. *Polarforschung* **63**, 2/3, pp. 183-201.

HOFMANN, J., KAISER, G., KLEMM, W. & PAECH, H.-J. 1980. K-Ar Alter von Doleriten und Metamorphiten der Shackleton Range und der Whichaway-Nunataks, Ost- und Südostumrandung des Filchner-Eisschelfs. *Zeitschrift für Geologische Wissenschaften* **8**, 9, pp. 1227-1232.

HOTTEN, R. 1993. Die mafischen Gänge der Shackleton Range/Antarktika: Petrographie, Geochemie, Isotopengeochemie und Paläomagnetik = The mafic dykes of the Shackleton Range/Antarctica: petrography, geochemistry, isotope geochemistry and palaeomagnetism. *Berichte zur Polarforschung* **118**.

HUANG, X., GOHL, K. & JOKAT, W. 2014. Variability in Cenozoic sedimentation and paleo-water depths of the Weddell Sea basin related to pre-glacial and glacial conditions of Antarctica. *Global and Planetary Change* **118**, pp. 25-41.

HÜBSCHER, C., JOKAT, W. & MILLER, H. 1996a. Crustal structure of the Antarctic continental margin in the eastern Weddell Sea. In *Weddell Sea Tectonics and Gondwana Break-up* (eds. Storey, B. C., King, E. C. & Livermore, R. A.). Geological Society London, London, Special Publications, **108**, pp. 165-174.

HÜBSCHER, C., JOKAT, W. & MILLER, H. 1996b. Structure and origin of southern Weddell Sea crust; results and implications. In *Weddell Sea Tectonics and Gondwana Break-up* (eds. Storey, B. C., King, E. C. & Livermore, R. A.). Geological Society London, London, Special Publications, **108**, pp. 201-211.

HUHMA, H., MÄNTTÄRI, I., PELTONEN, P., KONTINEN, A., HALKOAHO, T., HANSKI, E., HOKKANEN, T., HÖLTTÄ, P., JUOPPERI, H., KONNUNAHO, J., LAHAYE, Y., LUUKKONEN, E., PIETIKÄINEN, K.,

PULKKINEN, A., SORJONEN-WARD, P., VAASJOKI, M. & WHITEHOUSE, M. 2012. The age of the Archaean greenstone belts in Finland. In *The Archaean of the Karelia Province in Finland* (ed. Hölttä, P.). Geological Survey Finland, Espoo, Special Papers, **54**, pp. 74-175.

HUISMANS, R. S., PODLADCHIKOV, Y. Y. & CLOETINGH, S. 2001. Transition from passive to active rifting: relative importance of asthenospheric doming and passive extension of the lithosphere. *Journal of Geophysical Research: Solid Earth* **106**, B6, pp. 11271-11291.

HUMPHREYS, B., KEMP, S. J., LOTT, G. K., BERMANTO, D.A., D. & SAMSORI, I. 1994. Origin of grain-coating chlorite by smectite transformation: an example from Miocene sandstones, north Sumatra back-arc basin, Indonesia. *Clay Minerals* **29**, 4, pp. 681-692.

HURFORD, A. J. & GREEN, P. F. 1982. A users' guide to fission track dating calibration. *Earth and Planetary Science Letters* **59**, 2, pp. 343-354.

HURFORD, A. J. & GREEN, P. F. 1983. The zeta age calibration of fission-track dating. *Chemical Geology* **1**, pp. 285-317.

HUTTON, D. H. W. 2009. Insights into magmatism in volcanic margins: bridge structures and a new mechanism of basic sill emplacement – Theron Mountains, Antarctica. *Petroleum Geoscience* **15**, 3, pp. 269-278.

IKEDA, Y., SHIRAISHI, K. & YANAI, K. 1997. Petrogenesis of the meta-trondhjemites from Cape Hinode, East Antarctica. In *Proceedings of the NIPR Symposium on Antarctic Geosciences*. pp. 102-110.

IKEDA, Y. & SHIRAISHI, K. 1998. Petrogenesis of the tonalitic rocks from the Sør Rondane Mountain, East Antarctica. *Polar Geoscience* **11**, pp. 143-153.

ISBELL, J. L., COLE, D. I. & CATUNEANU, O. 2008. Carboniferous-Permian glaciation in the main Karoo Basin, South Africa: stratigraphy, depositional controls, and glacial dynamics. In *Resolving the Late Paleozoic Ice Age in Time and Space* (eds. Fielding, C. R., Frank, T. D. & Isbell, J. L.). Geological Society of America, Boulder, Colorado, United States, Special Paper **441**, pp. 71–82.

ISHIKAWA, M., KAWAKAMI, T., SATISH-KUMAR, M., GRANTHAM, G. H., HOKAZONO, Y., SASO, M. & TSUCHIYA, N. 2013. Late Neoproterozoic extensional detachment in eastern Sør Rondane Mountains, East Antarctica: implications for the collapse of the East African Antarctic Orogen. *Precambrian Research* **234**, pp. 247-256.

IWASAKI, A. & YAMANOUCHI, T. 1992. Meteorological data at Asuka Station, Antarctica in 1990. In *JARE Data Reports*. National Institute of Polar Research. Tokyo, No. 179.

JACKSON, S. E., PEARSON, N. J., GRIFFIN, W. L. & BELOUSOVA, E. A. 2004. The application of laser ablation-inductively coupled plasma-mass spectrometry to in situ U-Pb zircon geochronology. *Chemical Geology* **211**, pp. 47-69.

JACOBS, J. 1991. Strukturelle Entwicklung und Abkühlungsgeschichte der Heimefrontfjella (Westliches Dronning Maud Land/ Antarktika). *Berichte zur Polarforschung* **97**, p. 141 pp.

JACOBS, J., HEJL, E., WAGNER, G. A. & WEBER, K. 1992. Apatite fission track evidence for contrasting thermal and uplift histories of metamorphic basement blocks in western Dronning Maud Land. In *Recent Progress in Antarctic Earth Science* (eds. Yoshida, Y., Kaminuma, K. & Shiraishi, K.). Terra Scientific Publishing Company, Tokyo, pp. 323-330.

JACOBS, J., BAUER, W., SPAETH, G., THOMAS, R. J. & WEBER, K. 1996a. Lithology and structure of the Grenville-aged (~1.1 Ga) basement of Heimefrontfjella (East Antarctica). *Geologische Rundschau* **85**, 4, pp. 800-821.

JACOBS, J., KAUL, N. & WEBER, K. 1996b. The history of denudation and resedimentation at the continental margin of western Dronning Maud Land, Antarctica, during break-up of Gondwana. In *Weddell Sea Tectonics and Gondwana Break-up* (eds. Storey, B. C., King, E. C. & Livermore, R. A.). Geological Society London, London, Special Publications, **108**, pp. 191-199.

JACOBS, J., FALTER, M., WEBER, K. & JESSBERGER, E. K. 1997. ^{40}Ar-^{39}Ar evidence for the structural evolution of the Heimefront Shear Zone (Western Dronning Maud Land), East

Antarctica. In *The Antarctic Region: Geological Evolution and Processes* (ed. Ricci, C. A.). Terra Antartica Publication, Siena, pp. 37-44.

JACOBS, J., FANNING, C. M., HENJES-KUNST, F., OLESCH, M. & PAECH, H. J. 1998. Continuation of the Mozambique Belt into East Antarctica: Grenville-age metamorphism and polyphase Pan-African high-grade events in central Dronning Maud Land. *Journal of Geology* **106**, 4, pp. 385-406.

JACOBS, J. & LISKER, F. 1999. Post Permian tectono-thermal evolution of western Dronning Maud Land, E-Antarctica: an apatite fission-track approach. *Antarctic Science* **11**, 4, pp. 451-460.

JACOBS, J., BAUER, W. & FANNING, C. M. 2003a. Late Neoproterozoic/Early Palaeozoic events in central Dronning Maud Land and significance for the southern extension of the East African Orogen into East Antarctica. *Precambrian Research* **126**, pp. 27-53.

JACOBS, J., BAUER, W. & FANNING, C. M. 2003b. New age constraints for Grenville-age metamorphism in western central Dronning Maud Land (East Antarctica), and implications for the palaeogeography of Kalahari in Rodinia. *International Journal of Earth Sciences* **92**, 3, pp. 301-315.

JACOBS, J., FANNING, C. M. & BAUER, W. 2003c. Timing of Grenville-age vs. Pan-African medium- to high grade metamorphism in western Dronning Maud Land (East Antarctica) and significance for correlations in Rodinia and Gondwana. *Precambrian Research* **125**, 1–2, pp. 1-20.

JACOBS, J., KLEMD, R., FANNING, C. M., BAUER, W. & COLOMBO, F. 2003d. Extensional collapse of the late Neoproterozoic-early Palaeozoic East African-Antarctic Orogen in central Dronning Maud Land, East Antarctica in Proterozoic East Gondwana; supercontinent assembly and breakup. In *Proterozoic East Gondwana: Supercontinent Assembly and Breakup* (eds. Yoshida, M., Windley, B. F. & Dasgupta, S.). Geological Society London, London, Special Publications, **206**, pp. 271-287.

JACOBS, J. & THOMAS, R. J. 2004. Himalayan-type indenter-escape tectonics model for the southern part of the Late Neoproterozoic-Early Paleozoic East African-Antarctic Orogen. *Geology* **32**, 8, pp. 721-724.

JACOBS, J., BINGEN, B., THOMAS, R. J., BAUER, W., WINGATE, M. T. D. & FEITIO, P. 2008. Early Palaeozoic orogenic collapse and voluminous late-tectonic magmatism in Dronning Maud Land and Mozambique: insights into the partially delaminated orogenic root of the East African-Antarctic Orogen? In *Geodynamic Evolution of East Antarctica: A Key to the East-West Gondwana Connection* (eds. Satish-Kumar, M., Motoyoshi, Y., Osanai, Y., Hiroi, Y. & Shiraishi, K.). Geological Society London, London, Special Publications, **308**, pp. 69-90.

JACOBS, J. 2009. A review of two decades (1986–2008) of geochronological work in Heimefrontjella, and geotectonic interpretation of western Dronning Maud Land, East Antarctica. *Polarforschung* **79**, 1, pp. 47-57.

JACOBS, J., BAUER, W., WEBER, K., SPAETH, G. & THOMAS, R. J. 2009. Geology of the Sivorg Terrane, Heimefrontfjella (East Antarctica), and new U-Pb zircon provenance analyses of metasedimentary rocks. *Polarforschung* **79** 1, pp. 11-19.

JACOBS, J., ELBURG, M., LAEUFER, A., KLEINHANNS, I. C., HENJES-KUNST, F., ESTRADA, S., RUPPEL, A., DAMASKE, D., MONTERO, P. & BEA, F. 2015. Two distinct Late Mesoproterozoic/Early Neoproterozoic basement provinces in central/eastern Dronnning Maud Land, East Antarctica: the missing link, 15-21°E. *Precambrian Research* **265**, pp. 249-272.

JENKYNS, H., SCHOUTEN-HUIBERS, L., SCHOUTEN, S. & DAMSTÉ, J. S. 2012. Warm Middle Jurassic-Early Cretaceous high-latitude sea-surface temperatures from the Southern Ocean. *Climate of the Past* **8**, 1, p. 215.

JIANG, G., SOHL, L. E. & CHRISTIE-BLICK, N. 2003. Neoproterozoic stratigraphic comparison of the Lesser Himalaya (India) and Yangtze block (south China): paleogeographic implications. *Geology* **31**, 10, pp. 917-920.

JOCHUM, K. P., NOHL, L., HERWIG, K., LAMMEL, E., TOLL, B. & HOFMANN, A. W. 2005. GeoReM: a new geochemical database for reference materials and isotopic standards. *Geostandards and Geoanalytical Research* **29**, 3, pp. 333-338.

JOKAT, W., BOEBEL, T., KÖNIG, M. & MEYER, U. 2003. Timing and geometry of early Gondwana breakup. *Journal of Geophysical Research: Solid Earth* **108**, B9, pp. 2156-2202.

JÖNS, N. & SCHENK, V. 2008. Relics of the Mozambique Ocean in the central East African Orogen: evidence from the Vohibory Block of southern Madagascar. *Journal of Metamorphic Geology* **26**, 1, pp. 17-28.

JORDAN, T. A., FERRACCIOLI, F., ROSS, N., CORR, H. F. J., LEAT, P. T., BINGHAM, R. G., RIPPIN, D. M., LE BROCQ, A. M. & SIEGERT, M. J. 2013. Inland extent of the Weddell Sea rift imaged by new aerogeophysical data. *Tectonophysics* **585**, pp. 137-160.

JUCKES, L. M. 1972. The Geology of North-Eastern Heimefrontfjella, Dronning Maud Land. *British Antarctic Survey Bulletin* **65**, p. 44.

KAMEI, A., HORIE, K., OWADA, M., YUHARA, M., NAKANO, N., OSANAI, Y., ADACHI, T., HARA, Y., TERAO, M., TEUCHI, S., SHIMURA, T., TSUKADA, K., HOKADA, T., IWATA, C., SHIRAISHI, K., ISHIZUKA, H. & TAKAHASHI, Y. 2013. Late Proterozoic juvenile arc metatonalite and adakitic intrusions in the Sør Rondane Mountains, eastern Dronning Maud Land, Antarctica. *Precambrian Research* **234**, pp. 47-62.

KELLEY, N. M. & HARLEY, S. L. 2005. An integrated microtextural and chemical approach to zircon geochronology: refining the Archaean history of the Napier Complex, East Antarctica. *Contributions to Mineralogy and Petrology* **149**, pp. 27-84.

KETCHAM, R. A. 2005. Forward and inverse modeling of low-temperature thermochronometry data. *Reviews in Mineralogy and Geochemistry* **58**, 1, pp. 275-314.

KETCHAM, R. A., CARTER, A., DONELICK, R. A., BARBARAND, J. & HURFORD, A. J. 2007. Improved modeling of fission-track annealing in apatite. *American Mineralogist* **92**, 5–6, pp. 799-810.

KING, E. C. 2000. The crustal structure and sedimentation of the Weddell Sea embayment: implications for Gondwana reconstructions. *Tectonophysics* **327**, 3-4, pp. 195-212.

KLEINSCHMIDT, G., BUGGISCH, W. & FLÖTTMANN, T. 1992. Compressional causes for the Early Paleozoic Ross orogen - evidence from Victoria Land and the Shackleton Range. In *Recent Progress in Antarctic Earth Science* (eds. Yoshida, Y., Kaminuma, K. & Shiraishi, K.). Terra Scientific Publishing Company, Tokyo, pp. 227-233.

KLEINSCHMIDT, G., HELFERICH, S., HENJES-KUNST, F., JACJSON, C. & FRIMMEL, H. E. 2000. The pre-Permo-Carboniferous rocks and structures from southern Kirwanveggen, Dronning Maud Land, Antarctica. *Polarforschung* **66**, pp. 7-18.

KLEINSCHMIDT, G., BUGGISCH, W., LÄUFER, A. L., HELFERICH, S. & TESSENSOHN, F. 2002. The "Ross orogenic" structures in the Shackleton Range and their meaning for Antarctica. In *Antarctica at the Close of a Millennium* (eds. Gamble, J. A., Skinner, D. N. B. & Henrys, S.), Wellington. The Royal Society of New Zealand, Bulletin 35, pp. 75-83.

KOJIMA, S. & SHIRAISHI, K. 1986. Note on the geology of the western part of the Sør Rondane Mountains, East Antarctica. *Memoirs of the National Institute of Polar Research* **43**, pp. 116-131.

KÖNIG, M. & JOKAT, W. 2006. The Mesozoic breakup of the Weddell Sea. *Journal of Geophysical Research* **111**, B12012, pp. 1-28.

KÖNIG, M. & JOKAT, W. 2010. Advanced insights into magmatism and volcanism of the Mozambique Ridge and Mozambique Basin in the view of new potential field data. *Geophysical Journal International* **180**, 1, pp. 158-180.

KOVACS, L. C., MORRIS, P., BROZENA, J. & TIKKU, A. 2002. Seafloor spreading in the Weddell Sea from magnetic and gravity data. *Tectonophysics* **347**, 1–3, pp. 43-64.

KRATZMANN, D., CAREY, S., SCASSO, R. & NARANJO, J.-A. 2010. Role of cryptic amphibole crystallization in magma differentiation at Hudson Volcano, Southern Volcanic Zone, Chile. *Contributions to Mineralogy and Petrology* **159**, 2, pp. 237-264.

KRETZ, R. 1983. Symbols for rock-forming minerals. *American Mineralogist* **68**, 1–2, pp. 277-279.

KREUSER, T. 1995. Rift to drift evolution in Permian-Jurassic basins of East Africa. In *Hydrocarbon Habitat in Rift Basins* (ed. Lamblase, J. J.). Geological Society London, London, Special Publications, **80**, pp. 297-315.

KRISTOFFERSEN, M., ANDERSEN, T. & ANDRESEN, A. 2013. U-Pb age and Lu-Hf signatures of detrital zircon from Palaeozoic sandstones in the Oslo Rift, Norway. *Geological Magazine* **151**, pp. 816-829.

KRISTOFFERSEN, Y. & HAUGLAND, K. 1986. Geophysical evidence for the East Antarcitc plate boundary in the Weddell Sea. *Nature* **322**, 6079, pp. 538-541.

KRISTOFFERSEN, Y. & HINZ, K. 1991. Evolution of the Gondwana plate boundary in the Weddell Sea area. In *Geological Evolution of Antarctica; Proceedings of the 5th International Symposium on Antarctic Earth Sciences* (eds. Thomson, M. R. A., Crame, J. A. & Thomson, J. W.). Cambridge University Press, Cambridge, pp. 225-230.

KRISTOFFERSEN, Y., HOFSTEDE, C., DIEZ, A., BLENKNER, R., LAMBRECHT, A., MAYER, C. & EISEN, O. 2014. Reassembling Gondwana: a new high quality constraint from vibroseis exploration of the sub-ice shelf geology of the East Antarctic continental margin. *Journal of Geophysical Research: Solid Earth* **119**, 12, pp. 9171-9182.

KROHNE, N., LISKER, F., KLEINSCHMIDT, G., KLÜGEL, A., LÄUFER, A., ESTRADA, S. & SPIEGEL, C. 2016. The Shackleton Range (East Antarctica): an alien block at the rim of Gondwana? *Geological Magazine*, pp. 1-24.

KROHNE, N., LISKER, F., LÄUFER, A., RUPPEL, A., JACOBS, J., ELBURG, M., DAMASKE, D. & SPIEGEL, C. prepared for submission. Passive margin formation in Sør Rondane (East Antarctica). *Tectonics*.

KRÖNER, A., ROJAS-AGRAMONTE, Y., KEHELPANNALA, K. V. W., ZACK, T., HEGNER, E., GENG, H. Y., WONG, J. & BARTH, M. 2013. Age, Nd–Hf isotopes, and geochemistry of the Vijayan Complex of eastern and southern Sri Lanka: a Grenville-age magmatic arc of unknown derivation. *Precambrian Research* **234**, pp. 288-321.

KRUHL, J. H. 1996. Prism- and basal-plane parallel subgrain boundaries: a microstructural geothermobarometer. *Journal of Metamorphic Geology* **14**, 5, pp. 581-589.

KURITANI, T. 2001. Replenishment of a mafic magma in a zoned felsic magma chamber beneath Rishiri Volcano, Japan. *Bulletin of Volcanology* **62**, 8, pp. 533-548.

LASLETT, G., KENDALL, W., GLEADOW, A. & DUDDY, I. 1982. Bias in measurement of fission-track length distributions. *Nuclear Tracks and Radiation Measurements* **6**, 2–3, pp. 79-85.

LE MAITRE, R. W. 2002. Igneous Rocks - A Classification and Glossary of Terms. Cambridge University Press, Cambridge.

LEAT, P. T., LUTTINEN, A. V., STOREY, B. C. & MILLAR, I. L. 2005. Sills of the Theron Mountains, Antarctica: evidence for long distance transport of mafic magmas during Gondwana break-up. In *Dyke swarms - time markers of crustal evolution; 5th International Dyke Conference (IDC-5)* (eds. Hanski, E., Mertanen, S., Ramo, T. & Vuollo, J.), Rovaniemi, Finland, Jul 31-Aug 03. Taylor & Francis, pp. 183-199.

LEBAS, M. J., LEMAITRE, R. W., STRECKEISEN, A. & ZANETTIN, B. 1986. A chemical classification of volcanic-rocks based on the Total Alkali Silica diagram. *Journal of Petrology* **27**, 3, pp. 745-750.

LEINWEBER, V. T. & JOKAT, W. 2012. The Jurassic history of the Africa–Antarctica corridor – new constraints from magnetic data on the conjugate continental margins. *Tectonophysics* **530-531**, pp. 87-101.

LEITCHENKOV, G., GUSEVA, J., GANDYUKHIN, V., GRIKUROV, G., KRISTOFFERSEN, Y., SAND, M., GOLYNSKY, A. & ALESHKOVA, N. 2008. Crustal structure and tectonic provinces of the Riiser-Larsen Sea area (East Antarctica): results of geophysical studies. *Marine Geophysical Researches* **29**, 2, pp. 135-158.

LEITCHENKOV, G. L., MILLER, H. & ZATZEPIN, E. N. 1996. Structure and Mesozoic evolution of the eastern Weddell Sea, Antarctica; history of early Gondwana break-up. In *Weddell Sea Tectonics and Gondwana Break-up* (eds. Storey, B. C., King, E. C. & Livermore, R. A.). Geological Society London, London, Special Publications, **108**, pp. 175-190.

LEMASURIER, W. E. & REX, D. C. 1983. Rates of uplift and the scale of ice level instabilities recorded by volcanic rocks in Marie Byrd Land, West Antarctica. In *Antarctic Earth Science* (eds. Oliver, R. L., James, P. R. & Jago, J. B.). Australian Academy of Science, Canberra, pp. 663-670.

LI, Z., TAINOSHO, Y., SHIRAISHI, K., OWADA, M. & KIMURA, J.-I. 2001. Geochemical characteristics of two types of early Paleozoic granitoids from the Sør Rondane Mountains, East Antarctica. *Polar Geoscience* **14**, pp. 119-138.

LI, Z., TAINOSHO, Y., KIMURA, J.-I., SHIRAISHI, K. & OWADA, M. 2003. Pan-African alkali granitoids from the Sør Rondane Mountains, East Antarctica. *Gondwana Research* **6**, 4, pp. 595-605.

LI, Z., DU, Z., YANG, S., CHEN, H., SONG, B. & LIU, D. 2006. First report of zircon SHRIMP U-Pb dating from the Dufek granite in the Sør Rondane Mountains, East Antarctica. *Journal of Zhejiang University SCIENCE A* **7**, 2, pp. 315-319.

LISKER, F., SCHÄFER, T. & OLESCH, M. 1999. The uplift/denudation history of the Shackleton Range (Antarctica) based on fission-track analyses. *Terra Antartica* **6**, 3, pp. 345-352.

LISKER, F., VENTURA, B. & GLASMACHER, U. A. (eds.) 2009. Thermochronological Methods: From Palaeotemperature Constraints to Landscape Evolution Models. Geological Society London, London, Special Publications, **234**.

LISKER, F. & LÄUFER, A. L. 2013. The Mesozoic Victoria Basin: vanished link between Antarctica and Australia. *Geology* **41**, 10, pp. 1043-1046.

LIU, X., ZHAO, Y. & HU, J. 2013. The c. 1000-900 Ma and c. 550-500 Ma tectonothermal events in the Prince Charles Mountains-Prydz Bay region, East Antarctica, and their relations to supercontinent evolution. In *Antarctica and Supercontinent Evolution* (eds. Harley, S. L., Fitzsimons, I. C. W. & Zhao, Y.). Geological Society London, London, Special Publications, **383**, pp. 95-112.

LIVERMORE, R. A. & WOOLLETT, R. W. 1993. Seafloor spreading in the Weddell Sea and southwest Atlantic since the Late Cretaceous. *Earth and Planetary Science Letters* **117**, 3–4, pp. 475-495.

LUDWIG, K. 2008. User's Manual for Isoplot 3.6, a Geochronological Toolkit for Microsoft Excel. Berkeley Geochronology Center, Special Publication, **No. 4**, 78 pp.

MA, J. L., WEI, G. J., LIU, Y., REN, Z. Y., XU, Y. G. & YANG, Y. H. 2013. Precise measurement of stable (delta Sr-88/86) and radiogenic (Sr-87/Sr-86) strontium isotope ratios in geological standard reference materials using MC-ICP-MS. *Chinese Science Bulletin* **58**, 25, pp. 3111-3118.

MARSCHALL, H. R., HAWKESWORTH, C. J. & LEAT, P. T. 2013. Mesoproterozoic subduction under the eastern edge of the Kalahari-Grunehogna Craton preceding Rodinia assembly: the Ritscherflya detrital zircon record, Ahlmannryggen (Dronning Maud Land, Antarctica). *Precambrian Research* **236**, pp. 31-45.

MARSH 1985. Ice surface and bedrock topography in Coats Land and part of Dronning Maud Land, Antarctica, from satellite imagery. *British Antarctic Survey Bulletin* **68**, pp. 19-36.

MARTIN, A. K. 2007. Gondwana breakup via double-saloon-door rifting and seafloor spreading in a backarc basin during subduction rollback. *Tectonophysics* **445**, 3–4, pp. 245-272.

MATSUOKA, N., MORIWAKI, K., IWATA, S. & HIRAKAWA, K. 1990. Ground temperature regimes and their relationship to periglacial processes in the Sør Rondane Mountains, East Antarctica. *Proceedings of the NIPR Symposium on Antarctic Geosciences* **4**, pp. 55-66.

MATSUOKA, N., THOMACHOT, C., OGUCHI, C. T., HATTA, T., ABE, M. & MATSUZAKI, H. 2006. Quaternary bedrock erosion and landscape evolution in the Sør Rondane Mountains, East Antarctica: reevaluating rates and processes. *Geomorphology* **81**, 3–4, pp. 408-420.

MCCOURT, S., ARMSTRONG, R. A., GRANTHAM, G. H. & THOMAS, R. J. 2006. Geology and evolution of the Natal belt, South Africa. *Journal of African Earth Sciences* **46**, 1–2, pp. 71-92.

MCDOUGALL, I. & HARRISON, T. M. 1999. Geochronology and Thermochronology by the $^{40}Ar/^{39}Ar$ Method. Oxford University Press, New York.

MEERT, J. G. 2003. A synopsis of events related to the assembly of eastern Gondwana. *Tectonophysics* **362**, 1–4, pp. 1-40.

MEIER, S. 1999. Paleozoic and Mesozoic tectono-thermal history of central Dronning Maud Land, East Antarctica - evidence from fission-track thermochronology. *Berichte zur Polarforschung* **337**, p. 178.

MEIER, S. & OLESCH, M. 1999. Exhumation history of central Dronning Maud Land, East Antarctica; evidence from fission-track analysis of basement apatites. In *Workshop on Geological Records of Global and Planetary Changes*, International School Earth and Planetary Sciences. Terra Antartica Reports, 3, pp. 179-182.

MEIER, S., JACOBS, J. & OLESCH, M. 2004. Tectono-thermal evolution of the continental margin of central Dronning Maud Land, East Antarctica: apatite fission-track thermochronology. In *International GeoMaud Expedition of the BGR to central Dronning Maud Land in 1995/96 - Geological Results* (ed. Paech, H.-J.). E. Schweizerbart´sche Verlagsbuchhandlung (Nägele u. Obermiller), Stuttgart, B96, **Polar Issue No. 10**, pp. 423-448.

MESHIDA, S., AZUMA, N., YUKIMATSU, A. & YAMANOUCHI, T. 1991. Meteorological data at Asuka Station, Antarctica in 1989. In *JARE Data Reports*. National Institute of Polar Research. Tokyo, No. 164.

MIETH, M. 2014. Aerogeophysical constraints for the geodynamic evolution of Dronning Maud Land, East Antarctica. PhD thesis, Faculty of Geosciences, University of Bremen, Bremen.

MIETH, M., JACOBS, J., RUPPEL, A., DAMASKE, D., LÄUFER, A. & JOKAT, W. 2014. New detailed aeromagnetic and geological data of eastern Dronning Maud Land: Implications for refining the tectonic and structural framework of Sør Rondane, East Antarctica. *Precambrian Research* **245**, pp. 174-185.

MIETH, M. & JOKAT, W. 2014. New aeromagnetic view of the geological fabric of southern Dronning Maud Land and Coats Land, East Antarctica. *Gondwana Research* **25**, 1, pp. 358-367.

MIKHALSKY, E. V., BELIATSKY, B. V., SAVVA, E. V., WETZEL, H.-U., FEDOROV, L. V., WEISER, T. & HAHNE, K. 1997. Reconnaissance geochronologic data on polymetamorphic and igneous rocks of the Humboldt Mountains, central Queen Maud Land, East Antarctica. In *The Antarctic Region: Geological Evolution and Processes* (ed. Ricci, C. A.). Terra Antarctica, Siena, pp. 45-54.

MIKHALSKY, E. V. & JACOBS, J. 2004. Orthogneisses in central Dronning Maud Land, East Antarctica: their origin and tectonic setting. In *International GeoMaud Expedition of the BGR to central Dronning Maud Land in 1995/96 - Geological Results* (ed. Paech, H.-J.). E. Schweizerbart´sche Verlagsbuchhandlung (Nägele u. Obermiller), Stuttgart, B96, **Polar Issue No. 10**, pp. 49-76.

MIKHALSKY, E. V. & SHERATON, J. W. 2011. The Rayner tectonic province of East Antarctica: compositional features and geodynamic setting. *Geotectonics* **45**, 6, pp. 496-512.

MIKOVA, J. & DENKOVA, P. 2007. Modified chromatographic separation scheme for Sr and Nd isotope analysis in geological silicate samples. *Journal of Geosciences* **52**, 3–4, pp. 221-226.

MILISENDA, C. C., LIEW, T. C., HOFMANN, A. W. & KOHLER, H. 1994. Nd isotopic mapping of the Sri Lanka basement - update, and additional constraints from Sr isotopes. *Precambrian Research* **66**, 1–4, pp. 95-110.

MORKEL, J., KRUGER, S. J. & VERMAAK, M. K. G. 2006. Characterization of clay mineral fractions in tuffisitic kimberlite breccias by X-ray diffraction. *The Journal of The South African Institute of Mining and Metallurgy* **106**, 6, pp. 397-406.

MOYES, A. B., BARTON JR., J. M. & GROENEWALD, P. B. 1993. Late Proterozoic to Early Paleozoic tectonism in Dronning Maud Land, Antarctica: supercontinental fragmentation and amalgamation. *Journal of the Geological Society* **150**, 5, pp. 833-842.

NAKANO, N., OSANAI, Y., KAMEI, A., SATISH-KUMAR, M., ADACHI, T., HOKADA, T., BABA, S. & TOYOSHIMA, T. 2013. Multiple thermal events recorded in metamorphosed carbonate

and associated rocks from the southern Austkampane region in the Sør Rondane Mountains, East Antarctica: a protracted Neoproterozoic history at the Gondwana suture zone. *Precambrian Research* **234**, pp. 161-182.

NARDI, L. V. S., FORMOSO, M. L. L., MULLER, I. F., FONTANA, E., JARVIS, K. & LAMARAO, C. 2013. Zircon/rock partition coefficients of REEs, Y, Th, U, Nb, and Ta in granitic rocks: uses for provenance and mineral exploration purposes. *Chemical Geology* **335**, pp. 1-7.

NASDALA, L., ZHANG, M., KEMPE, U., PANCZER, M., GAFT, M., ANDRUT, M. & PLÖTZE, M. 2003. Spectroscopic methods applied to zircon. In *Zircon* (eds. Hanchar, J. M. & Hoskin, P. W. O.). Mineralogical Society of America, Washington, DC, Reviews in Mineralogy & Geochemistry, **53**, pp. 427-467.

NÄSLUND, J. O. 2001. Landscape development in western and central Dronning Maud Land, East Antarctica. *Antarctic Science* **13**, 3, pp. 302-311.

NOGI, Y., NISHI, K., SEAMA, N. & FUKUDA, Y. 2004. An interpretation of the seafloor spreading history of the west Enderby Basin between initial breakup of Gondwana and anomaly C34. *Marine Geophysical Researches* **25**, 3, pp. 221-231.

NORMAN, M. D., PEARSON, N. J., SHARMA, A. & GRIFFIN, W. L. 1996. Quantitative analysis of trace elements in geological materials by laser ablation ICPMS: instrumental operating conditions and calibration values of NIST glasses. *Geostandards Newsletter* **20**, 2, pp. 247-261.

OSANAI, Y., TAKAHASHI, Y. & SAKIYAMA, T. 1988. High-grade metamorphic rocks from the central part of the Sør Rondane Mountains, East Antarctica. In *Proceedings of the NIPR Symposium on Antarctic Geosciences*. 2, p. 170.

OSANAI, Y., SHIRAISHI, K. & TAKAHASHI, Y. 1992. Geochemical characteristics of metamorphic rocks from the central Sør Rondane Mountains, East Antarctica. In *Recent Progress in Antarctic Earth Science* (eds. Yoshida, Y., Kaminuma, K. & Shiraishi, K.). Terra Scientific Publishing Company, Tokyo, pp. 17-27.

OSANAI, Y., SHIRAISHI, K., TAKAHASHI, Y., ISHIZUKA, H., MORIWAKI, K., TAINOSHO, Y., TSUCHIYA, N., SAKIYAMA, T., TOYOSHIMA, T., M., O. & KOJIMA, H. 1996a. Geological map of the Sør Rondane Mountains, Antarctica. In *Antarctic Geological Map Series, Sheet 34*. National Institute of Polar Research, Tokyo. 1:250,000.

OSANAI, Y., SHIRAISHI, K., TAKAHASHI, Y., ISHIZUKA, H., MORIWAKI, K., TAINOSHO, Y., TSUCHIYA, N., SAKIYAMA, T., TOYOSHIMA, T., OWADA, M. & KOJIMA, H. 1996b. Explanatory text of Geological Map of Brattnipene, Sør Rondane Mountains, Antarctica. In *Antarctic Geological Map Series; Sheet 34*. National Institute of Polar Research, Tokyo. pp. 1-29.

OSANAI, Y., NOGI, Y., BABA, S., NAKANO, N., ADACHI, T., HOKADA, T., TOYOSHIMA, T., OWADA, M., SATISH-KUMAR, M., KAMEI, A. & KITANO, I. 2013. Geologic evolution of the Sør Rondane Mountains, East Antarctica: collision tectonics proposed based on metamorphic processes and magnetic anomalies. *Precambrian Research* **234**, pp. 8-29.

OTSUJI, N., SATISH-KUMAR, M., KAMEI, A., TSUCHIYA, N., KAWAKAMI, T., ISHIKAWA, M. & GRANTHAM, G. H. 2013. Late-Tonian to early-Cryogenian apparent depositional ages for metacarbonate rocks from the Sør Rondane Mountains, East Antarctica. *Precambrian Research* **234**, pp. 257-278.

OWADA, M., BABA, S., LÄUFER, A., ELVEVOLD, S., SHIRAISHI, K. & JACOBS, J. 2003. Geology of eastern Muehlig-Hofmannfjella and Filchnerfjella in Dronning Maud Land, East Antarctica: a preliminary report on a Japan-Norway-Germany joint geological investigation. *Polar Geoscience* **16**, pp. 108-136.

OWADA, M., BABA, S., OSANAI, Y. & KAGAMI, H. 2008. Geochemistry of post-kinematic mafic dykes from central to eastern Dronning Maud Land, East Antarctica: evidence for a Pan-African suture in Dronning Maud Land. In *Geodynamic Evolution of East Antarctica: A Key to the East-West Gondwana Connection* (eds. Satish-Kumar, M., Motoyoshi, Y., Osanai, Y., Hiroi, Y. & Shiraishi, K.). Geological Society London, London, Special Publications, **308**, pp. 235-252.

OWADA, M., SHIMURA, T., YUHARA, M., KAMEI, A. & TSUKADA, K. 2010. Post-kinematic lamprophyre from the southwestern part of Sør Rondane Mountains, East Antarctica: constraint on

the Pan-African suture event. *Journal of Mineralogical and Petrological Sciences* **105**, 5, pp. 262-267.

OWADA, M., KAMEI, A., HORIE, K., SHIMURA, T., YUHARA, M., TSUKADA, K., OSANAI, Y. & BABA, S. 2013. Magmatic history and evolution of continental lithosphere of the Sør Rondane Mountains, eastern Dronning Maud Land, East Antarctica. *Precambrian Research* **234**, pp. 63-84.

PALME, H. & O'NEILL, H. S. C. 2003. Cosmochemical estimates of mantle composition. In *Treatise on Geochemistry* (eds. Carlson, R. W., Holland, H. D. & Turekian, K. K.). Elsevier, New York, 2, pp. 1-38.

PASSCHIER, C. W. & TROUW, R. A. J. 2005. Microtectonics. Springer, Heidelberg.

PASTEELS, P. & MICHOT, J. 1968. Nouveaux résultats géochronologiques obtenus par la méthode U-Pb sur des zircons des monts Sør-Rondane (Antarctique). *Annales de la Société Géologique de Belgique* **91**, pp. 283-303.

PASTEELS, P. & MICHOT, J. 1970. Uranium-lead radioactive dating and lead isotope study on sphene and K-feldspar in the Sør-Rondane Mountains, Dronning Maud Land, Antarctica. *Eclogae Geologicae Helvetiae* **63**, 1, pp. 239-254.

PATCHETT, P. J. & TATSUMOTO, M. 1982. Lu-Hf total-rock isochron for the eucrite meteorites. *Nature* **288**, pp. 571-574.

PATTYN, F., HUYBRECHTS, P. & DECLEIR, H. 1989. Modeling glacier fluctuations in the Sør Rondane, Dronning Maud Land, Antarctica. *Zeitschrift für Gletscherkunde und Glazialgeologie* **25**, 1, pp. 33-47.

PATTYN, F., DECLEIR, H. & HUYBRECHTS, P. 1992. Glaciation of the central part of the Sør Rondane, Antarctica: glaciological evidence. In *Recent Progress in Antarctic Earth Science* (eds. Yoshida, Y., Kaminuma, K. & Shiraishi, K.). Terra Scientific Publishing Company, Tokyo, pp. 669-678.

PAULSSON, O. & AUSTRHEIM, H. 2003. A geochronological and geochemical study of rocks from Gjelsvikfjella, Dronning Maud Land, Antarctica – implications for Mesoproterozoic correlations and assembly of Gondwana. *Precambrian Research* **125**, pp. 113-138.

PAXMAN, G. J. G., JAMIESON, S. S. R., FERRACCIOLI, F., BENTLEY, M. J., FORSBERG, R., ROSS, N., WATTS, A. B., CORR, H. F. J. & JORDAN, T. A. 2017. Uplift and tilting of the Shackleton Range in East Antarctica driven by glacial erosion and normal faulting. *Journal of Geophysical Research: Solid Earth* **122**, 3, pp. 2390–2408.

PEARCE, J. A., HARRIS, N. B. W. & TINDLE, A. G. 1984. Trace element discrimination diagrams for the tectonic interpretation of granitic rocks. *Journal of Petrology* **25**, 4, pp. 956-983.

PEATE, D. W., PEARCE, J. A., HAWKESWORTH, C. J., COLLEY, H., EDWARDS, C. M. H. & HIROSE, K. 1997. Geochemical variations in Vanuatu Arc Lavas: the role of subducted material and a variable mantle wedge composition. *Journal of Petrology* **38**, 10, pp. 1331-1358.

PETERS, M. 1989. Die Vulkanite im westlichen und mittleren Neuschwabenland, Vestfjella und Ahlmannryggen, Antarktika. Petrologie, Geochronologie, Paleomagnetismus, geotektonische Implikationen. *Berichte zur Polarforschung* **61**.

PICCIOTTO, E., DEUTSCH, S. & PASTEELS, P. 1964. Isotopic ages from the Sør Rondane Mountains, Dronning Maud Land. In *Antarctic Geology* (ed. Adie, R. J.). North Holland Publishing Company, Amsterdam, pp. 570-578.

PIN, C. & ZALDUEGUI, J. F. S. 1997. Sequential separation of light rare-earth elements, thorium and uranium by miniaturized extraction chromatography; application to isotopic analyses of silicate rocks. *Analytica Chimica Acta* **339**, 1–2, pp. 79-89.

POOLE, I., CANTRILL, D. & UTESCHER, T. 2005. A multi-proxy approach to determine Antarctic terrestrial palaeoclimate during the Late Cretaceous and Early Tertiary. *Palaeogeography, Palaeoclimatology, Palaeoecology* **222**, 1–2, pp. 95-121.

POSCHER, G. 1992. Mikrotexturelle, sedimentpetrographische und geochemische Vergleichsuntersuchungen an jungpaläozoischen Diamiktiten der Ostantarktis, präkambrischen Diamiktiten Schottlands und glazialen Sedimenten der Ostalpen. *Jahrbuch der Kaiserlich-Königlichen Geologischen Reichsanstalt* **135**, pp. 493-511.

POWELL, C. M. & PISAREVSKY, S. A. 2002. Late Neoproterozoic assembly of East Gondwana. *Geology* **30**, 1, pp. 3-6.

PRENZEL, J., LISKER, F., BALESTRIERI, M. L., LÄUFER, A. & SPIEGEL, C. 2013. The Eisenhower Range, Transantarctic Mountains:evaluation of qualitative interpretation concepts of thermochronological data. *Chemical Geology* **352**, pp. 176-187.

PRENZEL, J. 2014. Burial and exhumation of the Terra Nova Bay region, Transantarctic Mountains. PhD thesis, Faculty of Geosciences, University of Bremen, Bremen.

PRENZEL, J., LISKER, F., ELSNER, M., SCHÖNER, R., BALESTRIERI, M. L., LÄUFER, A. L., BERNER, U. & SPIEGEL, C. 2014. Burial and exhumation of the Eisenhower Range, Transantarctic Mountains, based on thermochronological, sedimentary rock maturity and petrographic constraints. *Tectonophysics* **630**, pp. 113-130.

PURDY, J. W. & JÄGER, E. 1976. K-Ar ages on rock-forming minerals from the Central Alps. *Memorie degli Istituti di Geologia e Mineralogia dell'Università di Padova*, p. 31.

RAHN, M. K., BRANDON, M. T., BATT, G. E. & GARVER, J. I. 2004. A zero-damage model for fission-track annealing in zircon. *American Mineralogist* **89**, 4, p. 473.

RAO, D. R., RASHID, S. A. & PANTHULU, G. V. C. 2000. Origin of Mg-Metatholeiites of the Schirmacher Region, East Antarctica: constraints from trace elements and Nd-Sr isotopic systematics. *Gondwana Research* **3**, pp. 91-104.

RAO, G. D., RAMANA, M. V. & SARMA, K. V. L. N. S. 1992. Tectonic development of graben over the Astrid Ridge off Dronning Maud Land. In *Recent Progress in Antarctic Earth Science* (eds. Yoshida, Y., Kaminuma, K. & Shiraishi, K.). Terra Scientific Publishing Company, Tokyo, pp. 639-647.

RAVIKANT, V., BHASKAR RAO, Y. J. & GOPALAN, K. 2004. Schirmacher Oasis as an extension of the Neoproterozoic East African Orogen into Antarctica: new Sm-Nd isochron age constraints. *Journal of Geology* **112**, 5, pp. 607-616.

RAVIKANT, V. 2006. Sm-Nd Isotopic evidence for Late Mesoproterozoic metamorphic relics in the East African Orogen from the Schirmacher Oasis, East Antarctica. *Journal of Geology* **114**, pp. 615-625.

RAVIKANT, V., LAUX, J. H. & PIMENTEL, M. M. 2007. Sm-Nd and U-Pb isotopic constraints for crustal evolution during Late Neoproterozoic from rocks of the Schirmacher Oasis, East Antarctica: geodynamic development coeval with the East African Orogeny. In *10th International Symposium on Antarctic Earth Sciences* (eds. Cooper, A. K., Raymond, C. R. & 10th ISAES Editorial Team), Santa Barbara. USGS, Antarctica: a keystone in a changing world – Online proceedings for the 10th International Symposium on Antarctic Earth Sciences Open File Report 2007-1047.

READING, A. M. 2006. The seismic structure of Precambrian and early Palaeozoic terranes in the Lambert Glacier region, East Antarctica. *Earth and Planetary Science Letters* **244**, 1–2, pp. 44-57.

REEVES, C. V. 2014. The position of Madagascar within Gondwana and its movements during Gondwana dispersal. *Journal of African Earth Sciences* **94**, pp. 45-57.

REEVES, C. V., TEASDALE, J. P. & MAHANJANE, E. S. 2016. Insight into the eastern margin of Africa from a new tectonic model of the Indian Ocean. In *Transform Margins: Development, Controls and Petroleum Systems* (eds. Nemčok, M., Rybár, S., Sinha, S. T., Hermeston, S. A. & Ledvényiová, L.). Geological Society London, London, Special Publications, **431**, pp. 299-322.

REINERS, P. W., SPELL, T. L., NICOLESCU, S. & ZANETTI, K. A. 2004. Zircon (U-Th)/He thermochronometry: He diffusion and comparisons with $^{40}Ar/^{39}Ar$ dating. *Geochimica et Cosmochimica Acta* **68**, 8, pp. 1857-1887.

REINERS, P. W. 2005. Zircon (U-Th)/He thermochronometry. In *Low-Temperature Thermochronology: Techniques, Interpretations, and Applications* (eds. Reiners, P. & Ehlers, T. A.). Mineralogical Society of America, Geochemical Society, Chantilly, 58, **1**, pp. 151-179.

REINERS, P. W. & EHLERS, T. A. 2005. Low-Temperature Thermochronology: Techniques, Interpretations, and Applications. The Minerological Society of America, Chantilly, Reviews in Mineralogy and Geochemistry, **58**.

REUBI, O. & BLUNDY, J. 2009. A dearth of intermediate melts at subduction zone volcanoes and the petrogenesis of arc andesites. *Nature* **461**, pp. 1269-1273.

RIEDEL, S. 2009. Airborne-based geophysical investigation in Dronning Maud Land, Antarctica. PhD thesis, Faculty of Geosciences, University of Bremen, Bremen.

RIEDEL, S., JACOBS, J. & JOKAT, W. 2013. Interpretation of new regional aeromagnetic data over Dronning Maud Land (East Antarctica). *Tectonophysics* **585**, pp. 161-171.

RILEY, T. R. & KNIGHT, K. B. 2001. Review. Age of pre-break-up Gondwana magmatism. *Antarctic Science* **13**, 2, pp. 99-110.

RING, U., BRANDON, M. T., WILLETT, S. D. & LISTER, G. S. 1999. Exhumation processes. In *Exhumation Processes: Normal Faulting, Ductile Flow and Erosion* (eds. Ring, U., Brandon, M. T., Lister, G. S. & Willett, S. D.). Geological Society London, London, Special Publications, **154**, pp. 1-27.

ROBERT, C. & MAILLOT, H. 1990. Paleoenvironments in the Weddell Sea area and Antarctic climates, as deduced from clay mineral associations and geochemical data, ODP Leg 113. In *Proceedings of the Oceanic Drilling Programme, Scientific Results* (eds. Barker, P. F., Kennett, J. P. & al). Integrated Ocean Drilling Program, Texas, 113, pp. 51-70.

ROGENHAGEN, J., JOKAT, W., HINZ, K. & KRISTOFFERSEN, Y. 2005. Improved seismic stratigraphy of the Mesozoic Weddell Sea. *Marine Geophysical Researches* **25**, 3–4, pp. 265-282.

ROSA, D. R. N., FINCH, A. A., ANDERSEN, T. & INVERNO, C. M. C. 2009. U-Pb geochronology and Hf isotope ratios of magmatic zircons from the Iberian Pyrite Belt. *Mineralogy and Petrology* **95**, pp. 47-69.

RUBATTO, D. & GEBAUER, D. 2000. Use of cathodoluminescence for U-Pb zircon dating by ion microprobe: some examples from the Western Alps. In *Cathodoluminescence in Geosciences* (eds. Pagel, M., Barbin, V., Blanc, P. & Ohnenstetter, D.). Springer-Verlag, Heidelberg, pp. 373-400.

RUPPEL, A. 2012. Structural evolution of the Main Shear Zone in Sør Rondane, East Antarctica. Department of Geosciences, University of Bremen. Unpublished Master Thesis.

RUPPEL, A., LÄUFER, A., JACOBS, J., ELBURG, M., KROHNE, N., DAMASKE, D. & LISKER, F. 2015. The Main Shear Zone in Sør Rondane, East Antarctica: implications for the late-Pan-African tectonic evolution of Dronning Maud Land. *Tectonics* **34**, 6, pp. 1290-1305.

SALMAN, G. & ABDULA, I. 1995. Development of the Mozambique and Ruvuma sedimentary basins, offshore Mozambique. *Sedimentary Geology* **96**, 1, pp. 7-41.

SATISH-KUMAR, M., HOKADA, T., KAWAKAMI, T. & DUNKLEY, D. J. 2008. Geosciences research in East Antarctica (0°E–60°E): present status and future perspectives. In *Geodynamic Evolution of East Antarctica: A Key to the East-West Gondwana Connection* (eds. Satish-Kumar, M., Motoyoshi, Y., Osanai, Y., Hiroi, Y. & Shiraishi, K.). Geological Society London, London, Special Publications, **308**, pp. 1-20.

SATISH-KUMAR, M., HOKADA, T., OWADA, M., OSANAI, Y. & SHIRAISHI, K. 2013. Neoproterozoic orogens amalgamating East Gondwana: did they cross each other? *Precambrian Research* **234**, pp. 1-7.

SCHÄFER, T. 1998. Thermo-tektonische Entwicklung von Oates Land und der Shackleton Range (Antarktis) basierend auf Spaltspur-Analysen. *Berichte zur Polarforschung* **263**, p. 107.

SCHERER, E. E., MUNKER, C. & MEZGER, K. 2007. The Lu-Hf systematics of meteorites: consistent or not? *Geochimica et Cosmochimica Acta* **71**, 15, p. A888.

SCHNELLBACH, U. 1992. Neue Erkenntnisse der Hebungsgeschichte des Transantarktischen Gebirges mittels Spaltspurenanalyse. PhD thesis, Fachbereich Geowissenschaften, Universität Bremen, Bremen.

SHACKLETON, R. M. 1996. The final collision zone between East and West Gondwana: where is it? *Journal of African Earth Sciences* **23**, 3, pp. 271-287.

SHERVAIS, J. W. 1982. Ti-V plots and the petrogenesis of modern and ophiolitic lavas. *Earth and Planetary Science Letters* **59**, 1, pp. 101-118.

SHIRAISHI, K. & KAGAMI, H. 1992. Sm-Nd and Rb-Sr ages of metamorphic rocks from the Sør Rondane Mountains, East Antarctica. In *Recent Progress in Antarctic Earth Science* (eds. Yoshida, Y., Kaminuma, K. & Shiraishi, K.). Terra Scientific Publishing Company, Tokyo, pp. 29-35.

SHIRAISHI, K., OSANAI, Y., TAINOSHO, Y., TAKAHASHI, K., TSUCHIYA, N., KOJIMA, S., YANAI, K. & MORIWAKI, K. 1992a. Widerøefjellet. In *Antarctic Geological Map Series; Sheet 32* National Polar Institute, Tokyo. 1:100,000.

SHIRAISHI, K., OSANAI, Y., TAINOSHO, Y., TAKAHASHI, Y., TSUCHIYA, N., KOJIMA, S., YANAI, K. & MORIWAKI, K. 1992b. Explanatory text of Geological Map of Widerøefjellet, Sør Rondane Mountains, Antarctica. In *Antarctic Geological Map Series*. National Institute of Polar Research, Tokyo. pp. 1-28.

SHIRAISHI, K., ELLIS, D. J., HIROI, Y., FANNING, C. M., MOTOYOSHI, Y. & NAKAI, Y. 1994. Cambrian orogenic belt in East Antarctica and Sri Lanka: implications for Gondwana assembly. *The Journal of Geology* **102**, 1, pp. 47-65.

SHIRAISHI, K., OSANAI, Y., ISHIZUKA, H. & ASAMI, M. 1997. Geological map of the Sør Rondane Mountains. In *Antarctic Geological Map Series; Sheet 35*. National Institute of Polar Research, Tokyo. 1:250,00.

SHIRAISHI, K., HOKADA, T., FANNING, C., MISAWA, K. & MOTOYOSHI, Y. 2003. Timing of thermal events in eastern Dronning Maud Land, East Antarctica. *Polar Geoscience* **16**, pp. 76-99.

SHIRAISHI, K., DUNKLEY, D. J., HOKADA, T., FANNING, C. M., KAGAMI, H. & HAMAMOTO, T. 2008. Geochronological constraints on the Late Proterozoic to Cambrian crustal evolution of eastern Dronning Maud Land, East Antarctica: a synthesis of SHRIMP U-Pb age and Nd model age data. In *Geodynamic Evolution of East Antarctica: A Key to the East-West Gondwana Connection* (eds. Satish-Kumar, M., Motoyoshi, Y., Osanai, Y., Hiroi, Y. & Shiraishi, K.). Geological Society London, London, Special Publications, **308**, pp. 21-67.

SHUSTER, D. L., FLOWERS, R. M. & FARLEY, K. A. 2006. The influence of natural radiation damage on helium diffusion kinetics in apatite. *Earth and Planetary Science Letters* **249**, 3–4, pp. 148-161.

SINTON, J. M., FORD, L. L., CHAPPELL, B. & MCCULLOCH, M. T. 2003. Magma genesis and mantle heterogeneity in the Manus back-arc basin, Papua New Guinea. *Journal of Petrology* **44**, 1, pp. 159-195.

SKIDMORE, M. J. & CLARKSON, P. D. 1972. Physiography and glacial geomorphology of the Shackleton Range. *British Antarctic Survey Bulletin* **30**, pp. 69-80.

SLAMA, J., KOSLER, J., CONDON, D. J., CROWLEY, J. L., GERDES, A., HANCHAR, J. M., HORSTWOOD, M. S. A., MORRIS, G. A., NASDALA, L., NORBERG, N., SCHALTEGGER, U., SCHOENE, B., TUBRETT, M. N. & WHITEHOUSE, M. J. 2008. Plesovice zircon - a new natural reference material for U-Pb and Hf isotopic microanalysis. *Chemical Geology* **249**, 1–2, pp. 1-35.

SOBEL, E. R. & SEWARD, D. 2010. Influence of etching conditions on apatite fission-track etch pit diameter. *Chemical Geology* **271**, 1–2, pp. 59-69.

SÖDERLUND, U., PATCHETT, J. P., VERVOORT, J. D. & ISACHSEN, C. E. 2004. The Lu-176 decay constant determined by Lu-Hf and U-Pb isotope systematics of Precambrian mafic intrusions. *Earth and Planetary Science Letters* **219**, 3–4, pp. 311-324.

SOLLI, K., KUVAAS, B., KRISTOFFERSEN, Y., LEITCHENKOV, G., GUSEVA, J. & GANDJUKHIN, V. 2007. Seismic morphology and distribution of inferred glaciomarine deposits along the East Antarctic continental margin, 20°E–60°E. *Marine Geology* **237**, 3–4, pp. 207-223.

SORBADERE, F., SCHIANO, P., MÉTRICH, N. & BERTAGNINI, A. 2013. Small-scale coexistence of island-arc- and enriched-MORB-type basalts in the central Vanuatu arc. *Contributions to Mineralogy and Petrology* **166**, 5, pp. 1305-1321.

SPAETH, G., HOTTEN, R., PETERS, M. & TECHMER, K. S. 1995. Mafic dykes in the Shackleton Range, Antarctica. *Polarforschung* **63**, (2/3), pp. 101-121.

SPIEGEL, C., KOHN, B., BELTON, D., BERNER, Z. & GLEADOW, A. 2009. Apatite (U-Th-Sm)/He thermochronology of rapidly cooled samples: the effect of He implantation. *Earth and Planetary Science Letters* **285**, 1–2, pp. 105-114.

STACEY, J. S. & KRAMERS, J. D. 1975. Approximation of terrestrial lead isotope evolution by a two-stage model. *Earth and Planetary Science Letters* **26**, 2, pp. 207-221.

STEPHENSON, P. J. 1966. Geology, 1. Theron Mountains, Shackleton Range and Whichaway Nunataks (with a section on paleomagmatism of the dolerite intrusions by D.J. Blundell). The Trans-Antarctic Expedition Committee, London, Scientific Reports, **8**, 79 pp.

STERN, R. J. 1994. Arc-assembly and continental collision in the Neoproterozoic African Orogen: implications for the consolidation of Gondwanaland. *Annual Review of Earth and Planetary Sciences* **22**, pp. 319-351.

STERN, R. J. 2001. A new isotopic and trace-element standard for the ion-microprobe: preliminary thermal ionisation mass spectrometry (TIMS) U-Pb and electron microprobe data, current research 2001-F1. *Geological Survey of Canada*, pp. 1-11.

STUDINGER, M. & MILLER, H. 1999. Crustal structure of the Filchner-Ronne Shelf and Coats Land, Antarctica, from gravity and magnetic data: implications for the breakup of Gondwana. *Journal of Geophysical Research* **104**, B9, pp. 20,379-394.

SUDA, Y., KAWANO, Y., YAXLEY, G., KORENAGA, H. & HIROI, Y. 2008. Magmatic evolution and tectonic setting of metabasites from Lützow-Holm Complex, Antarctica. In *Geodynamic Evolution of East Antarctica: A Key to the East-West Gondwana Connection* (eds. Satish-Kumar, M., Motoyoshi, Y., Osanai, Y., Hiroi, Y. & Shiraishi, K.). Geological Society London, London, Special Publications, **308**, pp. 211-233.

SUGANUMA, Y., MIURA, H., ZONDERVAN, A. & OKUNO, J. I. 2014. East Antarctic deglaciation and the link to global cooling during the Quaternary: evidence from glacial geomorphology and ^{10}Be surface exposure dating of the Sør Rondane Mountains, Dronning Maud Land. *Quaternary Science Reviews* **97**, pp. 102-120.

SUGDEN, D. E., DENTON, G. H. & MARCHANT, D. R. 1995. Landscape evolution of the dry valleys, Transantarctic Mountains; tectonic implications. *Journal of Geophysical Research* **100**, B6, pp. 9949-9967.

SUGDEN, D. E., FOGWILL, C. J., HEIN, A. S., STUART, F. M., KERR, A. R. & KUBIK, P. W. 2014. Emergence of the Shackleton Range from beneath the Antarctic Ice Sheet due to glacial erosion. *Geomorphology* **208**, pp. 190-199.

SUKEGAWA, Y. & YAMANOUCHI, T. 1993. Meteorological data at Asuka Station, Antarctica in 1991. In *JARE Data Reports*. National Institute of Polar Research. Tokyo, No. 190.

SUN, S. S. & MCDONOUGH, W. F. 1989. Chemical and isotopic systematics of oceanic basalts; implications for mantle composition and processes. In *Magmatism in the Ocean Basins* (eds. Saunders, A. D. & Norry, M. J.). Geological Society London, London, Special Publications, **42**, pp. 313-345.

TAINOSHO, Y., TAKAHASHI, Y., ARAKAWA, Y., OSANAI, Y., TSUCHIYA, N., SAKIYAMA, T. & OWADA, M. 1992. Petrochemical character and Rb-Sr isotopic investigation of the granitic rocks from the Sør Rondane Mountains, East Antarcitca. In *Recent Progress in Antarctic Earth Science* (eds. Yoshida, Y., Kaminuma, K. & Shiraishi, K.). Terra Scientific Publishing Company, Tokyo, pp. 45-54.

TAKIGAMI, Y., KANEOKA, I. & FUNAKI, M. 1987. Age and paleomagnetic studies for intrusive and metamorphic rocks from the Sør Rondane Mountains, Antarctica. In *Proceedings of the NIPR Symposium on Antarctic Geosciences*. 1, pp. 169-177.

TAKIGAMI, Y. & FUNAKI, M. 1991. ^{40}Ar-^{39}Ar and K-Ar ages for igneous and metamorphic rocks from the Sør Rondane Mountains, East Antarctica. In *Proceedings of the NIPR Symposium on Antarctic Geosciences*. 5, pp. 122-135.

TANAKA, T., TOGASHI, S., KAMIOKA, H., AMAKAWA, H., KAGAMI, H., HAMAMOTO, T., YUHARA, M., ORIHASHI, Y., YONEDA, S., SHIMIZU, H., KUNIMARU, T., TAKAHASHI, K., YANAGI, T., NAKANO, T., FUJIMAKI, H., SHINJO, R., ASAHARA, Y., TANIMIZU, M. & DRAGUSANU, C. 2000. JNdi-1: a

neodymium isotopic reference in consistency with LaJolla neodymium. *Chemical Geology* **168**, 3–4, pp. 279-281.

TAYLOR, S. R. & MCLENNAN, S. M. 1985. The Continental Crust: Its Composition and Evolution. Blackwell Publishing Company, Carlton.

TESSENSOHN, F., KLEINSCHMIDT, G. & BUGGISCH, W. 1999a. Permo-Carboniferous glacial beds in the Shackleton Range. *Terra Antartica* **6**, 3, pp. 337-344.

TESSENSOHN, F., KLEINSCHMIDT, G., TALARICO, F., BUGGISCH, W., BROMMER, A., HENJES-KUNST, F., KRONER, U., MILLAR, I. L. & ZEH, A. 1999b. Ross-Age amalgamation of East and West Gondwana: evidence from the Shackleton Range, Antarctica. *Terra Antartica* **6**, 3, pp. 317-325.

THIRLWALL, M. F. & ANCZKIEWICZ, R. 2004. Multidynamic isotope ratio analysis using MC-ICP-MS and the causes of secular drift in Hf, Nd and Pb isotope ratios. *International Journal of Mass Spectrometry* **235**, pp. 59-81.

THORN, V. C. & DECONTO, R. 2006. Antarctic climate at the Eocene/Oligocene boundary – climate model sensitivity to high latitude vegetation type and comparisons with the palaeobotanical record. *Palaeogeography, Palaeoclimatology, Palaeoecology* **231**, 1–2, pp. 134-157.

TOYOSHIMA, T., OWADA, M. & SHIRAISHI, K. 1995. Structural evolution of metamorphic and intrusive rocks from the central part of the Sør Rondane Mountains, East Antarctica. In *Proceedings of the NIPR Symposium on Antarctic Geosciences*. 8, pp. 75-97.

TOYOSHIMA, T., OSANAI, Y., BABA, S., HOKADA, T., NAKANO, N., ADACHI, T., OTSUBO, M., ISHIKAWA, M. & NOGI, Y. 2013. Sinistral transpressional and extensional tectonics in Dronning Maud Land, East Antarctica, including the Sør Rondane Mountains. *Precambrian Research* **234**, pp. 30-46.

TRAIL, D., WATSON, E. B. & TAILBY, N. D. 2012. Ce and Eu anomalies in zircon as proxies for the oxidation state of magmas. *Geochimica et Cosmochimica Acta* **97**, pp. 70-87.

VAN ACHTERBERGH, E., RYAN, C. G., JACKSON, S. E. & GRIFFIN, W. L. 2001. Appendix 3, data reduction software for LA-ICP-MS. In *LA-ICP-MS in the Earth Sciences* (ed. Sylvester, P. J.). Mineralogical Association of Canada, Volume 29, pp. 239-243.

VAN AUTENBOER, T. 1964. The geomorphology and glacial geology of the Sør Rondane, Dronning Maud Land, Antarctica. *Medelingen van de Koninklijke Vlaamse Academie voor Wetenschappen, Letteren en Schone Kunsten van Belgie* **24**, 8, p. 91.

VAN AUTENBOER, T., MICHOT, J. & PICCIOTTO, E. 1964. Outline of the geology and petrology of the Sør-Rondane Mountains, Dronning Maud Land. In *Antarctic Geology* (ed. Adie, R. J.). North Holland Publishing Company, Amsterdam, pp. 501-514.

VAN AUTENBOER, T. & DECLEIR, H. 1978. Glacier discharge in the Sør-Rondane, a contribution to the mass balance of Dronning Maud Land, Antarctica. *Zeitschrift für Gletscherkunde und Glazialgeologie* **14**, pp. 1-16.

VAN LEEUWEN, T., ALLEN, C. M., KADARUSMAN, A., ELBURG, M., MICHAEL PALIN, J., MUHARDJO & SUWIJANTO 2007. Petrologic, isotopic, and radiometric age constraints on the origin and tectonic history of the Malino Metamorphic Complex, NW Sulawesi, Indonesia. *Journal of Asian Earth Sciences* **29**, 5–6, pp. 751-777.

VEEVERS, J. J. 1988. Gondwana facies started when Gondwanaland merged in Pangea. *Geology* **16**, 8, pp. 732-734.

VEEVERS, J. J. & POWELL, C. M. 1994. Permian-Triassic Pangean Basins and Foldbelts along the Panthalassan Margin of Gondwanaland. Geological Society of America, Boulder, CO, United States, Memoir, **184**.

VEEVERS, J. J. & TEWARI, R. C. 1995. Gondwana Master Basin of Peninsular India: Between Tethys and the Interior of the Gondwanaland Province of Pangea. Geological Society of America, Boulder, CO, United States, Memoir, **187**.

VEEVERS, J. J. 2012. Reconstructions before rifting and drifting reveal the geological connections between Antarctica and its conjugates in Gondwanaland. *Earth-Science Reviews* **111**, 3–4, pp. 249-318.

VERMEESCH, P. 2009. RadialPlotter: a Java application for fission track, luminescence and other radial plots. *Radiation Measurements* **44**, 4, pp. 409-410.

VERMEESCH, P. 2010. HelioPlot, and the treatment of overdispersed (U-Th-Sm)/He data. *Chemical Geology* **271**, 3–4, pp. 108-111.

VERVOORT, J. D., PATCHETT, P. J., SÖDERLUND, U. & BAKER, M. 2004. Isotopic composition of Yb and the determination of Lu concentrations and Lu/Hf ratios by isotope dilution using MC-ICPMS. *Geochemistry, Geophysics, Geosystems* **5**, 11, pp. 1-15.

VISSER, J. N. J. 1987. The palaeogeography of part of southwestern Gondwana during the Permo-Carboniferous glaciation. *Palaeogeography, Palaeoclimatology, Palaeoecology* **61**, pp. 205-219.

WAGNER, G. A. 1972. The geological interpretation of fission track ages. *Transactions of the American Nuclear Society* **15**, p. 117.

WHALEN, J. B., CURRIE, K. L. & CHAPPELL, B. W. 1987. A-type granites: geochemical characteristics, discrimination and petrogenesis. *Contributions to Mineralogy and Petrology* **95**, 4, pp. 407-419.

WIEDENBECK, M., P., A., CORFU, F., GRIFFIN, W. L., MEIER, M., OBERLI, F., VONQUADT, A., RODDICK, J. C. & SPEIGEL, W. 1995. Tree natural zircon standards for U-Th-Pb, Lu-Hf, trace-element and REE analyses. *Geostandards Newsletter* **19**, 1, pp. 1-23.

WILDMAN, M., BROWN, R., WATKINS, R., CARTER, A., GLEADOW, A. & SUMMERFIELD, M. 2015. Post break-up tectonic inversion across the southwestern cape of South Africa: new insights from apatite and zircon fission track thermochronometry. *Tectonophysics* **654**, pp. 30-55.

WILL, T. M., ZEH, A., GERDES, A., FRIMMEL, H. E., MILLAR, I. L. & SCHMÄDICKE, E. 2009. Paleoproterozoic to Paleozoic magmatic and metamorphic events in the Shackleton Range, East Antarctica: constraints from zircon and monazite dating, and implications for the amalgamation of Gondwana. *Precambrian Research* **172**, 1–2, pp. 25-45.

WILLBOLD, M., HEGNER, E., KLEINSCHRODT, R., STOSCH, H. G., KEHELPANNALA, K. V. W. & DULSKI, P. 2004. Geochemical evidence for a Neoproterozoic magmatic continental margin in Sri Lanka – relevance for the Rodinia-Gondwana supercontinent cycle. *Precambrian Research* **130**, 185-198.

WILSON, D. S., JAMIESON, S. S. R., BARRETT, P. J., LEITCHENKOV, G., GOHL, K. & LARTER, R. D. 2012. Antarctic topography at the Eocene–Oligocene boundary. *Palaeogeography, Palaeoclimatology, Palaeoecology* **335–336**, pp. 24-34.

WOLF, R. A., FARLEY, K. A. & SILVER, L. T. 1996. Helium diffusion and low-temperature thermochronometry of apatite. *Geochimica et Cosmochimica Acta* **60**, 21, pp. 4231-4240.

WOODHEAD, J. D. & HERGT, J. M. 2005. A preliminary appraisal of seven natural zircon reference materials for in situ Hf isotope determination. *Geostandards and Geoanalytical Research* **29**, 2, pp. 183-195.

YAMADA, R., TAGAMI, T., NISHIMURA, S. & ITO, H. 1995. Annealing kinetics of fission tracks in zircon: an experimental study. *Chemical Geology (Isotope Geoscience Section)* **122**, 1–4, pp. 249-258.

YAMADA, R., MURAKAMI, M. & TAGAMI, T. 2007. Statistical modelling of annealing kinetics of fission tracks in zircon; reassessment of laboratory experiments. *Chemical Geology* **236**, 1, pp. 75-91.

YAMANOUCHI, T., SHIBUYA, K. & SAKAI, R. 1988. Meteorological data at Asuka Camp, Antarctica in 1987. In *JARE Data Reports*. National Institute of Polar Research. Tokyo, No. 140.

YOGODZINSKI, G. M., LEES, J. M., CHURIKOVA, T. G., DORENDORF, F., WOERNER, G. & VOLYNETS, O. N. 2001. Geochemical evidence for the melting of subducting oceanic lithosphere at plate edges. *Nature* **409**, pp. 500-504.

YOSHIDA, M., FUNAKI, M. & PIYADASA, W. V. 1992. Proterozoic to Mesozoic East Gondwana: the juxtaposition of India, Sri Lanka and Antarctica. *Tectonics* **11**, 2, pp. 381-391.

YUAN, H. L., GAO, S., DAI, M. N., ZONG, C. L., GUNTHER, D., FONTAINE, G. H., LIU, X. M. & DIWU, C. 2008. Simultaneous determinations of U-Pb age, Hf isotopes and trace element

compositions of zircon by excimer laser-ablation quadrupole and multiple-collector ICP-MS. *Chemical Geology* **247**, pp. 110-118.

ZHANG, X., LUTTINEN, A. V., ELLIOT, D. H., LARSSON, K. & FOLAND, K. A. 2003. Early stages of Gondwana breakup: the $^{40}Ar/^{39}Ar$ geochronology of Jurassic basaltic rocks from western Dronning Maud Land, Antarctica, and implications for the timing of magmatic and hydrothermal events. *Journal of Geophysical Research* **108**, B9, p. 2449.

Appendix

A. Publication List

2012

Lucka, N. & Lisker, F. 2012. Mesozoic landscape development of Dronning Maud Land. Proceedings of the 35th meeting of the Deutsche Gesellschaft für Polarforschung, Jena, Germany. 4th-5th May 2012, p. 24-25.

2013

Elburg M. A., Andersen T., Jacobs J., Läufer A., Ruppel A. S., Lucka N, & Damaske D. 2013. Geochronological and geochemical constraints on the position of the Sør Rondane Mountains within East Antarctica. Geophysical Research Abstracts, Vol. 15, EGU2013-2155-1, 2013, EGU General Assembly 2013.

Lucka N., Lisker F., Läufer A. & Spiegel C. 2013. From basin to mountains: the uplift of the Shackleton Range. In: Pfeiffer EM, Kassens H, Scheinert M, Tiedemann R, Members of the DGP Advisory Board (eds.), Changing Polar Regions, 25th International Congress on Polar Research, 17th-22nd March, Hamburg, Germany, Berichte zur Polar- und Meeresforschung, 659, 2013, 106.

Lucka N., Lisker F., Spiegel C. & Läufer A. 2013. Exhumation of the Shackleton Range. Geophysical Research Abstracts, Vol. 15, EGU2013-7178, 2013, EGU General Assembly 2013.

Jacobs J., Läufer A., Clark C., Kleinhanns I., Elburg M. A. ., Ruppel A. S., Estrada S., Damaske D., Jokat W., Riedel S. & Lucka N. 2013. Neoproterozoic/Lower Paleozoic geodynamic evolution of Dronning Maud Land: integrating geology and geophysics. Geophysical Research Abstracts, Vol. 15, EGU2013-9188, 2013, EGU General Assembly 2013.

Jacobs J., Läufer A., Clark C., Kleinhanns I., Elburg M.A., Ruppel A.S., Estrada S., Damaske D., Jokat W., Riedel S. & Lucka N. 2013. Neoproterozoic/Lower Paleozoic geodynamic evolution of Dronning Maud Land: integrating geology and geophysics. In: Pfeiffer EM, Kassens H, Scheinert M, Tiedemann R, Members of the DGP Advisory Board (eds), Changing Polar Regions, 25th International Congress on Polar Research, 17th-22nd March, Hamburg, Germany, Berichte zur Polar- und Meeresforschung 659, 2013, 82-83.

Ruppel A.S., Läufer A., Lisker F., Jacobs J., Elburg M.A., Damaske D. & Lucka N. 2013. The Main Shear Zone in Sør Rondane: a key feature for the reconstruction of the geodynamic evolution of East Antarctica. Geophysical Research Abstracts, Vol. 15, EGU2013-9917, 2013, EGU General Assembly 2013.

Ruppel A.S., Läufer A., Lisker F., Jacobs J., Elburg M.A., Damaske D. & Lucka N. 2013. New constraints on the structural evoplution of East Antarctica: the Main Shear Zone of Sør Rondane, eastern Dronning Maud Land. In: Pfeiffer EM, Kassens H, Scheinert M, Tiedemann R, Members of the DGP Advisory Board (eds), Changing Polar Regions, 25th International Congress on Polar Research, 17th-22nd March, Hamburg, Germany, Berichte zur Polar- und Meeresforschung, 659, 2013, 145.

2014

Lucka, N., Lisker, F., Läufer, A. & Spiegel,C. 2014. The evolution of an Antarctic landscape during Gondwana breakup–an example from the Shackleton Range. Proceedings of the 37th Meeting of the Deutsche Gesellschaft für Polarforschung, Hannover, Germany. 8th-9th May 2014, p. 32-33.

Ruppel, A. S., Läufer, A., Lisker, F., Jacobs, J., Elburg, M.A., Damaske, D. & Lucka, N.. 2014. Combined structural, geochronological and electron microprobe analyses of the Main Shear Zone in Sør Rondane, East Antarctica. Proceedings of the 37th Meeting of the Deutsche Gesellschaft für Polarforschung, Hannover, Germany. 8th-9th May 2014, p. 47-48.

Lucka, N., Lisker, F. Läufer, A. Kleinschmidt, G. & Spiegel, C. 2014. The Shackleton Range, Antarctica: a Mesozoic basin at the Panthalassan margin of Gondwana. Schriftenreihe der Deutschen Gesellschaft für Geowissenschaften 85, p. 626.

Lucka N., Lisker, F., Läufer A., & Spiegel, C. 2014. Re-interpretation of the thermal history of the Shackleton Range, Antarctica, based on Ferrar volcanoclastic rocks. THERMO.2014–14th International Conference on Thermochronology, Charmonix-Mont Blanc. 8th-14th September 2014.

Jacobs J., Elburg M.A., Läufer A., Clark C., Kleinhans I., Andersen T., Mieth M., Ruppel A. S., Damaske D., Lucka N., Estrada S. & Jokat W. 2014. Geodynamic evolution of eastern Dronning Maud Land: research highlights from an international geological-geophysical approach. Geophysical Research Abstracts, Vol. 16, EGU2014-15694, 27th April – 02nd May, 2014, EGU General Assembly 2014.

2015

Elburg, M.A., Jacobs, J., Anderson, T., Clark, C., Läufer, A., Ruppel, A.S., Krohne, N., & Damaske, D. 2015. Early Neoproterozoic metagabbro-tonalite-trondhjemite of Sør Rondane (East Antarctica): implications for supercontinent assembly. Precambrian Research, **259**, 189-206.

Krohne, N., Lisker, F., Läufer, A. ,Jacobs, J., Elburg, M.A., Ruppel, A.S., Damaske, D. & Spiegel, C. 2015. First thermochronological results from Sør Rondane, Antarctica and implications on

regional exhumation. Proceedings of the 38th meeting of the Deutsche Gesellschaft für Polarforschung, Bremerhaven, Germany. 7th-8th May 2015, p 15-16.

Ruppel, A.S., Läufer, A., Jacobs, J., Elburg, M.A., Krohne, N., Eagles, G., Mieth, M. Jokat, W., Damaske, D. & Lisker, F. 2015. Pan-African strike-slip tectonics and combined aerogeophysical data as indicator for lateral extrusion of the East African–Antarctic orogen, East Antarctica. Proceedings of the 38th meeting of the Deutsche Gesellschaft für Polarforschung, Bremerhaven, Germany. 7th-8th May 2015, p 21-22.

Lisker, F., Krohne, N., Läufer, A., Kleinschmidt, G. & Spiegel, C. 2015. The evolution of an Antarctic landscape at the Weddell Sea margin of Gondwana? An example from the Shackleton Range. Proceedings of ISAES XII - 12th International Symposium on Antarctic Earth Sciences, Goa, India. 13th-17th July 2015, p. 44-45.

Elburg, M.A., Andersen, T., Jacobs, J., Läufer, A., Le Roux, P., Ruppel, A.S., Harris, C., Krohne, N., & Damaske, D. 2015. Spatial and temporal influences on the geochemical signature of Pan-African magmatism in the Sør Rondane Mountains (East Antarctica). Proceedings of ISAES XII - 12th International Symposium on Antarctic Earth Sciences, Goa, India. 13th-17th July 2015, p. 39-40.

Ruppel A.S., Läufer, A., Jacobs, J., Elburg, M.A., Krohne, N., Eagles, G., Mieth, M., Jokat, W., Damaske, D. & Lisker, F. 2015. Pan-African strike-slip tectonics in the Sør Rondane region, Dronning Maud Land, and lateral extrusion of the East African-Antarctic Orogen. Proceedings of ISAES XII - 12th International Symposium on Antarctic Earth Sciences, Goa, India. 13th-17th July 2015, p. 43

Krohne, N., Lisker, F., Läufer, A., Kleinschmidt, G. & Spiegel, C. 2015: Die langfristige Landschaftsentwicklung der Weddell Meer-Region. In: Eva-Maria Pfeiffer, Heidemarie Kassens, Christoph Mayer, Mirko Scheinert, Ralf Tiedemann and Members of the DGP Advisory Board: Berichte zur Polar- und Meeresforschung: High latitudes and high mountains: driver of or driven by global change?, 690, 26th International Congress on Polar Research, Munich, Germany. 6th-11th September 2015, p. 88-89.

Läufer, A., Jacobs, J., Elburg, M.A., Ruppel, A.S., Kleinhanns, I., Mieth, M., Jokat, W., Estrada, S., Henjes-Kunst, F., Eagles, G., Krohne, N., Damaske, D., Clark, C., Andersen, T., & Lisker, F. 2015. Connecting geology and geophysics: the geodynamic evolution of Dronning Maud Land from Rodinia to Gondwana. In: Eva-Maria Pfeiffer, Heidemarie Kassens, Christoph Mayer, Mirko Scheinert, Ralf Tiedemann and Members of the DGP Advisory Board: Berichte zur Polar- und Meeresforschung: High latitudes and high mountains: driver of or driven by global change?,

690, 26th International Congress on Polar Research, Munich, Germany. 6th-11th September 2015, p. 95-96.

Ruppel, A. S., Läufer A., Jacobs J., Elburg M., Krohne N., Eagles G., Mieth M., Jokat W., Damaske D. & Lisker, F. 2015. Lateral extrusion at the eastern margin of the East African-Antarctic Orogen in Dronning Maud Land, Sør Rondane. In: Eva-Maria Pfeiffer, Heidemarie Kassens, Christoph Mayer, Mirko Scheinert, Ralf Tiedemann and Members of the DGP Advisory Board: Berichte zur Poar- und Meeresforschung: High latitudes and high mountains: driver of or driven by global change?, 690, 26th International Congress on Polar Research, Munich, Germany. 6th-11th September 2015, p. 135-136.

Ruppel, A., Läufer, A., Jacobs, J., Elburg, M., Krohne, N., Damaske, D. & Lisker, F. 2015. The Main Shear Zone in Sør Rondane, East Antarctica: implications for the late-Pan-African tectonic evolution of Dronning Maud Land. *Tectonics* **34**, 6, pp. 1290-1305.

2016

Elburg, M., Andersen, T., Jacobs, J., Läufer, A., Ruppel, A., Krohne, N. & Damaske, D. 2016. One hundred fifty million years of intrusive activity in the Sør Rondane Mountains (East Antarctica): implications for Gondwana assembly. *The Journal of Geology* **124**, 1, pp. 1-26.

Krohne, N., Lisker, F., Kleinschmidt, G., Klügel, A., Läufer, A., Estrada, S. & Spiegel, C. 2016. The Shackleton Range (East Antarctica): an alien block at the rim of Gondwana? *Geological Magazine*, pp. 1-24.

B. Supplementary Material: The Shackleton Range (East Antarctica): an alien block at the rim of Gondwana?

B.1. Analytical Procedures

B.1.1. Thin section microscopy

Thin sections were prepared with a standard thickness of 25µm using epoxy resin. Analysis was carried by usage of LEICA DM EP petrographic miscroscope with maximum magnification of 400×.

B.1.2. XRD measurement

Mineral powder (>2µm crystallite size) was produced by hand using an opal mortar. The powder was loaded carefully into the sample holder, preventing any surface bias on the sample. Analysis was carried out at the crystallography research group of the University of Bremen. All measurement conditions valid for the machine are written in table S2.

B.1.3. Geochemistry

For X-ray fluorescence (XRF) analysis of major and some trace elements of sample SH08, about 0.6 g of sample powder and 3.6 g lithium tetraborate were mixed and fused beads produced. Analysis was carried out at University of Hamburg / Mineralogisch-Petrographisches Institut, using a Panalytical PW 2540. Most trace element contents were determined by inductively coupled plasma-mass spectrometry (ICP-MS) using a Thermo Element2 at University of Bremen / Department of Geosciences. About 50 mg of sample powder were digested in an ultrapure-grade HF-aqua regia mixture using an Evapoclean™ system with Savillex™ beakers. The analyte solution was spiked with 2.5 ng/ml indium as internal standard and contained 40 mg/l of total dissolved solid. In order to avoid mass interferences, the middle through heavy REE and Hf were measured at high resolution (10,000), the transition metals at medium (4,000) and all other elements at low (300) resolution.

B.1.4. ^{40}Ar–^{39}Ar analysis

Samples for ^{39}Ar–^{40}Ar measurement were prepared and measured by Dr. Y. Kapusta, Actlabs, Canada. Prior irradiation in the nuclear reactor the samples were wrapped in Al-foil and loaded in alumina vial with MCA-11 flux monitors. The Ar isotope composition was measured in a Noblesse Noble Gas static mass spectrometer (NU Instrument Ltd.). The 1300ºC blank of ^{40}Ar did not exceed n*10-11 cc STP.

B.1.5. Thermochronology

B.1.5.1. Mineral separation

Common lab pre-processing procedures for achieving apatite separates includes rock-crushing and sorting methods (Jaw Breaker, Wilfey Table), heavy liquid (LST fastfloat and Diiodmethane (CH_2I_2) and magnetic separation (Frantz Magnetscheider). Optional hand picking of apatites was conducted to enhance final purity.

B.1.5.2. Fission Track analysis

AFT analysis was carried out using the external detector method following the procedures described by Gleadow (1984) and Donelick *et al.* (2005), and by the zeta calibration approach by (Hurford & Green, 1982; Hurford & Green, 1983) with dosimeter glasses IRMM 540 (De Corte *et al.*, 1998). Zeta calibration was carried out on six Durango and Fish Canyon samples. Track length and D_{par} measurements followed the recommendations of Laslett *et al.* (1982), Donelick (1993) and Donelick *et al.* (2005). User length- and D_{par} calibration was applied on four samples with known track length distribution (annealed, mixed and induced lengths).

New samples were mounted in Petropoxy 154, polished and etched in 5 mol/l HNO_3 at 20°C for 20 seconds. Already mounted samples were prepared in the 1990ies and were etched in 1.13 mol/l HNO_3 for 60s at ambient room temperatures. D_{par} measurements of the already mounted samples were calibrated after recommendations of Sobel & Seward (2010) with a calibration factor of 0.14 and by direct D_{par} comparison of four samples treated with both etching conditions.

Thermal neutron irradiations were carried out in the reactor facility of FRM II (Garching, Germany) with a nominal neutron flux of 1×10^{16} n/cm^2 for all samples except for W68, W72 and W294 where a neutron flux of 1.2×10^{16} n/cm^2 was applied. Analysis was carried out with Zeiss Axioplan microscope using 1250× magnification, dry air objectives and the FT stage program of Dumitru (1993).

B.1.5.3. (U-Th-Sm)/He analysis

Selection of suitable apatite crystals followed recommendations after Farley (2002). This implies >60µm, inclusion and crack free euhedral crystals, wrapped into pre-cleaned Pt capsules. Selection was ensued at an Olympus SZX6 microscope (max. magnification of 143.75×) via transmitted and polarized light. Crystal dimensions were measured by application of the Cell A programme (Version 3.1; Olympus soft imaging solutions GmbH).

Measurement of ^{4}He, ^{235}U, ^{232}Th and ^{148}Sm was conducted at the department of sedimentology and environmental geology of Göttingen, following their laboratory procedures (http://www.sediment.uni-goettingen.de/thermochron/index.html).

B.2. Tables and Figures

Table S 1: Sample sites and lithologies

Sample Name	Latitude	Longitude	Elevation [m]	Lithology
SH 02	-80.4267	-21.7667	1065	Meta Turbidite
SH 03	-80.4217	-21.5333	1110	Meta Turbidite
SH 05	-80.5450	-20.7667	1305	Gneiss
SH 06	-80.5367	-20.5500	1255	Gneiss
SH 07	-80.6099	-20.8811	1470	Gneiss
SH 08	-80.5183	-19.0117	1355	Rhyolitc tuff
SH 09	-80.5450	-19.6033	1335	Gneiss
SH 10	-80.6396	-20.6249	1475	Gneiss
SH 11	-80.3705	-21.9687	915	Gneiss
SH 13	-80.4550	-22.2667	1105	Meta Turbidite
SH 15	-80.3467	-24.0388	1025	Gneiss
SH 16	-80.1183	-25.6333	540	Gneiss
SH 17	-80.1233	-25.7333	720	Gneiss
SH 19	-80.2567	-25.2500	890	Gneiss
SH 21	-80.3183	-24.9832	1065	Gneiss
SH 22	-80.3483	-25.0167	1010	Gneiss
SH 23	-80.3733	-25.1000	1340	Gneiss
SH 24	-80.6967	-22.6833	1515	Meta Turbidite
SH 25	-80.7333	-23.5667	1375	Meta Turbidite
W18e	-80.7157	-24.9425	1350	Pegmatite
W53	-80.7389	-25.0009	1100	Gneiss
W68	-80.7292	-25.0029	1220	Gneiss
W72	-80.6952	-24.5920	1250	Metadiorite
W181	-80.7406	-25.5275	1210	Granite
W294	-80.3860	-30.0130	570	Gneiss

Table S 2: XRD measurement conditions

Measurement Conditions:	
Comment	Configuration=Sample Spinner. Owner=User-1. Creation date=08.11.2002 10:25:05 Goniometer=PW3050/60 (Theta/2Theta); Minimum step size 2Theta:0.001; Minimum step size Omega:0.001 Sample stage=Spinner PW3064 Diffractometer system=XPERT-PRO Measurement program=C:\PANalytical\Data
scan-axis	Gonio
starting position [°2Th.]	3
end position [°2Th.]	85
step width [°2Th.]	0.017
step time [s]	100
scan Modus	Continuous
OED mode	Scanning
OED legnth [°2Th.]	2.12
offset [°2Th.]	0
divergence slot [°]	fixed
divergence slot [°]	0.2177
sample length [mm]	10
measurement temperature [°C]	25
anode material	Cu
generator settings	45 kV. 40 mA
Goniometer radius [mm]	240
primary beam-monochromator	no
sample rotation	yes

Table S 3: XRD reflex list

Pos. [°2Th.]	Height [cts]	FWHM [°2Th.]	d-value [Å]	Rel. int.[%]
6.21	475.9	0.1338	14.2329	0.59
10.4815	898.99	0.0836	8.44022	1.12
11.6489	843.46	0.0836	7.59689	1.05
12.4855	1039.63	0.1338	7.08967	1.29
13.3239	383.02	0.1004	6.64539	0.48
13.6288	885.22	0.1171	6.49738	1.1
13.8826	1867.37	0.0669	6.37916	2.32
15.0341	559.47	0.1673	5.89307	0.69
15.8782	296.95	0.1004	5.58163	0.37
18.0002	273.95	0.1338	4.92812	0.34
18.8368	406.29	0.1506	4.71109	0.5
19.8523	203.82	0.1004	4.47235	0.25
20.8748	19942.94	0.0836	4.25552	24.76
22.0606	5843.9	0.1004	4.0294	7.25
22.5191	1151.65	0.0836	3.94839	1.43
23.0745	1482.04	0.1004	3.85459	1.84
23.5656	6936.78	0.1171	3.77537	8.61
24.1893	3136.45	0.102	3.67637	3.89
24.2944	3774.65	0.0836	3.66373	4.69
24.5928	704.84	0.0836	3.61994	0.87
25.107	993.73	0.1338	3.54697	1.23
25.4123	1359.86	0.0669	3.50504	1.69
25.6942	3202.93	0.1673	3.46723	3.98
26.6512	80553.45	0.0669	3.34485	100
26.8573	5243.43	0.0669	3.31965	6.51
27.1129	3837.12	0.1171	3.28893	4.76
27.5707	6490.1	0.184	3.23535	8.06
27.7397	6742.54	0.0502	3.21603	8.37
27.9396	15332.14	0.1171	3.19347	19.03
28.1622	3535.33	0.0816	3.16611	4.39
28.2981	2467.51	0.1004	3.15383	3.06
29.1329	962.52	0.0502	3.06532	1.19
29.3909	846.55	0.0836	3.039	1.05
29.808	7406.1	0.1338	2.99742	9.19
30.1186	3188.93	0.1338	2.96722	3.96
30.4924	2456.55	0.1171	2.93168	3.05
30.8434	2448.02	0.1673	2.89912	3.04
31.2621	1023.88	0.0836	2.86124	1.27
31.8736	368.68	0.1338	2.80773	0.46
32.3186	1002.36	0.0836	2.77008	1.24
32.9409	347.89	0.1338	2.71915	0.43
33.9531	675.63	0.1004	2.64038	0.84

Table S 3(continued)

Pos. [°2Th.]	Height [cts]	FWHM [°2Th.]	d-value [Å]	Rel. int.[%]
34.3726	1310.3	0.1171	2.60911	1.63
34.8654	1992.48	0.1338	2.57335	2.47
35.0729	1945.53	0.0669	2.55859	2.42
35.4066	2228.05	0.102	2.53315	2.77
35.5076	2293.14	0.0669	2.52826	2.85
36.5554	5972.08	0.0612	2.45613	7.41
36.663	3291.91	0.0408	2.45525	4.09
37.3906	493.19	0.1224	2.40316	0.61
37.6644	622.34	0.2448	2.38632	0.77
38.8439	1058.19	0.0816	2.31653	1.31
39.476	4630.01	0.0816	2.28088	5.75
39.5861	2328.4	0.0408	2.28044	2.89
40.2996	2636.84	0.0612	2.23615	3.27
40.4123	1415.55	0.0612	2.23572	1.76
40.9156	246.88	0.1632	2.2039	0.31
41.2529	272.09	0.1632	2.18665	0.34
41.6541	832.01	0.2856	2.16651	1.03
42.4657	5422.02	0.0816	2.12696	6.73
42.5834	2826.59	0.0408	2.12663	3.51
42.7882	811.94	0.1632	2.11167	1.01
43.6136	359.36	0.2448	2.07361	0.45
44.2011	394.52	0.204	2.0474	0.49
44.9549	914.02	0.102	2.0148	1.13
45.8043	2912.78	0.0612	1.97939	3.62
45.93	1951.15	0.0612	1.97918	2.42
47.1263	493.66	0.2856	1.92691	0.61
48.2006	864.61	0.0816	1.88644	1.07
49.2292	706.04	0.1224	1.8494	0.88
50.1493	9085.3	0.0816	1.81761	11.28
50.288	4418.25	0.0612	1.81742	5.48
50.6363	1524.99	0.102	1.80126	1.89
50.7641	1591.27	0.102	1.80149	1.98
51.1638	1265.98	0.102	1.78392	1.57
51.3106	772.67	0.0612	1.78358	0.96
52.2225	327.64	0.4896	1.75022	0.41
52.5693	285.23	0.1224	1.73949	0.35
53.2064	543.25	0.2856	1.72015	0.67
54.8858	2716.69	0.0816	1.67142	3.37
55.0311	1468.08	0.0612	1.6715	1.82
55.335	1138.8	0.0816	1.65891	1.41
55.487	596.74	0.0612	1.65884	0.74
56.5354	732.21	0.2448	1.6265	0.91

Table S 3(continued)

Pos. [°2Th.]	Height [cts]	FWHM [°2Th.]	d-value [Å]	Rel. int.[%]
57.223	141.36	0.1224	1.60858	0.18
57.953	181.09	0.3264	1.59005	0.22
58.7049	469.86	0.204	1.57146	0.58
59.9666	6707.53	0.0816	1.54138	8.33
60.1315	3505.95	0.0612	1.54136	4.35
61.4823	496.25	0.1224	1.50696	0.62
61.9711	493	0.408	1.49624	0.61
63.5869	338.36	0.3264	1.46206	0.42
64.0467	1341.85	0.0612	1.45267	1.67
64.2236	784.28	0.0816	1.44909	0.97
65.1505	680.62	0.204	1.4307	0.84
65.7947	506.29	0.0612	1.41824	0.63
66.1681	404.27	0.4896	1.41114	0.5
67.1201	280.18	0.3264	1.39342	0.35
67.7516	3895.44	0.102	1.38196	4.84
67.9454	2187.1	0.0816	1.38192	2.72
68.1505	4218.5	0.0816	1.37484	5.24
68.3332	4999.33	0.102	1.37161	6.21
68.5193	1670.12	0.0816	1.37174	2.07
69.4692	393.41	0.1224	1.35193	0.49
70.9288	360.52	0.1224	1.32765	0.45
71.9924	200.36	0.816	1.31063	0.25
73.473	1426.93	0.0816	1.28783	1.77
73.6814	875.54	0.102	1.2847	1.09
74.0577	434.25	0.3264	1.27911	0.54
74.8561	337.94	0.2448	1.26743	0.42
75.6666	1997.32	0.102	1.25586	2.48
75.8839	1128.04	0.0816	1.25591	1.4
77.6798	911.07	0.0816	1.22826	1.13
77.9011	543.31	0.102	1.22837	0.67
79.8856	1491.47	0.0816	1.1998	1.85
80.1327	881.75	0.1632	1.19672	1.09
81.1775	1098.56	0.102	1.18394	1.36
81.491	1652.66	0.1428	1.18017	2.05
81.7369	842.32	0.102	1.18017	1.05
83.8305	857.69	0.102	1.15309	1.06
84.1003	432.82	0.0816	1.15293	0.54

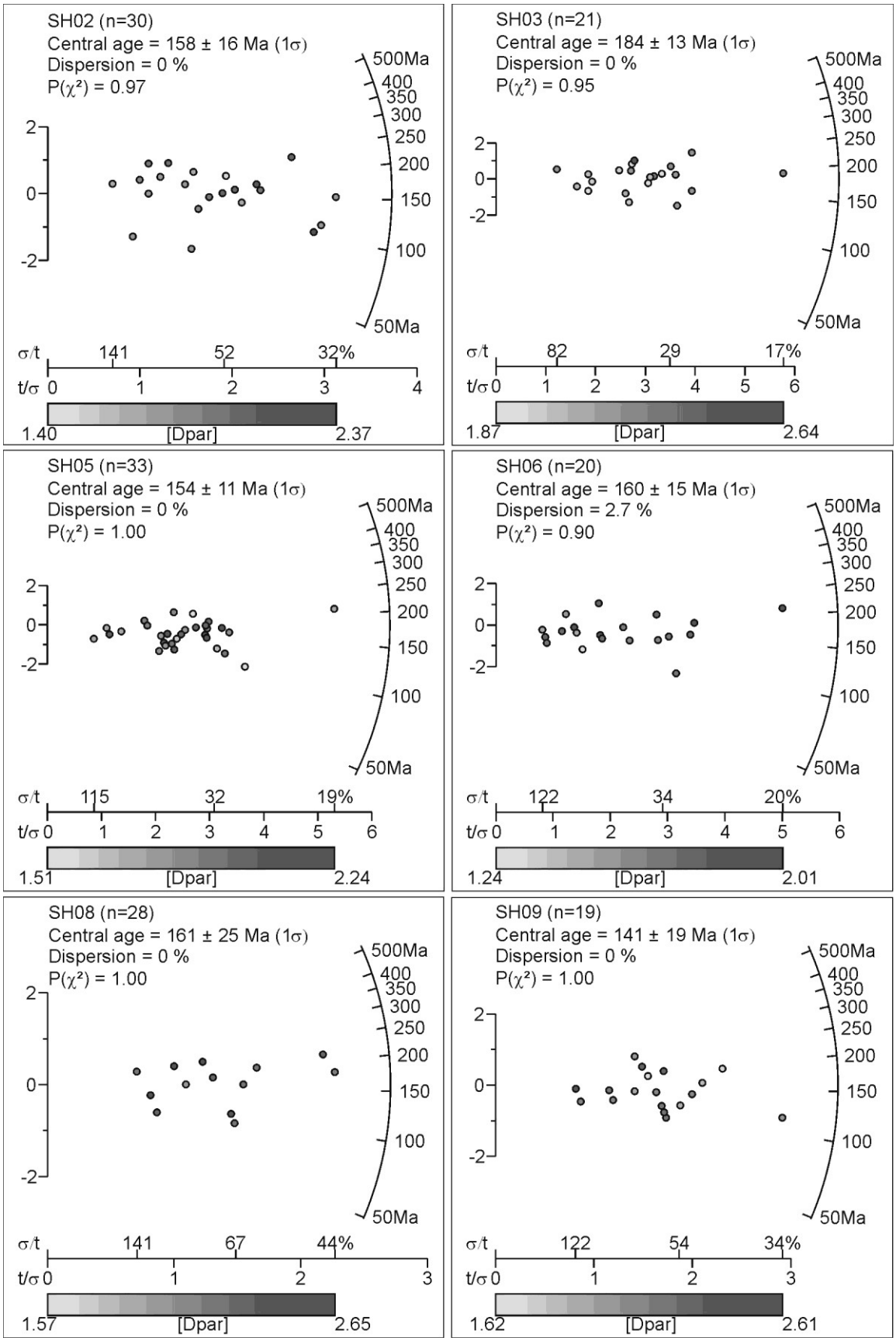

Figure S 1: Radial plots of the fission track samples. Plots were created using Radial plotter (Vermeesch, 2009). Single ages are coloured reflecting their individual D_{par} value.

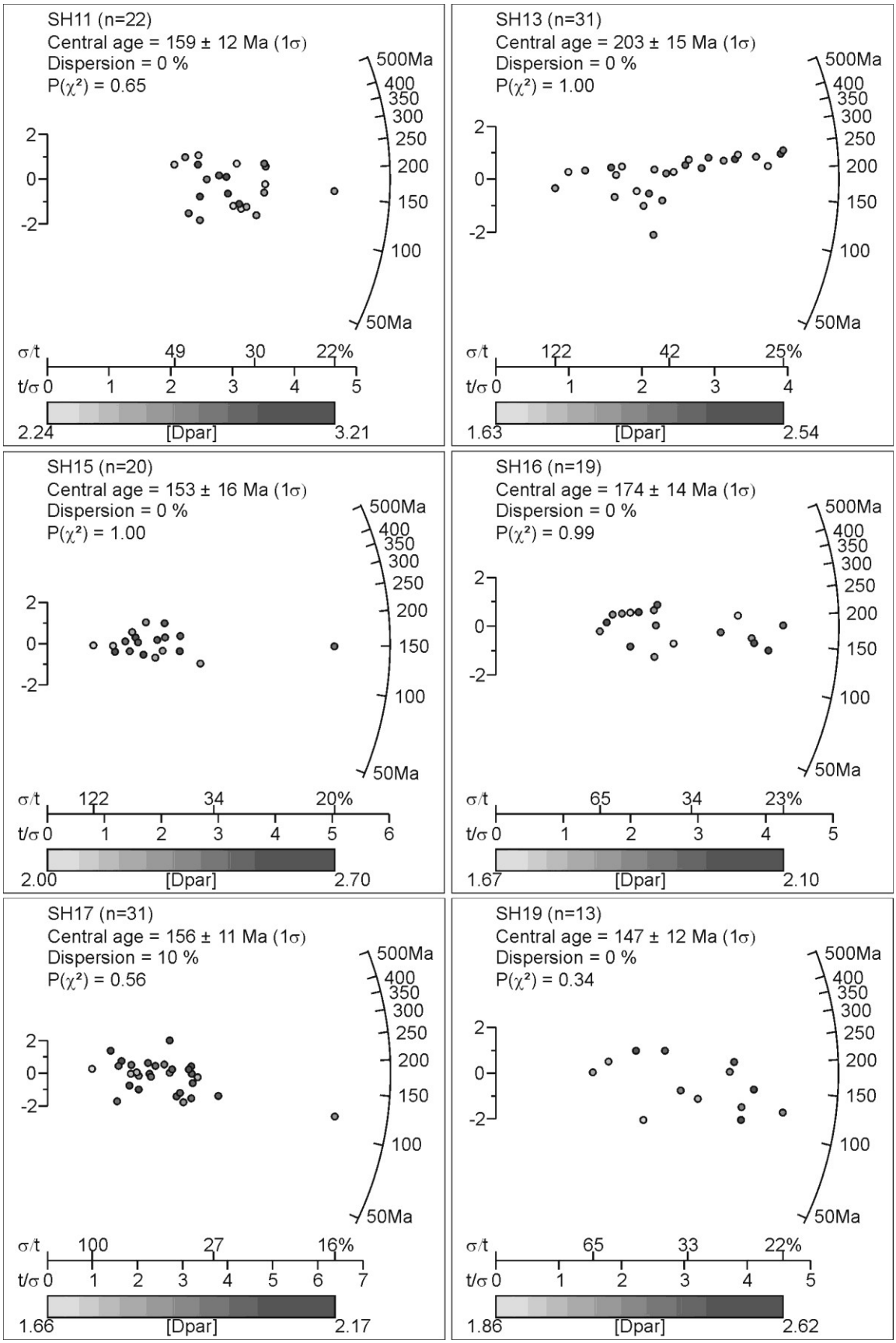

Figure S 1 (continued)

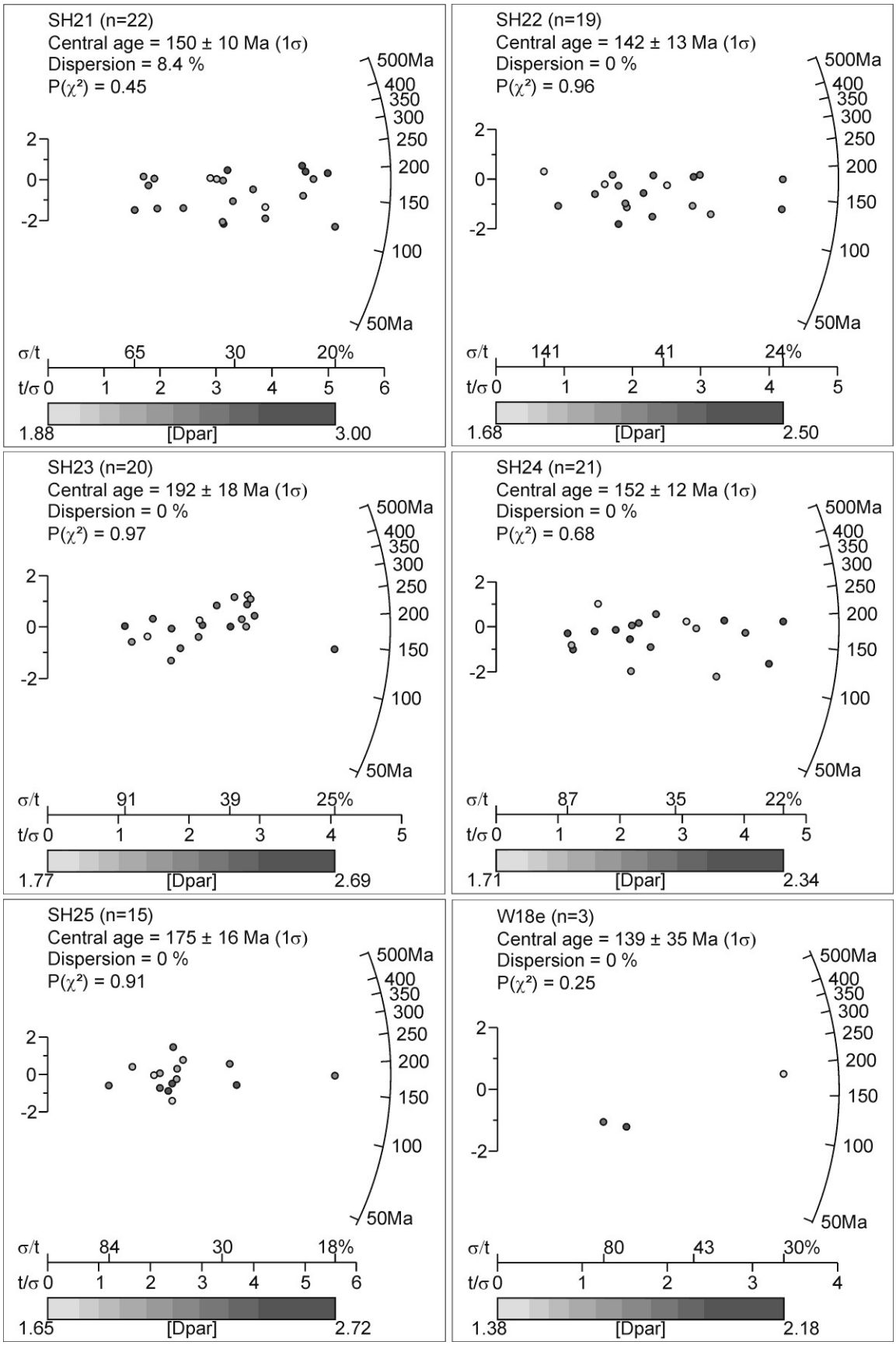

Figure S 1 (continued)

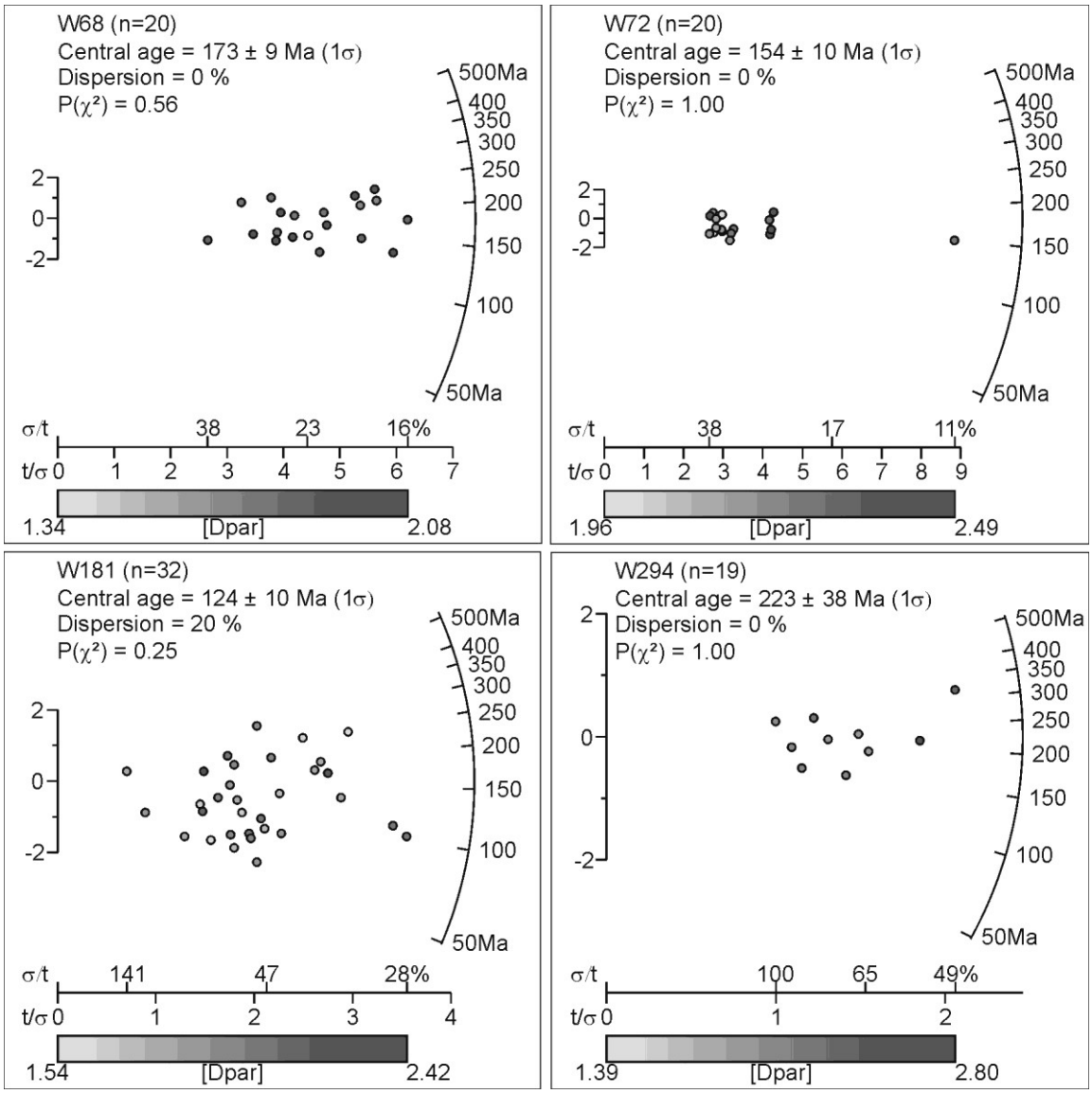

Figure S 1 (continued)

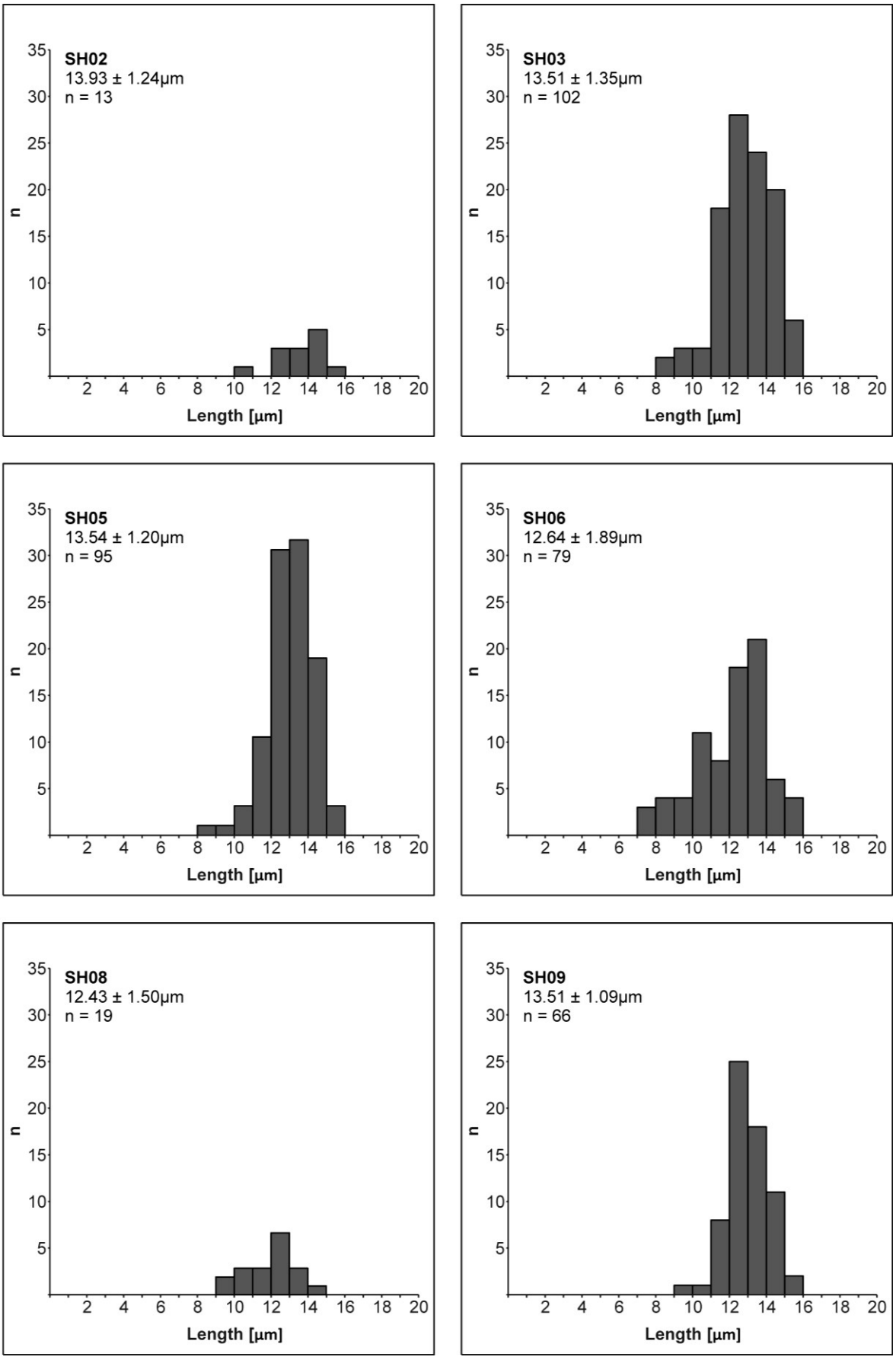

Figure S 2: Track length histograms. Showing track length histograms of the individual samples. Note that the values of the histograms are not c-axis projected.

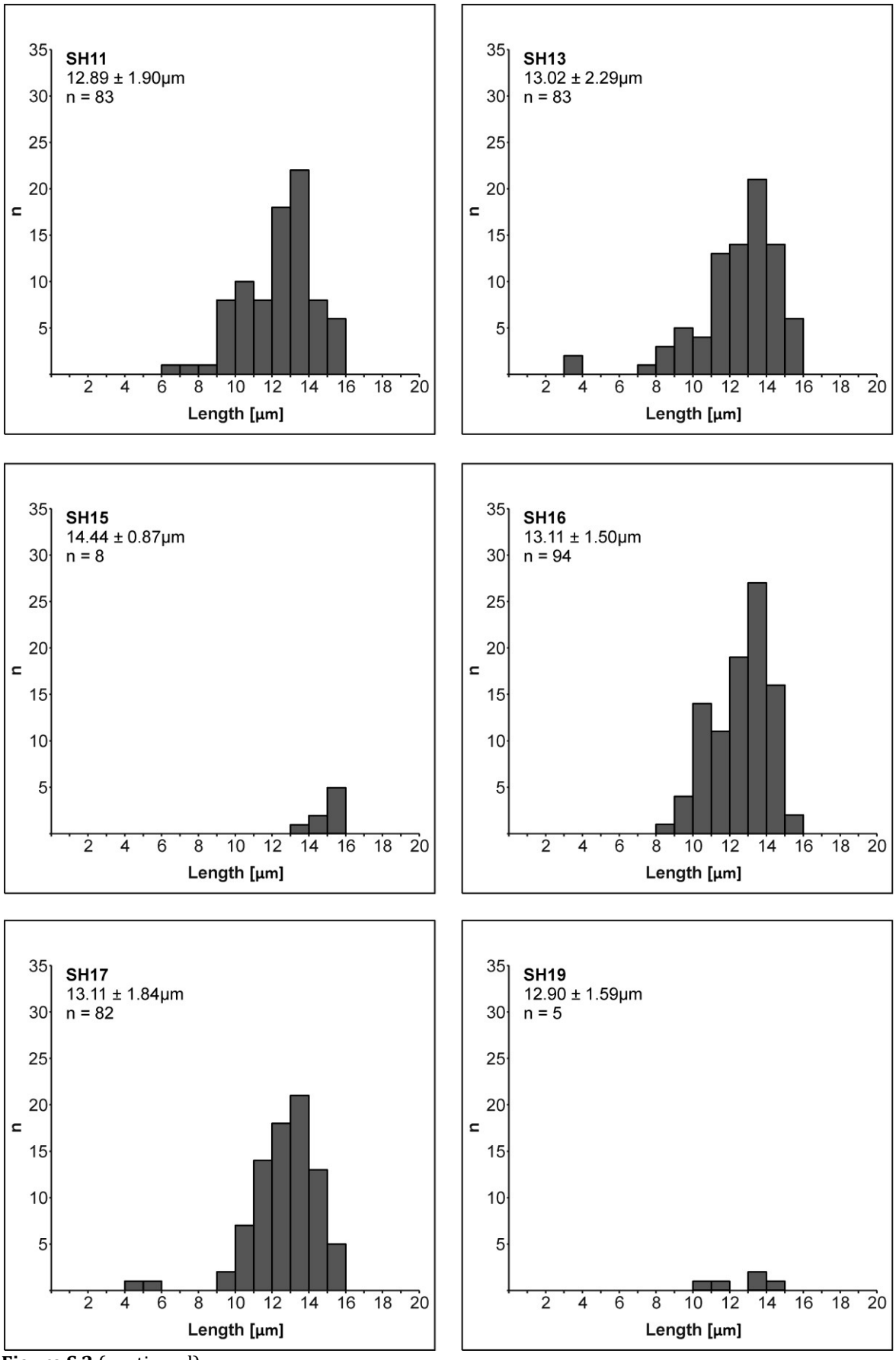

Figure S 2 (continued)

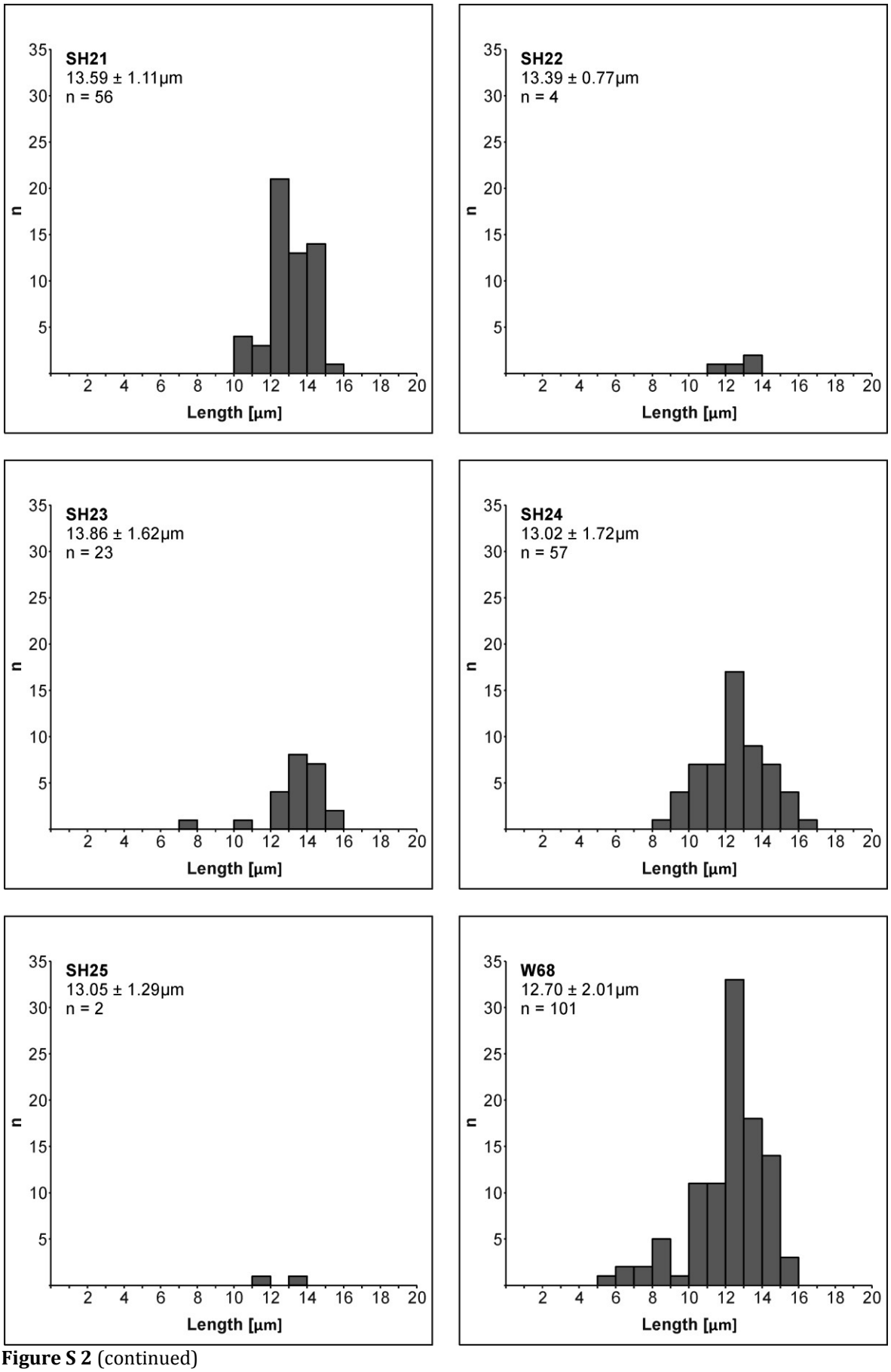

Figure S 2 (continued)

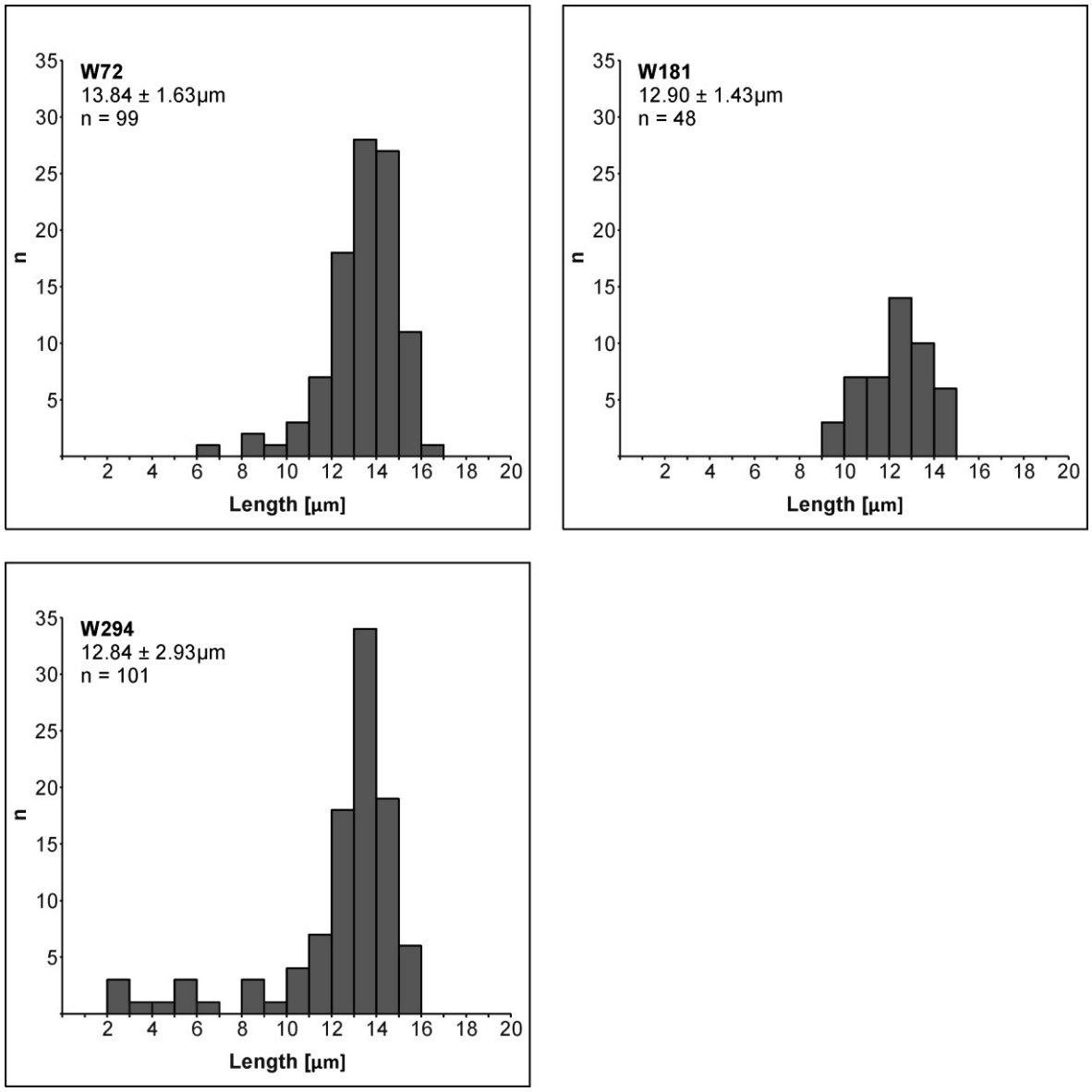

Figure S 2 (continued)

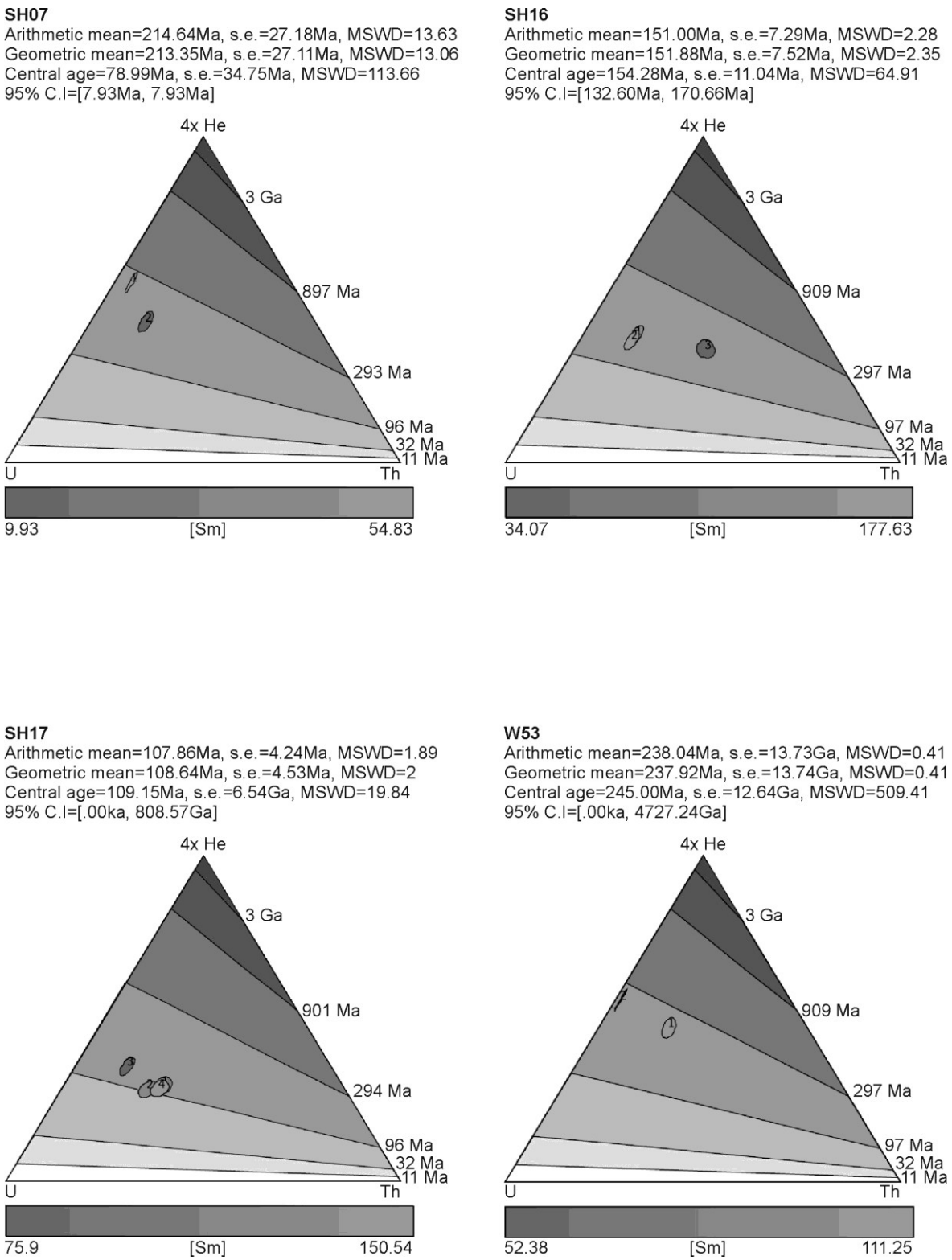

Figure S 3: U-Th- He ternary diagrams and age estimations. Ellipses illustrate the 2σ error. The diagrams were created using HelioPlot (Vermeesch, 2010).

W18e
Arithmetic mean=153.08Ma, s.e.=8.13Ma, MSWD=2.93
Geometric mean=153.67Ma, s.e.=7.97Ma, MSWD=2.79
Central age=181.48Ma, s.e.=17.68Ma, MSWD=873.52
95% C.I=[41.07Ma, 219.42Ma]

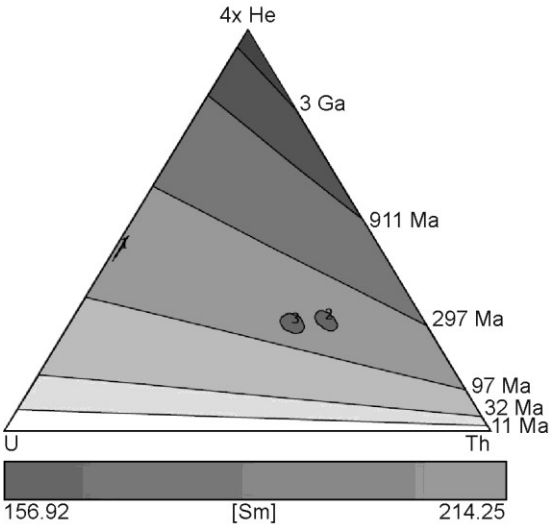

W181
Arithmetic mean=125.61Ma, s.e.=25.39Ma, MSWD=58.74
Geometric mean=117.26Ma, s.e.=23.02Ma, MSWD=46.16
Central age=130.33Ma, s.e.=3.62Ga, MSWD=180.03
95% C.I=[.00ka, 819.90Ga]

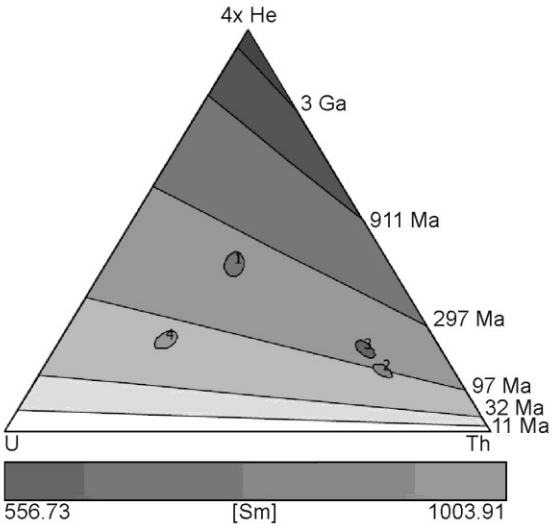

All aliquot points

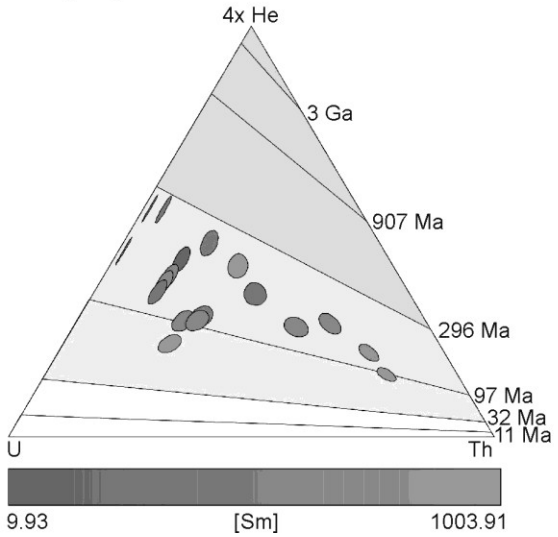

Figure S 3 (continued)

Table S 4: HeFTy preferences

ZFT	AFT	AHe
Annealing Model: Fanning Arrhenius (Yamada *et al.*, 2007)	Annealing model: Ketcham *et al.* (2007) Initial mean track length: 16.12 ± 0.06 µm Length reduction in stand-ards: 0.89 µm c-axis projection model: Ketcham *et al.* (2007)5.0M Length GOF: Kuipers Statistic Dpar Durango: 1.83 µm Calibration factor: 0.9196µm	AHe model: Farley (2000) or RDAAM, Flowers *et al.* (2009) Age α-correction: ejection Stopping distance: Farley *et al.* (2011)

Table illustrates the input preferences and annealing models used for thermal history modelling.

Table S 5: Input constraints inverse modelling - batch mode

Constraint	$Time_{max}$	$Time_{min}$	T_{max}	T_{min}	Mode
1	300	190	320	60	2Ev
2	200	170	40	0	2Ev
3	170	1	120	-40	2Ev
4	0	0	individual surface T.		-

Table showing the input constraints used for batch mode inverse modelling. Constraints 1, 2, and 4 were set because of geological evidence, whereas constraint 3 were set widely to allow all possible iteration steps. 2Ev segment parameters were used, implying 2 times iteration between segments, with episodic and monotonic variable style. This means that cooling as well as reheating is allowed (HeFTy user guide; Ketcham (2005)).

Table S 6: Individual annual mean recent surface temperatures

Sample	Latitude	Longitude	Elevation [m]	Mean surface temperature [°C]
SH 03	-80.422	-21.533	1110	-31±5
SH 05	-80.545	-20.767	1305	-33±5
SH 06	-80.537	-20.550	1255	-32±5
SH 07	-80.610	-20.811	1470	-35±5
SH 09	-80.545	-19.603	1335	-33±5
SH 10	-80.640	-20.625	1475	-35±5
SH 11	-80.370	-21.969	915	-29±5
SH 13	-80.455	-22.267	1105	-31±5
SH 16	-80.118	-25.633	540	-25±5
SH 17	-80.123	-25.733	720	-27±5
SH 21	-80.318	-24.983	1065	-31±5
SH 24	-80.697	-22.683	1515	-35±5
SH 25	-80.733	-23.567	1375	-34±5
W181	-80.741	-25.527	1210	-32±5
W68	-80.729	-25.003	1220	-32±5
W72	-80.695	-24.592	1250	-33±5
W294	-80.386	-30.013	570	-25±5

Table of the individual mean average surface temperature. This temperature was calculated using the mean annual temperature at sea level (ca. -18°C; Halley Station) and the orographic gradient of 0.98K/100m for dry adiabatic conditions.

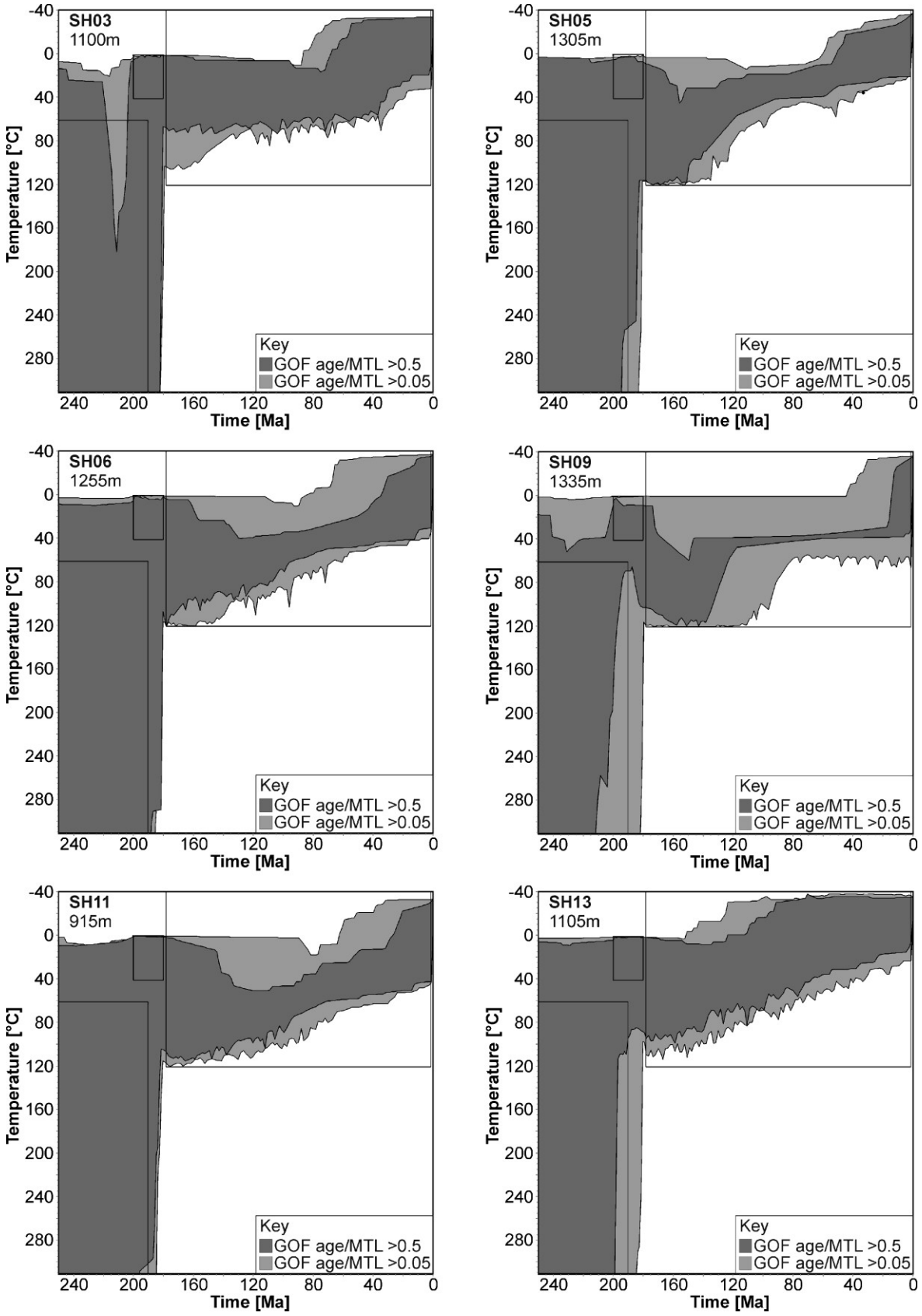

Figure S 4: Inverse thermal history modelling results.

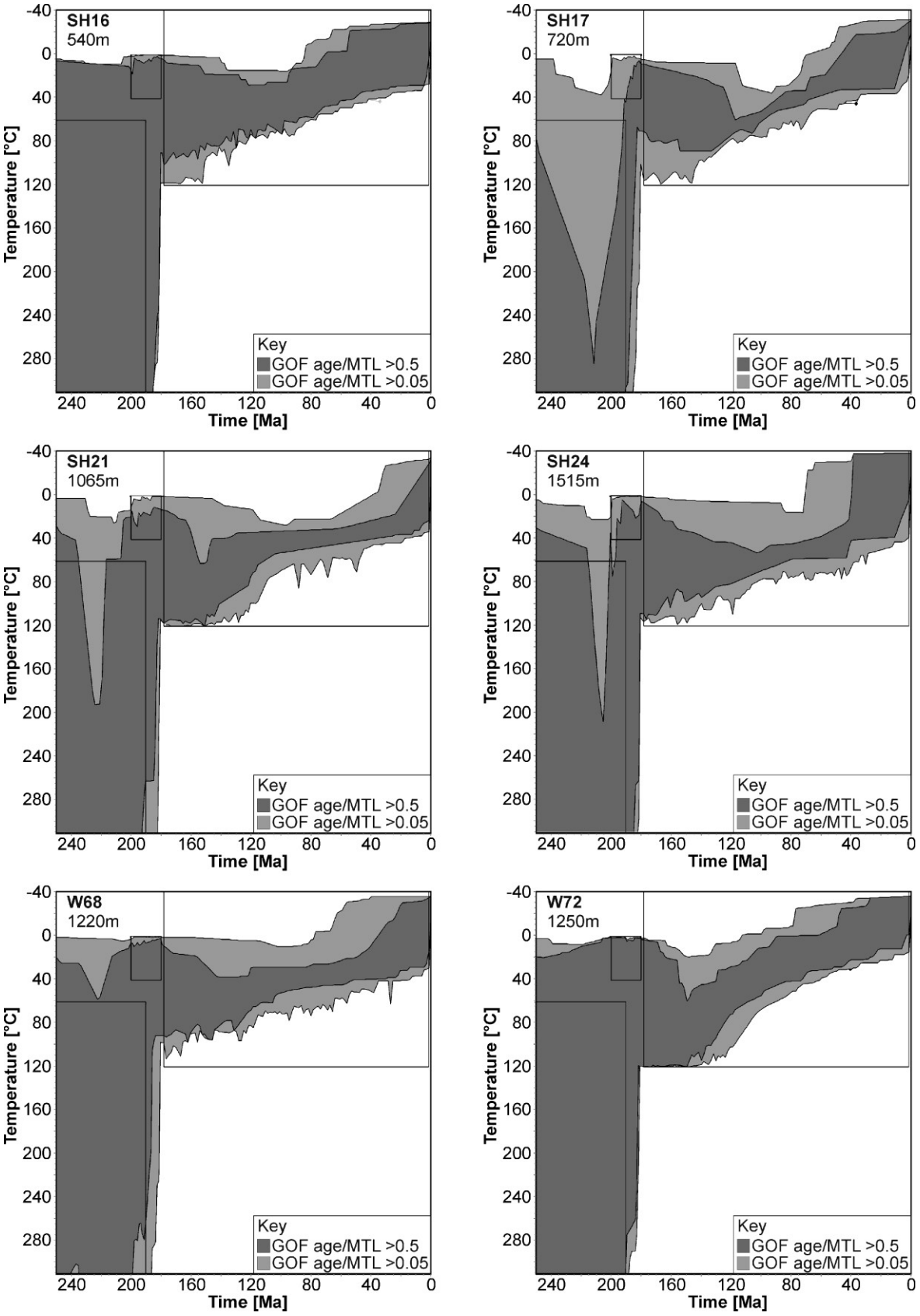

Figure S 4 (continued)

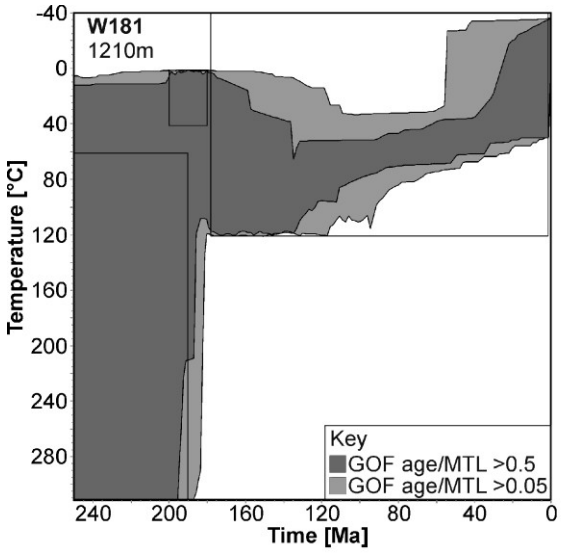

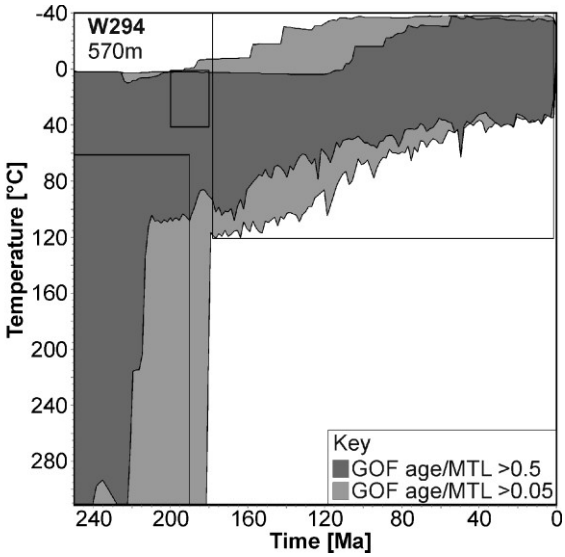

Figure S 4 (continued)

C. Supplementary Material: Passive margin formation in Sør Rondane (East Antarctica)

C.1. Analytical Procedures

C.1.1. Mineral separation

Separation of pure apatite from several basement lithologies includes rock-crushing and sorting procedures (Jaw Breaker, Wilfey Table), heavy liquid (LST fastfloat and Diiodmethane (CH_2I_2) and multi-stage magnetic separation (Frantz Magnetscheider). Hand picking of apatites was conducted to enhance final purity of the separates.

C.1.2. Fission Track analysis

AFT analysis was carried out using the external detector method following the procedures described by Gleadow (1984) and Donelick *et al.* (2005), and by the zeta calibration approach (Hurford & Green, 1982; Hurford & Green, 1983) with IRMM 540 dosimeter glasses (De Corte *et al.*, 1998). Zeta calibration was carried out on six Durango and Fish Canyon samples. Track length and D_{par} measurements followed the recommendations of Laslett *et al.* (1982), Donelick (1993) and Donelick *et al.* (2005). User length- and D_{par} calibration was applied on four samples with known track length distribution (annealed, mixed and induced lengths).

Samples were mounted in Petropoxy 154, polished and etched in 5 mol/l HNO_3 at 20°C for 20 seconds. Thermal neutron irradiations were carried out in the reactor facility of FRM II (Garching, Germany) with a nominal neutron flux of 1×10^{16} n/cm^2 for all samples. Analysis was carried out with Zeiss Axioplan microscope using 1250× magnification, dry air objectives and the FT stage program of Dumitru (1993).

C.1.3. (U-Th-Sm)/He analysis

Careful selection of suitable apatite crystals followed recommendations after Farley (2002). This implies >60 µm, inclusion and crack free euhedral crystals, wrapped into pre-cleaned Pt capsules. Selection was ensued at an Olympus SZX6 microscope (max. magnification of 143.75×) via transmitted and polarized light. Crystal dimensions were measured by application of the Cell A program (Version 3.1; Olympus soft imaging solutions GmbH).

Measurement of ^{4}He, ^{235}U, ^{232}Th and ^{148}Sm was conducted at the research groups 'Geodynamics of the Polar Regions' and 'Petrology of the Oceanic Crust' ;both Department of Geology - University of Bremen

^{4}He measurement was realized by mass spectrometry (Alphachron™ Automated Helium Thermochronometry, Quadrupole Mass spectrometry). Laser-controlled degassing at 900°C was realized by a 980nm diode laser, and isotope measurement by Quadrupole Mass spectrometry. The ^{4}He blank level is <0.02ncc and the resolution 0.5 AMU. Measurement of ^{235}U, ^{232}Th and ^{148}Sm with ICP-MS in solution by high-resolution double-focussing ICP mass spectrometer (ThermoFinnigan Element2). Detection limits are in the order of 1ppt, thus no spiking was necessary.

C.2. Tables and Figures

Table S 7: Individual mean average surface temperature.

Sample Name	Latitude	Longitude	Elevation [m]	Mean surface temperature [°C]
TC_01	72°07.126 S	23°11.575 E	1922	-34
TC_02	72°03.122 S	23°19.006 E	1406	-29
TC_03	72°04.553 S	23°25.727 E	1643	-31
TC_09	72°02.218 S	22°50.965 E	1642	-31
TC_10	72°01.273 S	22°47.083 E	1639	-31
TC_11	72°01.888 S	22°56.441 E	1545	-30
TC_12	72°05.863 S	23°11.040 E	1920	-34
TC_13	72°09.500 S	23°12.600 E	3120	-46
TC_14	72°9.389 S	23°12.071 E	2950	-45
TC_15	72°09.285 S	23°10.307 E	2710	-42
TC_16	72°08.850 S	23°09.178 E	2520	-40
TC_17	72°08.587 S	23°08.815 E	2390	-39
TC_18	72°08.339 S	23°08.273 E	2200	-37
TC_19	72°07.940 S	23°10.555 E	2257	-38
TC_20	72°07.773 S	23°10.523 E	2100	-36
TC_21	72°04.096 S	23°04.899 E	2153	-37
TC_22	72°03.897 S	23°10.651 E	1816	-33
TC_23	72°03.388 S	23°05.160 E	1741	-32
TC_24	72°04.033 S	23°06.227 E	2348	-38
TC_27	72°03.078 S	23°12.481 E	1344	-28
TC_28	72°03.497 S	23°08.339 E	1491	-30
TC_38	72°12.558 S	22°43.585 E	1696	-32
ME SR 110	72°20.263 S	23°13.490 E	2648	-41
02A-1	71°59.321 S	23°15.94 E	1338	-28
06B-3	71°52.858 S	22°44.873 E	1388	-29
10A-4	71°59.417 S	23°29.655 E	1350	-29
11B-6	72°5.891 S	23°12.341 E	1498	-30
12B-3	72°7.055 S	23°28.230 E	1607	-31
24B-1	71°59.580 S	23°11.042 E	1377	-29
25E 1	71°59.908 S	23°14.218 E	1376	-29
28B-2	72°2.275 S	23°7.112 E	1469	-30

The temperatures were calculated using the mean annual temperature at Asuka (~1000m) (Yamanouchi *et al.*, 1988; Aoki, 1989; Meshida *et al.*, 1991; Iwasaki & Yamanouchi, 1992; Sukegawa & Yamanouchi, 1993) and Princess Elisabeth Station (~1400m) and the orographic gradient of 0.98K/100m for dry adiabatic conditions.

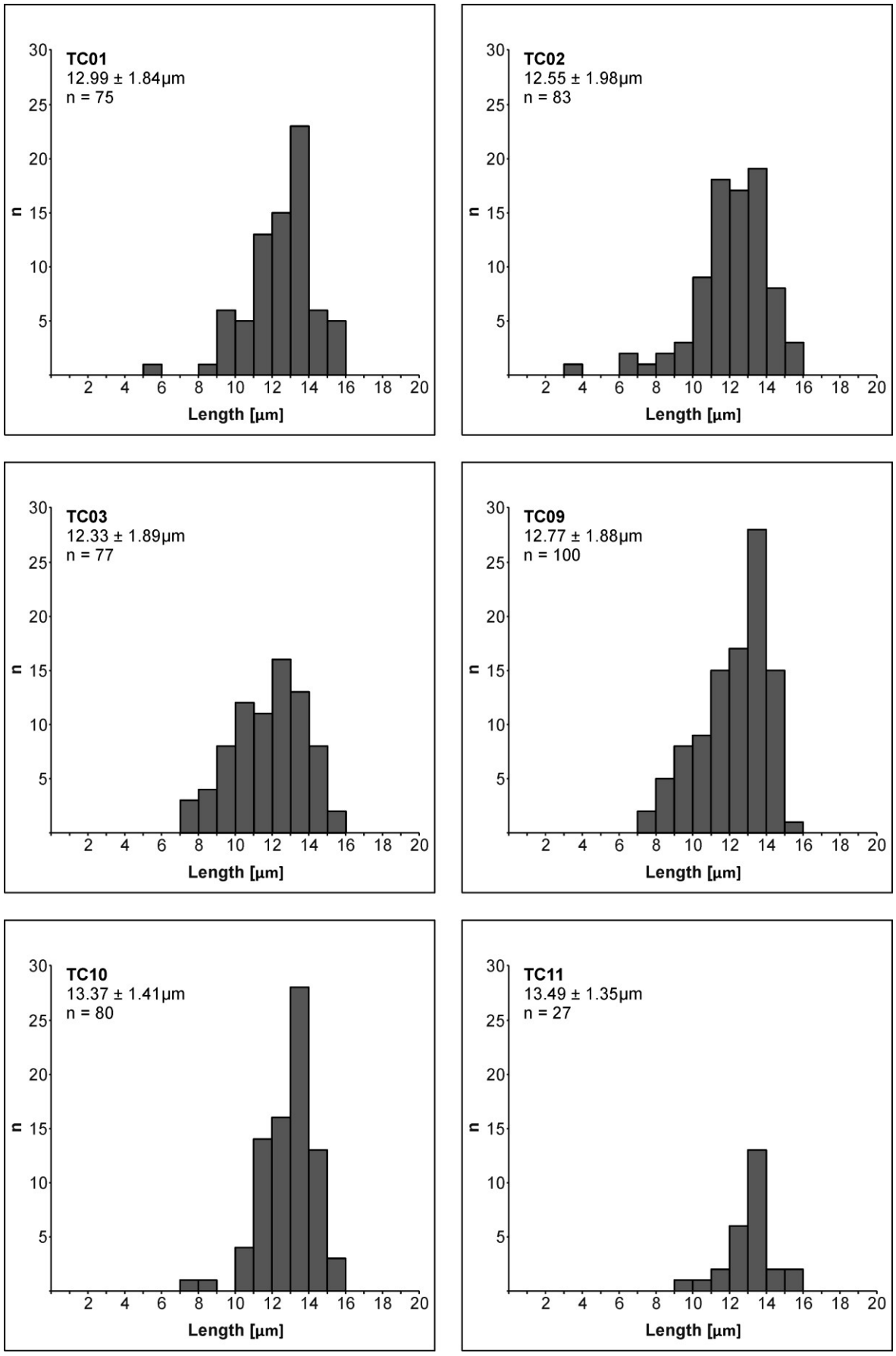

Figure S 5: Track length histograms of the individual samples. Note that the lengths are not c-axis projected.

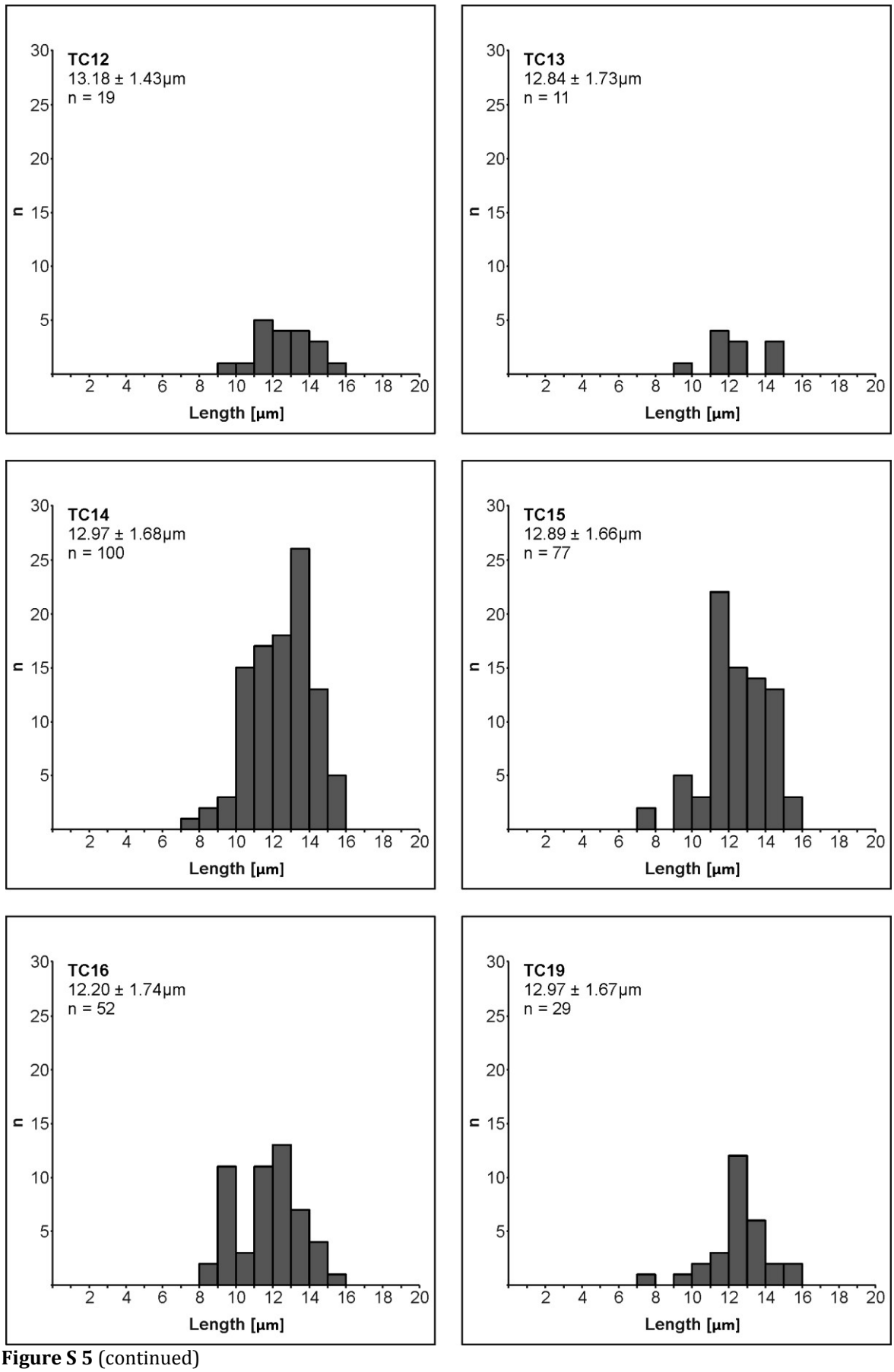

Figure S 5 (continued)

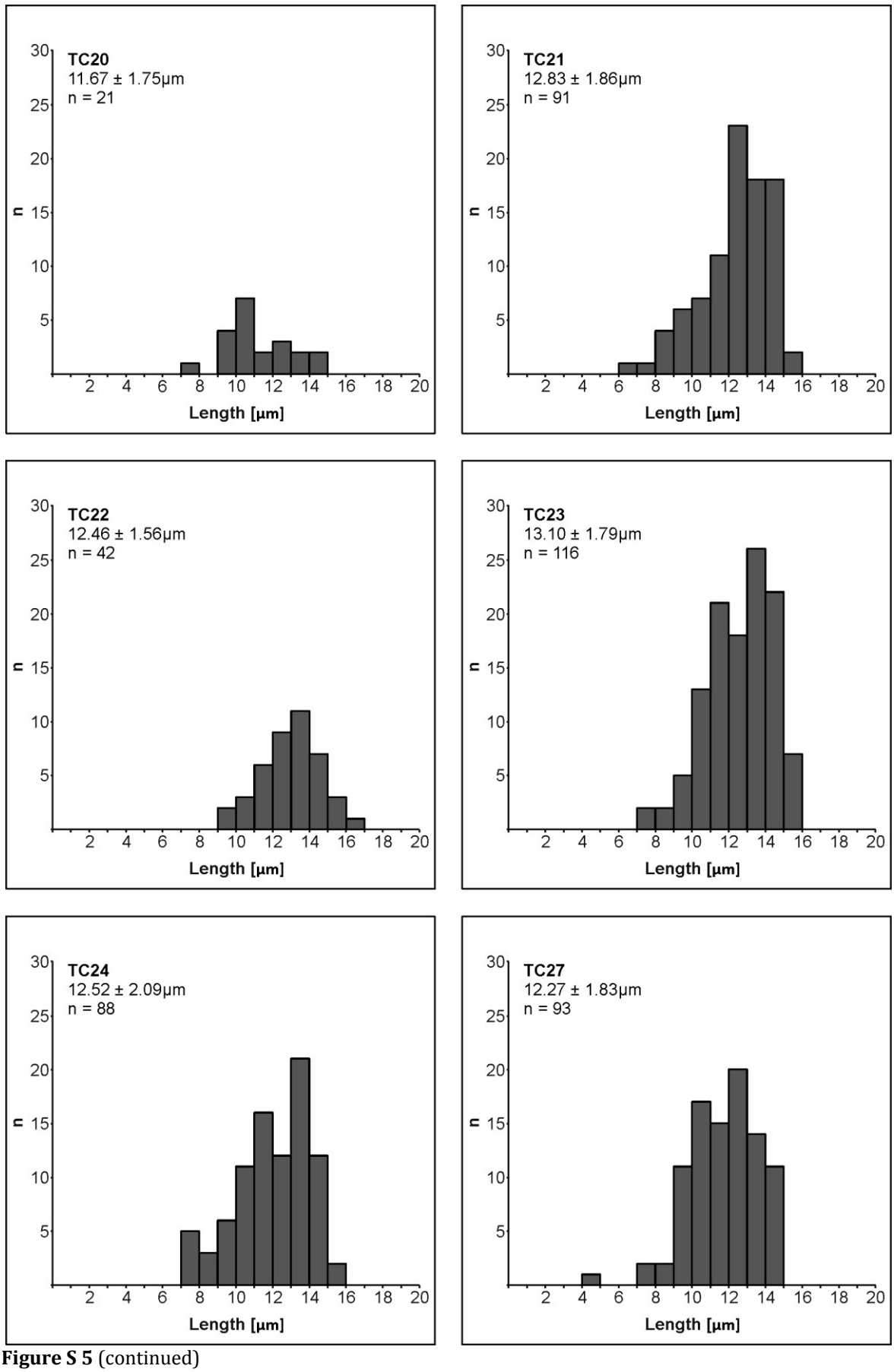

Figure S 5 (continued)

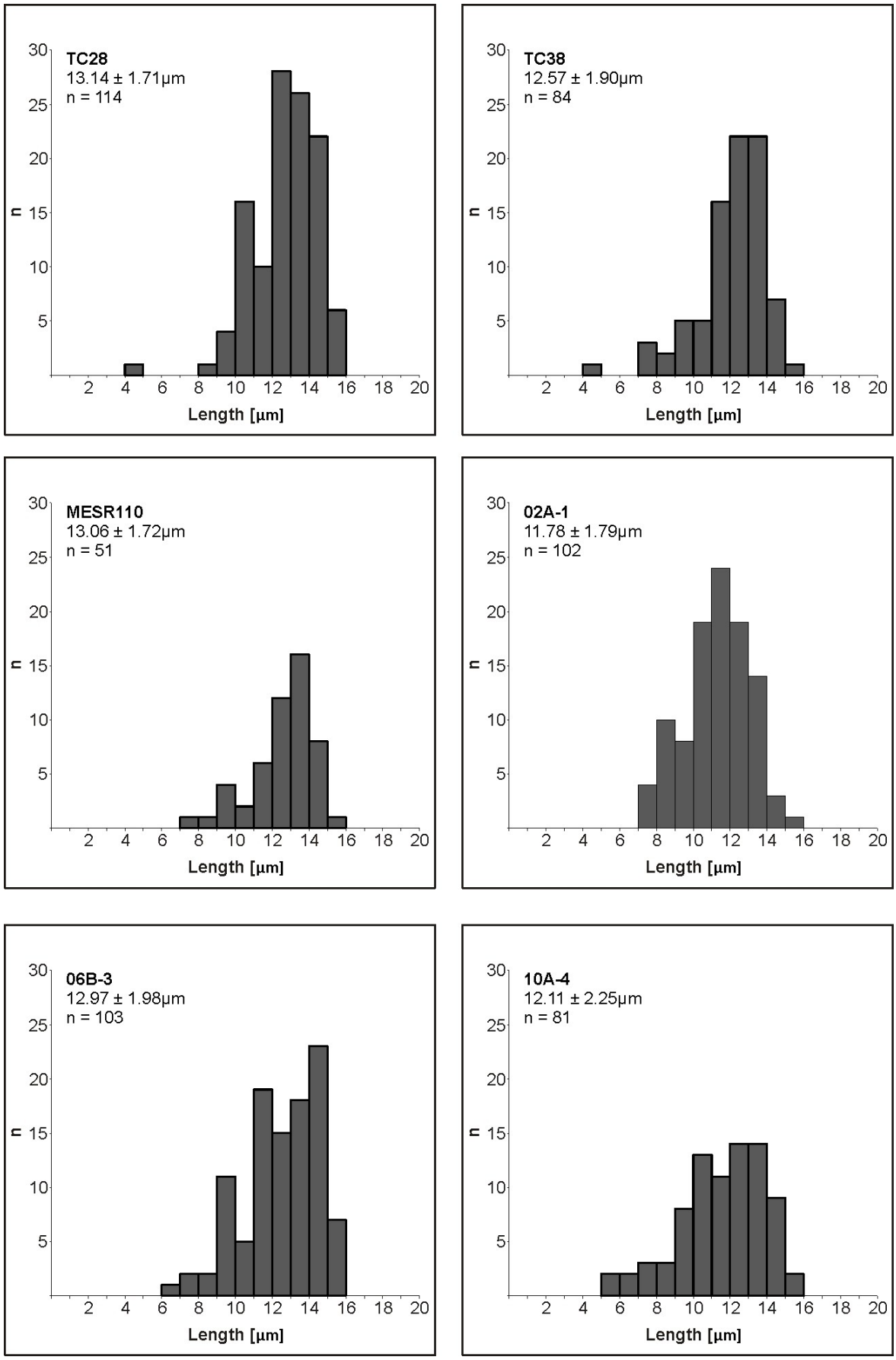

Figure S 5 (continued)

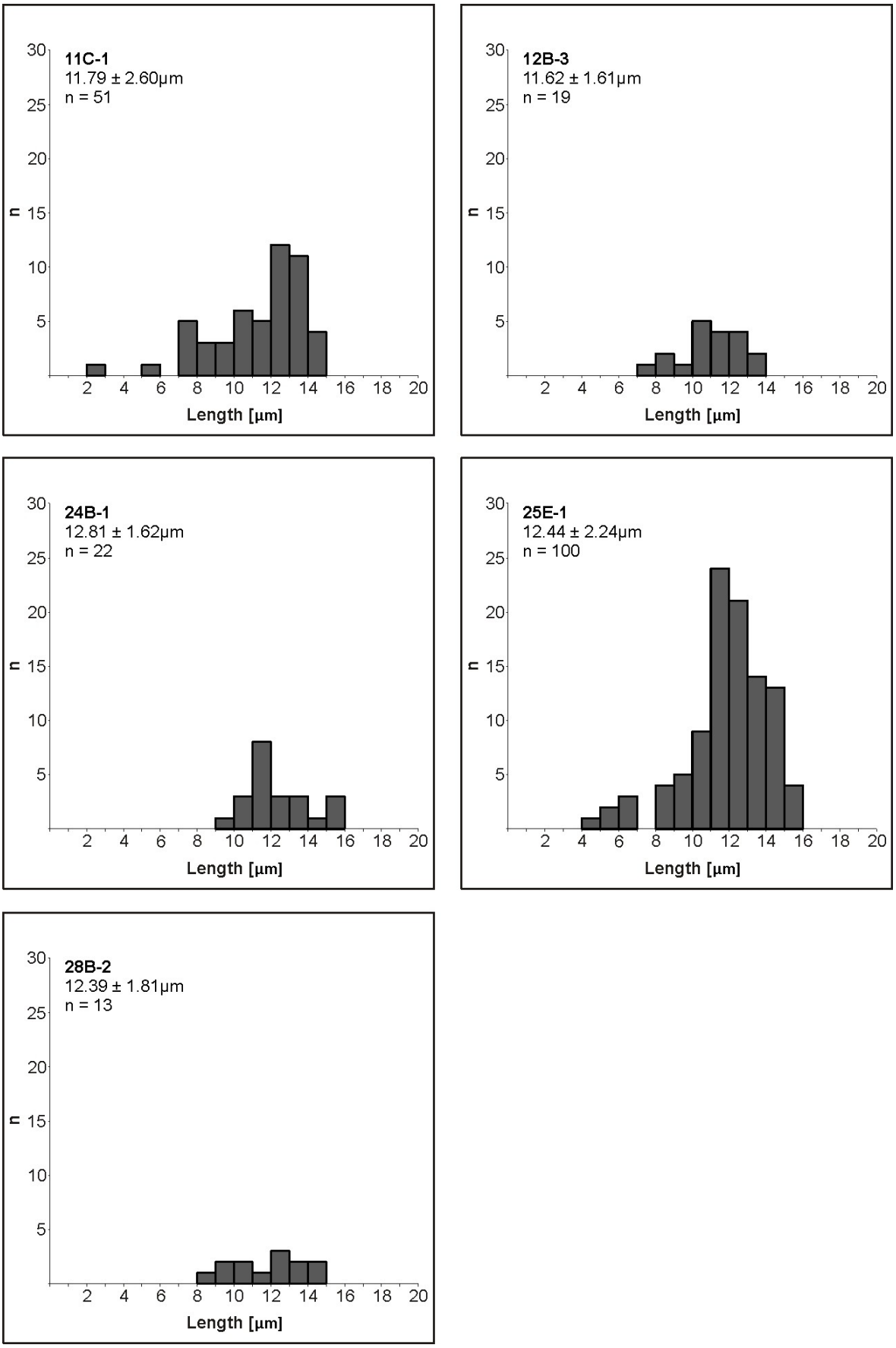

Figure S 5 (continued)

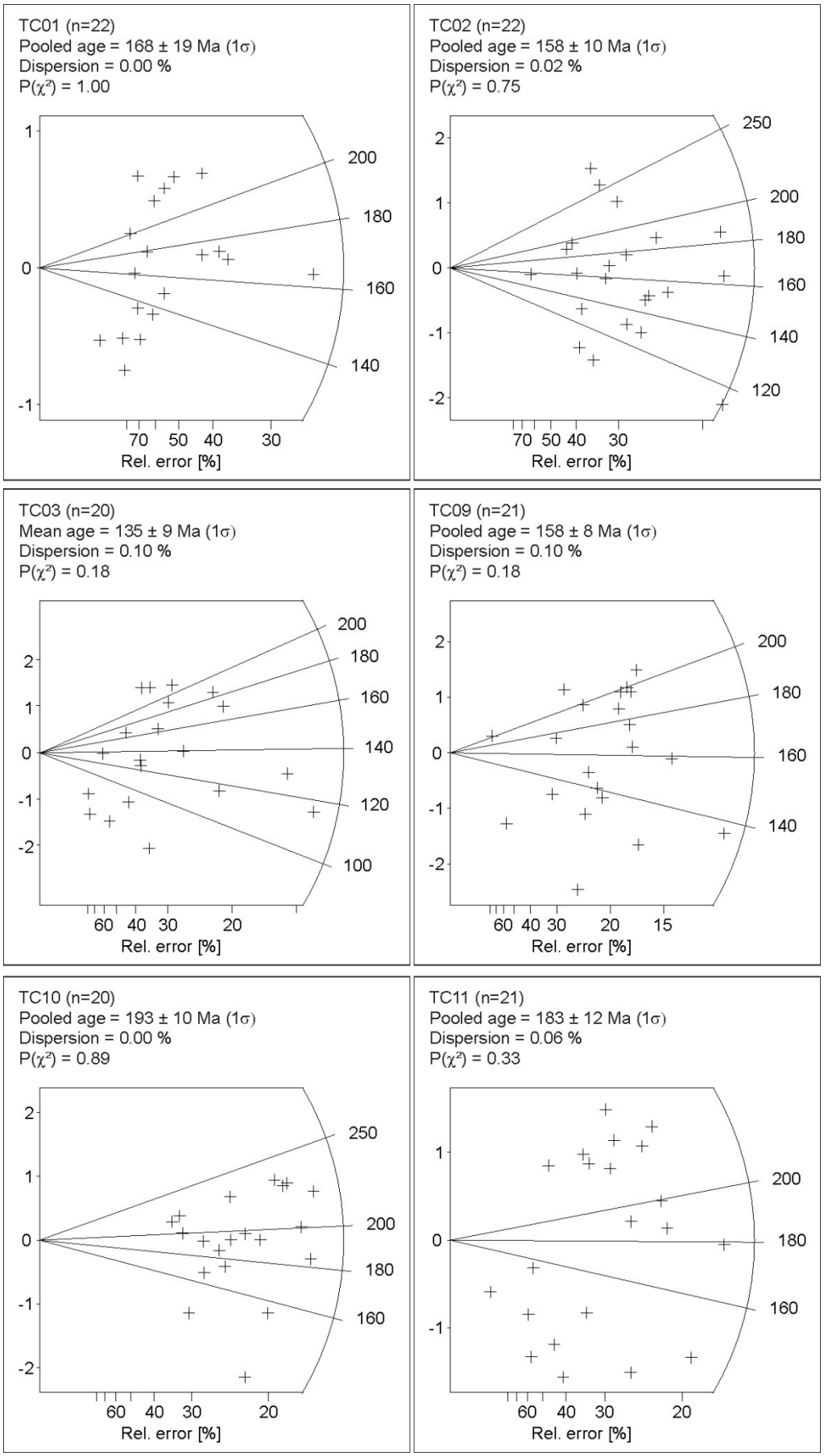

Figure S 6: Radial plots of the fission track samples. Plots were created using TRACKKEY (Dunkl, 2002).

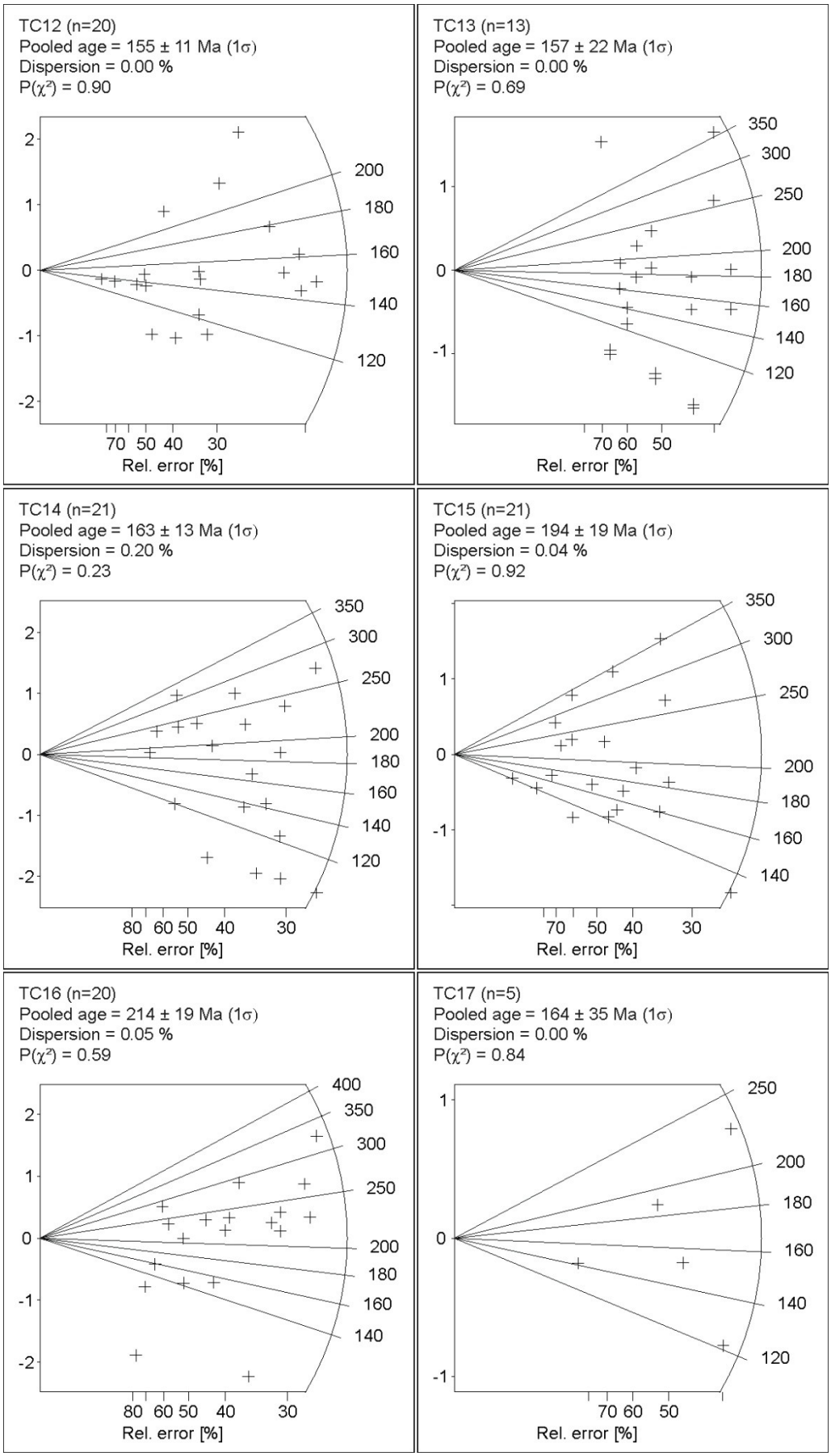

Figure S 6 (continued)

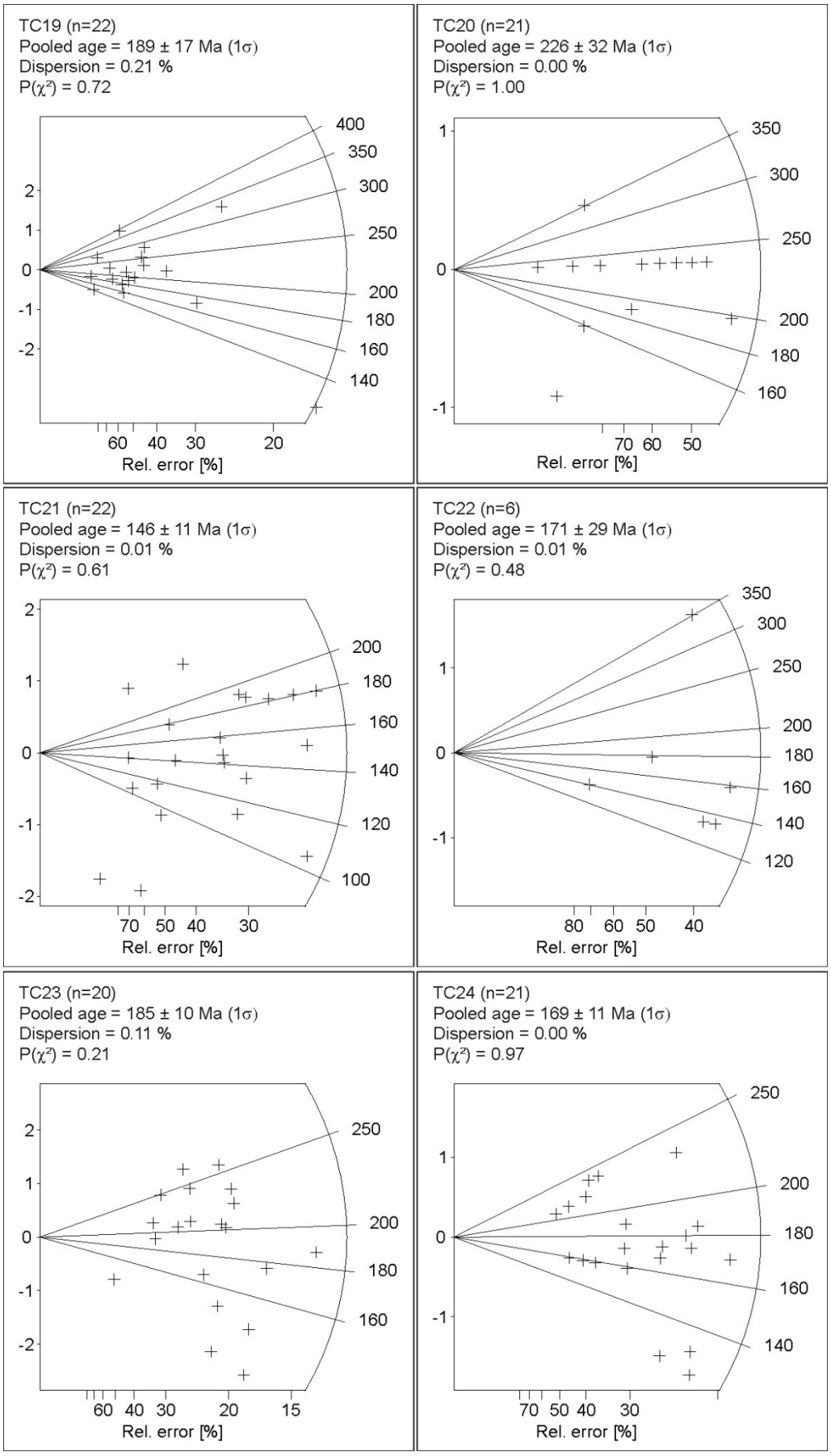

Figure S 6 (continued)

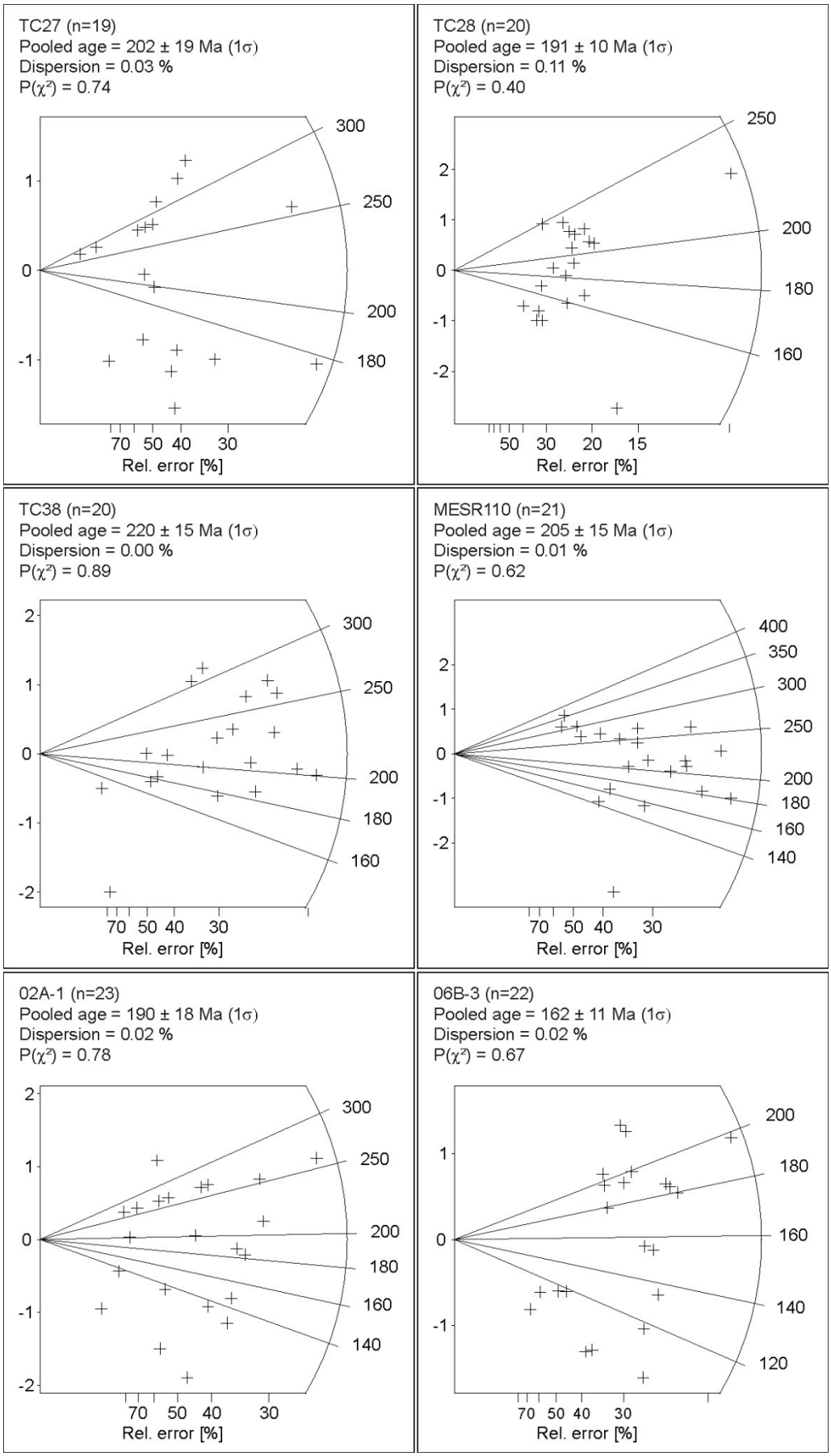

Figure S 6 (continued)

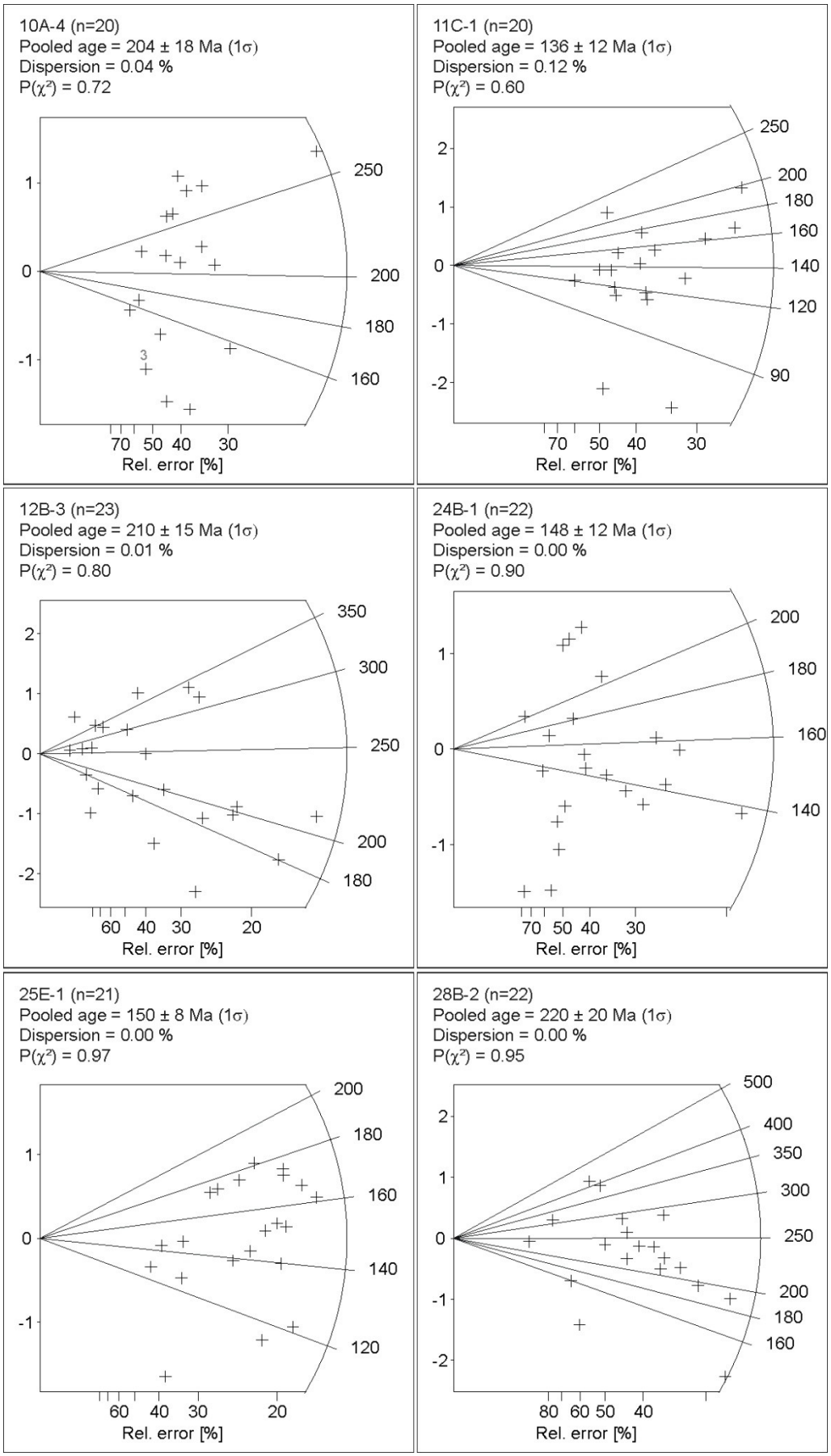

Figure S 6 (continued)

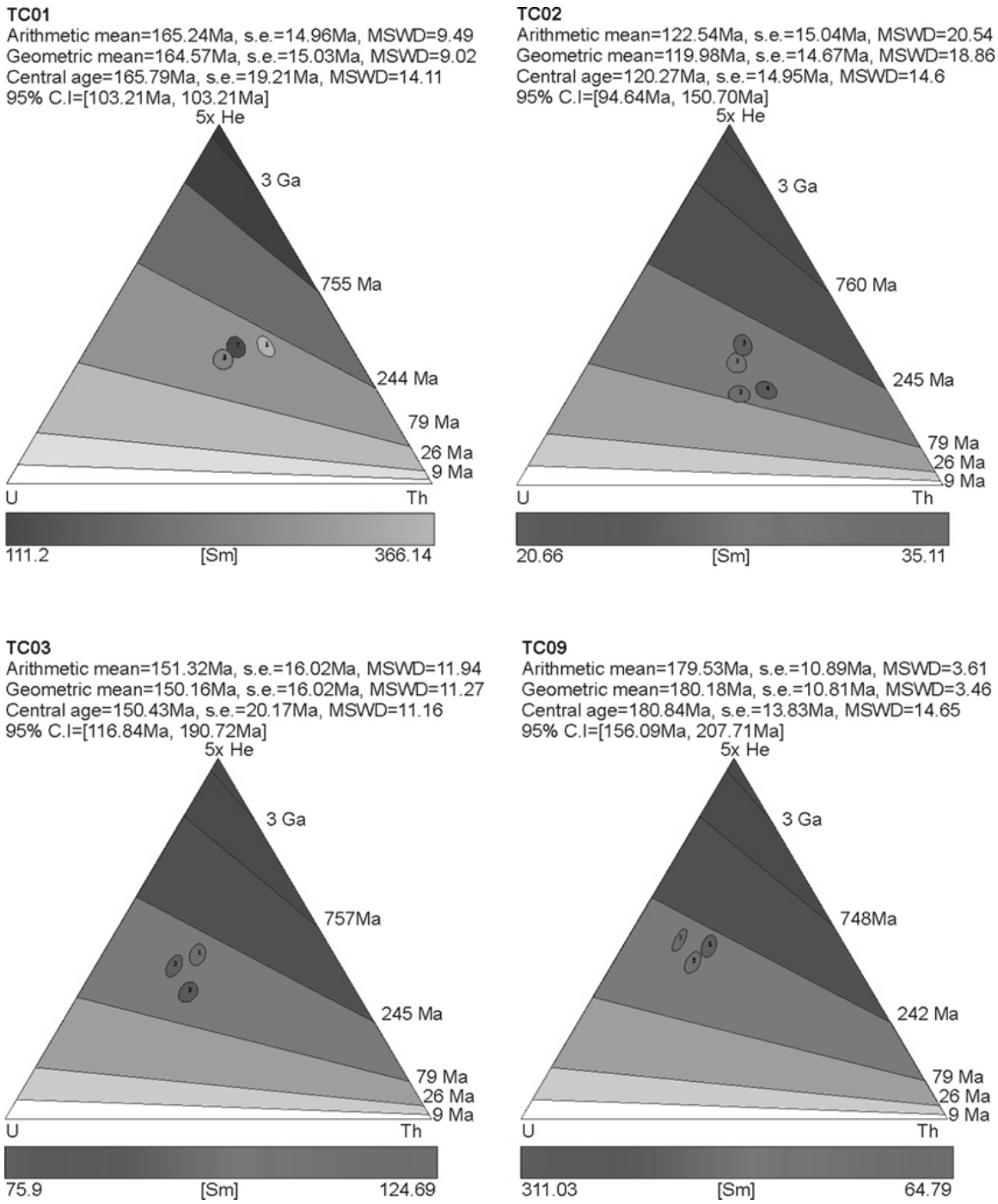

Figure S 7: U-Th- He ternary diagrams and age estimations. Ellipses illustrate the 2σ error. The diagrams were created using HelioPlot (Vermeesch, 2010).

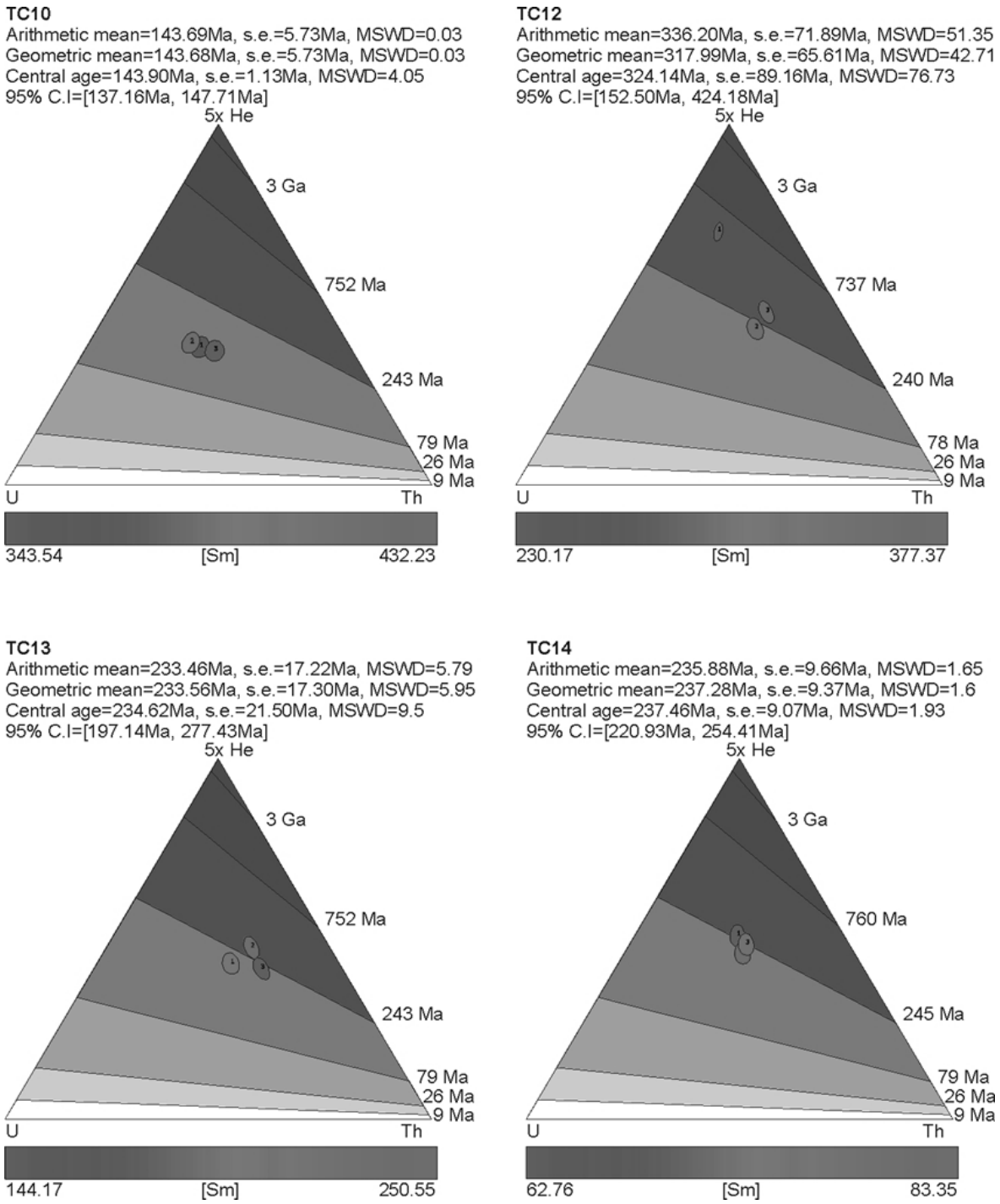

Figure S 7 (continued)

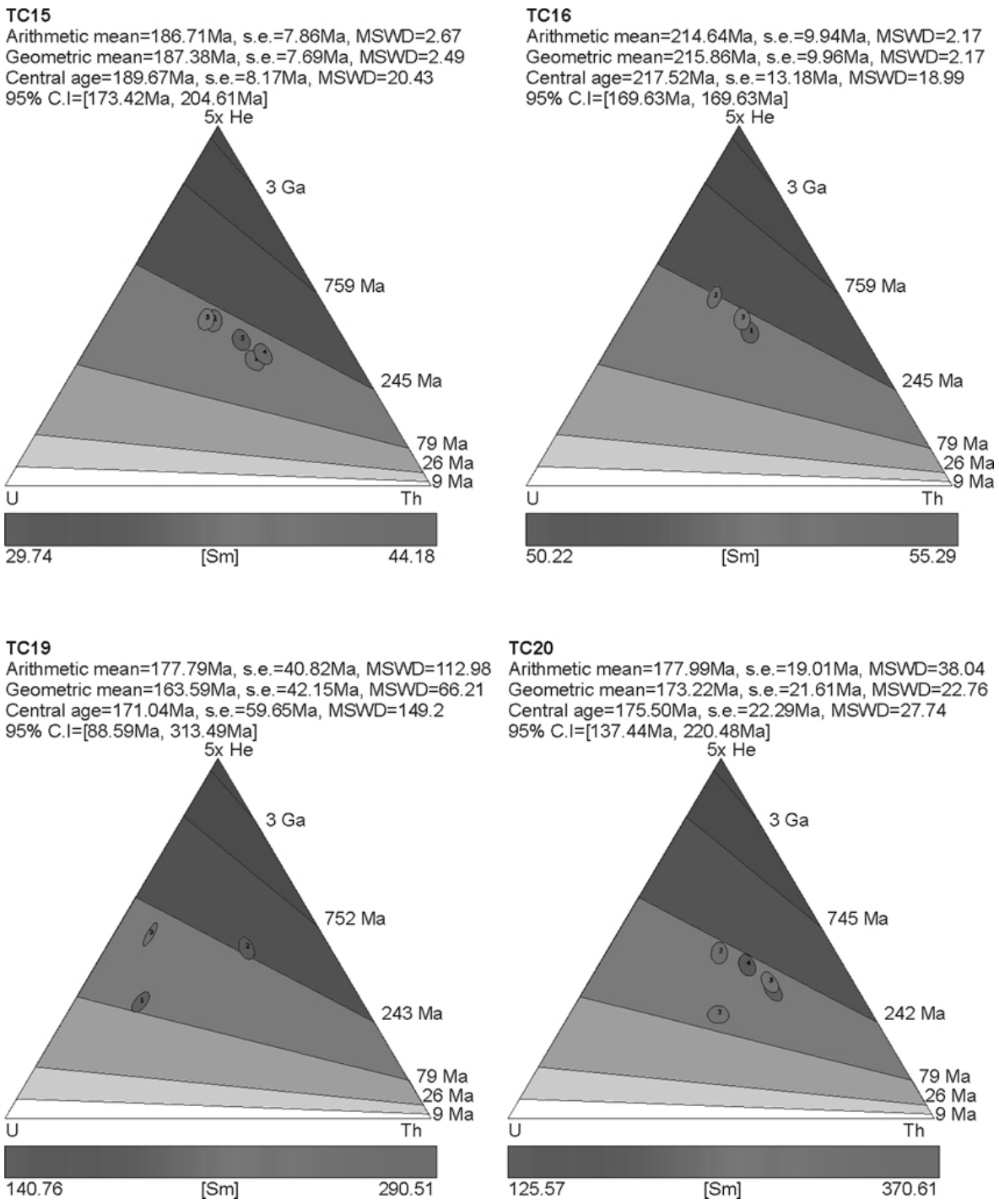

Figure S 7 (continued)

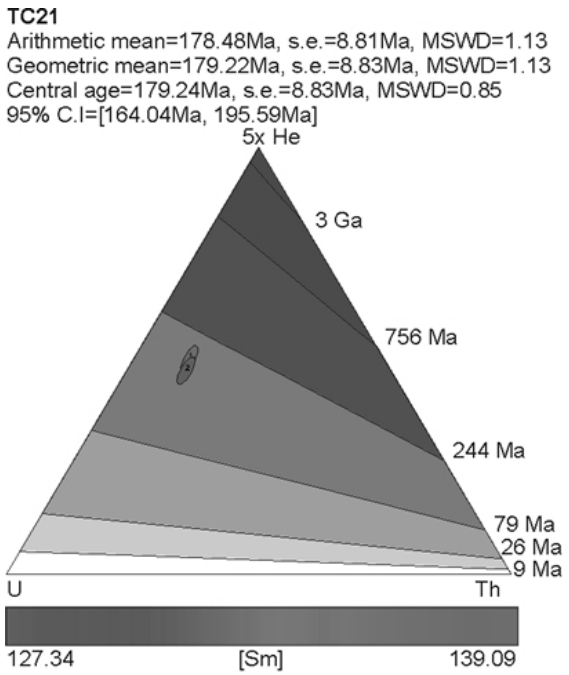

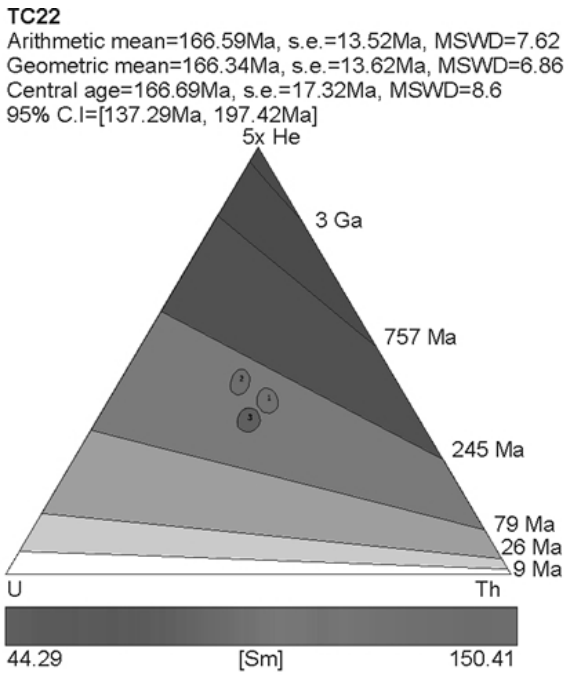

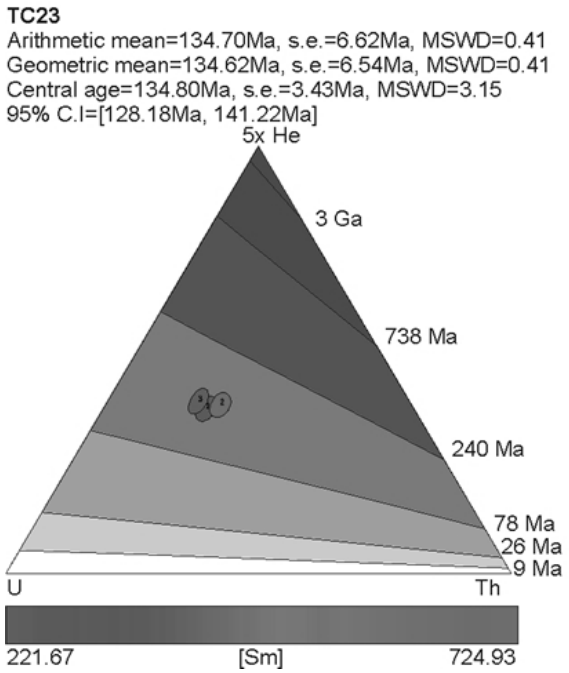

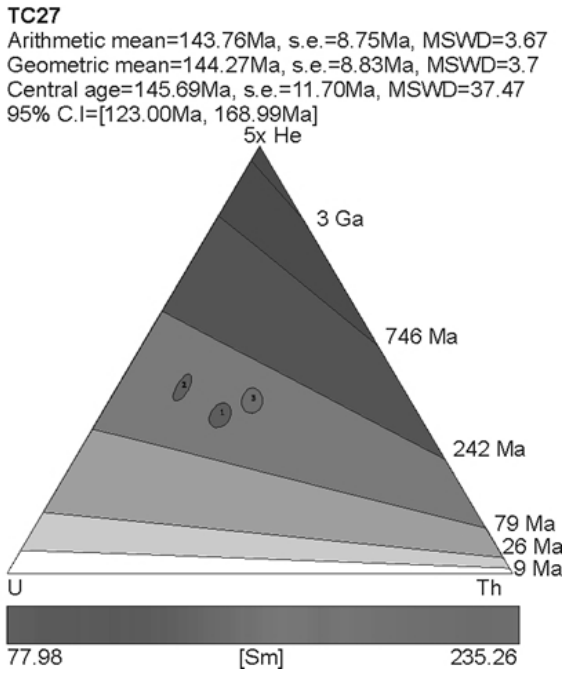

Figure S 7 (continued)

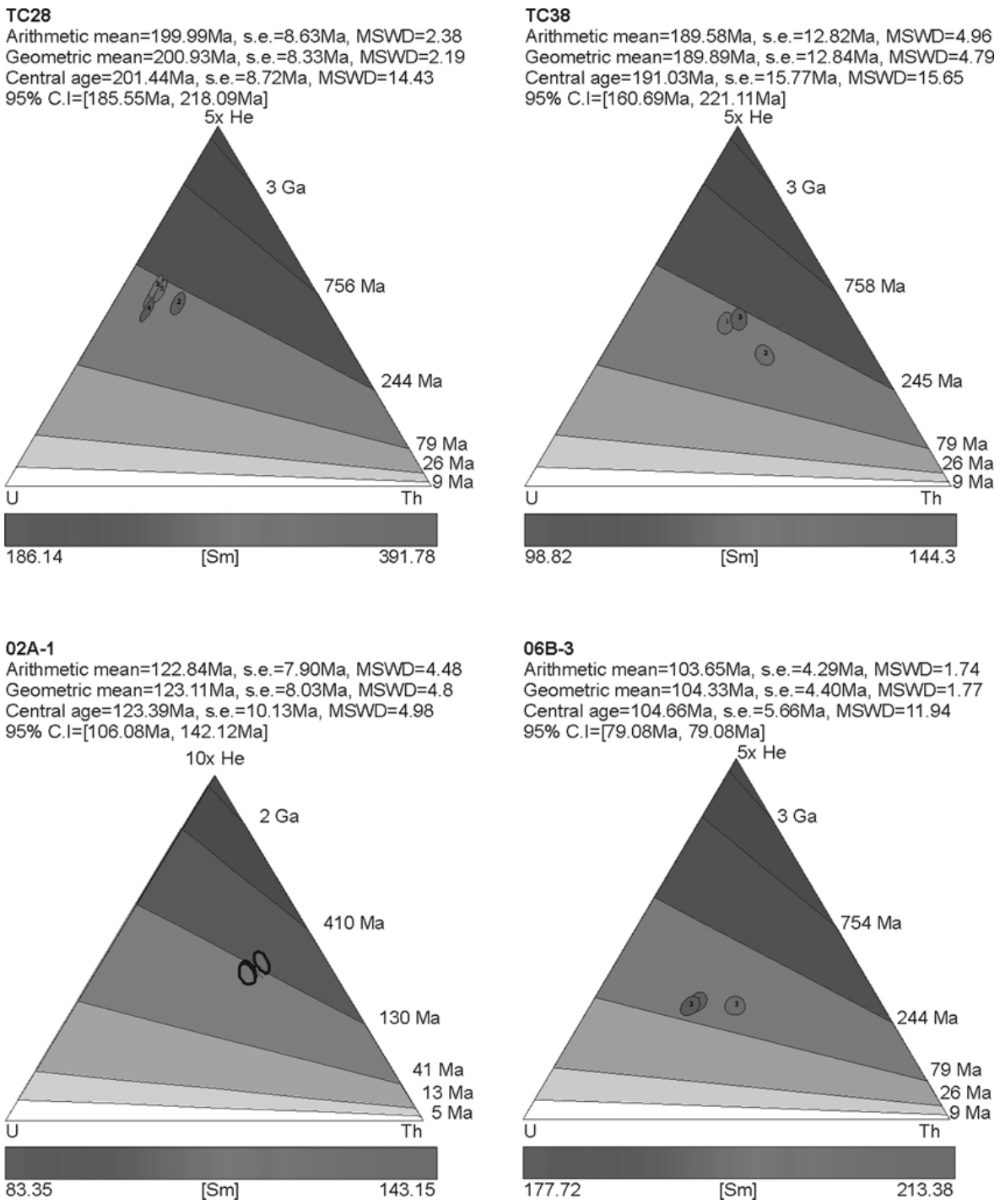

Figure S 7 (continued)

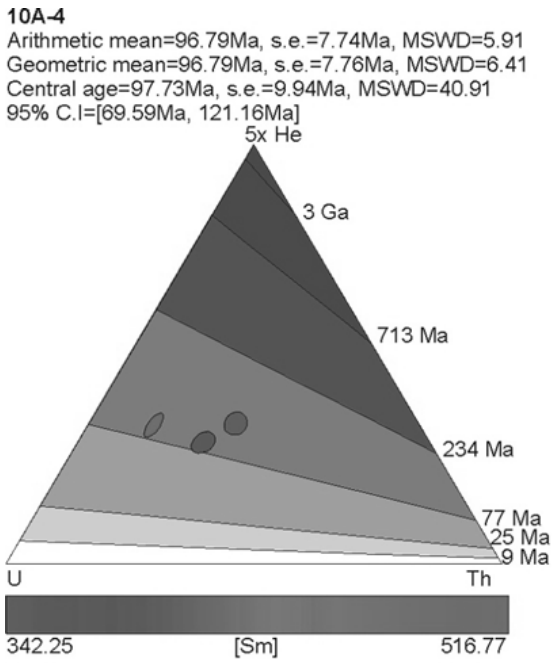

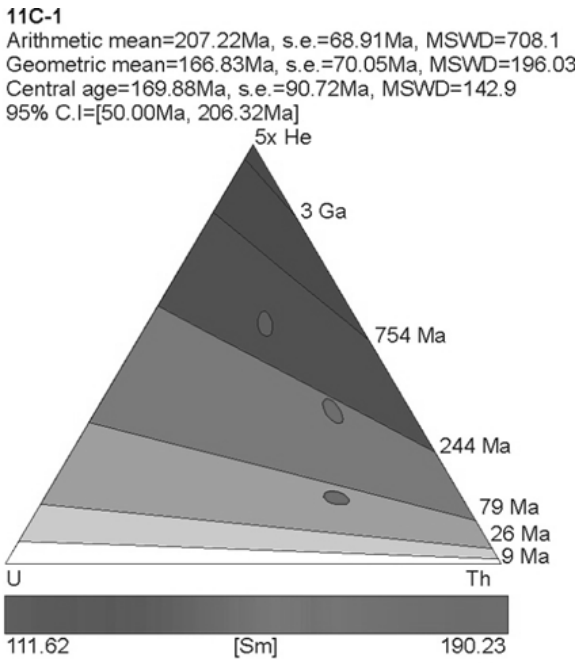

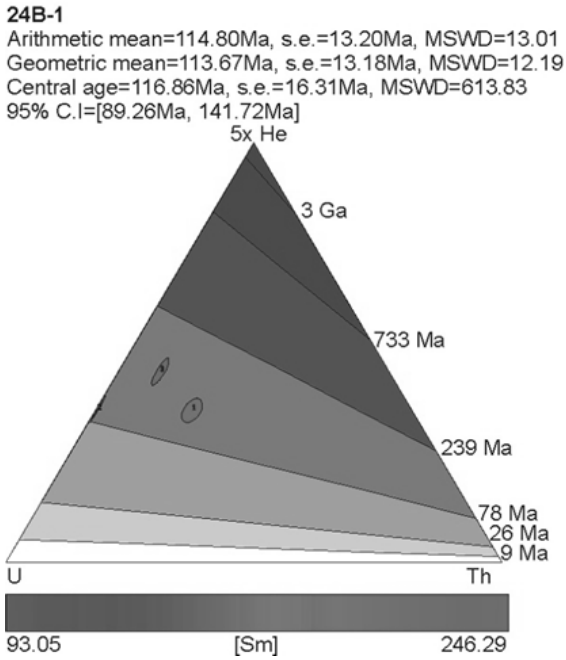

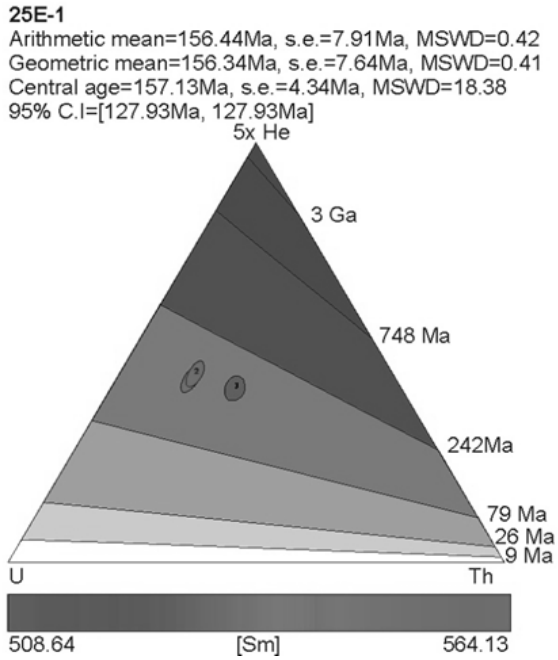

Figure S 7 (continued)

Table S 8: HeFTy preferences

AFT	AHe
Annealing model: Ketcham *et al.* (2007) Initial mean track length: 16.12 ± 0.06 µm Length reduction in standards: 0.89 µm c-axis projection model: Ketcham *et al.* (2007)5.0M Length GOF: Kuipers Statistic D_{par} Durango: 1.83 µm Calibration factor: 0.9196µm	AHe model: Farley (2000) or RDAAM, Flowers *et al.* (2009) Age α-correction: ejection Stopping distance: Farley *et al.* (2011)

Table illustrates the input preferences and annealing models used for thermal history modeling.

Table S 9: Input constraints inverse modelling–batch mode

Constraint	$Time_{max}$	$Time_{min}$	T_{max}	T_{min}	Mode
1	500	450	400	350	2Ev
2	450	200	20	15	2Ev
3	440	200	40	130	2Ev
4	190	175	50	15	2Ev
5	170	45	130	20	2Ev
6	40	20	130	0	2Ev
7	0	0	individual surface T.		-

Table showing the input constraints used for batch mode inverse modeling. 2Ev segment parameters were used, implying 2 times iteration between segments, with episodic and monotonic variable style. This means that cooling as well as reheating is allowed (HeFTy user guide; Ketcham (2005)).

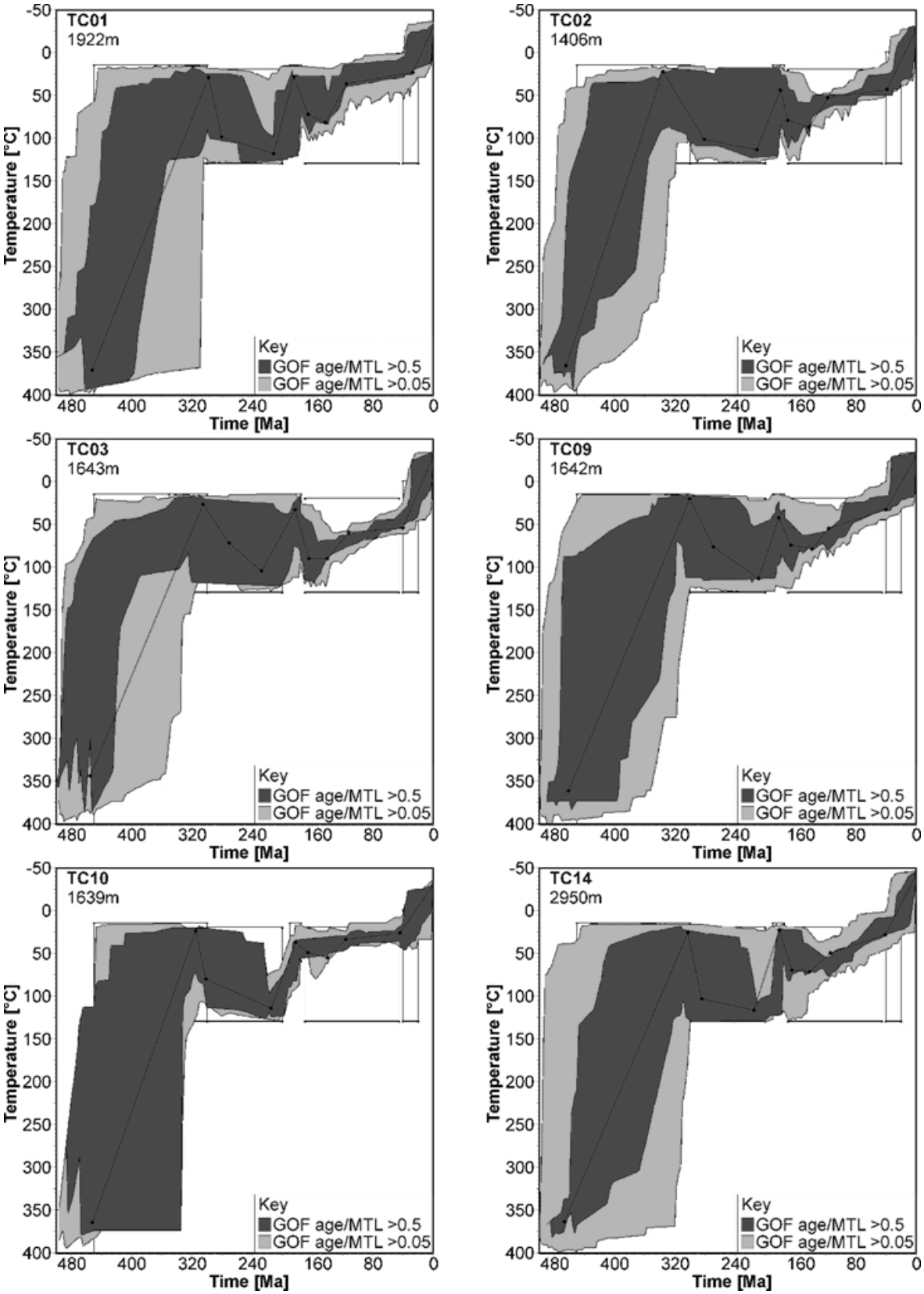

Figure S 8: Inverse thermal history modeling result.

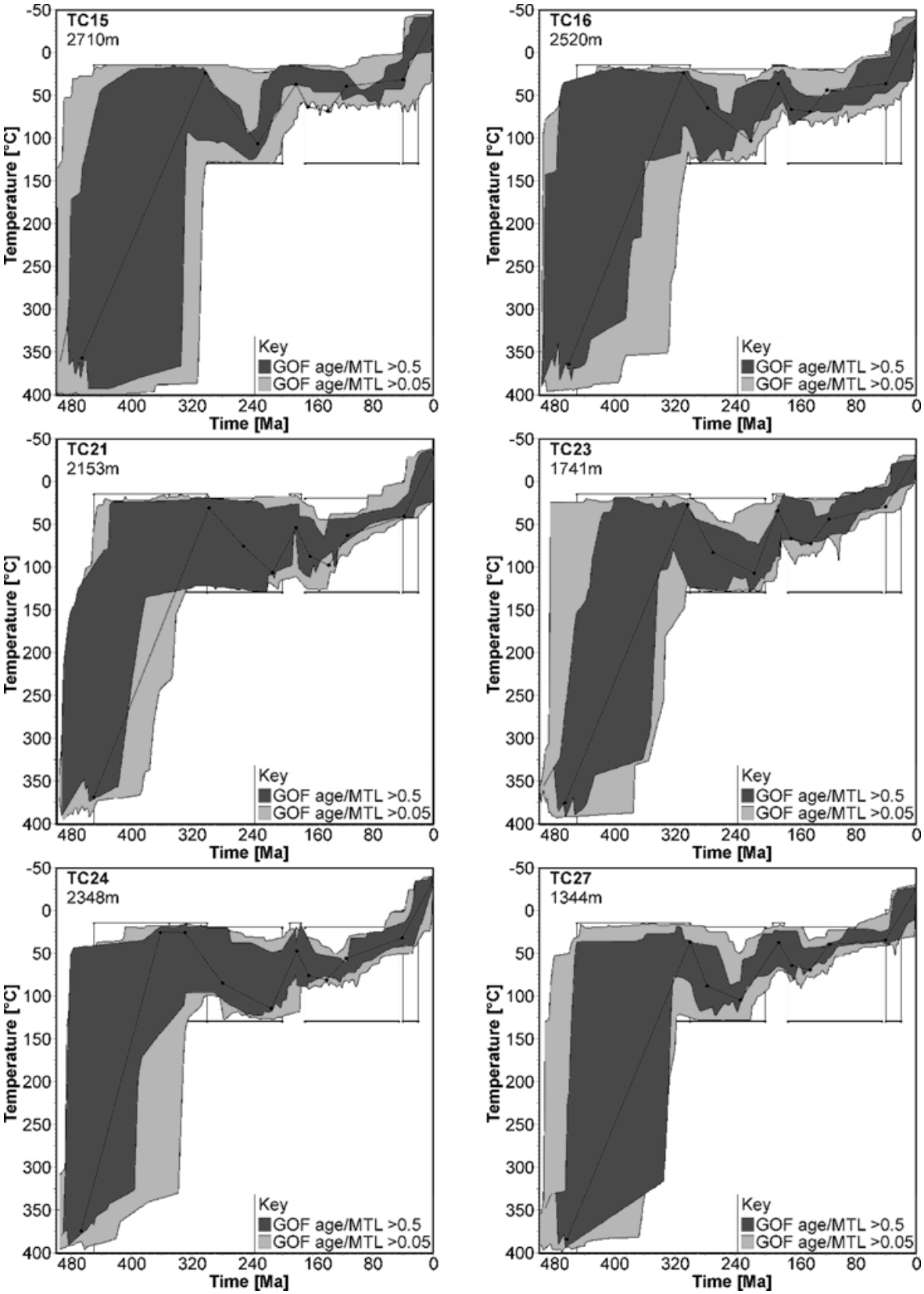

Figure S 8 (continued)

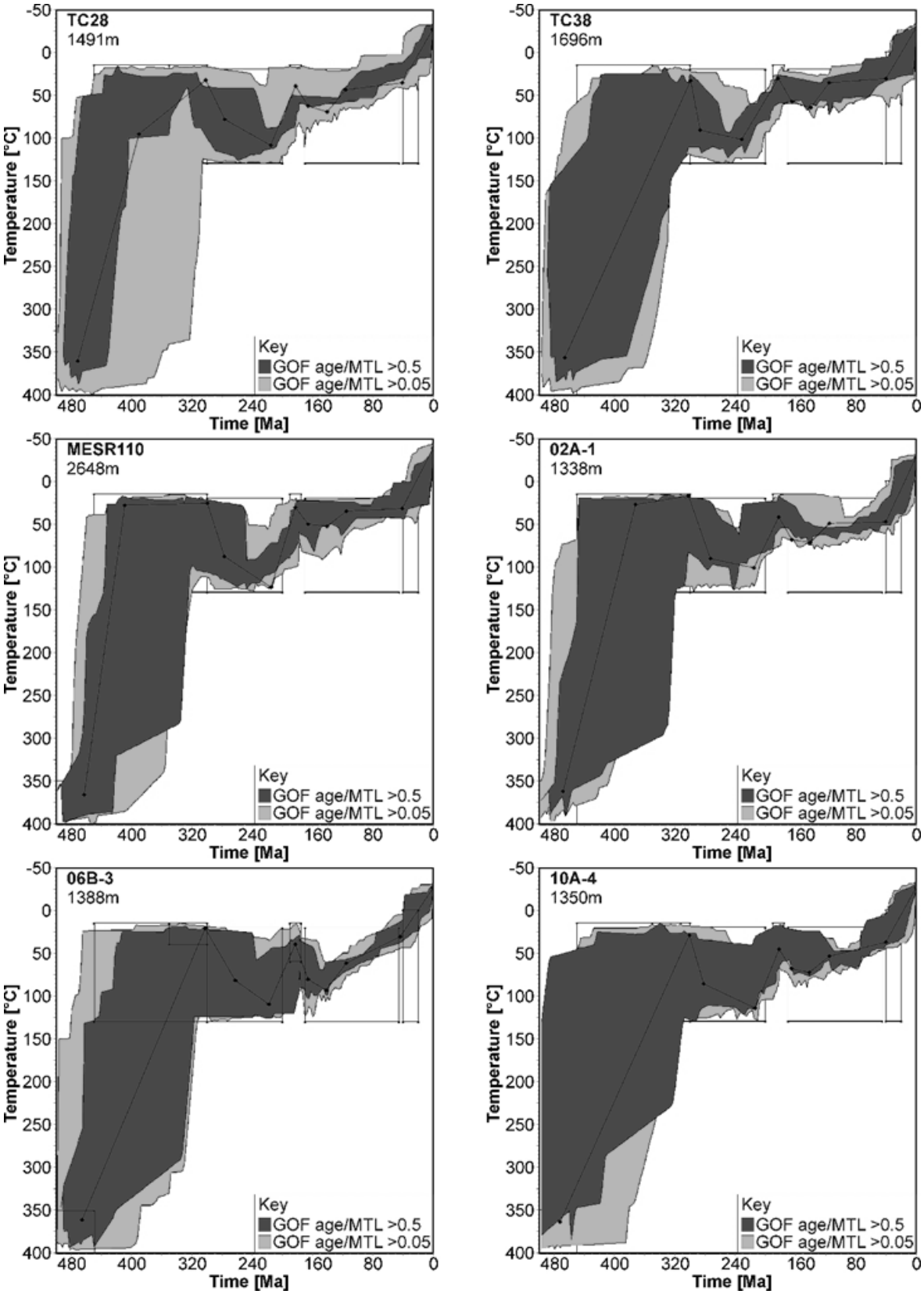

Figure S 8 (continued)

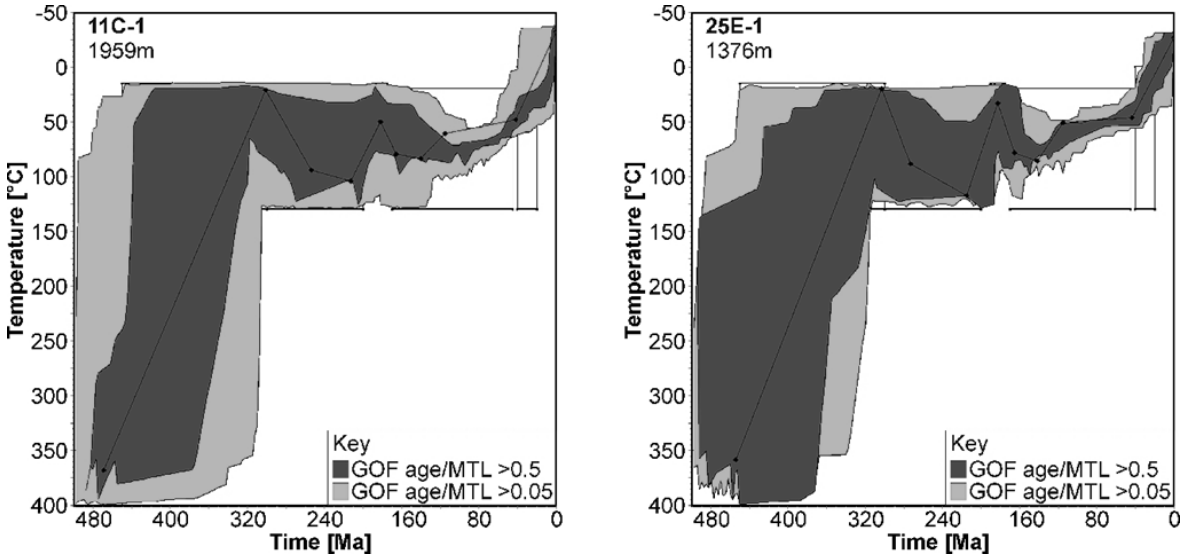

Figure S 8 (continued)

D. Supplementary Material for Chapter 6

D.1. Sample preparation

Samples collected varied in size between 1 and 3 kg, depending on their grain size. All samples were cut with a diamond-blade saw to remove any weathered rinds, and to obtain blocks that fit into the jaw crusher. The cleaned blocks were cleaned in an ultrasonic bath for 4-5 minutes and then dried at approximately 110ºC for 30 minutes. The material was put through a stainless steel jaw crusher, and a representative split was milled (using an agate swing mill) for approximately 1 hour to achieve the desired grain size of less than 2µm.

D.2. XRF analysis

Fused discs for major element analysis were made by melting the powered sample with a flux (66% lithiumtetraborate, 34% lithium metaborate), in a sample to flux ratio of 1:10, a platinum crucible at 1050ºC. The loss on ignition was determined by weighing before and after the melting process, and correcting for the amount of moisture lost from the flux. Pressed pellets for trace element analysis were made by mixing 9-10 grams of the powdered sample with 1 ml of binder (Mowiol). This mixture was pressed into a circular disc with a hydraulic press at a pressure of 5-6 tonnes and was held at this pressure for 30 seconds. These samples were left overnight to dry and then placed into the XRF machine for trace element analysis.

XRF analyses were performed with a Panalytical Axios sequential X-ray fluorescence spectrometer at the Discipline of Geological Sciences, SAEES, UKZN. Calibration lines for major element analyses were produced using both natural (USGS) and synthetic (WROXI) reference materials, spanning the full range of compositions encountered in the samples. Trace element analyses were calibrated against synthetic multi-element standards (Pro-Trace). Detection limits vary slightly according to the sample matrix, but are less than 50 ppm for the major oxides and 0.5-5 ppm for the trace elements.

Reference materials BCR-2 and JG-2 were analyzed with each batch of samples to check for accuracy (Table S 12 and Table S 13).

D.3. Whole rock trace element analysis LA fused disks

Additional to the suite of trace elements obtained by XRF analysis on pressed pellets, lower-abundance trace elements were analyzed by laser ablation inductively coupled plasma mass spectrometry of the fused disks used for XRF major element analysis at the Discipline of Geological Sciences, University of KwaZulu-Natal. Shards of the XRF disks were mounted in epoxy, together with shards from a blank disk (Li-meta/-tetraborate and anti-wetting agent

only) and from international standards (AGV-1, BCR-2, JG-2), prepared in the same way as the unknowns. NIST612 was used as a calibration standard–for some runs also in the form of a fused disk, and in others as the pure standard. No obvious difference was observed between the two approaches.

The analytical conditions for the laser and the ICP-MS are given in Table S 10. The flow of the carrier gas was adjusted to give a ThO^+/Th^+ ratio of 1%. Data reduction was done using the GLITTER software (van Achterbergh *et al.*, 2001), with the blank determined by analysing the blank disk for the fused disk samples, and a gas blank for the NIST612 standard. The NIST612 values of (Norman *et al.*, 1996) were used. Silicon was used as an internal standard, as determined by XRF analysis. The isotopes used and the counting time on each peak are given in Table S 11. Because of the high dilution factors of the fused disks (sample:flux ratio = 1:10) and the non-negligible blank for some elements, low level elements, such as the HREE with uneven atomic numbers, could not always be analyzed with a high level of precision. All samples were ablated 2-3 times and the data given are an average of the successful ablations. Table S 14 gives the average value and standard deviation for the BCR2 standard analyzed by this method.

D.4. Zircon trace element analysis LA

Zircon was ablated with a stationary beam and a 40 μm spot size, as far as possible in the same area as where the U-Pb and Lu-Hf ablations had been done. Standardisation was done against NIST612 glass, using Si as a normalising element. All zircons were assumed to contain 32.8 wt.% SiO_2. Zircon standard GJ (Elhlou *et al.*, 2006)was analyzed to check for accuracy and precision of the analyses (Table S 15).

Table S 10: Ablation and analysis parameters

LA	Trace elements WR	Trace elements zircon
Model	NWR UV-213	NWR UV-213
Wavelength	213 nm	213 nm
Repetition rate	20 Hz	10 Hz
Spot size	100 µm	40 µm
Analysis type	line scan, 10 µm/s	spot analysis
Energy density of sample	10 J cm^{-2}	6 J cm^{-2}
ICP-MS		
Model	Perkin-Elmer Nexion	Perkin-Elmer Nexion
Forward power	1500 W	1500 W
Plasma gas	Ar, 16l/min	Ar, 16l/min
Auxiliary gas	Ar, 1.375 l/min	Ar, 1.375 l/min
Carrier gas	Ar, 1.05-1.13 l/min	Ar, 1.05-1.13 l/min
Data acquisition		
Data acquisition protocol	Time-resolved analysis	Time-resolved analysis
Scanning mode	Peak hopping, 1 point per peak	Peak hopping, 1 point per peak
Detector mode	Dual detector	Dual detector
Time/scan	1.3 s	0.3 s
Data acquisition	ca. 106 s (65 s blank disk, 73 s sample)	ca. 60 s
Data reduction	GLITTER	GLITTER

Table S 11: Isotopes and counting times.

Element	isotope	counting time WR	counting time zircon
Si	29	30 ms	10 ms
Ca	43	30 ms	10 ms
Sc	45	30 ms	
Cr	53	30 ms	
Co	59	30 ms	
Ni	60	30 ms	
Rb	85	30 ms	
Sr	88	30 ms	
Y	89	30 ms	10 ms
Zr	90	30 ms	
Nb	93	30 ms	10 ms
Cs	133	30 ms	
Ba	137	30 ms	
La	139	30 ms	10 ms
Ce	140	30 ms	10 ms
Pr	141	30 ms	10 ms
Nd	146	30 ms	10 ms
Sm	147	30 ms	10 ms
Eu	153	60 ms	10 ms
Gd	157	60 ms	10 ms
Tb	159	60 ms	10 ms
Dy	163	60 ms	10 ms
Ho	165	60 ms	10 ms
Er	167	60 ms	10 ms
Tm	169	60 ms	10 ms
Yb	172	60 ms	10 ms
Lu	175	60 ms	10 ms
Hf	178	30 ms	10 ms
Ta	181	30 ms	10 ms
Pb	204		10 ms
Pb	206		10 ms
Pb	207		10 ms
Pb	208	30 ms	10 ms
Th	232	30 ms	10 ms
U	238	30 ms	10 ms

Table S 12: Major element concentrations standards by XRF of fused discs

Sample name	JG-2 (N=15)	1 sigma	BCR2 (N=15)	1 sigma
Majors XRF				
SiO2	76.68	0.117	53.67	0.207
TiO2	0.04	0.004	2.24	0.008
Al2O3	12.53	0.043	13.44	0.050
Fe2O3	0.99	0.007	13.76	0.057
Mn3O4	0.02	0.001	0.21	0.002
MgO	0.02	0.003	3.57	0.066
CaO	0.68	0.004	7.06	0.017
Na2O	3.57	0.138	3.22	0.131
K2O	4.89	0.020	1.82	0.013
P2O5	0.01	0.001	0.35	0.004

Table S 13: Trace element concentration standards by XRF of pressed pellets

Traces XRF	JG2 (N=14)	1 sigma	BCR2 (N=14)	1 sigma
Sc	3	0	30	2
V	3	0	429	3
Cr	4	1	18	2
Mn	134	4	1512	10
Co	7	2	36	3
Ni	4	1	13	2
Cu	4	1	20	2
Zn	11	1	134	2
Ga	19	1	24	1
Rb	303	1	50	1
Sr	16	0	349	1
Y	86	1	37	1
Zr	94	0	190	1
Nb	14	0	12	1
Mo	BDL		248	0
Ba	65	3	768	7
La	13	2	25	2
Ce	36	3	54	6
Nd	18	2	26	2
Hf	6	2	7	2
Pb	33	1	12	1
Th	32	1	7	1
U	7	1	3	1

Table S 14: Trace element concentrations standards by LA-ICPMS of fused discs

Traces LA ICPMS	BCR2 (N=13)	1 sigma
Rb	41.62	1.44
Sr	330.65	18.86
Y	37.67	1.72
Zr	187.52	9.93
Nb	11.67	0.92
Mo	234.97	9.98
Cs	0.92	0.15
Ba	627.80	48.92
La	27.19	1.36
Ce	53.57	2.65
Pr	6.91	0.39
Nd	31.02	1.72
Sm	7.03	0.86
Eu	1.94	0.17
Gd	7.21	0.58
Tb	1.09	0.09
Dy	7.21	0.42
Ho	1.45	0.11
Er	4.04	0.34
Tm	0.56	0.06
Yb	3.89	0.25
Lu	0.55	0.05
Hf	5.30	0.48
Ta	0.83	0.05
Pb	7.69	0.99
Th	6.55	0.45
U	1.50	0.29

Table S 15: Trace element analysis zircons by LA-ICPMS

Traces LA ICPMS	GJ zircon (N=18)	1 sigma
Ti	5.7	1.2
Y	257	29
Nb	2.4	0.6
La	0.03	0.03
Ce	15	1.7
Pr	0.05	0.03
Nd	0.61	0.17
Sm	1.4	0.3
Eu	0.84	0.17
Gd	6.5	1
Tb	1.8	0.24
Dy	20.6	3
Ho	7.1	0.8
Er	31.8	4.2
Tm	7	0.9
Yb	69	8
Lu	13.9	1.9
Hf	7554	1200
Ta	0.48	0.1
Pb204	0.15	0.06
Pb206	24.7	3
Pb207	1.55	0.20
Pb208	0.32	0.13
Th	10.2	1.35
U	263	41

D.5. Lu-Hf isotope analysis zircon

Lu-Hf isotope analyses were performed at the Department of Geosciences of Oslo University.

Masses 172 to 179 were measured simultaneously in Faraday collectors, using the Nu Plasma U-Pb collector block. Laser ablation conditions are: 55-60 µm static spot (aperture imaging mode), 5 Hz pulse frequency and ca. 2 J/cm^2 beam fluence. Each ablation was preceded by a 30 seconds on-mass background measurement. The total Hf signal obtained was in the range 1.5-4.0 V, and rarely as high as 6 V. Under these conditions, 120-150 seconds of ablation are required to obtain an internal precision of ≤ ±0.000020 (1SE).

Isotope ratios were calculated using the Nu Plasma time-resolved analysis software. The raw data were corrected for mass discrimination using an exponential law, and the mass discrimination factor for Hf (β_{Hf}) was determined assuming $^{179}Hf/^{177}Hf$= 0.7325 (Patchett & Tatsumoto, 1982).The invariant ratio $^{178}Hf/^{177}Hf$ was monitored during analytical sessions to monitor the quality of the data.

In order to obtain precise $^{176}Hf/^{177}Hf$ results, the isobaric interference from ^{176}Lu and ^{176}Yb on ^{176}Hf must be corrected. For a zircon with an average $^{176}Yb/^{177}Hf$ = 0.04, the total signal on mass 176 consists of about 87% ^{176}Hf, 13% ^{176}Yb and 0.2% ^{176}Lu, while for a REE-rich zircon

with $^{176}Yb/^{177}Hf$ = 0.25 the numbers will be 53%, 46.3% and 0.7% respectively. ^{176}Lu is calculated from the interference-free ^{175}Lu using $^{176}Lu/^{175}Lu$ = 0.02655 (Vervoort *et al.*, 2004) and f_{Hf}. ^{176}Yb is calculated from ^{172}Yb and the ratio $^{176}Yb/^{172}Yb$ = 0.58715 and the Yb mass discrimination factor (f_{Yb}). There are several possible Yb isotope ratios that can be used to calculate the f_{Yb} value; Yuan et al. (2008) Yuan *et al.* (2008)found that $^{173}Yb/^{171}Yb$ gave a better relative standard deviation for the calculated f_{Yb} than $^{173}Yb/^{172}Yb$ and $^{172}Yb/^{171}Yb$. The geometry of the Nu Plasma U-Pb collector block does not allow simultaneous measurement of mass 171 with the other masses of interest, therefore using the $^{173}Yb/^{171}Yb$ ratio for calculating f_{Yb} is not an option.

The mass discrimination factor *f* is defined by the expression $f = \frac{\log R_t / \log R_o}{\log(M_1 / M_2)}$, where R_t is a true, stable isotope ratio, R_o the corresponding observed value and M_1 and M_2 the masses of the isotopes ($M_1 > M_2$). In this expression, only R_o is subject to analytical error (s_{Ro}), and the resulting error in *f* (s_f) is given by: $s_f = \frac{s_{R_o}}{R_o \log(M_1 / M_2)}$. Assuming that two different stable isotope ratios of an element (R_1, R_2) can be measured with comparable internal precision, the ratio of uncertainties in mass discrimination factors calculated from the two pairs of isotopes will be given by $\frac{s_{f_1}}{s_{f_2}} = \frac{R_1}{R_2} \frac{\log(M_{1,2} / M_{2,2})}{\log(M_{1,1} / M_{2,1})}$, where isotopes with masses $M_{1,1}$ and $M_{2,1}$ are used to calculate f_1, and $M_{2,1}$ and $M_{2,2}$ to calculate f_2. An optimal value for *f* can therefore be determined from pairs of isotopes for which values of both *R* and M_1/M_2 are as high as possible.

Calculating f_{Yb} from the $^{174}Yb/^{172}Yb$ ratio gives an advantage in theoretical error of 75% compared to using the $^{173}Yb/^{172}Yb$ ratio, but is complicated by the isobaric overlap between ^{174}Yb and ^{174}Hf. For an average zircon the 174 mass will be 7% Hf and 93% Yb, and for the REE-rich case 1.4% Hf and 98.6% Yb. Stripping ^{174}Hf from ^{174}Yb is a much smaller correction than the ^{176}Hf isobaric correction. ^{174}Hf is calculated from the ratio $^{174}Hf/^{177}Hf$ = 0.008658 (Thirlwall & Anczkiewicz, 2004) and used for peak stripping ^{174}Yb before calculating f_{Yb} from $^{174}Yb/^{172}Yb$ = 1.46182.

The Yb isotope ratios used ($^{174}Yb/^{172}Yb$ = 1.46182 and $^{176}Yb/^{172}Yb$ = 0.58715) are in-house values. These values give the best fit for repeated runs of LV-11, which is a 10 mm euhedral crystal from the nepheline syenite pegmatite at Låven island in the Oslo Rift (290 Ma, source: Mineralogical collection of the Natural History Museum collection, University of Oslo). This crystal has a range of $^{176}Yb/^{177}Hf$ from 0.075 to 0.45 and solution analysis give a present-day $^{176}Hf/^{177}Hf$=0.282837±28 (Heinonen *et al.*, 2010a). A summary of the data obtained on standard zircons by the method outlines here is given in Table S 16.

The value for the decay constant of ^{176}Lu was taken as $1.867*10^{-11}$ a^{-1} (Söderlund *et al.*, 2004; Scherer *et al.*, 2007). The calculations of εHf were done using a present-day chondritic $^{176}Hf/^{177}Hf$ value of 0.282785 and $^{176}Lu/^{177}Hf$ of 0.0336 (Bouvier *et al.*, 2008)

Table S 16: Summary of zircon standards measured by laser ablation on the Oslo Nu MC-ICPMS, using the correction protocol described in the text, compared to solution data (Temora-2 and Mud Tank: Woodhead & Hergt, 2005)

	$^{176}Hf/^{177}Hf$	2SD	$^{178}Hf/^{177}Hf$	2SD	$^{176}Yb/^{177}Hf$	2SD	$^{176}Lu/^{177}Hf$	2SD	n	age	$^{176}Hf/^{177}Hf$ Solution
LV11	0.282836	0.000093	1.46725	0.00009	0.23	0.21	0.003	0.004	72	~290Ma	0.282837
Temora 2	0.282692	0.000070	1.46724	0.00005	0.058	0.043	0.0012	0.0008	28	418Ma	0.282686
Mud Tank	0.282511	0.000036	1.46726	0.00006	0.001	0.001	0.00002	0.00002	63	732Ma	0.282507

D.6. LA-MC-ICPMS U-Pb isotope analysis zircon

The analytical protocols presented by Rosa *et al.* (2009)and Andersen *et al.* (2009)were used for U-Pb geochronology of zircon, using the equipment at the Department of Geociences of the University of Oslo.

Mass number 204 was used as a monitor for common ^{204}Pb. In an ICPMS analysis, ^{204}Hg originating from the argon supply contaminates mass 204, giving a background counting-rate of ≤ 1000 cps. The contribution of ^{204}Hg from the plasma was eliminated by on-mass background measurement prior to each analysis. Analyses that yielded peak/background ratios at mass 204 of less than 1+3RSDB (where RSDB is the observed relative standard deviation of the on-peak background measurement) were considered to have common lead below the detection limit. At the low laser energy used, there was no observable increase in signal at mass 204 during ablation of reference zircons such as 91500 or GJ-1, which contain negligible common-lead. This suggests that there is insignificant excess ionization of ^{204}Hg from the gas supply during ablation, so that the on-mass background measurement is representative for the conditions during analysis. Where necessary, the observed signals at masses 206 and 207 were corrected for common ^{206}Pb and ^{207}Pb after integration of the signal, using observed ^{204}Pb and average common-lead composition given by the (Stacey & Kramers, 1975) global lead evolution curve at the uncorrected ^{206}Pb/^{238}U age.

Raw data from the mass spectrometer (converted to volts) were corrected for background, laser induced elemental fractionation, mass discrimination and drift in ion counter gains and reduced to U and ^{206}Pb concentrations and U-Pb isotope ratios by calibration to concordant reference zircons of known age, using protocols adapted from those of Jackson *et al.* (2004). The calculations were done off-line, using the in-house interactive spreadsheet NuAge.xlt.

Background-corrected signals for mass numbers 204, 206, 207 and 238 and the ^{207}Pb/^{206}Pb, ^{206}Pb/^{238}U and ^{207}Pb/^{235}U isotope ratios were plotted as traces of observed voltage and voltage ratios against ablation time. Time-intervals that were homogeneous in isotopic composition were interactively selected for integration, and calibrated against the corresponding time-interval for each mass in the reference zircon(s). To compensate for drift in instrument sensitivity and Faraday vs. electron multiplier gain during an analytical session, a linear correlation of signal vs. time was assumed for the reference zircons.

All isochrons and concordance ages were calculated using the program Isoplot (Ludwig, 2008), version 3.71 - r5.

During the analytical sessions, the reference zircon Plesovice (337.1 ± 0.4 Ma, Slama et al., 2008) as well as the in-hourse zircon standard C, with a concordant solution TIMS age of 553

± 0.4 Ma were analysed on a regular basis. The result for the Plesovice zircon gave a concordant age of 340 ± 1 Ma.

D.7. SHRIMP Th-U-Pb isotope analysis zircon

Zircon grains were separated from crushed rock samples by conventional magnetic and methylene iodide liquid separation. Grains were handpicked and mounted in epoxy resin discs that were coated with a thin membrane of gold that produced a resistivity of 10-20 Ω across the disc. The mounts were then imaged using a CL detector fitted to a Phillips XL30 scanning electron microscope at a working distance of 15 mm and using an accelerating voltage of 10 kV. The resulting images highlight distortions in the crystal lattice that are related to trace-element distribution and/or radiation damage (e.g. Rubatto & Gebauer, 2000; Nasdala *et al.*, 2003).

Zircon U-Th-Pb isotopic data were collected using the Sensitive High Resolution Ion Microprobe Mass Spectrometer (SHRIMP II) based in the John de Laeter Centre of Mass Spectrometry, Perth, Western Australia. The sensitivity for Pb isotopes in zircon using SHRIMP II was 18 cps/ppm/nA, the primary beam current was 2.5-3.0 nA and mass resolution was 5000.

Correction of measured isotopic ratios for common Pb was based on the measured ^{204}Pb in each sample and often represented a <1% correction to the ^{206}Pb counts (see % common ^{206}Pb in Electronic Appendix 2, available online). The common Pb component, being largely surface contaminant, was modelled on the composition of Broken Hill ore Pb.

Pb/U isotopic ratios were corrected for instrumental inter-element discrimination using the observed covariation between Pb+/U+ and UO+/U+ (Hinthorne *et al.*, 1979; Compston *et al.*, 1984) determined from interspersed analyses of the Perth standard zircon BR266. BR266 is a single zircon megacryst from Sri Lanka with an age of 559 ± 0.3 Ma, a 206Pb/238U = 0.09059, U and Th contents of 909 and 201 respectively (Stern, 2001).

D.8. Solution analysis trace elements, Sr and Nd isotopes

Solution analysis for trace elements and Sr and Nd isotopes were done at the Department of Geological Sciences of the University of Cape Town.

Approximately 50 mg of sample was dissolved in 2 ml of a 4:1 mixture of concentrated HF and HNO_3 in capped Teflon beakers, held at 140 °C for 48 hours. After drydown, the samples were converted to nitrate, by adding 2 ml of concentrated HNO3, and drying down again. This step was repeated once. The sample was taken up in 3 ml of 5% HNO_3, and approximately 10% was kept for trace element analyses, and the rest for isotope analysis.

Trace element analyses were performed on 5000x dilute 2% HNO_3 solutions, using a Thermo-Fisher X-Series 2 Q-ICPMS, tuned to minimise oxide production ($CeO^+/Ce < 5\%$) and doubly-charged species ($Ba^{2+}/Ba^+ < 1\%$). Calibration was performed using four solution standards. Analyses were performed in peak hopping mode, and counts for each isotope were integrated for 10 ms per sweep, with a 2 ms settling time. Each analysis consisted of 3 repeats of 100 sweeps each across the analysed mass range. An international powdered rock standard, JG-2, was dissolved and analysed in the same batch as the unknowns, and the results are given in Table S 17.

Table S 17: Data for the JG-2 standard analysed. The 2 sigma refers to the internal reproducibility.

	JG-2 measured	2 σ	JG-2 literature	JG2 literature 2σ
7Li	40.9	0.71	40.40	4.70
45Sc	1.63	0.06		
51V	0.62	0.01	3.00	
52Cr	2.78	0.03	6.00	4.00
59Co	3.77	0.08	4.30	0.10
60Ni	1.86	0.00		
65Cu	1.11	0.01	0.50	0.20
66Zn	11.7	0.28	12.30	1.10
85Rb	282	1.34	292.00	26.00
88Sr	15.0	0.22	16.40	1.10
89Y	59.2	0.66	88.00	21.00
90Zr	67.5	0.69	99.00	31.00
93Nb	12.3	0.07	16.10	3.40
137Ba	53.7	0.49	61.00	12.00
139La	17.6	0.21	19.10	1.70
140Ce	43.5	0.25	48.00	4.00
141Pr	5.50	0.09	6.30	0.90
144Nd	22.6	0.41	26.20	4.80
152Sm	6.86	0.07	8.30	2.00
153Eu	0.09	0.00	0.09	0.02
159Tb	1.42	0.01	1.65	0.22
160Gd	7.82	0.07	8.90	2.40
163Dy	9.64	0.05	11.10	1.40
165Ho	2.01	0.01	2.20	1.10
166Er	6.12	0.09	6.70	2.60
169Tm	0.89	0.04	1.01	0.44
174Yb	6.19	0.11	7.50	1.00
175Lu	0.89	0.04	1.25	0.20
178Hf	3.31	0.10	5.00	1.90
181Ta	1.92	0.01	2.00	0.50
208Pb	29.1	0.34	29.60	6.30
232Th	25.9	0.19	29.63	5.00
238U	8.36	0.04	10.70	2.50

Isolation of Sr and Nd for isotope analysis was done following the procedures described by

Mikova & Denkova (2007), adapted from Pin & Zalduegui (1997). The isotope ratio analyses were performed on a Nu Instruments NuPlasma HR multi-collector ICP-MS. Sr was analysed as a 200 ppb 0.2% HNO_3 solution. All isotopic mass discrimination, including that for Rb, was corrected using the exponential law and a $^{86}Sr/^{88}Sr$ ratio of 0.1194. Isobaric interference of ^{87}Rb on ^{87}Sr was corrected for by monitoring the signal of ^{85}Rb, and using the natural $^{87}Rb/^{85}Rb$ ratio. All runs consisted of 60 individual, 7 second readings. Analyses of reference material SRM987 bracketed sets of analyses of 5 unknowns, which were then normalised to a $^{87}Sr/^{86}Sr$ value of 0.710255 for these bracketing reference analyses. There are no published $^{87}Sr/^{86}Sr$ values from the GeoReM database (Jochum *et al.*, 2005) for international standard granite JG-2 (Japanese Geological Survey) which analysed with these unknowns gave a value of 0.759343 ± 18 (2σ). This value contrasts with the value of 0.758159±4 reported by (Ma *et al.*, 2013), indicating the probable inhomogeneous Sr isotope composition of JG-2 and explaining the absence of a reference $^{87}Sr/^{86}Sr$ value in the GeoReM database.

Nd was analysed as a 50 ppb 2% HNO_3 solution, with a DSN-100 desolvating nebuliser as an introduction system. Instrumental mass discrimination of all isotope ratios was corrected using the exponential law and a $^{146}Nd/^{144}Nd$ ratio of 0.7219. Isobaric interferences from Sm and Ce on all Nd isotopes were corrected by monitoring ^{140}Ce and ^{147}Sm, and using their natural isotope ratios. All runs consisted of 45 individual 7 second readings. As for Sr isotope analyses above, all measured $^{143}Nd/^{144}Nd$ ratios of unknowns were normalised to a value of 0.512115 for bracketing analyses of standard JNdi-1 (Tanaka *et al.*, 2000). Reference material JG-2, measured at the same time as the unknowns, gave a $^{143}Nd/^{144}Nd$ value of 0.512221 ± 9 (2σ), which compares well with published values from the GeoReM database (Jochum *et al.*, 2005).

For calculation of the εNd ratio, the $^{143}Nd/^{144}Nd$ ratio of CHUR was taken as 0.512638, and its $^{147}Sm/^{144}Nd$ ratio as 0.1967. The depleted mantle extraction age was calculated using a $^{143}Nd/^{144}Nd$ ratio of 0.513114, and its $^{147}Sm/^{144}Nd$ ratio as 0.222.

The $^{147}Sm/^{144}Nd$ and $^{87}Rb/^{86}Sr$ ratios were calculated from the trace element concentration analyses, and their uncertainty was calculated from the uncertainty on the concentrations using the quadrature rule. The uncertainty on these ratios and on the actual $^{143}Nd/^{144}Nd$ and $^{87}Sr/^{86}Sr$ values was taken into account when calculating the uncertainty on the initial ratio.

E. Supplementary Material

Table S 18: Apatite Fission Track Results

Sample / Location	Elev. [m] Lithology	N_D ρ_D *	N_s ρ_s *	N_i ρ_i *	$P(\chi^2)$ [%]	Age ± 1σ [Ma] N_G	MTL ± 1σ [µm] SD [µm]	N_L	D_{par} ± 1σ [µm] SD	U [ppm]
TC_33	2038	8380	109	218	100	138±17	12.32±0.15	80	1.57±0.02	18.56
Brattnipene		16.83				19	1.52		0.18	
TC_47	1213	8182	236	5.07	97	126±10	10.46±0.14	78	1.85±0.02	8.43
Vesthaugen	Granodiorite	1.643	4.23	9.09		21	2.69		0.12	

Table S 19: AHe Results

Sample	R_s	mass [mg]	^{4}He [ncc]	$^{238+235}$U [ppm]	^{232}Th [ppm]	^{147}Sm [ppm]	eU [ppm]	uncorr. Age [Ma]	SD [Ma]	F_T-factor	corrected Age [Ma]	SD [Ma]
TC46 #1	99.58	0.009	4.758	10.990	50.409	50.940	123.553	176.36	10.93	0.834	211.39	24.87
TC46 #2	60.30	0.003	0.699	7.568	25.762	20.686	65.088	120.67	7.48	0.711	169.65	19.96
TC46 #3	111.62	0.025	8.923	7.627	35.912	34.228	87.817	175.49	10.88	0.858	204.50	24.06
TC46 #4	76.56	0.007	2.419	8.942	28.137	39.915	71.784	180.61	11.20	0.791	228.39	26.87
TC47 #1	98.73	0.013	1.833	6.903	30.538	36.404	75.102	80.25	4.98	0.831	96.5	11.4
TC47 #2	133.49	0.022	4.798	8.514	39.238	38.813	96.131	99.23	6.15	0.876	113.3	13.3
TC47 #3	81.85	0.008	0.855	7.069	26.059	36.197	65.268	67.93	4.21	0.798	85.2	10.0

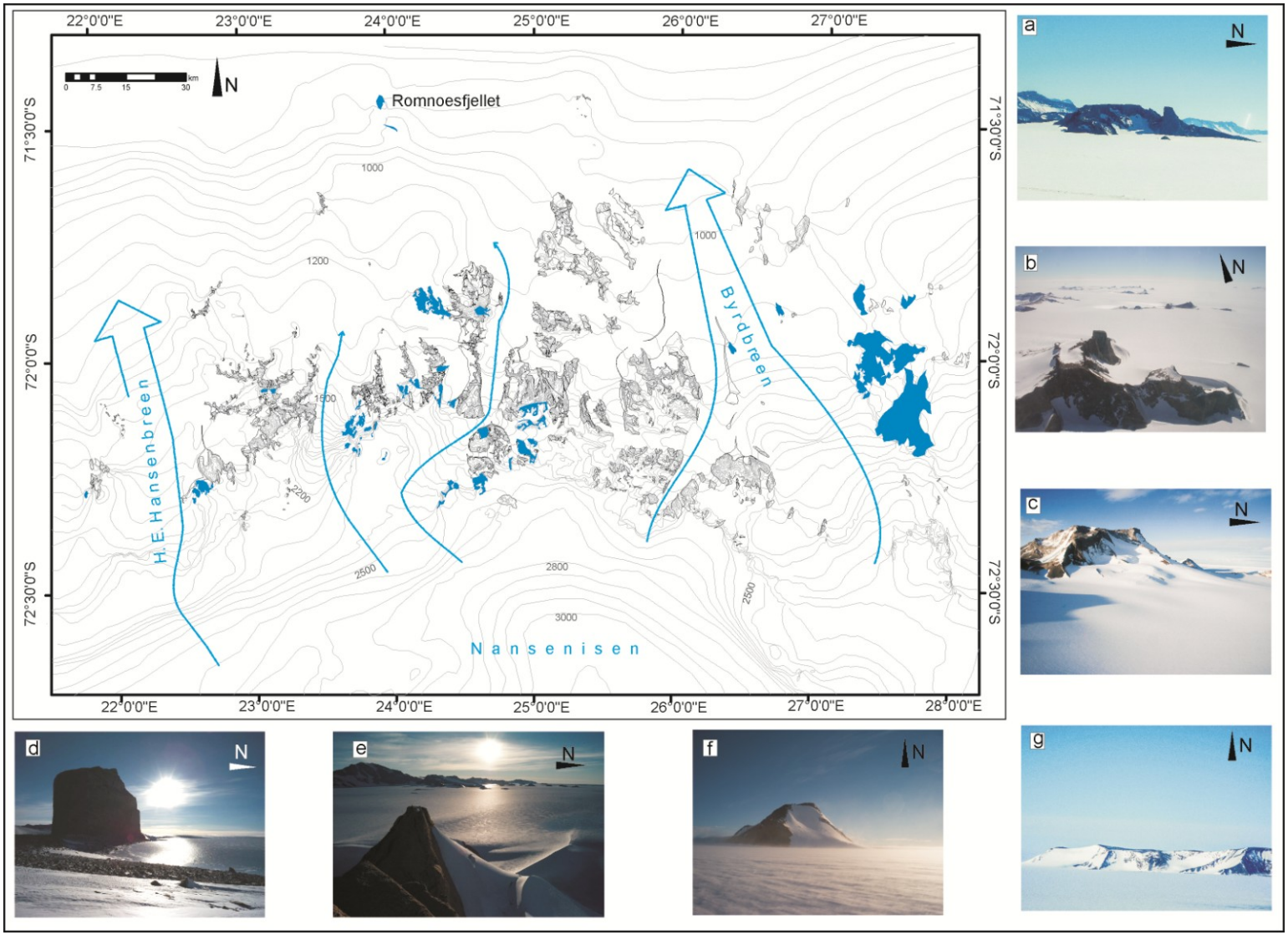

Figure S 9: Detailed geomorphological map of Sør Rondane. Blue areas indicating sides of flat topped surfaces (van Autenboer, 1964; van Autenboer & Decleir, 1978; Pattyn *et al.*, 1992). Arrows illustrate the direction of major ice discharge. Photographs a-g showing the different manifestations of the flat surfaces, occurring throughout the area. Picture d) was taken by René Robert.

Table S 20: Sample List Sør Rondane

Prefix	Sample No.	Outcrop_Name	Profile	Coordinates [dd°mm.mmm´]		ALT	Lithology
				Latitude [S]	Longitude [E]	[m]	
1126A	TC_01	Widerøefjellet	VA	72°07.126 S	23°11.575 E	1922	Granodiorite
1129A	TC_02	Ketelersbreen	Horizontal	72°03.122 S	23°19.006 E	1406	Grt-Bt-Amph-Gneiss
1130A	TC_03	Gunnestadbreen	Horizontal	72°04.553 S	23°25.727 E	1643	Bt-Amph-Gneiss (Grey Gneiss)
1202A1	TC_05	Smalegga	Horizontal	72°05.566 S	23°52.321 E	1702	Granodiorite
1202A2	TC_06	Smalegga	Horizontal	72°05.412 S	23°50.846 E	1752	Granodiorite
1202B1	TC_07	Smalegga	Horizontal	71°59.992 S	23°53.679 E	1392	Bt-Amph-Gneiss (Grey Gneiss)
1203C	TC_08	Yobuko Valley	Horizontal	72°04.700 S	23°49.037 E	1585	Mylonite, Protolith Granodiorite
1204A	TC_09	Tanngarden	Horizontal	72°02.218 S	22°50.965 E	1642	Bt-Amph-Gneiss (Grey Gneiss)
1204C	TC_10	Tanngarden	Horizontal	72°01.273 S	22°47.083 E	1639	Bt-Amph-Gneiss, contact with pegmatite
1204E	TC_11	Tanngarden	Horizontal	72°01.888 S	22°56.441 E	1545	Bt-Amph-Gneiss, fg-mg
1205A	TC_12	Ketelersbreen	Horizontal	72°05.863 S	23°11.040 E	1920	Granite (Vengen)
1208A	TC_13	Widerøefjellet	VA	72°09.500 S	23°12.600 E	3120	Granodiorite, cg
1208B	TC_14	Widerøefjellet	VA	72°9.389 S	23°12.071 E	2950	Granodiroite
1208C	TC_15	Widerøefjellet	VA	72°09.285 S	23°10.307 E	2710	Tonalite
1208D	TC_16	Widerøefjellet	VA	72°08.850 S	23°09.178 E	2520	Granodiorite
1208E	TC_17	Widerøefjellet	VA	72°08.587 S	23°08.815 E	2390	Amphbolilte
1208F	TC_18	Widerøefjellet	VA	72°08.339 S	23°08.273 E	2200	Granodiorite
1213A	TC_19	Widerøefjellet	VA	72°07.940 S	23°10.555 E	2257	Granodiorite/Tonalite
1213B	TC_20	Widerøefjellet	VA	72°07.773 S	23°10.523 E	2100	Granodiorite
1213C	TC_21	Vikinghøgda	VB	72°04.096 S	23°04.899 E	2153	Gneiss
1213D	TC_22	Vikinghøgda	VB	72°03.897 S	23°10.651 E	1816	Gneiss
1213E	TC_23	Vikinghøgda	VB	72°03.388 S	23°05.160 E	1741	Gneiss
1213F	TC_24	Vikinghøgda	VB	72°04.033 S	23°06.227 E	2348	Gneiss
1214A	TC_25	Bratnipane	VC	71°53.252 S	24°13.227 E	1549	Bt-Amph -Shist
1214B	TC_26	Bratnipane	VC	71°53.668 S	24°13.210 E	1589	Gneiss
1214C	TC_27	Vikinghøgda	VB	72°03.078 S	23°12.481 E	1344	Gneiss
1214D	TC_28	Vikinghøgda	VB	72°03.497 S	23°08.339 E	1491	Gneiss

Table S 20 (continued)

Prefix	Sample No.	Outcrop_Name	Profile	Coordinates [dd°mm.mmm´]		ALT	Lithology
				Latitude [S]	Longitude [E]	[m]	
1216A	TC_29	Bratnipane	VC	71°55.246 S	24°36.163 E	2244	Gneiss
1216B	TC_30	Bratnipane	VC	71°55.434 S	24°37.733 E	2354	Gneiss
1216C	TC_31	Bratnipane	VC	71°55.972 S	24°21.612 E	1318	Gneiss
1216D	TC_32	Bratnipane	VC	71°55.748 S	24°34.325 E	1864	Gneiss
1216E	TC_33	Bratnipane	VC	71°55.702 S	24°35.252 E	2038	Gneiss
1217A	TC_34	Lunckeryggen	Horizontal	72°01.981 S	24°35.857 E	1350	Syenite
1217B	TC_35	Ellisbreen ShearZone	Horizontal	72°03.197 S	24°17.982 E	1794	Mylonite
1219A	TC_36	Svindlandfjellet	Horizontal	72°05.746 S	23°44.082 E	1499	Granodiorite
1219B	TC_37	Verheyefjellet	Horizontal	72°12.155 S	23°41.808 E	2194	Granodiorite
1219D	TC_38	Nils-Larssenfjellet	Horizontal	72°12.558 S	22°43.585 E	1696	Tonalite/Granodiorite
1219E	TC_39	Nils-Larssenfjellet	Horizontal	72°16.336 S	22°36.543 E	1721	Tonalite/Granodiorite
1221A	TC_40	Dufekfjellet	VD	72°12.006 S	24°41.117 E	2993	Amphibolite
1221B	TC_41	Dufekfjellet	VD	72°11.693 S	24°40.338 E	2728	Granite
1221C	TC_42	Dufekfjellet	VD	72°11.645 S	24°39.201 E	2560	Granite
1221D	TC_43	Dufekfjellet	VD	72°10.576 S	24°38.456 E	2358	Granite
1221E	TC_44	Dufekfjellet	VD	72°10.278 S	24°37.791 E	2152	Granite
1221F	TC_45	Dufekfjellet	VD	72°10.052 S	24°38.512 E	1756	Granite
1221G	TC_46	Dufekfjellet	VD	72°10.077 S	24°46.149 E	1846	Granite
1223A	TC_47	Vesthaugen	Horizontal	71°41.607 S	23°33.582 E	1213	Granodiorite
1224A	TC_48	Mefjellet	Horizontal	72°02.697 S	25°02.787 E	1221	Granite
1224B	TC_49	Mefjellet	Horizontal	72°04.731 S	25°07.894 E	1924	Granite
1225C	TC_50	Yobuko Valley Süd	Horizontal	72°05.610 S	23°49.810 E	1943	Tonalite
1221C	MESR 110	Nunatak furthest south (Caussinknappen?)		72°20.263 S	23°13.490 E	2648	Tonalite
-	J1210C	Lågkollane	Horizontal	72°09.307 S	22°06.968 E	1674	Tonalite
-	J1210D	Lågkollane	Horizontal	72°08.596 S	22°06.306 E	1687	Gneiss
-	J1211A_1	Langekletten	Horizontal	72°24.376 S	20°55.215 E	2190	Garnet Shist
-	J1211B_1	Bergekongen	Horizontal	72°21.511 S	19°17.300 E	2262	Gneiss

Table S 20 (continued)

Prefix	Sample No.	Outcrop_Name	Profile	Coordinates [dd°mm.mmm´]		ALT	Lithology
				Latitude [S]	Longitude [E]	[m]	
-	J1211B_2	Bergekongen	Horizontal	72°21.490 S	19°17.330 E	2260	Gneiss
-	J1212A	Tonyknausane	Horizontal	72°12.846 S	20°11.878 E	1988	Gneiss
-	J1212B	Tonyknausane	Horizontal	72°12.757 S	20°11.097 E	1923	Gneiss
-	J1212C	Tonyknausane	Horizontal	72°12.756 S	20°10.966 E	1756	Gneiss
-	J1212E	Knøtten	Horizontal	72°09.003 S	20°19.265 E	1623	Granodiorite
-	J1212F_1	Vesalkletten	Horizontal	72°29.730 S	20°44.990 E	2390	Granodiorite (?)
-	J1213A	Taggen	Horizontal	72°08.996 S	21°18.382 E	1825	Tonalite
-	J1213B	Grandfluga	Horizontal	72°21.055 S	19°23.054 E	2164	Gneiss
-	J1213C	Bergtussen	Horizontal	72°20.252 S	19°28.338 E	2192	Gneiss
-	J1213D	van Autenboerfjellet	Horizontal	72°21.779 S	20°14.683 E	2135	Granitoide
-	J1213E_1	Taggen	Horizontal	72°08.116 S	21°35.808 E	1544	Greenschist
-	J1214A_2	Tertene	Horizontal	72°08.708 S	21°36.534 E	1550	Granitoide
-	J1214B	Tertene	Horizontal	72°17.081 S	21°26.114 E	1862	Granite
-	J1214C	Tertene NE	Horizontal	72°14.491 S	21°30.583 E	1695	Granitoide
-	J1214D	Tertene S	Horizontal	72°18.380 S	21°26.750 E	1864	Gneiss
-	J1214E	Høgekletten	Horizontal	72°27.713 S	20°44.882 E	2225	Gneiss
GEA I							
	02A-1	Ketelersbreen (E)	Horizontal	71°59.321 S	23°15.94 E	1338	
	06B-3	Perlebrandet (N-Tip)	Horizontal	71°52.858 S	22°44.873 E	1388	
	07A-1	Gunnestadbreen (E)	Horizontal	72°04.605 S	23°43.742 E	1400	
	10A-3	Teltet	Horizontal	71°59.417 S	23°29.655 E	1350	
	10A-4	Teltet	Horizontal				
	11B-6	Ketelersbreen (SW)	-	72°5.891 S	23°12.341 E	1498	
	11B-9	Ketelersbreen (SW)	-				
	11C-1	Ketelersbreen (SW)	-	72°5.482 S	23°10.445 E	1959	
	11C-3	Ketelersbreen (SW)	-				
	12B-3	East Widerøfjellet	Horizontal	72°7.055 S	23°28.230 E	1607	
	12B-4	East Widerøfjellet	Horizontal				

Table S 20 (continued)

Prefix	Sample No.	Outcrop_Name	Profile	Coordinates [dd°mm.mmm´]		ALT [m]	Lithology
	22A-1	Smalegga	-	72°4.625 S	23°48.413 E		
	26D-2	Duboisbreen (S)	-				
	28B-2	Gunnestadbreen (W)	Horizontal	72°2.275 S	23°7.112 E	1469	
	24B-1	Duboisbreen (NW)	Horizontal	71°59.580 S	23°11.042 E	1377	
	25E 1	Duboisbreen (NW)	Horizontal	71°59.908 S	23°14.218 E	1376	

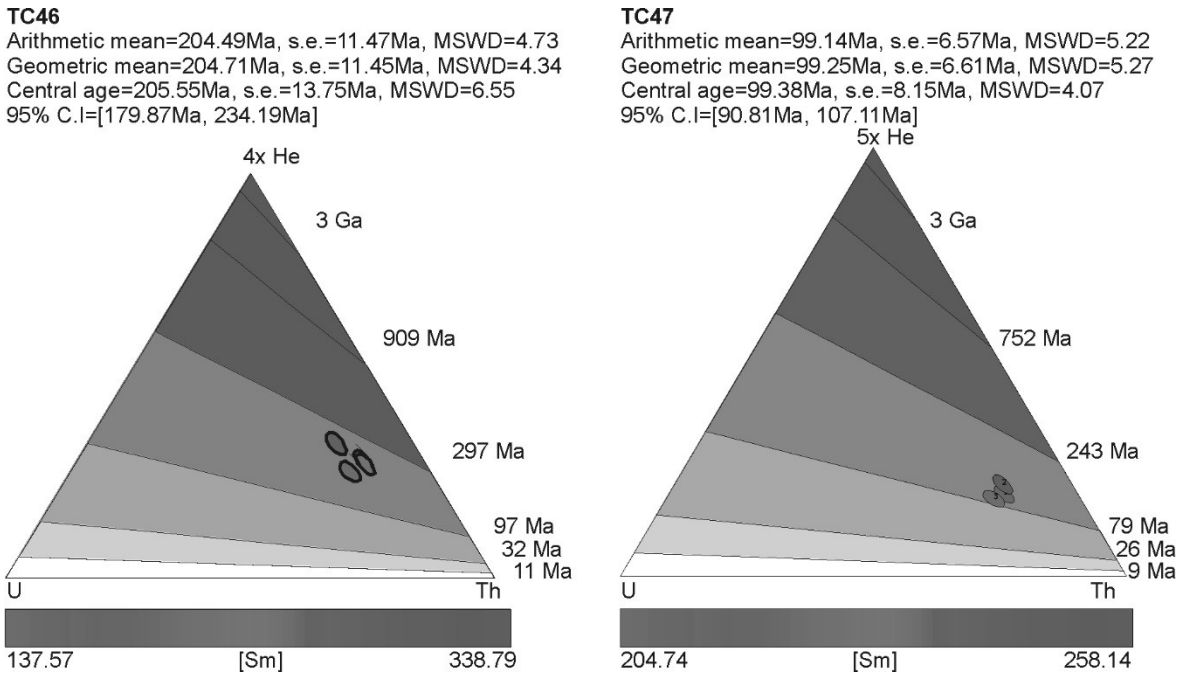

Figure S 10: U-Th-He ternary diagrams and age estimations. Ellipses illustrate the 2σ error. The diagrams were created using HelioPlot (Vermeesch, 2010).

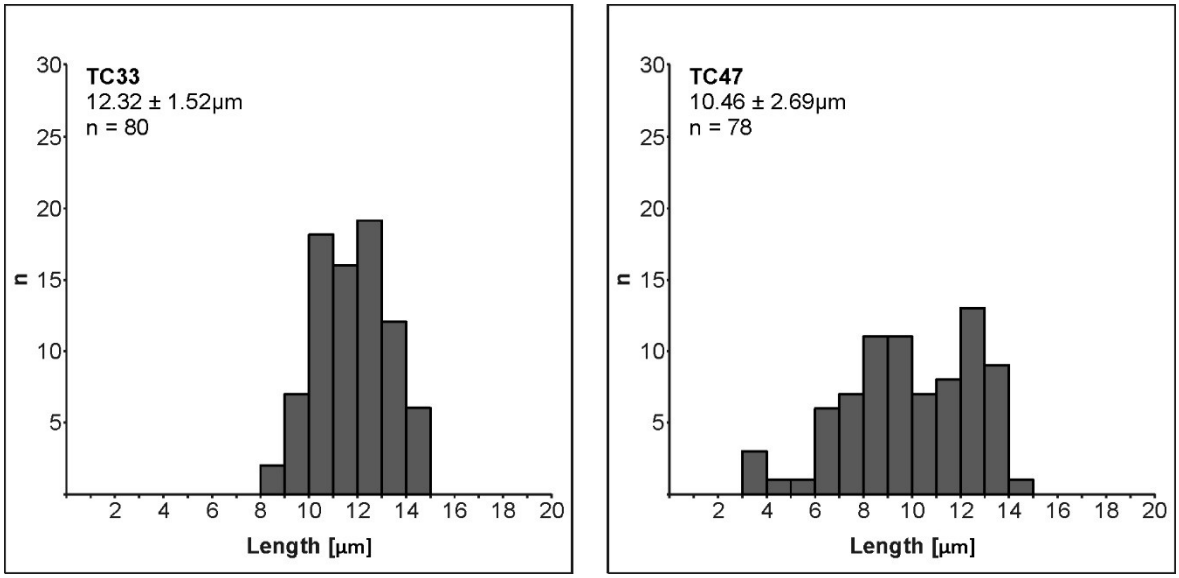

Figure S 11: Track length histograms of the individual samples TC33 and TC47. Note that the lengths are not c-axis projected.

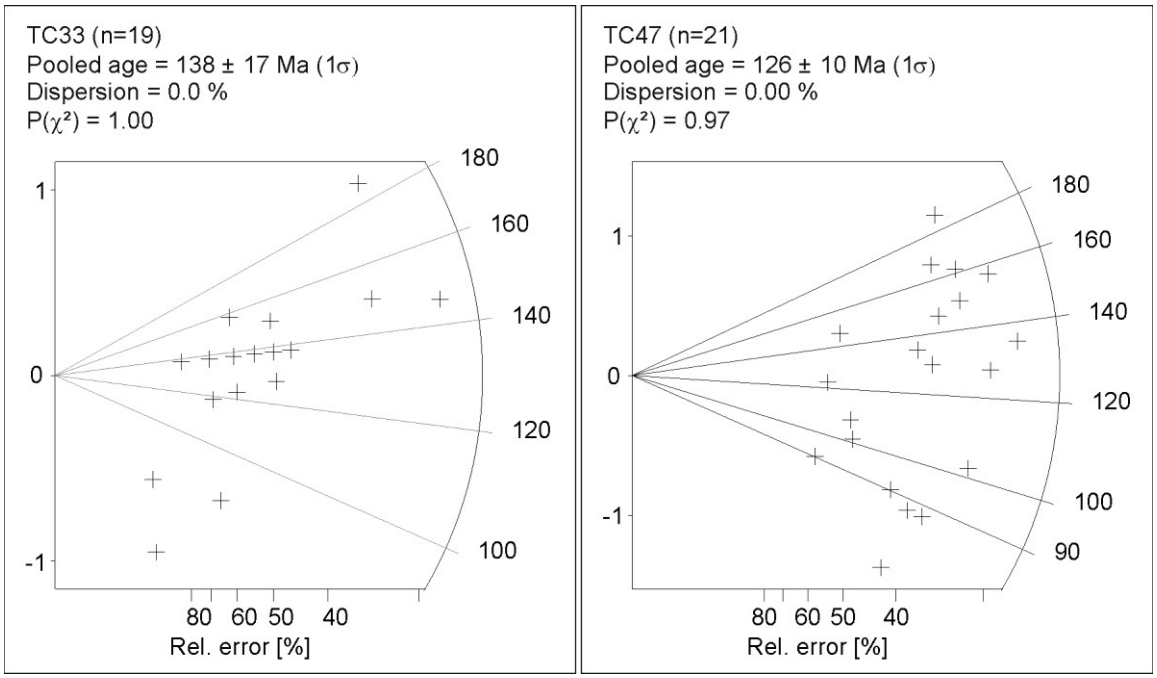

Figure S 12: Radial plots of the fission track samples TC 33 and TC47. Plots were created using TRACKKEY (Dunkl, 2002).

Erklärung

Hiermit versichere ich, dass ich

(I) die Arbeit ohne unerlaubte fremde Hilfe angefertigt habe,

(II) keine anderen als die von mir angegebenen Quellen und Hilfsmittel benutzt habe und

(III) die den benutzten Werken wörtliche oder inhaltlich entnommene Stellen als solche kenntlich gemacht habe.

Darüber hinaus erkläre ich hiermit, dass ich mich weder zuvor einem Promotionsverfahren unterzogen habe, noch ein solches beantragt habe.

Bremen, den 16.05.2017